SMSI 2021

Sensor and Measurement Science International

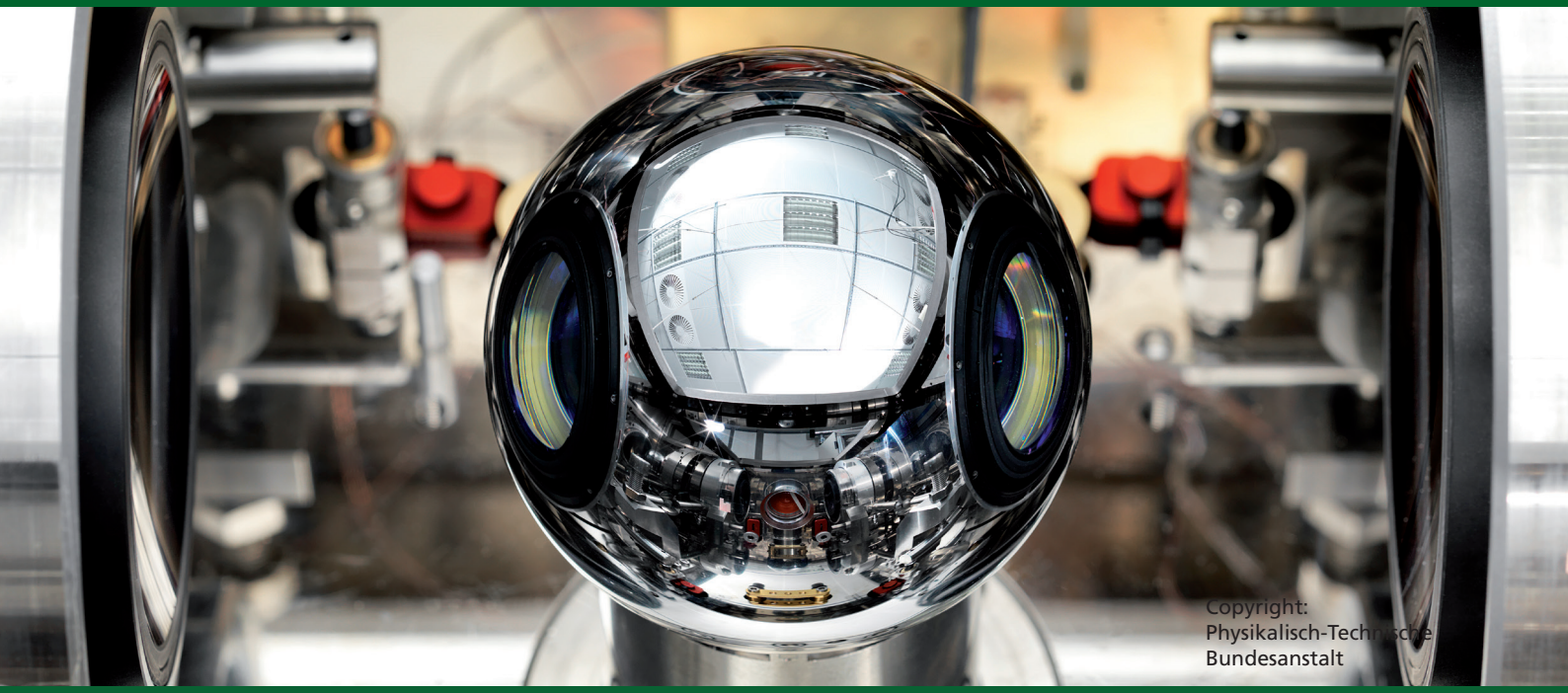

Proceedings

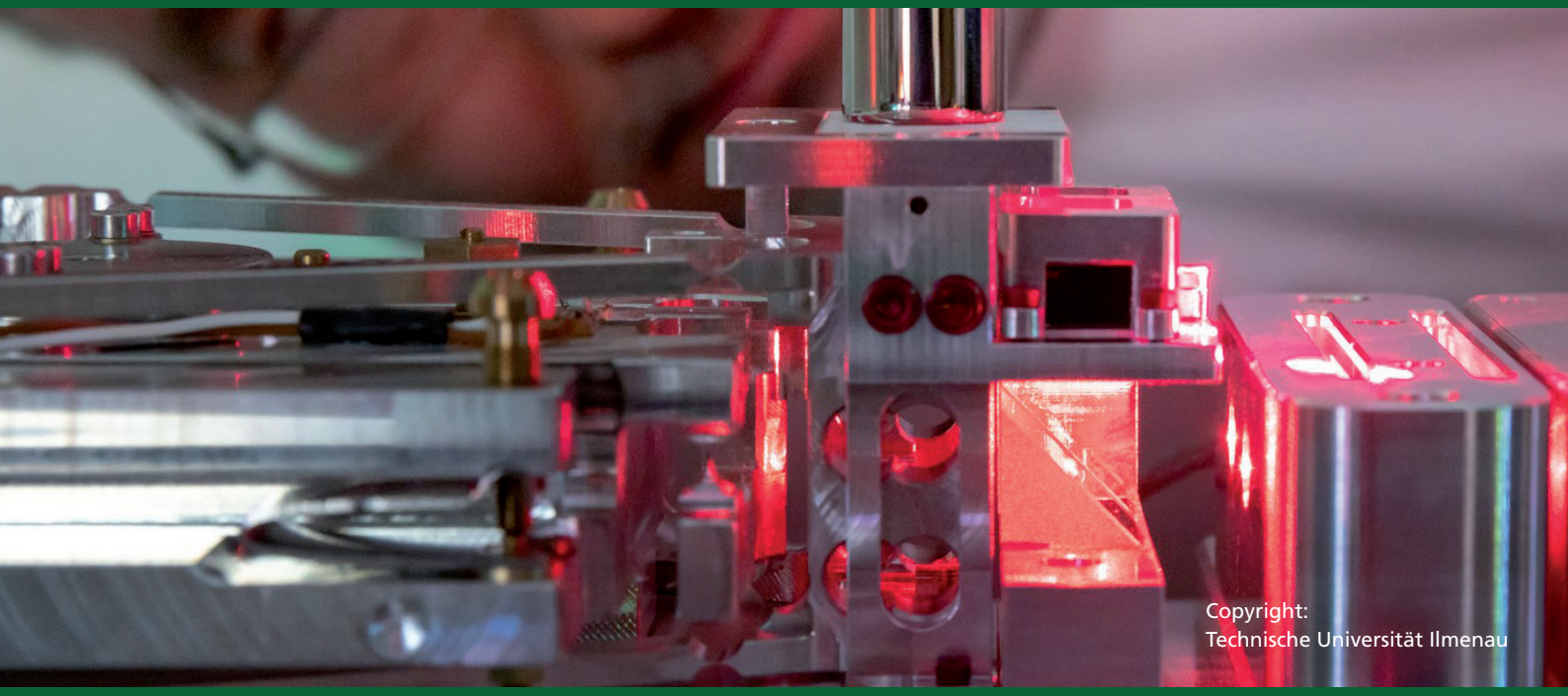

www.smsi-conference.com

AMA Association for Sensors and Measurement

Proceedings

SMSI 2021 Conference
Sensor and Measurement Science International

These proceedings cover the short papers of the digital lectures of the SMSI 2021 Sensor and Measurement Science International Conference.

The authors are responsible for form and content of the papers.

AMA Service GmbH accepts no responsibility for the correctness and completeness of the details and the consideration of private rights of third parties.

Herausgeber / Publisher:

AMA Service GmbH
Von-Münchhausen-Str. 49
31515 Wunstorf / Germany
Tel. +49 5033 9639-0
info@ama-service.com
www.ama-service.com / www.sensor-test.com
www.ama-science.org / www.smsi-conference.com

ISBN 978-3-9819376-4-0

SMSI 2021

Preface by the Conference Chairmen

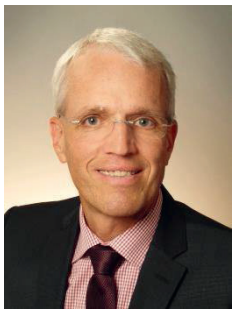

Gerald Gerlach

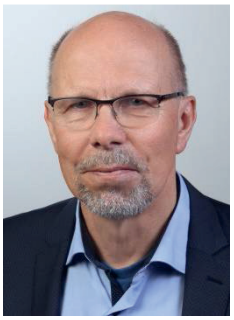

Klaus-Dieter Sommer

Information is the lubricant of our modern society and economy. The availability of information depends crucially on the relevant data sources. In particular, information is obtained through measurement; sensors and measuring systems are essential sources for obtaining relevant data. Without measurement data and, therefore, without measuring systems and sensors, neither Industry 4.0 nor the Internet of Things could be developed as targeted. For this reason it is not surprising that the number of sensors manufactured annually doubles currently every five years and now amounts to several tens of billions.

In the past the well-known AMA Conferences in Nuremberg, organized by AMA Association for Sensors and Measurement, parallel to the SENSOR+TEST, the world's largest trade fair of this industrial branch, so far is the annual highlights in the field of sensor technology in Germany and Europe.

However, to concentrate the power of the long-lasting experiences from these and other conferences, symposia and expert sessions in one common event and to advance the international visibility, the idea of the SMSI – Sensor and Measurement Science International – was born three years ago.

It is the central idea of this new conference to extend the previous more sensor-related topics by a much broader scope comprising the following three pillars:

- **Sensors and Instrumentation:** Sensor principles and quantities, Sensor materials and technology, Sensor interface electronics, Applications, Satellite Conference IRS² - Infrared Sensors and Systems,
- **Measurement Science:** Measurement foundations, Advanced methods and measurement systems, Networked and IoT-related measurement systems, AI approaches in measurement, Applications,
- **System of Units and Metrological Infrastructure:** Revised SI and its opportunities, Metrology and traceability, Advanced calibration and testing methods, Regulations, and Standards in metrology.

The first SMSI edition was planned for last year. However, the COVID-19 pandemic had obstructed our plans to hold the SMSI 2020 conference in June 2020. Nevertheless, many of the authors had already wished that the meeting should take place one year later. In particular, all plenary speakers have agreed to postpone their contributions to this year. We are therefore extremely pleased to be able to offer an exceptionally interesting program again this year, representing many of the latest developments in sensor technology, metrology and measurement.

With these Proceedings you hold the result of this SMSI 2021 Conference in your hands. It contains the two-page short papers as submitted by the authors to the Call for Papers. We hope you enjoy exploring the conference proceedings and gain many new insights.

Our special thanks go to the members of the SMSI Conference Committee, Topical Chairmen of the Conference Pillars, the session chairs, and in particular the authors. We really appreciate their commitment in bringing up this new Conference!

Gerald Gerlach
General Chair

Klaus-Dieter Sommer
General Co-Chair

SMSI 2021 Conference Committee

General Chair

G. Gerlach	Technische Universität Dresden (Germany)

General-Co-Chair

K.-D. Sommer	Technische Universität Ilmenau (Germany)

Sensors and Instrumentation - Including Satellite Conference IRS²

Topical Chairs

G. Gerlach	Technische Universität Dresden (Germany)
R. Lerch	Friedrich-Alexander-Universität Erlangen (Germany)
U. Schmid	Technische Universität Wien (Austria)

Members

J. Auge	Hochschule Magdeburg-Stendal (Germany)
C. Cavalloni	Kistler Instrumente AG (Germany)
J. Czarske	Technische Universität Dresden (Germany)
C. Corleto	STIL SAS (France)
M. da Silva	Federal University of Technology Parana (Brazil)
M. Deilmann	KROHNE Messtechnik GmbH (Germany)
G. Fischerauer	Universität Bayreuth (Germany)
M. Fleischer	Siemens AG (Germany)
J. Hollandt	Physikalisch-Technische Bundesanstalt (Germany)
B. Jakoby	Johannes-Kepler-Universität Linz (Austria)
U. Kaiser	Endress+Hauser AG (Switzerland)
U. Kienitz	Optris GmbH (Germany)
R. Kirchner	Technische Universität Dresden (Germany)
A. König	Technische Universität Kaiserslautern (Germany)
M. Kraft	University of Liege (Belgium)

Members

P. A. Lieberzeit	Universität Wien (Austria)
A. Lloyd Spetz	University of Linköping (Sweden)
W. A. Minkina	Czestochowa University of Technology (Poland)
R. Moos	Universität Bayreuth (Germany)
M. Penza	Italian National Agency for New Technology, Energy and Sustainable Economic (Italy)
L. Reindl	Albert-Ludwigs-Universität Freiburg (Germany)
S. J. Rupitsch	Albert-Ludwigs-Universität Freiburg (Germany)
V. Schauer	HENSOLDT Optronics GmbH (Germany)
J. Schieferdecker	Heimann Sensor GmbH (Germany)
A. Schütze	Universität des Saarlandes (Germany)
S. Semancik	National Institute of Standards and Technology - NIST - (USA)
E. Starke	SICK Engineering GmbH (Germany)
H. K.Trieu	Technische Universität Hamburg-Harburg (Germany)
G. Urban	Albert-Ludwigs-Universität Freiburg (Germany)
M. Vellekoop	Universität Bremen (Germany)
M. Walther	Fraunhofer-Institut - IAF - (Germany)
J. Wöllenstein	Fraunhofer-Institut - IPM - (Germany)
S. Zimmermann	Leibniz Universität Hannover (Germany)
J. Zosel	Kurt-Schwabe-Institut für Mess- und Sensortechnik e.V. Meinsberg (Germany)

Measurement Science

Topical Chairs

K.-D. Sommer	Technische Universität Ilmenau (Germany)
E. Benoit	Université Savoie Mont Blanc (France)
L. Mari	University Carlo Cattaneo (Italy)
B. Zagar	Johannes-Kepler-Universität Linz (Austria)

Members

Y. Aloimonos	University of Maryland (USA)
A. Chunovkina	VNIIMS D.I.Mendeleyev Institute for Metrology (Russia)
F. Fang	University of Dublin (Ireland)
A. Fischer	Universität Bremen (Germany)
A. Forbes	NPL National Physical Laboratory (Great Britain)
T. Fröhlich	Technische Universität Ilmenau (Germany)
C. Gulka	NCSL International Inc (USA)
E. Hazarian	California State University (USA)
M. Heizmann	Karlsruher Institut für Technologie KIT (Germany)
B. Henning	Universität Paderborn (Germany)
B. Jeckelmann	Eidgenössisches Institut für Metrologie (Switzerland)
W. Jian	National Institute of Metrology (China)
R. Kacker	National Institute of Standards (USA)
D. Knopf	Physikalisch-Technische Bundesanstalt (Germany)
A. König	Technische Universität Kaiserslautern (Germany)
A. Maier	Friedrich-Alexander Universität Erlangen-Nürnberg (Germany)
E. Manske	Technische Universität Ilmenau (Germany)
R. Morawski	Politechnika Warszawska (Poland)
A. Schäfer	Hottinger Brüel & Kjaer GmbH (Germany)
A. Schütze	Universität des Saarlandes (Germany)
R. Tutsch	Technische Universität Braunschweig (Germany)
J. Valdés	INTI - Instituto Nacional de Tecnologia Industrial (Argentina)

System of Units and Metrological Infrastructure

Topical Chairs

B. Jeckelmann	Muntelier (Switzerland)
M. Bartholmai	BAM Bundesanstalt für Materialforschung (Germany)
H. Busse	Physikalisch-Technische Bundesanstalt (Germany)
P. Neyeshmakov	COOMET (Ukraine)

Members

T. Bulygin	VNIIMS All-Russian scientific research institute for metrological service (Russia)
C. Corleto	STIL SAS (France)
A. Ganesh	CEN-CENELEC (Belgium)
E. Georgin	CETIAT - Centre Technique des Industries Aérauliques et Thermiques (France)
J. H. Hendricks	National Institute of Standards (USA)
J. Hollandt	Physikalisch-Technische Bundesanstalt (Germany)
A. Kuzin	VNIIMS All-Russian scientific research institute for metrological service (Russia)
F. Ogheard	CETIAT - Centre Technique des Industries Aérauliques et Thermiques (France)
G. Rietveld	VSL - Dutch Metrology Institute (Netherlands)
C. Tiebe	BAM Bundesanstalt für Materialforschung (Germany)
J. Unger	BAM Bundesanstalt für Materialforschung (Germany)
J. Zosel	Kurt-Schwabe-Institut für Mess- und Sensortechnik e.V. Meinsberg (Germany)

SMSI 2021: Planary Talks

Sensors and Instrumentation

A1: Piezoelectric High-temperature Sensors I (Special Session)

Chair: Y. Suhak, Clausthal Universit of Technology, Goslar (Germany)

A2: Piezoelectric High-temperature Sensors II (Special Session)

Chair: Y. Suhak, Clausthal Universit of Technology, Goslar (Germany)

A3: Load and Force Measurement

Chair: E. Starke, SICK Engineering GmbH, Ottendorf-Okrilla (Germany)

A4: Force, Pressure and Torque Measurement

Chair: J. Wilde, Albert-Ludwigs-Universität Freiburg, Freiburg (Germany)

A5: MEMS Sensors

Chair: R. Kirchner, Technische Universität Dresden, Dresden (Germany)

A6: Sensor Materials I

Chair: U. Schmid, Technical University Vienna, Vienna (Austria)

A7: Packaging and Integration of Sensors

Chair: R. Moos, Universität Bayreuth, Bayreuth (Germany)

A8: Ultrasonic Transducers and Measurement

Chair: S. Rupitsch, Albert-Ludwigs-University Freiburg, Freiburg (Germany)

A9: Ultrasonic and Acoustic Measurements

Chair: S. Rupitsch, Albert-Ludwigs-University Freiburg, Freiburg (Germany)

B1: Gas Sensors I

Chair: A. Schütze, Saarland University, Saarbrücken (Germany)

B2: Gas Sensors II

Chair: Anita Lloyd Spetz, University of Linköping, Linköping (Sweden)

B3: Gas Sensors III

Chair: A. Lieberzeit, University of Vienna, Vienna (Austria)

B4: Bio and Chemo Sensors

Chair: K. Trieu, Hamburg Univertiy of Technology, Hamburg (Germany)

B5: Chemosensor Applications

Chair: S. Zimmermann, Leibniz University of Hannover, Hannover (Germany)

B6: Flow Measurement

Chair: P. Neyezhmakov, National Scientific Centre “Institute of Metrology” - NSCIM, Kharkiv (Ukraine)

B7: Sensor Materials II

Chair: U. Schmid, Technical University Vienna, Vienna (Austria)

B8: Fiber Optic Sensors

Chair: A. Fischer, University of Bremen, Bremen (Germany)

B9: Optical Sensors

Chair: M. Heizmann, Karlsruher Institute of Technology – KIT, Karlsruhe (Germany)

B10: Optical Sensors and Measurement

Chair: R.Engelbrecht, Technische Hochschule Nürnberg, Nürnberg (Germany)

C1: IRS² Satellite Conference: Infrared Sensors

Chair: E. Manske, Technische Universität Ilmenau, Ilmenau (Germany)

C2: IRS² Satellite Conference: Thermal Imaging and Thermography

Chair: T. Fröhlich, Technische Universität Ilmenau, Ilmenau (Germany)

C3: IRS² Satellite Conference: Spectroscopy, Thermometry

Chair: V. Schauer, HENSOLDT Optronics GmbH, Oberkochen (Germany)

C4: Temperature Measurement

Chair: G. Machin, National Physical Laboratory (NPL), Teddington, Middlesex TW11 0LW (Great Britain)

C5: Process Monitoring

Chair: B. Jakoby, Johannes-Kepler-Universität Linz, Linz (Austria)

C6: Condition Monitoring

Chair: G. Fischerauer, University Bayreuth, Bayreuth (Germany)

C10: Magnetic Sensors

Chair: R. Slatter, Sensitec GmbH, Wetzlar (Germany)

D10: Advances in Sensor Electronics

Chair: A. König, Technical University of Kaiserslautern, Kaiserslautern (Germany)

Measurement Science

A10: Inverse Problems in Measurements (Special Session)

Chair: B. Henning, Paderborn University, Paderborn (Germany)

D2: Measurement Foundations I

Chair: E. Benoit, Université Savoie Mont Blanc, Chambéry (France)

D3: Measurement Foundations II

Chair: R. Morawski, Warsaw University of Technology, Warsaw (Poland)

D5: Deep Learning and Artificial Intelligence in Measurement

Chair: E. Rückert, Montanuniversität Leoben, Leoben (Austria)

D6: Advanced Methods and Measurement Systems

Chair: H. Bosse, Physikalisch-Technische Bundesanstalt (PTB), Braunschweig (Germany)

D8: Applications I

Chair: R. Tutsch, Technische Universität Braunschweig, Braunschweig (Germany)

D9: Applications II

Chair: G. Fischerauer, Universität Bayreuth, Bayreuth (Germany)

System of Units and Metrological Infrastructure

C7: Testing and Inspection

Chair: C. Tiebe, BAM Bundesanstalt für Materialforschung und -prüfung, Berlin (Germany)

C8: Testing and Diagnosis

Chair: T. Härtling, Fraunhofer-Institut für Keramische Technologien und Systeme (IKTS), Dresden (Germany)

C9: Advanced Testing Methods

Chair: V. Witkovsky, Slovak Academy of Sciences, Bratislava (Slovak Republic)

D1: Future Topics in Metrology (Special Session)

Chair: S. Eichstädt, Physikalisch-Technische Bundesanstalt (PTB), Berlin (Germany)

D4: Advanced Calibration Approaches

Chair: B. Jeckelmann, Muntelier (Switzerland)

Plenary Talks

DOI 10.5162/SMSI2021/PT1

New Opportunities for Measurement and Sensor Technology through Digitization

Ulrich Kaiser[1], Klaus-Dieter Sommer[2]
[1] Endress+Hauser AG, Kägenstr. 2, 4153 Reinach, Switzerland,
[2] Technische Universität Ilmenau, Ehrenbergstraße 29, 98693 Ilmenau, Germany
dr.ulrich.kaiser@gmail.com, klaus-dieter.sommer@tu-ilmenau.de

Summary:

Digitization offers completely new possibilities for the productivity, use and informative value of measurement and sensor technology. The most important requirement and achievement is that we have smart sensors with the necessary data pre-processing and communication capabilities with the "Internet of Things" in IoT EcoSystems. Therefore, many optimizations are possible regarding the statements of the measurement, utilizing redundant information, optimization calibration cycles and cost-optimized maintenance.

Keywords: Internet of Things, IoT Ecosystem, Soft Sensors, Smart calibration strategies and maintenance,

Industry 4.0 is comprised by the use of digital technologies, including especially the IoT technologies, in industrial automation and all spheres of life. This transformation will lead to enormous gains in productivity and flexibility. Measurement and sensor technology are not only an essential component of automation and is therefore doomed to participate in this transformation, but it will more and more influence our ordinary life - from leisure activities to life planning. Because of its late entry, however, it can rely on already existing, mature technologies and infrastructures, such as powerful hardware controllers, networks and cloud architectures from the IT and consumer world.

Smart sensors in an IoT Ecosystem

With a view to be able to maximum profit and benefit from the methods of digitization, several important prerequisites must be met: the essential elements have to be integrated component of the technical system, the sensors, but also the actuators must be "smart" [1]. They must have connectivity and communication capabilities to be part of the Internet of Things (IoT). And they must be capable of self-diagnosis and - as a goal - also be capable of their own maintenance, such as self-validation or even self-calibration. Then, an adapted architecture of the control system and a platform for the execution of the methods, the IoT ecosystem, is needed. For new technical systems to be created, this ecosystem can be including into the control system. However, still majority of today's implementations are based on the existing architecture of the automation/traceability pyramid and connect the IoT ecosystem via a separate communication channel at the field level.

Diagnostics and predictive maintenance

One potential, digitization offers is to move from preventive maintenance to real predictive maintenance, thus reducing maintenance costs and increasing the technical health of the system too. There are two different approaches. On the one hand, statistical methods, with which maintenance events can be predicted from a large amount of other information, and on the other hand - in knowledge of the underlying physical and chemical interrelationships - the recording of suitable indicators for maintenance requirements using sensors. In [2] the requirements for these sensors for condition monitoring and predictive maintenance for use in chemical process plants are clearly described.

Calibration and one-step traceability

To maintain its metrological quality, a sensor needs regular calibration, where its measured value must be traceable (within an appropriate measurement uncertainty) to a reliable reference and thus ultimately to the SI. In many cases, today, this requires the sensor to be removed from the system, which is (very) costly

and disadvantageous for operation. This traditional requirement is clearly opposed to the necessary sharp increase in the use and application of measuring and sensor systems in automated and partially autonomous production. Desirable here would be sensors that either ideally no longer need to be calibrated l or having exceptionally long calibration intervals that are in line with the maintenance cycles of the respective technical system. One approach to the solution is sensor-internal verification. This involves subjecting all or most of the components relevant to the metrological quality of a sensor to ongoing internal sensor verification based on the available sensor internal and external information, including the use of redundant information of the system under consideration., This therefore allows to reduce the probability of erroneous measurements combined with a reduction of the calibration effort. Of course, it would be ideal if a reference directly traceable to the SI were part of a sensor and calibration could be performed anywhere and anytime without external intervention. Such developments are already underway in some large metrology laboratories. There are interesting developments such as the NIST on a Chip [3] The NIST-on-a-Chip project [3] appears to be particularly advanced with microtechnologically realized traceable quantum-based reference standards built into the sensor [3].

Soft Sensors

Soft sensors are measuring systems where difficult to measure variables are determined from several more easily to measure variables (measurands). Either because the measurand cannot be measured directly, the measurement location is not accessible or a value to be measured in the future is required. The relationship of the measured quantities to the target quantity is either known, i.e., model-driven, or must be learned, i.e., data-driven. The latter is more appropriate, because it allows the mapping of complex dependencies with many input variables that are no longer easy to model [4]. However, there are also combinations of both methods in place. For the data-driven methods, the technique of machine learning comes into play. Machine learning has been booming in recent years. However, the necessary completeness and quality of training data is still a challenge. IoT Ecosystems are ideal platforms for implementing such Soft Sensors.

Information security for measurement and sensor technology

Smart sensors in IoT ecosystems are more vulnerable to cyberattacks than in isolated, proprietary systems because of their principle greater openness. Sensor data can be manipulated or unauthorized "overheard"; communication connections can be interrupted. Here too, measurement and sensor technology can build on the experience already acquired in information technology. A large arsenal of procedures and techniques is available for the information security of technical systems [5].

References

[1] Maiwald, Michael. Die Technologie-Roadmap „Prozess-Sensoren 4.0“ – Chancen für neue Automatisierungskonzepte und neue Geschäftsmodelle. ATP Plus - Das Magazin der Automatisierungstechnik (2016)

[2] U. Hampel et al. Sensorik für die Digitalisierung chemischer Produktionsanlagen. ProcessNet Fachgesellschaft, Dechema e.V. (2020)

[3] National Institute of Standards and Technology (NIST) (2018) https://www.nist.gov/pml/productsservices/nist-chip-portal/nist-chip-overview

[4] Michael Heizmann, Klaus-Dieter Sommer. Expertenforum Trends in der industriellen Mess- und Automatisierungstechnik – Von der Messung zur Information. tm – Technisches Messen 2019; 86(11): 619-622

[5] IEC 62443 Industrial communication networks

[6] Klaus-Dieter Sommer: One-Step-traceability – an indispensable Component for i4.o Ecosystems. Presentation on WebMeeting of the AMA-WG i4.0, April 2019 (based on information of B. Goldstein, NIST)

Plenary Talk
DOI 10.5162/SMSI2021/PT2

From Sensors to Standards: How NIST on a Chip is Transforming International Metrology

Barbara Goldstein[1]
[1] *National Institute of Standards and Technology, Physical Measurement Laboratory, 100 Bureau Drive, Gaithersburg, MD 20899, barbara.goldstein@nist.gov*

Summary:
What draws the line between a sensor and a standard? If precision measurement devices can be reduced to the size of a grain of rice, embedded directly in products, deployed on submarines or satellites without the need for periodic calibration, how does the international metrology framework need to change to adapt? And what commercial applications does it enable? These are the very questions raised by the successes of the NIST on a Chip program, which is transforming how precision measurements are being brought out of the lab and deployed at point of use through a suite of miniaturized, fit-for-purpose, quantum-based traceable sensors.

Keywords: Quantum Revolution, Metrology, Redefinition of the SI, Industry 4.0, Technology Readiness, Quantum Sensing

NIST on a Chip Vision

In the 1990s, when the world's best and only traceable measurements were made in laboratories filled with complex equipment that required highly skilled staff to operate, NIST researchers, together with U.S Defense Advanced Research Projects Agency (DARPA), had the bold notion that it might be possible to shrink an atomic clock down to a low cost, low-power chip-scale device. The successes arising from these early and sustained investments and industry collaborations[1] not only led to commercially available chip-scale atomic clocks, but motivated an entire research venture into developing chip-scale standards.

The NIST on a Chip program[2], or NOAC, is revolutionizing metrology by making precision measurements available at point-of-use through a suite of intrinsically accurate, quantum-based devices intended to be deployed nearly anywhere and anytime, performing uninterrupted without the need for NIST's traditional measurement services.

These quantum-based measurement technologies will enable users to make precision measurements referenced to the International System of Units (SI) wherever they're most needed – on factory floors, on satellites, in hospital diagnostic centers, in research labs, and ultimately in homes, automobiles, personal electronic devices, and more. NOAC is helping to "democratize" measurement technology, by drastically reducing the cost and increasing the availability of precision measurements that could previously only be delivered at the world's best metrology institutes.

The suite of ultra-compact, inexpensive, low-power devices being developed within the program can measure the full range of quantities including time and frequency, distance, mass and force, temperature and pressure, electrical and magnetic fields, current and voltage, and fluid volume and flow.

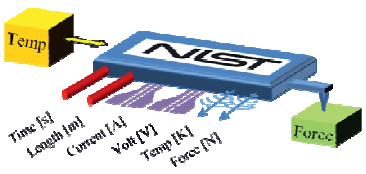

The program envisions eventually combining multiple measurement capabilities onto an integrated platform to enable, for example, a single, embeddable chip that senses absolute temperature, pressure, and humidity to immediately detect any excursions in safe storage conditions of sensitive goods, such as vaccines or food. Other applications will leverage inexpensive mass fabrication, leading to applications such as a chip-scale radiation monitor that could be embedded in every driver's license or other ID card to serve as a ubiquitous monitor or early-warning system for radiation exposure.

These NIST-pioneered technologies will be manufactured and distributed by the private

[1] https://www.nist.gov/noac/success-story-chip-scale-atomic-clock
[2] https://www.nist.gov/noac

sector, opening new technology transfer and lab-to-market opportunities in accordance with NIST's goal of strengthening U.S. economic competitiveness by supporting advanced manufacturing.

Defining Criteria for NOAC Devices

The quantum-based standards and sensors being developed within the NOAC program are designed to be:

Deployable to where customers need them, such as on the factory floor, embedded into products, in a laboratory environment, in space or at home.

Flexible, providing a broad range of "zero chain" SI-traceable measurements and standards that are configurable into a single small-form package and adaptable to customers' requirements.

Manufacturable, with production costs that scale appropriately for applications, such as low-cost/high-volume for broad deployment.

Reliable, providing either the right value of a measurement or no value at all.

Fit-to-Function, tending towards small size, low power consumption, rugged, easily integrated and operated, with an operating range and uncertainty required by the application.

Propitious Timing

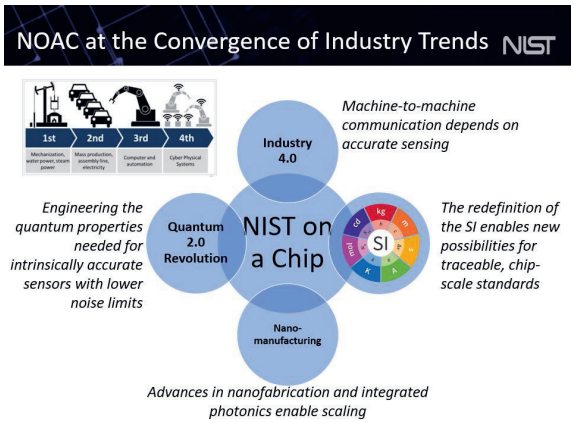

NOAC innovations will be increasingly valuable to industry, medicine, defense, and science because of the current convergence of major trends in technology advancement. For example, Industry 4.0 is an optimization strategy in which the machinery of industrial production no longer simply "processes" the product, but the product communicates with that machinery in a digital choreography of production.

This approach will come to redefine the consumer-manufacturer relationship, as products in the field (i.e., in the Internet of Things) communicate back to the manufacturing ecosystem that produced them (the Industrial Internet of Things) to influence everything from next-generation product design, supply chain management, peer-to-peer consumer networking, product maintenance and end-of-life. This new paradigm won't be possible without accurate sensors both in the field and in the plant to provide reliable information to drive automated, machine-to-machine communication and decision making.

At the same time, the emergence of the second quantum revolution – which depends on the control and manipulation of matter at the most fundamental levels – will spur a new generation of technologies based on phenomena such as entanglement and superposition. The preservation and manipulation of these very fragile quantum states will require reliable, in-situ sensors and measurements, a NOAC goal. In addition, advances in quantum information science will enable unprecedented advances in measurement precision and thus fuel a new generation of quantum-accurate standards and measurements.

Finally, the explosive demand for high-speed transfer of ever-larger volumes of data will benefit directly from NOAC's pioneering work in miniaturized photonic channels, novel signal transduction schemes, and accurate calibration standards for devices that must operate at unprecedented frequencies.

Opportunities for Partnerships

The NIST on a Chip program was built through collaboration. NOAC technologies are at varying stages of technology readiness. NIST is actively building partnerships with industry, both domestically and globally, to bring these innovations from lab to market. A portfolio of patents available for licensing are available at https://www.nist.gov/noac/patents. Potential partners are encouraged to explore opportunities for engagement.

Plenary Talk
DOI 10.5162/SMSI2021/PT4

Progress in Realising the Redefined Kelvin

Graham Machin[1], M. Sadli[2], J. Pearce[1], J. Engert[3], R. M. Gavioso[4]
[1]National Physical Laboratory (NPL), Teddington, TW11 0LW, UK
[2]LNE-CNAM, Laboratoire commun de métrologie, 93210 Saint-Denis, France
[3]Physikalisch-Technische Bundesanstalt (PTB), Abbestr. 2-12, 10587 Berlin, DE
[4]Istituto Nazionale di Ricerca Metrologica (INRIM), 91 Strada delle Cacce, 10135, Torino, Italy
Corresponding Author's e-mail address: graham.machin@npl.co.uk

Summary:
The redefinition of the SI unit the kelvin in May 2019 opened new possibilities for the realization, dissemination and measurement of temperature. Besides the two practical temperature scales that were in place before the redefinition, now, through the mechanism of the *mise en pratique* for the definition of the kelvin, temperature can be realized and disseminated through primary thermometry approaches with direct traceability to the redefined kelvin. Initial progress towards realizing the redefined kelvin will be discussed, with emphasis on temperatures >1235 K and <25 K.

Keywords: kelvin redefinition, primary thermometry, temperature scales, ITS-90, PLTS-2000

Introduction

The redefinition of the kelvin resulted from coordinated global activity by the thermometry community [1-4]. The redefinition, in terms of a defined value of the Boltzmann constant [1], opened new possibilities for realizing and disseminating temperature. Instead of the two defined scales, the International Temperature Scale of 1990 (ITS-90, [5]) and the Provisional Low Temperature Scale of 2000 (PLTS-2000, [6]), being the accepted means of attaining traceability, now a more flexible approach, by the *mise en pratique* for the definition of the kelvin (*MeP*-K-19) [7, 8], is possible. The *MeP*-K-19 details how to attain temperature traceability by means of primary thermometry without recourse to any defined scale.

In this paper the possibilities for temperature realization and dissemination, linked to the redefined kelvin, are discussed, mainly in the context of the European Metrology Programme for Innovation and Research (EMPIR) project "Realising the redefined kelvin" (Real-K) [9]. Initial results will be described, especially at high (>1235 K) and low (<25 K) temperatures. An outlook of the impact of the kelvin redefinition on the practice of thermometry in the short, medium and longer term, including on the practice of practical thermometry, is given.

Required progress and challenges

To turn the *MeP*-K-19 into a reality requires substantial research effort. The aim of the EMPIR Real-K project is to begin this process through the following research activities:

At high temperatures (>1235 K) indirect primary radiometry will link to the redefined kelvin, via high temperature fixed points (HTFPs) [2, 10]. HTFP blackbodies have been constructed for Fe-C (1426 K), Pd-C (1765 K), Ru-C (2226 K) and WC-C (3020 K) and performance assessed. In the next year low uncertainty thermodynamic temperatures will be determined, then dissemination of thermodynamic temperatures (>1235 K) with uncertainties comparable to ITS-90 (U<0.05%) will be demonstrated.

At temperatures <25 K the ITS-90 is complex to establish and disseminate. Primary thermometry techniques are being established for the realisation and dissemination of thermodynamic temperature from 1 K to 25 K to provide a direct link to the redefined kelvin, as well as ensuring a smooth transition to the PLTS-2000 range (i.e. <1 K). Progress will be by sensors (e.g., primary Johnson Noise and Coulomb Blockade thermometers) and gas-based thermometry.

To give time for primary thermometry techniques to become established in the intermediate temperature region (25 K – 1235 K) life extension research addressing two of the ITS-90's most pressing problems will be performed; namely reducing non-uniqueness uncertainty by 30 % in calibration of platinum resistance thermometers and preparing a suitable fixed-point replacement for the mercury triple point (e.g., CO_2, SF_6) including its integration within ITS-90.

To facilitate primary thermometry uptake in the intermediate temperature region (>25 K) thermophysical properties of noble gases (e.g., He,

Ne, Ar) are required over a wide range of conditions. These will be determined by *ab initio* calculations and experiment. These values will be used to reduce the attainable uncertainties by primary thermometry, which are generally currently uncompetitive with the ITS-90.

These are only the first steps towards realising the redefined kelvin. Progress will be reported to the CIPM Consultative Committee of Thermometry to ensure on-going fitness of realisation and dissemination of the temperature unit.

Impact of the kelvin redefinition

The potential impact of the kelvin redefinition, in the short to the long term, on the practice of thermometry is discussed below.

In the *short term* the current temperature scales will continue to be used to provide temperature traceability. For those requiring thermodynamic temperature, the $T - T_{90}$ and $T - T_{2000}$ data available in the *MeP*-K-19 annexes will allow users to access thermodynamic values.

In the *medium to long* term primary thermometry, directly linked to the redefined kelvin, could supplant the defined scales for realisation and dissemination of the unit. Primary thermometry will only do this when similar uncertainties to the current defined scales can be attained.

The developments described here may, by the mid-2020s, lead to the ITS-90 (>1235 K) being superseded by relative primary radiometry. On a similar timescale, for temperatures <25 K, different approaches to primary thermometry (variants of Johnson Noise <4 K, Coulomb blockade, acoustic gas or polarising gas thermometry <25 K) may provide sufficiently reliable low uncertainty thermodynamic temperatures so that the PLTS-2000 and the ITS-90 (<25 K) are superseded.

For a time primary thermometry, the ITS-90, and the PLTS-2000 will co-exist. But in the long-term (2030s+) progressive elimination of the defined scales may be possible as primary thermometry for temperature realisation and dissemination becomes increasingly adopted. The ITS-90 may possibly be the last defined temperature scale, though a future restricted-range scale may be needed at intermediate temperatures (the so-called ITS-20XX [11]). Nevertheless, the redefinition of the kelvin has opened the way for improvements in thermometry that can be introduced through the *MeP*-K-19 with no disruption to the user community.

In the longer term the kelvin redefinition, may lead to the advent of *practical* primary thermometry. Advances in practical Johnson Noise thermometry [12] are an early example. As *in-situ* practical primary thermometry becomes a reality then the need to calibrate temperature sensors would ultimately be un-necessary. These new sensing methods are essential if autonomous production is to be a reality.

Summary

The kelvin redefinition has ushered in a paradigm change in the field of thermometry. Temperature realization and dissemination will increasingly be based on direct linkage to primary thermometry and in the long-term users will turn to self-calibrating practical primary thermometry to address their thermometry needs.

Acknowledgement

This project 18SIB02 Real-K has received funding from the EMPIR programme co-financed by the Participating States and from the European Union's Horizon 2020 research and innovation programme.

References

[1] Fischer, J., *et. al*. "The Boltzmann Project", *Metrologia,* **55,** R1-R20 (2018)

[2] Machin, G., *et. al*. "Summary of achievements of the EMRP project implementing the new kelvin (InK)", *Measurement,* **94,** 149-156 (2016)

[3] Machin, G., "Towards implementing the new kelvin" *Phil. Trans R. Soc. A.* **374:** 20150053, (2016)

[4] Machin, G., *et. al.* "The European Metrology Programme for Innovation and Research project: Implementing the new kelvin 2 (InK2)", *XXII World Congress of the International Measurement Confederation (IMEKO 2018) IOP Conf. Series: Journal of Physics: Conf. Series* **1065** (2018) 122002

[5] Preston-Thomas, H., "The international temperature scale of 1990", *Metrologia*, **27**, 3-10 (1990)

[6] Rusby, R.L., *et. al.* "The provisional low temperature scale from 0.9 mK to 1 K the PLTS-2000", *J. Low. Temp., Phys.* **126**, 633-42 (2002)

[7] Fellmuth, B., *et. al.* "The kelvin redefinition and its *mise en pratique", Phil. Trans R. Soc. A.* **374:** 20150037 (2016)

[8] https://www.bipm.org/utils/en/pdf/si-mep/SI-App2-kelvin.pdf

[9] https://real-k.aalto.fi/

[10] Machin, G., "Twelve years of high temperature fixed point research: a review", *AIP Conf. Proc.* **1552**, 305 (2013)

[11] Machin, G., "The Kelvin redefined", *Meas. Sci. Technol.,* **29,** 022001 (11pp) (2018)

[12] Bramley, P., Cruickshank, D., Pearce, J., "The development of a practical, drift-free, Johnson-Noise Thermometer for industrial applications", *Int. J. Thermophys.,* **38,** 25 (2017)

Plenary Talk
DOI 10.5162/SMSI2021/PT6

Invariance in Measured Quantities across the Sciences

William P. Fisher, Jr[1]
[1] BEAR Center, Graduate School of Education, University of California, Berkeley, USA,
Senior Scientist, Research Institute of Sweden, & Living Capital Metrics LLC, Sausalito CA USA

wfisher@berkeley.edu, wpfisherjr@livingcapitalmetrics.com

Summary:
Basic physical quantities for mass, length, duration, and charge exhibit structural invariances not different in kind from those that also characterize probabilistically measured psychological and social quantities. For over 50 years, the theory and practice of additive conjoint models for measurement introduced in the 1960s have demonstrated that the scope of fundamental measurement is broader than was previously appreciated. This is especially apparent in the correspondences between the various log-interval scales employed in both the natural and the social sciences. These scales are conventionally treated in some fields as ratio scales by choosing convenient exponents, but are commonly expressed as log-odds interval scales in the social sciences. In recent years, a metrological perspective focused on defined quantity values using these kinds of scales has begun to emerge from collaborations of engineers and psychologists. The terms of the shared perspective on measurement concern a basis in modeling lawful regularities, predictive explanatory theories, and quality assured metrological traceability to consensus standards.

Keywords: measurement, modeling, metrology, history, log-interval scales

Interval Scales across the Sciences

Writing in 1986, Narens and Luce [1] say that mathematical models emerging in the 1960s provide "a basis for measuring a number of the basic physical quantities: mass, length, duration, and charge," observing "that much the same structure underlies the measurement of probability." The authors report that use of these models to obtain interval-scalable, fundamental measurements of non-extensive, nonphysical, psychological, and social constructs is "widely accepted." Given that 35 years have passed since that statement was made, the reader may well wonder why higher quality measurement has not yet been more widely achieved.

The class of additive conjoint models being referred to falls under the heading of log-interval scales, which S. S. Stevens [2] added as a fifth entry in his taxonomy of four scale types (nominal, ordinal, interval, and ratio). Narens and Luce note that this kind of scale is used in multiple examples across the sciences (such as decibels, the Richter scale, pH acidity, stellar magnitude, entropy, and information) contrary to common perceptions that it is rare.

Probabilistic models for measurement developed by Rasch [3-4] belong to this class of models [5-7] expressing interval units in log-odds form. Rasch [4] recounted that, when developing his initial model, "I imagined...that the reading ability of a student could be characterized in a quantitative way--not through a more or less arbitrary grading scale, but by a positive real number defined as regularly as the measurement of length."

These models, their estimation, fit assessment, software applications, implementations, and professionalization were significantly advanced by Wright [7-8], his students and colleagues [9], and Rasch's students [6, 10].

Models and Modeling Take Pride of Place

Nersessian [11] notes that "A significant segment of history and philosophy of science now gives models and modeling pride of place among scientific tools and practices." She and others [12-13] argue that reasoning with model systems takes place within socially distributed cognitive systems as constraint satisfaction processes in which mental and physical models co-evolve. A key point is that the conjoint interactions of mental and physical models do not occur in the isolation of a single person's mind but instead are integrated with cognitive resources embedded in the external shared social environment. These resources take the form of everyday languages' alphabets, dictionaries, phonemes, grammars, etc., as well as the more technically complex

standards of scientific languages' unit definitions, mathematical models, instrument calibrations, quality assurance methods, etc.

The similarity or goodness of fit of the model defines the relationship between mental and physical realities in much the same way they do for the relationships between mental and psychosocial models [15]. Successful models support local inferences and insights that cannot be entirely anticipated in research. Models are manipulated by changing their features and trying them out experimentally across contexts, with the aim of assessing their applicability, fit, and usefulness.

Nersessian establishes that scientific modeling does not enjoy any special advantage conferred by a supposed superior tractability of its objects of investigation. She focuses on the ways in which normal everyday cognitive operations are extended in science. Basic processes of analogy embedded in social and technical contexts work much the same way in normal language usage as they do in scientific language usage.

- **New Metrological Horizons**

Nersessian's account of the place of models and modeling in the history of science emphasizes the importance of models that are in principle identifiable: that are structured to have a capacity to locate, describe, and potentially explain repeatably reproducible phenomena. The primary focus of scientific models of this kind is not, then, descriptive, as in statistical modeling, but, rather, prescriptive. This orientation in modeling is important for the lesson learned from history: scientific laws are not discovered via measurement; rather, measurement requires that the laws are already in hand [15]. Thus we have the special significance of the fact that Rasch [3] intentionally structured his probabilistic models to have the same form as Maxwell's treatments of Newton's Second Law. The implications of this capacity to see the same mathematics in geometry, physics, and psychology [16] are increasingly explored in collaborations among metrologists and psychometricians [17-20].

References

[1] L. Narens, R. D. Luce, Measurement. *Psychological Bulletin*, 99(2), 166-180 (1986); doi: 10.1037/0033-2909.99.2.166

[2] S.S. Stevens, Mathematics, measurement, and psychophysics. In S. S. Stevens (Ed.), *Handbook of experimental psychology* (pp. 1-49). New York: Wiley (1951)

[3] G. Rasch, *Probabilistic models*, Chicago: University of Chicago Press, (1980)

[4] G. Rasch, On specific objectivity. *Danish Yearbook of Philosophy*, 14, 58-94 (1977)

[5] H. E. Brogden, The Rasch model, the law of comparative judgment and additive conjoint measurement. *Psychometrika*, 42, 631-634 (1977); doi: 10.1007/BF02295985

[6] G. H. Fischer, Applying the principles of specific objectivity and of generalizability to the measurement of change. *Psychometrika*, 52(4), 565-587 (1987); doi: 10.1007/BF02294820

[7] B. Wright, A history of social science measurement, *Educational Measurement: Issues and Practice*, 16, 33-52 (1997); doi: 10.1111/j.1745-3992.1997.tb00606.x

[8] B. D. Wright, Solving measurement problems with the Rasch model. *Journal of Educational Measurement*, 14(2), 97-116 (1977); https://www.jstor.org/stable/1434010

[9] W. P Fisher, B. D. Wright, (Eds.) Applications of probabilistic conjoint measurement. *International Journal of Educational Research*, 21(6), 557-664 (1994); doi: 10.1016/0883-0355(94)90010-8

[10] E. B. Andersen, Sufficient statistics and latent trait models. *Psychometrika*, 42(1), 69-81 (1977); doi: 10.1007/BF02293746

[11] N. J. Nersessian, Model-based reasoning in distributed cognitive systems. *Philosophy of Science*, 73, 699-709 (2006); https://doi.org/10.1086/518771

[12] N. J. Nersessian, *Creating scientific concepts*. Cambridge, Massachusetts: MIT Press (2008)

[13] B. Latour, *Science in action*. New York: Harvard University Press (1987)

[14] T. S. Kuhn, The function of measurement in modern physical science. Isis, 52(168), 161-193 (1961); doi: 10.1086/349468

[15] A. J. Stenner, W. P. Fisher, M. H. Stone, D. S. Burdick, Causal Rasch models. Frontiers in Psychology: Quantitative Psychology and Measurement, 4(536), 1-14 (2013); doi: 10.3389/fpsyg.2013.00536

[16] W. P. Fisher, A. J. Stenner, On the potential for improved measurement in the human and social sciences. In Q. Zhang & H. Yang (Eds.), Pacific Rim Objective Measurement Symposium 2012 Proceedings (pp. 1-11). Berlin: Springer (2013); doi: 10.1007/978-3-642-37592-7_1

[17] L. Mari, M. Wilson, An introduction to the Rasch measurement approach for metrologists, *Measurement*, 51, 315-327 (2014); doi: 10.1016/j.measurement.2014.02.014

[18] L. Pendrill, *Quality assured measurement*. Cham: Springer (2019)

[19] L. Pendrill, W. P. Fisher, Counting and quantification. *Measurement*, 71, 46-55 (2015); doi: 10.1016/j.measurement.2015.04.010

[20] L. Mari, M. Wilson, A. Maul, *Measurement across the sciences*. Cham: Springer (2021)

Plenary Talk
DOI 10.5162/SMSI2021/PT7

Quantum-Based Photonic Sensors for Pressure, Vacuum, and Temperature Measurements: A Vison of the Future with NIST on a Chip

J Hendricks, Z Ahmed, D Barker, K Douglass, S Eckel, J Fedchak, N Klimov, J Ricker, J Scherschligt
National Institute of Standards and Technology, Physical Measurement Laboratory, 1Sensor Science Division, Thermodynamic Metrology Group, 100 Bureau Drive, Gaithersburg, MD 20899-8363
E-mail: jayh@nist.gov

Summary:

The NIST on a Chip (NOAC) program's central idea is the idea that measurement technology can be developed to enable metrology to be performed "outside the National Metrology Institute" by the creation of deployed and often miniaturized standards. These standards, when based on fundamental properties of nature, are directly tracible to the international system of units known as the SI. NIST is also developing quantum-based standards for SI traceability known as QSI, or Quantum based International System of units. Specifically, this paper will cover NIST efforts in the area of thermodynamic metrology to develop NOAC standards for pressure, vacuum and temperature measurements.

Keywords:

Introduction

For pressure measurements, this paper will cover NIST efforts to eliminate mercury manometers with a photonic based measurement based on ultra-precise measurements of gas refractive index. For vacuum measurements, this paper covers NIST efforts to develop a new a vacuum standard for measuring and understanding the pascal at the lowest pressures through the development of a cold atom vacuum standard. For temperature measurements, this paper covers NIST efforts to develop a method of measuring temperature using a photonic-based method.

The unifying theme is that all these efforts are aimed at the development of standards and sensors that are small, deployable, and based on fundamental physics, or are quantum-based. This has been embodied within the "NIST on a Chip" or NOAC program. The core the idea of NOAC is that quantum-based measurements are fundamental and when employed in sensors will not require re-calibration. In this embodiment, the standards lab, or in this case "NIST", is "on a chip" and is powerful to industry and society as it means that large networks sensors (or sensors "integrated" into a product or device) can be deployed and trusted to provide accurate measurements without costly re-calibration.

Pressure

Moving forward, the next generation of pressure standards will provide a new route of SI traceability for the pascal. By taking advantage of both the properties of light interacting with a gas and that the pressure dependent refractive index of helium can be precisely predicted from fundamental, first-principles quantum-chemistry calculations, a new route of realizing the pascal has been demonstrated.

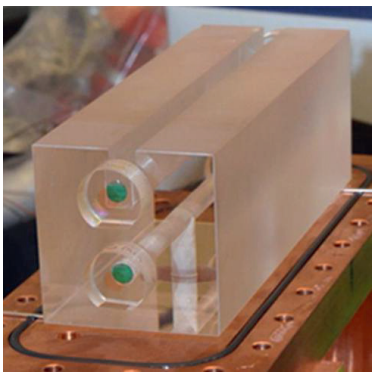

Figure 1: Fixed Length Optical Cavity (FLOC) will replace all mercury Manometers

DOI 10.5162/SMSI2021/PT7

This technique is very different from classical methods of realizing pressure that have served the metrology community well for the past 375 years. The new photonic-based pressure standards will enable the elimination of mercury manometers, replacing them with a smaller, lighter, faster, and higher precision standard. From a metrology standpoint, the new quantum-based SI pascal will move us from the classical force/area definition, to an energy density (joules per unit volume) definition. Should the technique be further miniaturized, it will lead to a revolution in pressure metrology, enabling a photonics-based device that serves both a gas pressure sensor and a portable gas pressure standard all in one. In the future, the mercury barometer will be replaced with a new standard based on quantum chemistry calculations.

The new method relies on a pair of optical cavities, each consisting of a set of mirrors on a spacer with the gas/vacuum filling the space between the mirrors. To improve upon this design, the reference cavity is always kept at vacuum to help eliminate noise and other systematic errors. This device, referred to as a Fixed Length Optical Cavity (FLOC), is shown in Figure 1. The FLOC is made out of a glass with Ultra-Low thermal Expansion (ULE) to prevent changes in interferometer length with temperature. The upper cavity consists of a slot to allow gas to easily flow in and out, whereas the reference cavity is a hole drilled through the glass block and sealed at either end via mirrors. [1-4]

Additionally, a vertical tube allows one to pump out the reference cavity through a vacuum pump. The glass cavity is placed inside a chamber to improve temperature stability and to ensure that the gas species is known, and therefore has a known refractivity. For gasses such as helium with simple electron structure and limited number of isotopes, the refractivity and density virial coefficients can be calculated through quantum mechanics [2]. This calculation can provide refractivity to an uncertainty better than 1 parts in 106. For other gasses, the values must be measured or will be calculated but with significantly larger uncertainties. Because the calculation of pressure is only dependant on refractivity and temperature, we can define the FLOC as a primary realization of pressure.

The FLOC is primary but does require corrections be carefully accounted for when making a high accuracy pressure measurement with the lowest possible uncertainties. The first correction is the distortion of the glass when pressure is applied. The glass experiences a bulk compression when forces to the outside surfaces occur. In addition to the bulk compression, the glass experiences a non-uniform bending due to the reference cavity being at a different pressure. While these distortion corrections are different for each glass cavity, the value can be determined experimentally and corrected with high accuracy. The second correction that must be accounted for is that helium can absorb into glass causing the glass to change its dimensions. By collection interferometer data the absorption can be traced over time and extrapolated back to zero, with high accuracy.

Overall a FLOC standard can achieve an uncertainty of 9 parts in 106 in nitrogen [4]. It is anticipated that a better determination of this index will soon allow this to be drastically reduced. Additionally, the best method to measure pressure distortions is to use several gasses of known refractive index at the same pressure. The distortions will be independent of gas species and can be solved to determine the magnitude of the error and even lower uncertainties. This means that as lower and lower uncertainty refractivity measurements are made by independent labs, the lower the uncertainty the FLOC method becomes world-wide. This is the power of quantum-based measurements.

Vacuum

For vacuum measurements, NIST efforts to develop a new vacuum standard for measuring and understanding the pascal at the lowest pressures is underway. To achieve this, the Cold- Atom Vacuum Standard (CAVS) has been developed which uses a cold atom trap to sense pressure. [5] Since the earliest days of neutral atom trapping, it has been known that the background gas in the vacuum limits the trap lifetime (the characteristic time that atoms remain trapped). NIST is inverting this problem to create a quantum-based standard and sensor.

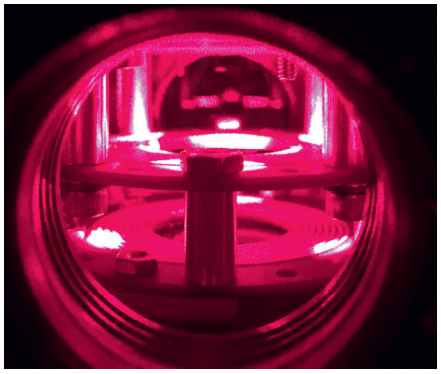

Figure 2: CAVS small portable version NIST prototype with a cloud of trapped Li atoms.

Because the measured loss-rate of ultra- cold atoms from the trap depends on a fundamental atomic property (the loss-rate coefficient, related to the thermalized cross section) such atoms can be used as an absolute sensor and primary vacuum standard. Researchers have often observed that the relationship between the trap lifetime and background gas can be an indication of the vacuum level, and several research groups have pursued using cold atom traps as vacuum sensors. [6,7] However, an absolute vacuum standard, sufficient for use as an international quality standard, has not yet been realized. To do this requires rigorous attention to all potential error sources, from both the atomic perspective and the vacuum perspective. Moreover, a primary CAVS requires the collision cross section between trapped ultra-cold atoms and the background gas to be traceable to an ab initio theoretical determination. NIST has built a laboratory-scale CAVS apparatus, developed the measurement scheme, and done preliminary theoretical calculations, all of which show promising early results. In addition, NIST is developing a small, portable version that uses a grating-based trap (shown in Figure 2) that will eventually enable users to realize and measure vacuum pressures in their lab without relying on calibrated sensor artifacts.

Temperature

For temperature measurements, NIST efforts to develop a method of measuring temperature using a photonic-based method are underway. Temperature measurements and sensors play a crucial role in various aspects of modern technology ranging from medicine and manufacturing process control, to environmental and oil-and-gas industry. Among various temperature measurement solutions, resistance-based thermometry is a time-tested method of disseminating temperature standards. [9]

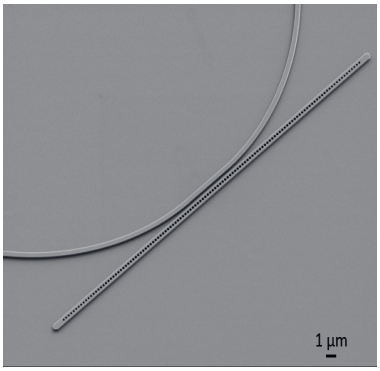

Figure 3. Silicon photonic crystal cavitythermometer fabricated at NIST

Although industrial resistance thermometers can routinely measure temperatures with uncertainties of 10 mK, their performance is sensitive to multiple environmental variables such as mechanical shock, thermal stress and humidity. These fundamental limitations of resistance thermometry, as well as the desire to reduce sensor ownership cost, have ignited a substantial interest in the development of alternative temperature measurement solutions such as photonics-based temperature sensors [10,11]. NIST is developing novel on-chip integrated silicon photonic temperature sensors with nanoscale footprint and ultra-high resolution as an alternative solution to legacy-based resistance thermometers. These sensors are Fabry-Perrot cavity type silicon photonic devices that are based on a Photonic Crystal nanobeam Cavity (PhCC), whose high-Q resonant frequency mode is highly sensitive to even ultra-small temperature variations. NIST has performed the first direct comparison of our photonic thermometers to Standard Platinum Resistance Thermometers, the best in class resistance temperature sensors used to disseminate the International Temperature Scale of 1990. The preliminary results indicate that our PhCC nanothermometers can detect changes of temperature as small as sub-10 µK and can achieve measurement capabilities that are on-par or even better than the state-of-the-art resistance thermometry.

References

[1] P. Egan, J. Stone, J. Hendricks, J. Ricker, G. Scace, G. Strouse, “Performance of a dual Fabry–Perot cavity refractometer,” Opt. Letters, Vol. 40, No. 17, August 2015

[2] M. Puchalski, K. Piszczatowski, J. Komasa, B. Jeziorski, K. Szalewicz, 2016, “Theoretical determination of the polarizability dispersion and the refractive index of helium,” Amer. Phys. Soc., Phys. Rev. A

[3] P. Egan, J. Stone, J. Ricker, J. Hendricks, 2016, “Metrology for comparison of displacements at the picometer level,” Amer. Inst. of Phys., Rev. of Sci. Inst. 87, 053113

[4] J. Stone, P. Egan. J. Hendricks, G. Strouse, D. Olson, J. Ricker, G. Scace, D. Gerty, 2015 “Metrology for comparison of displacements at the picometer level,” Key Eng. Mat. Vol. 625 p 79-84

[5] J. Scherschligt, J. A. Fedchak, D.S. Barker, S. Eckel, N. Klimov, C. Makrides, and E. Tiesinga, Metrologia 54, S125 (2017).

[6] D.E. Fagnan, J. Wang, C. Zhu, P. Djuricanin, B.G. Klappauf, J.L. Booth, and K.W. Madison, Phys. Rev. A - At. Mol. Opt. Phys. 80, 1 (2009).

[7] T. Arpornthip, C.A. Sackett, and K.J. Hughes, Phys. Rev. A - At. Mol. Opt. Phys. 85, 1 (2012).

[8] S. Eckel, D. Barker, J. Fedchak, N. Klimov, E. Norrgard and J. Scherschligt, Metrologia (submitted 2018).

[9] Strouse, NIST Spec. Publ. 250, 81 (2008).

[10] Kim et al., Opt. Express 18, 22215 (2010).

[11] Proceedings Volume 10923, Silicon Photonics XIV; 109230L (2019) https://doi.org/10.1117/12.2505898 Event: SPIE OPTO, 2019, San Francisco, California, United States

[12] Douglass, K.O. and D.A. Olson 2016 Towards a standard for the dynamic measurement of pressure based on laser absorption spectroscopy. Metrologia. 53(3): p. S96-S106.

[13] Ahmed, Z., D. Olson, and K.O. Douglass 2016 Precision Spectroscopy to Enable Traceable Dynamic Measurements of Pressure. CLEO: p. ATu1J.1.

[14] Hanson, E., et al. 2018 Towards traceable transient pressure metrology. Metrologia.

Plenary Talk
DOI 10.5162/SMSI2021/PT9

A white paper on quantum sensing with spins in diamond

Patrick Maletinsky[1], Gediminas Seniutinas[2], Mathieu Munsch[2]
[1]Department of Physics, University of Basel, Klingelbergstrasse 82, Basel CH-4056, Switzerland,
[2]Qnami AG, Hofackerstrasse 40B, CH-4132 Muttenz, Switzerland
patrick.maletinsky@unibas.ch

Summary:
We provide a high-level description of the emerging field of quantum sensing and magnetic imaging with "Nitrogen-Vacancy" (NV) electronic spins in diamond. This field has seen remarkable growth since its inception in 2008, and today forms one of the cornerstones of the "2nd quantum revolution", where control over single quantum entities is exploited to gain technological advantages. Nanoscale NV-based quantum sensors already led to key scientific discoveries and form a mature technology, which today is brought to the market by Qnami – a start-up company who co-authored this article.

Keywords: Quantum-sensing, Nanotechnology, Imaging, Spins, Diamond

As the old proverb says, "seeing is believing". Unfortunately, our eyes only capture a fraction of the surrounding world. Magnetism is one of these hidden domains. Despite magnetic fields being everywhere, from the one generated by the Earth and surrounding us, to the tiny ones within the molecules of our body, they remain invisible to human sight. Over the years, however, the development of sensing techniques allowing the observation, understanding and control of magnetism have led to a series of revolutions from the first compass used for navigation to the MRI scanner used every day in our hospitals. Yet, classical technologies are now reaching their limits

Measuring minute magnetic fields with NV centres in diamond

Quantum sensors, which leverage the extreme sensitivity of quantum systems to their environment, offer radically new performance. Their ability to measure weak signals down to the single molecule level unlock new perspectives in early-stage diagnostics, in the development of novel energy-efficient electronics circuits as well as in security. Among the existing technological platforms, quantum sensors based on so-called NV centres (or nitrogen-vacancy centres) in diamond stand out.

Diamond is a wonder material on many fronts. It is robust, inert and bio-compatible, allowing for nonperturbing measurement in the most challenging environments. Ultra-high-quality diamond is produced industrially while microfabrication processes allow to functionalize and cut the diamond with the same techniques as in the silicon industry. Diamond is also the perfect material for a quantum sensor. The diamonds used for quantum applications contain defects in their crystal lattice, where two carbon atoms have been swapped for a nitrogen atom and a vacant site immediately alongside. These defects are known as nitrogen-vacancy centres (NV centres) and can also occur in natural diamonds, where they impart a reddish colour to the precious stones (see Fig.2a and 2b). By trapping one extra electron, NV centres can be turned into a microscopic compass - a spin - with atomic size. Through precise manipulation and measurement of the state of this NV spin, one can measure the smallest changes in the surrounding magnetic field, a technique called NV magnetometry.

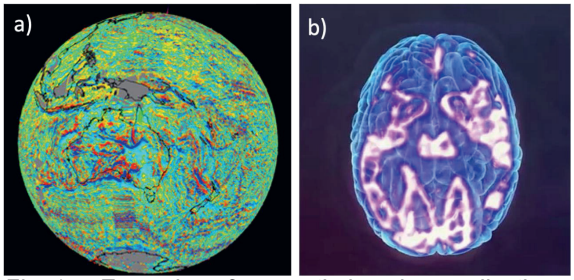

Fig. 1. Examples of magnetic imaging applications. a) Magnetic fields at the surface of the Earth (Credits Earth Bytes). b) Brain activity revealed by magnetic resonance imaging (MRI)

NV magnetometry: how it works

NV magnetometry relies on the interaction between the NV centre and the surrounding magnetic field. The presence of a magnetic field manifests by a modification of the energies of the NV centre spin states. Typical data from an NV magnetometer is shown in Fig.2c. The effect of the magnetic field is readily seen in the

DOI 10.5162/SMSI2021/PT9

modification of the NV centre microwave excitation spectrum. A crucial advantage of NV magnetometry comes from the well understood behaviour of the NV centre spin transition frequencies, which provide unambiguous information about the strength and the direction of the magnetic field. This ability to provide self-calibrated, quantitative data, combined with a very high reproducibility (each and every NV centre is the same) are key intrinsic features of NV-based quantum sensors.

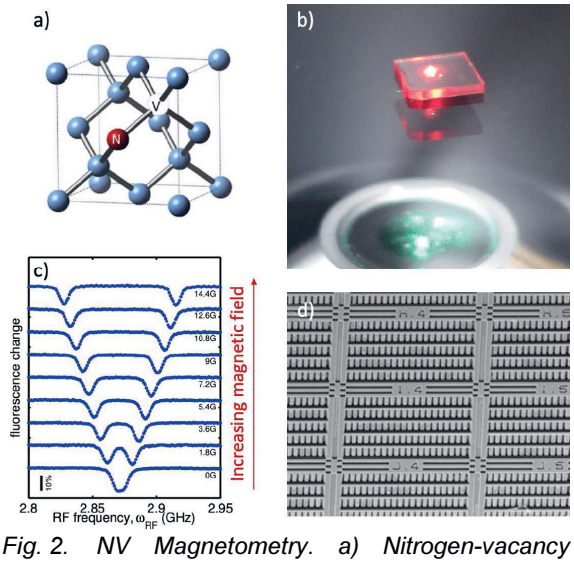

Fig. 2. NV Magnetometry. a) Nitrogen-vacancy centre in the diamond crystal. b) A diamond crystal (top) emits red light upon illumination with a green laser (bottom), the signature of NV centres in the crystal (Credits Hatano-Iwasaki Lab, Tokyo Institute of Technology) c) ODMR spectra as a function of the external magnetic field d) NV diamond by Qnami. The surface has been engineered into an array of scanning probes in a way to maximize light extraction while preserving the quantum coherence of the embedded NV centres. Both aspects contribute to a high sensitivity.

But the principal advantage of quantum sensors lies in their sensitivity to very small signals. Specifically, the sensitivity of an NV magnetometer to DC magnetic fields depends on 1) the density of NV centres within the diamond chip, 2) the quantum coherence of said NVs, and 3) the efficiency of the optical read-out. Theoretical sensitivities range from one micro Tesla per second integration time for single NV centres (used in high spatial resolution applications) down to a few pico-Tesla for dense NV ensembles. In practice though, reaching this level of performance can prove challenging. Indeed, the quantum coherence is a fragile property which is easily damaged when increasing the NV centre density or when engineering the diamond crystal itself. Using microfabrication techniques inspired by the silicon industry, the startup company Qnami (www.qnami.ch) has developed proprietary processes to produce advanced NV diamond chips which leaves their quantum properties intact (see Fig.2d).

The ability to measure small magnetic fields is key for a large variety of applications going from navigation to diagnostics, to electronics. For instance, NV sensors are being developed for navigation, where they allow for a reliable positioning on the surface of the Earth, similar to the GPS, but with the advantage of being free of any requirement of communication with an external device (like a satellite). Such navigation systems are not only of great importance for defence, but could also apply in the context of autonomous vehicles, as a safety back up for the cases of failing GPS connections. In healthcare, NV sensors are being developed to enable the detection of ultra-low concentrations of target biomarkers, removing the need for large test samples and offering new perspective in early diagnostics. Finally, in electronics NV sensors can be applied in quality control of integrated circuits. There, the measurement of magnetic field patterns allows tracing electrical currents in a microchip and potentially identifying manufacturing defects or deviations from the intended design.

The requirements on the NV sensors may vary depending on their use but such magnetometers always comprise the following core components:

- an NV diamond chip
- an optical excitation source (typically a green laser diode),
- a high sensitivity optical detector (typically a single photon counter),
- a tuneable microwave source (2.5-3.5GHz range).

Depending on the application, these elements can either be integrated around the diamond chip to make a compact sensor or left as separate components of a larger system. While the former option is well suited for the mobile measurement of weak, diffuse signals, the latter is favoured for the study of small signals with microscopic origin. In practice – and this represents an additional key feature of NV sensors – the atomic size of the NV centre offers the possibility to produce magnetic maps with nanometre spatial resolution. But such applications face a further challenge: the necessity to bring the NV sensors in extremely close proximity to the magnetic source.

DOI 10.5162/SMSI2021/PT9

Nanoscale NV magnetometry

In a similar way to classical magnetic field sensors, which are moved around the Earth by satellites and airplanes in order to map the Earth's magnetic field (see Fig.1), quantum sensors can be precisely maneuverer over tiny magnetic structures to map and visualize magnetic properties with nanoscale spatial resolution. This is achieved through a technique called Scanning NV Magnetometry.

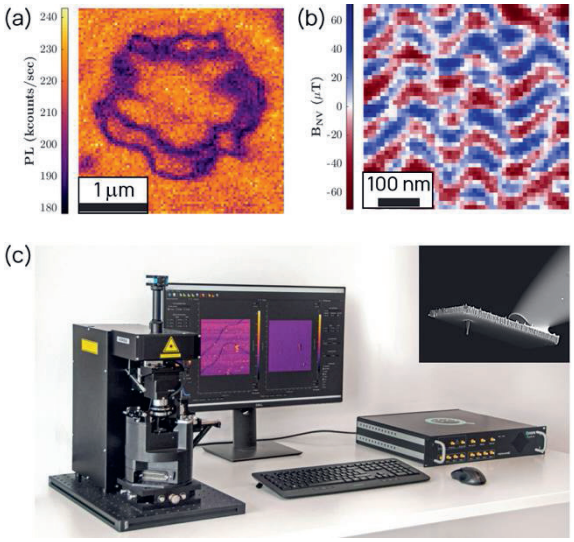

Fig. 3. Scanning NV Magnetometry. a) and b) show imaging examples of nanoscale magnetic images of state-of-the-art magnetic materials: "a synthetic antiferromagnet" in a and multiferroic $BiFeO_3$ film in b). These data were obtained using the Qnami ProteusQ (c), the first commercial scanning NV magnetometer, developed by Qnami in partnership with Horiba Scientific. The inset shows a scanning electron microscope image of an all-diamond scanning probe containing a single spin at the apex of its tip. For scale, the cantilever has a width of 2µm.

Scanning NV magnetometry relies on the use of a sharp, microscopic NV diamond tip, which is scanned at a controlled distance of just a few nanometre from a sample. As the tip flies over the surface, both the sample's topography and its magnetic textures are recorded, producing unique images in nanoscale resolution.

In order to provide the best spatial resolution, the NV centre is brought in very close proximity to the tip apex. Indeed, while the tip's radius of curvature determines the lateral resolution for the topography image, the distance between the NV centre and the sample surface determines the lateral resolution for the magnetic image. The patented Quantilever MX design from Qnami, brings the NV centre as close as ten nanometres away from the tip apex, offering the highest spatial resolution amongst all existing magnetometers. Remarkably, the Quantilever MX design simultaneously ensures an efficient routing of the NV optical signal, thereby maximizing sensitivity and overall performance.

Figure 3 illustrates the outstanding performance of scanning NV magnetometry. The images reveal the magnetic textures at the surface of a very special class of magnets known as antiferromagnets, whose peculiar properties have generated strong interest for the next generation of low-power electronic devices. Yet, despite the craze around such materials, the direct observation of their magnetic properties has remained a challenge, possible only with large scale instruments such as synchrotron light sources. Here, the data have been recorded using the Qnami ProteusQ, a complete quantum microscope and the first commercially available Scanning NV Magnetometer. This table-top system was developed by Qnami in partnership with Horiba Scientific. Compared to the previously available approach for nanoscale studies of antiferromagnets, which was based on synchrotron light sources, the Qnami ProteusQ offers simple operation, fast sample turnaround times, easy integration of Quantilevers as well as a leap in precision, through a 10x improvement in spatial resolution.

These features are key for the study of a new generation of advanced materials for spintronics applications, including ultra-thin ferromagnets, antiferromagnets, multiferroics, 2D materials and more. In addition, beyond the fundamental study of such materials, the on-going development of MRAM technology is shining light on the needs of the semiconductor industry to access new metrology tools and standards. While magnetic properties of materials have been largely ignored for electronic devices, the electronics of tomorrow is taking a new spin, and NV magnetometry will make decisive contribution.

References

Excellent reviews that discuss further aspects of NV based quantum sensors and magnetometry include the following

[1] John F. Barry, Jennifer M. Schloss, Erik Bauch, Matthew J. Turner, Connor A. Hart, Linh M. Pham, and Ronald L. Walsworth Sensitivity optimization for NV-diamond magnetometry, *Rev. Mod. Phys.* 92, 015004

[2] Francesco Casola, Toeno van der Sar, and Amir Yacoby Probing condensed matter physics with magnetometry based on nitrogen-vacancy centres in diamond, *Nature Reviews Materials* 3, 17088

Pillar

Sensors and Instrumentation

DOI 10.5162/SMSI2021/A1.1

Catangasite: piezoelectric single crystal for sensor applications at harsh conditions.

A.Sotnikov[1], R.Weser[1], B.P.Sorokin[2], Yu.Suhak[3], H. Fritze[3], M.Weihnacht[4], H.Schmidt[1]
[1]Leibniz IFW Dresden, SAWLab Saxony, Helmholtzstr. 20, 01069 Dresden, Germany
[2]Technological Institute for Superhard and Novel Carbon Materials, Tsentral'naya 7a, 108840 Troitsk, Moscow, Russia
[3]Institute of Energy Research and Physical Technologies, Clausthal University of Technology, Am Stollen 19 B, 38640 Goslar, Germany
[4]InnoXacs, Am Muehlfeld 34, 01744 Dippoldiswalde, Germany
h.schmidt@ifw-dresden.de

Summary:
Material parameters of catangasite (CTGS) piezoelectric single crystal are derived in extremely wide temperature range from 4.2 to 1173 K. A temperature sensor on the base of Y-cut CTGS SAW resonator is demonstrated.

Keywords: piezoelectric crystal, catangasite, langasite family, BAW, SAW, HBAR, temperature sensors.

Introduction

Piezoelectric single crystals are key materials for microacoustic devices and sensors of various physical quantities. Of particular interest are crystals which possess a reasonable piezoelectric response over an extremely wide temperature range from cryogenic to very high temperatures (1000°C and higher). Materials for use under these harsh conditions should maintain their material parameters over the entire operating temperature range. Among potential canidates, piezoelectric crystals of the langasite (LGS, $La_3Ga_5SiO_{14}$) family are very promising. For example, catangasite (CTGS, $Ca_3TaGa_3Si_2O_{14}$) crystal with ordered structure, demonstrates a combination of very attractive properties like relatively high piezoelectric coefficients, moderate dielectric constants, low acoustic loss and the absence of a structural phase transition up to the melting point of about 1450° C. In this communication, we present CTGS material parameters measured at 4.2 and 1173 K, an estimation of sound attenuation and viscosity tensor components including measurements in the GHz range as well as the characteristics of a SAW temperature sensor based on Y-cut CTGS crystal.

Crystal growth and sample preparation

CTGS single crystals were grown by FOMOS Materials (Moscow, Russia) and Leibniz IKZ (Berlin, Germany) using the Czochralski technique. For the ultrasonic wave velocity and attenuation measurements, cube-like samples and plates of different crystallographic orientation were prepared. For GHz frequencies, AlScN thin film piezoelectric transducers were deposited on the samples to realize High overtone Bulk Acoustic Resonators (HBAR). Finally, a demonstrator of SAW-based temperature sensor was realized by a one-port resonator chip comprising CTGS Y-cut crystal and advanced temperature stable electrodes on top.

Experimental procedure

Measurements of the bulk acoustic wave velocities propagating along certain directions were carried out by means of RITEC RAM-5000 and UT340 ultrasonic systems. Results at GHz frequencies were obtained using Agilent E5071C Network Analyzer. All temperature measurements were carried out using a continuous flow cryostat, a Carbolite tube furnace and a Linkam HFS600E temperature stage, respectively.

Results and discussion

The elastic C_{ij} and piezoelectric e_{ij} constants were derived using a system of relations between bulk velocities of different modes propagating along certain crystallographic directions considering dielectric constant ε_{ij} measured separately. As a result, elastic, piezoelectric and dielectric constants of CTGS single crystal at 4.2 K [1] and 1173 K are presented in Tab.1. Notice strong piezoelectric response of the crystal in a very wide temperature range including both cryogenic and high temperatures. Sound attenuation in GHz range is an important

parameter, especially for SAW sensors usually operating at microwave frequencies.

Tab. 1: Material parameters of CTGS single crystal at 4.2 and 1173 K.

Material constant	4.2 K	1173 K
C_{11} (GPa)	159.8	136.2
C_{12} (GPa)	83.15	57.9
C_{13} (GPa)	70.6	68.5
C_{14} (GPa)	1.2	0.52
C_{33} (GPa)	218.3	180.7
C_{44} (GPa)	39.02	42.9
C_{66} (GPa)	38.3	39.15
e_{11} (C/m^2)	-0.36	-0.435
e_{14} (C/m^2)	0.62	0.646
$\varepsilon_{11}/\varepsilon_0$	19.7	17.2
$\varepsilon_{33}/\varepsilon_0$	34.4	22.9

Fig. 1 shows as an example obtained attenuation coefficient α as a function of frequency for longitudinal mode on Y+45°-cut CTGS measured at room temperature.

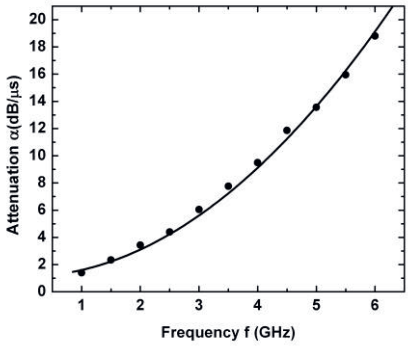

Fig. 1. Sound attenuation versus frequency for Y+45°-cut CTGS (Quasi-Longitudinal mode). Symbols: experiment, solid line: function ~ f² for comparison.

Note the well-defined square dependence of the attenuation versus frequency, which is also valid for X, Y, Z and Y-45° crystal cuts. Using the measured attenuation coefficients and elastic constants, the components of the dynamic viscosity tensor were derived in the 1-6 GHz frequency range. As for sound attenuation versus temperature, it was found to be low at 4.2 K while still reasonable at 1195 K. Fig. 2 shows as an example ultrasonic pulse-echo patterns for Y-cut CTGS at 298 and 1195 K, resp. The results were obtained using the intrinsic piezoelectric effect of the crystal for excitation and short (5 ns) ultrasonic pulses.

The temperature dependence of the resonance frequency of a SAW one-port resonator operated as temperature sensor in the range between 25°C and 600°C is depicted in Fig. 3. Note the very linear resonance frequency shift of the SAW device vs. temperature.

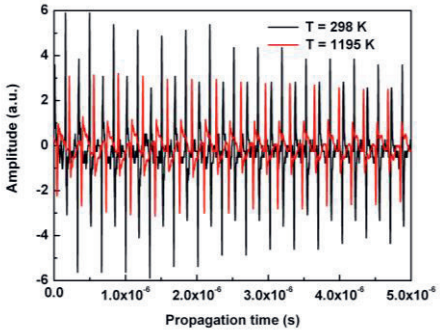

Fig. 2. Pulse-echo pattern for Y-cut CTGS single crystal at 298 K (black line) and 1195 K (red line).

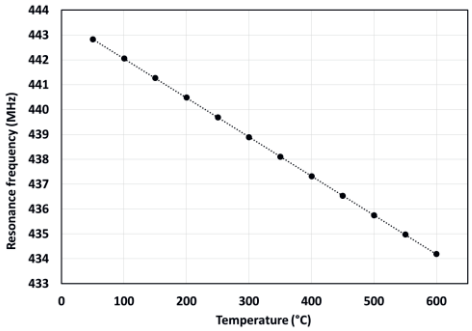

Fig. 3. Resonance frequency vs. temperature for SAW one-port resonator as temperature sensor.

Conclusion

Material parameters of CTGS single crystals were derived over extremely wide temperature range. Strong piezoelectric response as well as reasonable sound attenuation even in GHz frequency range predestine catangasite crystal as promising material for acoustic sensors capable of operating in a very wide temperature range. Temperature sensor behavior on the base of Y-cut CTGS SAW resonator was successfully demonstrated.

Acknowledgements

Financial support from the German Research Foundation (DFG grants SO 1085/2-2 and FR 1301/21-2) are gratefully acknowledged.

References

[1] A. Sotnikov, H. Schmidt, M.H. Haghighi, M. Gorev, Yu. Suhak, H. Fritze, S. Sakharov, Material parameters of $Ca_3TaGa_3Si_2O_{14}$ (CTGS) piezoelectric single crystal at extreme temperatures, *Proc. Joint Conf. Europ. Freq. and Time Forum and IEEE Int. Freq. Contr. Symp.,* 193-197 (2017); doi: 10.1109/FCS.2017.8088844.

DOI 10.5162/SMSI2021/A1.2

Oxygen Partial Pressure Dependent Electrical Conductivity of $LiNb_{1-x}Ta_xO_3$ Solid Solutions

Yuriy Suhak[1], Ahsanul Kabir[1], Dmitry Roshchupkin[2], Boris Red'kin[2], Steffen Ganschow[3], and Holger Fritze[1]
[1] Institute of Energy Research and Physical Technologies, Clausthal University of Technology, Am Stollen 19 B, 38640 Goslar, Germany
[2] Institute of Microelectronics Technology and High Purity Materials, Russian Academy of Science, Chernogolovka, Moscow District, 142432, Russia
[3] Leibniz-Institut für Kristallzüchtung, Max-Born-Str. 2, 12489, Berlin, Germany
ahsanul.kabir@tu-clausthal.de

Summary:
The electrical conductivity is investigated for piezoelectric single crystals of congruent lithium niobite ($LiNbO_3$, LN), lithium tantalate ($LiTaO_3$, LT), and their solid solutions ($LiNb_{1-x}Ta_xO_3$, LNT) at varying oxygen partial pressure in the range of 0.2-10^{-15} bar at a constant temperature of 900 °C. These crystals have been grown by the Czochralski and micro-pulling down method. At sufficiently low oxygen partial pressure, the LN sample demonstrates about two orders of magnitude larger electrical conductivity than LT. Such an outcome indicates a dominant n-type conductivity in the former. Moreover, the increase of the Nb/Ta ratio shows a tendency to decrease conductivity for LNT.

Keywords: piezoelectric single crystal, lithium niobate-tantalate solid solutions, electrical conductivity, high temperature

Background, Motivation, and Objective

High temperatures sensors and actuators enable a wide range of advanced technological applications in aerospace, automobile, energy conversion, and beyond [1,2]. Considering materials potentially suited for the above-mentioned devices, piezoelectric single crystals with large electromechanical coupling factors, high melting/phase transition temperatures, and cost-effective growth methods are essential [3,4]. However, state-of-the-art material such as quartz (α-SiO_2) is thermally unstable, showing a phase transition (α→β) at around 570 °C. In contrast, the family of langasite crystal displays no phase transformation up to the melting point (~1400 °C), but they possess a relatively low piezoelectric coefficient [2]. The ferroelectric lithium niobate (LN) and lithium tantalate (LT) have attracted significant interest because of their excellent dielectric, electro-optic, electro-acoustic, photoelectric, and piezoelectric properties [5]. Nevertheless, the high-temperature performance of these materials is restricted by thermo-chemical instability of LN and low curie temperature of LT. Meanwhile, few publications [6,7] and our preliminary work indicate that the properties of $LiNb_{1-x}Ta_xO_3$ (LNT) solid solutions can be tailored which includes refractive index, electroacoustic and electrooptic properties, melting point and curie temperature. In the current work, we investigate the oxygen partial pressure (pO_2) dependent high-temperature electrical properties of LN and LT crystals prepared by two different methods. Additionally, such experiments are also performed with LNT with different Nb/Ta ratios.

Description of the Method

The crystals investigated in this experiment were produced by the Czocharalski (CZ) and micro-pulling down (μ-PD) technique at the Institute of Microelectronics Technology and High Purity Materials (Russia) and at the Leibniz Institute for Crystal Growth (Berlin), respectively. The CZ crystals were then cut into a disc-shaped dimension (diameter 10 mm and thickness 1 mm) with a Z-cut orientation and polished. The μ-PD crystals were grown along Z-axis with about 15 mm in length and 1 mm in diameter. The samples were partially coated with Pt paste via screen printing and thermally treated at 1000 °C for 30 min. The electrical properties were measured by electrochemical AC impedance spectroscopy (Solartron 1260, UK) in a wide frequency range (10^6-10^0 Hz) under an alternative of bias of 100 mV at 900 °C and changing oxygen partial pressure (10^0-10^{-15} bar). The data were fitted using an equivalent circuit model consisting of a bulk resistor connected in parallel with a constant phase element. The conductivity was estimated using the equation, $\sigma = L/RA$ where R is the bulk resistance, A the electrode area, and L the sample thickness.

Results

The bulk electrical conductivity of LN and LT samples is represented in Fig. 1 as a function of pO_2 at 900 °C. As can be seen, the sample manufactured by the µ-PD method shows a higher electrical conductivity than the CZ sample. Such an outcome is expected due to a relatively high impurity content caused by rapid cooling during the µ-PD process. The latter prevents segregation and, thereby, lowering of impurity concentrations as expected for CZ growth. Further, LN possesses noticeably larger conductivity than LT, especially at low pO_2. For LT, the conductivity remains pO_2 independent down to 10^{-9} bar and increases slightly for increasingly reducing atmosphere. In contrast, a strong pO_2 dependent conductivity is observed for LN below about 10^{-3} bar, suggesting the LN system has a lower reduction enthalpy than LT. In general, the enhancement of the conductivity is typical for a mixed ionic-electronic conductor which exhibits an increasing electronic (n-type) conductivity as the pO_2 reduces [4,8].

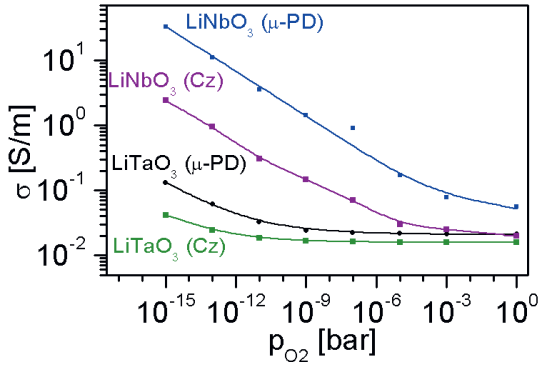

Fig. 1. Bulk electrical conductivity of LN and LT crystals grown by Czocharalski and micro-pulling down technique for varying oxygen partial pressure, measured at 900 °C.

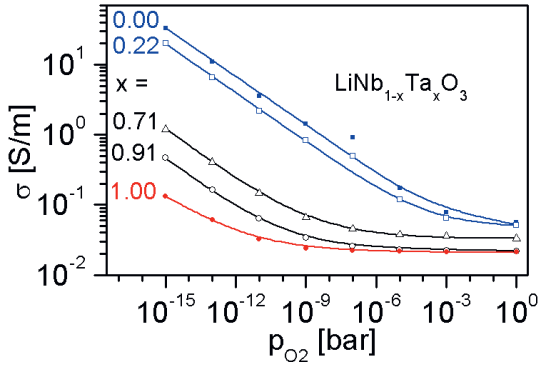

Fig. 2. Bulk electrical conductivity of LNT compounds with different Nb/Ta ratios prepared via micro-pulling down technique as a function of oxygen partial pressure, measured at 900 °C.

Fig. 2 illustrates the pO_2-dependent bulk electrical conductivity of LNT for different Nb/Ta ratios. The Nb-rich composition shows an identical reduction tendency to pure LN. The electrical conductivity is progressively dropped with increasing Nb/Ta ratio, and expectedly, the Ta-rich sample shows largely suppression of reduction like LT.

Conclusions

In summary, the electrical conductivity of LN, LT, and LNT solid solution was examined at a constant temperature of 900 °C with regards to different oxygen partial pressures. The outcome reveals a significant rise in conductivity for the LN sample than the LT at a low-oxygen partial pressure. The electrical conductivity can be tuned by the Nb/Ta ratio.

References

[1] R. C. Turner, P. A. Fuierer, R. E. Newnham, and T. R. Shrout, “Materials for high temperature acoustic and vibration sensors: A review,” *Appl. Acoust.*, vol. 41, no. 4, pp. 299–324, 1994, doi: 10.1016/0003-682X(94)90091-4.

[2] H. Fritze, “High-temperature piezoelectric crystals and devices,” *J. Electroceramics*, vol. 26, no. 1–4, pp. 122–161, Jun. 2011, doi: 10.1007/s10832-011-9639-6.

[3] H. Fritze, “High-temperature bulk acoustic wave sensors,” *Measurement Science and Technology*, vol. 22, no. 1. 2011, doi: 10.1088/0957-0233/22/1/012002.

[4] H. Seh and H. L. Tuller, “Defects and transport in langasite I: Acceptor-doped ($La_3Ga_5SiO_{14}$),” *J. Electroceramics*, vol. 16, no. 2, pp. 115–125, Mar. 2006, doi: 10.1007/s10832-006-4081-x.

[5] V. Y. Shur, “Lithium niobate and lithium tantalate-based piezoelectric materials,” in *Advanced Piezoelectric Materials: Science and Technology*, Elsevier, 2010, pp. 204–238.

[6] V. Bermúdez, C. Aragó, R. Fernández-Ruiz, and E. Diéguez, “Evolution of the structural properties in ferroelectric $LiNb_{1-x}Ta_xO_3$ compound with variation in Ta composition,” *Ferroelectrics*, vol. 304, pp. 159–162, 2004, doi: 10.1080/00150190490457852.

[7] I. G. Wood, P. Daniels, R. H. Brown, and A. M. Glazer, “Optical birefringence study of the ferroelectric phase transition in lithium niobate tantalate mixed crystals: $LiNb_{1-x}Ta_xO_3$,” *J. Phys. Condens. Matter*, vol. 20, no. 23, 2008, doi: 10.1088/0953-8984/20/23/235237.

[8] D. M. Smyth, “Defects and transport in $LiNbO_3$,” *Ferroelectrics*, 1983, doi: 10.1080/00150198308014437.

DOI 10.5162/SMSI2021/A1.3

Obtaining and investigation of the $LiNbO_3$, $LiNbO_3$:Mg, $LiTaO_3$ nanopowders doped with Pr ions

L. Vasylechko[1], V. Sydorchuk[2], S. Hurskyj[1], U. Yakhnevych[1], A. Lakhnik[3], I. I. Syvorotka[4], A. Luchechko[5], O. Buryy[1], D. Sugak[1,4], Ya. Zhydachevskyy[1,6], A. Suchocki[6], Yu. Suhak[7], H. Fritze[7]

[1] Lviv Polytechnic National University, 12 Bandera st., Lviv, Ukraine.
[2] Institute for Sorption and Problems of Endoecology, NASU, 13 Gen. Naumov st., Kyiv, Ukraine
[3] G.V.Kurdyumov Institute of Metal Physics NASU, 36 Acad. Vernadsky Bvd., Kyiv, Ukraine
[4] Scientific Research Company 'Electron-Carat', 202 Stryjska st., Lviv, Ukraine
[5] Ivan Franko National University of Lviv, 107 Tarnavskogo Str.,79017 Lviv, Ukraine
[6] Institute of Physics PAS, 32/46 Al. Lotnikow, Warsaw, Poland
[7] Clausthal University of Technology, 19B Am Stollen, Goslar, Germany
Corresponding Author's e-mail address: yakhnevych.u@gmail.com

Summary:

The samples of $LiNbO_3$:Pr, $LiNbO_3$:Mg,Pr, $LiTaO_3$:Pr nanopowders were obtained by the high-energy ball milling with subsequent annealing. Pellets were prepared from nanopowders by pressing for further investigation. The photoluminescence properties were studied using the SOLAR CM 2203 spectrofluorometer. The luminescence spectra of obtained samples in the red region of the spectrum in shape and spectral position coincide with the data for LN:Pr and LT:Pr single crystals and micropowders.

Keywords: lithium niobate, lithium tantalate, Pr ions, nanopowders, photoluminescence

Introduction

Lithium niobate ($LiNbO_3$, LN) and lithium tantalate ($LiTaO_3$, LT) single crystals doped by Pr ions have been attracting the attention of researchers since the 1990s [1, 2]. The reason for this is great interest in using of extraordinary physicochemical properties of LN and LT crystals in order to create multifunctional active elements for optoelectronic devices and sensors. In this context the results of recent years concerning the phenomenon of piezoluminescence in LN:Pr and LT:Pr are of particular interest to create, for example, a pressure sensors [3, 4]. It was found that the most intense mechano- and photoluminescence is observed in stoichiometric LN:Pr and LT:Pr samples. Also, attention was paid to the study of LN crystals, simultaneously doped by Pr and Mg [5]. Note that the investigation of the optical properties and photoluminescence of LN:Pr and LT:Pr was usually performed on single crystals of congruent composition grown by the Czochralski method. Whereas , the study of the mechano-luminescent properties of LN:Pr and LT:Pr was performed on samples of micropowders obtained by solid-phase synthesis from a mixture of the corresponding starting oxides and lithium carbonate. The current work focuses on obtaining of $LiNbO_3$, $LiNbO_3$:Mg, $LiTaO_3$ nanopowders doped with Pr^{3+} ions by high energy ball milling and subsequent studies of luminescent properties of ceramic samples made from these powders.

Experimental details

Based on the results of [6] nanopowders with nominal compositions $Li_{0,98}Pr_{0,02}NbO_3$ (denoted as LN:Pr), $Li_{0,93}Mg_{0,05}Pr_{0,02}NbO_3$ (LN:Mg,Pr), $Li_{0,98}Pr_{0,02}TaO_3$ (LT:Pr) were obtained by high-energy ball milling of the corresponding powders mixtures (Li_2CO_3, Nb_2O_5, Ta_2O_5, MgO, Pr_6O_{11}) taken in molar ratios corresponding to stoichiometric compositions. The milling was carried out by using of the planetary ball mill of Pulverisette-7 type (Fritsch, Germany). The rotation speed was equal to 600 rpm, and the duration of milling was about 15 h. The precursors obtained after milling were annealed in air at 700°C for 5 h. The control of structural parameters of nanopowders was performed by the XRD method on a DRON-3 diffractometer with the subsequent refinement of the x-ray patterns by the Rietveld method. Pellets with 6 mm diameter and 1.2 mm thickness were prepared from nanopowders by pressing. The pressure was about 190 MPa. It should be

noted that two types of samples were made: three pellets with different composition (see above) were pressed under an applied electric field (voltage of 1 kV) with simultaneous heating to about 200 °C; another three samples were pressed without the applied electric field at room temperature. Subsequently all the obtained pellets were annealed in air at 600°C for 6 h. The photoluminescence (PL) and photoluminescence excitation (PLE) spectra were studied using the SOLAR CM 2203 spectrofluorometer.

Results

XRD analysis of nanopowders showed that they all contain only one phase, which corresponds to the $LiNbO_3$ structure. According to XRD data the particle size was estimated to be about 20…80 nm. Similarly to [3, 4] the luminescent studies were performed in the red region of the spectrum. The excitation wavelength was 270 (LN) and 250 (LT) nm. All samples exhibited the emission band with a maximum of about 620 nm (Fig. 1) attributed to the $^1D_2 \rightarrow {}^3H_4$ transition of Pr^{3+} [1].

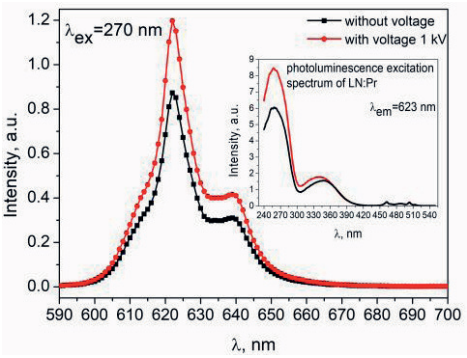

Fig. 1. The PL and PLE spectra of $LiNbO_3$:Pr

The most intense PL is observed in the LN:Pr samples (Fig. 1). Monitoring the 623 nm emission demonstrated that the excitation spectra were dominated by two broad UV bands centered at 258 and 345 nm (inset in Fig.1). Similar spectra of PL and its excitation were observed for both studied LN:Mg,Pr samples. The relative intensity of the PL was almost 10 times lower than that of the LN:Pr. There is a certain difference in the position of the UV excitation bands of red luminescence, namely, their maxima are shifted towards longer wavelengths compared to LN:Pr. In contrast to LN:Pr, in LT:Pr samples "red" luminescence has lower intensity, and its excitation bands at 240 nm and 290 nm are shifted towards shorter wavelengths (Fig. 2). Note that red luminescence in all samples is also excited in the processes of f-f transitions in Pr^{3+} ions, but the efficiency of such excitation is much lower than in the f-d transitions.

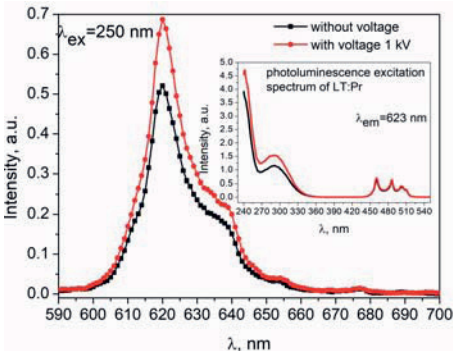

Fig. 2. The PL and PLE of $LiTaO_3$:Pr

Also, an important result is that the luminescence of Pr^{3+} and its excitation in the UV region are more intense in the samples, which were pressed with under applied field and temperature.

Conclusions

The single-phase nanopowders with nominal compositions $Li_{0.98}Pr_{0.02}NbO_3$, $Li_{0.98}Pr_{0.02}TaO_3$ and $Li_{0.93}Mg_{0.05}Pr_{0.02}NbO_3$ were obtained by the high-energy ball milling with subsequent annealing. The method of sample preparation significantly affects the results. The samples pressed under the voltage demonstrate higher relative photoluminescence intensity. One of the reasons for this may be the higher ordering of nanoparticles of ferroelectrics in the electric field.

Acknowledgements. The work is carried out in the frames of the joint German-Ukrainian project (M/48-2020) and partially supported by the grant No. 2019/33/B/ST8/02142 of the Polish National Science Center

References

[1] A. Lorenze, L. E. Bausa, J. Garcia Sole, Optical spectroscopy of Pr^{3+} ions in $LiNbO_3$, *Phys. Rev. B* 51, 16643-16650 (1995); doi: 10.1103/PhysRevB.51.16643

[2] W. Ryba-Romanowski, I. Sokólska, S. Gołab, T. Łukasiewicz, Photoluminescence of $LiTaO_3$:Pr, *Applied Phys. Lett.* 70, 686-687 (1997); doi: 10.1063/1.118899

[3] S. Lin, C. Xiong, D. Ma, H. Li, S. Long, B. Wang, Persistent luminescence found in Mg^{2+} and Pr^{3+} co-doped $LiNbO_3$ single crystal, *J. Materials Chemistry C* 6, 10067-10072 (2018); doi: 10.1039/C8TC03783C

[4] D. Tu, C.-N. Xu, A. Yoshida, M. Fujihala, J. Hirotsu, X.-G. Zheng, $LiNbO_3$:Pr^{3+}: A multipiezo material with simultaneous piezoelectricity and sensitive piezoluminescence, *Adv. Mater.* 1606914(1)-1606914(4) (2017); doi: 10.1002/adma.201606914

[5] G. Qiu, H. Ye, X. Wang, H. Fang, Y. Li, X. Yao, Intense piezoluminescence in $LiTaO_3$ phosphors doped with Pr^{3+} ions, *Ceramics International*. 45, 8553-8560 (2019); doi: 10.1016/J.CERAMINT.2019.01.173

[6] S. Khalameida, V. Sydorchuk, R. Leboda, J. Skubiszewska-Zięba, V. Zazhigalov, Preparation of nano-dispersed lithium niobate by mechanochemical route, *J Therm. Anal. Calorim.*, 115, 579-586 (2014); doi: 10.1007/s10973-013-3343-5

DOI 10.5162/SMSI2021/A1.4

Electrical and Electromechanical Properties of Single Crystalline Li(Nb,Ta)O_3 Solid Solutions up to 700 °C

Yuriy Suhak[1], Bujar Jerliu[1], Steffen Ganschow[2], Dmitry Roshchupkin[3], Boris Red'kin[3], Simone Sanna[4], Holger Fritze[1]
[1] Clausthal University of Technology, Am Stollen 19B, 38640, Goslar, Germany.
[2] Leibniz-Institut für Kristallzüchtung, Max-Born-Str. 2, 12489, Berlin, Germany.
[3]Institute of Microelectronics Technology and High Purity Materials, RAS, Academician Ossipyan str. 6, 142432, Chernogolovka, Russia.
[4]Justus Liebig University Gießen, Heinrich-Buff-Ring 16, 35392, Gießen, Germany
yuriy.suhak@tu-clausthal.de

Summary:
The electrical conductivity, resonance frequency and acoustic loss are determined for piezoelectric resonators which are based on Czochralski grown Li(Nb,Ta)O_3 solid solutions with different Nb/Ta ratios up to 700 °C. Experimental methods include impedance spectroscopy and resonant impedance spectroscopy. Further, the long-term behaviour of resonant properties is examined at high-temperatures. After operation for about 400 hours in air at 700 °C a $LiNb_{0.5}Ta_{0.5}O_3$ resonator shows an increase in resonance frequency only by 0.1 %.

Keywords: Piezoelectricity, high temperature, lithium niobate-tantalate, actuator, sensor.

Background, Motivation and Objective

Piezoelectric actuators that can be operated at high-temperatures are in high demand for e.g. energy conversion, aerospace or automotive industrial applications. Such devices can generate movements in micrometer range at relatively low voltage. For such materials, excellent thermal stability and large piezoelectric coefficients are required. However, common piezoelectrics are limited by their application temperature or suffer from low piezoelectric coefficients. For example, polycrystalline ceramics show thermal instability above about 300°C [1]. Quartz type crystals from langasite ($La_3Ga_5SiO_{14}$) family possess excellent thermal stability but their piezoelectric coefficients are too low for actuating applications [2]. Lithium niobate ($LiNbO_3$, LN) and lithium tantalate ($LiTaO_3$, LT) attract substantial scientific and industrial interest because of their excellent electro-optical, piezoelectric and acoustic properties. However, their high-temperature usage is limited by thermal instability of LN and low Curie temperature of LT. Recently, attention has been attracted by Li(Nb,Ta)O_3 (LNT) solid solutions that combine potentially the advantages of the end members of the material system [3]. The current work explores electrical conductivity, resonant frequency and loss of LNT resonators with different Nb/Ta ratios as a function of temperature and time

Specimens and Measuring Techniques

The crystals, used in this study were grown by Czochralski technique at the Institute of Microelectronics Technology and High Purity Materials, Russian Academy of Sciences, Moscow, and at the Leibniz Institute for Crystal Growth, Berlin. The high-temperature experiments are performed on platinum-electroded Y-cut and Z-cut samples in a gas-tight tube furnace.

The electrical conductivity σ is determined by impedance spectroscopy in the frequency range from 1 Hz to 1 MHz using an impedance/gain-phase analyzer (Solartron 1260). The investigations of acoustic losses are performed by means of resonant piezoelectric spectroscopy on Y-cut and Z-cut LNT resonators, operated in the thickness-shear mode and in the thickness mode, respectively, using a high-speed network analyzer (Agilent E5100A). Detailed description of measuring techniques is given elsewhere [4].

Results and Discussion

Electrical conductivity of $LiNb_{0.88}Ta_{0.12}O_3$ and $LiNb_{0.5}Ta_{0.5}O_3$ samples, measured in air in the temperature range 400–700 °C is shown in Fig. 1 and compared to that of LN and LT. As

seen from the figure, the samples exhibit similar conductivity that increases linearly in the Arrhenius presentation, indicating that it is governed by a single thermally activated process in the measured temperature range. The activation energies increase with the Ta-content in LNT system from 1.2 eV to 1.3 eV for LN and LT, respectively. The observation follows the general trend of similar conduction mechanisms in LN and LT at temperatures below 700 °C [5]. Earlier, it was shown in [6] that the electrical conductivity of congruent $LiTaO_3$ shows an activation energy of 1.2 eV in the temperature range of 350–800 °C. The authors concluded that the conductivity is governed by mobile lithium vacancies. Similarly, to $LiTaO_3$, our previous study shows that the lithium ion migration via lithium vacancies is the main transport mechanism in $LiNbO_3$ and the activation energy, determined for the congruent LN is equal to 1.3 eV [7].

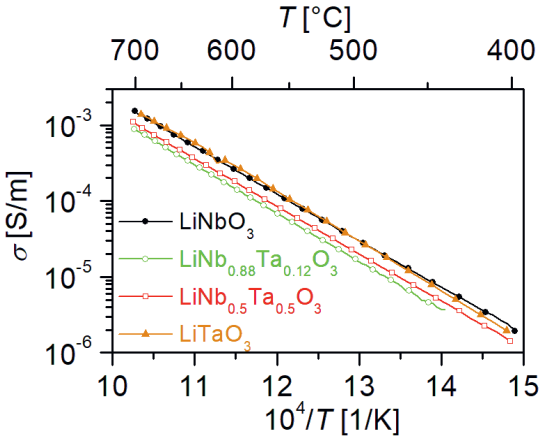

Fig. 1. Conductivity of Li(Nb,Ta)O_3 samples as a function of temperature.

Further, the measured acoustic losses of $LiNb_{0.88}Ta_{0.12}O_3$ and $LiNb_{0.5}Ta_{0.5}O_3$ specimens are shown in Fig. 2 in the Arrhenius plot and compared to those of pure LN, determined in [7]. As seen from Fig. 2, the losses in LNT are substantially lower in the measured range, which implies e.g. improved accuracy in frequency determination of such resonators.

Finally, in order to determine the stability of the resonant properties of LNT, the change of the resonance frequency (f_R) of the $LiNb_{0.5}Ta_{0.5}O_3$ sample is studied at 700 °C in air as a function of time during 400 h of uninterrupted thermal treatment. The measurements revealed, that f_R steadily increases with time, showing however a shift of less than 0.1% only, relative to f_0. The Q-factor at 700 °C equals 100 and 2000 for the 1st and the 3rd harmonics, respectively.

Conclusions

In summary, the electrical and electromechanical properties of LNT were investigated at high temperatures and low oxygen partial pressures. The conductivity measurements reveal similar magnitudes and activation energies for all measured samples that suggests similar conduction mechanisms. The losses in $LiNb_{0.5}Ta_{0.5}O_3$ resonators are found to be more than one order of magnitude lower, than those of congruent LN resonators. The change of resonance frequency of the $LiNb_{0.5}Ta_{0.5}O_3$ after about 400 operating hours at 700 °C in air is less than 0.1 %.

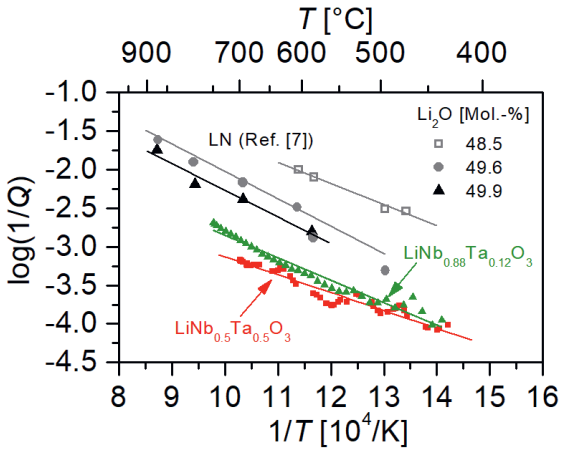

Fig. 2. Acoustic losses in Li(Nb,Ta)O_3 samples as a function of temperature.

References

[1] V. Segouin, B. Kaeswurm, K.G. Webber, L. Daniel, Temperature-dependent anhysteretic behavior of co-doped PZT, *J. Appl. Phys*. 124, 104103 (2018); doi: 10.1063/1.5040556.

[2] K. Shimamura, H. Takeda, T. Kohno, T. Fukuda, Growth and characterization of lanthanum gallium silicate $La_3Ga_5SiO_{14}$ single crystals for piezoelectric applications, *J. Cryst. Growth* 163, 388-392 (1996); doi: 10.1016/0022-0248(95)01002-5.

[3] I. G. Wood, P. Daniels, R. H. Brown, A. M. Glazer, Optical birefringence study of the ferroelectric phase transition in lithium niobate tantalate mixed crystals: $LiNb_{1-x}Ta_xO_3$, J. *Phys.: Condens. Matter* 20, 235237 (2008); doi: 10.1088/0953-8984/20/23/235237.

[4] H. Fritze, High-temperature bulk acoustic wave sensors, *Meas. Sci. Technol*., 22, 12002 (2011); doi: 10.1088/0957-0233/22/1/012002.

[5] A. Krampf, M. Imlau, Yu. Suhak, H. Fritze, S. Sanna, Polaronic structures, optical response and electrical conductivity of $LiTaO_3$, *In press*.

[6] A. Huanosta and A. R. West, The electrical properties of ferroelectric $LiTaO_3$ and its solid solutions, *J. Appl. Phys*. 61, 5386-5391 (1987); doi: 10.1063/1.338279.

[7] A. Weidenfelder, J. Shi, P. Fielitz, G. Borchardt, K. D. Becker, H. Fritze, Electrical and Electromechanical Properties of Stoichiometric Lithium Niobate at High-Temperatures, *Solid State Ionics* 225, 26-29 (2012); doi: 10.1016/j.ssi.2012.02.026

DOI 10.5162/SMSI2021/A2.1

Mechanisms of Anelastic Loss in Langasite at Temperatures from 113 K to 1324 K

Ward L. Johnson[1], Yuriy Suhak[2], and Holger Fritze[2]
[1]Applied Chemicals and Materials Division, National Institute of Standards and Technology, 325 Broadway St., MS 647, Boulder, CO 80305, USA
[2]Clausthal University of Technology, Am Stollen 19B, Goslar 38640, Germany
ward.johnson@nist.gov

Summary:
Synthetic piezoelectric crystals with the structure of langasite (LGS) are being pursued for resonant acoustic sensors that can operate at temperatures exceeding the range of conventional piezoelectric materials. The optimization of these crystals is currently focused primarily on minimization of acoustic loss, which degrades signal strength and resolution of sensors. This paper presents analysis and discussion of two sets of measurements of loss of LGS with a combined temperature range of 113 K to 1324 K. Physical mechanisms for the loss include intrinsic phonon-phonon interactions, multiple point-defect relaxations, piezoelectric/carrier loss, contact loss, and, perhaps, dislocation relaxations [1].

Keywords: acoustic loss, piezoelectric sensors, high temperatures, langasite, LGS, langatate, LGT catangasite, CTGS, quartz

Introduction

Traditional piezoelectric sensors are limited to operation at temperatures below several hundred degrees Celsius, because crystal transformations or degradation occur at higher temperatures in common commercially available piezoelectrics [2]. However, substantial research in recent decades has focused on synthesizing and optimizing innovative piezoelectric crystals that can be used in resonant sensors at temperatures exceeding 1000 K [3], including crystals with the structure of langasite ($La_3Ga_5SiO_{14}$, "LGS"), often termed members of the "langasite family."

The performance of resonators in sensing applications is limited by acoustic loss Q^{-1}. Within the langasite family of piezoelectric crystals, LGS has not been found to have the lowest Q^{-1}. For example, resonators of langatate ($La_3Ga_{5.5}Ta_{0.5}O_{14}$, "LGT") and langanite ($La_3Ga_{5.5}Nb_{0.5}O_{14}$, "LGN") at room temperature are reported to have lower loss than similarly manufactured LGS resonators [4]. Crystals of LGT [5] and catangasite ($Ca_3TaGa_3Si_2O_{14}$, "CTGS") [6] have also been found to have lower Q^{-1} at elevated temperatures (*e.g.*, above 200 °C) than that of any reported LGS specimen.

Despite the less-than-stellar quality factor of LGS, the available data on this material currently provide unique information on physical mechanisms that contribute to loss in crystals in the langasite family. Specifically, the range of temperatures over which Q^{-1} in LGS has been measured in the low megahertz range is exceptionally broad, enabling identification of contributions to the loss ranging from the small intrinsic loss associated with phonon-phonon interactions to conductivity-related loss five orders of magnitude larger at elevated temperatures. Analysis and discussion of these LGS data are the focus of this paper.

Results and Discussion

Figure 1(a) shows measurements of Q^{-1} of two Y-cut LGS crystals grown by different manufacturers [2,5]. Measurements on one crystal in vacuum were acquired from 113 K to 752 K with noncontacting electrodes at the National Institute of Standards and Technology (NIST, U.S.A.). Measurements on the other crystal in air were acquired from 309 K to 1324 K with Pt surface electrodes at Clausthal University of Technology (TUC, Germany).

This figure also shows the maximum Q^{-1} at 10 MHz reported for LGS at room temperature with noncontacting electrodes [4]. This Q^{-1} is an order of magnitude smaller than that measured near room temperature on the LGS specimen at NIST, indicating the presence of greater material loss in the NIST specimen. Q^{-1} of the specimen measured at TUC is an additional order of magnitude greater near room temperature. For the purpose of characterizing non-intrinsic contributions to the loss, the relatively high Q^{-1} of the NIST and TUC specimens is advantageous.

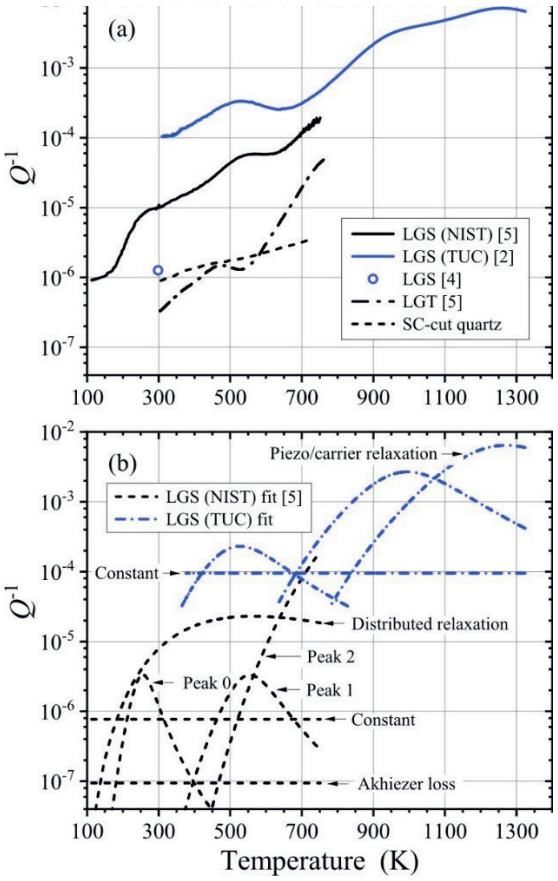

Fig. 1: (a) Q^{-1} of two LGS crystals measured at NIST [5] and TUC [2], an LGS crystal with lowest reported loss [4], an LGT crystal [5], and a swept SC-cut quartz crystal. The resonant frequencies near ambient temperature are, respectively, 6.1 MHz [5], 5.0 MHz [2], 10.0 MHz [4], 6.0 MHz [5], and 10.0 MHz. (b) Contributions to Q^{-1} of the NIST and TUC LGS crystals, determined from least-squares fits.

For comparison, Figure 1(a) also includes data on LGT from 302 K to 759 K [5] and data on swept SC-cut quartz from 306 K to 717 K, all obtained with noncontacting electrodes at NIST.

The LGS data from NIST in Fig. 1(a), along with simultaneously acquired data from two additional harmonics of this crystal, were fit to a function that includes intrinsic phonon-phonon (Akhiezer) loss (approximated as proportional to frequency and independent of temperature) [5], three anelastic point-defect relaxations [7], a constant frequency-independent background, and a broad relaxation consisting of a continuous set of Debye functions [7] with a log-normal distribution of activation energies. The physical mechanism responsible for the last term is hypothesized as arising from dislocations [5], consistent with the fact that no such term is required to fit the data in Fig. 1(a) for LGT, which has much lower dislocation density [5].

Results of fitting of the TUC data at the single measured harmonic are consistent with the NIST results for LGS, with respect to the temperatures of Peaks 1 and 2, considering the difference in resonant frequency. They reveal an additional large peak with a maximum near 1260 K, consistent in form with an expected relaxation involving the motion of charge carriers in acoustically generated piezoelectric fields [5,6]. The fit accurately matches the data without a broadly temperature-dependent term (*e.g.*, distributed relaxation). The constant term, which is inseparable from the Akhiezer term in the absence of measurements of additional harmonics, is two orders of magnitude greater than that determined for the LGS specimen at NIST. This difference is attributed primarily to greater mechanical contact.

Conclusions

Analysis of LGS data from 113 K to 1324 K reveals a number of anelastic loss mechanisms, including intrinsic loss, point-defect relaxations, piezoelectric/carrier relaxation, a constant background, and a broad background that may arise from dislocations. Similar effects have been reported in LGT and CTGS, even when the crystals are state-of-the-art, such as the LGT in Fig. 1(a). Despite the identification of the general nature of loss contributions, the optimization of these innovative piezoelectric materials for applications at elevated temperatures is far from complete. This situation is contrasted, here, with that of swept SC-cut quartz, which shows no evidence for point-defect relaxations over a more limited range of measured temperatures.

[1] This manuscript is a contribution of the National Institute of Standards and Technology and is not subject to copyright in the United States.

[2] Fritze, H., High-temperature bulk acoustic wave sensors, *Meas. Sci. Technol.* 22, 12002 (2011); doi: 10.1088/0957-0233/22/1/012002

[3] Johnson, W., Acoustic and Electrical Properties of Piezoelectric Materials for High-Temperature Sensing Applications, *Proc. SENSOR 2015*, 384-389 (2015); doi: 10.5162/sensor2015/C3.1

[4] Smythe, R. C., Langasite, langanite, and langatate bulk-wave Y-cut resonators, IEEE T. Ultrason. Ferr. 47, 355 (2000); doi: 10.1109/58.827420

[5] Johnson, W., Kim, S. A., Uda, S., and Rivenbark, C. F., Contributions to anelasticity in langasite and langatate, J. Appl. Phys. 110, 123528 (2011); doi: 10.1063/1.3672443

[6] Johnson, W. L., High-Temperature Electroacoustic Characterization of Y-Cut and Singly-Rotated $Ca_3TaGa_3Si_2O_{14}$ Resonators, *IEEE T. Ultrason. Ferr.* 61, 1433-1441 (2014); doi: 10.1109/TUFFC.2014.3052

[7] Nowick, A. S., and Berry, B. S., *Anelastic Relaxation in Crystalline Solids* (Academic, NY, 1972).

DOI 10.5162/SMSI2021/A2.2

Housed Temperature Sensors Based on Piezoelectric Resonators for High-Temperature Applications

M. Schulz[1], F. Kohler[2], J. Wilde[2], H. Fritze[1]
[1] Institute of Energy Research and Physical Technologies,
Clausthal University of Technology, Am Stollen 19 B, 38640 Goslar, Germany,
[2] Department of Microsystems Engineering – IMTEK,
University of Freiburg, Georges-Köhler-Allee 103-01-105, Germany.
michal.schulz@tu-clausthal.de

Summary:
A housed temperature sensor based on piezoelectric CTGS ($Ca_3TaGa_3Si_2O_{14}$) single crystals is presented. Here, temperature data is derived from the shift of the resonance frequency, obtained from an analysis of the impedance spectra of resonators prepared from CTGS. The device is operated up to 900 °C, exhibiting nearly linear temperature dependence of the resonance frequency of about 180 Hz/K in the entire temperature range.

Keywords: piezoelectricity, temperature sensor, resonance frequency, CTGS

Introduction and Objectives

Piezoelectric devices based on high-temperature stable single crystals allow to create sensors for measurement of temperature as well as other physical properties. Thereby, the devices withstand harsh environments such as extreme temperatures or highly reducing or oxidizing atmospheres. The measured property is the resonance frequency which is governed by e.g. the temperature of the environment.

Commonly used piezoelectric materials such as quartz or lithium niobate are not suitable for high-temperature applications. Strongly increasing damping and destructive phase transitions or decomposition of the crystals limit their use up to about 400-500 °C. Catangasite ($Ca_3TaGa_3Si_2O_{14}$, CTGS) is a commercially available member of the so-called langasite family. The crystal structure of CTGS is the same as of quartz. CTGS does not undergo any phase transitions up to its melting point at about 1350 °C [1] and exhibits an ordered crystal structure, yielding low electromechanical losses [2,3].

This paper focuses on preparation and characterization of high-temperature stable resonators based on Y-cut CTGS crystals and their integration in a gas-tight package. The temperature dependence of the resonance frequency and loss of as-prepared resonators and housed devices is compared and discussed.

Experimental

Polished Y-cut CTGS blanks with a diameter of 10 mm are purchased from Shanghai SICCAS High Technology Corporation (Shanghai, China) and from FOMOS Materials (Moscow, Russia). The thickness of about 250 µm is chosen for a resonance frequency of 5 MHz. Keyhole-shaped electrodes with a diameter of 5 mm are deposited using pulsed laser deposition (PLD) and screen printing techniques. In case of the former, a Pt/Rh alloy is deposited, as it exhibits improved stability in harsh environments [4]. In case of the latter, standard Pt paste (Ferro, 64120410) is used.

The resonators are pre-characterized in air at a ramp of 1 K/min in temperature range from RT up to 850 °C and 1000 °C for PLD and screen printed electrodes, respectively. Thereby, the impedance spectra in the vicinity of the resonance frequency is measured using an Agilent E5100A network analyzer. From this data, the peak maximum and full width at half maximum (FWHM) of the real part of admittance are calculated.

Subsequently, the resonators are mounted in a housing made of Al_2O_3 (see Fig. 1). Thereby, the CTGS is glass-soldered with a support structure. The electrical contact between connector pads and the resonator is realized using Pt bond wires. Finally, a cap is mounted over the resonator and sealed using glass solder technique.

The complete device is characterized in a furnace up to 900 °C. Thereby, the analysis as done during the pre-characterization is repeated. The obtained frequency data and loss are

compared with those of as-prepared Y-cut resonators.

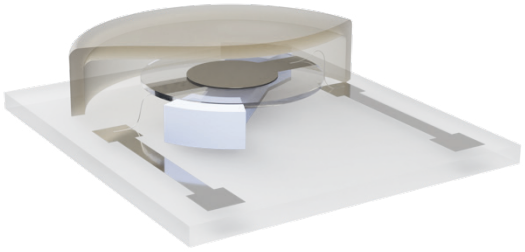

Fig. 1. Design of a temperature sensor based on CTGS.

Results and Discussion

The relative changes of resonance frequencies for as-prepared and housed resonators are shown in Fig. 2. Since the screen printed electrodes are fired in a furnace prior to the measurement, they introduce low mechanical strain to the resonator. In case of the PLD electrodes a small hysteresis of the resonance frequency is measured during first temperature ramp. The relative change of the frequency for two different crystal manufacturers is the same. The absolute data spreads by about 2 % between investigated samples. This is attributed to slight differences in the thickness of as-prepared blank Y-cuts.

The loss expressed in form of inverse Q factor [5] is shown in Fig. 3. Due to very narrow FWHM of the admittance peak, the calculated Q value at low temperatures exhibits large noise. The increase of Q^{-1} at 350-500 °C is attributed to anelastic relaxation of point defects [3]. At temperatures above 700 °C the loss is dominated by piezoelectric/conductivity relaxation [3]. As shown in Fig. 3, the loss measured for the housed device is nearly identical to those of an as-prepared SICCAS resonator. The FOMOS material exhibits significantly lower loss throughout entire temperature range.

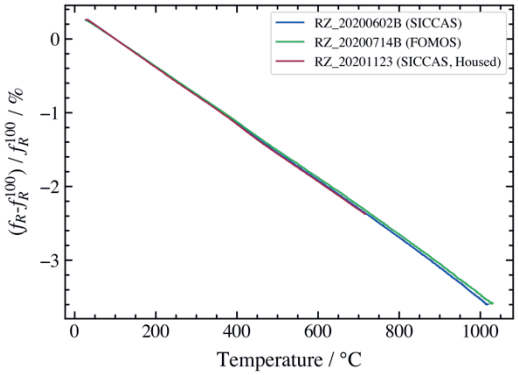

Fig. 2. Relative change of resonance frequency for CTGS manufactured by SICCAS and FOMOS as well as housed CTGS. Thereby, the housed resonator was annealed up to 700 °C only.

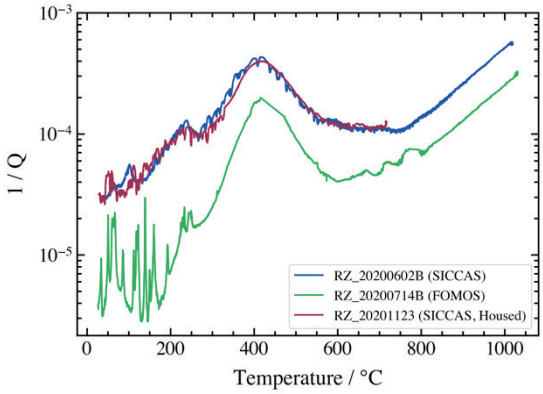

Fig. 3. Loss measured in CTGS samples and housed device as a function of temperature.

Conclusions

CTGS is a promising material for high-temperature stable sensor devices. Thanks to ordered crystal structure it exhibits low losses in comparison to some other members of langasite family. A nearly linear dependence of the resonance frequency from temperature of Y-cut CTGS simplifies the frequency to temperature conversion allowing to perform it even on low-cost microcontrollers. The housed sensor is tested up to 900 °C. The impact of the housing on resonators performance is negligible.

Acknowledgement

The authors thank the German Research Foundation (Deutsche Forschungsgemeinschaft, DFG) for financial support under grants FR 1301/35-1 and WI1987/6-1.

References

[1] F. Yu, S. Zhang, X. Zhao, D. Yuan, L. Qin, Q. Wang, T. R. Shrout, Investigation of Ca3TaGa3Si2O14 piezoelectric crystals for high temperature sensors, J. Appl. Phys. 109, 114103 (2011)

[2] Yu. Suhak, M. Schulz, W. L. Johnson, A. Sotnikov, H. Schmidt, H. Fritze, Electromechanical Properties and Charge Transport of $Ca_3TaGa_3Si_2O_{14}$ (CTGS) Single Crystals at Elevated Temperatures, *Solid State Ionics* 317, 221-228 (2018)

[3] Yu. Suhak, W. L. Johnson, A. Sotnikov, H. Schmidt, and H. Fritze, Transport and Electromechanical Properties of $Ca_3TaGa_3Si_2O_{14}$ Piezoelectric Crystals at Extreme Temperatures, *MRS Advances* 4, 515-521 (2019); doi: 10.1557/adv.2019.16

[4] D. Richter, M. Schulz, S. Sakharov, Z.J. Davis, H. Fritze, Surface Acoustic Wave Devices: Materials Stability in Harsh Environments, *MRS Proceed*. 1519 (2013)

[5] H. Fritze, High-Temperature piezoelelctric crystals and devices, *J. Electroceramics* 26, 122-161 (2011)

DOI 10.5162/SMSI2021/A3.1

Adjustment Concept for Compensating Stiffness and Tilt Sensitivity of a Novel Monolithic EMFC Weighing Cell

Markus Pabst[1], Maximilian Darnieder[2], René Theska[2], Thomas Fröhlich[1]
Technische Universität Ilmenau, Departement of Meachanical Engineering, Ilmenau, Germany
[1] Institute for Process Measurement and Sensor Technology,
[2] Institute for Design and Precision Engineering, Precision Engineering Group
markus.pabst@tu-ilmenau.de

Summary:
This paper describes the experimental investigation of a new adjustment concept for planar monolithic high precision electromagnetic force compensated weighing cells. The concept allows to adjust the stiffness and the tilt sensitivity of the compliant mechanisms to an optimum. A new prototype mechanism is set up and adjusted according to the developed mechanical model. For evaluation of the concept, the system was tested on a high precision tilt table and under high vacuum conditions.

Keywords: weighing cell; electromagnetic force compensation; flexure hinges; compliant mechanism; adjustment; stiffness; tilt sensitivity

Introduction

High precision mass comparison is a very recent issue. In 2019, the definition of the mass in the Système International d'Unités (SI) system of units was redefined by the use of fundamental physical and atomic constants [1]. With the redefinition the kilogram, as the last unit of the SI system, is no longer based on an artefact, the international prototype kilogram (IPK) [2]. This ensures an invariable definition. Nevertheless, there are uncertainty issues in determination of mass. The use of mass comparators for the determination of mass allows to shortcut some of the uncertainty sources. The heart of the mass comparators are electromagnetic force compensated (EMFC) weighing cells whose optimization in terms of sensitivity is the focus of this paper.

Description of the work

Further improvements in high precision mass comparison are subjects of investigation in the dissemination chain of the mass standard. One of the most precise methods of mass comparison is achieved by the use of high precision electromagnetic force compensated (EMFC) weighing cells as part of mass comparators. The mechanics of EMFC weighing cells are based on compliant mechanisms with concentrated compliances in form of flexure hinges. Total mechanical stiffness and tilt sensitivity are limiting factors with regard to the resolution of EMFC weighing cells. In order to optimize their performance, the stiffness and the tilt sensitivity of the systems need to be minimized. Due to manufacturing restrictions and robustness requirements, a further reduction of the thickness of the flexure hinges is not desirable. For a further optimisation of the mechanisms, a new adjustment concept is required.

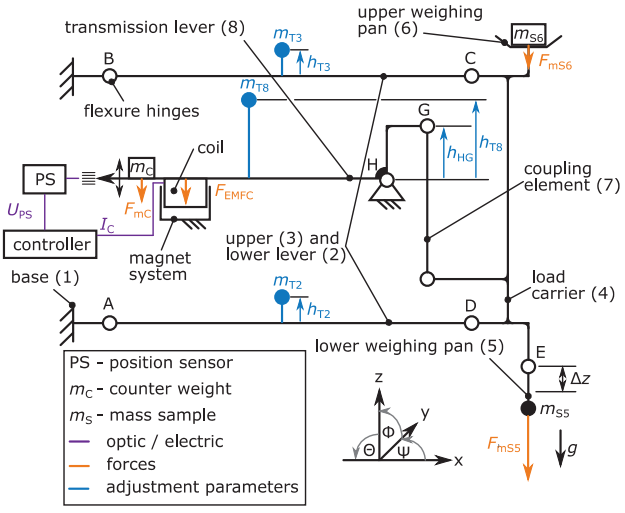

Fig. 1: Operating principle of prototype planar monolithic EMFC-weighing cell supplemented by adjustment possibilities.

In this paper, an alternative to reduce stiffness and tilt sensitivity by adding trim weights (m_{T2}, m_{T3}, m_{T8}) at certain heights in combination with an astasizing adjustment (h_{HG}) is presented in Figure 1. Based on the results of the investigations, a new planar monolithic mechanism for an EMFC weighing cell is designed, providing

the possibility to adjust trim masses. For the investigation, the weighing cell was set up on a precision tilt stage [3] (also see [4] and [5]) protected by an enclosure and a windshield to reduce the influence of air movement.
The new mechanism was adjusted according to the developed mechanical model [6]. A parameter combination for a total stiffness slightly above zero and a tilt sensitivity close to zero is found. For the evaluation of the adjustment success and the vacuum compatibility, the system is tested under high vacuum conditions.
For the evaluation of the adjustment concept, the investigated properties were compared to the values from the initial investigation of the structure. In the first step, the initial stiffness $C_{\mathrm{init.}} = 21.560\,\mathrm{N/m}$ was reduced by the manufactured adjustment parameter h_{HG} (from figure 1) to $C_{\mathrm{m0}} = -33.5\,\mathrm{mN/m}$ in the pre-adjusted state (results in Table 1).
Caused by astasizing the mechanism ($h_{\mathrm{HG}} \neq 0$) for an optimized stiffness, the initial tilt sensitivity changes. In the second step the tilt sensitivity of $D_{\mathrm{m0}} = 5.511\,\mathrm{mN/rad}$ in the pre-adjustet state was reduced to $D = 0.1\,\mathrm{mN/rad}$ in the fine-adjusted state by optimizing the parameters of h_{T8}, h_{T2} and h_{T3}. The final stiffness in the fine-adjusted state was reduced to $C = 5.1\,\mathrm{mN/m}$. At the end, the initial stiffness was reduced to $< 0.3\,‰$ and the tilt sensitivity to $< 2\%$ compared to the pre-adjusted state.

Summary

A new planar monolithic electromagnetic force compensated weighing cell, adjustable in its mechanical properties was designed, manufactured and investigated. The measurement procedure has proven the feasibility of the adjustment concept. The vacuum compatibility of the new mechanism was confirmed for further investigations in the environment of a vacuum mass comparator. Here, the performance of the system will be determined and compared to other systems. The knowledge about the manufacturing deviations in the mechanism will be used for further investigation and an advancement of the next prototype to be designed and manufactured.

References

[1] Stock, M., et al. "The revision of the SI—the result of three decades of progress in metrology." Metrologia 56.2 (2019): 022001.

[2] Quinn, T. J. "The kilogram: the present state of our knowledge." IEEE Transactions on Instrumentation and Measurement 40.2 (1991): 81-85.

[3] Rvero, M., and Kühnel, M. "High precision dual axis tilt stage." Proceedings of the 58th Ilmenau scientific Colloquium. 2014.

[4] Yan, N., et al. "Torsion balance-based system for high-precision force measurement in horizontal plane: part I. Development concept." Measurement Science and Technology 29.8 (2018): 084001.

[5] Yan, N., et al. "Torsion balance based system for high-precision force measurement in horizontal plane. Part II: Static and dynamic improvement." Measurement Science and Technology. 2019.

[6] Darnieder, M., et al. "Static behavior of weighing cells." Journal of Sensors and Sensor Systems 7.2 (2018): 587-600.

DOI 10.5162/SMSI2021/A3.2

Model Based Evaluation of Integrated DLC Based Sensor System for Load Measurement on Linear Guides

David Krampert[1,2], Sebastian Unsleber[1], Leonhard Reindl[2]
[1] Bosch Rexroth AG, Ernst-Sachs-Straße 100, 97424 Schweinfurt, Germany,
[2] Albert-Ludwigs-University Freiburg, IMTEK, Georges-Köhler-Allee 106, 79110 Freiburg, Germany
david.krampert@boschrexroth.de

Summary:
Having an accurate model of the load distribution in linear guides is crucial for both simulative purposes and accurate sensor based load measurement. In this work, such a model is employed to predict sensor signals of an integrated, Diamond Like Carbon (DLC) based sensor system directly beneath the raceways, in different load scenarios. Measurements were found to match the theoretical model predictions well. This both allows for model verification by direct load measurements as well as demonstrating the capability of the sensor system to successfully retrieve the applied load.

Keywords: Load Determination, Linear Guide Bearings, Industry 4.0, Piezoresistive DLC, Load Distribution Model

Background, Motivation and Objective

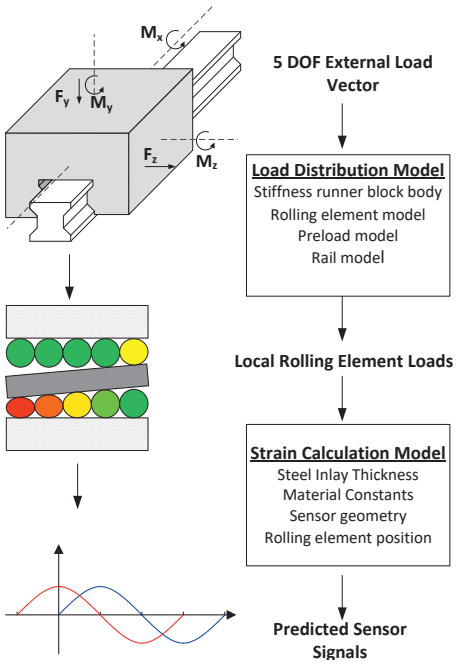

Fig. 1 Sensor signal calculation scheme

There are widespread efforts to integrate load measurement features in machine tools, e.g. for process monitoring [1]. Solutions such as a sensory spindle exist [2] but are highly specialized to the component at hand. Integrating load measurement into a standard machine part in the force flux, such as linear guides which provide a translational bearing, would significantly reduce required engineering efforts and cost. In [3] we presented an integrated strain sensor system based on Diamond-Like-Carbon (DLC), which is placed directly beneath the raceways, i.e. the place of load transmission. For evaluating sensor system performance, and in deployment for retrieving the applied load from the sensor signals, a model for the mapping of external loads to sensor signals has to be defined, as sketched in fig. 1. In [3], we have shown good agreement of the sensor signals with both strains obtained via finite element method simulation and an analytical strain calculation model, predicting strain depending on the local load on rolling elements beneath the sensors, i.e. the second step in fig. 1. The result is shown in fig. 2 for the difference signal between two neighboring sensors over different relative positions of the closest rolling element. The load distribution model, used for predicting those local loads dependent on an external five degrees of freedom load vector, is yet to be verified in the context of load measurement and at the center of this work.

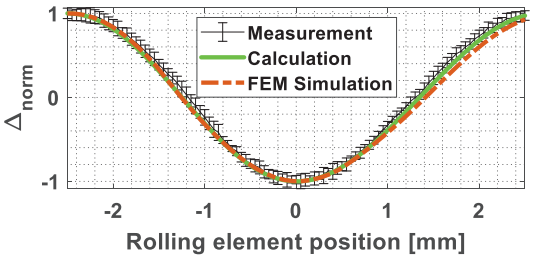

Fig. 2 Normalized difference signal Δ_{norm} for movement under constant load

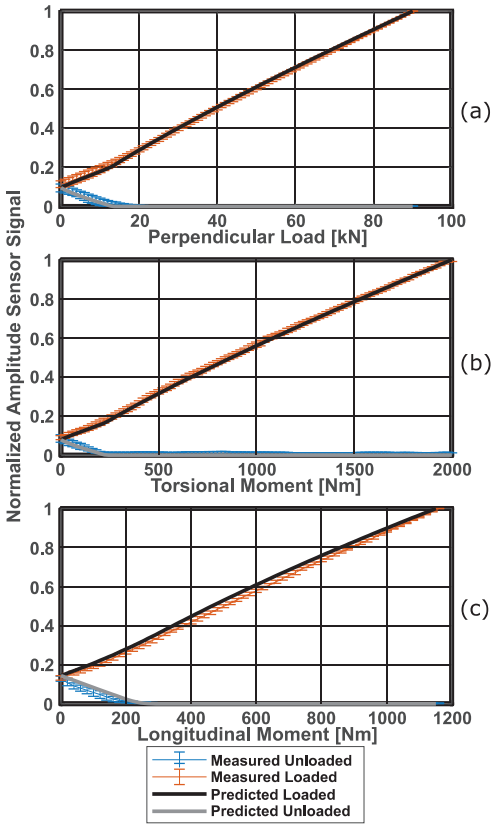

Fig. 3 Comparison of measured and calculated sensor signal amplitudes. (a) Perpendicular loading (b) Torsional moment (c) Longitudinal moment

Description of the New Method or System

The load-displacement relationship of the rolling elements is nonlinear. This prohibits linear superposition of the individual load components' effects. The load distribution model therefore establishes a mapping of the internal loads to the external loads, and then uses Gauss-Newton iterations until the discrepancy falls below a threshold. The core procedure is based on [4]. First major model assumptions have to be addressed. The runner block and the rail are assumed to be ideally rigid, i.e. all deformation only occurs at the rolling element contacts. A profiled, slice based model with 41 slices as in ISO/TS 16281 [5] where each slice is modeled according to [6] is employed. Preload is introduced in linear guides by design using oversized rolling elements and changes when loading the bearing. As load on some raceways increases by external loading, the other experience reduced load. This effect is integrated into the model by calculating the preload as a function of the load on rolling elements being less loaded then at a preload-only state, and is thus integrated into the iteration procedure. The calculated local loads are then used in the strain calculation model to predict the resulting sensor signals.

Results

Experiments have been performed loading two runner blocks type SNS size 45 from Bosch Rexroth, equipped with the sensor system. Normal loads are ranging from 0 kN to 90 kN, torsional moments from 0 Nm to 2000 Nm and longitudinal moments from 0 Nm to 1150 Nm, each applied in both directions. The sensor signal is dependent on the relative position of rolling elements, so experiments have been repeated at 13 positions, moving the runner block 1 mm in between. From this an amplitude is calculated, indicating the maximum sensor signal at a certain load. Sensor signal here refers to the difference of the relative resistance change between two sensors of a group, which is more robust to e.g. temperature changes [3]. Fig. 3 compares amplitudes normalized to the maximum value, from calculations and repeated measurements, for two sensor pairs per raceway, measurements ± one standard deviation. The measurements agree well with the predictions for both loaded and unloaded raceways. Note that for all predictions the same parametrization of the model has been used. The biggest discrepancy is found at unloaded raceways at longitudinal moments, see fig. 3(c), where the preload vanishes slightly faster than predicted.

The good overall consistency demonstrates the sensor systems capability to estimate the external load vector and for the first time allows for direct verification of the load distribution model.

References

[1] R. Teti, K. Jemielniak, G. O'Donnell, D. Dornfeld, "Advanced monitoring of machining operations",CIRP Annals,Volume 59, Issue 2,2010, doi: 10.1016/j.cirp.2010.05.010.

[2] Denkena, B., Dahlmann, D., Boujnah, H., "Tool Deflection Control by a Sensory Spindle Slide for Milling Machine Tools", Procedia CIRP 62, 2017. doi: 10.1016/j.procir.2016.06.059

[3] D. Krampert, S. Unsleber, C. Janssen und L. Reindl, "Load Measurement in Linear Guides for Machine Tools", Sensors, Vol. 19, No. 3411, 2019. doi: 10.3390/s19153411

[4] S. Lenssen und J. Sarfert, „Berechnung wälzgelagerter Linearführungen" Konstruktion , Vol. 46, pp. 209-214, 1994.

[5] ISO, „ISO/TS 16281 – Rolling Bearings – Methods for calculating the modified reference rating life for universally loaded bearings", 2008

[6] K. Kunert, „Spannungsverteilung im Halbraum bei elliptischer Flächenpressungsverteilung über einer rechteckigen Druckfläche," Forschung auf dem Gebiete des Ingenieurwesens, Vol. 27, pp. 165-174, 1961. doi: 10.1007/BF02561354

DOI 10.5162/SMSI2021/A3.3

Development of a Traceable Cantilever Calibration Device

Oliver Dannberg[1], Michael Kühnel[2], Thomas Fröhlich[1]
[1] Technische Universität Ilmenau, Ilmenau, Germany,
[2] SIOS Meßtechnik GmbH, Ilmenau, Germany
oliver.dannberg@tu-ilmenau.de

Summary:
This paper describes the development of a device that measures the force-displacement-curve of cantilevers to determine their stiffness. An interferometer detects the deflection of the cantilever while the force is measured by a novel EMK load cell with a soft mechanism to provide a high force resolution. The results of first cantilever calibrations with this device showed a low uncertainty and no detectable damage to the tip.

Keywords: Cantilever calibration, load cell, force measurements, interferometer

Introduction

The measurement of forces in the subnano- and nanonewton range is a strongly growing application in different fields of science such as biology, biophysics, medical- or materials science. Typically, these forces are determined by measuring the deflection of calibrated AFM cantilevers. However, an uncertainty of the cantilever stiffness has a direct impact to the force measurement.

This paper describes the development of a novel device that is able to do a traceable cantilever calibration with small uncertainties.

Cantilever calibration

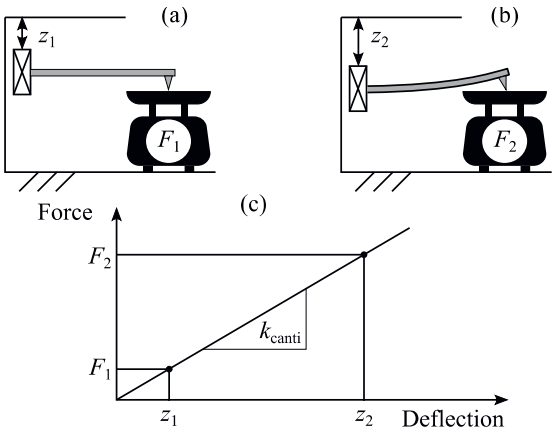

Fig. 1: Static experimental calibration setup for two load steps (a, b) with the corresponding force-deflection-curve (c).

The most accurate way to calibrate the stiffness of cantilevers is a static experimental calibration process [1] as shown in Figure 1. The cantilever is attached to a piezo stage and moved in z-direction while the tip is touching an electromagnetic force compensating (EMFC) balance. Since the weighting pan of the balance is always controlled to the same position the movement of the cantilever equals its deflection [2]. The slope of the force-deflection-curve represents the stiffness of the cantilever.

For the calibration process, the cantilever is clamped to a holder that is positioned in x, y and z while an interferometer measures its z-position. High calibration forces cause a nonlinear force-deflection-curve and wear of the cantilever tip [5]. Therefore, a high resolution load cell has been developed that achieves a small uncertainty, even for small calibration forces.

Force Measurement

The cantilever force is measured by a custom load cell that is optimized to have a high force resolution. Therefore it uses two major elements that are different, compared to commercial load cells:

1. a single joint mechanism with a low stiffness of 1 Nm^{-1} at the load button
2. a difference interferometer (SIOS SP 2000 DI) to measure the beam deflection with a resolution of 10 pm

Two mirrors (8) on top and bottom of the load cell (4) reflect the interferometer beams. Figure 2 shows the CAD model of the custom load cell. A deflection of the load cell increases the length of one beam while the other one decreases.

The symmetry of the optical path reduces the sensitivity for external disturbances such as changes in temperature, humidity and air pressure. An additional positioning sensor measures the absolute zero position (1) with an accuracy of 1 nm [3].

The center of gravity is adjusted in horizontal and vertical direction by means of two adjusting screws (3), (5). This makes the balance less sensitive to tilt and other disturbances.

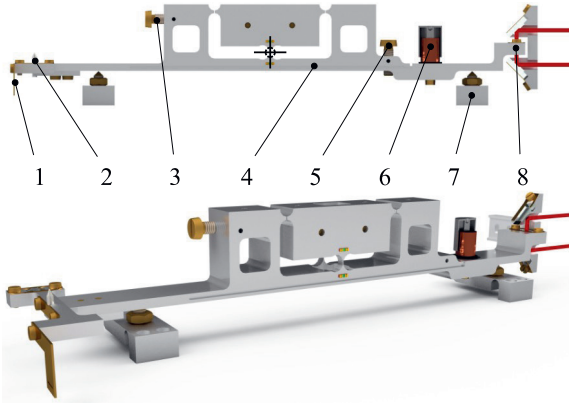

Fig. 2: CAD model of the single pivot beam balance: (1) Absolute position sensor; (2) Diamond load button; (3) Horizontal adjustment weight; (4) Monolithic beam; (5) Vertical adjustment weight; (6) Voice coil; (7) Mechanical limits; (8) Mirrors.

A voice coil (6) with a force constant of 26 mNA^{-1} generates a Lorenz force to compensate the cantilever force that is applied to a diamond load button (2) with the shape of a truncated cone. The tip touches the circular, flat surface with a diameter of 10 µm which ensures a constant leverage ratio.

Position measurement

For the cantilever calibration, the cantilever is clamped to a cantilever holder.

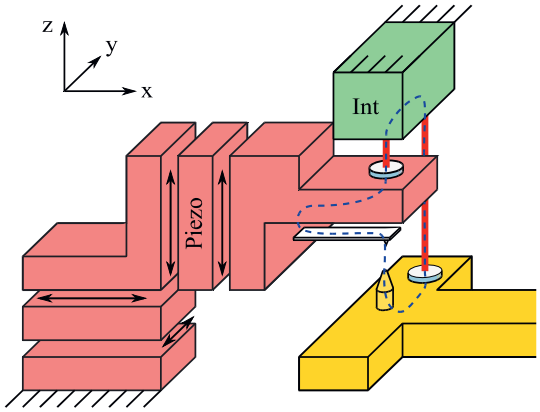

Fig. 3: Positioning of the cantilever and the measurement of its z-position with the measurement loop (blue)

A stack of three stages moves the cantilever in x, y and z direction to align the tip to the load button of the weighting cell. However, a piezo stage moves the cantilever during the calibration procedure.

The z position of the cantilever is measured with a second difference interferometer (SIOS SP 2000 DI). One of its beams is reflected on the beam balance while the other one hits the cantilever holder as shown in Figure 3.

This results in a short measurement loop (blue) that takes into account the thermal drift of the stages and the weighting cell.

Results

Figure 4 shows the force-deflection-curve of a cantilever that has been measured with the calibration device. Even with small calibration forces of less than 100 nN the relative uncertainty of the cantilever stiffness is 1.5% (k=2).

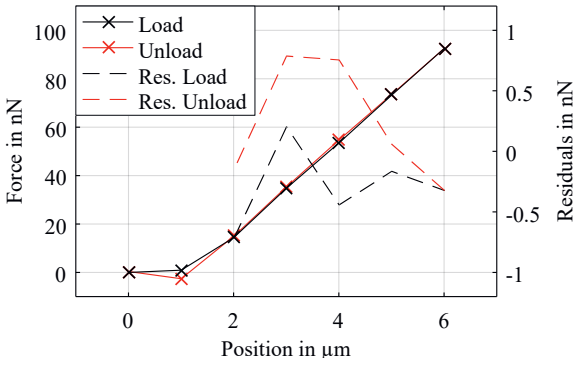

Fig. 4: Force-displacement-curve for one load cycle

After the calibration the cantilever tip has been examined under an electron microscope. The silicon tip with a 30 nm radius has not been damaged during the calibration process.

References

[1] C. A. Clifford et al., „The determination of atomic force microscope cantilever spring constants via dimensional methods for nanomechanical analysis“ Nanotechnology, 2005.

[2] C. Diethold, et al., „Determination of force to displacement curves using a nanopositioning system based on electromagnetic force compensated balances“ Measurement, 2014.

[3] C. Diethold, et al. „High precision optical position sensor for electromagnetic force compensated balances“ in Proceedings of IMEKO, 2010.

DOI 10.5162/SMSI2021/A3.4

A Control Concept of a Compensation Load Cell in Terms of Calibration a Cantilever

O. Dannberg [1], V. Cherkasova [2], T. Fröhlich [3]
Institute for Process Measurement and Sensor Technology, Technische Universität Ilmenau
PF 10 05 65, 98684 Ilmenau, Germany
[1] oliver.dannberg@tu-ilmenau.de
[2] valeriya.cherkasova@tu-ilmenau.de
[3] thomas.froehlich@tu-ilmenau.de

Summary:
The article proposes a concept of an automatic load cell control system with compensation of electromagnetic force for the tasks of precision force measurement. The following tasks were solved: mathematical modeling of mechanical processes in the compensation load cell when touching the cantilever, taking into account mechanical disturbances; identification of parameters and computer simulation of processes; development and simulation of the coil current control loop. The purpose of the control was to find a balance between precise control and reducing the oscillation of the control current.

Keywords: control system, load cell, electromagnetic force compensation, cantilever, bumpless control transfer

Introduction

There are many studies going on today and analyzes of scanning atomic force microscope (AFM). One of the important areas of research for improving the quality of the atomic force microscope is the calibration of the stiffness of the cantilever springs of the device [1], [2]. A force displacement measurement device for the determination of spring constants was developed at TU Ilmenau [3]. The research was continued in this subject [4]. In these developments the spring constant of AFM cantilevers is determined by using an electromagnetic force compensated (EMFC) load cell, for which analysis and control methods given in the article [5]. However, in the cited works, the concepts of control systems are not considered when changing the overall stiffness coefficient of the system.

The functional principle of the device and mathematical model of mechanical processes in the single joint load cell

The basic principle of measuring the cantilever force is based on a linear relationship between it and the compensation current of coil in the permanent magnet field attached to the weight beam. When touched by a cantilever, the balance beam deviates from the zero position, the deviation is fixed by an interferometer and transmitted to the controller, which in turn changes the current in the coil, thereby the Lorentz force returns the beam to zero.

The main research problem is the development of precise control of the coil current when the cantilever and the weighing beam are in contact. The stages of the position and impact of the cantilever are shown in Fig. 1 (I-III).

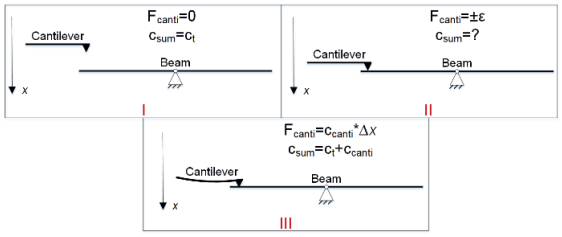

Fig. 1. I. The cantilever does not touch the beam. II. The moment of the contact of the cantilever and the beam. III. The cantilever touches the beam

In this figure: c_{sum} — the overall stiffness coefficient; c_t — the flexure hinge spring constant; c_{canti} — the cantilever stiffness coefficient.

A simplified representation of the device is shown in Fig. 2.

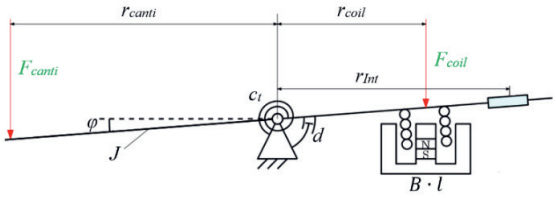

Fig. 2. Simplified mechanical representation of the beam

In this scheme: J — moment of inertia of the beam; d — the damping coefficient of the damper between flexure hinge and beam; φ — the beam angular displacement; r_{Int} — the distance between mirror of the interferometer and joint. Based on the balance moments of forces a system of differential equations is derived (1).

$$\begin{cases} \dot{q}_1 = q_2 \\ \dot{q}_2 = -\dfrac{c_t + c_{canti} r_{canti}^{\,2}}{J} q_1 - \dfrac{d}{J} q_2 + \dfrac{M_{canti}}{J} - \dfrac{M_{coil}}{J} \end{cases} \quad (1)$$

Computer model is performed in the Matlab / Simulink software.

Control system

As can be seen from Fig. 1, at the moment of cantilever contact with the weighing beam, the impact force and the total system stiffness coefficient are unknown. The dynamic behavior of the system changes suddenly. The main objective of the control is to improve the balancing of the beam at the touch of the cantilever, reduce the transient time and reduce the current oscillations. It is proposed to use bumpless control transfer between two discrete PID controllers. If the error modulus between the set position and the position signal from the interferometer is greater than selected error value, the fast controller is triggered, which adjusts the deviation faster, if the error modulus is less than selected error value, the slow controller is triggered.

Since the system error varies greatly when the cantilever comes in contact with the balance beam, the control system must take into account the moment the cantilever is touched and change the error value on the switch, an observer system is needed. The integral of the error squared between the signals from the object and the observer allows you to take into account additional noise at the object, which does not affect the observer in real time. The full structure of the control system consists from four PID controllers and three switches. The control frequency is 600 Hz.

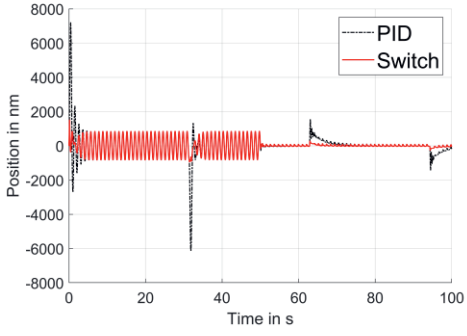

Fig. 3. Comparing simulated displacements of the beam balance with control

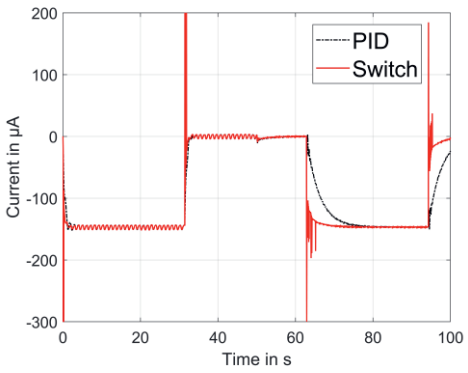

Fig. 4. Comparing simulated currents

Figures 3 and 4 show control results when comparing the developed control system and the slow PID controller. The response rate of the system at contact of the EMFC load cell with the cantilever is improved by 8.39 seconds, thus reducing the time of the transition process. Overshoot reduced by 72%. The control current oscillations are acceptable.

This work was supported by the Deutsche Forschungsgemeinschaft (DFG) in the scope of the Research Training Group "Tip- and Laserbased 3D-Nanofabrication in extended macroscopic working areas" (GRK 2182) at Technische Universität Ilmenau, Germany.

References

[1] J. R. Pratt et al., “Review of si traceable force metrology for instrumented indentation and atomic force microscopy,” Measurement science and technology, vol. 16, no. 11, p. 2129, 2005; doi:10.1088/0957-0233/16/11/002.

[2] Zhao, Yu Wen, et al. "Accurate and traceable calibration of the stiffness of various AFM cantilevers." Key Engineering Materials. Vol. 645. Trans Tech Publications, 2015; doi:10.4028/www.scientific.net/KEM.645-646.817.

[3] C. Diethold, M. Kühnel and T. Fröhlich (2014). Development of a Force Displacement Measurement Device for the Determination of Spring Constants. Universitätsbibliothek Ilmenau; urn: urn:nbn:de:gbv:ilm1-2014iwk-092:6.

[4] O. Dannberg, M. Kühnel and T. Fröhlich (2018, July). Nanonewton Force Measurements Based on Electromagnetic Force Compensated Balances (EMFC). In 2018 Conference on Precision Electromagnetic Measurements (CPEM 2018) (pp. 1-2). IEEE; doi: 10.1109/CPEM.2018.8501174.

[5] A. Amthor, I. Kaiser, N. Rogge and H. Weiss (2014). Analysis, physically motivated modeling and system identification of electromagnetic force compensated balances (EMFC). In Shaping the Future by Engineering: Proceedings; 58th IWK, Ilmenau Scientific Colloquium, Technische Universität Ilmenau, 8-12 September 2014 (Vol. 58); urn: urn:nbn:gbv:ilm1-2014iwk:3.

DOI 10.5162/SMSI2021/A4.1

A metrological atomic force microscope for large range measurements with sub-nanometre resolution

Yiting Wu, Elisa Wirthmann, Ute Klöpzig, Tino Hausotte
Institute of Manufacturing Metrology (FMT), Friedrich-Alexander-Universität Erlangen-Nürnberg (FAU)
Nägelsbachstr.25, 91052 Erlangen, Germany
yiting.wu@fmt.fau.de

Summary:
Calibration of standards is a very important task in dimensional metrology. In this paper large range measurements of pitch standards using a metrological atomic force microscope (MAFM) with combined deflection detection system, that comprises a homodyne interferometer and a tilt measuring system, are presented. The combination allows the simultaneous three-dimensional detection of tip position and cantilever bending and torsion. The combination of the MAFM sensor with the Nanopositioning and Nanomeasuring Machine allows improved quality in calibration of standards such as step height standards, pitch standards and flatness standards. This paper introduces its application for measurements of pitch standards working in contact mode (CM) and in intermitted contact mode (IM).

Keywords: metrological atomic force microscope, large range, nanomeasuring

Introduction

Scanning probe microscopy (SPM) is widely used in semiconductor, precision technology and biotechnology. As the most important member of SPMs atomic force microscopy (AFM) [1] has been used to meet the challenges for dimensional metrology in these areas. Different approaches such as optical beam deflection (OBD) systems, focus sensor detection systems and interferometric detection systems have been developed to measure the position or deflection of the cantilever [2, 3]. Measurements with a laser interferometer allow a traceability to the meter definition by means of the laser light wavelength.

A new version of a metrological laser interferometer-based AFM head has been developed at the Institute of Manufacturing Metrology (FMT). This MAFM sensor with a combined deflection detection system is not influenced by creep, hysteresis of piezo actuators, which occur in many AFM systems. The signal quality has been improved by using two wedge plates to reduce disturbing interference [3, 4]. The new measuring system uses two tiltable plane mirrors to adjust the direction and position of a focused laser beam on the backside of the cantilever [3].

The calibration of standards is a very important task in dimensional nanometrology. For surface roughness measurements a stylus profilometer is usually used. According to DIN EN ISO 4288 [5] a minimum scan length of 400 µm is required for assessment surface texture. The lateral resolution is limited by the tip radius of the stylus (typically 2 µm ~ 5 µm). Due to the small scan ranges, the conventional AFMs are rarely used for applications in the area of conventional roughness determination. Another very important task in dimensional nanometrology is the determination of the pitch. A key factor for better statistical results of the mean pitch is the long scanning range in order to measure over a large number of grating lines [7].

The nanomeasuring machine NMM-1 developed at the Ilmenau University of Technology and manufactured by SIOS Meßtechnik features a reliable measurement resolution of less than 0.1 nm and a positioning and measuring volume of 25 mm × 25 mm × 5 mm [6]. The combination of the MAFM sensor with the NMM-1 leads to improved quality in the calibration of standards. By the integration of the MAFM in the NMM-1, large-scale measurements over a range of 25 mm × 25 mm × 5 mm with sub-nanometre resolution are realizable.

In this short paper the application of the MAFM sensor in different working modes for large range measurements of pitch standards with sub-nanometre resolution is presented.

Calibration

In order to perform measurements, the signals of the MAFM sensor must be calibrated. In CM, the sensitivity of bending signal must be deter-

mined. In IM, oscillation amplitude of the bending signal must be calibrated. The characteristic curves of bending and oscillation amplitude sampled by the analogue digital converter of the NMM-1 are shown in Fig. 1 and Fig. 2. The working range, set point (needed for the force control by measurements in constant-force mode) and coefficients of the characteristic line (used for the calculation of the distance between the cantilever tip and the measured object) can be determined from the approach / retract curves, which also feature the typical snap-in and snap-out.

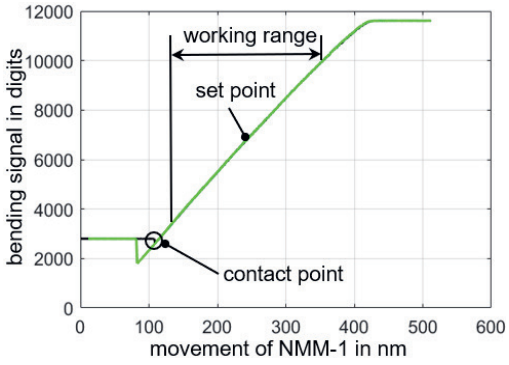

Fig. 1 Characteristic curve for bending

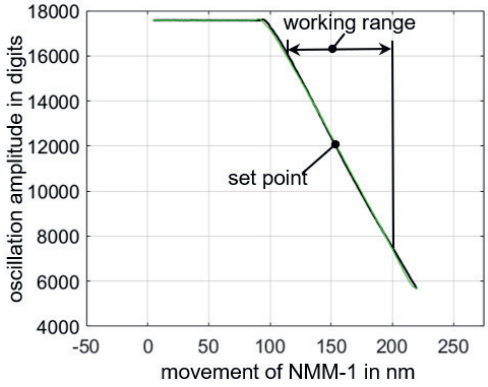

Fig. 2 Characteristic curve for oscillation amplitude

Application

The grating set TGZ series with a period of (3 ±0.01) µm from company NT-MDT were used in the CM and IM measurements. The measurements with scan length of 600 µm are conducted forwards (f) and backwards (b) perpendicular to the gratings for 10 times. When measuring in IM, the profile height (z-direction) is given as the difference between the calibrated amplitude signal and the z-axis position data of the NMM-1. For measurements in CM, the profile height (z-direction) is calculated as the difference between the calibrated bending signal and the z-axis position data of the NMM-1. The mean pitch was calculated using the Fourier transform method [3, 7]. Table 1 shows the determined mean pitch values (*m*) and standard deviations (*s*) of TGZ1 with a step height of (21.4 ±1.5) nm and of TGZ2 with a step height of (108 ±2) nm by forward and backward measurements. The deviations between the nominal values and measured values for the pitch are within the uncertainty of the nominal values. The deviation between CM and IM was less than 50 pm. Measurements at different positions showed, that the local deviations also play a role for the measurements results.

Tab. 1: Results for pitch on gratings

standard	*forward*		*backward*	
	m in nm	*s* in pm	*m* in nm	*s* in pm
CM				
TGZ1	3000.058	82.09	3000.053	84.03
TGZ2	3000.011	16.85	3000.056	74.16
IM				
TGZ1	3000.030	38.5	3000.038	65.3
TGZ2	3000.037	41.3	3000.023	24.3

References

[1] H.-U. Danzebrink, T. Dziomba, M. Xu, A. Pidduck, R. Leach, A. Yaccot, L. Koenders, Scanning Probe Microscopy, Scanning Electron Microscopy and Critical Dimension: Nanometrology Status and Future Needs within Europe, Nanometrology Discussion Papers Co-Nanomet, 55-57 (2009); ISBN 978-0-9566809-0-7

[2] A. Yacoot, L. Koenders, Recent developments in dimensional nanometrology using AFMS Measurement Science and Technology, 122001 (2011); doi: 10.1088/0957-0233/22/12/122001

[3] Y. T. Wu, E. Wirthmann, U. Klöpzig, T. Hausotte, Investigation of a metrological atomic force microscope system with a combined cantilever position, bending and torsion detection system, SMSI (2020); doi: 10.5162/SMSI2020/C6.3

[4] F.G. Balzer, T. Hausotte, N. Dorozhovets, E. Manske, G. Jäger, Tactile 3D microprobe system with exchangeable styli, Measurement Science and Technology, 094018 (2011); doi: 10.1088/0957-0233/22/9/094018

[5] DIN EN ISO 4288:1998-04, Geometrische Produktspezifikation (GPS) - Oberflächenbeschaffenheit: Tastschnittverfahren - Regeln und Verfahren für die Beurteilung der Oberflächenbeschaffenheit (ISO 4288:1996)

[6] T. Hausotte, Nanopositionier- und Nanomessmaschinen – Geräte für hochpräzise makro- bis nanoskalige Oberflächen- und Koordinatenmessungen, Ilmenau: Techn. Univ. Habilitationsschrift, Pro Business (2011); URL: https://www.fmt.tf.fau.de/forschung/publikationen/habilitationsschriften/#collapse_0

[7] G. Dai, L. Koenders, F. Pohlenz, T. Dziomba und H.-U. Danzebrink, Accurate and traceable calibration of one-dimensional gratings, Measurement Science and Technology, (2005); doi: 10.1088/0957-0233/16/06/001

DOI 10.5162/SMSI2021/A4.2

Development of a Non-invasive Pressure Sensor

Paul Szász[1], Vadim Migunov[1]
[1] ABB Corporate Research Center, Wallstadter Str. 59, 68526 Ladenburg, Germany
paul.szas@de.abb.com

Summary:
A novel solution for measuring pressure non-invasively is presented, offering new perspectives for retrofittable monitoring and optimization applications. The clamp-on sensor is based on measurement of the circumferential deformation of pressurized pipes, using a compliant pre-stressed metal clamp with strain gauges as sensing elements. The design concept of this measurement system is presented, including the underlying functional mechanisms. Its achievable measurement performance and applicability limitations have been derived from long-term validation tests.

Keywords: non-invasive, pressure, sensor, strain gauge, clamp,

Background, Motivation an Objective

While non-invasive sensors are increasingly available for process variables like temperature or flow, pressure sensing is still persistently invasive, needing direct fluid contact. Filling this gap in non-invasive sensing is expected to offer significant benefit, e.g. regarding increased safety and hygiene due to zero leakage risk, or improved process control at low cost due to easy retrofit even in running processes.

In patent literature, solutions for this task are present since the 1970ies. Still no product has emerged over all these years, indicating major technical obstacles. One main limiter is the international pressure vessel design regulation, leading to highly stiff piping which is supposed to suffer minimum effects by internal pressure variations. While this is favorable for safety and longevity of the piping, it actually strongly limits the use of a process pipe as sensing element. Transforming the pressure into a measurable signal appears to require very elaborate and costly technologies. ABB has taken the chance to pioneer in this field and present a sensing concept which can overcome many of the so far known limitations at an acceptable cost level.

Measurement Principle

After analyzing the vast variety of physically conceivable measurement principles, strain gauge sensing of the pipe circumferential strain was selected as promising option. Strain gauge sensing offers not only sufficient resolution of the very small pipe deformations, but it is also widely available at moderate cost and well understood, so development could concentrate on the realization of a sensor system with sufficient robustness and reliability. Pipe circumferential strain is also favorable as measurand, as it is fully independent of the pressurizing fluid offering so a broad use range.

Technical solution

Direct strain gauge application to process pipes in the field is not practical for an industrial sensing device. So, a solution for transferring the pipe deformation to a sensor structure with a well-defined transfer function was developed. I.e. the deformation of this structure deviates in a predictable way from the deformation of the pipe. A flexible thin steel strip is wrapped around the pipe and pre-stressed to a degree which makes it fully compliant to the pipe surface (Fig.1).

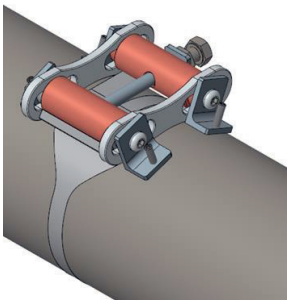

Fig. 1. Strain and pressure sensing clamp

As result, the strains on the clamp strip surface will always be almost identical to the pipe surface deformation. Having a small thermal mass and good contact to the pipe, the clamp also will have the same temperature, reducing temperature induced errors. Variations of the strain in the clamp over the circumference and especially due to the discontinuity at the tensioning mechanism can be accounted for using a transfer function determined by calibration, as they are constant properties of the clamp.

The tensioning mechanism is an especially sensitive part, requiring high long-term stability and minimized influence on the actual transfer function. Its design included aspects of thermal and elastic tailoring, ease of handling and reliability.

Temperature compensation

Temperature induced signal variations are inherent to strain gauge sensing and are typically solved by using full Wheatstone bridge circuitry. However, on curved surfaces and especially on pressurized pipes there is no way to create such a self-compensating circuitry. Only a diagonal half bridge solution was applicable, measuring the circumferential strain on two locations of the clamp. Consequently, a solution was developed to quantify the thermal response of the clamp in a calibration step. The generated temperature dependent calibration values can subsequently be subtracted from the actual measured values, allowing the correction of the temperature induced error.

Measurement of pressure step change

The strain gauge clamp solution was thoroughly tested to provide information on the expectable measurement performance.

Pressure step changes, i.e. discrete pressure changes within defined time periods give a highly linear strain signal (Fig. 2).

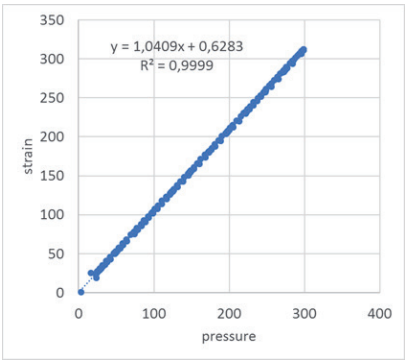

Fig. 2. Strain is a linear function of pressure

The strain signal is corrected by the known transfer function of the clamp to yield the actual pipe strain value. Knowing geometric and elastic properties of the pipe (described by according constants k_{geom} and k_{elast}) any strain change $\Delta\varepsilon$ can be analytically transformed into a corresponding pressure change Δp with an accuracy within 1 – 2 % of the rated pressure of the considered pipe (eq. (1)).

$$\Delta p = \Delta\varepsilon_{pipe} \times k_{elast} \times k_{geom} \quad (1)$$

Long term stability

Experiments over several months showed that long term stability does not come up to the level of pressure step change measurement accuracy. Though drifts in the mechanical setup were excluded by design, two inherent stability issues are still prevalent. First, the accuracy of thermal calibration cannot fully exclude signal fluctuations in the order of up to 5 % of the rated pressure of the pipe due to “stress augmented thermal activation” in the interfaces, leading to temperature gradient dependent reversible creep and friction phenomena. Additionally, long term slow drift of the zero signal was observed (inherent to glued strain gauges, especially on highly stressed components), leading to about 0.5 % drift per month, which can be compensated by periodic zero reset.

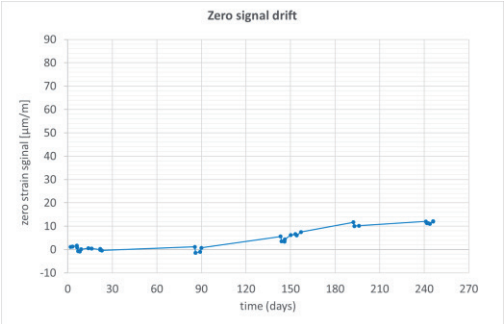

Fig. 3. Long term signal fluctuation and drift

Applicability conclusions

The developed clamp-on pressure sensor is scalable for pipe sizes exceeding DN50 based on the developed design rules. It is applicable for all pressure ratings exceeding 10 bars. For lower pressure piping the small deformations limit the achievable resolution and accuracy strongly.

It is important to note that the non-invasive pressure measurement always measures a pressure difference related to a defined starting point, usually the mounting state or an arbitrary zero setting. I.e. a one-point calibration (knowing the real pressure value at a given time) is essential to enable this measurement.

This non-invasive pressure sensor can detect and quantify short term pressure changes with an accuracy of 1 – 2 %, making it suited for monitoring of e.g. pump or valve functions, flow obstructions or leakage. Alternatively, for known pressure steps the system can recognize pipe wall thickness variations as may occur due to long-term corrosion.

Its long-term accuracy of 5 to 10 % limits its use as absolute pressure sensor to applications with regular zero resetting possibility (e.g. batch processes) and small temperature variations, where the absolute accuracy can be < 2 % of the pipe pressure rating over longer periods.

DOI 10.5162/SMSI2021/A4.4

Theoretical Analysis of Measurement Flexures at the 5 MN·m Torque Standard Machine at PTB

Kai Geva[1], *Holger Kahmann*[1], *Christian Schlegel*[1], *Rolf Kumme*[1]
[1] *Physikalisch-Technische Bundesanstalt, Braunschweig, Germany*
[1] *kai.geva@ptb.de*

Summary:
A hinge flexure for measuring purposes is presented. Its usage in the 5 MN·m torque standard machine at PTB is described. Essential measurement uncertainty influences such as interferometer, retroreflector position and deflection line deviation are discussed.

Keywords: force measurement, torque measurement, multicomponent measurement, stiffness measurement, flexure hinge, compliant mechanism, beam theory

Introduction

At the PTB a new 5 MN·m torque standard machine (TSM) is built to calibrate torque transducers [1]. The machine's measurement system has a lever where the torque transducer under test is flange-mounted to. The lever itself is jointed on six hinge flexures (also called measurement flexures (MF) hereafter) to receive the lever forces axially and measure them with attached transducers. The MF support force transducers measuring either lever forces of torque moment (TM) or bending moment (BM). In this context, it is enough to focus only on the bending moment MF (BMMF, see Figure 1). Not only do these hinge flexures reduce bending moments and torsion onto the force transducer but their deflection helps measuring them. The transversal force and the torsion they receive account to a small amount of the overall calibration moment that needs to be measured and can't be neglected for accuracy reasons. The deflection caused by transversal force and torsion at MF is measured by an interferometer because strain gauge measurement lacks the needed precision due to high crosstalk. The stiffness is calibrated in a MF calibration set-up (CSU), the required force and torsion is measurable [2]. To provide a traceable calibration moment the MF force and torsion measurement must be characterized by a measurement uncertainty analysis.

Measurement Uncertainty Analysis

An uncertainty measurement analysis for the reaction force and torsion for is performed. Table 1 depicts all quantities which contribute to the uncertainty budget. The following sections discuss the most essential uncertainty quantities.

Measurement flexure calibration

There are two different calibration cases: Bending moment and torsion. Both calibration moments are always combined with a transversal force. This force is measured indirectly by the deflection. Thus, it is important that the deflection line in calibration setup and TSM operation match. The crucial question to the effectiveness of this approach is how reliantly the mass-lever system "imitates" the load within TSM operation and result in the same deflection line.

In the CSU a simple mass-lever system is used. The force is introduced on the height of the middle of the MF. This causes a linear decrease of

Table 1 List of measurement uncertainty influences

MF Calibration	Calibration uncertainty	
	Deflection line deviation	Different Load
		Additional TSM Load
	Assembly	
	Alignment	
	Fixation	
Interferometer	Calibration uncertainty	
	Environment	
	Retroreflector (RR)	
	Resolution	
	User	
RR Position	CSU Lever	Force
		Torsion
	TSM Lever	Deformation RR
		Deformation MF
		Lever Rotation angle

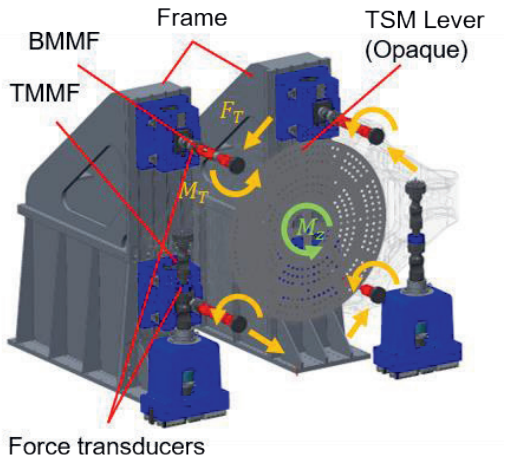

Figure 1 Parasitic MF Loads during TSM operation

bending moment with zero moment in the middle of the MF (see Figure 2). In TSM operation, it is rather a forced displacement at the MF's end producing the same force and moment reaction as in CSU. To comprehend why both load scenario match, an analytical model is created. Flexure hinges are widely investigated in the field of precision positioning. There exist various theories to describe the deflection of beams. The resulting deflection line and the preceding presumptions differ, and a literature research is performed to find the most appropriate theory [2],[4].

The analytical model is used to validate the FE-models made in ANSYS. The FE-models are used to analyze if additional axial force, orthogonal bending moment or torsion have an influence on the deflection line in TSM operation. Furthermore, the FE model quantifies the linearity.

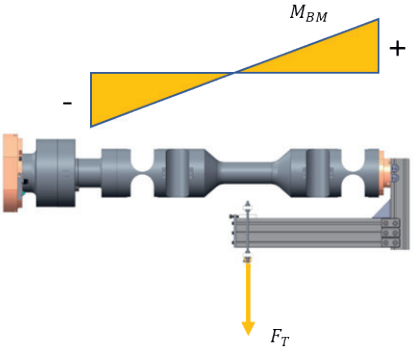

Figure 2 Measurement flexure calibration set-up

Interferometer

For displacement measurements a SIOS interferometer MI5000 is used. It is equipped with two retroreflectors and was calibrated at PTB. The calibration incorporates uncertainty influences the environment quantities and the retroreflector as well. The uncertainty of the interferometer depends on the distance between the laser and the reflector. The uncertainty of the interferometer influences the MF's overall uncertainty at two stages: When the MF is calibrated and when then MF displacement is measured during TSM operation. All three displacement measurements need to be analyzed.

Retroreflector position

Not only the retroreflector's distance to the laser but also the positions where the measurement takes place adds up to the uncertainty. Because the points of interest can't be measured directly the measurements are taken at a place that have a linear correlation to the points of interest. During MF calibration, the reflector is placed close to the cantilever depending on the calibration desired. The FE analysis reveals the relative displacement difference between set point and measured point and its impact on the measurement uncertainty.

During TSM operation the reflector can't be placed at the MF because it is covered by a mounting plate. Thus, the MF displacement correlates with the lever rotation angle α. The angle measurement α is approximated by two simple distance measurements which must be addressed in the measurement uncertainty analysis. The movement of the lever and the additional deformation of the lever under load lead to a deviation from idle rotation which must be added in the uncertainty budget. All the deviations from idle rotation are extracted from a FE analysis.

Summary

The usage of an interferometer to measure reaction force and moment of measurement flexures were discussed. The key components of the measurement uncertainty budget were presented. The influence of the retroreflector positions was discussed. The method how to estimate the deflection line deviation by an analytical and a FE-model were described, and the deflection measurement deviation quantified.

References

[1] H. Kahmann, C. Schlegel, R. Kumme, and D. Röske, Principle and Design of a 5 MN·m Torque Standard Machine, *Proc. of the IMEKO 2017 TC3 Conference*.

[2] K. Geva, H. Kahmann, C. Schlegel and R. Kumme, Analysis of the Measurement Uncertainty of a New Measurement Flexure Calibration Set-Up, *ACTA IMEKO TC3 Special Issue,* ***not published yet***

[3] J. Gallego, J. Herder, Classification for Literature on Compliant Mechanisms: A Design, *Proc. of the ASME 2009*, DOI: 10.1115/DETC2009-87334

[4] D. Kern, Neuartige Drehgelenke für reibungsarme Mechanismen, Diss., Karlsruhe Institut für Technologie, DOI: 10.5445/KSP/1000036442

DOI 10.5162/SMSI2021/A5.1

Design, Simulation, Fabrication and Characterization of Piezoelectric MEMS Cantilever for Gas Density and Viscosity Sensors Applications

A. Mehdaoui[1], C.Huber[1], J.Becker[1], F.Schraner[1], L.G.Villanueva[2]
[1] TrueDyne Sensors AG, Reinach BL, Switzerland
[2] Ecole Polytechnique Fédérale de Lausanne, Advanced NEMS Laboratory, Lausanne, Switzerland
alexandre.mehdaoui@truedyne.com

Summary:
A MEMS cantilever based resonant device for gas monitoring actuated and sensed piezoelectrically, has been designed, simulated, fabricated and tested. Aluminum Nitride (AlN) has been used as active material to implement the piezoelectric actuator and sensor. Simulation performed using COMSOL and measurements show a very good agreement. The final system, the full sensor for gas monitoring, allows the measurement of gas density and viscosity at temperatures between 0 and 65 °C and pressures between 1 and 10 bar abs. with accuracies of <0.03 kg/m^3 and 6% respectively. The second technological run has shown significant results at the same conditions, respectively of < 0.02 kg/m^3 and < 2% for density and viscosity.

Keywords: MEMS, resonator, cantilever, piezoelectric actuation, piezoelectric sensing, density, viscosity, gas monitoring

Background, Motivation an Objective

Micromachined sensors are widely used to meet the increasing demand for miniaturized sensors for measuring physical parameters of gases, such as the density and viscosity. Also the realisation of ultra-precise scales in the field of inert gases e.g. welding gas or modified atmospheric packaging gas mixing application is of high interest. The use of standard silicon technology allows miniaturization at reduced costs, thus pushing the entry into new sensor markets such as low-power handheld systems [1]. The core of the sensor is an oscillating micro-cantilever which is fabricated at the Center of MicroNanotechnology (EPFL). The peak resonance response frequency f_r and the quality factor Q of a microcantilever are the two main dynamic characteristics that are very sensitive to the density and viscosity of the surrounding fluid [2]. Therefore, the viscosity and density of a fluid can be determined by analyzing the frequency response of a cantilever immersed in the fluid [3,4].

Description of the System: Design&Process

In this paper, a MEMS cantilever resonator (the core of the sensor), actuated and sensed piezoelectrically, has been designed, simulated, fabricated and tested. A piezoelectric transduction, Aluminum Nitride (AlN), is integrated on top of the cantilever to enable actuation and detection of devices (resonance frequency and Q factor). Platinum (Pt) has been used as top and bottom metal contacts between which AlN has been sandwiched to form the actuating and sensing electrodes and also the temperature sensor. Indeed, as the temperature has to be well measured and controlled during the evaluation of the gas thermophysical properties, we need to define the temperature sensor as close as possible of the density and viscosity sensors. The cantilever investigated in this paper was fabricated on a SOI wafer with a 10 μm thick device layer and with a length of L=600 μm and a width of W=202 μm. Fig. 1 shows the detailed process flow.

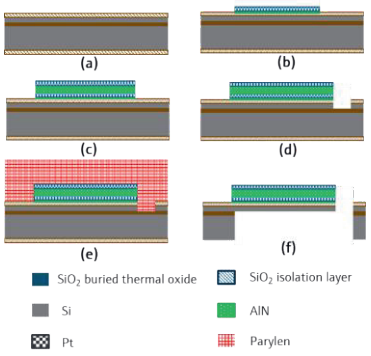

Fig. 1. AlN cantilever fabrication process: (a) thermal oxidation isolation layer, (b) adhesion AlN layer and bottom Pt metal deposition and patterned by lift-off, (c) active AlN layer and top Pt metal deposition

by sputtering and patterned by Cl_2/Ar dry etch, (d) cantilever shape patterning by CF4 and Cl_2 dry etch, (e) Parylen deposition for the front side protection during the deep back side etching, (f) cavity patterning by dry Si and wet SiO_2 etching, cantilever release by plasma O_2

Results

Fig. 2a shows the SEM image of the fabricated AlN cantilever. Fig. 2b shows the MEMS chip bonded on a PCB, following by the glob-top encapsulation.

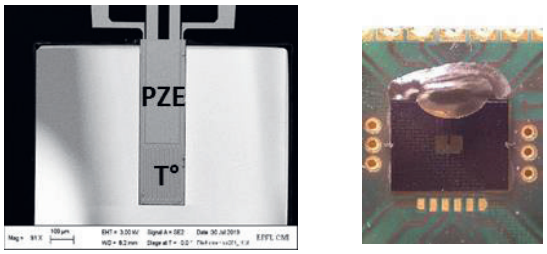

(a) b)

Fig. 2. MEMS Piezoelectric cantilever: (a) SEM image: Temperature sensor (T°) and Piezoelectric transducer (PZE), (b) MEMS sample + PCB

Fig. 3 a and b show respectively the simulated impedance real and imaginary parts performed in COMSOL and the measured frequency response, both amplitude and phase of the signal. We can see a good agreement between the simulation (f_r = 43.7 kHz, Q = 882) and measurement results (f_r = 41.1 kHz, Q = 724).

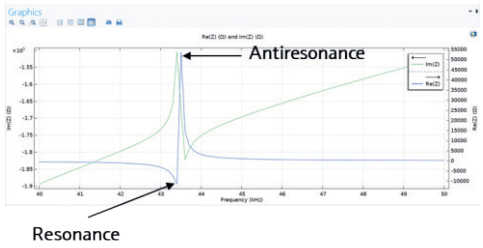

(a)

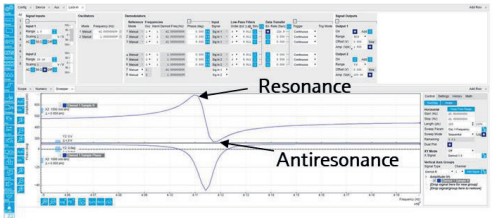

(b)

Fig. 3. Piezoelectric resonance and Q factor in Air: (a) simulated impedance in COMSOL, (b) Measured frequency response using lock-in amplifier

For the measurement in gases, we have manufactured a special PCB containing a MEMS chip, a pressure and temperature sensors. This PCB can be screwed into a gas tight metal cylinder that serves as a gas cell, see Fig. 4. For a standard density and viscosity calibration, 4 different gases (N_2, CO_2, Ar and He) are measured at temperatures between 0 and 60 °C and pressures between 1 and 10 bar abs. We can measure the gas density with an abs. accuracy <0.03 kg/m^3 and the dynamic viscosity with a relative accuracy of 6%. The second technological RUN has shown better accuracies, respectively of < 0.02 kg/m^3 and < 2% for density and viscosity, by changing the Si device layer thickness from 10 μm to 5 μm and 3 μm. The measuring performance of the final sensor is shown in Fig. 5.

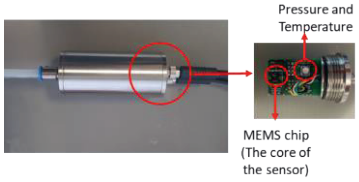

Fig. 4. Sensor PCB mounted in a pressure tight gas cell with electric connections on the right and fluidic connections on the left

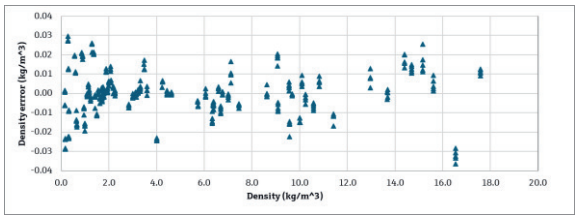

(a)

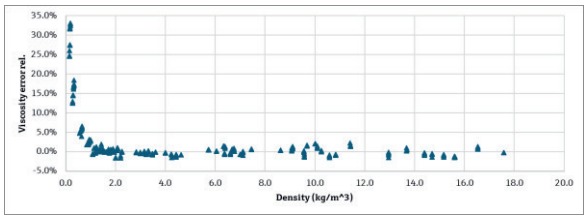

(b)

Fig. 5. (a) Density and (b) viscosity measuring accuracy

References

[1] M. Kucera and all, Characterization of multi roof tile-shaped out of plane vibrational modes in aluminum nitride actuated self-sensing micro-resonators in liquid media, *Applied Physics Letters 107*, 053506 053506 (2015), doi: 10.1063/1.4928429

[2] H. Qiu et al., Hydrodynamic analysis of piezoelectric microcantilevers vibrating in viscous compressible gases, *Sensors and Actuators A*, 238 (2016), 299-306

[3] A. Badarlis et al., Measurement and evaluation of the gas density and viscosity of pure gases and mixtures using a micro-cantilever beam, *Sensors*, 15 (2016), doi: 10.3390/s150924318

[4] C. Huber et al., Gas density and viscosity measurement with a micro-cantilever for online combustion gas monitoring, 19. GMA/ITG-Fachtagung Sensoren and Messsysteme, 2018

DOI 10.5162/SMSI2021/A5.2

Swarm-Based Multi-Objective Design Optimization of Single-Plate Condenser MEMS Microphone

Qummar Zaman[1], Senan Alraho[1], Andreas König[1]
[1]Lehrstuhl Integrierte Sensorsysteme (ISE), TU Kaiserslautern Deutschland,
qummar@eit.uni-kl.de

Summary:
This work presents a multi-objective optimization of MEMS microphone using the PolyMUMPS fabrication technology. The proposed method handles simultaneous optimization of performance parameters such as sensitivity, lower cut-off frequency, resonance frequency, linearity and noise level. An agglomerative method is being used for multi-objective optimization due to its simplicity. While for efficient exploration of complex search space of MEMS microphone, the traditional particle swarm optimizer has been amended by adaptively adjusting its social and personal best coefficients.

Keywords: MEMS condenser microphone, Machine learning for microsystems, An agglomerative method, Particle swarm optimizer, Multi-objective optimization, PolyMUMPS technology

Background, Motivation an Objective

A microelectromechanical system (MEMS) based condenser microphone also known as silicon microphone [1] is widely used as an acoustic wave (sound, pressure waves, etc.) sensor [2]. The applications of a MEMS microphone include hearing aids, vibration, security surveillance instruments, voice control devices and machine conditioned monitoring in industry 4.0 [3,4]. The main reasons for this trend are their small size, compatibility with the standard CMOS process, low noise level, low power consumption, flat frequency response and high sensitivity [5].

Several parameters (sensitivity, lower cut-off frequency, resonance frequency, linearity and noise level) affect the performance of MEMS-based microphones [6]. Hence, multiple objectives need to be explored simultaneously. So, the main objective of this research is to analyze the multi-objective performance optimization of a MEMS-based microphone. Many researchers have worked on the optimizations of the MEMS microphone [1] [6-10] but none of them covered all the optimization parameters at the same time. MEMS design implies a search space complexity, that makes it challenging to find the suitable optimum using traditional optimization algorithms [8]. To handle this problem, metaheuristic and evolutionary algorithms are found promising alternatives for the optimization of such a complex landscape. Additionally, they showed promising results in many engineering optimization problems. For this reason, Particle Swarm Optimizer (PSO) is selected as an evolutionary optimizer for this research. The multi-objective optimization of a microphone is presented in [8] that simultaneously considers the trade-off between noise floor and sensitivity. Similarly, [1] used evolutionary genetic algorithm to optimize three objective functions for MEMS microphone but did not consider linearity and noise level optimization.

Proposed Methodology

The proposed work presents a novel PSO method to optimize a microphone due to its enhanced exploration capabilities through adaptive value adjustment of personal and social coefficients presented in [11]. PSO begins with random initialization followed by the evolution of cost function. Then the particle's personal or global best is being amended in case of better fitness value. The cognitive and social scaling factors are being updated according to the following equations

$$c_1 = c_2 = F(D) = \frac{a}{1 + e^{-c(D-d)}} + b$$

where $a = 0.5$, $b = 1.5$, $c = 0.000035 \times$ search range (distance between upper & lower bound of particle), $d = 0$ and $D = P_{p\,or\,g}(k) - x_i(k)$ which represent the distances of the particle to its p_{best} or g_{best} at k_{th} iteration. After that, the particle's velocity and position are being updated, this procedure continues until maximum iterations.

Also, we applied an agglomerative method for multi-objective optimization [12] of a microphone. The weight parameters of all optimization

objective for an agglomerative method are defined equally. The 3D structure of a microphone is designed in coventor mems+ [13] using PolyMUMPS technology as shown in Fig. 1.

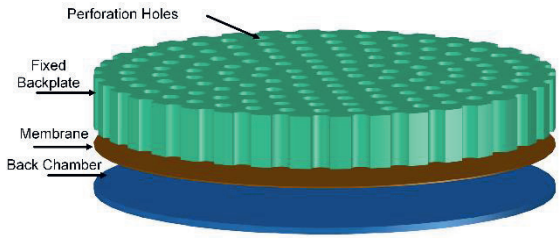

Fig. 1. A 3D structure of condenser MEMS microphone.

Results

The design specification for MEMS microphone and results achieved after optimization along with search variables' range and step size are presented in Tables 1 and 2 respectively. For this experiment we used 10 particles and 100 number of iterations.

Tab. 1: Design specifications for MEMS microphone.

Specifications	Target design	Achieved
Sensitivity	$\geq 5\ fF(Pa)^{-1}$	$\geq 5.34\ fF(Pa)^{-1}$
-3dB low frequency (f_1)	$\leq 20\ Hz$	$3.433\ Hz$
Resonance frequency (f_2)	$\geq 20\ kHz$	$59.71\ kHz$
DC capacitor	$\geq 1\ pF$	$2.13\ pF$
Linearity	$1\ to\ 20\ Pa$	$1\ to\ 20\ Pa$
Noise level	$\leq 40\ pV(Hz)^{-1/2}$	$37.11\ pV(Hz)^{-1/2}$

Tab. 2: Range of search space variables.

Design Variables	Range		
	From	To	Step Size
Membrane thickness	0.5 µm	5 µm	100 nm
Membrane Radius	500 µm	750 µm	100 nm
Backplate thickness	2.5 µm	8 µm	100 nm
Backplate conductive factor	0.5	0.75	0.05
Air gap thickness	1 µm	8 µm	100 nm
Perforation hole radius	2.5 µm	25 µm	100 nm
Perforation distance	2.5 µm	25 µm	100 nm
Ventilation radius	1 µm	5 µm	100 nm

The output sensitivity graph is shown in Fig. 2 which clearly illustrates the flattened response of sensitivity and makes it perfectly applicable for audio frequency applications. The outlook to this work will be the introduction of self-x (self-calibration, self-healing) properties to the MEMS microphone [14] along with its electronic readout circuit to address the problem of device performance tolerances or drift due to static and dynamic effects.

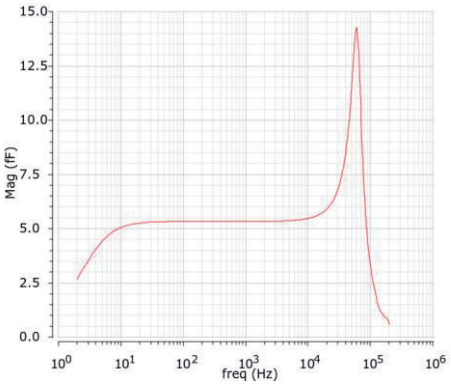

Fig. 2. Frequency response of output sensitivity.

References

[1] G. M. Sessler, "Silicon microphones," J. Audio Eng. Soc. 44, 16–22 (1996).
[2] M. Saadatmand and J. Kook, "Multi-objective optimization of a circular dual back-plate MEMS microphone: tradeoff between pull-in voltage, sensitivity and resonance frequency," Microsyst. Technol. 2019.
[3] S. Babaei Sedaghat, B. Azizolla Ganji, and R. Ansari, "Design and modeling of a frog-shape MEMS capacitive microphone using SOI technology," Microsyst. Technol., vol. 24, Jun. 2017.
[4] Shaffer, Derek, et al. "Investigation of the feasibility of using microphone arrays in monitoring machining conditions." Manufacturing Letters 15 (2018).
[5] M. A. Shah, I. A. Shah, D. G. Lee, and S. Hur, "Design approaches of MEMS microphones for enhanced performance," J. Sensors, vol. 2019, 2019.
[6] Farnsworth, Michael, et al. "An efficient evolutionary multi-objective framework for MEMS design optimisation: validation, comparison and analysis." Memetic Computing 3.3 (2011): 175.
[7] Wang, Pan, Qibing Lu, and Zhun Fan. "Evolutionary design optimization of MEMS: a review of its history and state-of-the-art." Cluster Computing 22.4 (2019): 9105-9111." IEEE Sensors Journal 19.15 (2019).
[8] Papila, Melih, et al. "Piezoresistive microphone design pareto optimization: tradeoff between sensitivity and noise floor." Journal of MEMS 15.6 (2006).
[9] Shah, Muhammad Ali, et al. "Design approaches of MEMS microphones for enhanced performance." Journal of Sensors 2019 (2019).
[10] Zhu, Jianxiong, et al. "Development Trends and Perspectives of Future Sensors and MEMS/NEMS." Micromachines 11.1 (2020): 7.
[11] Liu, Weibo, et al. "A Novel Sigmoid-Function-Based Adaptive Weighted Particle Swarm Optimizer." IEEE transactions on cybernetics (2019).
[12] Kammara, Abhaya Chandra, Lingaselvan Palanichamy, and Andreas König. "Multi-objective optimization and visualization for analog design automation." Complex & Intelligent Systems 2.4 (2016): 251-267.
[13] "MEMS Microphone Design — Coventor MEMSplus." https://www.coventor.com/mems-solutions/microphones/. Accessed: 26-11-2020.
[14] Clark, Jason. "Self-Calibration and Performance Control of MEMS with Applications for IoT." Sensors 18.12 (2018): 4411.

DOI 10.5162/SMSI2021/A5.3

Designing Low Power Systems with Digital MEMS Sensors

Petr Stukjunger
STMicroelectronics, Pobrezni 620/3, Prague, Czech Republic,
petr.stukjunger@st.com

Summary:
Design of low power systems has been significantly improved by recent innovations in the field of digital MEMS sensors. System engineers can take advantage of sensors' embedded features and parameters that enhance and simplify power consumption optimization at both sensor and system level.

Keywords: low power, system design, MEMS sensor, application, machine learning

Introduction

More and more features and functionalities are expected from modern embedded systems. At the same time, it is required to minimize power consumption. These requirements are contradictory and often difficult to fulfill.

Applications that are utilizing digital MEMS sensors to measure environmental, motion and other types of data, can take great benefits by utilizing sophisticated features of these sensors.

In this paper we will discuss the features of digital MEMS sensors and system level techniques that designers may exploit to minimize power consumption of their systems.

Low power sensor and features

Wide popularity of battery-operated nodes motivated manufactures of MEMS sensors to develop devices with ultra-low current consumption. The newest accelerometers can measure movements while consuming less than one microamp. Even larger improvements have been made in the design of gyroscopes, where we have seen more than 10times drop in their current consumption just over last couple of years.

Digital MEMS sensors are very flexible in their configuration offering variety of operating modes with associated output resolution and wide range of applicable data rates. Designers can therefore select the most suitable configuration for each application case. Some sensors are even capable to switch their operating mode and data rate autonomously based on an external motion event. Even though these improvements are of substantial help in low power system design, the newest MEMS sensors bring even more features that can help.

Motion detection features like wake-up (for system activation based on a motion), free fall (detection of device falling down), orientation detection (used daily in our mobile phones), single & double tap (for enhanced user interface) became almost industry standard. More and more common are also features like step counter or pedometer, tilt detection etc.

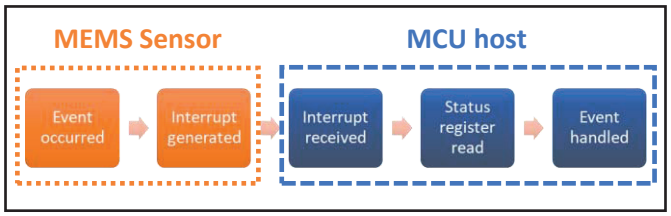

Fig. 1. Utilizing interrupt of digital MEMS sensor.

The above-mentioned features allow to offload microcontroller from continuous acquisition and evaluation of sensor data bringing a substantial decrease in system power consumption. It is simply achieved by the utilization of interrupt signals routed from the sensor to the microcontroller. The microcontroller is not anymore involved in nonstop data acquisition, instead it is solely waiting for a signal from the sensor raised just in the moment when there was a new event to be handled by the system.

Advanced Embedded Features

The latest six axis inertial measurement units (IMUs) from STMicroelectronics bring system power reduction to a next level as discussed in [1]. Thanks to Finite State Machine and Machine Learning Core blocks it is possible to move medium complex algorithms from microcontroller inside the sensor itself and consequently reduce not just microcontroller's current consumption and load, but also traffic on communication bus.

Finite State Machine

Finite State Machine (FSM) block provides to system designers possibility of creating their own state programs, where in each state two conditions may be evaluated, or a command executed. The conditions evaluate sensor output data with respect to a user-defined threshold or time-related execution based on internal timers. The FSM is well suited for implementation of gesture recognition algorithms or enhanced control mechanisms based on the sensor data.

Machine Learning Core with AI

Machine Learning Core (MLC) is a hardware implementation of decision trees inside digital MEMS sensor. The sensor can run motion classification algorithms by its own and take the advantage of machine learning techniques well known from the field of artificial intelligence.

The utilization of the MLC follows common machine learning process. It starts by data collection and labeling followed by identification and extraction of the features that characterize the movements to be recognized. Then any conventional machine learning tool is executed to generate decision tree. Finally, the decision tree is converted into set of values, which are then loaded into sensor's configuration registers to run the decision tree algorithm.

The overall system current consumption is dramatically reduced as can be seen from the following example. We took human activity recognition algorithm and compared its implementation as microcontroller library vs. decision tree inside the MLC. In this comparison we have used STM32L476, ultra-low-power 32bit Cortex-M4 MCU, and LSM6DSOX, high-performance 6axis IMU with embedded MLC core, from STMicroelectronics.

As shown in table Tab 1. in both cases the sensor needs 15 µA to sample data. Running the algorithm inside the MLC increases sensor's current consumption just by a few extra micro amps. When the microcontroller is running activity recognition library, it needs to collect sensor data at certain rate (16Hz in this case) and run the classification algorithm. On the other hand, when the MLC is running the activity recognition, the microcontroller can be left in a very low power mode for most of the time and wakes-up only upon notification from the sensor that a new motion class has been detected. In our example we considered that the class (user activity in this case) will change on average every 30 seconds. We can see that the overall system current consumption is greatly reduced by offloading the microcontroller and prolonging its stand-by time.

Tab. 1: Current consumption of an embedded system when running activity recognition algorithm. Comparing implementation inside STM32L476 32bit MCU vs. MLC of LSM6DSOX 6axis IMU.

	MCU library implementation	MLC implementation
Sensor data chain	15 µA	15 µA
Sensor MLC block	0 µA	4 µA
MCU stand-by time	63 ms (1/16Hz)	30 s
MCU consumption	51 µA	0.7uA
Total	**66 µA**	**19.7 µA**

From Low Power Sensor to Low Power System

We have seen that sensors offer many options to optimize overall system current consumption. There are several methods how to save current also at the system level as discussed in [2]. The output data shall be read from the sensor using so-called data ready interrupt instead of continuously polling a status register to check whether new data has been sampled. Communication on the serial bus between the sensor and the microcontroller is another contributor to the overall system power consumption. SPI interface is therefore preferred over I^2C. Brand new sensors are equipped with MIPI $I3C^{SM}$ bus that combines benefits of SPI, i.e. speed, and I^2C, i.e. number of wires. Power supply level shall be as low as possible because it decreases the current consumed by the sensor itself.

Conclusion

The ultra-low current consumption of modern MEMS sensors and their embedded features like FSM and MLC are handy tools for designers of low power systems. By employing optimizations also at system level, the overall power consumption budget is reduced multiple times. These mechanisms open new approaches to design of embedded systems including edge computing, in case of the MLC brought really to the very source of the sensor data.

References

[1] M. Castellano, R. Bassoli, M. Bianco, A. Cagidiaco, C. Crippa, M. Ferraina, M. Leo, S.P. Rivolta, Embedded Algorithms for Motion Detection and Processing, proceedings of embedded world 2018 exhibition&conference

[2] Vladimir Janousek, Petr Stukjunger, Low-power application design with ST's MEMS accelerometers, design tip, Rev 1, February 2019

DOI 10.5162/SMSI2021/A5.4

Self-excited Contact Resonance Operation of a Tactile Piezoresistive Cantilever Microprobe with Diamond Tip

Michael Fahrbach[1], Min Xu[2], Uwe Brand[2] and Erwin Peiner[1]
[1] Technische Universität Braunschweig, Institute of Semiconductor Technology (IHT), Hans-Sommer-Straße 66, 38106 Braunschweig, Germany and Technische Universität Braunschweig, Laboratory for Emerging Nanometrology (LENA), Langer Kamp 6A/B, 38106 Braunschweig, Germany
[2] Physikalisch-Technische Bundesanstalt (PTB), Bundesallee 100, 38116 Braunschweig, Germany
m.fahrbach@tu-bs.de

Summary:
In this work, a self-exciting tactile cantilever sensor for contact resonance applications is described. The design integrates heating resistors with the aim to enable high-speed measurements on large workpieces. For this purpose, higher-order out-of-plane bending modes of the cantilever are favorable. Consequently, the position of the actuators is optimized using finite-element modelling to achieve uniform signal amplitudes for a range of materials when using the third vibration mode. Preliminary measurements with thin polymer films show the basic function of the design.

Keywords: MEMS, microprobe, thermal actuator, piezoresistive cantilever, contact resonance

Motivation

In industrial environments, where surfaces can be covered with contaminants like lubricants or cooling liquids, monitoring of workpieces using optical techniques is often difficult or not possible. Here, piezoresistive microprobes with integrated silicon tips are promising as they can scan surfaces at velocities up to 15 mm/s [1]. However, their silicon tip quickly wears down during measurements and, if mechanical characterization of the sample using contact resonance (CR) techniques are to be performed, external actuators are necessary.

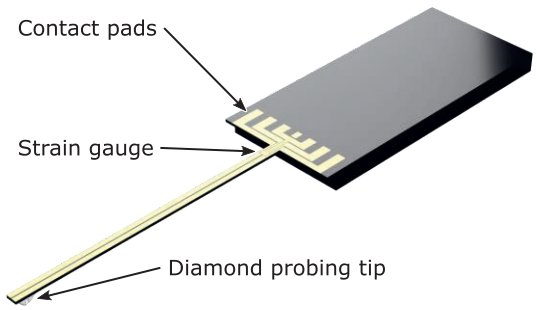

Fig. 1. Render of the microprobe design.

The European EMPIR project MicroProbes is developing new sensors, that aim to improve on the shortcomings of previous designs [2]. These new sensors shall be able to efficiently measure mechanical properties using CR. Then, they shall be calibrated on reference samples.

Design of the microprobe

The basic shape of our new probes is based on previous designs [3], with the cantilevers being 5 mm long, 200 µm wide and 50 µm thick. As shown in Fig. 1, the probes integrate a strain gauge near the clamped end of the beam and contact pads close to the edge of the base. Additionally, wear resistant diamond probing tips are included close to the free end of the beam and, as shown in Fig. 2, heating resistors are distributed across the length of the cantilever

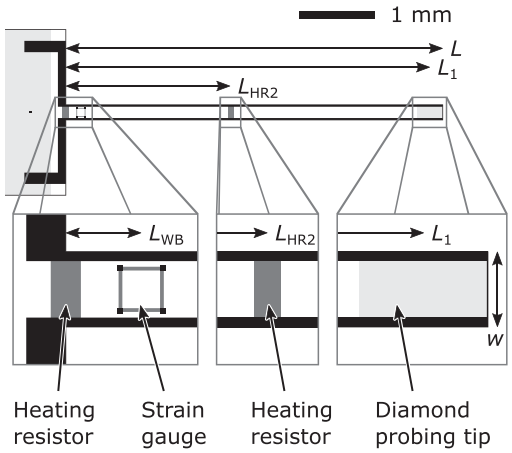

Fig. 2. Overview of the microprobe design. The metal contact lines are not shown to maintain visibility.

Previous measurements using a commercial CAN50-2-5 probe (CiS Forschungsinstitut für Mikrosensorik GmbH, Erfurt, Germany) [4] are used to evaluate the performance of different CR vibration modes. Here, the third flexural vibration

mode at 53 kHz is a good compromise of resolution, measurement speed and ease of use.

To actuate this vibration mode more efficiently, this design is changed by two heating resistors placed on the cantilever. Their locations are optimized to enable uniform signal amplitudes when analyzing a large range of materials [5].

The strain gauge is located close to the clamping at $L_{\mathrm{WB}} = 185\ \mu\mathrm{m}$ and distanced from the adjacent heater by 100 µm to minimize parasitic thermal coupling [6].

FEM simulations of contact mechanics

After completing the sensor design, finite element modelling (FEM) simulations of the sensor in contact with the surface of a sample are performed using COMSOL 5.4. As shown in Fig. 3, large frequency shifts are expected for the first three CR-modes when analyzing samples with Young's moduli up to 10 GPa. Consequently, compliant layers on stiff substrates, such as polymers on silicon, can be measured with high resolution.

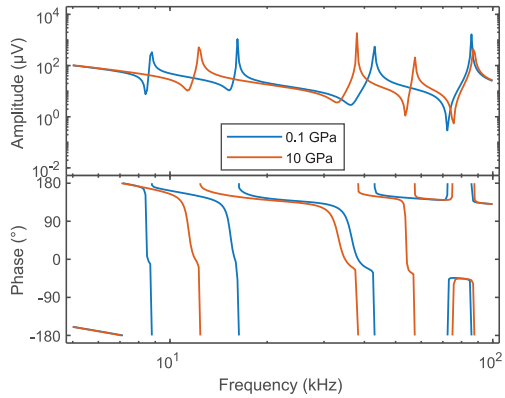

Fig. 3. FEM frequency response of the strain gauge output for sample Young's moduli of $E = 0.1$ GPa and $E = 10$ GPa.

Fabrication and Test

First sensor samples with a thickness of approximately 100 µm are fabricated. Due to the increased thickness, the measured resonance frequencies of these sensors are approximately 2.5 times higher than calculated using FEM. One of these probes is shown in as shown in Fig. 4.

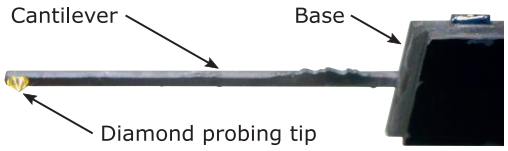

Fig. 4. Photograph of the bottom side of a prototype microprobe.

Then, preliminary measurements on a thin polymer film are conducted. The results are shown in Fig. 5. Here, CR spectra are acquired at different probing forces on the same sample. As expected, the CR frequency increases with increasing probing force.

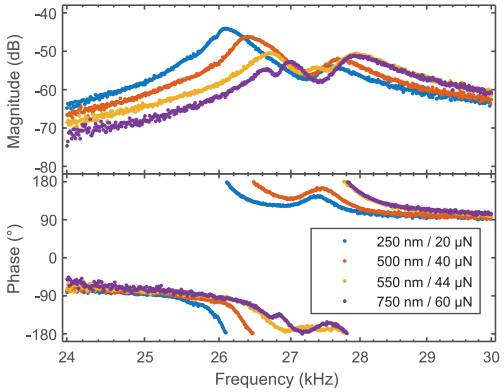

Fig. 5. Measured fundamental mode CR frequency responses on a thin polymer film for different probing forces given by the respective cantilever deflections.

As the next step, measurements on reference samples will be performed to calibrate the microprobes for enabling a quantitative analysis.

Acknowledgements

This project has received funding from the EMPIR programme co-financed by the participating states and from the European Union's Horizon 2020 research and innovation programme under no. 17IND05 MicroProbes.

References

[1] H. S. Wasisto et al., Ultra-high-speed cantilever tactile probe for high-aspect-ratio micro metrology, *2015 Transducers - 2015 18th International Conference on Solid-State Sensors, Actuators and Microsystems (TRANSDUCERS)*. IEEE. (2015); doi: 10.1109/transducers.2015.7181109

[2] 17IND05 MicroProbes Multifuntional ultrafast microprobes for on-the-machine measurements. (2018). Retrieved from https://www.ptb.de/empir2018/microprobes/

[3] E. Peiner et al., Slender Tactile Sensor for Contour and Roughness Measurements Within Deep and Narrow Holes, *IEEE Sensors Journal* 8, 1960-1967 (2008); doi: 10.1109/jsen.2008.2006701

[4] M. Fahrbach et al., Calibrating a high-speed contact-resonance profilometer *Journal of Sensors and Sensor Systems* vol. 9, no. 2, Art. no. 2 (2020); doi: 10.5194/jsss-9-179-2020.

[5] M. Fahrbach, E. Peiner, Higher-Mode Contact Resonance Operation of a High-Aspect- Ratio Piezoresistive Cantilever Microprobe, *SMSI 2020 - Sensors and Instrumentation* (2020); doi: 10.5162/SMSI2020/A6.3.

[6] A. Setiono et al., Phase optimization of thermally actuated piezoresistive resonant MEMS cantilever sensors. *Journal of Sensors and Sensor Systems 8*, 37-48 (2019); doi: 10.5194/jsss-8-37-2019

DOI 10.5162/SMSI2021/A6.1

Full Stress Tensor Measurement by Photoelasticity in Silicon

Markus Stoehr[1], Gerald Gerlach[2], Thomas Härtling[2,3], Stephan Schoenfelder[1]
[1] University of Applied Sciences Leipzig, Faculty of Engineering Sciences
[2] Technische Universität Dresden, Institut für Festkörperelektronik
[3] Fraunhofer Institute for Ceramic Technologies and Systems IKTS
markus.stoehr@htwk-leipzig.de

Summary:
Photoelasticity offers a promising measurement tool for the in-line measurement of semiconductor materials such as silicon. Photoelasticity is a contactless, optical and full-field measurement method based on stress-induced birefringence. However, it is in principle only capable of measuring stress differences and therefore not able to determine the quantitative stress state inside a material. In this work a method is presented to separate this stress difference using modified equations of the mechanical equilibrium in conjunction with the Finite-Difference-Method. This method takes into account the anisotropic photoelastic law for mono-crystalline silicon and enables a full separation of the mechanical stresses with a single measurement.

Keywords: photoelasticity, stress measurement method, full-field, contactless, semiconductors

Introduction

Photoelasticity is regarded a promising measurement principle to characterize stress fields inside thin substrates. It is based on stress-induced birefringence, which causes a material to split an incoming light wave into two light waves each with different coefficients of refraction. In general, only the stress difference $(\sigma_{11} - \sigma_{22})$ and the shear stresses σ_{12} can directly be measured with this. However, a full stress tensor information gives the often more desirable full image of the stress state inside a material or component.

In this work a method is developed to separate the full stress tensor information from a single photoelastic measurement. Since silicon shows a mechanically and photo-elastically anisotropic behavior, first the photo-elastical law for mono-crystalline silicon is developed. A general approach and the explicit stress-optical relationship for several crystalline orientations are derived. With those, the stress differences and the shear stresses can be measured. Second, a method is developed to separate the stress difference into the single stress components by solving modified equations of the mechanical equilibrium. These 2nd-order partial differential equations are approximated by the Finite-Difference-Method. Applying FDM to the differential equations and using known initial values, the stress difference $(\sigma_{11} - \sigma_{22})$ can further be separated into the single stress components σ_{11} and σ_{22}.

This method is demonstrated for the full stress tensor determination of a silicon wafer under diametrical load and for the measurement of residual stresses in a multi-crystalline silicon slab.

Methods

Photoelasticity can be described using a phenomenological approach suggested by Pockels [1, 2]. This model states that mechanical stresses lead to a change of the impermeability tensor B_{ij} which describes the optical properties. The change of impermeability is proportional to the stress tensor σ_{ij} by the stress-optical tensor π_{ijkl} and adds to the unstressed impermeability B_{ij}^{o}:

$$B_{ij} = B_{ij}^{o} + \pi_{ijkl}\sigma_{kl} \qquad (1)$$

The change of impermeability depends also on the crystalline orientation and the load direction. Therefore, the stress-optical tensor has to be transformed accordingly.

In this work, a general stress-optical relation and explicit relations for a (100), (110) and (111) crystalline orientation are developed. The necessary stress-optical material parameters $(\pi_{11} - \pi_{12})$ and π_{44} are determined using a (100) silicon wafer under diametrical load inside a grey-field polariscope.

With this, the stress difference $(\sigma_{11} - \sigma_{22})$ and the shear stress σ_{12} can be measured. To further separate this difference into its single stress

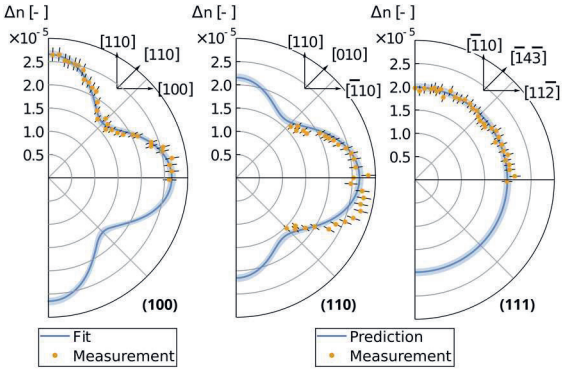

Fig. 1: Stress-optical relations (blue) for a (100), (110) and (111) orientation of silicon with measurement results (yellow)

components a modified equation of the mechanical equilibrium is used [3]:

$$\frac{\partial^2 \sigma_{11} + \sigma_{22}}{\partial x_1^2} + \frac{\partial^2 \sigma_{11} - \sigma_{22}}{\partial x_1^2} + 2\frac{\partial^2 \sigma_{12}}{\partial x_1 \partial x_2} = 0. \quad (2)$$

The Finite-Difference-Method is applied to this equation in a central difference scheme to approximate the derivations over a discretized domain. This gives a set of equations for each discretized point that can be solved to obtain the single stress components σ_{11} and σ_{22}. For this, initial values are necessary that can be taken from free edges of the measured component.

Results

The stress-optical material parameters are measured using a (100) silicon wafer under diametrical load as $(\pi_{11} - \pi_{12}) = (12.4 \pm 0.3) \cdot 10^{-7}\mathrm{MPa}^{-1}$ and $\pi_{44} = (7.7 \pm 0.3) \cdot 10^{-7}\mathrm{MPa}^{-1}$. With those material parameters and with the respective theoretical derivation a prediction is made for the stress-optical law for the (110) and (111) orientation. This prediction follows closely the measurement results of the respective crystalline orientations, as shown in fig. 1.

The separation of the stress difference $(\sigma_{11} - \sigma_{22})$ into the single stress components was tested for the (100) silicon wafer under diametrical load. The stress components were found to be in good agreement with a Finite-Element-Analysis of the same test, as can be seen in fig. 2.

Additionally, the method was applied to a silicon slab that was cut from a multi-crystalline silicon ingot. The stress-optical law was averaged for the various orientations of the crystallites. With that, the determined stresses are very similar to

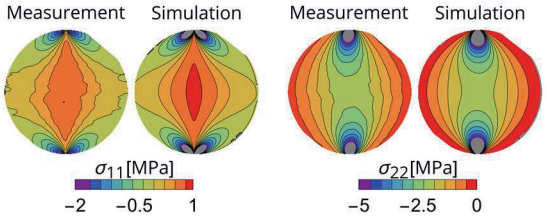

Fig. 2: Stress components for a (100) silicon wafer under diametrical load

experimental works by Bär et al. [4] using the stress-relation method.

Discussion and Conclusion

In this work a method is presented that enables a full-field quantitative stress characterization of thin silicon substrates with a single photo-elastical measurement.

The method was tested and validated using a (100) silicon wafer under diametrical load. The determined stresses correspond well to the stresses simulated by means of FEM. Furthermore, this method was applied to the measurement of residual stresses in a multi-crystalline silicon slab where it showed a good agreement to previous experimental works. However, the experimental effort for photo-elastical measurements is considerably lower compared to the laborious stress-relaxation method used previously by Bär et al.

While this approach was demonstrated for silicon, it can be applied to a variety of different semiconductor materials. Therefore, this method presents interesting opportunities for the application to in-line measurements in production or for academic purposes.

References

[1] K. Neumann, Die Gesetze der Doppelbrechung des Lichts in comprimirten oder ungleichförmig erwärmten unkrystallinischen Körpern, Annalen der Physik und Chemie, **54**, 12 , 449 - 476, 1841

[2] F. Pockels, Ueber den Einfluss elastischer Deformationen, speciell einseitigen Druckes, auf das optische Verhalten krystallinischer Körper, Annalen der Physik, **273**, 6, 269 - 305, 1889

[3] L. J. Segerlind, Stress-difference elasticity and its application to photomechanics, Experimental Mechanics, **11**, 440 - 445, 1971

[4] T. Bähr et al., Residual stresses in multicrystalline silicon, In: 27th European Photovoltaic Solar Energy Conference and Exhibition; 642-646

DOI 10.5162/SMSI2021/A6.2

Adding Seebeck coefficient measurements to an existing high temperature device for Hall constant and electrical conductivity measurements

Robin Werner[1], Jaroslaw Kita[1], Michael Gollner[2], Florian Linseis[2], Ralf Moos[1]
[1] Department of Functional Materials, University Bayreuth, 95440 Bayreuth, Germany
[2] Linseis Thermal Analysis, 95100 Selb, Germany
functional.materials@uni-bayreuth.de

Summary:
An already existing high temperature device to determine the electrical conductivity and the Hall constant has been extended for thermoelectric Seebeck coefficient measurements. The sample holder made in thick-film technology is equipped with two platinum heaters. Whereas the primary heater allows to reach the desired measuring temperature, the second one allows measurements at variable temperature differences. Measurements on constantan, a certified reference material, confirm the functionality of the Seebeck measurements with this new measurement setup.

Keywords: Seebeck coefficient, Hall constant, electrical conductivity, high temperature, low-cost

Motivation

For electrical material characterization, the electrical conductivity, the carrier density, the carrier mobility, and the Seebeck coefficient are of great importance. Especially challenging is the characterization at high temperatures. Current commercial instruments can either determine the electrical conductivity and the Hall constant or determine the electrical conductivity and the Seebeck coefficient. Often, expensive and slow furnaces are needed. Furthermore, expensive electromagnets are used. A novel sample holder design developed with the help of FEM simulations and manufactured in thick-film technology, makes it possible to characterize all of the above-mentioned parameters within one measuring device and eliminates the need for expensive furnaces and electromagnets. This contribution describes an extension of an existing system for thermoelectric Seebeck coefficient measurements.

Description of the New System

The basic structure of the new sample holder is a 635 µm thick alumina ceramic substrate with four electrodes on the upper side. The electrodes are spring mounted and moveable, which allows to contact samples of any geometry within a sample area with a maximum diameter of 12.7 mm according to the van der Pauw measuring method [1]. Gold screen-printed conductor lines and the contact pads are located on the reverse side of the sample holder. A screw-nut combination with an integrated spring serves as a through-hole connection between both sides of the substrate. For connection with the electronics, a standard card-edge connector is used.

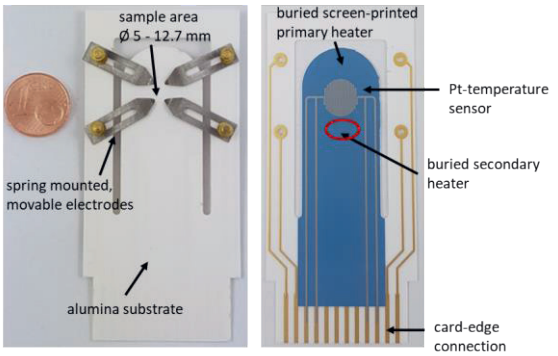

Fig. 1. Sample holder for conductivity, Hall constant and thermoelectric Seebeck measurements with two buried heaters

Fig. 1 shows the front and reverse side of the sample holder. Besides the mentioned gold conductors and contacts, a screen-printed platinum resistive temperature sensor is visible. For precise resistance measurement, a four-wire technique is used. The temperature in the sample area is determined via a four-wire resistance measurement by a previously done one-time resistance-temperature calibration. The temperature within this area is generated by two platinum heaters located under the blue cover layer. The desired measuring temperature can be generated by Joule heating via the primary heater. The secondary heater can be used to generate a variable temperature difference within the sample area. The necessary measurement of the con-

tact point temperature, as well as the thermoelectric voltage for Seebeck measurements is realized by gold-platinum thermocouples, which can be clamped between the electrode tip and the sample.

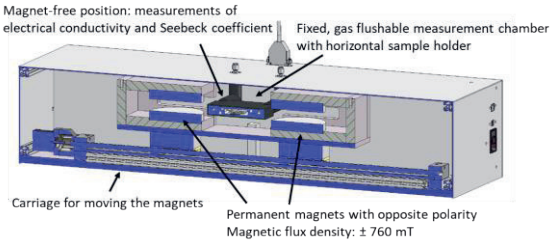

Fig. 2. Measurement setup: two movable permanent magnetic yoke systems with +/- 760 mT and a magnet-free position for electrical conductivity and thermoelectric Seebeck measurements

The presented sample holder, including all components, has a height of only a few millimeters and can be installed inside a small gas flushable aluminum measuring chamber that can be seen in Fig. 2. The system additionally contains two magnetic yoke systems made of permanent magnets with different polarity, with which the electrical conductivity and the charge carrier density could be measured up to 600 °C as described in [2].

Seebeck Coefficient Measurements

For the measurements of the Seebeck coefficient and to test the functionality of the new system, a sample of constantan was chosen, which is well known in the thermoelectric community as a reference material. For the measurements, the sample holder was heated up to 700 °C in 100 °C steps by the primary heater. Afterwards, the temperature difference over the sample was varied by varying the secondary heater. The resulting thermoelectric voltage within the sample is measured via the platinum wires of the gold-platinum thermocouples. The Seebeck coefficient can be calculated from the ratio of the thermoelectric voltage and the temperature difference between the thermocouples, considering the temperature of the reference junction and the thermoelectric voltage of the platinum wire. Fig. 3 shows experimental results of the absolute Seebeck coefficient measurements up to 700 °C. The Seebeck coefficient increases with increasing temperature. The measurement was performed twice, with an intermittent sample change. The measurements show the same trend as the known values of the certificate. Also, the absolute values differ by only a few percent, which is why the functionality of the measurement setup can be called functional.

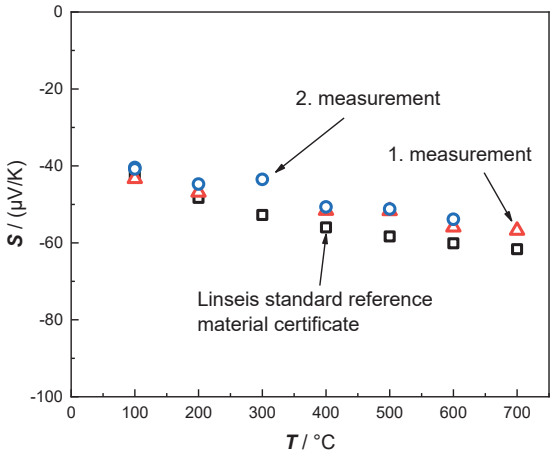

Fig. 3. Measurement of the Seebeck coefficient of constantan up to 700 °C

Conclusion and Outlook

By adding a second screen-printed heater and two gold-platinum thermocouples, an already existing measurement setup for the measurement of the Hall constant and the electrical conductivity could be extended by an arrangement to determine the Seebeck coefficient. Measurements on constantan as a certified reference material with known temperature dependent Seebeck coefficient have shown that the Seebeck coefficient can be determined up to 700 °C with the here-investigated setup.

In future, all mentioned material parameters will be determined in one measurement cycle to validate the functionality of this new combined low-cost measurement instrument. Furthermore, a continuous increase of the maximum measuring temperature is envisaged.

References

[1] L.J. van der Pauw, A Method of Measuring Specific Resistivity and Hall Effect of Discs of Arbitrary Shape, *Semiconductor Devices: Pioneering Papers*, 174-182 (1991); doi: 10.1142/9789814503464_0017

[2] R. Werner, J. Kita, M. Gollner, F. Linseis, R. Moos, Development of a new Measurement System for Electrical Conductivity and Hall Constant, *SMSI Sensor and Measurement Science International, cancelled conference, 22-25 June 2020, Nuremberg, Germany,* doi: 10.5162/SMSI2020/A5.4

Acknowledgements

The presented results have been achieved in the scope of the project ESB-1607-0002//ESB040/001. It has been funded by the Bavarian Ministry of Economic Affairs and Media, Energy and Technology, VDI/VDE-IT Electronic Systems Program.

DOI 10.5162/SMSI2021/A6.3

Epitaxial graphene on SiC: a versatile sensing platform for high sensitivity applications

Marius Rodner[1,2], *Donatella Puglisi*[1], *Alberto Zilli*[1], *Jens Eriksson*[1]
[1] *Applied Sensor Science Unit, Department of Physics, Chemistry and Biology, Linköping University, 58183 Linköping, Sweden*
[2] *Lab for Measurement Technology, Department of Systems Engineering, Saarland University, 66123 Saarbrücken, Germany*
marius.rodner@liu.se

Summary:
Epitaxial graphene on silicon carbide has become more available through the increased throughput and reduced price of 4 inch SiC-wafers lately. Particularly if used as a transducer and not directly as the sensing material, the graphene surface can be modified to tailor the sensing properties to the desired application. Herein we show that the low-noise and highly sensitive transduction renders epitaxial graphene on SiC a suitable platform for a range of environmental monitoring applications requiring trace-level detection.

Keywords: epitaxial graphene, chemical gas sensor, environmental monitoring

Background

Two-dimensional materials, such as graphene, offer a unique platform for sensing where extremely high sensitivity is a priority, since even minimal chemical interaction can cause significant change in the electronic or optical state [1]. The high sensitivity and resolution of 2D materials to chemical species stems from being essentially all surface and volume free. For many practical applications the material needs to be tailored to generate sensitivity to specific analytes, and the high sensitivity must be complemented with selectivity, fast response times and for some applications resilience in harsh environments. These requirements can be addressed for graphene through e.g. defect-generation, functionalization, or hybrid 2D material-metal or metal-oxide films or nanoparticles. The tailored sensors can then be used to monitor gas- and liquid phase toxic pollutants at concentrations of relevance to environmental monitoring.

Methods and materials

As basis, a semi-insulating, on-axis, 4H-SiC (0001) substrate is used and graphene is epitaxially grown on the Si-terminated silicon carbide surface via a sublimation process [2]. The sensor resistance is measured over time and the response is defined as the difference in % between the equilibrated/last resistance signal compared to the baseline resistance before exposure towards the analyte. Depending on the measurement environment, i.e. dry or wet, the sensor setup itself may vary.

Results

The sensor performance of chemical gas sensors usually highly depends on the sensing environment. We have investigated the variation of operating temperature, relative humidity in the ambient or additional UV-irradiation during the measurement on the sensor properties of surface modified epitaxial graphene on SiC [3]. In a previous study, we have found that a Fe_3O_4 nanoparticle decoration of the graphene surface leads to single-ppb detection of toxic VOCs (volatile organic compounds) such as benzene and formaldehyde. Decoration with a nanolayer of Fe_3O_4 covering the whole sensor surface shows a similar and slightly higher response towards benzene (compare Figure 1).

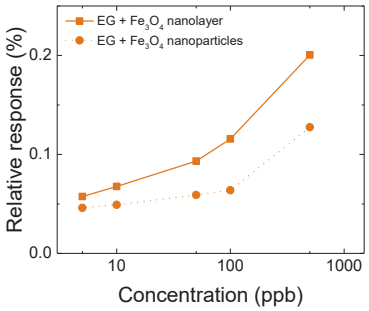

Fig. 1. Relative response of Fe_3O_4 decorated epitaxial graphene sensors towards benzene at 150 °C and 0 %RH based on [4].

Instead of functionalizing the graphene surface with additional materials, one can also alter the graphene lattice itself to change sensing behav-

ior. A defect generation by breaking up the carbon-carbon bonds, thus creating more available surface reaction sites, can increase the sensor response as well up to a certain point. We found that for the detection of NH_3 or NO_2, an Ag^- ion implantation with a fluence of 10^{13} ions/cm^2 shows the best sensor response whereas more or less defect generation decreases it again [5]. An even more radical approach to optimize the sensor performance is to substitute the graphene lattice with another two-dimensional material. 2D platinum, grown on the same substrate as the mentioned epitaxial graphene, was shown to exhibit similar outstanding sensor properties again with detected VOC species in the single-digit ppb level and theoretical detection limits in the range of hundreds of ppt [6].

In its pristine form, epitaxial graphene is rather inert, but it does not need to chemically bind to an analyte to be able to detect its presence. When an ion, e.g. a dissolved heavy metal ion, is in physical contact with the graphene lattice, the local doping changes and thus a change in resistance can be measured. We have previously reported this principle for heavy metal detection in liquids, where the heavy metal is diluted in a buffer solution and then pumped through a lab-on-chip device. As soon as the solved ions come in contact with the exposed graphene surface in the detection chamber, the resistance of graphene changes [7].

Another advancement is the use of epitaxial graphene in bio-inspired applications. Figure 2 shows the response of pristine epitaxial graphene towards HSA (human serum albumin) diluted in buffer. As shown, the sensor reacts rather fast to the analyte exposure with a stable baseline and the response is repeatable. The idea is to eventually substitute HSA with other proteins that are important for medical applications where the exact determination of analytes reflects the health status.

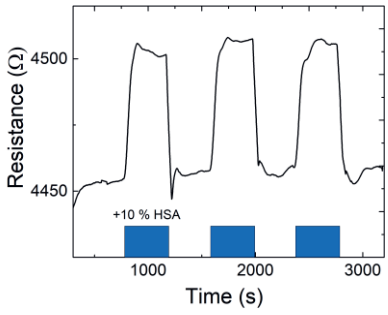

Fig. 2. Response of epitaxial graphene to 10 % HSA in buffer solution at room temperature.

Depending on the desired application, epitaxial graphene on SiC can be used as-grown or surface modified to accommodate specific sensor properties, especially when used only as the transducing and not the sensing material itself. Here we show that Epitaxial graphene on SiC can be used as a platform for highly sensitive and tailorable sensor applications, thus can have a bright future in upcoming sensor applications.

References

[1] C. Anichini, W. Czepa, D. Pakulski, A. Aliprandi, A. Ciesielski, P. Samorì, Chemical sensing with 2D materials, Chem. Soc. Rev. 47 (2018) 4860–4908. doi:10.1039/c8cs00417j.

[2] G.R. Yazdi, T. Iakimov, R. Yakimova, Epitaxial graphene on SiC: A review of growth and characterization, Crystals. 6 (2016). doi:10.3390/cryst6050053.

[3] M. Rodner, A. Icardi, M. Kodu, R. Jaaniso, A. Schütze, J. Eriksson, Metal Oxide Nanolayer-Decorated Epitaxial Graphene: A Gas Sensor Study, Nanomaterials. 10 (2020) 1–12. doi:10.3390/nano10112168.

[4] M. Rodner, D. Puglisi, S. Ekeroth, U. Helmersson, I. Shtepliuk, R. Yakimova, A. Skallberg, K. Uvdal, A. Schütze, J. Eriksson, Graphene decorated with iron oxide nanoparticles for highly sensitive interaction with volatile organic compounds, Sensors (Switzerland). 19 (2019). doi:10.3390/s19040918.

[5] P.D. Kaushik, M. Rodner, G.B.V.S. Lakshmi, I.G. Ivanov, G. Greczynski, J. Palisaitis, J. Eriksson, P. Solanki, A. Aziz, A.M. Siddiqui, R. Yakimova, M. Syväjärvi, G.R. Yazdi, Surface functionalization of epitaxial graphene using ion implantation for sensing and optical applications, Carbon N. Y. 157 (2020) 169–184. doi:10.1016/j.carbon.2019.09.071.

[6] K.H. Kim, H. He, M. Rodner, R. Yakimova, K. Larsson, M. Piantek, D. Serrate, A. Zakharov, S. Kubatkin, J. Eriksson, S. Lara-Avila, Chemical sensing with atomically-thin metals templated by a two- dimensional insulator, Adv. Mater. Interfaces. 1902104 (2020) 1–7. doi:10.1002/admi.201902104.

[7] M.F. Santangelo, I. Shtepliuk, D. Filippini, D. Puglisi, M. Vagin, R. Yakimova, J. Eriksson, Epitaxial graphene sensors combined with 3D-printed microfluidic chip for heavy metals detection, Sensors (Switzerland). 19 (2019) 1–13. doi:10.3390/s19102393.

DOI 10.5162/SMSI2021/A7.1

Smart Sensor Systems for Extremely Harsh Environments

H. Kappert[1], S. Schopferer[2], R. Döring[3], S. Ziesche[4], A. Olowinsky[5], F. Naumann[6], M. Jägle[7], A. Ostmann[8]
[1] Fraunhofer Institute for Microelectronic Circuits and Systems IMS
[2] Fraunhofer Institute for High-Speed-Dynamics, Ernst-Mach-Institut EMI
[3] Fraunhofer Institute for Electronic Nanosystems ENAS
[4] Fraunhofer Institute for Ceramic Technologies and Systems IKTS
[5] Fraunhofer Institute for Laser Technology ILT
[6] Fraunhofer Institute for Microstructure of Materials and Systems IMWS
[7] Fraunhofer Institute for Physical Measurement Techniques IPM
[8] Fraunhofer Institute for Reliability and Microintegration IZM
holger.kappert@ims.fraunhofer.de

Summary:
Sensors systems are key elements for capturing environmental properties and are increasingly important in industry 4.0 for the intelligent control of processes. However, under harsh operating conditions like high temperatures, high mechanic load or aggressive environments, standard electronics cannot be used. Eight Fraunhofer institutes have therefore bundled their competencies in sensors, microelectronics, assembly, board design, laser applications and reliability analysis to establish a technology platform for sensor systems working under extreme conditions.

Keywords: harsh environments, high temperature, ceramic sensors, integrated circuits, assembly

Introduction

Reliable sensor systems are increasingly important in the industry for the intelligent control of industrial processes. Fig. 1 shows a typical example of a generic sensor system. A number of sensors take information from the environment and transform them into electrical signals. A dedicated signal conditioning circuitry performs e.g. offset compensation, amplification, filtering and analog to digital conversion. Further processing is often done by a microcontroller with calculation and storage capacity for identification and calibration data. Standard interfaces like CAN or RS485 are commonly used for the connection to a higher level system making them capable to interact with Industry 4.0 processes.

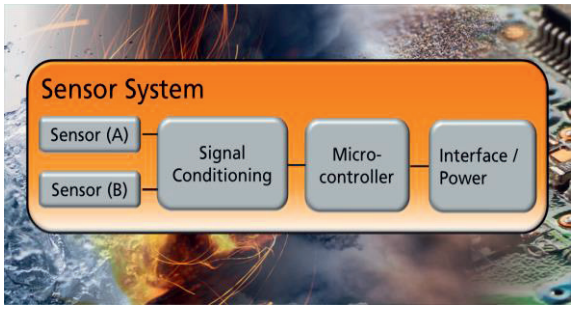

Fig. 1: Typical sensor system with analog and digital signal conditioning and interfacing.

While in many everyday objects highly integrated sensor systems are already state of the art, the situation in an industrial environment is clearly different. Up to now, the use of sensor systems here was often impossible, because the extreme ambient conditions of industrial processes like high operating temperatures, strong mechanical load or a humid or chemically aggressive environment do not allow reliable operation of sensitive electronic components.

However, due to the need for energy and resource savings as well as featuring environmentally friendly processes, detailed process control is necessary and monitoring of vital process parameters under extreme conditions becomes more and more essential. Applications can be found in various fields like steel treatment, jet engines, stationary turbines as well as deep drilling for oil, gas or geothermal energy.

Scope of the Lighthouse Project ‘eHarsh’

The realization of such sensor systems requires a multidisciplinary approach including e.g. the design of reliable sensor elements, high temperature integrated circuits, and appropriate assembly and housing techniques. Therefore eight Fraunhofer Institutes have concentrated

their competencies and have initiated the Fraunhofer Lighthouse Project ‘eHarsh’.

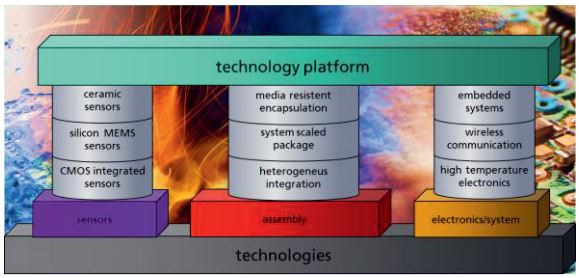

Fig. 2: Technological basis of the ‘eHarsh’ project.

‘eHarsh’ is a common approach involving all necessary technologies for the design of robust sensor systems for harsh environments. Two demonstrators are planned to show the successful implementation of the technology platform: the first is a pressure sensor system with sensor, microelectronics and dedicated ceramic board design for temperatures up to 300 °C with peek temperatures at the tip of the sensor up to 500 °C for avionic applications. The second is a sensor system for geothermal applications at temperatures up to 300 °C and under high pressure.

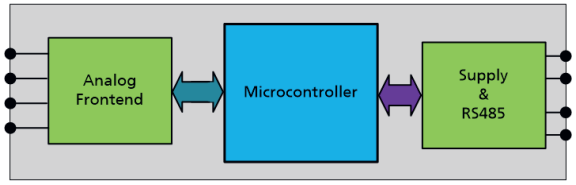

Fig. 3: Integrated chipset for the ‘eHarsh’ demonstrators.

In the project various technologies and components have been investigated like high temperature ceramic based pressure and temperature sensors, an integrated chipset (Fig. 3) for signal conditioning and processing featuring operating temperatures of up to 300 °C as well as various assembly and board technologies. Special focus is on the application of well-known technologies even for high temperature operation like flip chip assembly in combination with ceramic circuit boards and the application of embedding in combination with high temperature printed circuit boards. Special emphasis was on hermetic sealing of the sensor using laser beam micro welding of the metallic casing and glass-based connection between ceramic and metal.

All developments have been gone along with comprehensive characterization as well as simulation and analysis for reliability. In addition, new test and characterization methods have been investigated.

Fig. 4 shows a model of the high temperature sensor for avionic applications with integrated electronics.

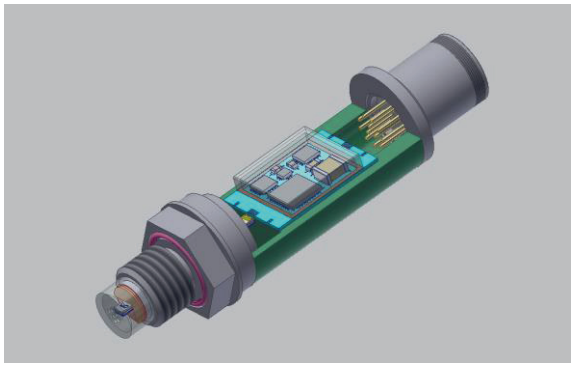

Fig. 4. Demonstrator for avionic applications.

Current status

In the first part of the project, the development of the envisaged technologies has been performed and verified. In the current second phase the demonstrators are assembled and first measurements have been made. In the remaining project time, demonstrators will be finished and extensively tested under the harsh conditions of the envisaged applications.

Acknowledgements

This work was supported as a Fraunhofer LIGHTHOUSE PROJECT.

References

[1] H. Kappert: ‘Sensor Systems for Extreme harsh Environments’, Plenary Session, International Conference and Exhibition on High Temperature Electronics (HiTEC 2018), Albuquerque, New Mexico, USA

[2] S. Ziesche, et al.: ‘On-turbine multisensors based Hybrid Ceramic Manufacturing Technology’, High Temperature Electronics Network (HiTEN 2019), Oxford, UK

[3] H. Kappert, et al.: ‘High Temperature SOI CMOS Technology and Circuit realization for Applications up to 300 °C’, IEEE International Symposium on Circuits and Systems (ISCAS), pp. 1162-1165, May 2015

DOI 10.5162/SMSI2021/A7.2

Evaluation of high temperature ceramic sensor packages

Paul Gierth, Lars Rebenklau, Henry Barth
Fraunhofer IKTS, Winterbergstrasse 28, 01277 Dresden, Germany
paul.gierth@ikts.fraunhofer.de

Summary:
Modern sensor elements could in many cases withstand very high environmental temperatures. Their only limitations are caused by packaging concepts. Therefore, novel-ceramic packaging concepts seem a promising platform for reaching the next application level. This work discusses technologies, materials and evaluation methods for reaching high temperature stable package solutions. Especially materials for sensor chips mounting inside ceramic packages and package connector mounting up to 600 °C were focused and discussed.

Keywords: high temperature, packaging, ceramic, interconnection, brazing

Motivation

Every kind of industrial process can only be performed if enough sensor signals could be used to control this process. Therefore, many sensors need to withstand very harsh environments, like high pressures, acid atmospheres or simply high temperatures.

Existing packaging technologies are based on integrating a sensor element in a metallic or ceramic package and hermetically sealing it. All therefore needed process steps needs to be further developed to fulfill requirements of higher environmental temperatures. The complete sensor packaging process can be splitted into five separate steps according Fig. 1.

Fig. 1. Process flow of sensor element packaging.

Packaging process is divided into package material selection (step 1), package connection if needed (step 2), assembling of the sensor element inside the package (step 3), interconnection between package and sensor element (step 4) and hermetical package enclosing (step 5). Influence of high temperatures on packages and their electrical characteristics is already discussed in [1]. Long time stability of welded interconnection joints at high temperatures was evaluated in [2] and first connecting and assembling results were shown in [3].

Present study is further focusing on assembling and sealing technologies. Main aim of this work is to discuss active brazing as high temperature sealing technology.

Characterization of assembling joints up to 600 °C

Active brazing joints, sintering materials, or ceramic adhesives could be used to realize high temperature stable sensor assembling inside a ceramic package. Ceramic adhesives show nearly identical thermal expansion to the ceramic package itself whereby they should be preferred. Mechanical stability of these kind of joints could only be inspected before and after a high temperature storage, but not under real conditions. Therefore, a high temperature shear-strength measurement setup has been developed (Fig. 2).

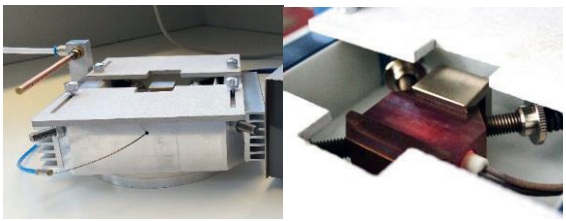

Fig. 2. High temperature shear test rig. left: complete rig with cooling airflow and temperature control, right: core heating table heated up to 600 °C.

The developed test rig was mounted on a Dage Series 4000 shear-force measurement tool and different high temperature adhesives were evaluated. It could be found that all kind of ceramic adhesives show completely different mechanical joint characteristics und different test temperatures (Fig. 3). Even promising materials, which should withstand temperatures up to over 900 °C, could show enormous interface degradations und real conditions (Fig. 3 SiO_2).

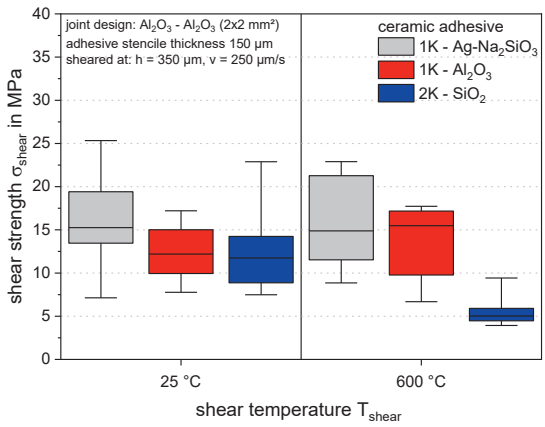

Fig. 3. Comparison of assembling adhesive joint strength at different test temperatures

High temperature packaging sealing

Sealing of packages can be performed in different ways. Metal-cap packages often use welding technologies for sealing. Soldering could also be a suitable solution but is only possible if solderable metallic surfaces are applied on the package and the sealing element. An alternative high temperature stable sealing strategy could be the use of active brazing materials. These materials can be used to interconnect ceramics directly. The fundamental working principle is based on generating a solderable surface on the ceramic during the brazing process by adding an active element into the material. For example, silver-copper-titanium compositions are often used as active brazing material. Silver and copper itself are not able to attach to a ceramic substrate. But titanium is interacting with the ceramic itself and generating a solderable surface layer during the brazingprocess. Eutectic AgCuTi brazing paste is applied directly on the ceramic surface of the package. The ceramic lid is placed into the paste and fixed by using a graphite mounting element. After an optimized drying process, a vacuum brazing step toke place between 850 – 925 °C to optimize the joint adhesion.

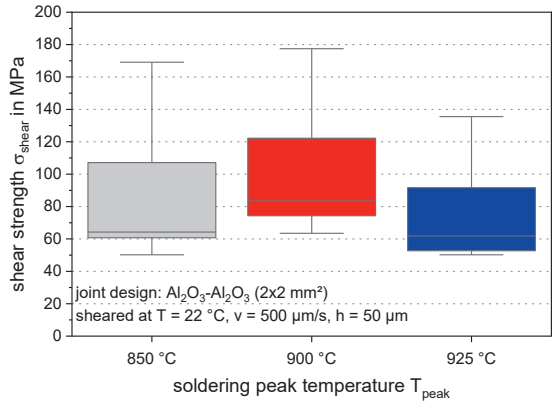

Fig. 4. Comparison of active brazing joint strength at different brazing temperatures

Fig. 4 shows very high joint strengths under all evaluated conditions, which indicates excellent adhesion between brazing material and ceramic. Most fracture modes were ceramic breakage. Cross sections were prepared to further investigate the joining quality (Fig. 5).

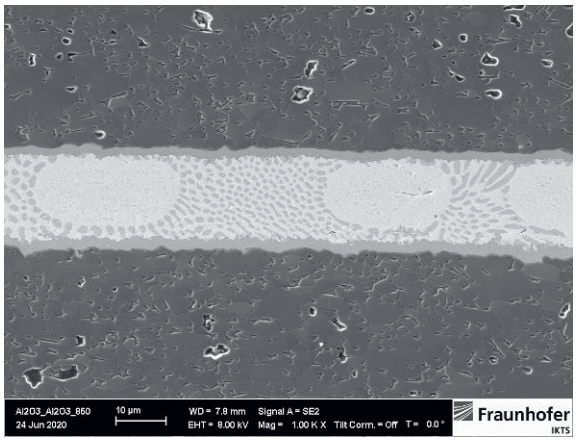

Fig. 5. Cross section of a ceramic-ceramic hermetic sealing using a AgCuTi active brazing material

As can be seen, a hermetical sealing between the ceramic elements could be realized with active brazing material. The very thin titanium layer and the ceramic surface is nearly not visible but the brazed copper film on this titanium layer can clearly be seen. The complete joining area consisting of a mixture between silver and copper, which shows a different morphology in dependency of the joining temperature.

As last thermal process during the production of high temperature stable packages, all previously applied technologies needs to withstand the joining temperature of the sealing. To prevent an overheating of the components, an alternative sealing brazing material could also be chosen, which are available in many different compositions starting from nearly 600 °C up to 1000 °C

References

[1] L. Rebenklau, P. Gierth, H. Barth, High-Temperature Packaging for Sensors, PCIM Europe 2019, 1-7 (2019); ISBN: 978-3-8007-4938-6

[2] P. Gierth, L. Rebenklau, Development and analysis of high temperature stable interconnections on thick films using micro resistance welding for sensors and MEMS, 7th Electronic System-Integration Technology Conference (ESTC), 1-5 (2018), doi: 10.1109/ESTC.2018.8546509.

[3] P. Gierth, L. Rebenklau, H. Barth, Validation of High-Temperature Stable Sensor Packaging Materials and Methods, SMSI 2020, 244-245 (2020), doi: 10.5162/SMSI2020/P2.10

DOI 10.5162/SMSI2021/A7.3

pH measurement system-on-foil aided with a mixed signal processor

Mustapha Fahem[1], Matthias Steinmaßl[1], Eva-Maria Korek[2], Karl Neumeier[1], Ralf Brederlow[2], Ignaz Eisele[1]
[1]Silicon technologies and devices, Fraunhofer EMFT, Hansastr. 27D, 80797 Munich, Germany
[2]Chair of Circuit Design, TU München, Arcisstr. 21, 80333 Munich, Germany
Corresponding author: matthias.steinmassl@emft.fraunhofer.de

Summary:
A microcontroller with an analog front-end is integrated with 3 on-chip FG-ISFETs sensors produced at the EMFT on a pH measurement system-on-foil. The MCU offers the ability to fully control the ISFETs by keeping them at constant biasing through a software configured feedback loop. The pH sensor precision and stability are highly enhanced by reading 2 ISFETs at a time. By the differential measurement, the drift and noise compensations are achieved. The whole system can be integrated on a 10 x 10 mm flexible printed circuit board.

Keywords: FG-ISFET, pH sensor, MSP430, system-on-foil, packaging

Introduction

During the last 50 years since the invention of the ion sensitive field effect transistor (ISFET) [1] many research groups proposed different configurations and techniques to realize an ISFET device on the aim of achieving stable measurements of ion concentrations, mainly pH. An ISFET is a device where the gate electrode of a normal FET is replaced by the liquid under study. If the potential of the liquid with respect to the reference electrode changes due to a pH change, the threshold voltage of the FET changes accordingly. For the floating gate ISFET (FG-ISFET) a floating extended gate is pinned electrically between back-gate and reference electrode. With the introduction of the back-gate control electrode adjustment of the bias conditions for the MOSFET is possible (see fig.1). Common readout systems either set V_{ds} and I_d constant and measure gate voltage proportionally related to pH, or measure I_d at constant voltages. In this case, it is exponentially correlated to the pH value [2]. The encapsulation methods used with such devices have an effect on the sensor performance [3], therefore drift-free pH measurement requires a fluid-tight packaging which integrates also the reference electrode. The most challenging part is the packaging of the active contact area between fluid and chip [4], often done by drop casting with epoxy resins.

Materials and Methods

We present pH sensor chip realized at the EMFT clean room that contains 3 FG-ISFETs with different pH sensitivity, an on-chip reference electrode made of screen-printed Ag/AgCl paste as well as an operational amplifier for each FG-ISFET to allow direct potential measurement. A simplified configuration of the electrical setup is shown in fig 1. The chip dimensions are 4.5 x 4.5 mm and the active area where the ISFETs and the reference electrode are placed is 2 mm. The chip is packaged by a flip-chip bonding to a flexible printed circuit board (FPCB) as shown in a previous work [5]. The main objective of this work is to prove compatibility of the packaged chip and the readout realized by the Texas Instruments MSP430FR2355 using its analog I/Os and a circuit concept similar to [2]. It provides a system-on-foil, stable, drift & noise immune pH measurement as well as the compatibility of the readout realized by the MCU.

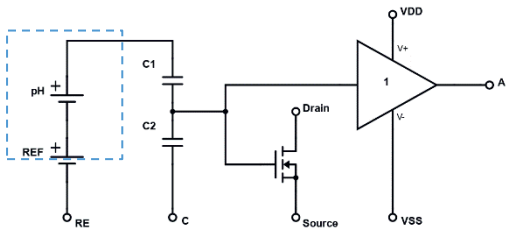

Fig. 1. One of three ISFETs featuring an on-chip op-amp to monitor FG potential. The dashed blue line represents the liquid, C1&C2 are capacitances between liquid-membrane interface and the floating gate and control electrode with floating gate respectively.

The floating gate together with the drain-source potential will set the drain current of the MOSFET. The medium potential is pH dependent. When it varies it will change the floating gate voltage and thus the drain current. A feedback loop needs to be implemented to control the

biasing drain current. The working principle of this configuration is similar to the PG-ISFET described in [6]. The MSP430FR2355 offers configurable on-chip operational amplifiers and a couple of analog I/Os which make it useful for handling the readout as already shown by [2]. We keep monitoring the drain and source voltages. With the help of an external 10 kΩ resistor shunted with a 10 nF capacitor, we can measure the drain current. Our configuration contains a 2 channel 4:1 MUX to measure all of the three on-chip FG-ISFETs. A key experiment in this work is the reliance on 2 ISFETs with different sensitivity what is so called FET/REFET [1] configuration where one ISFET acts as a reference to the other. By differentiating the two measured signals a more stable and noise-free signal is obtained. The governing equation between electrical and chemical forces is the Nernst equation which is defined as

$$E = E^0 + \frac{RT}{nF} ln \frac{[Ox]}{[Red]}.$$

Results and discussion

All ISFETs were conditioned in pH 7 buffer solution for at least 15 min. The black curve on fig.2 represents the measured potential at the ISFET2 and the red one at the ISFET1, used as reference. From the Nernst equation, the pH sensitivity is ~59mV/pH at room temperature, the so-called Nernst limit. According to fig. 1 we are making use of the capacitive amplification, for ISFET1 C1/C2~2.55 and for ISFET2 C1/C2~2.73. Fig. 2 shows the output voltage versus time. Respecting the capacitive gain, the sensitivity is between 30 and 40 mV/pH, which corresponds to the sub-Nernst regime. The used SiN membrane layer is not the best sensitive material for the purpose of pH measurement [1]. Fig. 3 shows the subtraction of ISFET2 minus the ISFET1. This technique reduces noise and drift which makes it very promising to rely on.

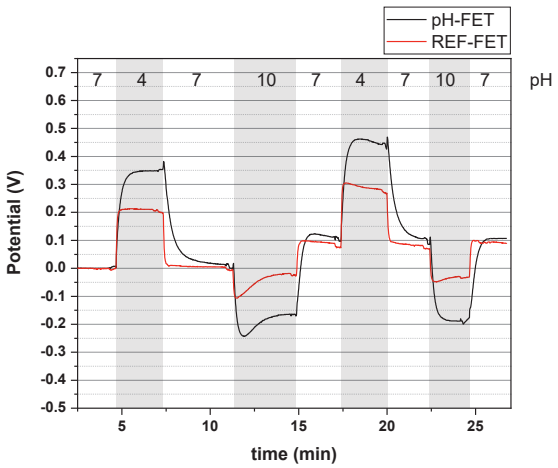

Fig.2 pH measurement using FET/REFET configuration. Black is the measurement of ISFET2 (pH-FET) and red is the one of ISFET1 (REF-FET)

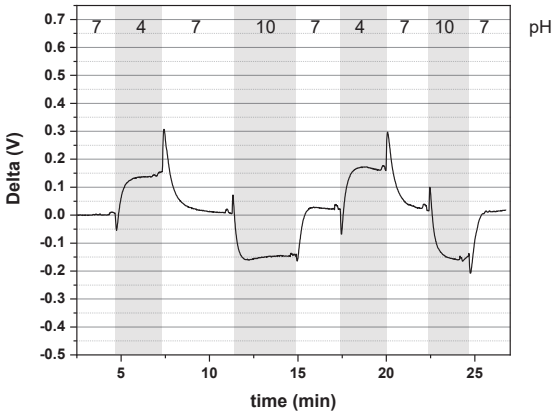

Fig.3 Differential pH measurement between FET/REFET

Conclusion and Outlook

This work shows the integration of the differential concept in a pH measurement system-on-foil. We used 2 ISFETs for measuring the pH. By introducing the MCU, a 10 x 10 mm system-on-foil can be established. Other ion concentration could be determined in principle by choosing the adapted sensitive membrane. After proving the concept, the next challenge would be the integration of all sensor and circuit components in a standalone easy to use system. The idea of integrating the packaging of each component on a system PCB on foil is being considered and is in the process of being realized.

Acknowledgement

Part of this work was financially supported by the FhG internal program [BioPat] and by the the Federal Ministry of Education and Research [project reference numbers 16FMD01K, 16FMD02, and 16FMD03]. We thank Markus Hefele (TUM) for support on the MSP430 programming and circuitry, Waltraud Hell (EMFT) for doing the flip-chip bonding and the EMFT cleanroom to fabricate the FG-ISFET.

References

[1] P. Bergveld, “Thirty years of ISFETOLOGY,” *Sensors and Actuators B: Chemical*, vol. 88, no. 1, pp. 1–20, 2003

[2] M. Hefele, “Integrated multipurpose analog front-end for electrochemical ISFET sensors,” *IEEE NEWCAS*, Munich, 2019.

[3] W. Oelßner *et al.,* “Encapsulation of ISFET sensor chips,” *Sensors and Actuators B: Chemical*, vol. 105, no. 1, pp. 104–117, 2005

[4] T. Datta-Chaudhuri et al, “Packaging commercial CMOS chips for lab on a chip integration,” *Lab on a chip*, vol. 14, no. 10, 2014

[5] I. Bose et al, “Low Profile Open MEMS and ASIC Packages manufactured by Flexible Hybrid Integration in a Roll-to-Roll compatible process,” in *ESSDERC 2018*, Dresden, 2018, pp. 102–106.

[6] P. Georgiou and C. Toumazou, “CMOS-based programmable gate ISFET,” *Electronics Letters*, vol. 44, no. 22, pp. 1289–1290, 2008

DOI 10.5162/SMSI2021/A7.4

Miniaturization of Mobile GPR Antenna Assembly

Di Shi[1], Albert Nadal Zaragoza[2], Taimur Aftab[1], Gunnar Gidion[1], Leonhard Reindl[1]
[1] University of Freiburg, Georges-Köhler-Allee 106, 79110 Freiburg, Germany,
[2] Polytechnic University of Catalonia, Carrer de Jordi Girona, 1-3. 08034 Barcelona, Spain
di.shi@imtek.uni-freiburg.de

Summary:
For miniaturizing a mobile ground penetrating radar (GPR) antenna assembly, an electromagnetic band gap (EBG) structure to reduce the transmitting and receiving cross-talk is proposed. The antenna assembly works around 2.45 GHz and supposed to detect motions though concrete and other building materials. Dimension of the required EBG-structure for both air-coupled and ground-coupled scenarios are analytically estimated. Finite element method based radio frequency simulations are conducted to verify the estimations and to find the optimal dimensions.

Keywords: GPR, planar antenna, miniaturization, RF-cross-talk isolation, electromagnetic band gap

Introduction

A ground penetrating radar (GPR) is capable of detecting motion even through layers of material. After an earthquake, a GPR can be used to find survivors that trapped under collapsed buildings by detecting the body motion caused by their respiration. The most volume consuming part of a traditional GPR is the transmitting and receiving (Tx- and Rx-) antenna assembly. Beside the physical size of the antenna itself, the Tx- and Rx-antennas usually need to be spatially separated by a certain distance to reduce the cross-talk which would otherwise obliterate the signals of interest. However, increasing the Tx- and Rx antennas distance will increase the volume of the assembly, which impacts the mobility of the system.

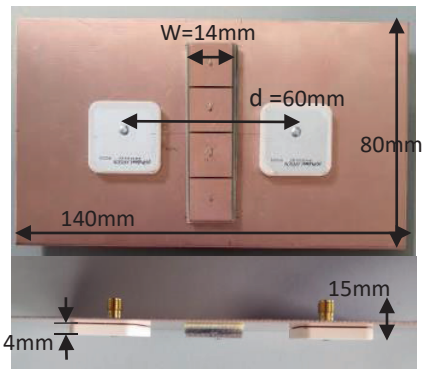

Fig. 1. Tx- and Rx-antenna assembly with a 4-element EBG structure, $W = 14\,mm$. Top: front view. Bottom: side view.

For a coplanar antenna assembly, the cross-talk occurs as surface waves between the Tx- and Rx antenna. In studies of metamaterial, it was found that some structures exhibit band-stop features for surface electromagnetic waves, this kind of structure is called electromagnetic band gap (EBG). There are various kinds of EBG structures, among them the mushroom-like EBG earned increasing attention in the recent decade, as first published in [2]. The mushroom-like EBG consists of evenly distributed metallic patches of the same shape, a ground plane in parallel and conducting vias (see Fig. 1. and 2). This special metallic structure introduces an LC resonator and the capacitance and inductance are determined as [2]:

$$L = \mu_0 \cdot h, \qquad (1)$$

$$C = \frac{W\varepsilon_0(1+\varepsilon_r)}{\pi}\cosh^{-1}\left(\frac{2W+s}{s}\right), \qquad (2)$$

in which h is the EBG substrate height, W is width of one EBG element, s is the gap between elements and ε_r is the relative permittivity of the substrate.

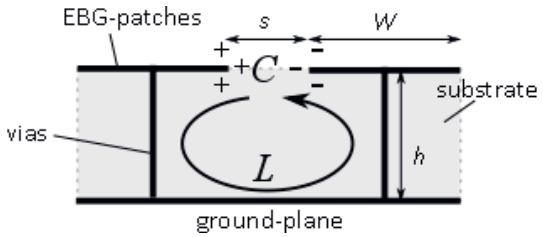

Fig. 2. Schematic side-view of a mushroom-like EBG structure with two elements. [2]

By cascading these elements, a high-order band-stop filter can be built. In [3], simulations show that the EBG provides better isolation than other surface wave reduction approaches, such as substrate removal or cavity-backed structure.

Method

Here we work with two commercial 2.45 GHz ceramic patch antennas [1] and restrict the analysis on single row mushroom-like square shape EBG structure (see Fig. 1). The EBG substrate is FR4 with the same height as the antenna: 4 mm, gap between elements is 0.5 mm. The Tx- and Rx-antennas share a 0.8 mm thick ground plane with a width of 80 mm and a length of 140 mm. Center to center distance of the two antennas is 60 mm. By using the resonance frequency of a simple LC-circuit:

$$f_{stop} = \frac{1}{2\pi\sqrt{LC}}, \qquad (3)$$

together with eq. (1) and (2), the required width of EBG-element W can be estimated. The desired f_{stop} is 2.45 GHz. For the air-coupled case, the required capacitance is about 0.84 pF and the W should be about 12 mm. For ground-coupled case, the permittivity of ground $\varepsilon_{r,grd}$ should be considered in the equation for capacitance as:

$$C = \frac{W\varepsilon_0\varepsilon_{r,grd}(1+\varepsilon_r)}{\pi}\cosh^{-1}\left(\frac{2W+s}{s}\right) \qquad (4)$$

The relative permittivity of common building material is between 2 and 9 [4]. For $\varepsilon_{r,grd} = 2, 4$ and 6, the required W shall be 7 mm, 4 mm and 3 mm respectively.

To verify the estimation, the model is analyzed with FEM based RF simulation. For air-coupled case, the number of EBG-elements is kept as 4, W varies from 10 mm to 18 mm. For ground-coupled cases, the number of elements is kept as 8, W varies from 2 mm to 9 mm.

Results

The transmission coefficient S_{21} indicates the mutual coupling between Tx- and Rx- antenna.

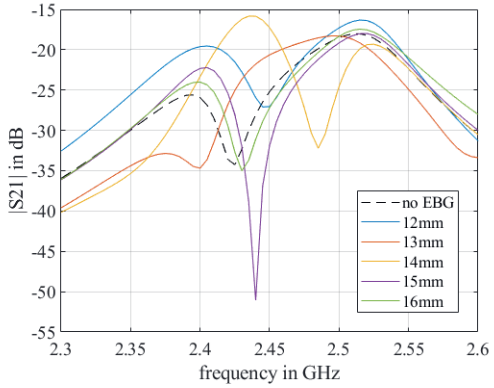

Fig. 3. S_{21} of air-coupled simulation. Comparison between no EBG and a 4-element EBG of various widths.

From the air-coupled simulation (see Fig. 3), that only EBG structure with a width of 15 mm forms a stopband around 2.45 GHz. In the measurement, the antenna assembly with 14 mm EBG has the weakest mutual coupling at 2.45 GHz. From the ground-coupled simulation with $\varepsilon_{r,grd} = 4$ (see Fig. 4), 8 mm width EBG is most suitable to isolate the cross-talk around 2.45 GHz. However, in both scenarios the band-stop frequency is very sensitive to the EBG width, only 1 mm difference could lead to completely different mutual coupling in the desired frequency band.

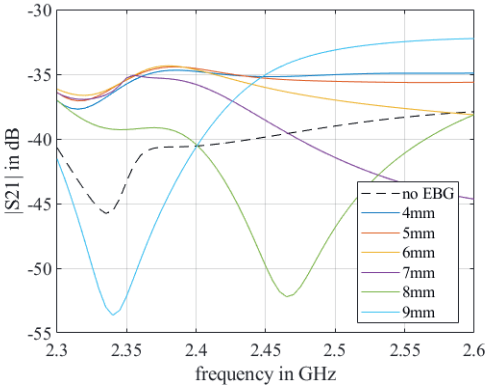

Fig. 4. S_{21} of ground-coupled $\varepsilon_{r,grd} = 4$ simulation,. Comparison between no EBG and an 8-element EBG of various widths.

Conclusion

In this work, a single-row EBG structure is implemented to reduce the cross-talk between planar Tx- and Rx- antennas. Simulations and measurements exhibit that the implemented EBG could reduce antenna mutual coupling by up to 10 dB.

Acknowledgment

This research is part of the German research project SORTIE, and is supported by the Federal Ministry of Education and Research.

References

[1] 2.45 GHz Pulse Lasern antenna W3229, https://www.pulselarsenantennas.com/

[2] D. Sievenpiper, High-impedance electromagnetic surfaces, Ph.D. dissertation, Dept. Elect. Eng., Univ. California at Los Angeles, CA, 1999.

[3] F. Yang, Y. Rahmat-Samii, Microstrip antennas integrated with electromagnetic band-gap (EBG) structures: a low mutual coupling design for array applications, *IEEE Transactions on Antennas and Propagation*, Oct. 2003, doi: 10.1109/TAP.2003.817983.

[4] Robert, A. Dielectric permittivity of concrete between 50 Mhz and 1 GHz and GPR measurements for building materials evaluation. J. Appl. Geophys. 1998, 40, 89–94, doi:10.1016/S0926-9851(98)00009-3.

DOI 10.5162/SMSI2021/A8.1

Electrostatic Transducer for Ultrasound Ranging Based on In-Plane Electrode Motion

Jorge M. Monsalve[1], Franziska Wall[1], Marcel Jongmanns[1], Sergiu Langa[1], Marco Kircher[1], Bert Kaiser[1], Hermann A.G. Schenk[2]
[1] Fraunhofer Institute for Photonic Microsystems, Maria-Reiche-Str. 2, 01109 Dresden, Germany,
[2] Arioso Systems GmbH, Maria-Reiche-Str. 1, 01109 Dresden, Germany
jorge.mario.monsalve.guaracao@ipms.fraunhofer.de

Summary:
A Micromachined Ultrasound Transducer (MUT) based on in-plane actuation is presented in this paper. Its building block, unlike membrane-based MUTs, is a Coulomb-actuated microbeam that is deflected in the in-plane direction. This system is designed to operate at low-frequency ultrasound waves, aiming for gesture recognition applications. The sensing function is demonstrated in this work, complementing an earlier report on its transmission characteristics.

Keywords: ultrasound detection, electrostatic transducers, gesture recognition, Duffing oscillator, capacitive measurement

Introduction

Ultrasound ranging has been proven an effective means to detect hand gestures and thus control electronic devices without the need of physical contact with a screen [1]. This detection strategy is based on the periodical emission of ultrasound pulses that are reflected by the motion of the hand and detected by an array of sensors at different positions, obtaining a measurement of the time of flight of the pulse [2]. The building unit of such a device is a Micromachined Ultrasound Transducer (MUT) designed to oscillate at frequencies in the low ultrasound range (near 40 kHz), so that absorption losses are diminished [2]. The two main types of MUTs (piezoelectric [1-4] and capacitive [5-7]) have been implemented for the generation (and detection) of low-frequency ultrasound waves; however, we argue that these two categories belong to the family of *out-of-plane* transducers, in contrast to *in-plane* ones. Whereas out-of-plane transducers excite a membrane in the direction of the propagation of sound, in-plane transducers oscillate perpendicular to this direction and can therefore use the *transverse* area (depth) of the device to displace a volume of air, instead of its *surface*—which heavily determines the cost of a chip. In-plane transduction has already been implemented in the acoustic range, both for a capacitive all-silicon loudspeaker [8] and a piezoresistive microphone [9]. Here we present an extension of this principle to the ultrasound range with a capacitive transducer based on clamped-clamped microbeams tuned to operate at 40 kHz and requiring a low bias voltage (24V).

Description of the System

The building block of this transducer is a classical Coulomb-actuated microbeam [10], i.e. a prismatic beam of dimensions in the µm-range that is moved towards a fixed electrode by means of a Coulomb force (See Fig. 1). As the beam is deflected, it displaces a volume of air towards a slit. Each microbeam behaves, therefore, as a moving wall between two acoustic chambers. A certain leakage across the beam is expected to occur, but the narrow clearance (1 µm) makes this flow negligible. The microbeams are fabricated by deep reactive ion etching on a silicon-on-insulator substrate, using a similar procedure as reported in [8] for the *nano e-drive* microspeaker—we thus codename this transducer as NED-MUT.

A closely packed array of 258 of these beams actuated with the same voltage comprises one transmitter unit. For the receiving units, two design options were explored: one with clamped-clamped beams (152 in total), and one with clamped-free beams (410 in total). The resonance frequency of the transmitter beams lies at 53 kHz to ensure stability when oscillating near 40 kHz, around which the resonance of the receivers was tuned. The whole device consists of 9 units of 3x3mm²: 4 receiver units on the corners of the chip and 5 transmitter units elsewhere. The electrostatic gap, which is limited by the DRIE etching process, was set to 2.5 µm. The arrangement of the transmitter

units allows modifying the irradiation pattern by introducing phase shifts.

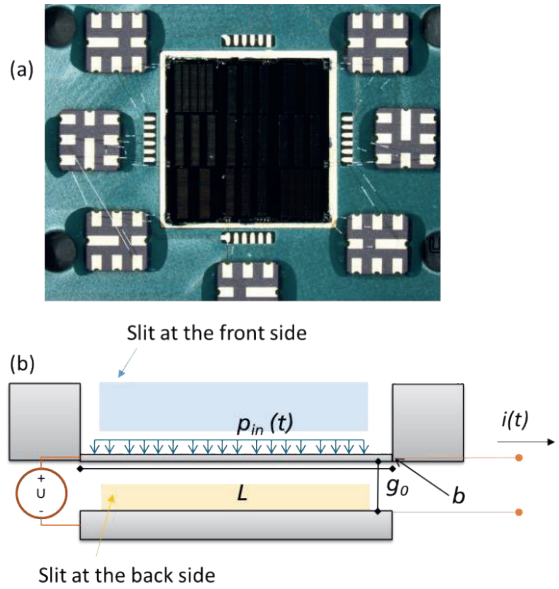

Fig. 1. (a) Photograph of the electrostatic NED-MUT and (b) scheme of one of its clamped-clamped beams acting as ultrasound receiver.

We already reported a first characterization of the transmitter function, reaching a pressure[1] of 87 dB at a distance of 8.9 cm with an excitation of 24V DC and 24V AC [11]—very similar to the pressure reported in [5] but using a much lower bias voltage. Here we further report on the function of the sensing units, therefore showing that this device is capable of performing pulse-echo tests.

Results

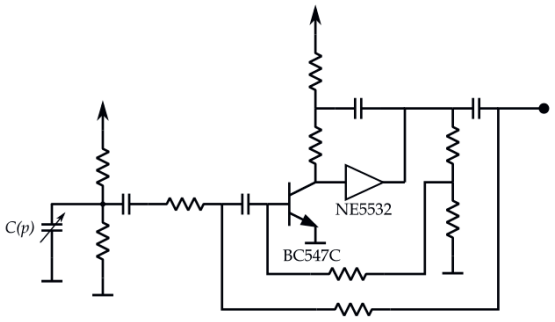

Fig. 2. Illustration of the amplifier topology used to measure the output of the in-plane ultrasound transducer.

In order to test the sensing function of the NED-MUT, a ceramic transmitter (UST-40T) was set 10 cm apart from the chip, hence generating a pressure of 60 Pa rms at 40 kHz (see datasheet [12]). The sensing unit was connected to the amplifier shown in Fig. 2, which relies on the h_{fe} factor of the transistor to amplify the signal. An output signal of 4.5 V peak-to-peak was measured with this procedure. When no pressure is excited, a noise level of 0,5 Vpp is measured at 38 kHz, and if a reflective object is placed in-between, the amplitude of the 40 kHz signal is nearly halved. The NED-MUT is thus capable of acting a as ultrasound receiver.

[1] relative to 20 µPa rms

References

[1] D. Horsley, Beyond Touch: Tomorrow's Devices Will Use MEMS Ultrasound to Hear Your Gestures, *IEEE Spectrum*, (2016) Available: https://spectrum.ieee.org/semiconductors/devices/beyond-touch-tomorrows-devices-will-use-mems-ultrasound-to-hear-your-gestures.

[2] D. M. van Willigen, E. Mostert and M. A.P. Pertijs, In-Air Ultrasonic Gesture Sensing with MEMS Microphones, *SENSORS 2014 IEEE* (2014)

[3] P. Gijsenberg, A. Halbach, Y. Jeong *et al.*, Characterization of polymer-based piezoelectric micromachined ultrasound transducers for short-range gesture recognition applications, *J. Micromech. Microeng.*, vol. 29 (2019); doi: 10.1088/1361-6439/ab1f41

[4] M. Saad, C. J. Bleakley, V. Nigram, P. Kettle, Ultrasonic hand gesture recognition for mobile devices, *J. Multimodal User Interfaces*, vol. 12, pp 31-39, (2016) DOI: 10.1007/s12193-017-0257-8

[5] I. O. Wygant, M. Kupnik, J. C. Windsor *et al.*, 50 kHz Capacitive Micromachined Ultrasonic Transducers for Generation of Highly Directional Sound with Parametric Arrays, *IEEE T. Ultrason. Ferr.*, vol. 56, no. 1, (2009).

[6] A. Unger, Air coupled ultrasonic transducers for industrial applications, *Ph. D. dissertation*, Dept. Elec. Eng., T. U. Darmstadt, Darmstadt, Germany, (2019)

[7] H. Zhang, D. Liang, Z. Wang, *et al*, Fabrication and Characterization of a Wideband Low-Frequency CMUT Array for Air-Coupled Imaging, *IEEE Sensors Journal* vol. 20, no. 23 (2020); doi: 10.1109/JSEN.2020.3007068

[8] B. Kaiser, S. Langa, L. Ehrig *et al.*, Concept and proof for an all-silicon MEMS micro speaker utilizing air chambers, *Microsystems & Nanoengineering*, vol. 5, no. 43 (2019).

[9] J. Czarny, Conception, fabrication and characterization of a MEMS microphone, *Ph. D. dissertation*, Lyon INSA, France (2015).

[10] M. I. Younis and A. H. Nayfeh, A study of the nonlinear response of a resonant microbeam to an electric actuation, *Nonlinear Dynamics*, vol. 31, pp. 91-117, (2003).

[11] J. M. Monsalve, M. Kircher, F. Wall *et al*, First Time of nanoscopic electrostatic drives pushing for ultrasonic transmission for gesture recognition, *2020 IEEE International Ultrasonics Symposium (IUS)* (2020); doi: 10.1109/IUS46767.2020.9251316

[12] 400RT/R160 Air Ultrasonic Ceramic Transducers

DOI 10.5162/SMSI2021/A8.2

Measurement and simulation of Lamb waves in adhesive-bonded multilayer systems

Henning Zeipert[1], Leander Claes[1], Sarah Johannesmann[1], Manuel Webersen[1]
Yevgeniya Lugovtsova[2], Jens Prager[2], Bernd Henning[1]
[1] Measurement Engineering Group, Paderborn University,
Warburger Straße 100, 33098 Paderborn, Germany
[2] Div. Acoustic and Electromagnetic Methods, Bundesanstalt für Materialforschung und –prüfung,
Unter der Eichen 87, 12205 Berlin, Germany
zeipert@emt.uni-paderborn.de

Summary:
Lamb waves are a common tool in the field of non-destructive testing and are widely used for material characterisation. Further, the increasing computational capability of modern systems enables the simulation of complex and detailed material models. This work demonstrates the possibility of simulating an adhesive-bonded multilayer system by characterising each layer individually, and introduces an approach for determining the dispersive behaviour of acoustic waves in a multilayer system via real measurements.

Keywords: Adhesive bonds, Lamb waves, material parameter, non-destructive testing, ultrasound

Motivation

Adhesive bonding of different materials is a common method in modern technologies. To ensure those bonds meet the expectations, it is necessary to investigate their quality. A possible approach is the analysis of mode repulsion points of Lamb waves as presented by Lugovtsova et al. [1]. Methods like these rely on both precise measurements and simulations of the respective systems. The investigation presented in this contribution considers a two-layer system of an aluminium plate (3 mm) and a polycarbonate plate (4 mm). After a characterisation of each individual plate, the two samples are bonded using an epoxy adhesive and investigated as a multilayer system.

Experimental method

The measurements for this investigation are conducted with the setup developed by Claes et al. [2]. The setup uses a short laser pulse, which, due to the photoacoustic effect, generates broadband mechanical waves inside a plate-shaped specimen, which are detected using a piezoelectric transducer. Optical components, which focus the laser beam as a thin line onto the specimen's surface, are mounted on a linear actuator. This enables a variation of the point of excitation on the plate sample, allowing for the acquisition of two-dimensional measurement data in temporal and spatial domain. The application of a two-dimensional Fourier transform yields information in frequency and wavenumber domain. A possible depiction of this data is called "dispersion map" and visualizes the detected lamb modes as ridges (Fig. 1).

Material characterisation

Dispersion diagrams for this investigation are calculated via the SAFE method [3], assuming a plane-strain isotropic model for the individual layers. To determine the material parameters of the layer specimens, an inverse procedure is used [4]. In an inverse procedure, the sound velocities of the material are optimised to match the dispersion curves to the ridges of the dispersion map (Fig. 1).

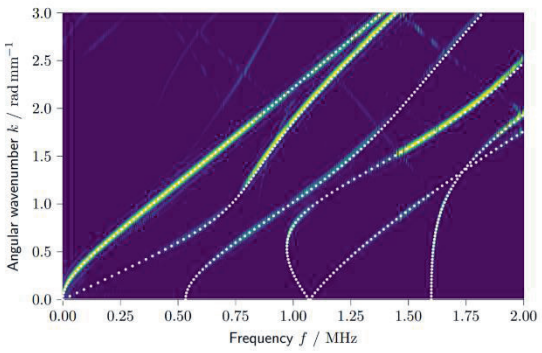

Fig. 1. Dispersion curves (white dots) based on optimised transversal and longitudinal wave velocities match the measurement based dispersion map (image) of the aluminium (3 mm) plate.

Multilayer system

The dispersive propagation of Lamb waves inside the aluminium-polycarbonate-system is simulated with a SAFE model [3], which is built

by stacking the two models of the layer specimens using the individually determined material parameters. The adhesive layer is neglected, thus assuming an ideal coupling of the layers. The Lamb wave excitation for the measurements are performed on the polycarbonate layer while the detecting transducer is placed on the aluminium layer. For the sake of improved visibility, Fig. 2 displays only a part of the resulting dispersion map of such a measurement, overlaid with the simulated dispersion diagram. The simulation results for the multilayer specimen are in general in good agreement with the measurement data, despite the simplifying assumption of the adhesive layer.

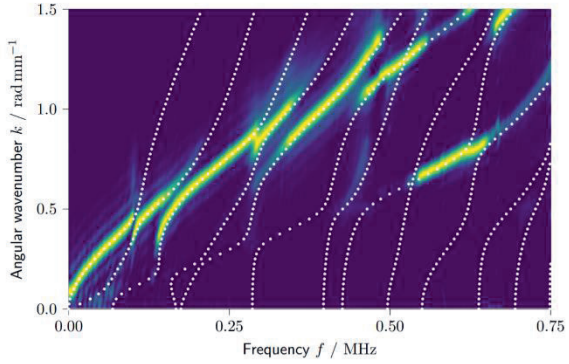

Fig. 2. Comparison of simulation (white dots) and measurement (image) of the aluminium-polycarbonate-system. The ridges in the dispersion map (image) and the simulated dispersion curves are in good agreement of one another.

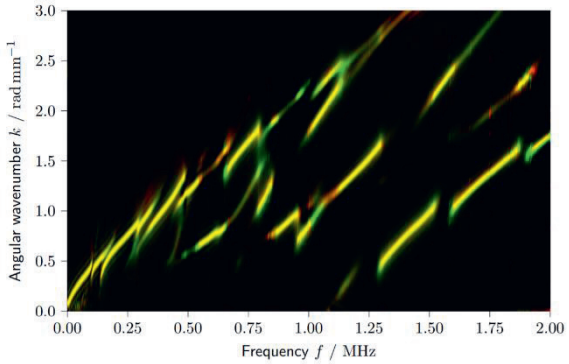

Fig. 3. Color-coded comparison of measurement results of the same specimen after 48 h (red) and 120 h (green) of adhesive curing. Yellow regions indicate matching data in both results while red/green regions are predominantly contributed by one of the results.

Adhesive curing

Since it is possible to investigate the Lamb wave propagation of multilayer systems, it will further be determined whether one can recognise a difference in the material behaviour in different stages of adhesive curing. Therefore, two different measurements of the specimen are performed. The first one about 48 h after application of the adhesive and a second one after about 120 h after bonding. To compare those two measurements, their resulting dispersion maps are overlaid in Fig. 3 using a color-coded depection. In this, the two dispersion maps are each assigned to one RGB-channel (48 h red, 120 h green) and the third channel (blue) is set to zero. Due to this coding, the depiction displays black values where the two measurement are identically zero and yellow values where both feature intense signal data. For the most part the displayed measurements are identical and both feature the same modes. Further, the 120 h cured system provides signal data for those modes over a slightly larger range. Therefore, most of the yellow ridges start and end with a green extension, indicating an improved coupling of both plates and lower absorption.

Conclusion

The investigation at hand shows that it is possible to get detailed measurements of ultrasonic waves in adhesively bonded multilayer systems using non-destructive testing methods with laser-induced Lamb waves. Further, is it possible to simulate the dispersive behaviour of those waves if the material properties of the included layers are known in advance. Additionally, it is possible to use this measurement setup to investigate changes in the material behaviour during the curing of the adhesive bonding. For further investigations, the authors aim to derive test methods for adhesive bonding strength from the observed changes in the dispersive properties.

Acknowledgements

The authors would like to thank the German Research Foundation (DFG) for financial support of the research project 449607253.

References

[1] Y. Lugovtsova, S. Johannesmann, B. Henning, J. Prager, Analysis of Lamb wave mode repulsion and its implications to the characterisation of adhesive bonding strength, International Congress on Ultrasonics (2019); doi: 10.1121/2.0001074

[2] L. Claes, T. Meyer, F. Bause, J. Rautenberg, B. Henning, Determination of the material properties of polymers using laser-generated broadband ultrasound, Journal of Sensors and Sensor Systems (2016), doi: 10.5194/jsss-5-187-2016

[3] I. Bartoli, A. Marzani, F. Di Lanza Scalea, E. Viola, Modeling wave propagation in damped waveguides of arbitrary cross-section, Journal of Sound and Vibration (2006), doi: 10.1016/j.jsv.2006.01.021

[4] M. Webersen, S. Johannesmann, J. Düchting, L. Claes, B. Henning, Guided ultrasonic waves for determining effective orthotropic material parameters of continuous-fiber reinforced thermoplastic plates, Ultrasonics (2018), doi: 10.1016/j.ultras.2017.10.005

DOI 10.5162/SMSI2021/A8.3

A Hardware Simulator for the Generation of Ultrasonic Transmission Test Signals

Michael Vogt[1], Martin Gevers[2], Rogier Geerders[3], Jan Förster[2]
[1] KROHNE Messtechnik GmbH, Ludwig-Krohn-Str. 5, 47058 Duisburg, Germany,
[2] KROHNE Innovation GmbH, Ludwig-Krohn-Str. 5, 47058 Duisburg, Germany,
[3] KROHNE New Technologies BV, Kerkeplaat 12, 3313 LC Dordrecht, The Netherlands
m.vogt@krohne.com

Summary:
The quality and characteristics of the transmission signals in ultrasonic transit-time flowmeters are important with regard to the accuracy of the time of flight and the flow measurements. In this contribution, a hardware simulator for generating ultrasonic transmission signals is presented, which allows for testing the sensor electronics of the flowmeter at zero flow and under well-defined and highly reproducible conditions. The concept is to replace the liquid by a block of polymethylmethacrylate as ultrasound propagation medium. The resulting effects on the transmission signal are analyzed and discussed.

Keywords: Ultrasonic flowmeter, testing, transmission attenuation, time of flight

Introduction

In ultrasonic transit-time flowmeters, ultrasound waves are propagated downstream and upstream a flowing fluid (liquid or gas). Based on the measured *times of flight* (TOFs), the volumetric flow rate is calculated. The ultrasound transducers play an important role for the time domain characteristics (amplitude, shape, duration, etc.) of the transmission signals. Because various operating conditions (pressure, temperature, etc.) have to be considered in the transducer design, the signal characteristics is largely transducer-specific. For testing of the sensor electronics, realistic transmission signal measurements are required. The below presented hardware simulator has been designed for performing test measurements at zero flow under well-defined and highly reproducible conditions.

Concept of the Hardware Simulator

In Fig. 1 a), the transmission path of an ultrasonic transit-time flowmeter containing a liquid is illustrated. Two transducers are positioned opposite to each other with the flowing liquid (SOS: *speed of sound* c_L, AI: *acoustic impedance* Z_L, AC: *attenuation coefficient* $\alpha_L(f)$) in-between. The concept of the hardware simulator in Fig. 1 b) is to replace the heavy flowmeter and the liquid by a block of *polymethylmethacrylate* (PMMA) plastic (SOS c_P, AI Z_P, AC $\alpha_P(f)$) and using the same transducers as in the flowmeter in Fig. 1 a). The motivation behind using the plastic is that no liquid must be handled and that the testing is performed under more reliable and reproducible conditions.

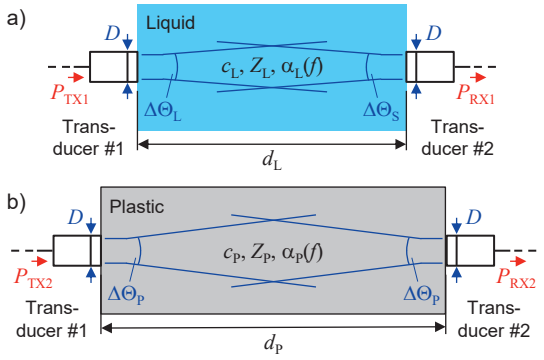

Fig. 1. Ultrasound transmission paths: a) Flowmeter (liquid), b) hardware simulator (plastic block).

In the following, the two setups in Fig. 1 are compared to each other by theoretically analyzing the characteristics of both different ultrasound transmission paths. Finally, the proposed concept has been experimentally evaluated and according measurement results are presented.

Ultrasound Transmission Path

For the same *absolute TOF*, the *distance* d_P between the transducers in the plastic must be chose as follows (distance d_L in the liquid):

$$d_P = d_L \cdot c_P / c_L \quad (1)$$

Using the same transducers (*aperture diameter* D, *frequency* f) in both setups, the *angular beam widths* $\Delta\theta_L$ and $\Delta\theta_P$, respectively, are different:

$$\Delta\theta \sim \frac{c}{D \cdot f}, \quad \Delta\theta_P = \Delta\theta_L \cdot \frac{c_P}{c_L} \quad (2)$$

Accordingly, the *transmission attenuation* a_{US} also depends on the SOS c (transmit and receive

powers P_{TX} and P_{RX}; aperture and electrical efficiencies η_{ap} and η_{el}, respectively; AC $\alpha(f)$) [1]:

$$a_{US} = \frac{P_{TX}}{P_{RX}} = \frac{16 \cdot c^2 \cdot d^2}{\pi^2 \cdot D^4 \cdot f^2 \cdot \eta_{ap}^2 \cdot \eta_{el}} \cdot e^{2 \cdot \alpha(f) \cdot d} \quad (3)$$

The *acoustic coupling* between the transducers and the propagation medium depends on the matching between the AIs of both. Likewise, the decay of the transducer 'ringing', i.e. multiple reflections inside the transducer, over TOF depends on the matching. With the hardware simulator, the ringing is expected to decay faster compared to the flowmeter, because of the better matching of the plastic.

Measurement Results

The two different setups have been tested using water ($d_L = 55$ mm, $c_L = 1480$ m/s, $Z_L = 1.48$ MRayl) and PMMA plastic ($d_P = 100$ mm, $c_P \approx 2700$ m/s, $Z_P \approx 3.2$ MRayl). The same transducers ($f_0 = 2$ MHz center frequency, $D = 10$ mm aperture diameter) have been used in both cases. Transmission measurements have been performed with a calibrated *vector network analyzer* (model Bode 100; OMICRON electronics GmbH, Klaus, Austria). Time domain transmission signals $s_{21}(t)$ have been calculated from the measured frequency domain transmittances $S_{21}(f)$ by means of the inverse Fourier transform [2]. In Fig. 2, the measured transmission signals are shown:

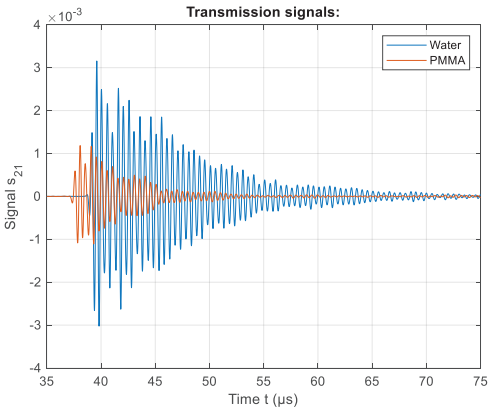

Fig. 2. Measured transmission signals: Water (blue), PMMA block (red).

As can be seen, almost the same TOFs are given, as the distance d_L has been chosen according to (1). Both signals have a very similar shape, except of the different amplitudes and decays over TOF. With the different SOSs, the transmission attenuation of the hardware simulator is expected to be 5.22 dB larger compared to with the water path, see (3). The *envelopes* of the measured transmission signals over TOF in Fig. 3 show an amplitude difference of 8.4 dB. This difference is because the AC of the PMMA is significantly larger compared to that of the water, and so the transmission attenuation in (3).

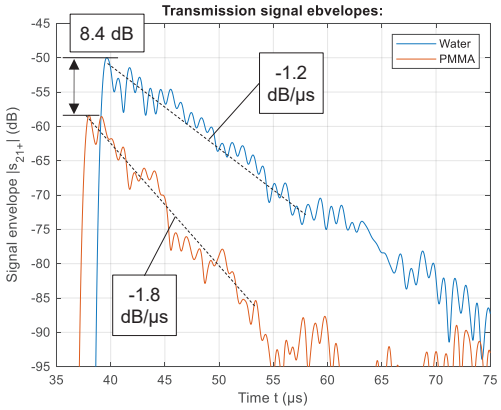

Fig. 3. Envelopes of measured transmission signals: Water (blue), PMMA block (red).

The transmission signal from the water path decays with about 1.2 dB/µs over TOF. With the PMMA, a faster decay of about 1.8 dB/µs is given. This difference is found, because the decay of the transducer ringing is the faster the better the acoustic matching between the sound propagation medium and the transducer is. The AI of the PMMA is more than twice large as the AI of water. Accordingly, the hardware simulator is much better matched to the high AI of the transducer.

Summary and Conclusions

In this contribution, a hardware simulator with PMMA as sound propagation medium for testing the sensor electronics of ultrasonic flowmeters has been presented and discussed. Measurements with a vector network analyzer have been performed to compare this setup with the flowmeter containing water. Transmission signals in both cases show a similar shape but different amplitudes. The latter is because of the different transmission attenuation linked to the different SOSs and the different attenuation coefficients. Furthermore, both transmission signals show different decays over TOF, what is caused by the different matching between the sound propagation medium and the transducers in the two cases. The findings from the experimental evaluation of the concept are in good agreement with expectations from the theoretical modeling. The realized hardware simulator allows for reliable transmission signal measurements with featuring well-defined conditions.

References

[1] B.R. Tittmann, Ultrasonic Sensor Viscosity of Mineral Oil for Built-in Pipe Applications, *Sensor+Test Conf.*, 171-176 (2011); doi: 10.5162/sensor11/a7.3

[2] M. Vogt, H. Ermert, Quantitative Analysis of Liquids and Emulsions by Means of High-Frequency Ultrasound (15-35 MHz), *IEEE Ultrason. Symp.*, 68-71 (2011); doi: 10.1109/ULTSYM.2011.0018

DOI 10.5162/SMSI2021/A8.4

Acoustophoresis in suspensions with local- and time-discrete sound fields based on the time reversal technique

Philipp Hörnlein[1], Sebastian Wöckel[1], Hendrik Arndt[1], Jörg Auge[2]
[1] Institute for Automation and Communication (ifak) e. V., 39106 Magdeburg, Germany
[2] University of Applied Sciences Magdeburg-Stendal, 39114 Magdeburg, Germany
Philipp.Hoernlein@ifak.eu

Summary:
This contribution presents a new approach concerning the acoustic 3D-manipulation of particles in a liquid filled volume. Based on simulation studies and a physical model, the realization of acoustophoresis using the acoustic radiation force (ARF) on particles in a liquid-filled vessel is discussed. The discrete local acoustic pressure field, that is required for the acoustophoresis, is generated by a time reversal mirror consisting of 24 piezoceramic transducers.

Keywords: acoustophoresis, acoustic tweezers, levitation, particle manipulation, time reversal

Motivation

The manipulation of particles and cells in fluids has numerous applications in medicine and biotechnology. This complies amongst the sorting and separation in sense of size and material, especially the exact positioning of single cells for further investigation or biochemical treatment. In this context the acoustophoresis is a proven method that works contactless, biocompatible and label-free [1]. Existing methods use either volume waves, surface waves or focused fields (acoustic vortexes) [2] to manipulate objects. Focused acoustic fields can be used to achieve a very specific stationary force effect on one or more objects (acoustic tweezers). Such previous rely either on phased array technology [3], passive systems (resonator [4], phase plate [5], diffraction grating [6]) or special transducer geometries [7]. However, these techniques have limitations when focusing is to be performed in a closed room or vessel (cavity). In addition, passive systems and special transducer geometries provide stationary acoustic fields only and do not allow an electronic translational displacement of the objects.

Methods

In order to circumvent the previous limitations, this contribution discusses the use of the ultrasonic time reversal (TR) technique to generate a transient sound field in a liquid-filled vessel. In the variant of the time reversal technique used here, the transfer function or impulse response from the piezoceramic ultrasonic transducers to the desired focal points is determined by means of a suitable measurement setup (calibration) [8]. By time reversal of the impulse responses, the time reversal signal is formed, whose emission at the associated transducer leads to a high-quality focusing on the target point. Almost any sound field geometry can be generated by simultaneous response of several focus points. The advantage is that, especially in small vessels – like bioreactors –, the reflection processes in the cavity contribute significantly to the focusing effect, which is not the case with previous realizations. In addition, the sound field geometry and its position can be varied (moved) arbitrarily within the cavity.

Results

The feasibility of the transient time-reversal focusing and the generation of specific complex sound field geometries, in the sense of particle traps, were investigated using 3D-simulations with COMSOL Multiphysics. On the basis of these parameter studies it could be shown, that a so-called bottle trap represents an ideal sound field geometry for this purpose in terms of local pressure field, reproducibility and particle force vector. The trap consists of six focus points which are excited simultaneously. In the case of the bottle trap, there are two focus points in each axis of a cartesian coordinate system, which are opposite each other at a defined distance – depending on the physical parameters of the particle and the surrounding medium. The object to be manipulated is located between the focal points. In this way, a three-dimensional force effect based on the ARF is achieved. The investigation shows that such a sound field based on the time reversal technique is basically feasible if the time reversal signals are at least as long as a sound wave needs to pass through the largest dimension of

the vessel five times. Furthermore, it becomes clear that focal points which are close to each other and have the same phase position merge to one focal point. It is therefore obvious that opposite focal points have an inverse sound pressure amplitude. If opposing focus points have an additional distance of λ/2, an acoustic field is realized which in principle corresponds to a locally limited standing wave in three dimensions (Fig 1). By high-frequency repetition of the time reversal signals, a quasi-stationary sound field can be generated. As prove of example, investigations with 24 single element transducers (in the range from 250 kHz to 1 MHz) show, that force effects in all three dimensions (F0), which allow a levitation and manipulation of particles from various plastics, glass and graphite in the order of λ/10, are already achievable with low excitation voltages of 20 V_{PP}.

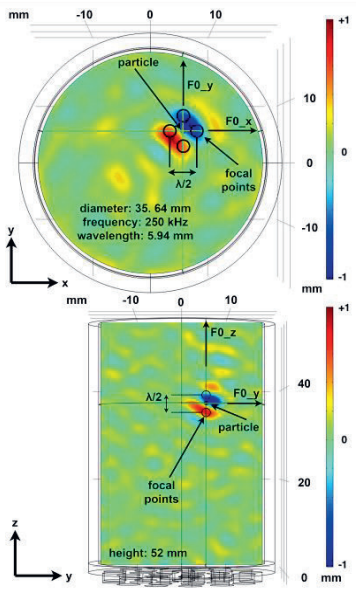

Fig. 1. Simulation-example at 250 kHz: Intensity plot of the acoustic pressure field of the bottle trap (top) in the XY and (bottom) in the YZ plane in a cylindrical vessel with piezoceramic transducers on the bottom.

Experimental Setup and Outlook

Based on the results of the simulations a demonstrator has been realized (Fig. 2). It consists of a cylindrical vessel (diameter 35.64 mm, height 52 mm) made of PMMA (wall thickness 1.36 mm) with 24 piezoceramic transducers (PIC255) with a diameter of 4.9 mm each coupled to its bottom side. The transducers operate at a frequency of 1 MHz. The vessel is filled with distilled water and the bottom serves as a λ/4 matching layer for low-reflection coupling of the transducers to the liquid. In the further course of the work a suitable control system has to be designed and realized. This will probably consist of an FPGA and a multi-channel amplifier.

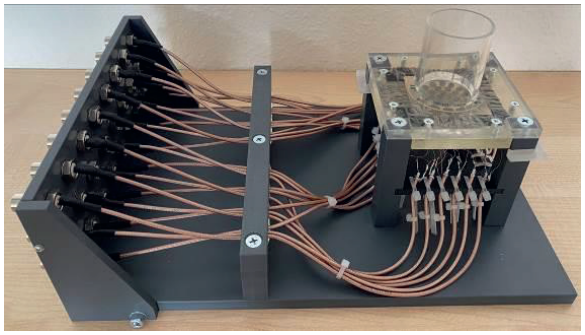

Fig. 2. TR demonstrator for 1 MHz with 24 single transducers and a cylindrical cavity for liquid fillings.

Conclusion

Within the work it could be shown by means of simulation studies, that on the basis of the time reversal technique an acoustic field can be realized which enables the transient acoustophoresis in liquid filled vessels. The so-called bottle trap, which can be moved translatorily in the vessel, was determined as the ideal sound field geometry. In addition, a suitable structure in the form of a demonstrator was shown, for which a suitable control system needs to be developed afterwards.

References

[1] A. Lenshof *et al.*, “Acoustophoresis,” in *Encyclopedia of Nanotechnology*, B. Bhushan, Ed. Dordrecht: Springer Netherlands, 2014, pp. 1–6

[2] A. Ozcelik *et al.*, “Acoustic tweezers for the life sciences,” *Nature Methods*, vol. 15, no. 12, pp. 1021–1028, 2018, doi: 10.1038/s41592-018-0222-9

[3] A. Marzo *et al.*, “Holographic acoustic elements for manipulation of levitated objects,” *Nature Communications*, vol. 6, no. May, pp. 1–7, 2015, doi: 10.1038/ncomms9661

[4] X. Jiang *et al.*, “Convert Acoustic Resonances to Orbital Angular Momentum,” *Physical Review Letters*, vol. 117, no. 3, 2016, doi: 10.1103/PhysRevLett.117.034301

[5] M. E. Terzi *et al.*, “Generation of a vortex ultrasonic beam with a phase plate with an angular dependence of the thickness,” *Moscow University Physics Bulletin*, vol. 72, no. 1, pp. 61–67, 2017, doi: 10.3103/S0027134916050180

[6] N. Jiménez *et al.*, “Formation of high-order acoustic Bessel beams by spiral diffraction gratings,” *Physical Review E*, vol. 94, no. 5, pp. 1–18, 2016, doi: 10.1103/PhysRevE.94.053004

[7] M. Baudoin *et al.*, “Folding a focalized acoustical vortex on a flat holographic transducer: Miniaturized selective acoustical tweezers,” *Science Advances*, vol. 5, no. 4, pp. 1–7, 2019, doi: 10.1126/sciadv.aav1967

[8] Y. D. Sinelnikov *et al.*, “Time reversal in ultrasound focusing transmitters and receivers,” *Acoustical Physics*, vol. 56, no. 2, pp. 183–193, 2010, doi: 10.1134/S1063771010020107

DOI 10.5162/SMSI2021/A9.1

Excitation of Guided Acoustic Waves Using Ignition Sparks

Sandro Krempel, Alexander Backer, Florian Dötzer, Klaus Stefan Drese
Coburg University of Applied Sciences and Arts, Institute of Sensor and Actuator Technology (ISAT),
Am Hofbräuhaus 1b, 96450 Coburg, Germany
sandro.krempel@hs-coburg.de

Summary:
Many sensor principles are based on the excitation and detection of guided acoustic waves (GAW). These are usually generated by mechanical coupling of piezoceramic transducers with the help of thin coupling layers. With electromechanical transducers (EMAT) or pulsed lasers, GAW can also be excited without a coupling layer or direct coupling. A further, very cost-effective possibility to excite Lamb waves on thin sheets without direct contact is shown here in the experimental setup by means of electric sparks.

Keywords: contactless excitation, guided acoustic waves (GAW), spark plug, electric spark, thermoacoustic wave excitation

Introduction

Pulsed GAW, excited by piezoceramic transducers, are frequently used in the field of material or damage analysis, but also for layer detection [1]. If individual samples are to be measured without contact, the expensive principle of thermoacoustic excitation of GAW by means of pulsed laser radiation is frequently used [2]. Korolev, Krasilnikov and Krylov have already shown that Rayleigh waves can also be excited in the material by spark discharge in air over thicker metal samples. The main effect seems to be the pressure wave generated above the material [3]. Focused pressure waves generated by sparks are also directed onto material surfaces in other places, generating bulk and Rayleigh waves [4, 5].

The approach presented here focuses on the experimental setup of a device using a very low-cost, commercial ignition coil and spark plug. The spark is generated directly between the spark plug and a thin metal sheet whereby Lamb waves are excited on the sheet. The excitation and propagation of the waves is detected by a laser vibrometer.

Methodology

The test setup is shown in Fig. 1. A self-developed electronic switchbox (3) is supplied with 16.4 V voltage via a power supply EA-PS 2016-100 (1) and delivers the necessary current for charging the non-suppressed ignition coil 12V-QM50QT-6(A) (4). An Agilent 33500B function generator (2) generates a voltage pulse with a pulse width of 80 µs as a control signal, which is sent to the switchbox at a recovery rate of 20 Hz. At the same time it also sends the trigger pulse to the laser vibrometer Polytec PSV400-M (7) to start the measurement. A suppressed iridium spark plug A7TC-QM50QT-6(A) with the counter electrode removed (5) is used for spark excitation.

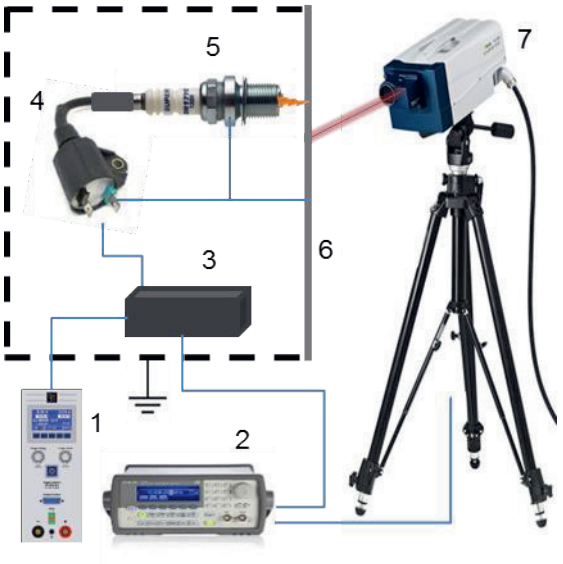

Fig.1. Illustration of the measurement setup

As the spark discharge of the spark plug causes large EM interference in the surrounding area, the switchbox as well as the coil and spark plug were installed in a closed stainless steel box. The test sample (6) is a 0.5 mm thick stainless steel sheet which also serves as a cover of the steel box and as a counter electrode of the spark plug. The distance of the spark plug electrode to the test sample is 0.7 mm. To detect the generated wave, the

outer side of the test sample is scanned with the laser vibrometer.

Results and Discussion

The vibrometer signal detected by the VD-09 velocity decoder at the point of excitation is shown in Fig. 2. After interruption of the coil current at 80 µs there is a short time delay until the spark is formed, then the oscillation of the plate surface can be detected.

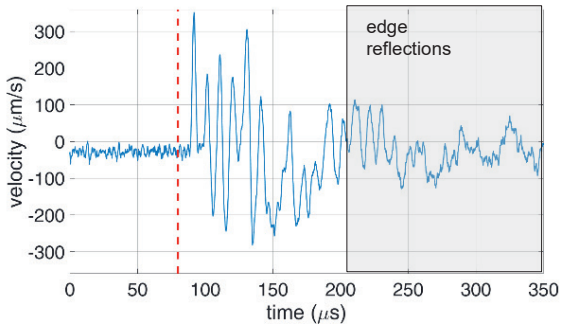

Fig.2. Time signal of the laser vibrometer measurement

From approx. 200 µs onwards, interactions with edge reflections occur in the time signal. The Lamb waves excited by the point impulse show a radially symmetrical propagation (Fig. 3).

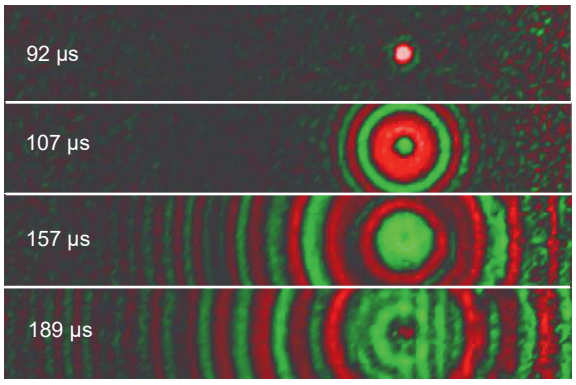

Fig.3. Surface scanning by laser vibrometer at different times.

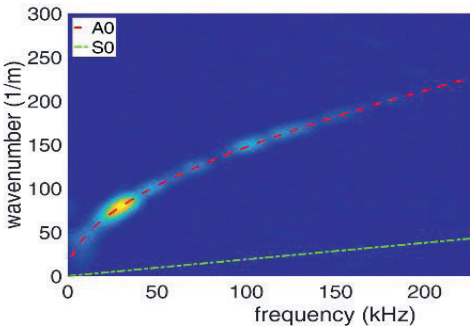

Fig.4. 2D FFT along the time and horizontal spatial axis (at the vertical center)

Using a 2D FFT of the time and horizontal position (vertical: centered) dependent from the same measurement series as used for Fig. 3, the waves excited in the measurement can be compared with the dispersion behavior of the Lamb modes calculated for a 0.5 mm thick stainless steel plate (Fig. 4). It can be seen that the one-sided impulse excites almost exclusively the antisymmetric A0 mode. In addition to the dominant frequency of approx. 30 kHz frequency components up to approx. 200 kHz are also visible.

Conclusion and outlook

The experimental investigations have shown that even with a very simple and inexpensive ignition coil - spark plug design (<100 €) it is possible to excite guided acoustic waves in a metal plate without contact and broadband, but above all at very low frequencies. This would, for example, open up new possibilities in the field of sensor technology for structural health monitoring. In further investigations, the following points are to be clarified more precisely: local position accuracy and repeatability of the spark impact, potential material removal on the sample, electrode geometry and position relative to the sample, extension of the frequency range, investigation of the contribution of various excitation mechanisms to the formation of GAWs (thermal expansion, pressure waves).

Acknowledgments

The authors thank the various supporters of the project at ISAT, especially Frank Ritter, Tobias Köstner, Andrej Schumacher, Sabrina Tietze and the European Fund of Regional Development (EFRE) within the project "InnoTerm".

References

[1] G. Lindner, M. Schmitt, K. Schmidt, H. Faustmann, S. Krempel, J. Schubert, Detection of coatings and measurement of coating thickness on technical substrates using surface acoustic waves in a waveguide configuration, *Proc. Sensor 2009 (1)*, 35–40 (2009); doi: 10.5162/sensor09/v1/a1.3

[2] F. Singer, Laser-Acoustic Characterization of Coatings, *AMA Conferences 2015 - SENSOR 2015 and IRS2 2015*, 119-123; doi: 10.5162/sensor2015/A5

[3] S. V. Korolev, V. A. Krasilnikov, V. V. Krylov, Mechanism of sound generation in a solid by a spark discharge near the surface, *Sov. Phys. Acoust. 33 (4)*, 774-776, (1987)

[4] X. Dai, J. Zhu, M. Haberman, A focused electric spark source for non-contact stress wave excitation in solids, *JASA Express Letters*, 2013; doi: 10.1121/1.4826913

[5] S. V. Korolev, V. V. Krylov, Efficient excitation of Rayleigh waves by a strong shock wave initiated by a spark in air, *Sov. Tech. Phys. Lett. 14 (11)*, 1945-1949, (1988)

DOI 10.5162/SMSI2021/A9.2

Fouling Detection in Polymerization Processes by Ultrasound Echo Measurements

Jan Förster[1], Marco Osenberg[2], Jan Tebrügge[1], Stephan Westerdick[2], Esther von Grotthuss[3], Frank Behrendt[3], Michael Vogt[4]
[1] KROHNE Innovation GmbH, Ludwig-Krohne-Str. 5, 47058 Duisburg, Germany
[2] Ruhr-Universität Bochum, Chair of Electronic Circuits, 44780 Bochum, Germany
[3] Covestro Deutschland AG, 51365 Leverkusen, Germany
[4] KROHNE Messtechnik GmbH, Ludwig-Krohne-Str. 5, 47058 Duisburg, Germany
j.foerster@krohne.com

Summary:
Growth of fouling in polymerization processes is an unwanted event, reducing the energy- and resource-efficiency during fabrication. To improve cleaning cycles due to fouling, operators of these processes request for measurement techniques for reliable in-line detection of fouling. A very promising approach for this problem is using ultrasound-based measurement technique. A basic measurement setup based on an ultrasonic pulse-echo method is introduced and its proof of principle is demonstrated by first experiments where formation of fouling was detected.

Keywords: Ultrasound, Fouling Detection, Polymerization

Introduction

Many applications, where fluids flow inside pipes or where fluids react in mixing structures, suffer from the growth of fouling. Of course, these fouling represent unwanted impurities to the products in such processes [1]. This leads to product contamination and eventually to reduced process yields as contaminated products must be removed. Furthermore, fouling often appears as layers at the inner surfaces of pipes or mixing structures and thus act as a thermal insulator. This decreases the energy efficiency of these processes noticeably [2]. Both, the reduced yield and the reduced energy efficiency causes the operator financial losses.

In the field of the chemical process industry, polymerization processes have been identified to be of high interests and often suffering from fouling [3]. As fouling cannot be prevented, the operators are forced to apply cleaning procedures to their plants on a regular basis. Unfortunately, no suitable sensors for early detection of fouling are available for these processes. For this reason, the operators so far only rely on their experience to decide whether cleaning procedures must be applied. As this requires permanent surveillance of the process, measurement technique to reliably detect the formation of fouling in an early stage is strongly desired.

Ultrasound-based sensors have already been suggested as a possible solution to this problem. Thus, this work aims on the analysis of the suitability of using ultrasound to detect fouling in polymerization processes.

Exemplary Polymerization Process

For the proof of concept, the oligomerization of isocyanates was chosen as an exemplary polymerization process. In a first approach, this process was analyzed regarding its compatibility with ultrasonic measurement technique. In general, this process is suitable for ultrasonic measurements, because no outgassing occurs and no inhomogeneities exist. Furthermore, it is operated at low pressure and slow flow velocity. Besides these conditions, the process needs to have significant differences in the acoustic impedances of the fluid and the fouling to achieve a noticeable contrast in the measured ultrasonic echo signals. Some of the parameters of the relevant chemicals are already known from literature, such as the density ρ_{fl} = 1050 kg/m^3 [4]. However, other parameters had to be determined by experiments. Therefore, samples of the fluid with and without fouling were placed into a container. An ultrasonic transducer (3 mm aperture diameter, 19.2 MHz center frequency, 12.2 MHz bandwidth; Olympus Corp., USA; model V316-SM) was immersed to a certain depth into the investigated samples. A pulser-receiver (Metrotek Inc., USA; model MP203, MR101) was used to generate a short

pulse. The received echo was recorded using an oscilloscope (Rohde & Schwarz GmbH, Germany; model RTO 1004). The speed of sound (SOS) c of the fluid and of the fouling was then extracted from the echo measurement. The determined values for the fluid and the fouling at room temperature are c_{fl} = 1430 m/s and c_{fo} = 2920 m/s, respectively. Furthermore, the fouling has a density of approximately ρ_{fo} = 1030 kg/m^3. Both, the difference in SOS c and in density ρ lead to a significant difference in the acoustic impedances Z:

$$Z = \rho \cdot c \qquad (1).$$

Measurement Setup

For the proof of principle, the growth of fouling had to be detected in-line by the ultrasonic measurement technique. Therefore, the measurement setup had to be integrated into the process setup. An in-line measurement cell built of polyether ether ketone (PEEK) including an inner fluid channel with a square cross section of d_{cell} = 10 mm was constructed. As illustrated in Fig. 1, the ultrasonic transducer was installed in the PEEK body perpendicularly to the flow direction of the fluid. For a good separation of the relevant echoes from multiple reflections the transducer was placed at a distance d_{delay} = 20 mm from the inner channel. An inspection glass was installed upstream the measurement cell to visually survey the growth of fouling.

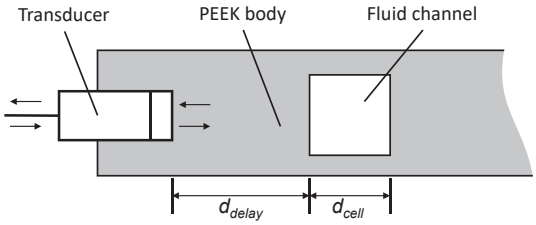

Fig. 1 Schematic drawing of the in-line measurement cell used for the experiments. The flow direction is perpendicular to the illustrated plane.

The ultrasound echo signals were recorded using the same measurement equipment as for the determination of the acoustic parameters of the polymerization process. To improve the SNR, 10 successive echo measurements were averaged before further processing. A digital bandpass filter with upper and lower cutoff frequencies of 1 MHz and 39 MHz, respectively, was applied and the envelope signal was calculated using the Hilbert transformation.

Results

During the experiments, some local fouling grew at the surface of the backside of the channel in the ultrasonic path. The envelope of signals obtained before and after the formation of this fouling are shown in Fig. 2. As can be seen, the first echo occurs at the transition

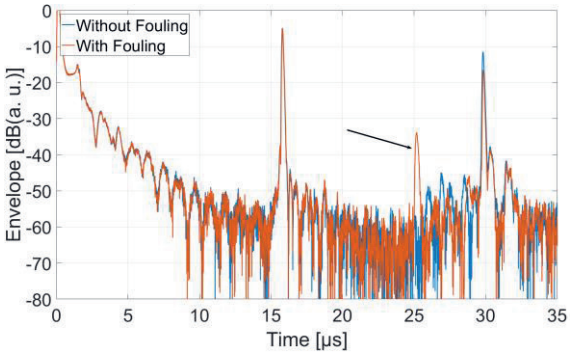

Fig. 2. Envelope of the received signals without and with formation of fouling (arrow indicates additional echo by fouling)

between the PEEK body and the fluid at about 16 µs. At approx. 30 µs, the echo of the transition between the fluid and the PEEK body is visible. In addition, the envelope of the echo signal obtained with the fouling shows an additional echo at about 25 µs. Thus, the fouling is clearly detectable in this case.

The thickness of the fouling can be determined from the time difference between the different echoes. Taking the SOS c_{fl} = 1430 m/s of the fluid into account, a thickness of 3.38 mm was calculated for the fouling. Verification with a vernier caliper later confirmed this measurement.

Conclusion

Proof of principle for ultrasound-based detection of fouling in polymerization processes was demonstrated. Further work will now deal with determining the minimal detectable fouling thickness and the transfer of this method to other polymerization processes.

Acknowledgment

The German Federal Ministry for Economic Affairs and Energy (BMWi) is acknowledged for funding this research as part of the ENPRO2.0 initiative. (Support code: 03EN2004E)

References

[1] A. Hohlen, W. Augustin, S. Scholl, Quantification of Polymer Fouling on Heat Transfer Surfaces During Synthesis, *Macromolecular Reaction Engineering,* (2019) doi: 10.1002/mren.201900035

[2] M. Bohnet, Fouling of heat transfer surfaces, *Chem. Eng. Technol.,* vol. 10, 113-125 (1987)

[3] H. J. Harwood, Principles of polymerization (Odian, George*), Journal of Chem. Ed.* (1971), doi:10.1021/ed048pA734.1

[4] GESTIS-Stoffdatenbank, Hexamethylen-1,6-diisocyanat, http://gestis.itrust.de/nxt/gateway.dll/getis_de/013120.xml?f=templates$fn=default.htm$3.0, called at 20.11.2020

DOI 10.5162/SMSI2021/A9.3

Dual Electrochemical Quartz Crystal Microbalance with Dissipation Monitoring

Rafael Ecker[1], Nikolaus Doppelhammer[1], Bernhard Jakoby[1], Erwin K. Reichel[1]
[1]Institute for Microelectronics and Microsensors, Johannes Kepler University Linz, 4040 Linz, Austria
rafael.ecker@jku.at, nikolaus.doppelhammer@jku.at, bernhard.jakoby@jku.at, erwin.reichel@jku.at

Summary:
We report on the design and fabrication of a dual electrochemical quartz crystal microbalance sensor unit with dissipation monitoring (EQCMD). Applying an electrical field between two oppositely placed quartz surfaces facilitates particle separation and monitoring the deposition of oppositely charged particles on the electrodes during or after the colloidal synthesis of silicalite-1 zeolites. By evaluating the resonance frequencies and quality factors of the quartz crystals, several properties of the test liquid are monitored indirectly. We demonstrate the measurement of electrical conductivity and viscosity.

Keywords: EQCMD; crystallization monitoring; zeolite; viscosity measurement; fluid conductivity

Introduction

The quartz crystal microbalance with dissipation monitoring (QCMD) and the associated electrochemical version (EQCMD) are nowadays often used to detect very tiny mass changes on the surface, for example in a deposition process [1], or to characterize mechanical properties of materials [2].

The purpose of this work is to build a setup for monitoring the synthesis of zeolites. This process is based on emerging colloidal nanoparticles in an alkaline solution that grow by consuming a silicate source present as tetra(ethyl)orthosilicate (TEOS). This solution is particularly aggressive such that measurement cells have to be designed carefully including the selection of suitable materials. Besides other techniques, viscosity sensing is used to track the crystallization progress [3]. The presented setup aims at integrating the in-situ measurement of electrochemical properties and mass loading at electrodes. In particular, this setup differs from previous similar approaches by using two mass-sensitive devices facilitating the measurement of potential deposits and surface effects at each of the two electrodes used for impedance spectroscopy and viscosity sensing.

Setup

The reactor chamber is constructed as shown in Fig. 1. Top, middle and lower part are 3D printed using an Objet30 Pro 3D printer. For the fabrication of the inner chamber, castable silicone and 3D printed molds are used. This reactor chamber is surrounded by temperature-controlled aluminum housing, Peltier elements, PT100 temperature sensors, heat sinks, fans and thermal insulation.

The control task itself is executred by a Raspberry PI computer with additional evaluation electronics. Two quartz disk resonators operating in thickness shear mode (Tai Tien Electronic S-CAAAB-5MG03 or LapTech Precision Inc. WTiAu0514) are installed as sensors. An evaluation unit (MicroResonant QCM50) and a multiplexer are used to evaluate the resonance frequencies and the quality factors of these quartz crystals.

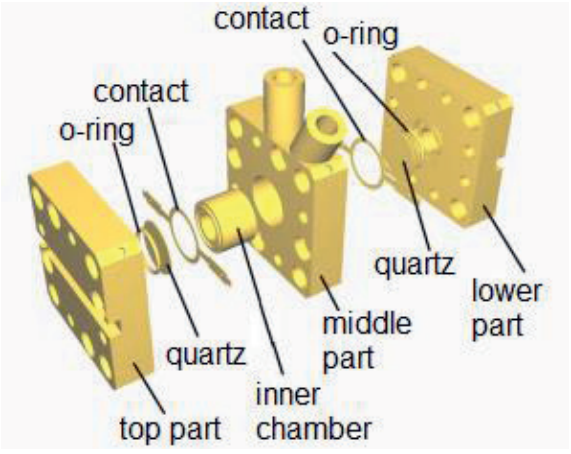

Fig. 1. Design of the reactor chamber

Methods

To determine the viscosity from the measured values of resonance frequency and quality factor, the acoustic impedance for Newtonian flu-

ids is used [3]. This requires two reference measurements in known fluids or gases and the density of the test liquid at a known temperature.

A Reference 600+ potentiostat from Gamry Instruments is used to measure the electrical impedance of the sample between those two electrodes of the quartz sensors which are in contact with the sample. We utilized a first order model for the impedance of the liquid in terms of a resistor, modeling the ohmic resistance of the liquid, in series with a capacitance, modeling the electrochemical double layer at the electrode-liquid interface. For high frequencies the capacitance is short-circuited. Consequently, this impedance solely represents the ohmic resistance *R* of the sample and serves as a measure for electrical conductivity.

Measurements

To test the setup, we started with viscosity and electric conductivity measurements using sodium hydroxide (NaOH) solutions in various concentrations and compared our results to data from literature [4,5]. The results show that the measured values are in reasonable agreement with reference values.

Next, we did measurements monitoring the crystallization of a zeolite precursor liquid (ZPL) with a reactor temperature of 60°C. After the first measurement we noticed that the gold electrodes of both quartz crystals, contacting the strong alkaline ZPL solution, were partly destroyed (little holes). Consequently, we covered these sides of the quartzes with a thin, about 1-2 µm thick, polymethyl methacrylate (PMMA) layer using a spin coating process. . In Fig. 2 the results with and without this protection layer are shown. Comparison of the two curves shows that the sensitivity of the quartz crystals decreases because of the PMMA layer. Otherwise both measurements show a similar course. The decreasing resonance frequency and quality factor indicates the growth of the crystals on the quartz surfaces. The reason for the regularly swings in all curves is not known yet. Measurements with the lye potassium hydroxide (KOH), 40% in water, have shown these effects too. With pure water no swings are monitored. We therefore assume that these swings are not directly related to crystallization process. But occur generally in connection with alkaline solutions. We are currently studying this phenomenon further.

Conclusion

In this paper, we presented a setup designed for the monitoring of zeolite syntheses using the principle of a dual EQCMD setup. To demonstrate its capabilities, viscosity and electrical

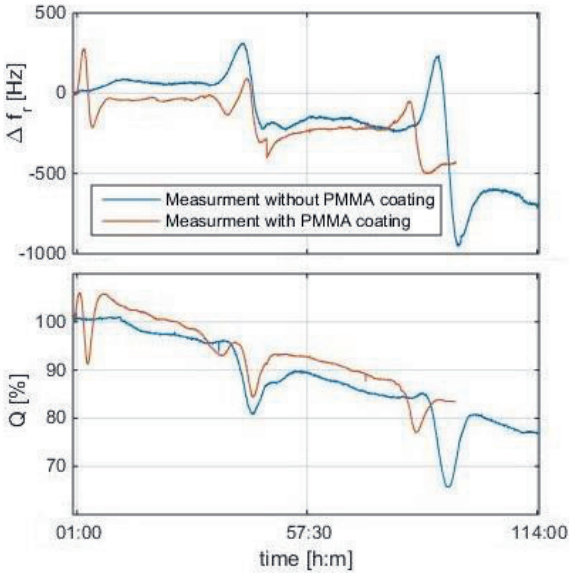

Fig. 2. Measurement result with ZPL and a reactor temperature of 60°C using a PMMA coated and an uncoated quartz crystal. Top graph changes in resonance frequency vs time, bottom graph quality factor vs time.

conductivity for various NaOH solutions are measured. We compared the results to known values from literature, where measurements agree particularly well with literature data. Our cell has the potential to monitor chemical reactions such as zeolite formation in alkaline precursor liquids or to detect other phenomena, like the regularly swings in measurement data, which we are currently investigating.

References

[1] D. Dudášová, A. Silset, J. Sjöblom, Quartz Crystal Microbalance Monitoring of Asphaltene Adsorption/Deposition, Journal of Dispersion Science and Technology 29, 139-146 (2008); doi: 10.1080/01932690701688904

[2] N. Shpigel, M.D. Levi, D. Aurbach, EQCM-D technique for complex mechanical characterization of energy storage electrodes: Background and practical guide, Energy Storage Materials 21, 399- 413(2019); doi: 10.1016/j.ensm.2019.05.026

[3] L.R. Follens, E.K. Reichel, C. Riesch, J. Vermant, J.A. Martens, C.E. Kirschhock, B. Jakoby, Viscosity sensing in heated alkaline zeolite synthesis media, *Physical chemistry chemical physics* 11, 2854- 2857 (2009); doi: 10.1039/B816040F

[4] P.M. Sipos, G. Hefter, P.M. May, Viscosities and Densities of Highly Concentrated Aqueous MOH Solutions (M+) Na+, K+, Li+, Cs+, (CH3)4N+) at 25.0 °, *J. Chem. Eng. Data* 45, 613- 617 (2000); doi: 10.1021/je000019h

[5] Y. Shao, M. Hellström, A. Yllö, J. Mindemark, K. Hermansson, J. Behler, C. Zhang, Temperature effects on the ionic conductivity in concentrated alkaline electrolyte solutions, *Phys Chem Chem Phys.* 22, 10426- 10430 (2020); doi: 10.1039/C9CP06479F

DOI 10.5162/SMSI2021/B1.1

Innovative hydrogen sensors in fuel cell vehicles

Olaf Kiesewetter[1], Alexander Kraußer[1], Nils Kiesewetter[1], Jürgen Müller[1], Marcus Bose[1], , Matthias May[1]
[1] UST Umweltsensortechnik GmbH, Dieselstr. 2 und 4, 99331 Geratal OT Geschwenda
o.kiesewetter@umweltsensortechnik.de

Summary:
For the measurement of H_2 concentrations in the exhaust gas of automotive fuel cells and in its vehicle environment an active diversified-redundant hydrogen gas sensor system will be developed. The combination of a selective metal oxide semiconductor gas sensor and a thermal conductivity detector as well as suitable signal preprocessing enables an application-specific H_2 sensor system with high sensitivity, selectivity, stability and safety. Based on updated application specific sensor requirements the work status and current results of the project focused on the current development state of the ambient gas sensor including measurement results will be presented.

Keywords: H_2-sensor, fuel cell, monitoring, ambient, exhaust gas, automotive, diversified-redundant

Used gas sensor principle for H_2 measurement

Technical objectives, requirements and basics for the development of a highly integrated miniaturized humidity compensated H_2 sensor systems for the use in exhaust gas and ambient monitoring systems of automotive fuel cells are described in [1]. The gas sensor systems to be realized are based on an innovative combination of a H_2 selective metal oxide semiconductor gas sensor and a thermal conductivity detector as well as a suitable signal preprocessing [2]. Based on this patented Semicon® principle application-specific H_2 sensor systems with high sensitivity, selectivity, stability and safety for various applications are realizable [3]. Following up [1] in this paper the current development state of the ambient gas sensor is described.

Application specific sensor requirements

For the intended automotive application of H_2 sensors various properties and technical parameters of the sensors must be realized. These are in particular, additional to the described active diversified-redundance [1] [2], integrated safety related functions (e.g. errors will be signaled during the measurement procedure), icing resistance (ready for operation after defrosting), resistance to deionized water (as condensate of the fuel cell), certifiability for use in safety-critical systems, perspective suitability of the sensor concept for large series production, the validatability for automotive applications up to compliance with the target costs. Tab 1 shows target parameters for both the H_2 sensor types to be developed.

Tab. 1: Selected technical target parameters for the H_2 Sensors (Ambient and Exhaust)

Parameter	H_2 Sensor Ambient	H_2 Sensor Exhaust
H_2 measurement range	1 ppm - 10 Vol%	
Accuracy	± 30 % from measured value (≤ 1 % H_2), ± 10 % from measured value (> 1 % H_2)	
Operating hours	≥ 8.000 h	≥ 6.000 h
Lifetime	≥ 15 Years	≥ 10 Years
On/Off cycles	≥ 45.000	≥ 30.000
Mileage	≥ 300.000 km	
Resistances to chemical substances	CO, C_6H_6, C_7H_8, NH_3, NO, NO_2, O_3, SO_2, ammonium sulphates/nitrates, HMDS, …	
Ready for operation after defrosting	≤ 5 s	
Operating temperature	-40°C - +85 °C/+125°C	
Dew point	≤ 40°C	≤ 80°C – 95°C
Power supply U_b	12 V DC – 16 V DC	

Laboratory sample of the ambient H_2 sensor

Fig.1 shows the block diagram of a first laboratory sample of an integrated H_2 sensor system for ambient monitoring. In the sensor is an ceramic one-chip H_2 MOX/TCD gas sensor element and a platinum thin-film temperature sensor element as reference sensor as well the sensor electronics for sensor control, signal

preprocessing, communication, I²C-interface and power supply integrated. The sensor elements are realized in hybrid-technology: ceramic carrier substrate (Al_2O_3) with a microstructured platinum thin-film layer, covered with a passivation layer, specific layers for contacts and locking as well as a gas-sensitive metal oxide (MOX) layer (H_2-selective) for the MOX gas sensor element [1] [2] [4].

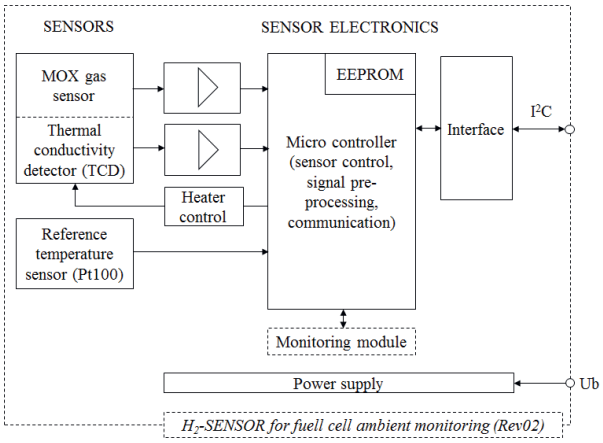

Fig. 1 H_2 Semicon® sensor for ambient monitoring of an automotive fuel cell – block diagramm

Fig. 2 shows an exploded view of the first laboratory sample of the H_2 sensor for ambient measurement, Fig. 3 shows the PCB with the sensor elements and the capped sensor sample (LxWxH ca. 17x13x7 mm).

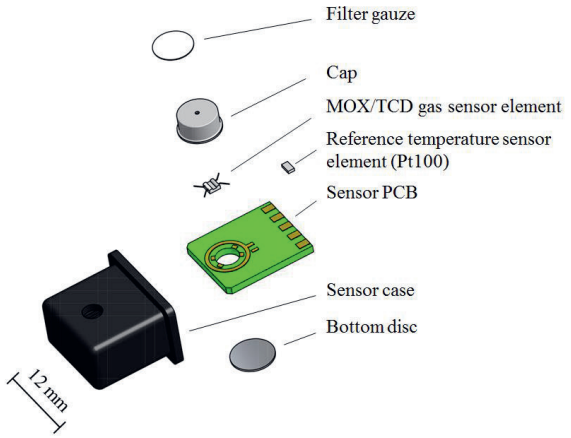

Fig. 2 H_2 Semicon® sensor for ambient monitoring of an automotive fuel cell – exploded view

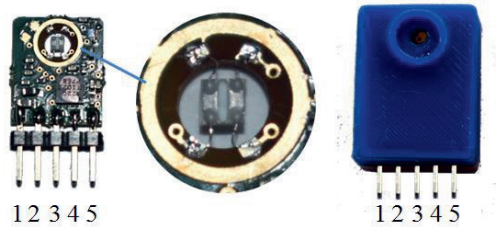

1: GND, 2: VCC (operating voltage), 3: SDA (I²C), 4: SCL (I²C), 5: Hz (heater)

Fig. 3 H_2 Semicon® sensor for ambient monitoring of an automotive fuel cell – left: PCB with gas sensor element; right: sample H_2 sensor capped

During measurements in the laboratory test environment the H_2 sensor system was exposed to various H_2 concentrations. Fig. 4 shows the reactions of the MOX gas sensor and the TCD as raw signals. These raw signals can be application specific further processed.

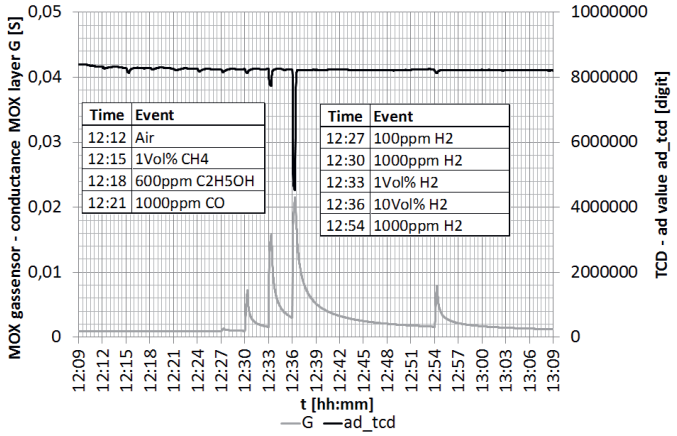

Fig. 4 Laboratory measurement of H_2 Semicon® sensor sample for ambient monitoring

Results and outlook

The presented results show that the realized and tested ambient H_2 gas sensor sample is promising for further development. Sensor concept and design as well in particular the possibility of an easy sensor gas calibration are basically for a successful future development as serial product and the following transfer in serial production. Furthermore some results will be suitable for the ongoing development of the H_2 gas sensor for exhaust gas monitoring systems of automotive fuel cells.

References

[1] Kiesewetter, O., Kraußer, A., Kiesewetter, N., Müller, J., Bose, M., Schenk, St., May, M., "H_2-Sensors for Automotive Fuel Cell Application", Short paper, SMSI 2020, 12.05.2020

[2] Kiesewetter, O., Kraußer, A., Kiesewetter, N., Müller, J., Bose, M., Schenk, St., May, M.: „Innovative H_2-Sensorik für Brennstoffzellen-Fahrzeuge", Tille, T. (Herausgeber), Automobil-Sensorik 3, pp. 97-114, ISBN 978-3-662-61259-0, Springer-Vieweg, Springer Verlag GmbH, Berlin, 2020

[3] Ewert, A., Kiesewetter, O., Kittelmann, S., Melchert, V., „Verfahren zur Erfassung brennbarer Gase, insbesondere zur Erfassung von Wasserstoff / Method for detecting combustible gases, in particular hydrogen", European Patent, No. EP000001621882B1, 02.06.2005.

[4] Kiesewetter, O., Kohl, C.-D., Melchert, V., Bauersfeld, D., May, M., „Innovative Plattform für keramische Sensoren als Basis für automotive Applikationen", In: Tille, T., et al., Sensoren im Automobil IV, 236-259, Haus der Technik Fachbuch Band 119, ISBN 978-3-8169-3066-2 , Expert-Verlag, 2011.

DOI 10.5162/SMSI2021/B1.2

Failure analysis of overloaded coulometric hydrogen sensor

Andreas Graff [1], Wolfram Münchgesang [1,2], Frank Altmann [1], Cameliu Himcinschi [2], Thomas Köhler [2], Pramit Sood [3], Jens Zosel [3] and Michael Mertig [3]

[1]Fraunhofer Institute for Microstructure of Materials and Systems (IMWS), 06120 Halle, Germany
[2]Technische Universität Bergakademie Freiberg, 09599 Freiberg, Germany
[3]Kurt-Schwabe-Institut für Mess- und Sensortechnik Meinsberg e.V., Kurt-Schwabe-Straße 4, 04736 Waldheim, Germany

Summary:

An irreversible degradation of a coulometric hydrogen sensor is observed after operation at high electrical load. Microstructural investigations were performed on the YSZ ceramic tube of the sensor with outer and inner electrodes to find the root causes for the degradation. Local color changes (blackening) were observed caused by the reduction of the YSZ by oxygen diffusion at grain boundaries under chemical and electrical potential. Crack formation and phase transitions in the YSZ ceramic from cubic to monoclinic can explain the irreversible degradation of the solid electrolyte sensor.

Keywords: gas chromatography, coulometry, hydrogen sensor; Yttria-stabilized zirconia (YSZ)

Background, Motivation and Objective

Hydrogen is a convenient candidate to store energy produced by surplus green electricity. The key component for converting the electrical energy into chemical energy of hydrogen is the electrolyzer which splits water into hydrogen and oxygen. To ensure the safety during the production, storage, transport and usage of hydrogen gas sensors are mandatory. For the electrolyzer, hydrogen sensors must have a sensitivity of 100 vol.-ppm up to a concentration of 4 vol.-% hydrogen in an oxygen atmosphere or in air at pressures up to 30 bar and temperatures up to 90 °C. Coulometric solid electrolyte sensors for hydrogen provide the required sensitivity and withstand these operation conditions. To suppress the cross sensitivity against other gases the substances can be separated in advance by gas chromatography. Such sensors have to sustain under harsh environment and high electrical fields causing degradation of the sensor materials and limiting the life time. This study focusses on the solid electrolyte YSZ in the coulometric measurement cell and its structural changes during extreme load conditions.

Description of the Methods

Microstructural investigations are performed on a gas-tight YSZ ceramic tube (Friatec, 8 mol% Y) after electrical overload. The YSZ tube is the central part of a coulometric sensor device (Zirox GmbH). The oxygen transport in and out the tube is controlled by two pairs of Pt (99.99% pure) electrodes fixed by YSZ cement to the inner and outer wall of the tube. One pair is used for measurement and the other one as reference. The electrodes are also used to measure the difference of the chemical potential between inside and outside the tube. The microstructure of the YSZ ceramic was mainly determined by electron microscopy (SEM Zeiss Supra, TEM FEI Titan) combined with diffraction and analytical methods (Trident EBSD-EDX, EDAX). Additional structural information was obtained by XRD and Raman spectroscopy.

Results

The experiments started with the conditioning of the sensor under high electrical load. Starting with oxygen transport from outside air to a reforming gas (50 vol.-ppm H_2 in N_2) inside the tube for 60 s at 750 °C. The transport was forced by a voltage of 11 V and the current was limited to 0.6 A. During the conditioning the tube gets damaged by elevated local current densities and developed remarkable oxygen gas diffusion through the tube wall. After conditioning the voltage at the electrodes was reversed automatically to establish a low oxygen partial pressure inside the tube. Due to the unnoticed gas leakage, a high pumping current was applied for more than 60 min. The structural changes caused by this experiment were investigated in detail.

3.1. Defect localization and blackening

To localize the positions of the gas leakage and assumed electrical shorts sites have to be found where the color of the YSZ changes from opaque to black. Known as blackening-effect occurring in reduction atmosphere [1]. After removing the electrodes blackening could be observed only at single spots on the tube surface. To localize more positions laser cross sectioning and inside

illumination have been performed (Fig.3) before the tube was separated by sawing to get cross sections for further investigations. At cross sections blackening could be observed at the inner electrode. At some positions the blackening reaches the outer surface of the tube indicating possible sites of gas leakage and electrical shorts (Fig.1).

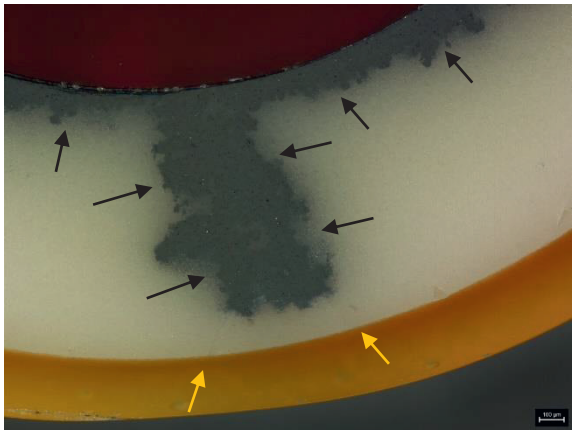

Fig. 1 Light microscope image of mechanical cross section of the YSZ tube. Blackening and cracks are visible in the YSZ ceramic starting at inner surface.

3.2. Microstructural investigation

Different analysis methods were applied to correlate the blackening with changes in the microstructure of the YSZ. To determine the grain structure back scatter electron (BSE) imaging and EBSD was applied to identify the different phases of the ceramic. In comparison to unaffected areas void formation and cracks at the grain boundaries could be found in the blackening areas (Fig.2). EBSD analysis reveal the hexagonal Alumina structure of the darker precipitates (Fig.4) seen in the BSE images. Raman measurements indicate the monoclinic Zirconia phase in the blackening areas in contrast to the cubic and tetragonal phases at the reference sites.

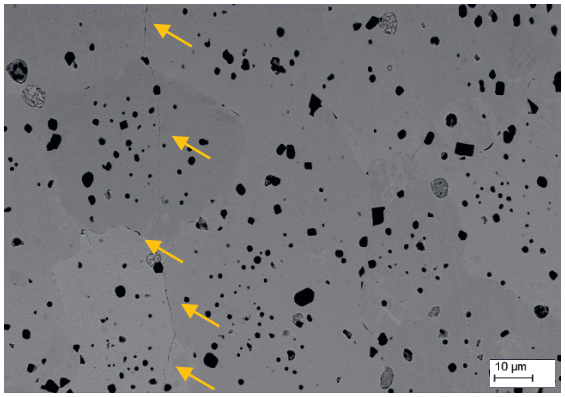

Fig. 2 BSE image of the cross section with grain structure and Al_2O_3 inclusions. Micro cracks have formed (left side) in the black regions.

References

[1] J. Janek.; C. Korte. Electrochemical blackening of yttria-stabilized zirconia – morphological instability of the moving reaction front. Solid State Ionics, 1999, 116, 181-195.

Acknowledgments

This research was funded by the German Federal Ministry of Education and Research, grant numbers 03ZZ0724A, 03ZZ0724E and 03ZZ0724I within the “HYPOS – Hydrogen Power Storage & Solutions East Germany” project.

Illustrations, Graphs, and Photographs

A.

B.

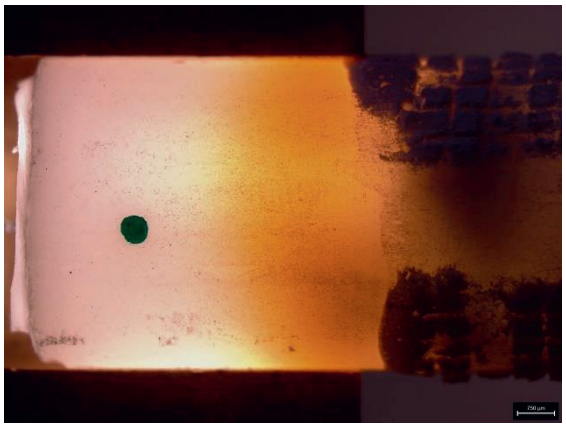

Fig. 3. **A.** Overview of the sawn YSZ tube with electrodes. **B.** Part of the ceramic tube with inside illumination at the electrode position. Blackening inside the tube is visible.

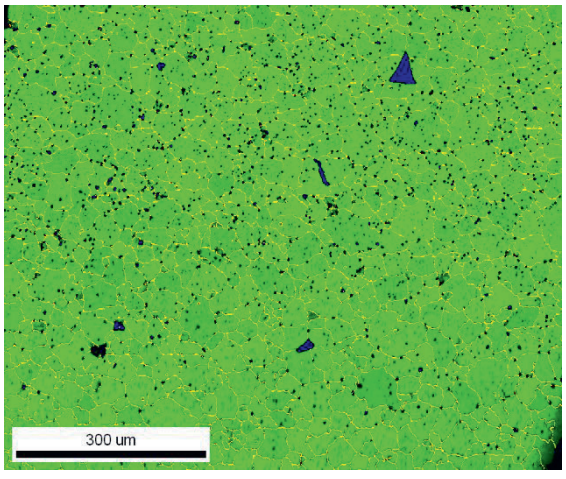

Fig. 4 EBSD phase and quality image of the cross section with grain structure and Al_2O_3 (blue) inclusions as well as YSZ (green).

DOI 10.5162/SMSI2020/B1.3

Long-Term Monitoring of Gaseous Ammonia with a Semi-automatic Measuring Device

Kornelia Gawlitza[1], Sergej Johann[2], Maria Mansurova[1], Harald Kohlhoff[2], Carlo Tiebe[2], Jérémy Bell[1], Matthias Bartholmai[2], Knut Rurack[1]
[1] Div. 1.9 Chemical and Optical Sensing, Federal Institute for Materials Research and Testing (BAM), Richard-Willstätter-Str. 11, 12489 Berlin, Germany,
[2] Div. 8.1 Sensors, Measurement and Testing Methods, Federal Institute for Materials Research and Testing (BAM), Unter den Eichen 87, 12205 Berlin
kornelia.gawlitza@bam.de

Summary (max. 6 lines):

In the present paper the development of a semi-automated device for long-term monitoring of gaseous ammonia is described. A sensor material was produced that changes its optical properties in the presence of low concentrations of ammonia in air. The implementation into an electronic device enables precise, simple, economic and fast monitoring of low concentrations of harmful gases, like ammonia, and hence can help to improve the climate monitoring in livestock housing, barns or stables.

Keywords (max. 5): spectroscopy, embedded sensor, environment, air quality

Introduction

It is known since years that low concentrations of ammonia in the air not only smell intensively but also can cause considerable damage to human health and ecosystems. Because most of this gas is emitted in the agriculture sector (up to approx. 95 %), the EU regulation on national emission maxima (NEC-Directive 2016/2284) involves a reduction of ammonia emissions by 29 % in 2030 compared to 2005. In addition, the German Federal Ministry for the Environment, Nature Conservation and Nuclear Safety specifies a limit concentration value in an exhaust gas of 30 mg m^{-3} equal to 41 µmol mol^{-1} for ammonia [1]. Hence, reliable and cost-effective sensors for gaseous ammonia with sensitivities in the lower ppm range are required for continuous monitoring of air quality. Besides being miniaturizable, the developed sensors should be usable on-site for in-the-field measurements by untrained personnel over long periods.

The present work contributes to the development of a more precise, less expensive, simpler and faster sensor for ammonia in air, that can be used, for instance, to monitor the climate in barns. The implementation of a developed chemical sensor material, changing its optical properties in the presence of gaseous ammonia, into an in-house-build electronic device usable directly in the field is described.

Chemical Sensor Material

To be able to produce a chemical sensor material that can change its optical properties in the presence of gaseous ammonia, the fluorescent signaling unit, 1,3,5,7-tetramethyl-2,6-diethyl-boron-dipyrromethene (BODIPY) or dye **1**, was used as basic component in the presented study (Fig. 1). This dye has unique properties like high fluorescence quantum yields and excitation and emission maxima at reasonably long wavelengths in the visible spectral range (529 nm and 545 nm respectively) and was thus already described for the development of ammonia and pH sensors [2-4].

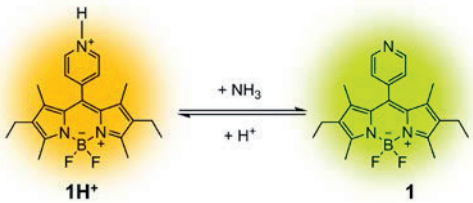

*Fig. 1. Scheme of sensor dye **1** and the fluorescence change (λ_{ex} 365 nm) in presence of ammonia.*

A detailed description of the preparation of the sensor material can be found elsewhere [2]. Briefly, 20 µL of a hydrogel-ethanol-water-mixture and 50 µL of **1H⁺** in ethanol (1 mM) were filled into the wells of a black 96-well microtiter plate with a transparent bottom and dried twice for 12 h. To avoid contamination

before the actual measurement, the plate was hermetically sealed with an aluminum foil.

Semi-automatic Measuring Device

A Fluorescence Spectrum Gas Injection Microtiter Plate Measuring Device (FS-GIMMD) being able to hold six 96-well microtiter plates has been developed (Fig. 2). Conclusively, one fully equipped device can be used to run up to 567 measurements. The easy replacement of the plates can be done by untrained personnel and allows the use of the setup for long term tracking of ammonia, for instance to monitor the air in barns. Each sensor material, being prepared in the wells as described before, can be illuminated by an excitation light (LED 500 nm) and the produced change in fluorescence signal in the presence of ammonia can be tracked by the optical head containing a C12666MA microspectrometer from Hamamatsu [2]. The validation was performed by generation of different concentrations of gaseous ammonia as well as varying relative humidity by an automated mechanical-electrical device. The gas mixing system is described in more detail elsewhere [2]. A typical measurement was performed by piercing the aluminum cover foil with two needles and passing a defined ammonia concentration over the sensor material for a defined time at a certain relative humidity. Afterwards, the identical procedure was carried out at the next position.

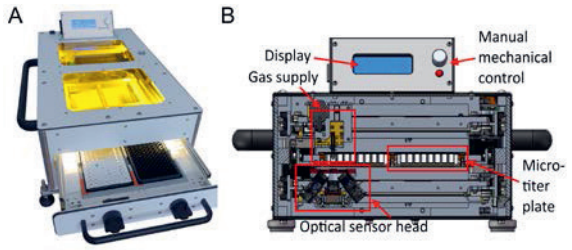

Fig. 2. Picture (A) and a scheme of the main mechanical parts (B) of the FS-GIMMD prototype.

Results and Discussion

As schematically shown in Fig. 1, dye **1** is highly fluorescent in the neutral state while protonation induces a change in emission [2]. A hydrogel matrix being polar and humid enough to accumulate gaseous ammonia was used to embed the protonated dye **1H$^+$**. Due to a pKa of 2.15 ammonia deprotonates **1H$^+$** leading to a fluorescence increase at 570 nm when excited at 500 nm. First tests with increasing concentrations of ammonia from 0 to 20 µmol mol^{-1} and at relative humidity of 0 %, 10 % and 25 % were performed with the developed FS-GIMMD. Measurements of the entire emission range (525 nm to 800 nm) over a time period of 60 minutes revealed that saturation is reached after 10 min. Fig. 3A exemplarily shows the emission spectra of one sensor material purged with 20 µmol mol^{-1} ammonia over 10 minutes and demonstrates the increase in fluorescence at 570 nm. Identical experiments were performed with increasing concentrations of ammonia (0, 1, 5, 10, 20 µmol mol^{-1}). The corresponding change in fluorescence at 570 nm plotted as a function of the concentration shows a linear increase (Fig. 3B). It was also observed that the calibration curve depends on the relative humidity and thus parallel tracking of the humidity is essential to determine real ammonia concentrations. In addition, the long-term stability of the sensor material in the microtiter plates has been validated over 1 year.

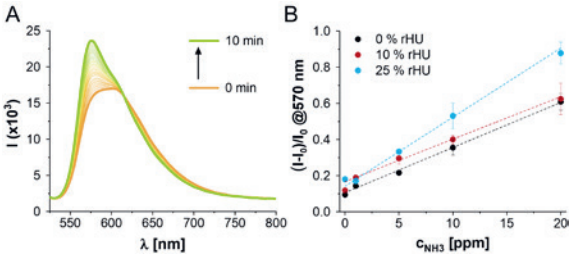

Fig. 3. Time dependent response in presence of 20 µmol mol^{-1} ammonia (A) and fluorescence change at 570 nm at different ammonia concentrations and relative humidity after 10 min (B) measured with the developed FS-GIMMD (λ_{ex} = 500 nm).

Conclusion

In conclusion, a semi-automated approach to long-term monitor low concentrations of gaseous ammonia in livestock housing, barns or stables, in a simple, precise, economic and fast manner has been developed. After implementation of the humidity dependent calibration curves, the sensor device could be easily adapted to other harmful gases which enables the use in a broad range of applications.

References

[1] https://www.umweltbundesamt.de/sites/default/files/medien/1/dokumente/taluft_stand_200207241.pdf, 23.01.2020

[2] S. Johann, H. Kohlhoff, K. Gawlitza, J. Bell, M. Mansurova, C. Tiebe, M. Bartholmai, Semi-automatic Gas Measurement Device based on Fluorescent Multi-gas Sensors, *IEEE Sensors*, 1-4, (2019); doi: 10.1109/SENSORS43011.2019.8956664

[3] K. Gawlitza, C. Tiebe, U. Banach, R. Noske, M. Bartholmai, K. Rurack, Novel sensor for long-term monitoring of ammonia in gas phase, *13. Dresdner Sensor-Symposium Proceedings*, 272–276 (2017); doi: 10.5162/13dss2017/P4.02

[4] R. Gotor, P. Ashokkumar, M. Hecht, K. Keil, K. Rurack, Optical pH Sensor Covering the Range from pH 0–14 Compatible with Mobile-Device Readout and Based on a Set of Rationally Designed Indicator Dyes, *Analytical Chemistry* 89, 8437-8444(2017); doi: 10.1021/acs.analchem.7b01903

DOI 10.5162/SMSI2020/B1.4

A humidity-independent photoacoustic sensor

Emilio Ambra[1], Genny A. Pang[1], Christoph Haish[1]
[1] Institute of Hydrochemistry Technical University of Munich, Germany,
emilio.ambra@tum.de, genny.pang@tum.de, haisch@tum.de.

Summary:
Photoacoustic spectroscopy is routinely used to characterize absorption of gas and aerosols in various environments. To obtain accurate absorption measurements in atmospheric science, where variations in humidity exist, the photoacoustic signal's dependence from relative humidity must be investigated in-depth. For this purpose, we used a resonant photoacoustic cell embedded with a piezoMEMS microphone, which is insensitive to humidity. We scanned the light modulation frequency around the theoretical resonance value and acquired the microphone signal through a lock-in amplifier. From the results, we can affirm that the overall photoacoustic sensor response is independent of the humidity parameter only if we consider the photoacoustic signal amplitude at the exact resonance frequency, which shifts with humidity.

Keywords: photoacoustic effect, piezo MEMS, QCL laser, relative humidity, post-processing signal.

Introduction

Photoacoustic spectroscopy (PAS) is a technique based on the optical absorption of modulated light by solids, liquids or gases. The absorption leads to thermal expansion of the absorber at the modulation frequency of the light ("photo"), causing a pressure wave to be formed and detected by an acoustic transducer ("acoustic") (Fig.1) [1]. Gases or aerosols samples are commonly confined inside an acoustically resonant photoacoustic cell for measurement, and the resulting sound wave intensity is directly proportional to the amount of those absorbers. Therefore, PAS is routinely applied for absorption measurements in atmospheric science.

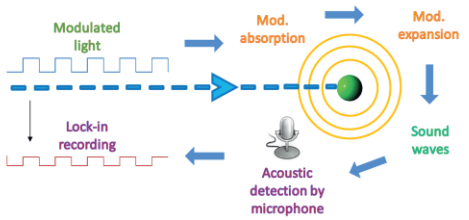

Fig. 1. Representation of the photoacoustic principle

The goal of our research is to improve the fundamental understanding of the PAS signal generation process and its dependence on atmospheric parameters. In this paper, we investigate whether a humidity-insensitive photoacoustic sensor can be developed with a piezoMEMS microphone. We tested the efficiency of the PAS sensor to measure ethanol absorption at varying humidity levels.

Methods and Materials

The experimental setup consists of a PAS cell with a piezo MEMS PMM-3738-CM1000-R microphone positioned in the center of the 4 cm long resonator (Fig 2). While electret microphones are commonly used in PAS cells, these are sensitive to humidity [2]. Therefore, we chose a microphone with a humidity-insensitive piezoelectric crystal in the piezo MEMS.

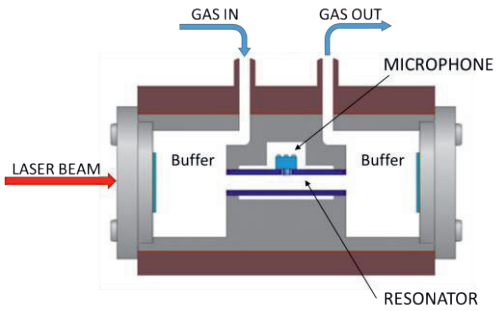

Fig. 2. Resonant photoacoustic cell with resonator and buffer volumes used in this study.

The sample is excited by an intensity-modulated QCL at 9.47 µm. Ethanol vapor was used as the absorbing sample due to its strong absorption in the infrared range. We used nitrogen as carrier gas, and the gas mixture was humidified by flowing through the headspace of a flask filled with distilled water. Different relative humidity (RH) levels were reached by dilution with dry nitrogen. RH was measured with a sensor (HYTE-ANA10V) at the inlet of the PAS cell. The ethanol concentration of was measured with a FTIR spectrometer (Fig.3).

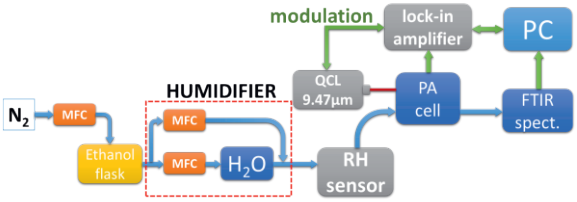

Fig. 3. Scheme of the experimental setup. MFC – mass flow controller.

The presence of water in the sample leads to a change of speed of sound of the gas sample and, consequently, to a shift of the resonance frequency. To identify the exact resonance peak at different RH values, the laser modulation frequency was swept from 3.9 to 4.2 kHz. Photoacoustic (PA) signals were measured for RH levels from 1% up to 50%.

Results

In Fig. 4, curves with red shades depict PA signals detected at low RH (1-22%), while blue curves represent higher RH (30-50%). The signals at the exact resonance peak are marked with red diamonds, and are shifted to higher frequency with increasing RH. This is in agreement with the change of the speed of sound in gas mixtures in the presence of humidity [3]. Moreover, a variation of the signals amplitudes is observed, because of variations in ethanol concentration at different RH levels.

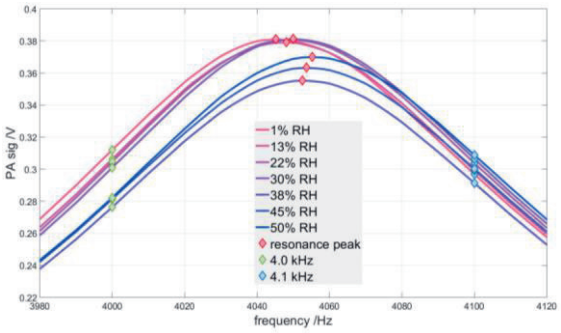

Fig. 4. Photoacoustic signal acquired sweeping the frequency at different relative humidity.

We analyzed the PA signal measured at three different modulation frequencies (marked in Fig. 4): the shifting peak resonance frequency (red diamonds), a fixed f = 4.0 kHz (green diamonds), and a fixed f = 4.1 kHz (blue diamonds). A plot of the PA signal as a function of ethanol concentration at each of these frequencies is shown in Fig. 5 (data points). For comparison, we also show the PA signal vs. ethanol concentration, measured under dry conditions at the three specified frequencies (solid lines).
The PA signal measured at the exact resonance frequency peak at different level of humidity (red points) are consistent with the calibration curve at dry conditions for all concentrations of ethanol.

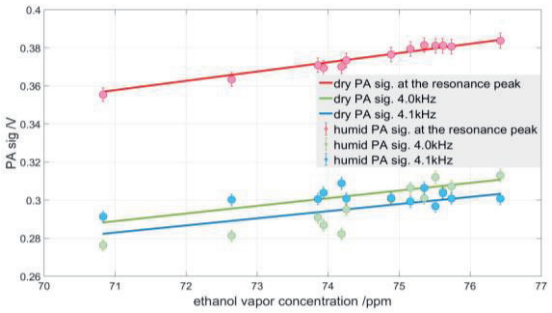

Fig. 5. Amplitude of the photoacoustic signal in humid conditions compared to the calibration curves obtained in dry conditions.

The results indicate that at the condition of ideal resonance, the signals measured from our PAS sensor are insensitive to changes in RH, and all variations in amplitude are attributed to changes in absorber concentration. On the other hand, data acquired at a fixed frequency, which is typically done in PAS measurements, show a deviation between the dry calibration line and the humid sample measurements, as shown by our data at f = 4.0 kHz (green) and f = 4.1 kHz (blue). Measuring the PA signal at a fixed modulation frequency, therefore, could create an apparent dependence of the signal on humidity.

Conclusion

We investigated PA signals generated at different humidity conditions. PA signals were shown to be completely independent from humidity in exact resonant conditions. Future applications of this work include studying the humidity dependence of the PA signal generation from aerosols. In particular, in the case of hygroscopic particles, light absorption leads to not only the formation of pressure waves but also a partial evaporation of volatile compounds and water, and a humidity-insensitive PAS sensor is needed to quantitatively study this behavior.

References

[1] A. Miklós, P. Hess, and Z. Bozóki, Application of acoustic resonators in photoacoustic trace gas analysis and metrology, *Review of Scientific Instruments* **72**, 1937 (2001), doi: 10.1063/1.1353198.

[2] J.M. Langridge, M.S. Richardson, D.A. Lack, C.A. Brock, D.M. Murphy, Limitations of the photoacoustic technique for aerosol absorption measurement at high relative humidity. *Aerosol Science and Technology*, 47:11, 1163-1173, (2013) doi: 10.1080/02786826.2013.827324

[3] Owen Cramer, The variation of the specific heat ratio and the speed of sound in air with temperature, pressure, humidity, and CO2 concentration, *Journal of the Acoustical Society of America*, 93, 2510, (1993), doi: 10.1121/1.405827

DOI 10.5162/SMSI2021/B2.1

Multiple gas detection by dynamic electrochemical methods

A. Ruchets[1], N. Donker[2], D. Schönauer-Kamin[2], R. Moos[2], J. Zosel[1], U. Guth[3], M. Mertig[1,3]
[1]Kurt-Schwabe-Institut für Mess- und Sensortechnik Meinsberg e.V., Kurt-Schwabe-Straße 4, 04736 Waldheim, Germany
[2]Department of Functional Materials, University of Bayreuth, Universitätsstraße 30, 95440 Bayreuth, Germany
[3]Institute of Physical Chemistry, Technische Universität Dresden, 01062 Dresden, Germany
anastasiya.ruchets@ksi-meinsberg.de

Summary:
Multiple redox gas detection such as carbon monoxide, nitrogen monoxide and oxygen by solid electrolyte gas sensors (SESs), operated in a dynamic detection regime, is reported. To this aim, an oxygen-pumping SES was used in cyclic voltammetry mode at different operational conditions and gas concentrations. The obtained results demonstrate the possibility of selective detection of CO and NO in nitrogen gas flow with one device.

Keywords: Yttria-stabilized zirconia (YSZ), carbon monoxide, nitrogen oxide, cyclic voltammetry, solid electrolyte sensor (SES)

Motivation

One common source of toxic gas exposure is the incomplete combustion of fuels in combustion engines. Exhaust gases usually contain mixtures of redox-active gases, for example CO and NO. In order to detect such redox active gases selectively and simultaneously, electrochemical sensors operated in dynamic mode can be applied. The advantage of dynamic measurements is the utilization of different electrode reaction kinetics, which are not visible in static mode of operation with signals corresponding to the total equilibrium between the gases [1, 2].

In the presented work, a Pt/YSZ/Pt-based solid electrolyte gas sensor is used for multiple redox-active gas detection by means of dynamic electrochemical measurements for the example of cyclic voltammetry in combination with static open circuit potential measurements in the gas outflow.

Experimental setup

The set-up described in [3] was modified to establish and detect NO, CO, and O_2 concentrations in nitrogen gas flow (see Figure 1). The total flow rate and the analyte concentrations were regulated by mass flow controllers. In contrast to this control, the O_2 concentrations were established by means of constant polarization of SES 1. All dynamic electrochemical measurements were carried out in SES 2 at different experimental settings. SES 3 was used to measure open circuit potentials in the outlet gas.

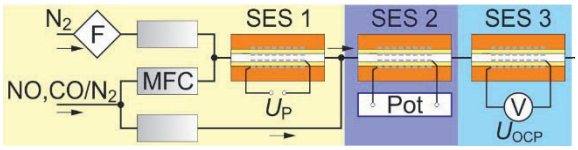

Fig. 1. Experimental setup. MFC – mass flow controller, SES – solid electrolyte sensor, Pot – electrochemical measuring system, F – triple filter.

Results

The curves given in Figure 2 show cyclic voltammograms (CVs) recorded at SES 2 at 700 °C in dry gas flow with a mixture of different concentrations of CO and NO and at $c(O_2)$ = 65 ppmv in N_2. The gas concentrations have been changed from 150 to 0 ppmv of each gas in the mixture. For each concentration, CVs with three cycles were recorded. For NO detection every second cycle was taken, while the CO peak of the first cycle was taken for peak quantification.

Curves in Figure 2A were measured at a scan rate 1000 mV/s, while this parameter was optimized for NO gas detection in previous work [4]. As the NO gas concentration increases, the NO-related peak also increases (see inset in Fig. 2A), showing cross-selectivity to CO gas in the concentration range between 0 and 150 ppmv.

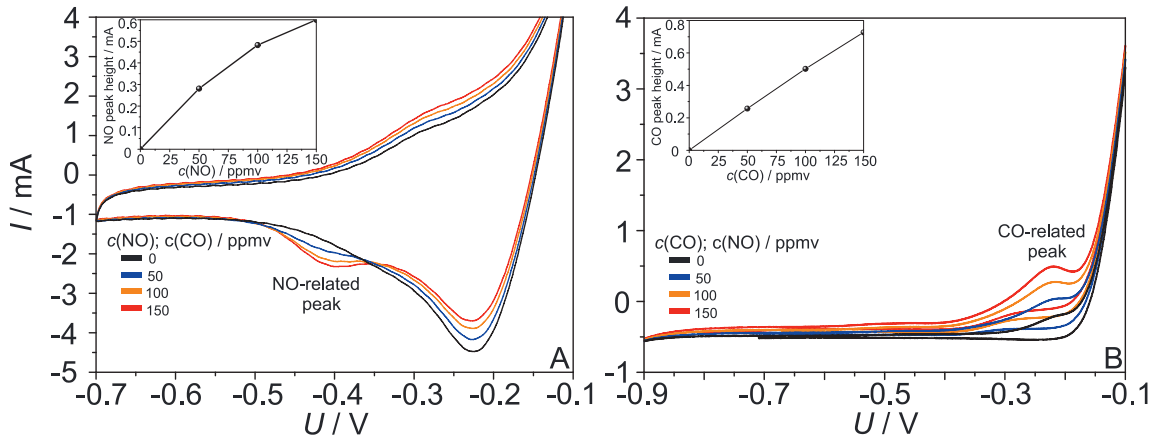

Fig. 2. Cyclic voltammograms in the gas mixture of NO and CO gases diluted in nitrogen at (A) 1000 mV/s scan rate and (B) at 20 mV/s scan rate. Sensor temperature T = 700 °C; flow rate = 20 sccm; c(O_2) =65 ppmv.

Curves in Figure 2B have been recorded at 20 mV/s scan rate, in order to detect carbon monoxide in presence of oxygen and nitrogen monoxide. Linear concentration dependency was observed for the detected CO-related peak in the concentration range between 0 and 150 ppmv.

Monitoring of the open circuit potential U_{OCP} in the outlet gas during measurements and pauses between experiments is plotted in Figure 3 as a temporal course. The baseline shift due to gas concentration changes can be clearly seen on the curves as well as the changes of U_{OCP} during each cycle of cyclic voltammograms. During taking the voltammograms at 1000 mV/s scan rate, the potential was changed to more positive values, illustrating an increase of oxygen concentration during NO detection. In contrast to that, very negative potentials, e.g. reducing conditions have been reached for CO detection at cyclic voltammograms at 20 mV/s.

References

[1] X. Zhang, H. Kohler, M. Schwotzer, Y. Wu, U. Guth, Mixed-potential gas sensor with layered Au,Pt-YSZ electrode: Investigating the sensing mechanism with steady state and dynamic electrochemical methods, *Sensors and Actuators B: Chemical* 252, 554-560 (2017); doi: 10.1016/j.snb.2017.05.168

[2] T. Ritter, J. Lattus, G. Hagen, and R. Moos, Effect of the Heterogeneous Catalytic Activity of Electrodes for Mixed Potential Sensors, *Journal of The Electrochemical Society* 165, B795-B803 (2018); doi: 10.1149/2.0181816jes

[3] A. Ruchets, N. Donker, D. Schönauer-Kamin, R. Moos, J. Zosel, U. Guth, M. Mertig, Selectivity improvement towards hydrogen and oxygen of solid electrolyte sensors by dynamic electrochemical methods, *Sensors and Actuators B: Chemical* 290, 53-58 (2019); doi: 10.1016/j.snb.2019.03.063

[4] A. Ruchets, N. Donker, D. Schönauer-Kamin, R. Moos, J. Zosel, U. Guth, M. Mertig, Cyclic and square-wave voltammetry for selective simultaneous NO and O_2 gas detection by means of solid electrolyte sensors, *Journal of Sensors and Sensor Systems* 9, 355-362 (2020); doi: 10.5194/jsss-9-355-2020

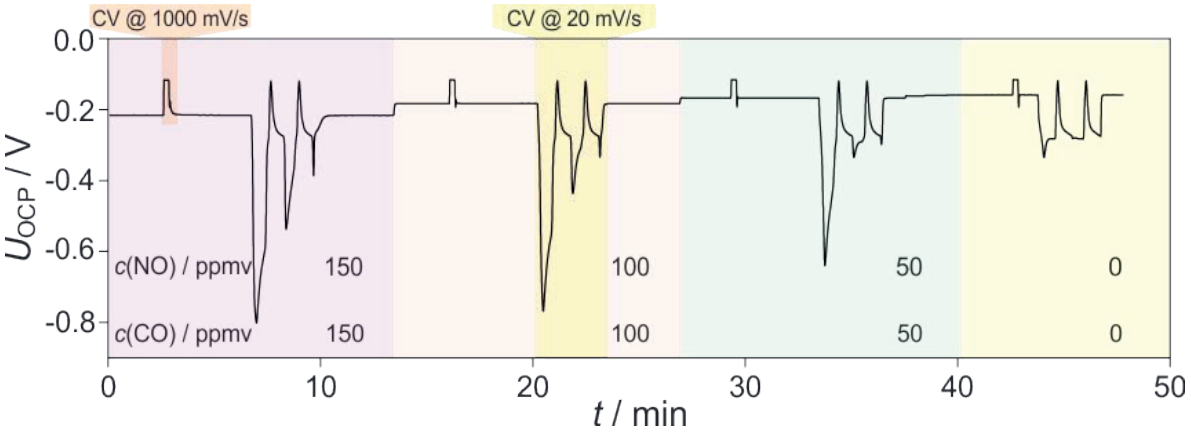

Fig. 3. OCP measurement in the outlet gas flow with SES 3.

DOI 10.5162/SMSI2021/B2.2

Pulsed polarization on Au|YSZ NO_x-sensors with and without catalytic layer

Nils Donker[1], Anastasiya Ruchets[2], Daniela Schönauer-Kamin[1],
Jens Zosel[2], Ulrich Guth[3], Ralf Moos[1]
[1] Department of Functional Materials, University of Bayreuth, 95440 Bayreuth, Germany
[2] Kurt-Schwabe-Institut für Mess- und Sensortechnik Meinsberg e.V., 04736 Waldheim, Germany
[3]Dresden University of Technology, Department of Chemistry and Food Chemistry, Dresden, Germany
funktionsmaterialien@uni-bayreuth.de

Summary:
Sensors of the type Au|YSZ|Au were produced, and some of them were covered with an additional Pt containing catalyst layer. These sensors were operated in the pulsed polarization mode. Their sensitivity to NO_x was investigated. The pure gold sensor showed almost no NO signal, but a clear signal towards NO_2. The catalyst-coated sensor responded to both gases, NO and NO_2. Therefore, we assume that NO_2 is essential for the sensor effect, which could not have been explicitly shown in previous studies.

Keywords: pulsed polarization, Au | YSZ, NO_x detection, exhaust gas sensor, dynamic method

Motivation

Gaseous components from combustion processes are among the main pollutants in our environment. Therefore, it is important to measure them for continuous optimization of the combustion process. Newer approaches for the detection of such gases are directed towards dynamic instead of static methods. This is expected to lead to further improvements in selectivity. Examples for such methods are cyclovoltammetry [1], thermocyclic operation [2] or pulsed polarization [3]. In the latter case, nitrogen oxides could be detected selectively, but the exact mechanism is still unclear. In this method, catalytically active Pt-electrodes are polarized at 400 °C and the subsequent self-discharge behavior is evaluated. It is expected that NO and NO_2 are present in thermodynamic equilibrium at the electrode, independent of the actual concentrations [4]. In this work, the influences of the NO/NO_2-equilibrium on the sensor signal will be investigated in more detail.

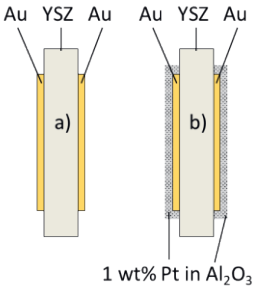

Fig.1. Schematic view of the sensors a) without and b) with catalytic layer

Experimental

The here-used sensors consist of screen-printed Au-electrodes (area = 5 x 5 mm²) that are applied to both sides of an 8YSZ substrate and fired at 850 °C (see Fig. 1). A catalytic layer was then added to some of the electrodes. It consists of 1 wt% Pt added to porous Al_2O_3. These catalytic layers were fired at 700 °C, whereby the sensors without catalytic layer were also fired in order to avoid influences by the firing process.

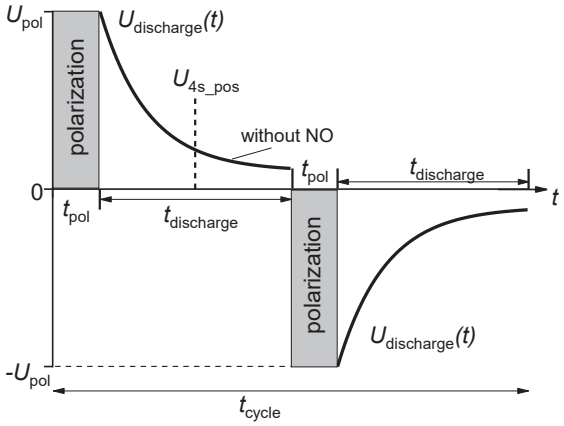

Fig. 2. Overview of a pulsed polarization cycle

Then, the sensors were operated by pulsed polarization. For this purpose, the sensor was polarized for a polarization duration t_{pol} = 1 s with a polarization voltage U_{pol} = 1 V. Afterwards the self-discharge was measured as an open circuit potential, OCP, for $t_{discharge}$ = 10 s. These polarization and self-discharge phases were repeated continuously, always polarizing with alternating

polarity. To generate a sensor signal from these cycles, the discharge voltage is evaluated at a fixed point in time in the cycle, for example 4 s after positive polarization U_{4s_pos} (Fig. 2).

A mixture containing 10% O_2 and 2% H_2O in N_2 was used as base gas. Additionally, 50-400 ppm NO and NO_2 were added stepwise. All measurements were performed at 400 °C in a tube furnace.

Results

The results of two measurements of Au|YSZ|Au are shown in Fig. 3. Fig 3a shows the discharge voltages of an Au-sensor without catalyst layer 1 s and 9 s after positive polarization. It can be seen that this sensor almost does not respond to NO. Thus, on the 1 s curve almost no NO influence is visible. After 9 s a slight change to more positive voltages can be seen, which means a slowing down of the self-discharge. With added NO_2, however, clear change to more negative voltages can be seen. This indicates an accelerated self-discharge. These NO_2 signals are visible after 1 s as well as after 9 s and show a similar effect as observed for sensors with Pt-electrodes [3].

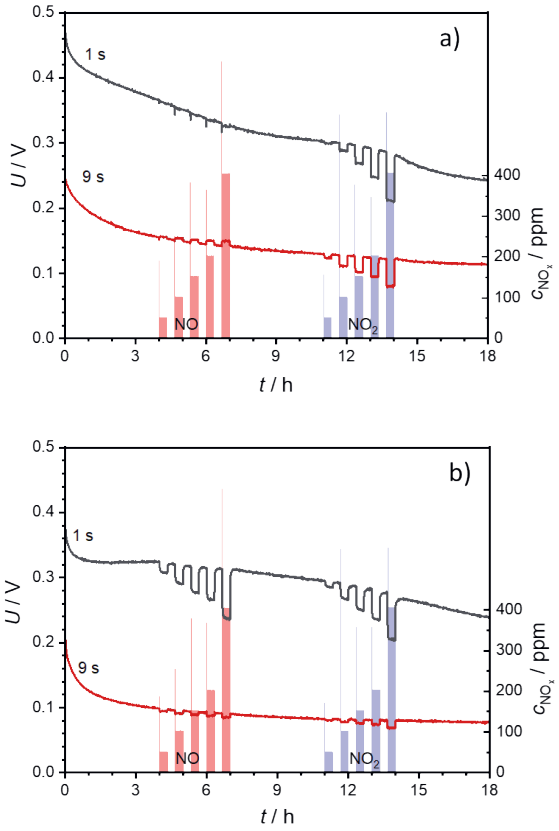

Fig. 3. Depolarization voltages after 1 and 9 s after positive polarization at Au|YSZ|Au sensors a) without and b) with additional catalytic layer on both electrodes.

Fig. 3b shows the discharge curves of a sensor with a catalytic layer on top of both gold electrodes. Here, a clear signal for NO as well as for NO_2 can be seen. This is particularly pronounced 1 s after polarization. Here, the effects of NO and NO_2 hardly differ.

Discussion

These results show that an Au sensor without catalyst hardly responds to NO but clearly responds to NO_2. Only with a catalytic layer, which oxidizes a part of the NO to NO_2 due to the thermodynamic equilibrium, NO becomes measurable. Since the electrodes of Pt sensors are catalytically active themselves, they may also react primarily to NO_2, which is formed by oxidation of NO directly at the electrode.

Conclusion

It could be shown that NO_2 in contrast to NO at 400 °C has a direct influence on the self-discharge of the sensor. In order to further investigate this effect, measurements with single-sided catalytic coated electrodes as well as measurements at other temperatures will be performed.

References

[1] A. Ruchets, N. Donker, D. Schönauer-Kamin, R. Moos, J. Zosel, U. Guth, M. Mertig, Selectivity improvement towards hydrogen and oxygen of solid electrolyte sensors by dynamic electrochemical methods, Sens. Actuators B 290 (2019) 53–58.

[2] X. Zhang, H. Kohler, M. Schwotzer, U. Guth, Mixed-potential gas sensor with PtAu-8YSZ sensing electrode: Electric potential difference measurements at isothermal and thermo-cyclic operation, Sens. Actuators B 217 (2015) 107–112.

[3] N. Donker, A. Ruchets, D. Schönauer-Kamin, J. Zosel, U. Guth, R. Moos, Influence of Pt paste and the firing temperature of screen-printed electrodes on the NO detection by pulsed polarization, J. Sens. Sens. Syst. 9 (2020) 293–300.

[4] T. Ritter, J. Lattus, G. Hagen, R. Moos, On the influence of the NO_x equilibrium reaction on mixed potential sensor signals: A comparison between FE modelling and experimental data, Sens. Actuators B 296 (2019) 126627.

Acknowledgement

We thank the German Research Foundation (DFG) for financial support under grants MO 1060/30-1 and ZO 139/3-1

DOI 10.5162/SMSI2021/B2.3

Impedimetric NO_x sensor for exhaust applications with internal lambda correction

Julia Herrmann[1], Gunter Hagen[1], Jaroslaw Kita[1], Frank Noack[2], Dirk Bleicker[2], Ralf Moos[1]
[1] Department of Functional Materials, University of Bayreuth, D-95440 Bayreuth, Germany
[2] CPK Automotive GmbH&Co. KG, D-48157 Münster, Germany

Abstract

Due to current developments in the automotive industry, more attention has to be paid to exhaust aftertreatment. Robust and cost-effective sensors for monitoring and controlling the exhaust aftertreatment systems are required, especially for NO_x detection. We suggest an impedimetric NO_x sensor which is fully manufactured in planar thick film technology. The impedance of a functional layer ($KMnO_4$ supported on Al_2O_3) reacts selectively to the NO_x concentration in the exhaust. However, this mechanism depends on the air-fuel-ratio (Lambda). For this reason, a resistive O_2-sensitive functional layer (BFT) is additionally applied to the sensor element. Using this signal of the O_2-sensitive functional layer, the existing lambda can be determined and thus the lambda dependency of the NO_x-sensitive functional layer can be corrected.

Keywords: impedimetric gas sensor, oxygen sensor, exhaust gas sensor, NO_x sensor, O_2 sensor

Introduction

In the course of the current developments in the automotive industry, it is necessary to pay special attention to efficient exhaust aftertreatment. For NO_x abatement of the exhaust gases, there are different possibilities (storage catalytic converters or SCR-concepts). All of these aftertreatment systems need to measure the NO_x concentration in the exhaust gas as a variable. Available NO_x sensors are based on electrochemical ZrO_2 cells. Design and production of such sensors are complex and cost-intensive. In this study, an impedimetric sensor concept is proposed. It can be fully realized in planar thick film technology. [1-2]. The sensitivity of the measured signal depends not only on the nitrogen oxide concentration but also on the lambda value of the exhaust gas. For this reason, the sensor element is extended by an additional O_2 sensor layer. Thus, in addition to the NO_x signal, information about the oxygen content of the exhaust gas can be determined. Now, a correction of the impedimetric signal of the NO_x measurement is possible [3].

Description of the sensor setup

Sensor elements are completely built in planar thick film technology on Al_2O_3 substrates. On the front side there is a NO_x-sensitive functional layer of potassium permanganate ($KMnO_4$) supported on Al_2O_3 (Figure 1, brown).

The contacting of the functional layer is realized by planar interdigital electrodes, which allows an impedance-based measurement. In addition to the NO_x-sensitive functional layer, an O_2-sensitive functional layer of barium iron tantalate (BFT) is screen-printed on the front side of the sensor (Figure 1, black). This functional layer is contacted by two electrodes and can be measured resistively. A meander-shaped heater structure is applied on the reverse side. It heats up the sensor to the required operating temperature. For more details on the sensor design see Ref. [3].

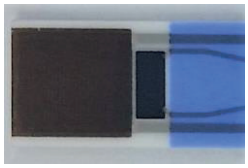

Figure. 1: Top view of the functional part of the sensing element (brown: NO_x-sensitive functional layer, black: O_2-sensitive functional layer).

Experimental

The sensor is installed in a lab test bench (atmospheres by gas dosing from cylinders) and heated to an operating temperature of 650 °C via the heater structure on the reverse side. The base gas (total flow 6000 ml/min) contains 10 % O_2, 3 % CO_2 and 2 % H_2O with N_2 as carrier gas (yellow background in Figure 2). By mass-flow-controllers (MFCs), first NO

(100 ppm, 300 ppm, 600 ppm) and then NO_2 (100 ppm, 300 ppm) is added to the base gas. After that, the base gas is changed to N_2 with 2 % O_2, 7 % CO_2 and 2 % H_2O (blue background in Figure 2). The stepwise dosing of NO and NO_2 is repeated here.
For the NO_x-sensitive functional layer, the bulk resistance of the functional layer acts as the sensor signal. It is calculated from the impedimetric signal as follows, assuming a semi-circle behaviour in the complex plane (Equation 1):

$$R = |\underline{Z}| / \cos(\varphi) \quad (1)$$

Both sensor signals (NO_x and O_2) were evaluated as relative change based on the resistance R_0 before test gas dosing to compare the results.

Results and Discussion

Figure 2 shows the sensor signals of both functional layers for NO_x variation in two gas atmospheres. The black curve (Figure 2) shows the signal of the NO_x-sensitive functional layer. The signal reacts clearly to the addition of NO and NO_2 in both gas atmospheres. However, the sensitivity of the NO_x-sensitive functional layer decreases with an decreased lambda value. The O_2-sensitive functional layer shows a dependency on lambda and thus on the present O_2 content. Additionally, a slight cross-sensitivity to NO_2 can be recognized. This could be caused by a too low temperature at the functional layer [4]. However, the signal of the O_2-sensitive functional layer can now be used to correct the lambda dependency of the NO_x-sensitive functional layer.

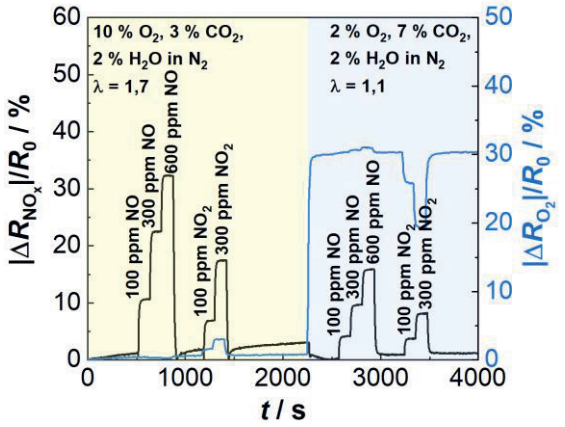

Figure 2: Sensor signal of both functional layers at two different gas atmospheres (base gas: 10 % O_2, 3 % CO_2, 2 % H_2O in N_2; atmosphere 2: 2 % O_2, 7 % CO_2, 2 % H_2O in N_2) with a variation of NO (100 ppm, 300 ppm, 600 ppm) and NO_2 (100 ppm, 300 ppm).

For this purpose, NO_x-dependent characteristic curves at different lambda atmospheres were measured and a lambda-dependent characteristic curve of the O_2-sensitive functional layer was recorded in further experiments. By using these characteristic curves, the signal of the NO_x-sensitive functional layer can be corrected and converted into a NO_x-concentration. The result of this correction is shown in figure 3.

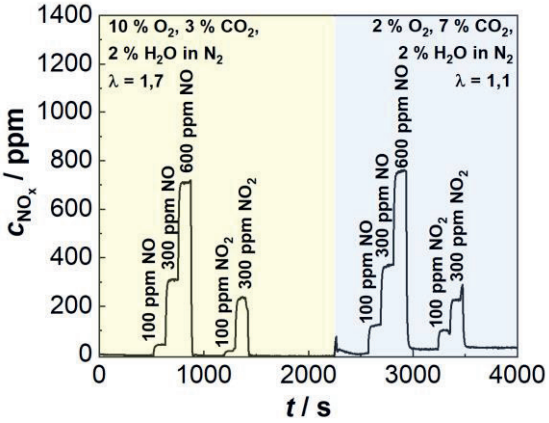

Figure 3: Result of the corrected sensor signal of the NO_x-sensitive functional layer.

Conclusion

The described sensor element can be used as an alternative NO_x sensor in exhaust applications. However, since the NO_x-sensitive signal depends on the predominant lambda, an additional O_2-sensitive functional layer is integrated. With this setup, it is possible to correct the lambda dependence of the NO_x-sensitive sensor signal and to convert the signal into a NO_x concentration.

References

[1] Hagen, G., Müller, A., Lattus, J., Kita, J., Moos, R., Noack, F., Bleicker, D.: Impedanz-basierter NO_x-Sensor für Abgasanwendungen, in: Proceedings of Sensoren und Messsysteme 2019, 2.4.4, 25.–26. Juni 2019, Nürnberg, 197–200, doi: 10.5162/sensoren2019/2.4.4, 2019

[2] Bleicker, D., Noack, F., Costa, L., Rühl, S.: NO_x-Sensor für Nfz und mobile Maschinen, ATZ, 01/2020, 38–41, 2020

[3] Herrmann, J., Hagen, G., Kita, J., Noack, F., Bleicker, D., and Moos, R.: Multi-gas sensor to detect simultaneously nitrogen oxides and oxygen, J. Sens. Sens. Syst., 9, 327–335, https://doi.org/10.5194/jsss-9-327-2020, 2020

[4] Bektas, M.; Hanft, D.; Schönauer-Kamin, D.; Stöcker, T.; Hagen, G.; Moos, R. (2014): Aerosol-deposited $BaFe_{0.7}Ta_{0.3}O_{3-\delta}$ for nitrogen monoxide and temperature-independent oxygen sensing. J. Sens. Sens. Syst. 3 (2), pp. 223–229, DOI: 10.5194/jsss-3-223-2014

DOI 10.5162/SMSI2021/B3.1

Planar Bragg Grating Sensors Functionalized with Cyclodextrins for Trichlorofluoromethane Sensing

Stefan Belle[1], Stefan Kefer[1], Siegfried R. Waldvogel[2] and Ralf Hellmann[1]
[1]Applied Laser and Photonics Group, Aschaffenburg University of Applied Sciences, Wuerzburger Strasse 45, 63743 Aschaffenburg, Germany
[2]Instituite of Organic Chemistry, Johannes Gutenberg University Mainz, Duesbergweg 10-14, 55125 Mainz, Germany
Corresponding author's e-mail address: ralf.hellmann@th-ab.de

Summary:
This contribution summarizes on recent findings of planar Bragg grating sensors, functionalized with cyclodextrins, for the detection of ozone depleting trichlorofluoromethane. Detection limits as low as 5 ppm are feasible whereas sensitivity and dynamic depend on the employed cyclodextrin class. The prospect of transferring the technology from silicas to polymer-based devices is also presented.

Keywords: Optical Sensor, Bragg Grating, Evanescent Field, Cyclodextrin, Trichlorofluoromethane

Introduction

Once an auspicious chlorofluorocarbon, widely employed as propellant and refrigerant, the usage and fabrication of trichlorofluoromethane, also referred to as CFC-11 or R-11, is now strictly prohibited due to its vast ozone depletion potential [1]. Nevertheless, the substance is still released nowadays, for example during the recycling of obsolete cooling devices or even in illegal production plants [2].

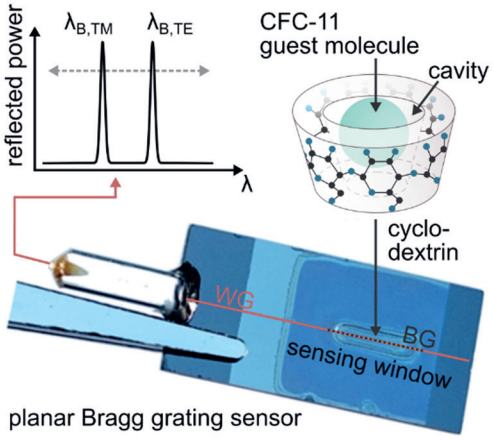

Fig. 1. Working principle of a planar Bragg grating sensor functionalized for CFC-11 sensing via cyclodextrin coatings.

Thus, reliable and sensitive detection of CFC-11 is still of vital importance for the society and yet continuously a technological challenge for modern sensors. Optical Bragg gratings constitute a promising technology for this task, since, besides low weight, they offer outstanding electromagnetic, chemical and thermal resistance. However, they necessitate functionalization for the detection of CFC-11, which can be achieved by coating the sensitive Bragg grating region with cyclodextrins (CDs). Due to their molecular structure and composition, CDs are able to form a non-covalent host-guest complex with CFC-11, as illustrated in Fig. 1. Coating a planar Bragg grating (PBG) device with CDs enables quantification of the CFC-11 molecule abundance via the evanescent field interaction of guided mode and functional coating, which leads to a shift of the PBG's modal Bragg reflection peaks $\lambda_{B,TE}$ and $\lambda_{B,TM}$. Based on their composition, CDs are classified as α-, β- or γ-cyclodextrin. Further modification of its solubility, viscosity and selectivity, is adapted by substitution of the CD's hydroxyl groups.

Sensor Response

An overview of the employed CD derivatives is given in Tab. 1 , while Fig. 2 depicts the respective Bragg wavelength shift $\Delta\lambda_B$ of both modal reflection peaks as a function of the CFC-11 content, diluted in nitrogen. It is found that, in all cases, the maximum response of the TE reflection peak is about ten times larger than that of the TM signal. *Per*-methyl substituted derivatives exhibit maximum wavelength shifts up to

Tab. 1: Per-substituted cyclodextrin derivatives.

Substitute	α-CD	β-CD	γ-CD
Methyl	CD1	CD2	CD3
Ethyl	CD4	CD5	CD6
Allyl	CD7	CD8	CD9

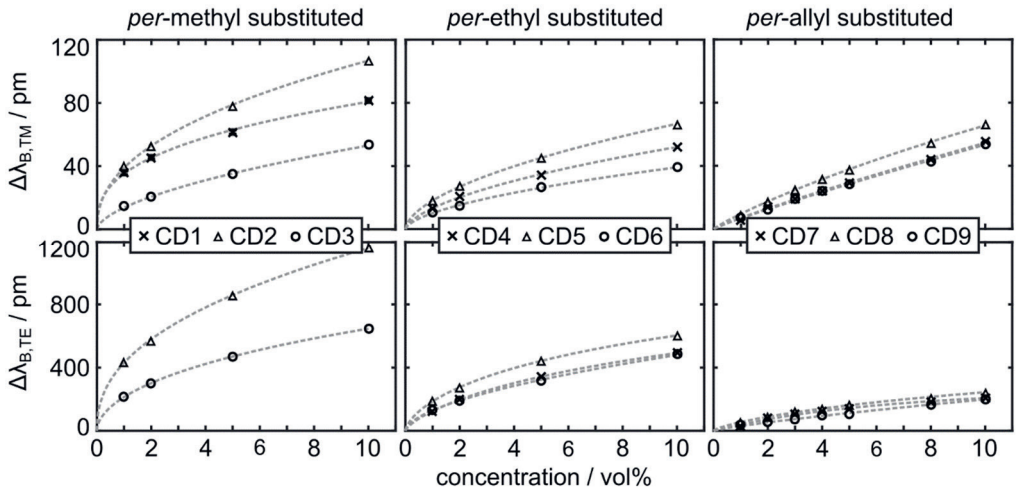

Fig. 2. Bragg wavelength shift of both modal (TE & TM) reflection peaks as a function of CFC-11 concentration in nitrogen, for α-, β- or γ-cyclodextrin derivative coatings with various hydroxy substitutions.

1200 pm (CD2), which results in a detection limit of 5 ppm. This value is about 400 times larger than that of an uncoated PBG. The signal deflection of *per*-ethyl- and *per*-allyl substituted derivatives, however, is reduced. Albeit, in contrast to the determined sensitivities, these derivatives show a significantly faster temporal response when the sensor is exposed to CFC-11 in nitrogen. For example, the rise times for CD2, CD5 and CD8, at 1 vol% CFC-11, are 1435 s, 71 s and 45 s, respectively. Consequently, it is feasible to tailor the functionalized PBG's behavior by employing the appropriate CD coating [3].

Spontaneous Crystallization

Exposing a PBG coated with CD1 to a CFC-11 content of at least 35 vol% leads to spontaneous crystallization of CFC-11 on the surface of the PPBG, as depicted in Fig. 3.

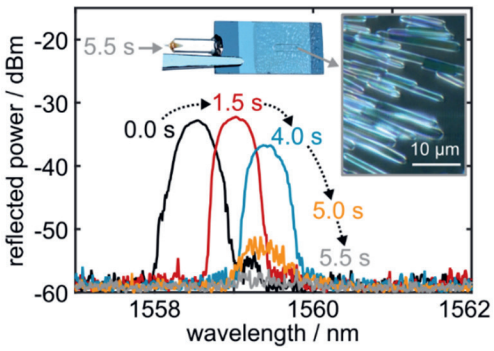

Fig. 3. Signal loss due to spontaneous crystallization. Inset: Sensor with crystallized surface and microscopic image thereof.

Within a timeframe of 5.5 s, this leads to complete signal loss due to a drastic refractive index increase of the functionalization coating and / or scattering losses by the structural reconfiguration of the crystallized surface [4].

Conclusion and Outlook

In conclusion, PBGs functionalized with CDs are well-suited for the detection of volatile trichlorofluoromethane, whereas sensor sensitivity and response time can be adapted by employing appropriate CD derivatives. CFC-11 quantities above 35 vol% lead to spontaneous crystallization of the coating which can be exploited for the development of new filter and storage concepts [5]. While all PBGs used in this study are SiO_2 based, future research will focus on transferring the demonstrated methodology on polymer-based planar devices and the development of new affinity materials.

Acknowledgements

We thank M. Girschikofsky (today with Heraeus Nexensos) and S. Hessler (alp group Aschaffenburg) for their valuable contributions to this research.

References

[1] M. Prather et al., The ozone layer: the road not taken, *Nature* 381, 551–554 (1996); doi: 10.1038/381551a0.

[2] I. Papst, *Global Banks of Ozone Depleting Substances: A Country-Level Estimate,* Deutsche Gesellschaft für Internationale Zusammenarbeit (GIZ) GmbH, 2017.

[3] M. Girschikofsky et al., Optical Sensor for Real-Time Detection of Trichlorofluoromethane, *Sensors* 19 (2019); doi: 10.3390/s19030632.

[4] D. Ryvlin et al., Methyl-Substituted α-Cyclodextrin as Affinity Material for Storage, Separation, and Detection of Trichlorofluoromethane, *Global Challenges* 2, 1800057 (2018); doi: 10.1002/gch2.201800057.

[5] M. Girschikofsky et al., "Planar optical sensor for trichlorofluoromethane," in *SPIE Future Sensing Technologies* (SPIE, 2019 - 2019), 13; doi: 10.1117/12.2542013.

DOI 10.5162/SMSI2021/B3.2

Compensating the quantitative signal of metal oxide semiconductor gas sensors in temperature cycled operation under the influence of siloxane poisoning

Caroline Schultealbert, Tobias Baur, Tilman Sauerwald[1], Andreas Schütze
Lab for Measurement Technology, Saarland University, Saarbrücken, Germany
c.schultealbert@lmt.uni-saarland.de

Summary:
We present a method for quantifying the degradation state due to siloxane poisoning of a metal oxide semiconductor gas sensor using temperature cycled operation. The time constant for the generation of surface charge at high temperature increases through poisoning and is only slightly dependent on the gas atmosphere. In addition to indicating a necessary sensor replacement, this signal can also be used for drift compensation based on the relation between sensor signal and this time constant.

Keywords: metal oxide semiconductor, gas sensor, siloxanes, poisoning, stability

Motivation

Metal oxide semiconductor (MOS) gas sensors are promising candidates for several applications due to their excellent sensitivity towards many reducing gases. This of course brings along some drawbacks like poor selectivity but also stability issues. Well-known poisons for MOS sensors are siloxanes [1]. Due to their broad occurrence in personal care and household products problems arise in several applications [2]. The impact of siloxanes on sensors operated at constant temperature have been studied extensively, but investigations on temperature cycled sensors are rarely found. We recently presented first results [3]. However, these measurements involved only very high siloxane dosages, the relatively uncommon siloxane HMDS (hexamethyldisiloxane) and only a small set of gases. Here we present a systematic study on the effect of the more prevalent D_4 (OMCTS, octamethylcyclotetrasiloxane, [4]) on MOS sensors in temperature cycled operation (TCO) and an approach for self-compensation.

Experimental setup

Measurements were conducted with our gas mixing apparatus (GMA). The sensors were exposed to a concentration of 2 ppm OMCTS for 1-3 hours several times followed by complex characterization measurements. The following gases and concentration ranges were selected: humidity (30-70 %RH), H_2 (500-2300 ppb), CO (40-1750 ppb), acetone (0-800 ppb), ethanol (0-700 ppb), acetaldehyde (0-900 ppb) and toluene (0-1200 ppb). Gas exposures were generated as described in [5], offering all mentioned gases simultaneously at a randomly chosen concentration within the associated range. 50 mixtures were measured, each held for 20 min. 16 sensors in total were studied (6 different types, 2 working modes, 4 using different types of diffusion barriers). The results presented here focus on the AS-MLV-P2 sensor (ScioSense B.V., NL) in TCO with a cycle length of 120 s. The cycle itself is derived from the differential surface reduction (DSR, described in [6]). This means that the sensor is oxidized at high temperature (here 400 °C, 10 s) followed by fast cool down to a lower temperature (100, 150, 200, 250, 300 °C, 14 s each) where the surface reduction (DSR signal, $k_{reduction}$), which is proportional to the concentration of reducing gases, is measured directly via differentiation of the logarithmic conductance:

$$\frac{d}{dt}\ln(G) \propto k_{reduction} \qquad (1)$$

Turning the DSR method around gives the opportunity to evaluate the simplified time constant t_{50} for generation of surface charge (differential surface oxidation, DSO). This procedure is more stable (higher signal to noise ratio) than using an exponential fit.

Results

One cycle with the same, constant gas atmosphere is shown in Fig. 1 after different siloxane dosages. Dosage 6.84 ppm·h is excluded here for better overview but agrees with other results.

[1] currently at: Fraunhofer Institute for Process Engineering and Packaging IVV, Freising, Germany.

The mean value of the cycle is shifted due to the siloxane exposure and the dynamic response at high and low temperatures (DSR and DSO) is slowed down. This indicates that all processes on the sensor surface become slower due to siloxane poisoning, which corresponds to the deactivation of catalyst and other active surface sites. For quantification of the degradation state the time constant t_{50} for oxidation at high temperature was evaluated, which is – according to the underlying gas sensor model [6] – independent from the ambient gas atmosphere. Fig. 2 shows the mean value of $\overline{t_{50}} \pm \sigma$ for the characterization measurements evaluated during the first high temperature phase in each cycle. σ mainly originates from the fact that t_{50} still depends slightly on the atmosphere, but the effect is sufficiently small to allow quantification of the sensor state, e.g., to indicate the need for sensor replacement. Before replacing the sensor, the signal needs to be corrected to allow correct gas quantification. The DSR signal at 200 °C initially shows a correlation of 0.90 with the total concentration, which is lowered only slightly by poisoning (5 % after 1.33 ppm·h). In contrast, the sensitivity of the signal is lowered fast by about 50 % after 1.33 ppm·h (see Fig. 3, blue data points). To perform that correction a relation between the relative change of the DSO signal and the relative change of the DSR-signal is linearly fitted for the first three datapoints (0-1.33 ppm·h). Using higher dosages needs a fit of the form $f(x) = \frac{1}{x}$ but the signal to noise ratio becomes very poor in this case. Applying this compensation to the data points projects them back on the original characteristic line extending the lifetime of the sensor by providing correct quantification results before a replacement is needed.

Outlook

If the found compensation factor can be transferred to new unpoisoned sensors or is individual for every single device needs to be evaluated. Additionally, the presented results include only a small part of the collected data from the corresponding study. More results including other sensors and operating modes, selectivity of MOS sensors and classification as well as other concepts to deal with siloxane poisoning are in preparation.

References

[1] G. Korotcenkov, B. K. Cho, *Sensors Actuators, B Chem.*, 156 (2011); doi: 10.1016/j.snb.2011.02.024

[2] D. Rüffer, F. Hoehne, J. Bühler, *Sensors (Switzerland)*, 18 (2018) doi: 10.3390/s18041052

[3] C. Schultealbert, I. Uzun, T. Baur, A. Schütze, T. Sauerwald, *J. Sens. Sens. Syst.* 9, 283-292 (2020), doi: 10.5194/jsss-9-283-2020

[4] C. Rücker, K. Kümmerer, *Chem. Rev.*, 115 (2015); doi:10.1021/cr500319v

[5] T. Baur, M. Bastuck, C. Schultealbert, A. Schütze, T. Sauerwald, *J. Sens. Sens. Syst.* 9, 411-424 (2020), doi:10.5194/jsss-9-411-2020

[6] T. Baur, C. Schultealbert, A. Schütze, T. Sauerwald. *J. Sens. Sens. Syst*. 7, 411-419 (2018); doi: 10.5194/jsss-7-411-2018

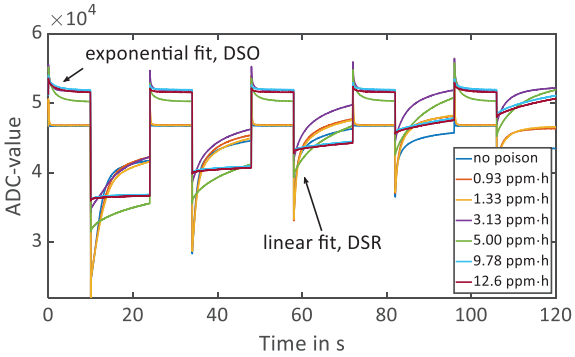

Fig. 1. Signal of one cycle under constant gas atmosphere for different siloxane dosages.

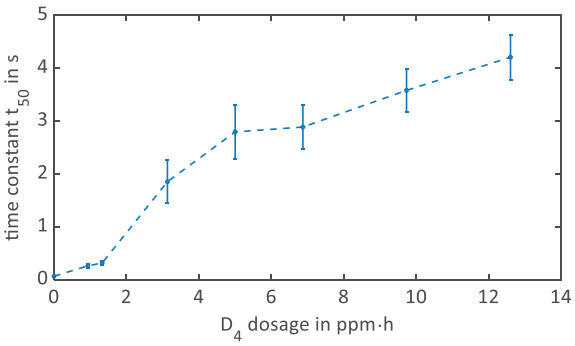

Fig. 2. The DSO signal evaluated on the first high temperature phase as a mean value over all 50 gas exposures and the corresponding standard deviation as error bars. A quantification of the poisoning state is easily possible by this feature.

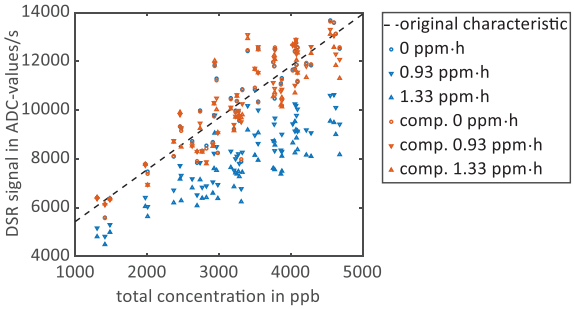

Fig. 3. DSR signal at 200 °C over total concentration: blue (original measured values at 0, 0.93 and 1.33 ppm·h) and red (compensated values). Each data point represents the mean value of one gas exposure.

DOI 10.5162/SMSI2021/B3.3

Monitoring Food Aging in a Refrigerator with GC/MS and Gas Sensor Systems

Julian Joppich[1], My Sa Marschibois[1], Tobias Baur[1], Oliver Brieger[1], Caroline Schultealbert[1], Martin Leidinger[2], Thorsten Conrad[2], Andreas Schütze[1]
[1] Saarland University, Lab for Measurement Technology, Saarbrücken, Germany
[2] 3S GmbH – Sensors, Signal Processing, Systems, Saarbrücken, Germany
j.joppich@lmt.uni-saarland.de, m.marschibois@lmt.uni-saarland.de

Summary:
We are targeting novel smart gas sensor systems to reduce food waste mainly from end consumers. To identify characteristic components and adequate sensors and sensor operation modes suitable for determination of these gas patterns during storage and aging, studies with different foods have been conducted. Besides a GC/MS, the test setup consists of several gas sensors, located both behind the chromatography column and parallel to the GC/MS, i.e. without separation of the compounds. First results show that emissions of aging food can be detected both by the GC/MS and by the gas sensors.

Keywords: food aging, food waste, gas chromatography/mass spectrometry (GC/MS), metal oxide semiconductor sensor, smart gas sensor

Background, Motivation

Approximately a third of the global food production is wasted while approx. one billion people worldwide are suffering hunger. In Europe, mostly fruit and vegetables go to waste or are discarded during production. Around 50 % of overall food waste is due to consumer behaviour, and more than 50 % of that waste is avoidable [1]. Since food waste accounts for 3.3 billion tons of CO_2 emissions, it is also a huge burden for the environment [2]. Against the backdrop of today's climate crisis, this is another reason to minimize food waste.

Low-cost gas sensor systems could help consumers reduce food waste. Different solutions seem possible, i.e. handheld devices for immediate analysis of dairy products after opening instead of relying on the "best before" date or continuous monitoring of the inside of a refrigerator. Specific gas emissions could, e.g., help determine when specific foods should be consumed. These sensor solutions could therefore prevent disposing of edible food or spoilage of food during storage.

Materials and Methods

To be as realistic as possible, a large commercial refrigerator is used and modified to our needs, see also Fig. 1: it is equipped with 32 closed storage boxes, containing different food samples. The storage boxes are connected to a valve block, which allows sampling the headspace of each box individually. At defined intervals, gas samples are automatically drawn from the sample boxes by a pump. Pump and valves are controlled by a multi gas sensor system supplied by the company 3S GmbH (D); the device contains two metal oxide semiconductor (MOS) gas sensors. The sample air is also passed through an additional, custom-built sensor system [4], equipped with a SGP30 (Sensirion AG, CH), a BME680 (Bosch Sensortec GmbH, D) and a ZMOD4410 (Renesas Electronics Corporation, JPN); all are operated using TCO (temperature cycled operation, [3]).

Parallel to these sensor systems, the gas composition is analysed by a GC/MS (Thermo Fisher Scientific, Trace 1300 Gas Chromatograph, ISQ 7000 Single Quadrupole Mass Spectrometer; TG-624 60 m/0.25 mm/1.4 µm column, temperature program, S/SL injector, headspace injection). To ensure a reliable synchronisation of the GC/MS with the valve operation, a trigger is provided by a custom-built controller. In addition, further MOS gas sensors (an AS-MLV-P2 (ScioSense, NL, former ams AG), a SGP30 and a ZMOD4450) are located parallel to the MS behind the GC column and run at constant temperature, i.e. they are supposed to detect separated compounds. The split between sensors and MS is approximately between 8:10 and 9:10.

The food to be tested, including different fruits (banana, citrus fruits), meat and fish, was stored in the storage boxes for up to 14 days, the box

headspace was analysed at least once a day. The temperature of the refrigerator is set to 6 °C.

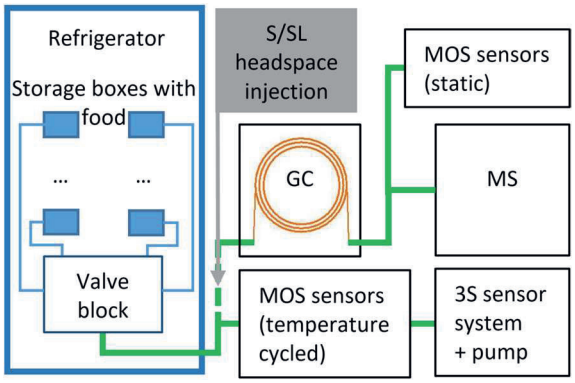

Fig. 1: Sketch of the measurement setup including storage boxes in the refrigerator, valve block, GC/MS and gas sensor systems.

Results

The exemplary results from the banana boxes (day 10) show that the chromatogram of the GC/MS and the peaks of the MOS sensor (AS-MLV-P2) correspond very well (see Fig 2).

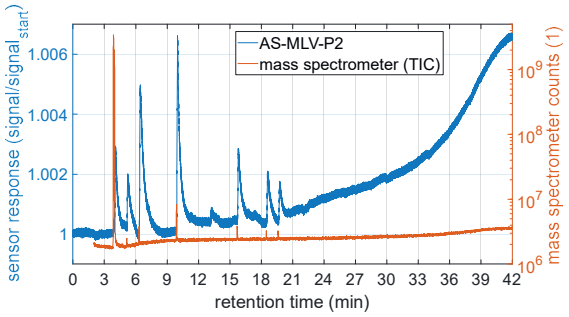

Fig 2: Chromatogram of a banana box after 9 days of storage and corresponding MOS sensor signal.

In fact, the MOS sensor has a higher sensitivity and detects additional peaks that are not visible in the MS signal (e.g. at about 13 minutes), although the split between the MS and the MOX sensors provides a higher flow to the MS. However, the sensor shows tailed peaks, which might originate from effects of the sensor chamber or from the sensitive layer. The ascending baseline might be ascribed to increasing column bleeding with increasing column temperature and flow. Moreover, while the first two peaks (the peaks of the permanent gases) do not grow over the course of the days, almost all other peaks grow or occur as the food (banana) ages. The assignment of peaks to substances is summarized in Tab. 1.

The temperature cycled sensors show a distinct response during exposure to the atmospheres of the boxes, and different foods and degrees of aging result in different patterns.

Tab. 1: Identified peaks in the chromatogram of Fig. 2.

Retention time (min)	most probable substance(s)
3.85 - 3.88	O_2, N_2, Ar
3.96	CO_2
5.14	acetaldehyde
6.32	ethanol
9.90	ethyl acetate
13.12	presumably pentanone (only MOS sensor)
15.70	isobutyl acetate
18.49	2-pentanol acetate
19.61	1-butanol-3-methyl acetate

Summary and Outlook

The results of the first measurements with the complete setup indicate that the sensors are suitable to detect components emitted by aging food that can be assigned to spoilage. GC peaks were successfully detected by the MOS gas sensors, further work on improving the peak shape and quantification abilities are foreseen. Data of the temperature cycled gas sensors have to be evaluated by means of pattern recognition. Finally, the ongoing systematic measurements will give an insight in the compounds and patterns of the emissions of various types of food needed to determine the degree of aging over a longer time. An additional challenge in the future will be the reliable recognition of these gas patterns in presence of a variety of cross influences inside a normal refrigerator.

Acknowledgment

This work is sponsored by the DBU – Deutsche Bundesstiftung Umwelt in the frame of the project SiVERiS under reference 34806/01-36.

References

[1] S. Noleppa *et al.*, Das große Wegschmeißen: Vom Acker bis zum Verbraucher, Ausmaß und Umwelteffekte der Lebensmittelverschwendung in Deutschland, WWF Germany (2015)

[2] Food and Agriculture Organization of the United Nations, Food Wastage Footprint: Impacts on Natural Resources: Summary Report, FAO (2013); ISBN: 978-92-5-107752-8

[3] A. Schütze *et al.*, Dynamic operation of semiconductor sensors, in: Raivo Jaaniso and Ooi Kiang Tan (eds.): *Semiconductor Gas Sensors*, Woodhead Publishing, 2nd Edition, 385-412 (2020); ISBN: 9789176850039, doi: 10.1016/B978-0-08-102559-8.00012-4

[4] T. Baur *et al.*, Device for the detection of short trace gas pulses, *Tech. Mess.* 85(7-8), 496-503 (2018); doi: 10.1515/teme-2017-0137

DOI 10.5162/SMSI2021/B3.4

Impact of cobalt oxide morphology on the thermal response to methane examined by thermal analysis

Olena Yurchenko[1,2], Hans-Fridtjof Pernau[1], Laura Engel[1], Benedikt Bierer[1], Martin Jägle[1], Jürgen Wöllenstein[1,2]

[1]Fraunhofer Institute for Physical Measurement Techniques IPM, Georges-Koehler-Allee 301, 79110 Freiburg, Germany,
[2]Department of Microsystems Engineering—IMTEK, University of Freiburg, Georges-Koehler-Allee 102, 79110 Freiburg, Germany
olena.yurchenko@ipm.fraunhofer.de

Summary:
In the present talk, we will demonstrate the impact of particle size and morphology of a metal oxide catalyst on its catalytic ability towards methane oxidation examined in a wide temperature range at dry environmental conditions. The investigations were performed by differential thermal analysis (DTA) technique delivering the thermal response of different cobalt oxide samples differing in particle size. The obtained results demonstrate the reliability of the method for preselection of catalysts for their application in catalytic gas sensors by the example of cobalt oxide, which is a promising catalyst for methane oxidation.

Keywords: metal oxide catalysts, catalytic activity, catalytic gas sensor, Differential Thermal Analysis (DTA), catalyst preselection.

Background, Motivation and Objective

Catalytic gas sensors, so-called “pellistors“, are commonly used for detection of combustible gases in order to warn the formation of potentially explosive atmospheres. In pellistors, combustible gases are detected by the heat produced through their catalytic oxidation on the active sensor coated with a catalytic layer. To initiate the catalytic oxidation of gases on the catalyst, the sensor is held at a specific operation temperature. The currently pellistors usually operate at high temperatures (>450°C) to ensure the proper detection of methane, which is the most inert combustible gas.

However, the high operation temperatures entail some disadvantages such as high power consumption and lowered catalyst stability. Reducing the operating temperature will contribute to a decrease in power consumption and an increase of the sensor’s operating life due to the decelerated catalyst aging. For the reduction of the operation temperature, catalysts of high activity and stability are required, especially for detection of methane.

Pd or Pt particles finely dispersed on aluminum oxide is the most common choice of catalyst material for pellistors [1]. However, recent advances in catalytic combustion evidences that some metal oxides could have certain advantages over aluminum oxide based catalysts. Thereby, the particle size and morphology of catalytic material have a determining effect on its catalytic behavior.

In this context, we investigated systematically the effect of particle size distribution and morphology of Co_3O_4 catalysts on their catalytic activity to methane oxidation and their thermal stability. The focus of investigation was on lower operation temperatures (<400°C). Spinel Co_3O_4 was reported as a promising catalyst for methane combustion [2]. Differential Thermal Analysis (DTA) was used as investigation method that provides a voltage signal in case of an oxidation reaction of the test gas on catalyst surface [3]. Two different methods were applied to produce Co_3O_4 catalysts with different particle size and morphology, a grinding of micro-sized particles and a direct synthesis.

The investigations aim at the ascertainment of Co_3O_4 applicability as catalyst or as support of metallic catalyst in pellistors that achieve low operation temperatures.

Description of the New Method

The commercially available STA (NETZSCH, STA 409 CD-QMS 403/5 SKIMMER) equipped with a DTA sample carrier was adapted for the investigation of catalytic activity at dry environmental conditions. Thereby, the temperature difference between the sample and reference crucible is measured as a voltage at defined environmental temperature (isothermal conditions) and gas atmosphere. The temperature difference between reference and sample crucible (contained ≈20 mg sample) was converted by software in a DTA signal (µV/mg) corresponding to the catalytic activity. Due to the heat release during the catalytic oxidation, the DTA signal shows a negative output. The signal normalization on the sample weight allows systematic investigation and direct comparison between different samples.

To investigate the effect of particle size distribution on catalytic activity, commercial Co_3O_4 (400 mesh, 37 µm) was wet grinded in a zircon jar by means of a planetary ball mill for different durations (between 0.5h and 16h). Additionally, Co_3O_4 was synthesized by precipitating procedure obtaining nanosized particles.

Results

Fig. 1 illustrates the dependence of the DTA response of commercial Co_3O_4 on the grinding time at different temperatures. The increase of the grinding time leads to successive improvement in the catalytic activity, especially during the first four hour of grinding. Further increase of the grinding time has no significant effect on improving the catalytic activity.

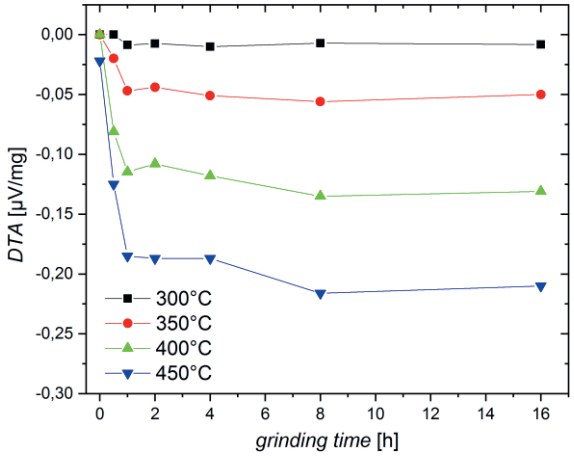

Fig. 1. DTA response as a measure of catalytic activity obtained at CH_4 oxidation (1 vol.% in dry air) on commercial Co_3O_4 catalysts as a function of grinding time and operation temperature.

Fig. 2 shows the thermal response of commercial catalyst grinded for 8h in comparison to response of synthetized Co_3O_4. It is visible that for the grinded catalyst, a pronounced activity is observed at 400°C and 450°C. In contrast, the synthetized Co_3O_4 with initially nanosized particles already shows a significantly higher activity at 350°C.

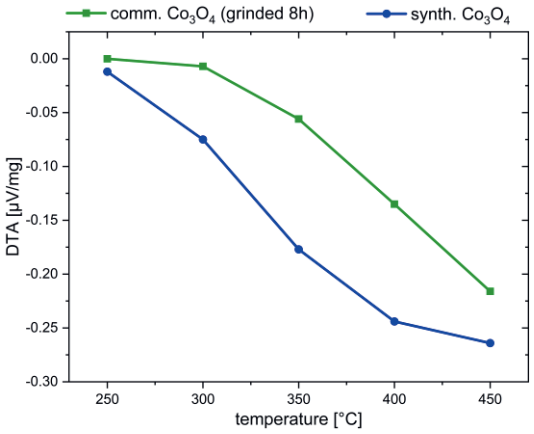

Fig. 2. DTA response obtained at CH_4 oxidation (1 vol.% in dry air) on commercial Co_3O_4 catalyst grinded for 8h and synthetized Co_3O_4 catalyst at different operation temperatures.

For both kinds of catalyst, thermal stabilty tests (synthetic air/methane alternation at 350°C and 450°C) were undertaken. The results indicate that synthetisized nanosized Co_3O_4 exhibits a slighly lower thermal stability than the commercial one originated by operation at high temperatures (450°C).

References

[1] F. Bíró, A.E. Pap, I. Bársony, Cs. Dücsó, Micropellistor with integrated porous alumina catalyst support. *Procedia Engineering* 87, 200–203 (2014); doi: 10.1016/j.proeng.2014.11.618.

[2] Z. Pu, H. Zhou, Y. Zheng, W. Huang, X. Li, Enhanced methane combustion over Co_3O_4 catalysts prepared by a facile precipitation method: Effect of aging time. Appl. Surf. Sci. 410, 14-21 (2017); doi:10.1016/j.apsusc.2017.02.186.

[3] Le Parlouër, P.: Thermal Analysis and Calorimetry Techniques for Catalytic Investigations, in: Calorimetry and Thermal Methods in Catalysis, vol. 154, edited by: Auroux, A., 52 pp., Springer, https://doi.org/10.1007/978-3-642-11954-5_2, 2013.

DOI 10.5162/SMSI2021/B4.2

Sensing Penicillin V in aqueous media with MIP nanoparticle coatings on QCM

M. Bagheri, O. Gatterbauer, P. A. Lieberzeit

University of Vienna, Faculty for Chemistry, Department of Physical Chemistry, Vienna, Austria
Peter.lieberzeit@univie.ac.at

Summary:

Molecularly imprinted polymers (MIP) based on an acrylic system have proven useful for sensing Penicillin V in aqueous solvents by the means of quartz crystal microbalances (QCM). Herein we carry that concept further by synthesizing molecularly imprinted polymer (MIP) nanoparticles (NPs) as sensitive matrices due to some considerable properties including high surface-to-volume ratio, low cost and straightforward preparation and handling. Herein, we report the sensitivity and selectivity results of MIP NPs with rapid screening method based on QCM. The approach indicates selective response of sensors to Pen V toward similar molecular structures and clearly reveals concentration-dependent reversible signals in terms of different concentration of target.

Keywords: Penicillin V, Molecularly Imprinted Polymer, Quartz Crystal Microbalance, Polymer Nanoparticles

Introduction

Most pharmaceuticals are deposited in the environment through human consumption and excretion, and are often filtered ineffectively by municipal sewage treatment. Persistence of pharmaceuticals and active drugs in wastewater are detrimental, because they are not only potential environmental pollutants, but are also pharmaceutically active. They also have the potential to accumulate in soil and plants that have been irrigated with wastewater and reclaimed water. Especially antibiotics are considered harmful for promoting the development of antibiotic-resistant bacteria in nature. Various analytical techniques can be utilized for measuring concentrations of antibiotics in wastewater effluent. Molecular imprinting is a comparably recent method for generating artificial recognition matrices toward both biological and synthetic species. Combined with suitable transducers, e.g. QCM, they allow for rapid and reproducible sensing [1]. The project underlying this presentation aims at sensing the antibiotic Penicillin V (Pen V) with both MIP nanoparticles and bulk MIP via QCM measurements. During the first stage, we studied corresponding MIP thin films based on radical polymerization of acrylic monomers. QCM sensor characteristics revealed a limit of detection at 0.02 mg/ml. Selectivity was investigated against Penicillin G and Amoxicillin, which have similar chemical structures [2].

The second step involves preparation of polymer Nanoparticles (NPs). The advantages of MIP NPs compared to bulk polymer is to enhance sensing efficiency due to their increased surface-to-volume ratio: it provides larger number of accessible binding sites for molecular recognition. This study reports on synthesis methods for improving the recognition properties of MIP NPs.

Preparing Penicillin V MIP NPs

Herein, MIP NPs were synthesized by precipitation polymerization of methacrylic acid (MAA) as the functional monomer, and trimethylolpropane trimethacrylate (TRIM) as the cross-linker and Pen V as the template in the acetonitrile. After thermal polymerization at 60°C, particles in the size range of 200 nm were prepared and spin-coated onto QCM electrodes. The corresponding non-imprinted (NIP) sensor was prepared in the same manner without template.

Results

Fig. 1 shows the outcome of MIP particle synthesis: one can clearly see that the process leads to large numbers of uniform particles in the size range of 200nm. In a first step towards generating the sensor it is necessary to extract the template from the polymer to reveal cavities. For that purpose, we stirred the particles in a mixed solution of Methanol and Acetic acid for 24 hours.

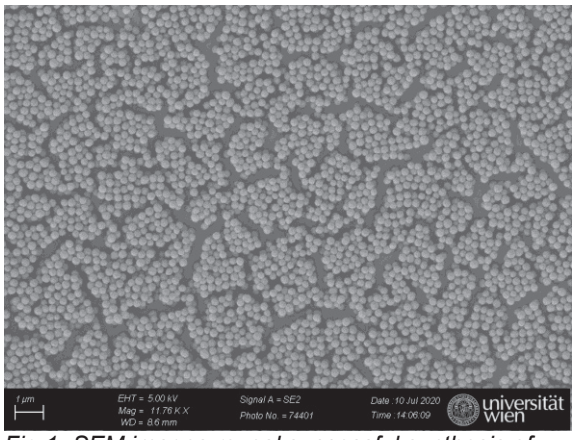

Fig.1. SEM images reveal successful synthesis of NPs in the size range of 200 nm

Then, QCM measurements served to assess sensitivity and selectivity of the sensors. Figure 2 shows the outcome of a sensitivity test: the sensor signals depend on the concentration of Pen V: they are roughly twice as large at 50mM, than at 25mM. After each injection we removed the analyte by washing with distilled water. To ensure reproducibility of the QCM response, every measurement repeated three times for each concentration. This led to a standard deviation of 1.2.

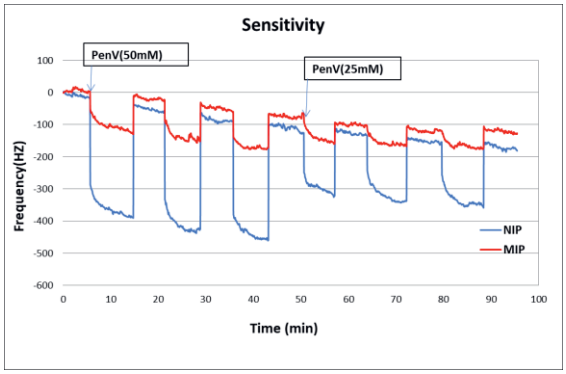

Fig.3. MIP and NIPQCM results at concentrations of 50 mM and 25 mM Pen V, respectively

For every signal, the frequency shifts recorded for MIP NPs are higher than those of NIP NPs: it exceeds the latter by a factor of three.

Fig. 2 summarizes the QCM selectivity pattern of the MIP NPs. To investigate selectivity, we utilized Penicillin G and Amoxicillin as competitive analytes against Pen V, because their structures are very similar to each other, as can be seen in Figure 2.

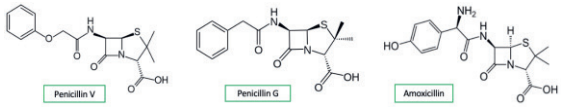

The results shown the highest response obtained when the sensors exposed to Pen V at a concentration of 50mM with selectivity factors around 1.3 each.

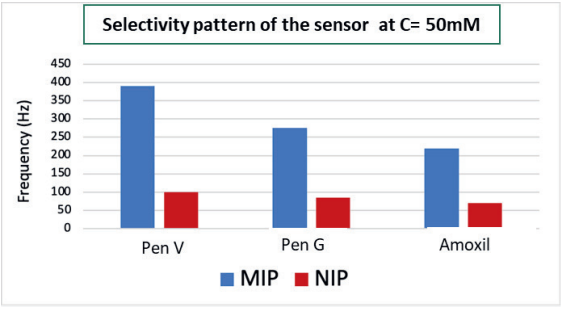

Fig.2. Selectivity of sensors at a concentration of 50 mM towards competing analytes.

In summary, we successfully developed MIP NPs that selectively bind Pen V and thus are potentially useful for establishing sensor systems for detecting wastewater effluents.

Acknowledgement

Authors gratefully acknowledge funding of this work by the Austrian Research Promotion Agency (FFG) through project AquaNOSE (Grant agreement no. 864893)

References

1. Vasapollo, G., Sole, R. D., Mergola, L., Lazzoi, M. R., Scardino, A., Scorrano, S., & Mele, G. (2011). Molecularly imprinted polymers: present and future prospective. *International journal of molecular sciences*, *12*(9), 5908–5945. doi:10.3390/ijms12095908

2. S. Haghdoust and P. Lieberzeit, Molecularly Imprinted Thin Films for Detecting Penicillin V, 10th International Congress Nanotechnology in Biology & Medicine, Graz, Austria. (2019)

DOI 10.5162/SMSI2021/B4.3

Cognitive Integrated Sensor Systems for In-Hive Varroa Infestation Level Estimation based on Temperature-Modulated Gas Sensing

Andreas König[1]
[1] *Institute of Integrated Sensor Systems, TU Kaiserslautern, Kaiserslautern, Germany*
koenig@eit.uni-kl.de

Summary:
Bees are recognized as an indispensable link in the human food chain and general ecological system. Numerous threats, from pesticides to parasites, endanger bees and frequently lead to hive collapse. The varroa destructor mite is a key threat to bee keeping and the monitoring of hive infestation level is of major concern for effective treatment. Sensors and automation, e.g., as in condition-monitoring and Industry 4.0 with machine learning offer help. Here, from our **IndusBee4.0** project, an integrated in-hive gas sensing system, denoted as **BeE-Nose**, for infestation level estimation and its application to a colony in the bee season 2020 from July to September is presented with first results of varroa infestation level estimation and automated treatment need detection.

Keywords: Temperature-modulated gas sensor, varroa infestation level, treatment need detection, digital bee keeping, in-hive measurement, cognitive sensor systems

Introduction

Major issues from environmental pollution to invasive species are threatening our ecological system and the human food supply. Insects, and honey bees in particular, play a decisive role, e.g., for pollination. The varroa mite parasite is a major threat to bee keeping and the cause of many bee colony losses. The monitoring of the varroa infestation level is one important task of conventionally operating bee keepers. Though there is a community practicing treatment free bee keeping [1], the majority of bee keepers follows standard treatment practice, e.g., by formic acid, which needs to know the right time to start treatment based on the hive infestation level. Sensors and automation, like in home automation, condition-monitoring and Industry 4.0, can both alleviate hive keeping and also make it much more effective. Thus, in the last 10-15 years numerous approaches to digital bee keeping can be observed [1]. In our **IndusBee4.0** project, small, effective, and affordable cognitive integrated sensor systems for continuous in-hive-monitoring and state estimation, e.g., monitoring and reporting the varroa infestation level, are pursued. In particular, integrated gas sensors, e.g., the BME680, are investigated for this purpose in the following.

Conventional Varroa Monitoring Methods

There are several standard methods available for conventional varroa infestation level estimation (VILE). They all have in common, that they imply substantial effort for the bee keeper and deliver results only at larger time steps. The analysis of hive debris including mites, dropping from the hive bottom and collected on a slider or varroa board, is most common. Usually, three days are expended until a manual, or more recently (semi) automated vision-based analysis, of the debris for the number of varroa can be conducted. The hive infestation level can be estimated from this count [1]. Another common approach, also denoted as flotation method, extracts a bee sample from the hive and drowns them to separate bees and varroa. The powder sugar and the CO_2-based sedation are two alternative more bee-friendly variants. Again, hive infestation level can be estimated from the count. Sample adequateness will probably depend on the location of extraction in the hive. More recent principle approaches try to scrutinize in and out going bees at the flight hole for varroa mites clinging to them, e.g., [3, 1]. In this paper, the standard counting on the varroa board will be applied to obtain the required ground truth for VILE and the automated treatment need detection (ATND).

Indirect Gas Sensor-Based VILE

Basic investigations in the past have revealed, that both the sound patterns emitted by bees as well as the air composition inside the hive host information, that correlates with the varroa infestation level, as determined by the conven-

tional methods from the previous section. Hive sound patterns also allow to detect hints on 'missing queen', advent of 'swarming mood' etc. Thus, in our and many others previous work, microphones and signal processing and analysis have been applied, see e.g., [1]. MEMS microphones deliver in our Pi Zero W based **SmartComb** in-hive measurement system [1] the acoustical information on hive state, including continuous cues for VILE. Recent intriguing work, based on a set of Figaro gas sensors and an external measurement system confirmed the existence and usefulness of a correlation of hive air analysis results and varroa infestation level [2] [4]. With the advent of highly integrated gas sensing systems, e.g., Sensirion SGP30 multi-pixel sensor system [1] or the BOSCH Sensortec BME680, the possibility of VILE by in-hive low-cost gas sensing system and direct or indirect indicators from hive air analysis over the bee season was added to our **IndusBee4.0** system. **Fig. 1** shows the **SmartComb** measurement systems, non-obtrusive to the bees, and continuously delivering registrations at any desirable rate, with the **BeE-Nose** extension in stable 'bee climate'.

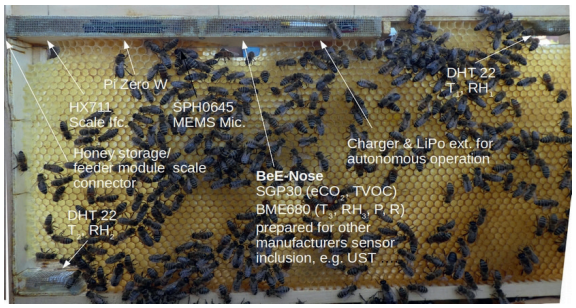

Fig. 1. ***SmartComb*** *with SGP30 and BME680*

The BME680 allows the control of sensor heating, i.e., it can be modulated for temperature cycles in measurement (Virtual sensors).

Experiments and Results

One **SmartComb** module (as exemplified in **Fig. 1**) has been deployed in a mature hive, that had released as swarm, and data (T, RH, weight, hive sound, and gas sensor data from hive air) from July to September until formic acid treatment, has been collected. **Fig. 2** shows gas sensing results complemented with varroa counting data as ground truth for this campaign. A subset of this data has been sampled in a train and a test set with 1047 samples each and 8 measurements from a temperature modulation with 8 equidistant levels from 50° C to 400° C have been employed as raw features for the first VILE and ATND. For VILE, four classes, *No_Varroa*, *Low_Varroa*, *Mid_Varroa*, *Treatment_!*, have been introduced.

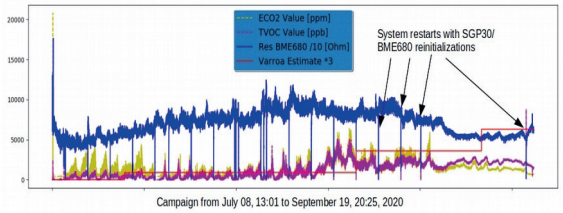

Fig. 2. Three months of SPG30 eCO_2, TVOC, & BME680 resistance data @400° C with varroa count.

For ATND, the first three classes are merged to *SubTh*. **Fig. 3** shows a scatter plot of the first two BME680 T-modulated outputs.

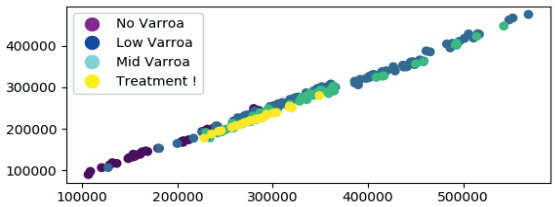

Fig. 3. BME680 resistance data scatter plot of first two of 8 T-modulated channels with four classes.

Fig. 3 shows only a weak support for the VILE. A kNN classification of all 8 channels with k=3 gave 83,73 % resubstitution and 70.33 % generalization recognition rate. For the two classes of ATND and the selected BME680 channels 2, 6, 7, and 8, resubstitution of 91.86 % could be achieved with 99.25 % for 934 *SubTh* and 92.3 % of 113 *Treatment_!* true positive patterns.

Conclusions

Honoring the importance and challenging of honey bees, an in-hive close to brood nest sensing system has been applied for a substantial time of the 2020 bee season. First VILE and ATND results on indirect hive air cues were obtained. Validation, robustness investigation, and multi-sensing is required next. The approach is potentially generalizable to foulbrood, SHB etc.

References

[1] A. König, IndusBee4.0 – Integrated Intelligent Sensory Systems for Advanced Bee Hive Instrumentation and Hive Keeper's Assistance Systems, S. & Trans. J., 237.9-10,*109-121 (2019)*

[2] A. Szczurek, M. Maciejewska, B. Bąk, J. Wilk, J. Wilde, M. Siuda, Detection Level of Honeybee Desease: Varroosis Using a Gas Sensor Array, SEIA'2019, Tenerife, 25-27 Sep. 255-256 (2019).

[3] L. Chazette, M. Becker and H. Szczerbicka, Basic algorithms for bee hive monitoring and laser-based mite control, 2016 IEEE SSCI, 1-8 (2016)

[4] Szczurek, A., Maciejewska, M., Bąk, B., Wilk, J., Wilde, J., and Siuda, M.: Detecting varroosis using a gas sensor system as a way to face the environmental threat, Science of The Total Environment, Vol. 722, 2020

DOI 10.5162/SMSI2021/B4.4

Proof of Concept Validation of a Swimming Multi Sensor Platform for In-Situ Ocean Monitoring

Julius Harms, Thorsten A. Kern
Institute for Mechatronics in Mechanics (iMEK)
Hamburg University of Technology (TUHH), 21073 Hamburg
Corresponding author: Julius.harms@tuhh.de

Summary:

A concept for a modular multi sensor platform to collect various measurement data at the interface of air and water is presented in this paper. Besides position tracking and wave height measurement, the drifting buoy allows individual integration of different sensors by its scalable design. A wave energy converter and solar modules provide redundant energy harvesting sources for long time applications. The concept was tested in the Baltic Sea off the coast of Fehmarn, by a first prototype equipped with low-cost temperature and salinity sensor. Drifting behaviour was compared to the CARTHE Drifter.

Keywords: In-Situ, Monitoring, Drifter, Modular, Platform, Maritime, Ocean

Introduction

Existing drifter platforms, used to gather ocean current information by tracking the buoy's position, lack the ability to measure individual parameters, have a limited energy source or are too expensive for the use in large quantities. Big experiments like LASER [1], using 1000 drifter at the same time, show that there is a great need for low-cost platforms. The used CARTHE drifter, like others, miss the ability to acquire further measurement data like e.g. temperature or salinity. At the same time, measurement data with high space resolution present a great advantage for many applications like analysation of submesoscale dynamics. The here presented concept is the development of an affordable multi-sensor platform with high modularity in its use.

Concept Description

The modularity of the concept is given by the system reduction to the most important standardized components, combined with an extension concept for customized components. Figure 1a shows the schematic of the Affordable Multi Sensor Drifter (AMuSeD) with the main unit as the central component. With the integrated GPS-Module and a small MEMS IMU, the position and wave height is always acquired. If further measurement data is required, the embedded master controller requests measurement data from additional sensor unit, replying according to a standardized protocol. This protocol allows exchange of the sensors on the sensor unit without touching the main unit. The main unit processes the received data and transmits the full data set via satellite communication. This modularity allows research groups to use the main unit as their key component and adjust only the sensor unit according to their individual needs. Besides the data processing, the main unit provides a power supply for all peripherals, which can be implemented using energy harvesting methods if long time measurement is required. Since solar power, in some areas, is not sufficient, a wave energy converter (WEC) adds redundancy to the supply. The WEC is based on a specially developed linear generator and the planned implementation can be seen in Figure 1b. The energy is gained from a relative movement between stator and translator, due to the difference in the wave orbital velocity exciting the buoy and drogue. The concept was tested in a wave channel and the generator simulated based on electromagnetic FEM software. The promising results will be presented in the scope of a different work.

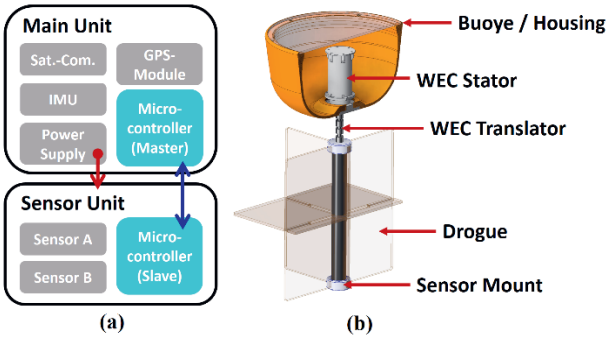

Figure 1: (a) Schematic for the sensor interfacing (b) of the AMuSeD prototype

Prototype Test

In a proof of concept experiment, a prototype of AMuSeD was built and tested. The complexity of the main unit was reduced to electronics for the acquisition of GPS position and acceleration. The connected sensor unit consists of low-cost temperature and conductivity sensors. The temperature sensor was implemented by a PT1000 (~15€) with the RTD-Digital converter MAX31865 (~5€). The integrated ADC allows a resolution of 0.03°C and a total accuracy over all operating conditions of 0.5°C. Conductivity was measured by the Atlas Scientific Conductivity K1.0 Kit (~230€), which gives an accuracy of +/- 2%.

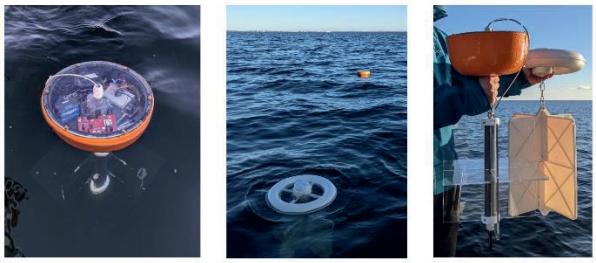

Figure 2: (a) Top view AMuSeD (b) deployed CARTHE & AMuSeD (c) comparison AMuSeD (l.) CARTHE (r.)

This 2-electrode conductive sensor allows an inexpensive use, but has the disadvantage of being more susceptible to bio fouling and polarization. For this reason, the authors of this paper are researching on low-cost inductive salinity sensors [2]. Two of the AMuSeD drifters, one with full electronics and one with GPS tracking only, were deployed on the 27th of November 2020 together with two CARTHE drifter off the coast of Fehmarn (Fig. 2b/c). For the duration of 280 minutes, the drifter covered a distance of ~2.5 km (Fig. 3a) while one was tracking measurement data every minute. After the simultaneous deployment, the measuring platforms drifted close together during the entire period. At the time of collection, the CARTHE drifters were 150m further east than the AMuSeD, which may be due to the slightly different sizes of the drogues and the waves coming from the northwest. The tracked temperature and conductivity data (Fig 3b) is used to calculate the water salinity (Fig 3c) based on the practical salinity scale [3]:

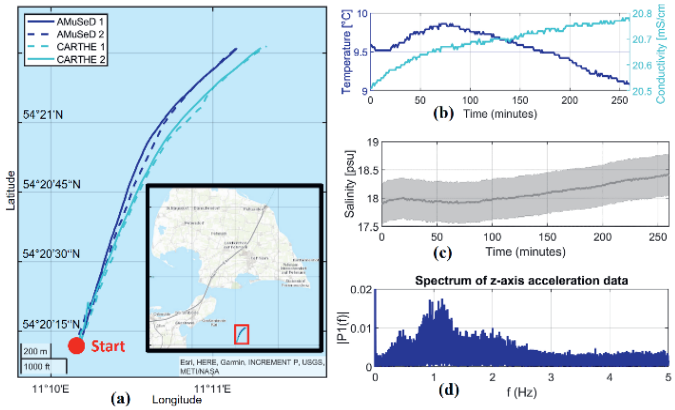

Figure 3: (a) Comparison of GPS-tracks (b) temperature & conductivity over time (c) calculated salinity with error band (d) frequency spectrum of vertical acceleration data

$$S = a_0 + a_1 K^{\frac{1}{2}} + a_2 K + a_3 K^{\frac{3}{2}} + a_4 K^2 + a_5 K^{\frac{5}{2}}$$

Where the salinity S is calculated from the empirical parameters a_0 to a_5 and the conductivity ratio K of the sample to a standard *KCl*-solution at 15°C. With the given the measurement uncertainties, this leads to an propagated uncertainty of +/-0.035 psu (~2%) for the present water conditions of around 9.5°C temperature and a water conductivity of 20.600$\mu S/cm$. A spectral analysis of the acceleration data (Fig 3c) gives information about sea state, wave height and period.

Results and Conclusion

The collected measurement data allow a much better interpretation than a mere observation of the position data. Despite the low-cost sensors, the additional measurement data achieve accuracy values to identify disturbances like changing sea states and temperature jumps that affect the drift behaviour. This is especially relevant for remote long-term measurements. The executed test is a successful proof of concept. In the next steps, the modular electronics will be integrated by a PCB design and the energy supply will be ensured by energy harvesting. In addition, the housing will be reduced in size and optimized for better drift behavior while being easy to produce. The ultimate goal is to use biocompatible materials in the manufacturing process so that even when large quantities are used, the oceans are not polluted. In addition to the main unit development, research on low-cost sensors, especially inductive conductivity sensors, with high resolution is going to be performed.

References

[1] Novelli et al. ”A Biodegradable Surface Drifter for Ocean Sampling on a Massive Scale” . J. Atmos. Oceanic Technol. (2017) 34, 2509–2532; doi:10.1175/JTECH-D-17-0055.1

[2] Harms et al. “Theory and Modelling of eddy current type Inductive Conductivity Sensors” MDPI Eng. Proc. (2021) (accepted)

[3] E. Lewis, "The practical salinity scale 1978 and its antecedents" IEEE Journal of Oceanic Engineering, vol. 5, no. 1, pp. 3-8, January 1980, doi:10.1109/JOE.1980.1145448.

DOI 10.5162/SMSI2021/B5.1

Determination of the Dielectric Properties of Ceria and Soot Powders by the Microwave Cavity Perturbation Method

Stefanie Walter[1], Carsten Steiner[1], Gunter Hagen[1], Ralf Moos[1]
[1] Department of Functional Materials, University of Bayreuth, 95447 Bayreuth, Germany
functional.materials@uni-bayreuth.de

Summary:
A comprehensive method to determine dielectric properties using the microwave cavity perturbation method (MCP) is presented. It is applicable to a wide range of sample geometries and properties. First tests with typical materials for exhaust aftertreatment have already been carried out successfully. The application of the method can provide further knowledge for radio frequency-based analysis of catalysts and filter systems.

Keywords: radio frequency (RF), microwave cavity perturbation, material characterization, dielectric properties, depolarization

Introduction

In order to meet the increasingly stringent emission standards, the application of automotive exhaust gas aftertreatment systems is essential. To ensure correct operation, knowledge of the state of a catalytic converter or the soot loading of a filter is necessary. A method suitable for this purpose is the radio frequency (RF)-based state diagnosis. This measuring system is based on the change in the dielectric properties of the catalyst or filter depending on their current state. The applicability of this system has already been shown in several studies [1,2].

In order to optimize the technical application of this measuring approach, a deeper understanding of the electrical properties of the used materials in exhaust gas aftertreatment systems is necessary. Recently, a test bench was presented, that enables the characterization of small amounts of powder materials under defined conditions using the microwave cavity perturbation (MCP) method [3].

The exact calculation of the material properties for the investigated samples using the resonance properties is not trivial, since often not all assumptions of the classical microwave cavity perturbation theory (MCPT) are fulfilled. While in previous publications a simplified approach was sufficient to investigate the relative change of the polarization ε_r' and the dielectric losses ε_r'', this work aims to show, using the example of ceria and soot, that a more precise determination of material properties is possible with an extended method.

Microwave Cavity Perturbation

The determination of the material parameters by the MCP is based on the change of the resonant mode properties due to the introduction of a small material sample into the resonance cavity. The setup shown in Fig. 1 was designed to ensure that the TM_{010} and TM_{020} modes have a constant electric field along the resonator axis and thus in the sample area [3].

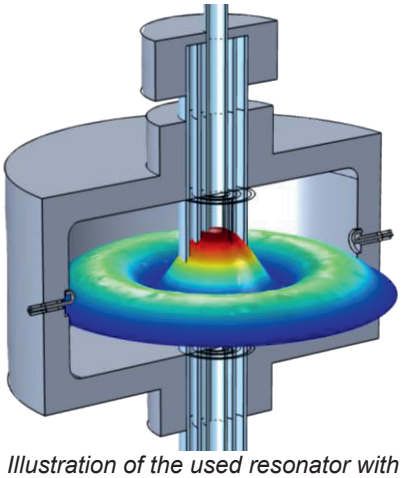

Fig. 1. Illustration of the used resonator with the electric field distribution of the TM_{020} mode.

In the simplified MCP theory, the material polarization ε_r' can be calculated from the shift of the resonant frequency Δf due to the sample, the sample volume V_S and an effective resonator volume V_{eff}, that is dependent on the field distribution of the resonant mode:

$$\frac{\Delta f}{f_0} = (\varepsilon_r' - 1)\,\frac{V_S}{2V_{eff}} \qquad (1)$$

Moreover, the dielectric losses can be calculated from the change in the inverse resonant quality:

$$\Delta\left(\frac{1}{Q}\right) = \varepsilon_r'' \frac{V_S}{V_{eff}} \quad (2)$$

These equations can only be applied to a, corresponding to the MCP theory, ideal system. If these preconditions are not fulfilled, various correction terms have to be applied for a correct determination of the dielectric properties. For the setup described in this work, especially the following three points should be considered [4]:

- Deviations of the field distribution of the real setup compared to a perfectly cylindrical resonator lead to a wrong V_{eff}. These are caused, e.g., by the openings required for heating or by the quartz glass tubes used to place the material sample. However, the correct determination of V_{eff} can be obtained by a simulation of the field distribution.
- Depolarization effects can lead to a field weakening inside the sample. In consequence, the resonant parameters are influenced to a smaller extent by the sample than assumed in the simplified theory. This effect can be corrected if the sample geometry is known.
- To determine the effective dielectric properties of porous samples, such as powders, the portion of the different components has to be considered by a mixing model. In the literature a large number of various models is described (e.g. Wiener, Looyenga, …). Which of these can be applied to the measured material can be analyzed almost exclusively by further measurements.

Results

In addition to solid oxide fuels cells, ceria is frequently used for three-way catalytic converters in automobiles. In this application, ceria serves as an oxygen storage material. Since its dielectric properties depend on its oxygen stoichiometry, the investigation of ceria using MCP is particularly important for RF-based state diagnosis. Tab. 1 shows the results for a ceria powder sample in the resonator at room temperature. The calculation of ε_r' with both approaches clearly shows that the extended approach is necessary to calculate the known properties of ceria. The extended method uses a simulation-determined V_{eff}, the mixture model according to Looyenga and considers the depolarization effect.

Tab. 1: Permittivity ε_r' of ceria at 25 °C and 20 % O_2

mode	simplified theory	extended theory	literature[5]
TM_{010}	3.95	22.6	23
TM_{020}	9.92	23.6	

The determination of an applicable mixture model for an investigated material represents a great effort. It depends not only on the material itself, but also on other parameters such as its particle size distribution.

The mixture model for a soot loaded particulate filter, for example, can be determined by measuring different mixtures of synthetic soot (PrintexU) and cordierite in the resonator setup.

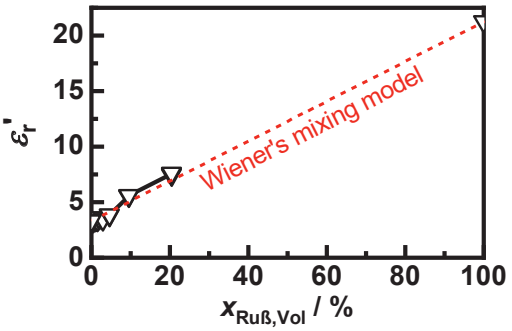

Fig. 2. Permittivity of different PrintexU – cordierite mixtures at room temperature.

The measured permittivity in Fig. 2 show a behavior equivalent to Wiener's mixing model. Thus, this model can be used in further measurements to determine directly the permittivity of pure soot.

References

[1] R. Moos, Microwave-Based Catalyst State Diagnosis - State of the Art and Future Perspectives, *SAE Int. J. Engines* 8, 1240–1245 (2015); doi: 10.4271/2015-01-1042.

[2] R. Moos, et al., Automotive Catalyst State Diagnosis Using Microwaves, *Oil Gas Sci. Technol.* 70, 55–65 (2015); doi: 10.2516/ogst/2013203.

[3] M. Dietrich, et al., A Laboratory Test Setup for in Situ Measurements of the Dielectric Properties of Catalyst Powder Samples under Reaction Conditions by Microwave Cavity Perturbation: Set up and Initial Tests, *Sensors* 14, 16856–16868 (2014); doi: 10.3390/s140916856.

[4] C. Steiner, et al., Determination of the Dielectric Properties of Storage Materials for Exhaust Gas Aftertreatment Using the Microwave Cavity Perturbation Method, *Sensors* 20, 6024 (2020); doi: 10.3390/s20216024.

[5] N. I. Santha, et al., Effect of Doping on the Dielectric Properties of Cerium Oxide in the Microwave and Far-Infrared Frequency Range, *J. Am. Ceram. Soc.* 87, 1233–1237 (2004); doi: 10.1111/j.1151-2916.2004.tb07717_33.x.

Funding

This research was funded by the Deutsche Forschungsgemeinschaft DFG, (MO 1060/29-1 and FR 1301/23-1) and the Bayerische Forschungsstiftung BFS (AZ-1288-17).

DOI 10.5162/SMSI2021/B5.2

Simultaneous Quality and Flow Rate Monitoring of Diesel Exhaust Fluid by Using A Platinum Thin Film Sensor

Ralf E. Bernhardsgrütter[1,2], Christoph Hepp[1], Katrin Schmitt[2,3], Jürgen Wöllenstein[2,3]
[1] Innovative Sensor Technology IST AG, Ebnat-Kappel, Switzerland,
[2] Department of Microsystems Engineering IMTEK, University of Freiburg, Freiburg, Germany
[3] Fraunhofer Institute for Physical Measurement Technique IPM, Freiburg, Germany
ralf.bernhardsgruetter@ist-ag.com

Summary:
The monitoring of the quality and the flow rate of the diesel exhaust fluid is essential for an efficient selective catalytic reduction in diesel combustion. This article presents a platinum thin film sensor using a combination of the constant temperature anemometry and the 3ω-method to measure continuously the urea content and the flow rate with compensated fluid dependence. The urea content can be determined within 3 % by weight and the flow rate within 4 % full scale. The presented method allows continuous monitoring of two main parameter in the selective catalytic reduction.

Keywords: Diesel exhaust fluid, flow measurement, quality monitoring, 3ω-method, anemometry

Motivation and Background

The selective catalytic reduction (SCR), an aftertreatment method to reduce the emission in diesel combustion engines, can convert the harmful detrimental nitrous oxide into water and nitrogen by using a so-called diesel exhaust fluid (DEF), known as the trademark “AdBlue”. The DEF consists of 32.5 % urea and 67.5 % water. The ratio of urea and water is crucial for an optimal aftertreatment and an inappropriate ratio breaks the SCR down and the emission reduction fails.

Reported DEF quality sensors, based on optical principles [1], ultrasonic [2] and sinusoidal heating measurement [3], are not sensitive to flow or are driven at non-flow condition due to a cross correlation between flow and fluid composition.

The claims of this paper are: A method using a combination of the constant temperature anemometry (CTA) and the 3ω-method to (1) measure simultaneously flow and (2) determine the urea concentration. (3) The measurement deviations are better than 4 % full scale for the flow measurement and better than 3 % for the urea concentration measurement. (4) The sensor is suitable for on-the-fly measurements in e.g. vehicles.

Method

On one side, the CTA [4] is a well-known flow measurement method. However, the state-of-the-art thermal flow measurement are highly dependent on the fluid and the sensor must be calibrated for each fluid. On the other side, the 3ω-method is a well-known method to measure thermal conductivity and heat capacity [5], but the signal has usually a flow cross sensitivity. A crucial quantity in the field of the 3ω-method is the penetration depth δ which depends on the surrounding, e.g. thermal conductivity and flow, and on the frequency ω as following,

$$\delta \propto \sqrt{\frac{1}{\omega}}\,. \qquad (1)$$

Because the flow velocity changes perpendicular to the flow direction and is zero at the wall boundaries, a frequency range might exist where the fluid dependence is still visible, and dominant compared to the flow dependence. This article shows that such a frequency exists and can be used to measure the composition of a binary mixture and to compensate the fluid dependence of the CTA-measurement.

Experiment & Result

The investigated sensor (see figure 1) bases on platinum thin film technology.

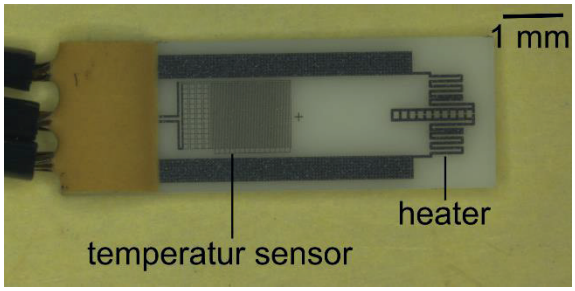

Figure 1: Platinum thin film element consists of a temperature sensor with 1200 Ω at 0 °C and a heating element with 45 Ω at 0 °C.

The sensor consists of two structure, a heater and a temperature sensor. Both structures have a temperature-to-resistance coefficient of 3900 ppm/K. The setup consists of an electronic circuit able to do the CTA-mode and the 3ω-mode.

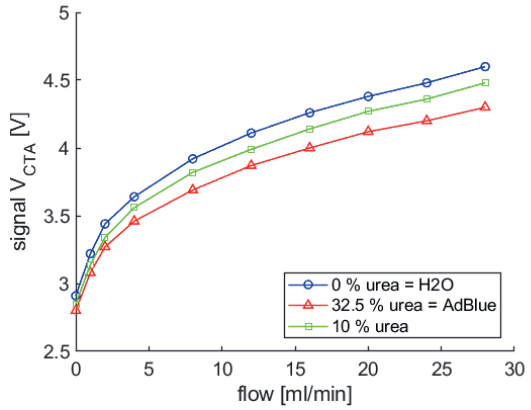

Figure 2: CTA-signal for different fluids, namely water, a urea-water mixture of 32.5 % urea and a urea-water mixture of 10 % urea as function of flow.

The experiment was done for three mixtures, namely water, a urea-water mixture of 32.5 % urea (pure DEF) and a urea-water mixture of 10 % urea. The sensor calibration was done with pure DEF. Figure 2 shows the uncompensated CTA-signal for these fluids and the fluid dependence is highly visible which leads to a measurement error of the linearized flow of around 50 % full scale in a state-of-the-art thermal flow meter.

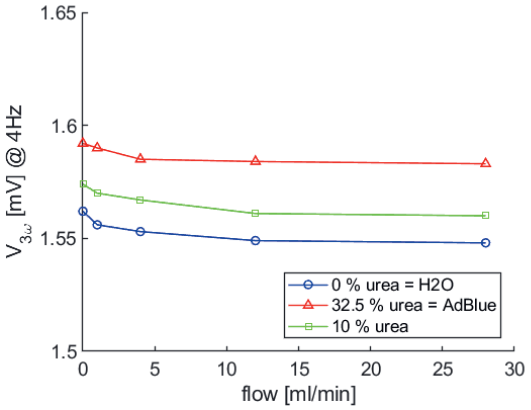

Figure 3: 3ω-method signal for a drive frequency of 4 Hz as function of flow. The fluid dependence is dominant compared to the flow dependence.

The 3ω-method investigations showed that the flow dependence is reduced for increasing drive frequency due to the decrease of the penetration depth (see eq. 1), however, the signal strength reduces as well. Therefore, a trade-off between flow dependence and signal strength exists. For the given setup and at a drive frequency of 4 Hz, the 3ω-signal (see figure 3) is still fluid dependent, but the flow dependence is strongly reduced. Given the base lines of water and pure DEF, the urea content of the 10%-mixture is determined to be between 10% and 13 % urea for the entire flow range.

Using the extracted information of the 3ω-method, the fluid dependence can be compensated. In this investigation, the dependence between the 3ω-signal of a mixture at the given drive frequency of 4 Hz and its urea concentration is approximated to be linear. Figure 4 shows the compensated and linearized flow signal and the deviation with respect to the calibration with pure DEF. The deviation is smaller than 4 % with respect to the calibration with pure DEF. Therefore, the deviation due to fluid dependence is reduced by more than a factor of 10 compared to the state-of-the-art thermal flow sensor without fluid compensation.

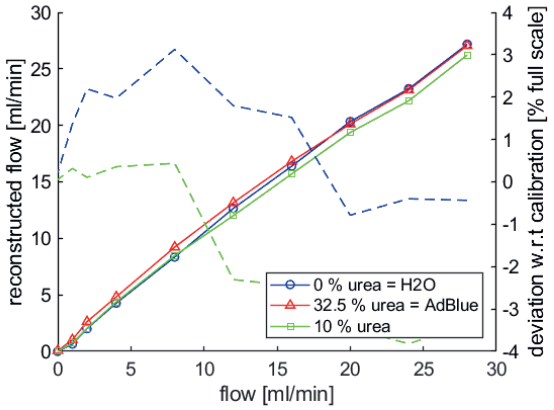

Figure 4: Linearized signal regarding flow, where the fluid dependence is reduced. Solid lines correspond to the linearized signal, dashed lines correspond to the deviation being smaller than 4 % full scale with respect to the calibration curve of pure DEF.

References

[1] N. Kumawat, et al., Quality monitoring of diesel exhaust fluid in vehicles using diffractive interference sensors, *SENSORS IEEE*, 1676-1678 (2014); doi: 10.1109/ICSENS.2014.6985343

[2] P. Gurusamy, et al. Measurement of diesel exhaust fluid concentration in urea-SCR after-treatment system. *Int. J. Precis. Eng. Manuf. 18*, 1085-1092 (2017); doi: 10.1007/s12541-017-0127-zFdgsf

[3] R.E. Bernhardsgrütter, et al., Inline Quality Monitoring of Diesel Exhaust Fluid (AdBlue) by Using the 3w-Method, SMSI 2020, 79-80 (2020); doi: 10.5162/SMSI2020/A5.2

[4] S. Sosna, et al. A Temperature Compensation Circuit for Thermal Flow Sensors Operated in Constant-Temperature Mode, *IEEE Transaction on Instrumentation and Measurement* 59, 1715-1721 (2010); doi: 10.1109/TIM.2009.2025988

[5] D.G. Cahill, et al. Thermal conductivity of α-SI:H thin films, *Phys. Rev. B 50*, 6077-6081 (1994); doi: 10.1103/PhysRevB.50.6077

DOI 10.5162/SMSI2021/B5.3

Examination of New Catalysts for Catalytic Combustible Gas Sensors by Thermal Analysis

Olena Yurchenko[1,2], Hans-Fridtjof Pernau[1], Laura Engel[1], Benedikt Bierer[1], Martin J ägle[1], J ürgen Wöllenstein[1,2]

[1]Fraunhofer Institute for Physical Measurement Techniques IPM, Georges-Koehler-Allee 301, 79110 Freiburg, Germany,
[2]Department of Microsystems Engineering—IMTEK, University of Freiburg, Georges-Koehler-Allee 102, 79110 Freiburg, Germany
olena.yurchenko@ipm.fraunhofer.de

Summary:
DTA was used to investigate cobalt oxide (Co_3O_4) catalysts, which differ essentially in terms of particle morphology, to their thermal response towards methane (CH_4) oxidation in dry air. Moreover, the thermal stability and the effect of hydrogen sulfide (H_2S) inhibitor on the thermal behavior of the Co_3O_4 catalyst was examined by DTA. A comparison of the DTA measurement with a MEMS pellistor based on a modified Co_3O_4 catalyst shows a similar behaviour of their responses to CH_4 and H_2S. The obtained results demonstrate the reliability of the method for preselection of catalysts for their application in catalytic gas sensors.

Keywords: metal oxide catalysts, catalytic gas sensor, poisons, Differential Thermal Analysis (DTA).

Background, Motivation and Objective

In the field of safety technology, catalytic sensors, so-called »pellistors«, are commonly used for detection of flammable gases such as hydrocarbons. The heat produced during catalytic oxidation of the combustible gas on the catalytic layer corresponds to its concentration in environment. Currently, pellistors usually operate at high temperatures (>450°C) to ensure the proper detection of methane, which is the most inert combustible gas.

The high operation temperatures as well as the presence of catalyst inhibitors like hydrogen sulfide (H_2S) and sulfur dioxide (SO_2) or poisons like silicones lead in turn to a high power consumption, short or long-term deactivation of catalyst and thus a shortened sensor life. Novel catalysts are required to lower the operating temperature and extend the service life. However, the development of new catalysts for the targeted gas sensor applications turns out to be difficult due to various factors influencing the sensor response, which are not easy to differentiate [1].

To overcome the limitations, existing by investigations of pellistor gas sensors, Differential Thermal Analysis (DTA) [2] can be used for preselection and investigation of possible catalyst materials [1]. The thermal response of a catalyst powder induced through oxidation of target gas can be measured and used for direct comparison of different catalysts.

Here, we demonstrate DTA investigations on the impact of particle size and morphology of Co_3O_4 catalysts on their thermal response to CH_4 oxidation and the thermal stability as well as the effect of H_2S exposure. The pellistor response of Co_3O_4 related catalyst deposited on MEMS-based hotplate sensor [3] to CH_4 and H_2S is shown for comparison. The focus of the examinations was on lower operation temperatures (<400°C). Spinel Co_3O_4 is used for investigations due to its promising catalytic properties for CH_4 combustion [4].

Description of the New Method

The commercially available DTA device (NETZSCH, STA 409) was adapted for the investigation of catalyst´s gas reaction at dry conditions. The DTA signal is measured as voltage signal normalized to sample weight (µV/mg) and correlates with the temperature difference between empty reference and sample crucible resulted from a heat release or heat uptake. If heat is released (exothermic oxidation reaction) the DTA signal shows a negative output.

Results

In order to investigate the impact of particle size and morphology on the thermal response, wet

grinded commercial Co_3O_4 with spherical nanoparticles and Co_3O_4 synthesized by precipitation exhibiting nanoparticles of random shape were used for investigations. Fig. 1 illustrates the DTA response of commercial Co_3O_4 in comparison to the synthesized one to the exposure of 1 vol. % CH_4 for 30 min at different temperatures. While the commercial Co_3O_4 shows a pronounced activity firstly at 450°C, the synthetized Co_3O_4 with particles of random shape exhibits already at 350°C a considerable response. For both catalysts, the thermal stabilty test (synthetic air/methane alternation at 350°C and 450°C) were undertaken. The synthetisized Co_3O_4 exhibits a slighly lower thermal stability than commercial one originated from operation at high temperatures (450°C).

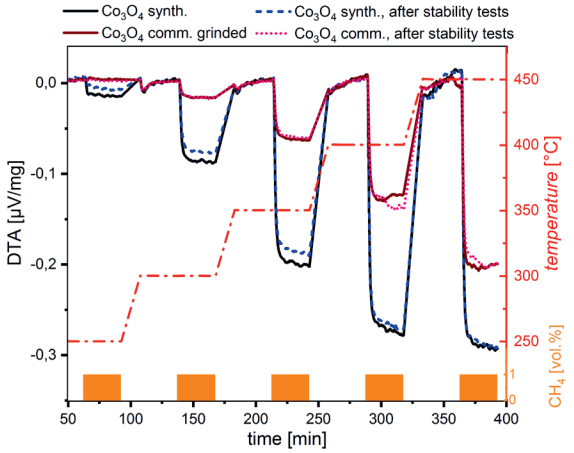

Fig. 1. DTA response to the exposure of 1 vol.% CH_4 in dry air for 30 min at temperatures between 250-450°C for two different Co_3O_4 catalysts before and after thermal stability investigations.

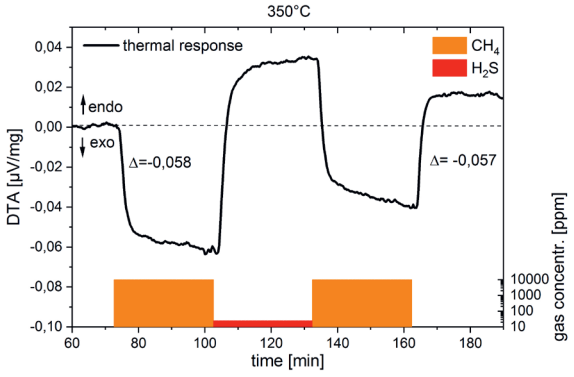

Fig. 2. DTA response of commercial Co_3O_4 catalyst to the exposure of 1 vol.% CH_4 and 25 ppm H_2S in dry air for 30 min each at 350°C. A purge with synthetic dry air for 30 min was used to achieve a base line.

Furthermore, the effect of H_2S exposure on thermal response of commercial Co_3O_4 catalyst to methane was examined (Fig. 2). In particular, when H_2S is introduced into the chamber after methane, the positive output is observed, which indicates the endothermic reaction taking place on the catalyst. When CH_4 is introduced directly after H_2S, the same signal output as before H_2S exposure is obtained with some baseline drift evidencing that short H_2S exposition times have no effect on the catalytic reaction. The same thermal behavior towards CH_4 and H_2S was observed by testing of Co_3O_4 related catalyst in pellistor (Fig. 3), with exception of the baseline shift. In pellistor measurements, the positive output corresponds to the exothermic oxidation of CH_4.

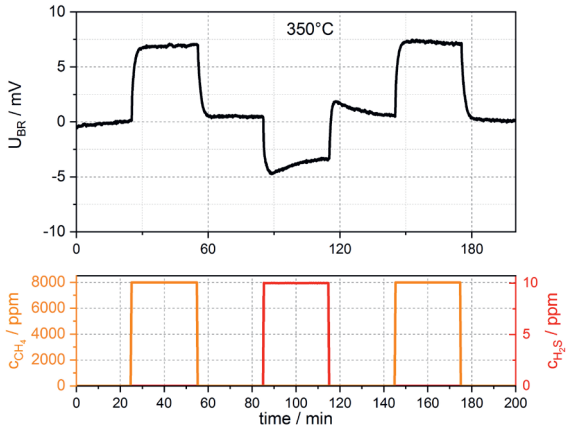

Fig. 3. Pellistor sensor output to 8000 ppm CH_4 and 10 ppm H_2S in dry air at 350°C for Co_3O_4 related catalyst.

The obtained results illustrate the applicability of DTA measurements for previous testing of catalysts offering many opportunities for further investigations.

References

[1] O. Yurchenko, H.-F. Pernau, L. Engel, B. Bierer, M. Jägle, J. Wöllenstein, Systematic Investigations on the Reaction Potential of Catalytic Sensor Materials, *SMSI 2020 Proceedings*, 201–202 (2020); doi: 10.5162/SMSI2020/P1.4

[2] P. Le Parlouër, Thermal Analysis and Calorimetry Techniques for Catalytic Investigations. In: A. Auroux (eds.) Calorimetry and Thermal Methods in Catalysis, Springer Series in Materials Science, vol. 154 (2013); doi:10.1007/978-3-642-11954-5_2

[3] B. Bierer, D. Grgic, O. Yurchenko, L. Engel, H.-F. Pernau, L. Reindl, J. Wöllenstein, Wireless low-power warning system for the detection of flammable gases *SMSI 2020 Proceedings*, 121–122 (2020); doi: 10.5162/SMSI2020/B4.3

[4] Z. Pu, H. Zhou, Y. Zheng, W. Huang, X. Li, Enhanced methane combustion over Co_3O_4 catalysts prepared by a facile precipitation method: Effect of aging time. Appl. Surf. Sci. 410, 14-21 (2017); doi:10.1016/j.apsusc.2017.02.186.

DOI 10.5162/SMSI2021/B6.1

Improved Gas-liquid Flow Meter Using a Neural Network

Aluísio do Nascimento Wrasse[12], Eduardo Nunes dos Santos[12], Rigoberto E. M. Morales[2], Marco Jose da Silva[12]
[1] Department of Electrical Engineering (CPGEI), Federal University of Technology – Paraná (UTFPR), Curitiba, Brazil,
[2] Multiphase Flow Research Center (NUEM - UTFPR), Curitiba, Brazil
mdasilva@utfpr.edu.br

Summary:
This paper presents an improved gas-liquid flow rate meter based on gas fraction, pressure drop measurements, and an Artificial Neural Network (ANN). The available database comprises 416 sets of data, in which 50% is applied to train, 10% to validate and 40% to test the ANN. We evaluated the performance of the network considering 10 neurons at the hidden layer. Quantitative results are presented, regarding gas and liquid flow rate estimation, showing significant improvements compared to a previous methodology based on algebraic approximations.

Keywords: gas-liquid flow, flow rate measurement, gas fraction, pressure drop, artificial neural network

Introduction

The knowledge of parameters such as phase fractions and phase flow rates is necessary for control and optimization strategies in petroleum production and processing. Multiphase inline flow meters (MPFM) have been proposed to measure the flow rate of individual phases (e.g. gas and oil) by applying several technologies, among others for instance through arranging different sensors in the pipeline and applying correlation models to obtain the desired parameters. Artificial Neural Networks (ANN) are used in a variety of problems occurring either in research or in the industry [1]. Here, we describe the application of an ANN to reduce the uncertainty of a previously presented MPFM, as a first step towards an intelligent calibration routine since only a few parameters are required to train the neural network.

Gas-liquid Flow Rate Meter

In our earlier work, a gas-liquid flow rate meter [2] was introduced with the purpose of being simple and having no dependency on reference measurements or on calibration procedures as is usual for other solutions. Hence, the flow rate meter considers simple and direct algebraic approximations (AA) to compute gas and liquid superficial velocities (J_G and J_L) based on capacitance readings of the twin sensor, pressure drop fluctuations through a Venturi tube and, pressure and temperature information, as summarized in Fig. 1. For details on implementation and results, please refer to [2].

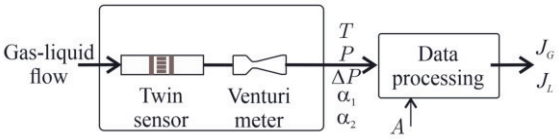

Fig. 1. Schematic illustration of the gas-liquid flow meter [2].

We chose the superficial velocity J as the target parameter because it is a more usual and general parameter than flow rate, considering that it is independent of the pipe diameter, as J is the ratio of the phase volumetric flow rate to the pipe cross-section area.

Experimental Database

The gas-liquid flow meter proposed in [2] was tested in a horizontal test bench located at NUEM/UTFPR, Brazil. A total of 416 experimental points were measured during 60 seconds in a 1-inch pipe inner diameter. Most of the experimental points developed slug flow regimes. The database comprises average parameters of the acquisition interval such: the cross-sectional gas fraction α of the capacitive sensor; the gas mean velocity v_G; the pressure fluctuations ΔP through a Venturi tube; pressure and temperature information of the two-phase mixture and, reference values of gas and liquid flow rate.

Artificial Neural Network

In this work, we apply an ANN in the data processing step, represented in Fig. 1, to accomplish the computation of the gas and liquid flow rate. The ANN reproduces the Levenberg Mar-

quardt algorithm with backpropagation to propagate errors from the output layer back to the input layer by a chain rule. This process performs adjustments of its synaptic weights and bias levels in the learning process through an iterative process. The ANN configuration, represented in Fig. 2 has (i) 2 inputs: phase fraction readings and pressure fluctuations ΔP (ii) 10 neurons at hidden layer and (iii) 2 outputs, as gas and liquid flow rates. The mapping between input parameters and target data is performed throughout layers of neurons with a non-linear sigmoid activation function. As a common practice in neural networks, we divided the database into training, validation and test datasets. Since the targets are a function of only two parameters, it seems not to be a complex task to fit the model. Thus, we use only 50% of the database for training, keeping in mind that the selected data have to cover the full range of targets. With the hypothesis that the model will have few hyperparameters and, consequently it will be easy to validate and tune it, we can reduce the size of the validation dataset and have a good amount of data for testing and comparison with our results presented in [2]. Therefore, we split the rest of the database into 10% for validation and 40% for testing.

Results

The performance of the proposed ANN is analyzed based on the root mean-squared deviation (RMSD) of the output values relative to the target parameters. The results are an RMSD for training, validation and testing data of 0.0508, 0.0555 and 0.0463 m/s, respectively. In Fig. 3 we show the results for testing data - 166 operating points. Dotted lines represent a deviation of 10%. We also compare the same operating points with the AA result from our previous work [2]. As one can notice, the flow rate estimation was clearly improved by the proposed methodology, mainly for the lower range of liquid superficial velocity and for the higher range of gas superficial velocity. Quantitatively, the percent RMSD decreased from 16.2% to 8.6% for gas and from 18.1% to 5.4% for liquid flow rate.

Conclusions

In this work, we introduced an ANN-based method applied in a gas-liquid flow rate meter. The gas and liquid superficial velocities are mapped using only two measured parameters, the gas fraction and pressure drop through a Venturi tube. Ten neurons at the hidden layer, two at the output layer and 50% of the experimental basis were sufficient to achieve improvements in the gas and liquid flow rate estimation. Representing 7.6% and 12.7% of reducing in the RMSD%, for gas and liquid respectively. As a next step of the work, we aim to expand the proposed methodology to a larger database, in which fluid properties significantly change over the experimental points.

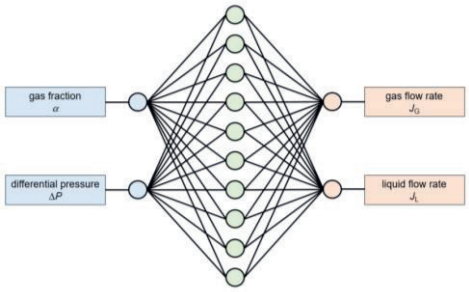

Fig. 2. Representation of the designed ANN to obtain gas and liquid flow rates.

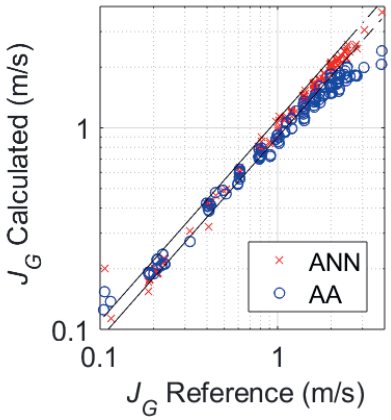

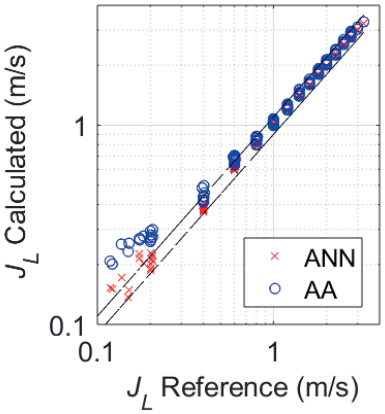

Fig. 3. Improved results of gas and liquid flow rate estimation based on the ANN model.

References

[1] Y. Yan, L. Wang, T. Wang, X. Wang, Y. Hu, and Q. Duan, "Application of soft computing techniques to multiphase flow measurement: A review," *Flow Meas. Instrum.*, vol. 60, pp. 30–43, Apr. 2018; doi: 10.1016/j.flowmeasinst.2018.02.017

[2] A. do N. Wrasse, D. Bertoldi, E. N. Dos Santos, R. E. M. Morales, and M. J. Da Silva, "Gas–Liquid Flow Rate Measurement Using a Twin-Plane Capacitive Sensor and a Venturi Meter," *IEEE Access*, vol. 7, pp. 135933–135941, 2019; doi: 10.1109/ACCESS.2019.2942772

DOI 10.5162/SMSI2021/B6.2

A hermetic sensor concept for measuring condensing fluid flows

Philipp Radler[1,2], Jan Ringkamp[1,2], Dr. Philipp Lebhardt[1], Dr. Jens Langejürgen[1]
[1] Fraunhofer IPA, Project Group for Automation in Medicine and Biotechnology, Group for Biomedical Sensors and Microsystems, Theodor-Kutzer-Ufer 1-3 (Cubex41), 68167 Mannheim, Germany
[2] Medical Faculty Mannheim, Heidelberg University, Theodor-Kutzer-Ufer 1-3, 68167 Mannheim, Germany

Summary:
We present a novel, fully encapsulated sensor concept, which is specially designed for the measurement of condensing gas flows. The sensor concept is based on the Magnus forces working on a magnetically levitated and rotated cylinder at high speeds. Our first experimental results have successfully shown the feasibility of this sensor concept.

Keywords: Magnus effect, flow sensor, condensing gas flow, high humidity, hermetic sensor

Introduction

Robust gas and liquid flow measurement is a crucial requirement for production-related industries as well as in medical applications. Despite the wide range of available sensors, in applications where condensing or corrosive gas flows need to be measured, the range of available sensors narrows down significantly. Water droplets that accumulate on a sensor element i.e. of MEMS or dP-Sensors often negatively affect accuracy or lead to complete malfunction of the sensor. In this paper, we present a novel flow sensor concept based on the Magnus effect. A major advantage of this approach is that the sensor element is in constant rotation and thus robust against influences of condensation on the sensor surface. In addition, it allows a fully encapsulated construction of the sensor with a single-use sensor element with magnetically coupled driver and read-out. With these features, the sensor concept is suitable for medical applications and for the use in corrosive media.

Materials and Methods

Measurement principle:

Figure 1 illustrates a gas flow from bottom to top through a tube around a cylinder, which is rotating at an angular velocity ω. This results in the two forces F_D and F_M that work on the cylinder. The first is in the direction of the flow caused by drag. The second is due to the Magnus effect that acts orthogonally to the flow velocity vector and can be described as:

$$F_M = S(\omega \times v)$$

S is the air resistance coefficient across the surface of the cylinder. Both forces would lead to a displacement of the cylinder off its rotating axis. The aim is to drive the cylinder and measure these forces with our proposed sensor concept.

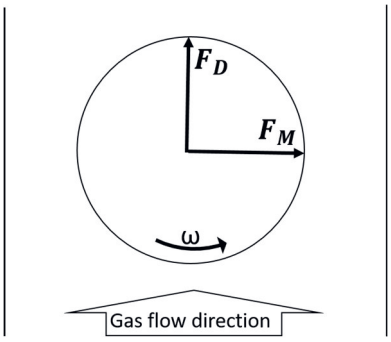

Fig. 1. Magnus (F_M)and drag (F_D) forces on a rotating cylinder with angular velocity ω

Sensor concept:

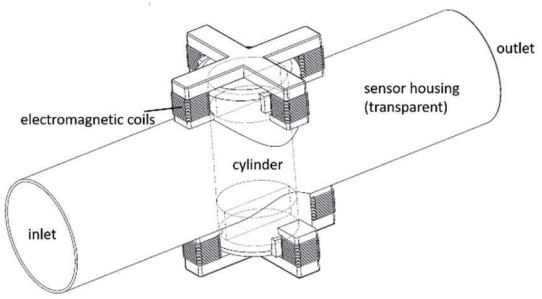

Fig. 2. Magnus sensor concept (overview)

Figure 2 and 3 illustrate the sensor concept. The sensor element consists of a cylinder that has

two magnets integrated on either end. This cylinder is fully encapsulated by a sensor housing, which guides the gas flow from the inlet around the cylinder to the outlet. The cylinder is being levitated and rotated by multiple electromagnetic coils that are placed around the poles of the cylinders permanent magnets. Additional sensors measure the current angle and displacement of the cylinder. The individual coil currents are controlled such that the cylinder is levitated in the center and driven at a variable rotational speed.

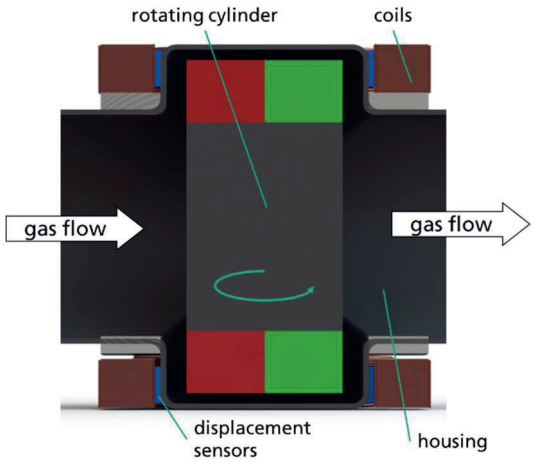

Fig. 3. Magnus sensor concept (cross-section)

Experimental Setup:

We used an existing medical rotary pump with displacement sensors and electromagnetic coils. We replaced the pump impeller by a 3D-printed cylinder and pump housing accordingly. We built a custom electromagnetic driver and implemented a custom PID-controller on an embedded microcontroller (TI, TMS320F28379D). This system controls the levitation and rotation of the cylinder. The inlet of the Magnus sensor was connected through a reference flow meter (Sensirion, SFM3000) to a gas source (pressurized air). The sensor signal is derived from the force that is necessary to counteract the respective Magnus and drag forces.

Results

First results in Figure 4 show the forces working on the cylinder rotating at 5000RPM as a result of Magnus and Drag forces. Combining these two forces yields a linear resultant force signal that is proportional to the fluid flow.

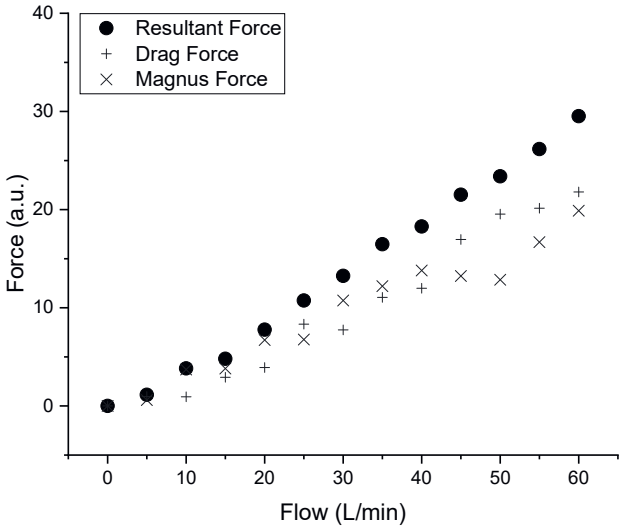

Fig. 4. Force signal for varying volume flows of 0-60 L/min at a rotational speed of 5000RPM

Discussion

Our first experiments have successfully shown that it is possible to independently measure Magnus and Drag forces imposed on a cylinder by a gas flow with the proposed hermetic setup. The achievable sensitivity and resolution of the sensor is currently limited because of the relatively large dimensions of the setup. A dedicated coil geometry is expected to increase resolution and linearity significantly.

The presented sensor can be constructed as two separate parts. The more expensive driver electronics can be reused and have no parts prone to failure because none of them are mechanically moving or in contact with the fluid. The second unit is a low cost, fully encapsulated, single-use unit consisting of the rotating cylinder and housing. This enables the elimination of any possible cross contamination and maximizes sterility.

DOI 10.5162/SMSI2021/B6.3

Towards standalone attitude estimation for instrumented flow followers

Lukas Buntkiel[1], Sebastian Reinecke[1], Uwe Hampel[1,2]
[1] Helmholtz-Zentrum, Dresden-Rossendorf (HZDR), Bautzner Landstr. 400, 01328 Dresden,Germany,
[2] Chair for Imaging Techniques in Energy and Process Engineering, Technische Universität Dresden, 01062 Dresden, Germany
l.buntkiel@hzdr.de

Summary:
A concept for 3D-motion tracking of instrumented flow-following sensor particles, equipped with a gyroscope, accelerometer, magnetometer and pressure sensor, has been developed. Consisting of an error state Kalman filter (ESKF) the algorithm can track the attitude of the sensor particle in relation to a reference coordinate system. In this short paper we investigated if the estimated attitude returns to the reference trajectory after experiencing motion similar to a motion that is expected to be found in the multidisperse fluid flows of a biogas fermenter or a waste water treatment basin. Results show the feasibility of the proposed method. However, the strategy of the measurement update in the ESKF needs improvement.

Keywords: error state kalman filter, motion tracking, fluid dynamics, sensor particle, soft sensor

Motivation

The investigation of the fluid flow in large-scale plants or vessels like biogas fermenters or activated sludge tanks, is limited because currently applied instrumentation only measures locally. To optimize the use of energy and resources in such plants, the flow patterns inside the vessels need to be known. To overcome the limitations of local sensors, the concept of instrumented flow-following sensor particles has been developed at HZDR [1].

The aim is, to recover the acceleration, velocity and position of the sensor particle in the vessel over time, to track the flow pattern. Therefore, sensor particles are equipped with an accelerometer, a gyroscope, a magnetometer and a pressure sensor. Since the measurements are taken in body coordinates, the reconstruction of the attitude of the sensor particle in relation to the vessel is of fundamental importance. An absolute attitude is obtained by combining the measurement of acceleration due to gravitation and earth magnetic field aiding the attitude calculated from the measured angular velocity.

In this short paper, we show that an error state Kalman filter (ESKF) as presented in [2] can be used to estimate the attitude of the sensor particle after an experienced motion with a maximum angular velocity of 55.7 °/s and a maximum acceleration of 13.2 m/s².

Method

To investigate the developed algorithm, a customized inertial measurement unit (IMU) was build from an accelerometer ADXL355, a gyroscope IAM-20380, a magnetometer MMC5883MA and an Arduino Due. The IMU was strapped to a hexapod, as shown in fig. 1.

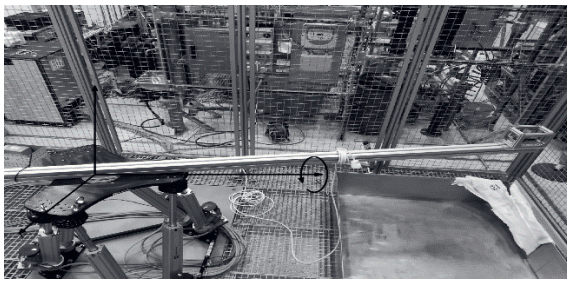

Fig 1: Experimental setup for a circular motion of sensor particles on a hexapod. The length of the arm was 195 cm.

The setup measures body acceleration, angular velocity and the earth magnetic field with a sampling rate of 500, 250 and 100 Hz, respectively and then low pass filtered with a cutoff frequency of 5 Hz. To use the local magnetic field as an aiding attitude element, a proper calibration of the magnetometer data was performed by using the initial parameter estimation for the bias and misalignment of the algorithm described in [3]. The local magnetic field reference was taken at the initial position (φ = 15 °) and was $\boldsymbol{B_0} =$

$[-12.5\ 26.6\ 23.6]$ nT. The bias of the inertial sensors was obtained by taking the mean over 5 seconds when the IMU was at rest. The inertial sensors noise characteristics was identified with the allan variance method [4].

All these quantities were then used by the ESKF to estimate the attitude in vessel coordinates.

As an example of an expected motion in agitated vessels, such as biogas digesters, a circular motion in the y-z-plane of radius 0.5 m was chosen. The motion was generated by manipulating the angles yaw (φ), pitch (θ) and roll (ψ) with a sinusoidal signal with a frequency of 0.25 Hz (φ, θ) and 0.40 Hz (ψ) and a magnitude of 15 °, 15 ° and 20 °. One motion cycle had a duration of 60 seconds with an appended pause of 12 s. This motion was repeated for 20 times. The resulting angular movement for 2 cycles is depicted in fig. 2. The ESKF was intended to perform the measurement update in the pause of the motion as soon as the norm of the measured acceleration and the norm magnetic field deviated less than 0.001% to gravity and the norm local magnetic field, respectively.

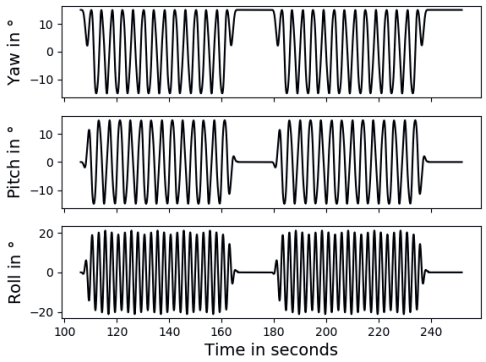

Fig 2: Extract of the attitude reference trajectory in Euler angles.

Results

To evaluate the quality of the attitude estimation, the error between the reference trajectory and the estimated trajectory and the raw integrated angular velocity, respectively are shown in fig. 3. It is evident, that the raw integrated angular velocity drifts off from the reference trajectory since the error is not symmetric with respect to the reference. The filtered result from the ESKF does not show this drift. But the error margin is still too large with a maximum deviation of Δφ=19 °, θΔ=14.3 °, Δψ=23.5 ° to obtain a valid velocity or position from the measured acceleration. Due to noise and changes of the local magnetic field in the area of motion the updates were sometimes performed at the period at the motion and not only in the pause. This then leads to a wrong attitude. The filter corrected this in the next pause.

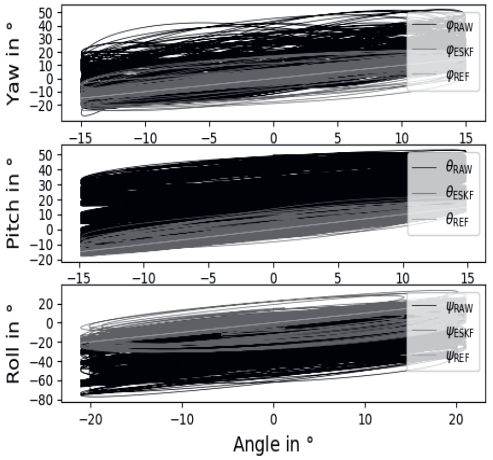

Fig 3: Error of the estimated attitude for each Euler angle.

Conclusion

The motion-tracking algorithm introduced in [2] can reconstruct the attitude of the sensor particle in relation to the vessel. This allows to calculate the acceleration in vessel coordinates and, due to the pressure sensor, allows a statistical analysis of the vertical acceleration profile. Further development will focus on a better calibration and noise estimation of all sensors. Also, we aim to develop a proper strategy for the measurement update since we expect disturbances of the magnetic field next to deviation of gravity and measured acceleration.

Acknowledgments

This research is part of the project ‘NeoBio’ funded by the Federal Ministry of Food and Agriculture under the funding code FKZ 22032618.

References

[1] Thiele, S., Da Silva, M. J., & Hampel, U. (2010). Autonomous sensor particle for parameter tracking in large vessels. *Measurement Science and Technology*, *21*(8), 085201.

[2] Buntkiel, L., Reinecke, S. F., & Hampel, U. (2019). 3.5-Inertiale Lage-und Bewegungsverfolgung für instrumentierte Strömungsfolger zur Strömungscharakterisierung. *Tagungsband*, 52-58, DOI: 10.5162/14dss2019/3.5.

[3] M. Kok and T. B. Schön, "Magnetometer Calibration Using Inertial Sensors," in *IEEE Sensors Journal*, vol. 16, no. 14, pp. 5679-5689, July15, 2016, doi: 10.1109/JSEN.2016.2569160.

[4] N. El-Sheimy, H. Hou and X. Niu, "Analysis and Modeling of Inertial Sensors Using Allan Variance," in *IEEE Transactions on Instrumentation and Measurement*, vol. 57, no. 1, pp. 140-149, Jan. 2008, doi: 10.1109/TIM.2007.908635.

DOI 10.5162/SMSI2021/B6.4

Spectral response of MEMS plate resonators exhibiting non-conventional vibrational modes in fluids

Daniel Platz[1], *André Gesing*[1] *and Ulrich Schmid*[1]
[1]*TU Wien, Institute of Sensor and Actuator Systems, Gußhausstraße 27-29, 1040 Vienna, Austria*
daniel.platz@tuwien.ac.at

Summary:
Understanding of the fluid-structure interaction between a MEMS resonator and a surrounding fluid is key for understanding and predicting the dynamics of MEMS resonators in fluids. Here, we present a numerical method for modelling the fluid-structure interaction between a viscous fluid and vibrational eigenmodes of a plate-like MEMS resonator. The dynamics of the MEMS resonator is determined using a finite element method while the fluid flow is obtained from a boundary integral formulation. With this method we compute the spectral response of MEMS plate resonators in fluids.

Keywords: fluid sensing, MEMS resonators, fluid-structure interaction, finite elements, simulation

Background, Motivation an Objective

The characterization of fluid properties like density or viscosity is a focal area in fluid sensing. Density and viscosity sensors based on micromechanical systems (MEMS) have the potential for widespread use in various applications, like the monitoring of technical fluids like motor oil or medical diagnosis in lab-on-chip systems, due to their low-production cost and high integrability in complex sensor systems. The measurement of fluid properties requires an interaction between the MEMS sensor and the fluid environment. Such an interaction is readily established by exciting a vibrational eigenmode of a MEMS resonator. MEMS resonators often exhibit relatively simple geometries like cantilever beam structures. A typical vibrational eigenmode of a cantilever beam structure is shown in figure 1a. Advantages of beam structures are that they can be relatively simple fabricated and that their vibrational eigenmodes are readily modeled with Euler-Bernoulli beam theory. However, the quality factor of beam-like MEMS resonators is usually very low in liquids. This implies that reliable measurements of fluid properties are often difficult or even not feasible, especially in highly viscous fluids. A possible solution to this problem is the use of vibrational modes which are commonly not considered for fluid sensing. An example of such a non-conventional mode is depicted in figure 1b. These non-conventional vibrational modes exhibit extraordinary high quality factors in fluids [1, 2] which allows for measurements even in highly viscous fluids. Quality factors can be directly determined from the spectral response of a MEMS resonators in fluids. However, a method for quantitatively predicting the spectra of MEMS resonators exhibiting non-conventional modes in fluids has been missing. Here, we introduce a numerical method for determining this spectral response by numerically computing the fluid-structure interaction between non-conventional vibrational modes and a surrounding fluid.

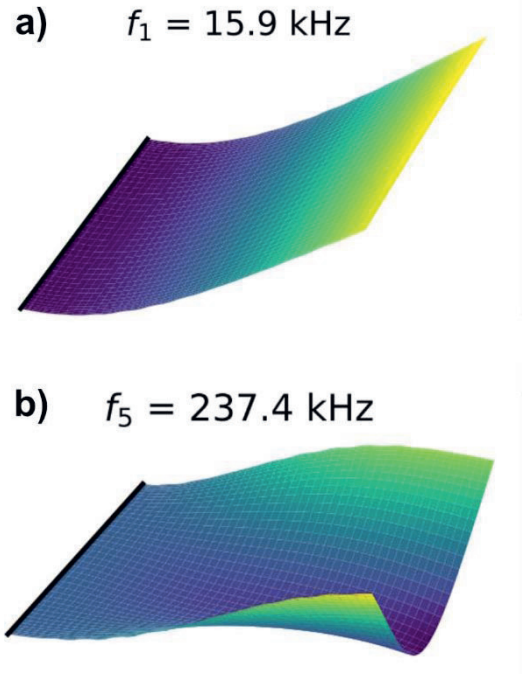

Fig. 1. Numerical simulation of vibrational eigenmodes of a cantilevered plate resonator clamped at the right edge (marked by thick black line). The mode in (a) is also observed in one-dimensional

beam structures whereas the mode in (b) can only be found in two-dimensional structures.

Description of the Method

Two components are required for modelling the fluid-structure of non-conventional eigenmodes: the elastic dynamics the resonator and the flow of a viscous fluid around the resonator. While the elastic dynamics of conventional eigenmodes are well described by Euler-Bernoulli beam theory, the two-dimensional character of non-conventional mode requires the use of Kirchhoff-Love plate theory. To solve the underlying Kirchhoff-Love plate equation we use a continuous/discontinuous finite element method. This method allows for weakly imposing to the solution both the boundary conditions of a cantilevered structure and the physically motivated continuity conditions.

For MEMS resonators in the kHz regime the fluid flow is approximated as a Stokes flow of a viscous incompressible fluid. Moreover, due to the kinematics of non-conventional modes in slender cantilever structures, the fluid flow can be considered as approximately two-dimensional. We employ a two-dimensional stream function description of the fluid flow in planes parallel to the clamped edge of the resonator as depicted in figure 2. This description yields a boundary integral which we solve numerically.

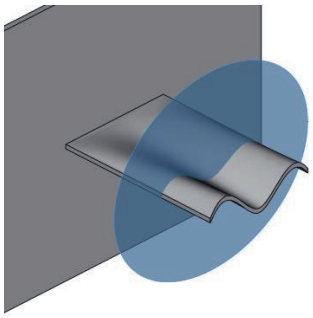

Fig. 2. Non-conventional mode of a cantilevered MEMS resonator. The blue disk indicates the plane of two-dimensional fluid flow.

Using this approach, we are able to determine the spectral response of non-conventional modes of MEMS resonators while taking into account two-dimensional plate dynamics. This has not been possible with conventional methods since most conventional methods are only applicable to one-dimensional beam modes of MEMS resonators [3].

Results

We apply the proposed method to a cantilevered plate resonator with a size of 300 × 300 × 5 µm^3 immersed in water. The plate is excited at one of its free corners with a force of 1 µN and we compute the amplitude spectrum at this corner using the method described above. The resulting spectral is shown in figure 3 (orange line). To compare our results with conventional theory we also plot the corresponding results based on beam theory (blue line). The peak at the lowest frequency is the fundamental flexural mode which is predicted by both beam and plate theory. Both curves thus coincide. The second peak is a torsional mode not described by Euler-Bernoulli beam theory. This mode is only predicted by the plate-based theory. The peak at 100 kHz corresponds to the second flexural mode and consequently both methods agree again with each other. The mode at 237 kHz is the non-conventional mode shown in figure 1b and its response can only be predicted with the proposed method.

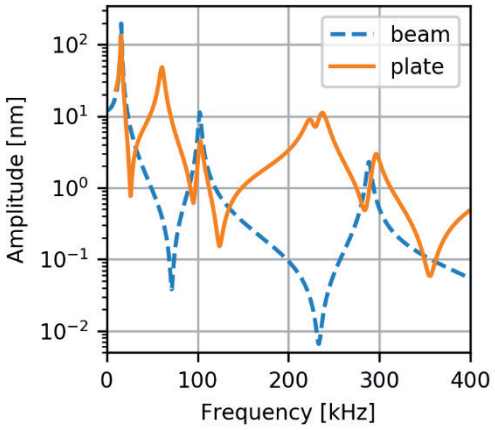

Fig. 3. Spectral response of a MEMS resonator immersed in water using beam and plate theory.

Conclusion

We present a method for modelling the fluid-structure interaction of MEMS plate resonators. With this method we are able to predict the spectral response of non-conventional modes of MEMS resonators in liquids. These spectra pave the way for quantitative measurements of fluid properties and novel designs of fluid sensors which go beyond one-dimensional beam geometries.

References

[1] Kucera, M. et al. Characterisation of multi roof tile-shaped out-of-plane vibrational modes in aluminum-nitride-actuated self-sensing micro-resonators in liquid media. Appl. Phys. Lett. 107, 053506 (2015).

[2] Pfusterschmied, G. et al. Temperature dependent performance of piezoelectric MEMS resonators for viscosity and density determination of liquids. J. Micromechanics Microengineering 25, 105014 (2015).

[3] Sader, J. E. Frequency response of cantilever beams immersed in viscous fluids with applications to the atomic force microscope. J. Appl. Phys. 84, 64–76 (1998).

DOI 10.5162/SMSI2021/B7.1

Highly stable pressure sensors made of <110> silicon

Th. Frank, R. Röder, S. J agomast, H. Übensee, A. Cyriax, Th. Ortlepp
Forschungsinstitut für Mikrosensorik GmbH, Konrad-Zuse-Straße 14, 99099 Erfurt, Deutschland,
tfrank@cismst.de

Summary:
A pressure sensor chip of <110> p-silicon is described. The piezoresistive measuring resistors run, in <110> direction. They have only a noticeable longitudinal effect. This is the first prerequisite for an ideal mirror-image arrangement of a measuring bridge. Thus it is possible to achieve an ideal symmetrical change in resistance due to the compressive load. These sensors were manufactured, the effectiveness is presented.

Keywords: silicon, piezoresistive, pressure sensor, stability, linearity

Highly stable pressure sensors made of <110> silicon

For miniaturized sensors based on silicon and MST technologies, the piezoresistive measuring principle has proven to be versatile and robust. The measuring principle is of great importance for pressure sensors. The basic structure of silicon-based, piezoresistive pressure sensors is well known. The integrated piezoresistive measuring resistors react to strain or mechanical stress. Therefore, they are integrated in a bending plate, which changes its mechanical stress state pressure-dependent in a very selective way. The measuring resistors are arranged as a measuring bridge to increase the sensitivity and to compensate the temperature dependence.

For high-precision pressure measuring cells, the effort for calibration over the entire application range is approx. 20-30 % of the manufacturing costs. Especially the nonlinear dependencies of the measurement signal on pressure and temperature lead to this high effort. Thus these costs exceed the chip price many times over. Therefore it makes sense to reduce especially these costs. If e.g. the linearity is increased, a reduction of the degree of the polynomial, this expenditure is reduced substantially. This means there are less calibration points, less pressure-temperature pairs, necessary for calibration. Further possibilities are to reduce the effort for signal processing:

- Temperature coefficient of the zero point
- Temperature coefficient of the measuring span
- Influence of the mechanical mounting stresses

One starting point is the optimization of the measuring bridge, which means that an ideally designed measuring bridge compensates all influencing variables which are identical at all four measuring points. Most silicon-based, piezoresistive pressure sensors consist of p-type measuring resistors in an n-type substrate of orientation <100>. The measuring resistors are sensitive in longitudinal and transverse direction in relation to the flowing current. These properties result in the classical arrangement of the measuring resistors on the bending plate of silicon-based piezoresistive pressure sensors. Since the piezo coefficients of the magnitude are only similar and not identical in the mechanical stress field, the selection of a suitable design is accordingly complex and often cannot be optimized over the entire measuring range. This can be seen in the linearity of the pressure characteristic curve and the temperature dependence of the measuring span. In this paper an almost completely symmetric bridge design shall be investigated. For this purpose p-type measuring resistors in an n-type substrate of orientation <110> are used.

Fig. 1 shows the direction dependent piezo coefficients of <110> p-silicon, the transversal effect in direction <110> is minimal.

DOI 10.5162/SMSI2021/B7.1

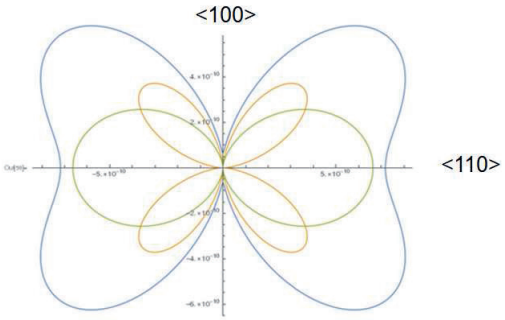

Fig. 1: Directional piezo coefficient of <110> p-silicon, longitudinal effect (σ_{xx}): $\pi_{l(110)}$ and the transverse effect (σ_{yy}): $\pi_{t(110)}$, blue: directional longitudinal effect (for σ_{xx}), orange: directional transverse effect (for σ_{yy}), green: directional transverse effect (for σ_{zz})

If the measuring resistors are oriented in the direction <110> only the longitudinal effect is effective, a completely symmetrical layout can be realized. First measurements on a demonstrator show that the system has a good linearity and a good long term stability.

DOI 10.5162/SMSI2021/B7.2

Influence of the Gas Velocity on the Temperature Homogeneity of Transducers for Gas Sensors

Julia Herrmann, Thomas Kern, Gunter Hagen, Ralf Moos
Department of Functional Materials, University of Bayreuth, D-95440 Bayreuth, Germany

Abstract

High-temperature gas sensors need homogeneous heating in the functional sensing area. Varying gas flow characteristics lead to cross-effects and signal instability. Utilizing a special sensor transducer, these effects can be proven experimentally. FEM modelling further supports the understanding. Proper protection caps solve cross-sensitivity problems but also cause decreasing sensor response.

Keywords: Exhaust gas sensors, Thermoelectric gas sensors, FE simulation.

Introduction

Gas sensors provide necessary information in several processes of daily life. Air quality measurements for safety reasons, exhaust gas detection for controlling aftertreatment systems or for on-board-diagnosis, evaluation of flue gas in biomass combustion processes for modern energy technology but also medical breath analysis require stable and reliable sensor signals. Most chemical sensors therefore must be operated at defined temperatures.
In fact, this temperature has to be homogeneous over the whole sensor area (i.e. that region of the sensing element, where the gas interacts with the applied gas sensitive functional materials) and may not be influenced by external parameters like, e.g., gas velocity. The temperature and its homogeneity must be kept constant also during dynamic changes of the environmental conditions, i.e. in all possible working points.
On the other hand, gas contact is highly desired for both fast response and high sensitivity. In the present contribution, general aspects concerning sensor housing and heating are highlighted. Basically, for experimental investigations, a thermoelectric sensor device is used which is an ideal candidate to identify typical problems. As well, simulations were made to verify the results.

Setup: Sensor and Experiments

The here used sensor transducers are derived from thermoelectric hydrocarbon sensors, developed for automotive exhaust measurements [1] and investigated also in the flue gas of wood burning processes [2]. The sensor measures a temperature difference between two areas within the sensor tip and therefore gives a direct measure of the temperature homogeneity in the interesting region (fig. 1).

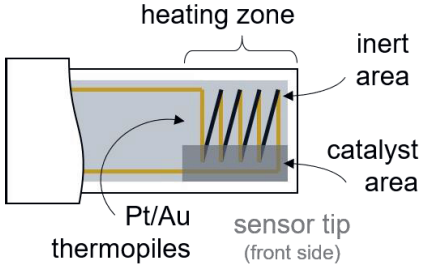

Figure 1: Sketch of the sensor tip.

If one of these areas is catalytically activated and the other region is covered by an inert layer, exothermic reactions generate a temperature gradient between both areas. This gradient is measured by serially connected screen-printed thermopiles in form of a thermovoltage in the µV-range. Without test gas, temperature gradients (coming from changing flow conditions any kind of inhomogeneous heating or thermal flow) are measured as well. In former work, it was shown that laminar and symmetric flow characteristics around the sensor tip might avoid cross sensitivities [3]. Here, the described thermoelectric sensors are operated at 600 °C. This absolute sensor temperature is adjusted with a thick-film heater, connected in four-wire technique and located on the reverse side of the substrate. The four-wire resistance is kept constant and so is also the temperature on the reverse side. To evaluate the gas flow

influence on the front (sensing) side of the substrate, measurements were conducted with different flow rates (compressed air, gas flow directly facing the sensors front side) and under variation of the mounting position (rotating the sensor by a defined angle concerning the gas flow direction) as well as the use of different housings.
Finite-Element-Simulations were made with COMSOLMultiphysics. The here presented data show the gas velocity distribution, regarding the effects around and inside a porous (sintered metal) protection cap (fig. 2). Test gas measurements with propene (C_3H_6) show the influence of this protection cap concerning the gas flow but also sensitivity.

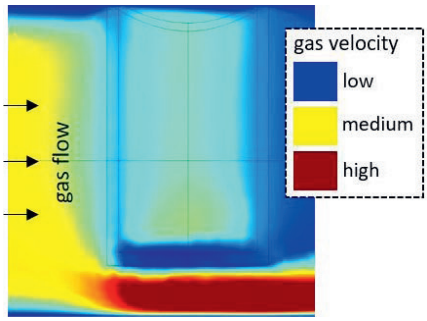

Figure 2: FEM-modelling of the gas flow characteristic around the housed sensor tip.

Results and Conclusions

In a first experiment, sensors were operated in different gas flows without a protection cap. The gas flow varied between 0 and 50 l/min in a tube of 1" diameter. Sensors were mounted from above ("hanging") with its front side facing the gas flow. Even here, within the sensor tip temperature differences of 5 °C occure. It gets worse by rotating the sensor orientation +/- 45° (gradients up to 20 °C), coming from non-symmetric cooling effects. By using a porous protection cap around the sensor, this influence is minimized (< 0.5 °C) due to low and more homogeneous gas velocities inside the cap (fig. 2). Secondly, the sensor results were measured with admixing test gas (mounting in 0°-position, i.e. directly facing the gas flow, but under 20 and 40 l/min). Results were evaluated regarding the sensor sensitivity *S*, with is the slope in the characteristic curve (fig. 3). It could be shown that without the protection cap, both parameters – the gas flow as well as the test gas concentration – influence the sensor signal in similar height. Using the cap, the gas flow influence can be avoided, but a loss in sensitivity must be taken into account. Reasons therefore could be heterogeneous catalytic effects on the cap surface or transport controlled diffusion through the porous cap. Several other types of protection caps were also tested and simulated. It is necessary to find an ideal configuration for sensor mounting, heater design and protection cap depending on the particular application.
These findings should be transferred to all other kinds of chemical gas sensors where flow characteristics and heating play a role. Temperature gradients on the sensors surface influence directly all mechanistic processes in resistive, amperometric, mixed-potential or potentiometric type sensors.

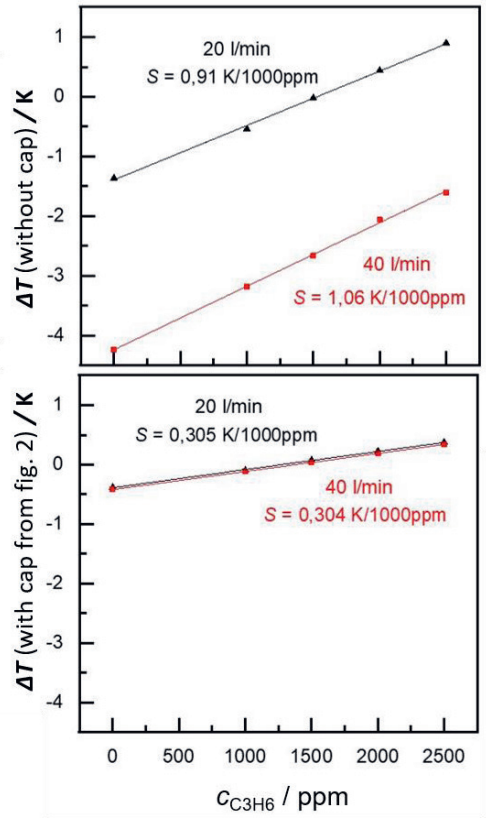

Figure 3: Sensor characteristic with and without cap depending on the gas flow.

References

[1] S. Wiegärtner, G. Hagen, J. Kita, W. Reitmeier, M. Hien, P. Grass, R. Moos, Thermoelectric hydrocarbon sensor in thick-film technology for on-board-diagnostics of a diesel oxidation catalyst, Sens. Act. B, 214 (2015) 234–240. doi: 10.1016/j.snb.2015.02.083.
[2] B. Ojha, G. Hagen, H. Kohler, R. Moos, Exhaust Gas Analysis of Firewood Combustion Processes: Application of a Robust Thermoelectric Gas Sensor, Proceedings 1 (2017) 457. doi: 10.3390/proceedings1040457.
[3] G. Hagen, A. Harsch, R. Moos, A pathway to eliminate the gas flow dependency of a hydrocarbon sensor for automotive exhaust applications, J. Sens. Sens. Syst. 7 (2018) 79–84. doi: 10.5194/jsss-7-79-2018.

DOI 10.5162/SMSI2021/B7.3

Influences of the Microstructure on the Drift velocity of Electromigrating Aluminum through Molybdenum disilicide Thin films

Julia Baldauf[1], Martin Schädel[1]
[1] CiS Forschungsinstitut für Mikrosensorik GmbH, Konrad-Zuse-Straße 14, 99099 Erfurt, Germany, jbaldauf@cismst.de

Summary:
A difference of the drift velocity of aluminum could be observed for polycrystalline thin film conductor lines made of molybdenum disilicide with different grain sizes in the scanning electron microscope.

Keywords: electromigration, thin film

Background and Motivation

Because of its high melting point molybdenum disilicide ($MoSi_2$) [1] is often used in MEMS hotplates [2,3], which can be applied as IR light source in NDIR gas measurement systems. Electromigration and diffusion within the $MoSi_2$ or the materials of the electric contact pads through the resistive heating layer are reasons for device failures and limits for long term stability and life time [3]. Electromigration properties of $MoSi_2$ thin films are hardly investigated in the literature. Some findings described in [4,5,6] show the electromigration of aluminum of the electrical contact pads through $MoSi_2$ thin films, without giving detailed information about the drift velocity of the aluminum. Here we address the issue of the drift velocity of aluminum through molybdenum disilicide thin films. The knowledge of the drift velocity allows to make predictions of the life time of devices using molybdenum disilicide layers.

Experiments

A 70 nm thick layer of silicon oxide was grown on n-type silicon wafers were used as a substrate. A 500 nm thick layer of silicon nitride was deposited via low pressure chemical vapour deposition. A 100 nm thick layer of molybdenum disilicide was magnetron sputtered from a stoichiometric target without use of substrate heating at a pressure of $5x10^{-3}$ mbar.

The molybdenum silicide layer was annealed under different conditions shown in Table 1.

Tab. 1: Annealing conditions

Sample	Atmosphere: temperature (time)
A	100% N_2: 500°C (60 min) + 900°C (120 min)
B	100% H_2: 500°C (60 min) + 800°C (60 min) + 900°C (120 min)
C	100% N_2: 500°C (60 min) + 800°C (60 min) + 900°C (120 min)
D	100% H_2: 500°C (60 min)

The resulting crystal structure was analyzed via electron backscatter diffraction (EBSD). For samples A, B, and C the annealing caused the amorphous molybdenum silicide layer to transform into a polycrystalline layer of grains of the tetragonal crystal phase of molybdenum disilicide with different grain sizes. The average grain size of sample A (0.343 µm diameter) was smaller and the distribution of the grain size was narrower than the grain sizes of samples B and C. With samples B and C having similar grain sizes and distributions. Sample D stayed amorphous. After the annealing step the molybdenum silicide layer was structured and electrical contacts made of aluminum silicon alloy were deposited. Schematics of the test structures are shown in Figure 1.

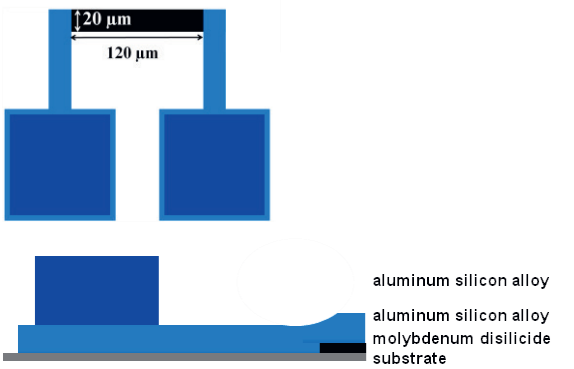

Fig. 1 Schematic of the test structures, top view and cross section.

Test structures have been stressed with current densities from $1.7x10^6$ A/cm² up to $3.0x10^6$ A/cm². While applying a constant current the cathode end of the molybdenum disilicide stripe was monitored via scanning electron microscope to investigate the time needed for the formation of hillocks. Because of the structure geometry the aluminum forming the hillock can only be aluminum which was formerly present at the anode and has electromigrated through the molybdenum silicide test stripe. Figure 2 shows a cathode before and after the growth of a hillock.

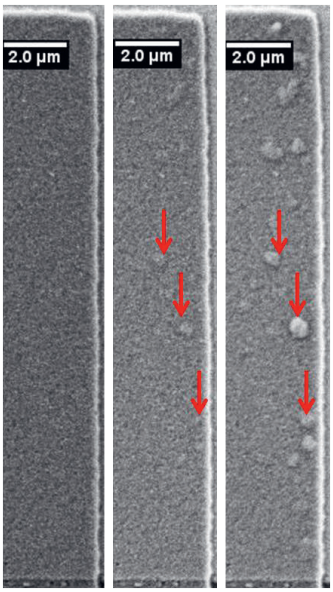

Fig. 2 Aluminum alloy cathode end before (left) and after (middle, and right) formation of hillocks.

From this observation an average drift velocity could be calculated. The drift velocities of the aluminum through the test structure ranged from $1.04x10^{-7}$ m/s to $8.57x10^{-6}$ m/s depending on the current density and the microstructure of the thin film (see Figure 3).

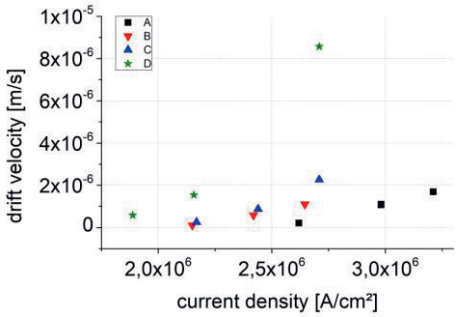

Fig. 3 Drift velocity of aluminum in the test structures depending on the current density.

B and C have similar grain structures and behaviors of drift velocity. Sample A showed lower drift velocities. The electromigration of aluminum being strongly dependent on the grain boundaries has also been reported in [6]. With annealing it is possible to tune the grain structure and reduce the electromigration of aluminum through the molybdenum disilicide layer.

References

[1] A. B. Gokhale, G. J. Abbaschian, R.W. Olesinski and G. J. Abbaschian, In Binary Alloy Phase Diagrams, vol. 2, T. B. Massalski (editor) (ASM, Ohio, 1986) pp. 1631, 2062.

[2] G. Beensh-Marchwicka, E. Prociów, and T. Berlicki, Thin film heater and thermopile built up using some silicides under thermal test, 2006 29th International Spring Seminar on Electronics Technology, St. Marienthal, 2006, pp. 475-478; doi: 10.1109/ISSE.2006.365152.

[3] Y. Ito, M. Sato, K. Wakisaka, and S. Yoshikado, Improvement of heating characteristics of molybdenum silicide thin film electrical heaters, Electrical Engineering in Japan 168 (2007),11-19; DOI: 10.1002/eej.20806

[4] A. Zehe, A. Ramirez, Electromigration of Aluminium through Quasi Bamboo- Like Grain Blocked Silicide Interconnects, Cryst. Res. Technol. 35 (2000), 557-562; doi: 10.1002/1521-4079(200005)35:5<557::AID-CRAT557>3.0.CO;2-M

[5] A. Zehe, The stress-induced escape of migrating aluminium from silicide interconnects, Semicond. Sci. Technol. 16 (2001), 817-821; DOI: 10.1088/0268-1242/16/301

[6] A. Zehe, A. Ramirez , A. Corona, Migration-forced metal extrusion from passivated molybdenum disilicide interconnects, Materials Letters 57 (2002), 55-58; doi:10.1016/S0167-577X(02)00698-5

Acknolodgements

Thanks are due to A. Graff, and D. Zwanzig, Fraunhofer IMW, Halle, for EBSD measurements.

Parts of this research were funded by the german “Bundesministerium für Wirtschaft und Energie” (BMWi) within the ongoing project „EMIR“ (Innokom, 49MF190017).

DOI 10.5162/SMSI2021/B8.1

Improvements in Thermal Profiling Using High-Definition Fiber Optic Sensing

David Potter[1], Andreas Stern[2], Aida Rahim[1]
[1]Luna Innovations, Blacksburg, VA, U.S.A.
[2]Luna Innovations, Pfullingen, Germany
potterd@lunainc.com, sterna@lunainc.com, rahima@lunainc.com

Summary:
One of the main challenges of using distributed fiber optic sensing technologies is their sensitivity to both strain and temperature. This paper describes a new development in high-definition distributed fiber optic sensing (based on Rayleigh backscatter and OFDR instrumentation) that provides for the automatic compensation of mechanical strain when measuring distributed temperature, enabling broader adoption of the technology in embedded and surface mounted measurement applications.

Keywords: Temperature, fiber optic, strain, distributed

Background and Motivation

Fiber optic sensing (FOS) have become relatively common in a wide range of testing and monitoring applications, due to their many benefits and advantages, such as EMI immunity, passivity, reduced cabling and very small, flexible sensors. High-definition (HD) fiber optic sensors additionally deliver the highest spatial resolution for distributed measurements. For example, commercially available systems can resolve strain or temperature along a fiber with a gage pitch, or spacing, as low as 0.65 mm.

One challenge of using most fiber optic sensing technologies comes from the fact that the sensors react to both mechanical strain and temperature. Therefore, when it is difficult to physically isolate strain from the fiber, accurate and reliable temperature measurements can be difficult in many applications. In particular, applications involving attaching or embedded longer sensor fibers to a surface with bends or curves can experience measurement errors due to strain.

This paper describes an important improvement to high-definition temperature sensing that compensates for strain and delivers more reliable and accurate temperature measurements when subjected to mechanical strain.

Fiber Optic Sensing - Measurement Theory

The temperature sensor is formed by standard off-the-shelf optical fiber composed of a monolithic fused silica core and cladding and a protective coating. An individual sensing fiber can be many meters in length and provide thousands of strain measurements at points distributed along its length. Measurements are made using the Rayleigh scatter in the fiber, a random but stable pattern of reflections inherent to each fiber as a result of small-scale non-homogeneities in the fiber. This random pattern of reflections is unique to each fiber and constant for the life of the fiber, forming a reflection 'fingerprint'. Temperature changes experienced by the sensor results in variations of both its refractive index (due to the thermo-optic coefficient, dn/dT) and its length (due to the coefficient of thermal expansion, CTE). Both these effects result in an apparent stretching of this 'fingerprint', which translates to a shift in the spectral content of the 'fingerprint'.

Sensors are interrogated using optical frequency domain reflectometry (OFDR), an interferometric technique which can distinguish sensors or scattering points at different locations along the fiber. Figure 1 describes the basic OFDR network. Light from a swept-tunable laser is split between the measurement path and a reference path by a fiber optic coupler. Light

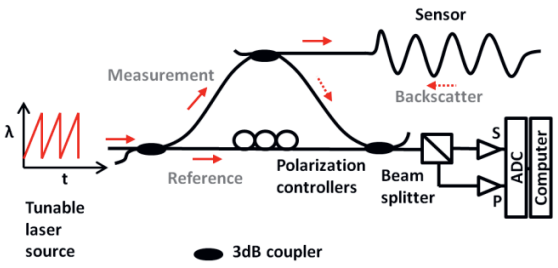

Figure 1. Basic OFDR system for measurement of temperature and strain in optical fiber

reflected from the sensing fiber returns through the coupler and is recombined with light from the reference path. This combined signal then passes through a polarization beam splitter, which splits the light into orthogonal states recorded at the S and P detectors. A Fourier transform of these signals yields the phase and amplitude of the signal as a function of length along the fiber, i.e. the fiber 'fingerprint'.

To calculate temperature change, the spectral content of the fiber's 'fingerprint' is compared between the measurement and reference state. Complex Fourier transform data is windowed around a desired measurement location. An inverse Fourier transform of the windowed data gives the spectral content from a particular gage in the sensing fiber (which is cross-correlated with the spectrum from the same location of fiber in a baseline state). Finally, the cross-correlated shift is converted to temperature change using a calibration coefficient. This process is repeated along the length of the fiber, forming a distributed measurement.

Strain Compensation when Measuring Temperature with Distributed FOS

This paper describes the effectiveness of an improvement to this OFDR system to essentially separate and remove the impact of strain on the measurement signal.

The high-definition strain-compensated (HD-SC) system utilizes the advanced polarization capabilities of the described OFDR system, combined with specialty fiber-based temperature fiber, taking advantage of polarization effects, to decouple strain and temperature for more reliable and accurate temperature measurements.

Verification of Strain Compensation

In order to demonstrate the strain compensation capabilities of the HD-SC sensor, a 5 m fiber sensor was fixtured into a system, shown in Figure 2, which is able to selectively apply strain and temperature to different sections of the fiber optic sensor. The sensor is routed along a pulley system (configured to apply set amounts of strain) and then into a controllable temperature chamber. Therefore, there are sections of the fiber sensor that are subject to applied strain (at room temperature), elevated temperature and strain, and temperature only (loose fiber, no strain). A Luna Innovations ODiSI optical interrogator is used to acquire and compute the temperature measurements.

Figure 3 shows a summary of the results. In the regions where mechanical strain is applied to the sensor, the non-compensated (standard) temperature sensor registers very large errors which increase with the amount of applied

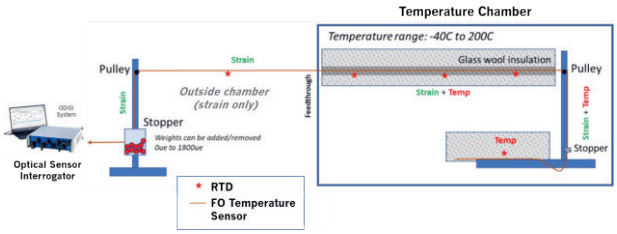

Figure 2. Experimental setup to verifiy strain compensation

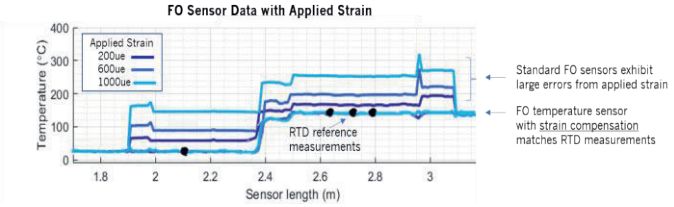

Figure 3. Experimental results, showing data with strain compensation and without

strain. However, the strain-compensated HD-SC temperature sensor is largely unaffected and returns measurements that match the reference RTD measurement.

Applications of High-Definition Temperature Measurements

With increased accuracy and measurement reliability provided by the strain-compensation capability, HD temperature measurements should prove even more effective in key applications, such as:

- Monitoring of battery cell/packs and power electronics
- High-resolution thermal profiling of precision reactors
- In-situ monitoring of thermoplastic welding processes

The high-resolution thermal profiles, with hundreds or more distinct sensing points per meter of fiber, provides a unique measurement capability for these challenging applications.

References

[1] J. Bos, J. Klein, M. Froggatt, S. Sanborn, D. Gifford, Fiber Optic Strain, Temperature and Shape Sensing via OFDR for Ground, Air and Space Applications, *Proc. SPIE 8876, Nanophotonics and Macrophotonics for Space Environments VII*, September 24, 2013.

[2] A. Rahm, J. Pandher, N. Coppola, V. Penumetsa, M. van Tooren, In-Situ Monitoring and Control of Induction Welding in Thermoplastic Composites Using High Def Fiber Optic Sensors, *CAMX Conference Proceedings,* September 2019.

DOI 10.5162/SMSI2021/B8.2

Tunable Nanopillars as surface enhanced Raman scattering (SERS) active structure for optical quartz glass fiber

E. Melekhov, V. Abb, T. Weidauer, M. Kammler, A. Lechner
Regensburg University of Applied Sciences, Centre of Excellence NanoChem
evgeny.melekhov@oth-regensburg.de

Summary:
In this work, a simple cost effective method to create tunable self-assembled three-dimensional nanostructure array-like nanoantennas on a tip of an optical quartz glass fiber is described. The structures are prepared using lithography-less dry etching. Gold nanoparticles are used as an etching mask using a thin metal-film thermal dewetting technique. The structures are applied as sensor for label-free analysis of organic substances in ppb range, such as drug residues in groundwater. The measurements are carried out by means of a Surface-enhanced Raman scattering (SERS) effect, an exchangeable sensor head, and a portable Raman device. This method allows in situ applications. Parathiocresol is used as a model substance to characterize the SERS cells. For metallization, gold and silver are compared. Reproducible SERS enhancement factors up to 10^7 are evaluated.

Keywords: Surface-enhanced Raman scattering (SERS); Nanostructuring; Analytical spectroscopy; Plasmonics; optical quartz glass fiber

Background, Motivation an Objective

Raman spectroscopy is a vibration spectroscopic technique using the inelastic scattering of light by vibrating molecules. Metallic nanostructures can induce a strong amplification of Raman signals by generation of local electrical fields induced by laser irradiation. Such signal amplification is caused on the one hand by localized surface plasmon resonances (LSPRs), and on the other hand by a charge transfer between substrate and molecules attached to the surface. Thus, it becomes possible to detect molecules by an amplification factor up to 10^{11}.

Design of measuring device

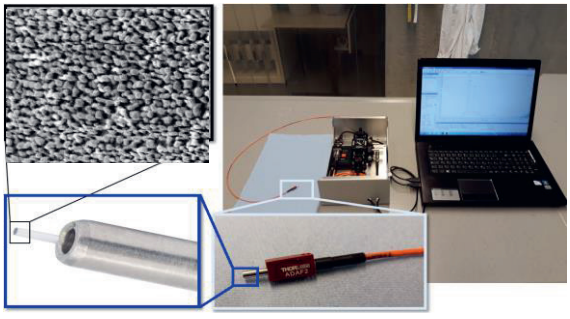

Fig. 1. Construction of a portable SERS-analyzer

The laser of λ_{ex}=785nm is connected on one side to the excitation fiber and on the other side to the fiber coupler. The beam of the laser is collimated via an excitation collimator and passes through a line filter to the dichroic mirror deflecting the light to the lens. The lens focuses the beam onto the sample surface. The same lens collimates the scattered Raman light from the SERS surface. The low energy stokes bands pass through the dichroic mirror, the high energy anti-stokes bands are almost completely suppressed. The dichroic mirror and the edge filter also reduce the highly intense Rayleigh bands and the excitation beam. The dichroic mirror deflects the light to the collimator, and in turn through an optical fiber to the spectrometer. The power supply for the system is provided via an USB cable from a laptop that is also employed for control of the laser and spectrometer.

Procedure of SERS-cells preparation

The following chapter describes a method for nanostructuring of SERS active areas on quartz substrates like plates or optical fibers (Fig. 2).

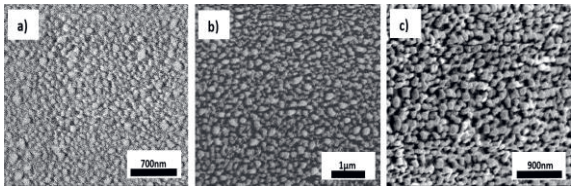

Fig. 2. Tilted SEM images of the preparation procedure of nanopillar arrays on a quartz plate: a) two-dimensional nanoislands, fabricated by thermal annealing of a gold layer; b) glass nanopillars, created by dry etching; c) quartz glass nanopillars after metallization with an additional silver film on top of the pillar array

The SERS substrate is prepared by reactive ion etching of quartz glass using nanoislands as an etching mask and an additive metallization with gold or silver. Creation of nanoislands is based on self-assembly structuring by annealing of a thin metal layer [1]. This can also be used for structuring of the tip of an optical quartz glass fiber.

Initially, a quartz substrate, e.g. a plate or an optical glass fiber, is covered with a thin gold film as a thermal dewetting layer via e-beam evaporator. In the next step, the metallized substrate is annealed to form closely packed gold nanostructures. During annealing, the thin gold layer breaks up forming nanoislands. These self-assembled structures serve as a mask [2] for etching the quartz glass substrate by CHF_3/Ar plasma.

Results

For Raman measurements, the samples are immersed in 10^{-4} mol/l solution of p-thiocresol in ethanol. After the sample solution is evaporated, the SERS spectrum is recorded.

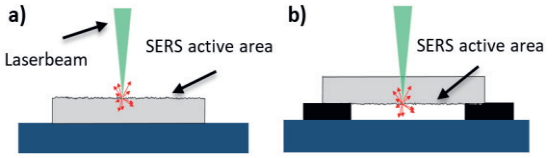

Fig 3: Schematic representation of the SERS measurements of quartz substrates from a) the upper side and b) from the underside of the substrate (comparable with a SERS-measurement using an optical fiber)

Figure 4 illustrates SERS-spectra of p-thiocresol using quartz plates covered by gold (right) or silver (left) on the top of the pillars from the underside (dashed red lines) and from the upper side (solid blue lines) of substrates (see Fig. 3).

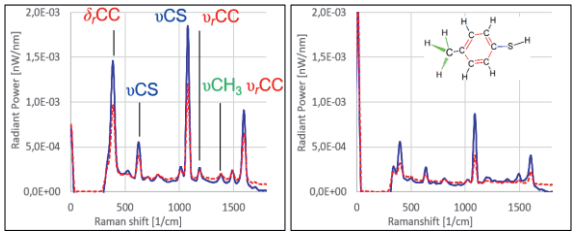

Fig 4: SERS Spectra of p-thiocresol with a concentration of 10^{-4} mol/l measured on structured quartz glass substrate. Dashed red lines represent SERS measurements from the underside of the substrates. The solid blue lines correspond to the measurements from the upper side of the substrates. Structures are metallized with 50 nm Ag (left) and 50nm Au (right)

Figure 5 shows SERS spectra of p-thiocresol recorded using a structured quartz glass fiber. In this figure, the solid blue line represents the background spectrum of the glass fiber immersed in pure ethanol. The dashed red line represents the overlay of the Raman spectrum of the quartz glass fiber and the SERS spectrum of p-thiocresol with a concentration of 10^{-4} mol/l. The corrected SERS spectrum of p-thiocresol after subtracting the background spectrum of the quartz glass fiber is illustrated on the right.

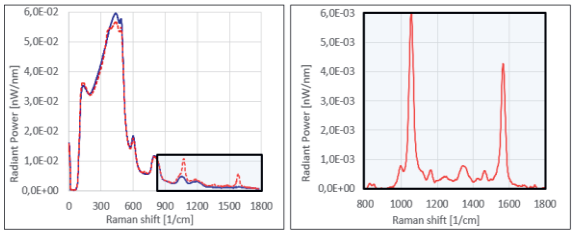

Fig 5: Raman spectrum of a SERS active structured quartz glass fiber immersed in ethanol as background spectrum (solid blue line) and SERS spectrum of thiocresol (dissolved in ethanol) with a concentration of 10^{-4} mol/l overlaid with the Raman spectrum of the glass fiber (dashed red line, left); SERS spectrum of p-thiocresol solution 10^{-4} mol/l (background Raman spectrum from the glass fiber already subtracted)

Conclusion

By thermal dewetting technology, quartz glass substrates such as optical fibers can be structured over large areas homogeneously in order to prepare nanopillars at low temperature. The pillars have diameters between 30nm und 80nm with the depth of 200nm. For creation of SERS activity, these pillars can be covered with silver or gold. In this way, nanogaps between metallized tops of pillars can be precisely adjusted.

Using the presented construction of the portable analyzer, SERS measurements can be performed in the field. With the measuring device and the SERS-active structure, p-thiocresol with a concentration of 10^{-8} mol/l dissolved in ethanol could be determined. The measurement results show that the organic substances can be measured in the ppb range.

References

[1] R. P. V. Duyne, J. C. Hulteen und D. A. Treichel, „Atomic force microscopy and surface-enhanced Raman spectroscopy.I. Ag island films and Ag film over polymer nanosphere surfacessupported on glass,“ *The Journal of Chemical Physics,* pp. 2101-2115, 1993.

[2] T.-W. Chang, M. R. Gartia, S. Seo, A. Hsiao und G. L. Liu, „A wafer-scale backplane-assisted resonating nanoantenna array SERS device created by tunable thermal dewetting nanofabrication,“ *Nanotechnology 25,* 2014.

DOI 10.5162/SMSI2021/B8.3

Influence of Temperature on Distributed Strain Sensing with OTDR in Polymer Optical Fibers

S. A. Dengler[1], N. Schmidt[1], M. Luber[1], J. Fischer[1], H. Hangen[2], O. Ziemann[1], R. Engelbrecht[1]
[1] Polymer Optical Fiber Application Center (POF-AC),
Technische Hochschule Nürnberg Georg Simon Ohm,
Wassertorstraße 10, 90489 Nuremberg, Germany,
[2] HUESKER Synthetic GmbH,
Fabrikstraße 13-15, 48712 Gescher, Germany.
simon.dengler@pofac.th-nuernberg.de

Summary:
Strain in ground and earthworks can be measured by polymer optical fibers (POF) applied to geotextiles. We measure the increase of backscatter (IOB) in the fiber under strain using optical time domain reflectometry (OTDR). The effect of temperature on this measurement principle is investigated. The local backscatter changes by 0.003 dB/K for common ambient temperature. In addition it is shown, that temperature depended viscoelastic properties of the polymer does affect IOB.

Keywords: optical time domain reflectometry, structural health monitoring, strain sensing, geotextiles, polymer optical fiber

Background

Condition monitoring of critical earthworks as for example dams, dikes and disposal sites is a challenging yet not satisfactorily solved measuring task. A possible sensor consists of a POF applied to a geotextile [1]. Geotextiles are fabrics made of polymer fibers, which are used to absorb stress within the soil and therefore, are ideal to transfer a soil movement to a strain of the sensor fiber.

When straining the POF, the level of optical backscattering within the fiber increases along strained sections [2, 3]. Spatially distributed measurements of backscattering, and thus, strain are possible using OTDR.

However, numerous side effects influence measurement accuracy significantly [4]. We previously analyzed relaxation processes that may result from adaptation of the POF material to external force [5]. Additionally, the IOB is affected by temperature and humidity [4]. We will therefore investigate the influence of temperature in this contribution. At first, we will analyze the change of optical backscattering level due to temperature at static unstrained conditions. Secondly, the influence of temperature on IOB due to strain is investigated.

Method

The backscatter response to temperature is tested on a 20 m fiber sample. The fiber section between 5 m to 15 m is placed in a climate chamber. The temperature is increased from 25°C to 30°C, 40°C, 50°C, 60°C then cooled down to 50°C, 40°C, 30°C, 25°C, 10°C, 0°C, -10°C, -20°C and finally increased to -10, 0°C, 10°C, 25°C again. At each step, the temperature is kept constant for 3h. Arrows in Fig. 1 also indicate the temperature cycle. The ambient temperature was kept constant as well with a conventional air condition unit at 22°C. OTDR traces were taken automatically in intervals of 10 minutes. The IOB is then determined as the difference between backscatter level inside and outside of the climate chamber (at reference temperature 22°C).

In the second experiment, five fibers were strained in identical manner, but exposed to different temperatures. The fibers were acclimatized at measurement temperature for at least 1 h. An automated measurement program strained the fiber at constant time steps of 1 h. In order to transfer the strain to the fiber, two rods were glued to it using a two-component epoxy, where motorized linear drives apply the elongation. Strain was applied at the position 10.0 m – 10.1 m increasing over time from 0% to 10% in steps of 0.1%. The IOB is calculated as the maximum value above the mean of backscattering level.

For all measurements, we used the same standard PMMA-POF with 1 mm diameter (Mitsubishi GH-4001-P) and a commercially available POF OTDR (Luciol LOR-220) at 520 nm wavelength.

Results

The temperature dependence of backscattering is shown in Fig. 1. A linear dependence has been estimated.

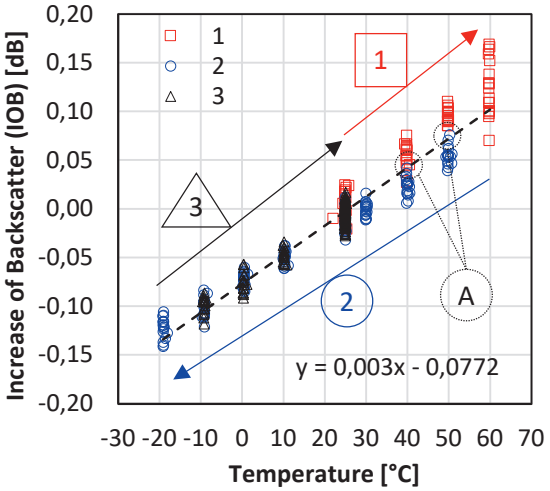

Fig. 2. Temperature dependence of backscattering. 1: increasing temperature, 2: decreasing temperature, 3: increasing temperature, A: hysteresis.

In this approximation, the backscattering raises by 0.003 dB/°K compared to the reference temperature. The measured values have a standard deviation of ±0.015 dB, from the fit. Heating can lead to a hysteresis. In the measurement data of Fig. 1. some deviations at 40°C and 50°C are noticeable, indicated by “A” in Fig. 1.

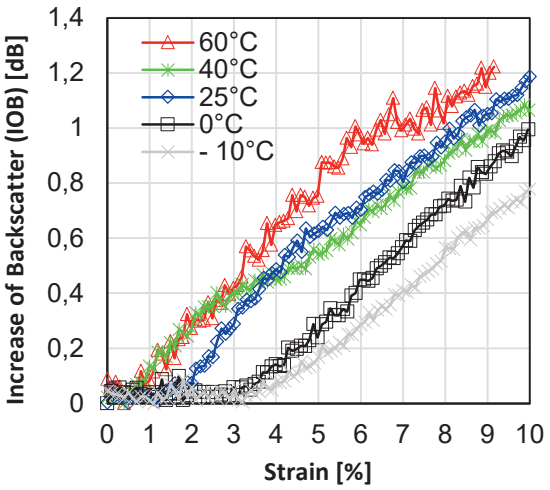

Fig. 2. IOB due to strain at different temperatures

Fig. 2. shows the IOB due to strain at different temperatures. As a noticeably trend, higher slopes and amplitudes correspond to higher temperatures. However, no straight relationship could be derived from the experiment. As the IOB at <3% strain does not increase in low temperatures, we additionally measured the force and can confirm that strain was actually applied.

Temperature affects viscoelastic properties and the IOB by strain behavior respectively, as the viscoelastic stress at the fiber changes. The strained interval of 10cm is beyond the spatial resolution limit of the OTDR. This affects the results in two ways. First, the absolute value of IOB is higher than in Fig. 2. Second, a small IOB could not be detected accurately. However, the 10 cm interval was limited due to mechanical restrictions of the climate chamber.

Conclusion

Temperature could be measured by the change of local backscatter. At this point it is not possible to distinguish strain from temperature. As the effect is small, it adds a measurement uncertainty for strain measurement. There is little uncertainty for small local temperature differences in the application, of soil depth >1 m, and might therefore be neglectable in most cases.

The altering IOB due to strain properties at different temperatures is an interesting result, which has the potential, to provide deeper understanding on viscoelastic and optical properties of POF. Despite of that, it is a challenge to correct the effect for strain sensing, if necessary.

Acknowledgements

This work has been funded by the Federal Ministry of Education and Research, funding program Forschung an Fachhochschulen (FHprofUnt) under contract number 13FH137PX6, “Optische Sensoren zur Überwachung von Erdstrukturen (SmartOSE).”

References

[1] S. Liehr, P. Lenke, K. Krebber, M. Seeger, E. Thiele, H. Metschies, B. Gebreselassie, J. Ch. Münich and L. Stempniewski, Distributed strain measurement with polymer optical fibers integrated into multifunctional geotextiles, Proc. SPIE 7003, 7003-02–7003-15 (2008).

[2] I. R. Husdi, K. Nakamura and S. Ueha, Sensing characteristics of plastic optical fibres measured by optical time domain reflectometry, Meas. Sci.Techn. 15 (8), 1553-1559 (2004)

[3] S. Liehr, Ph. Lenke, M. Wendt, K. Krebber, M. Seeger, E. Thiele, H. Metschies, B. Gebreselassie and J. Ch. Münich; Polymer Optical Fiber Sensors for Distributed Strain Measurement and Application in Structural Health Monitoring, IEEE Sensors J. 9 (11), 1330 – 1338 (2009).

[4] S. Liehr, M. Breithaupt, and K. Krebber; Distributed humidity sensing in PMMA optical fibers at 500 nm and 650 nm wavelengths; Sensors 17.4 (2017): 738.

[5] S. Dengler, N. Schmidt, M. Luber, J. Fischer, H. Hangen, O. Ziemann and R. Engelbrecht; Influence of Temporal Strain Evolution on Distributed Strain Sensing with OTDR in Polymer Optical Fibers, SMSI (2020): 75-76.

DOI 10.5162/SMSI2021/B8.4

12 nm spectral shift with a VCSEL in the near infrared in a 10 µs time interval

Gregor Saur, Roman Kruglov, Rainer Engelbrecht
Polymer Optical Fiber Application Center (POF-AC),
Technische Hochschule Nürnberg Georg Simon Ohm,
Wassertorstr. 10, 90489 Nuremberg, Germany
rainer.engelbrecht@th-nuernberg.de

Summary:
An optical wavelength tuning range up to 12 nm has been achieved within 10 µs, using VCSELs operating in the near infrared. The range has been measured with an interferometric setup and an optical spectrum analyzer respectively. Potentially, low-cost sensor systems based on tunable diode laser absorption spectroscopy or coherent optical frequency domain reflectometry could be realized, achieving sub-mm two-point range resolution or even better single-point range precision within a few microseconds for a single measurement.

Keywords: tunable lasers, semiconductor lasers, fiber optics, wavelength shift, VCSEL

Tuning of laser diodes

We present a method to tune the wavelength of a VCSEL in the near infrared (NIR) by 12 nm in a time interval of 10 µs. The heat dissipation from a current pulse induces a shift in the emission wavelength. This enables use in applications such as coherent optical frequency domain reflectometry (c-OFDR) or tunable diode laser absorption spectroscopy (TDLAS).

Previous publications in this field aim to tune a wide range of wavelengths within nanoseconds [2]. Another research focus is the linearization of wavelength sweeps [3].

The method presented here offers various advantages over other approaches of wavelength tuning and its linearization over time. The experimental setup is very simple and consists of only few and commercially available components. The overall spectral shift of 12 nm is considerably high for dynamic tuning in the microsecond range. The short duration of the pulse provides a possibility for measurements with only limited time available for data acquisition. Moreover, the lifetime of the laser diode (LD) increases by a low duty-cycle. Compared to wavelength tuning with nanosecond pulses, more energy is available due to the longer pulse duration, which potentially improves the signal-to-noise ratio.

Measurement setup

We measure both the overall spectral shift and the instantaneous wavelength during a 10 µs time interval.

The fundamental wavelengths of the used Vertilas VCSEL-LDs in TO-46 packages are 1577 nm and 1545 nm, respectively.

A laser diode controller (Thorlabs LDC 202C) injects a current into the LD. A signal generator applies a square pulse to its analog modulation input. The limited 3 dB-bandwidth of the LDC creates a gentle rise in the LD current, which is composed of the bias current i_B and a pulse amplitude i_P (Fig. 1). A temperature controller regulates the LD equilibrium temperature to approximately 21°C (thermistor $R_\mathrm{TH} = 12\,\mathrm{k\Omega}$). A fiber optic isolator prevents reflection of optical power into the LD.

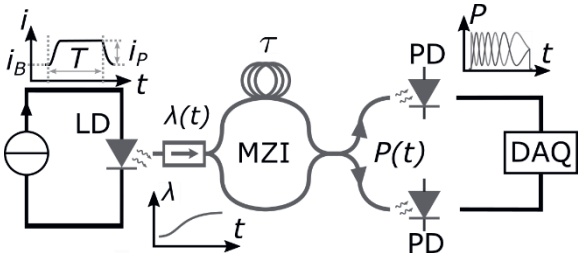

Fig. 1. Measurement of the instantaneous wavelength applying the Hilbert Transformation Compensation Method.

The optical signal passes through a fiber optic Mach-Zehnder-interferometer (MZI) with an imbalance τ of $1\,\mathrm{ns}$. We record the oscillating optical power (interferogram) at the two outputs with photodetectors DET08CFC from Thorlabs (PD) and a Keysight oscilloscope MSOX3104T. The instantaneous wavelength is then calculated using Hilbert Transformation Compensation

Method [1] (HTCM). The overall spectral shift $\Delta\lambda$ corresponds to the difference between the end and start value of the instantaneous wavelength. The results for the overall spectral shift have been validated with an optical spectrum analyzer.

Results

Increasing the peak LD current to approximately double the recommended current limit results in a maximum of 12 nm overall spectral shift for the VCSEL at 1545 nm (11 nm for the VCSEL at 1577 nm). Higher currents are of no benefit for pulse lengths of 10 µs. The optical power drops significantly due to the excess heat, so that no usable spectral components are emitted (thermal roll-off).

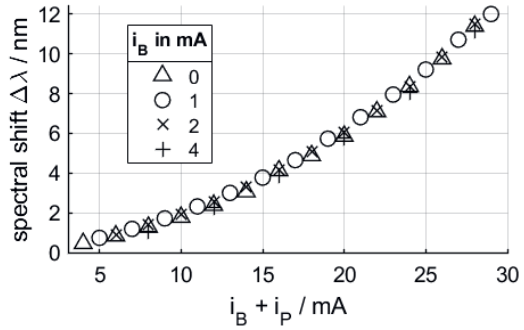

Fig. 2. The overall spectral shift within 10 µs depends on the sum of the current pulse amplitude i_P and bias current i_B (VCSEL at 1545 nm).

The overall spectral shift depends on the sum of the bias current and pulse amplitude (Fig. 2). A variation of the bias close to the laser threshold (approximately $1\,\mathrm{mA}$) does not influence the maximum overall spectral shift. Instead, thermal roll-off occurs when the sum of the currents exceed a critical level.

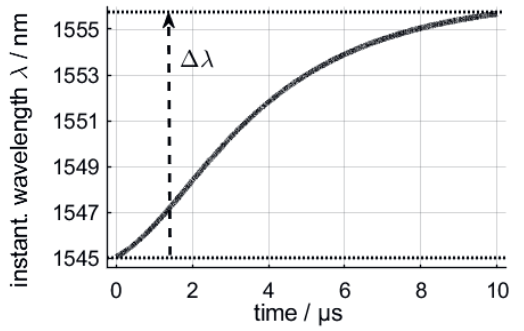

Fig. 3. Instantaneous wavelength and overall spectral shift during a 10 µs interval ($i_P = 26\,mA$, $i_B = 1\,mA$).

While a square pulse leads to an exponential increase in instantaneous wavelength [4], the gentle rise of the LD current leads to a more linear wavelength sweep as depicted in Fig. 3.

Tab. 1. Overall spectral shift depending on the equilibrium temperature for the VCSEL at 1577 nm

$\boldsymbol{i_B = 1\,\mathrm{mA}, i_P = 10\,\mathrm{mA}}$					
$\boldsymbol{R_{TH}\,/\,\mathrm{k\Omega}}$	8	10	12	14	16
$\boldsymbol{\vartheta\,/\,°C}$	30	25	21	17	15
$\boldsymbol{\Delta\lambda\,/\,\mathrm{nm}}$	1.36	1.33	1.32	1.30	1.29

The overall spectral shift varies in the range of tenths of a nanometer for temperatures between 15°C and 30°C (Tab. 1).

Conclusion

In this work, a method for tuning the wavelength of a VCSEL over 12 nm within 10 µs was presented.

The overall spectral shift depends on the peak current (sum of bias and pulse amplitude). The equilibrium temperature has no noticeable influence on the width of the overall spectral shift. An increase in the pulse amplitude beyond a critical value leads to the thermal roll-off of the LD, so that no further increase in overall spectral shift can be observed.

The gentle rise of the LD current produces a more linear wavelength sweep compared to a square pulse LD current. Therefore, detector electronics with smaller bandwidths can be used.

Acknowledgment

This project is funded by "Bayerisches Staatsministerium für Wissenschaft und Kunst" within the "Programm zur Förderung der angewandten Forschung und Entwicklung an Hochschulen für angewandte Wissenschaften" under contract no. H.2-F1116.NÜ/56/3 (FasoDynE).

References

[1] Ahn T., Kim D. J., Analysis of nonlinear frequency sweep in high-speed tunable laser sources using a self-homodyne measurement and Hilbert transformation, Appl. Opt. Vol. 46, 13, 2394-2400 (2007), doi: 10.1364/AO.46.002394

[2] M. Njegovec, D. Donlagic, Rapid and broad wavelength sweeping of standard telecommunication distributed feedback laser diode, *Optics Letters*, Vol. 38, 11, 1999-2001 (2013); doi: 10.1364/OL.38.001999

[3] Xiaosheng Z., Pouls J., Wu M.C., Laser frequency sweep linearization by iterative learning pre-distortion for FMCW LiDAR, Opt. Express Vol. 27, 7, 9965-9974 (2019), doi: 10.1364/OE.27.009965

[4] Passy et al., Coherent OFDR with semiconductor laser sources, Journal of Lightwave Technology, Vol. 12, 9, Sep 1994; doi: 10.1109/50.320946

DOI 10.5162/SMSI2021/B9.1

Optoelectronic nociceptive sensors based on heterostructured semiconductor films

Mohammad Karbalaei Akbari[1], Serge Zhuiykov[1],
[1] Gent University Global Campus, 119 Songdomunhwa-ro, Yeonsu-gu, Incheon 21985, South Korea
serge.zhuiykov@ugent.be

Summary:
A visible light optical nociceptive sensor was developed based on the heterostructured plasmonic Au/G_2O_3/TiO_2 semiconductor films. The incorporation of nitrogen atoms and the following phase transformation of G_2O_3 ultra-thin film during rapid thermal annealing enabled the nociceptive characteristics in heterostructured G_2O_3/TiO_2 plasmonic visible light sensor. The fabricated nociceptor showed the post-synaptic current, nociceptive threshold and non-adaption modes in normal states.

Keywords: Heterostructured Semiconductors, Nociceptors, Optical Sensing, Atomic Layer Deposition

Introduction

Bio-inspired nano-electronic technology is the fundamental knowledge toward the development of advanced artificial intelligence systems. The visual light reception and nociception are among the main functionalities of human eye sensory system where the accurate detection, processing and realization of optical signals lead to the visual cognition. The human eye is composed of thousands of visible light sensors and receptors which receives the environmental visible light signals, turn them into chemical pulses and send them to brain via optic nerve. Nociceptors are one of the key sensory receptors in human body with the capability of smart sensing of harmful stimuli. The human cornea has the highest number of nociceptors which generate warning signals through the neural system to brain to eventually trigger the human sensorimotor responses and then to minimize the potential sensitization (Fig. 1) [1]. The main component of such a sensory system is natural synapses, where the ultra-fast and ultra-low energy transfer of presynaptic pulses via ionic neurotransmitters through synaptic gaps enables the functionalities of human nervous system. A developed analogous artificial synaptic device composed of a nano-scaled semiconductor film sandwiched between conductive layers. Here, the ionic transfer in sandwiched semiconductor film changes the resistive switching (RS) mechanisms in the film, which resembles the transfer of ionic pulses in natural synaptic gaps. In the same concept, a heterostructured G_2O_3/TiO_2 synaptic film was deposited on the Au substrate. The heterostructured semiconductor film acts as the synaptic junction, where the Au substrate acts as plasmonic antenna which receives the visible light and transfer optically generated pulses to semiconductor body (TiO_2). The heterointerface engineering is the main strategy here to manipulate the heterointerfaces and to control the charge transfer between semiconductors and Au film of nociceptors.

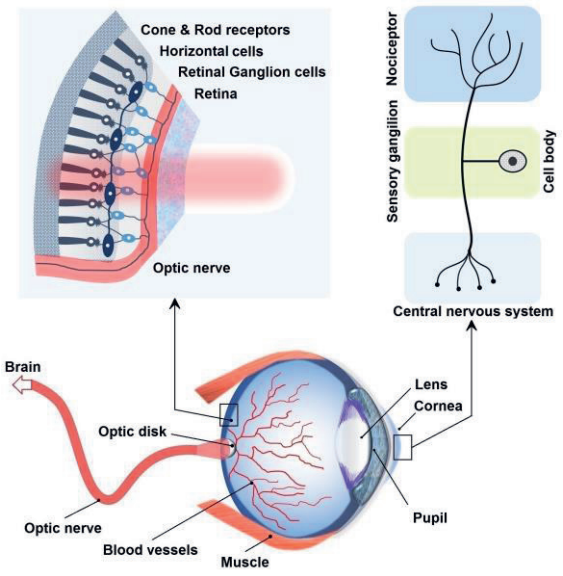

Fig. 1.The graphical scheme shows the structure of natural light receptors and nociceptors in human eye.

Results

Atomic layer deposition was used to deposit 4.0 nm thick Ga_2O_3 film on the Au substrate. The following rapid thermal annealing of Ga_2O_3 film in nitrogen at 450°C was accompanied by the phase transformation of film. In the Raman spectra, the characteristic peak of Ga-N bonding (E_2) was detected at binding energy of 515 cm^{-1}. XPS results demonstrated that the N_2 incorporation into gallium oxide film was

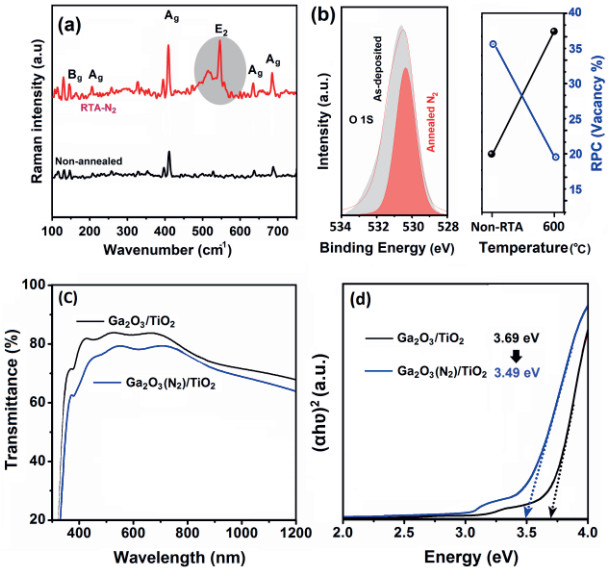

Fig. 2. (a) The Raman Spectra of as-deposited and N_2 annealed Ga_2O_3 films. (b) The XPS spectra of the similar samples including their Vacancy percentage. (c) The transmittance spectra and (d) bandgap of heterostructured Ga_2O_3/TiO_2 films.

accompanied by the decrease of intensity of O 1s peak and following shift of peak to lower binding energies. It confirms the replacement of oxygen vacancies with atomic nitrogen (Fig. 2b). The investigation of transmittance spectra of Ga_2O_3 (4.0 nm) / TiO_2 (19.0 nm) samples showed a high level of transparency in both samples in visible light region, with a slight decrease of transparency after nitrogen incorporation in Ga_2O_3 film. The measurement of bandgap energy via transmittance spectra of heterostructured samples showed the decease of bandgap from 3.69 eV to 3.49 eV. Considering the bandgap values of heterostructured Ga_2O_3/TiO_2 and Ga_2O_3 $(N_2)/TiO_2$ films, the UV source is required to excite the electrons from valence band to conduction bands of semiconductors. However, by using an Au antenna as plasmonic substrate it is possible to use the visible light to generate plasmonic hot electrons at the heterointerfaces between Au and Ga_2O_3. These hot electrons can be later transmitted to the main semiconductor body (TiO_2). This plasmonic heterostructured semiconductor acts as a resistive switching layer where the transfer of photogenerated charges between two conductive electrodes through semiconductor film enables the resistive switching characteristics. In this case, a tunable visible light (λ=650 nm) was used to excite the photoelectrons in Au/Ga_2O_3 $(N_2)/TiO_2$ heterostructured films. The following optoelectronic measurements confirmed that the Au/Ga_2O_3 $(N_2)/TiO_2$/ ITO (indium tin oxide) optoelectronic sensor showed the relaxation phenomenon which is a nociceptive characteristic. (Fig. 3a). It was also found that the

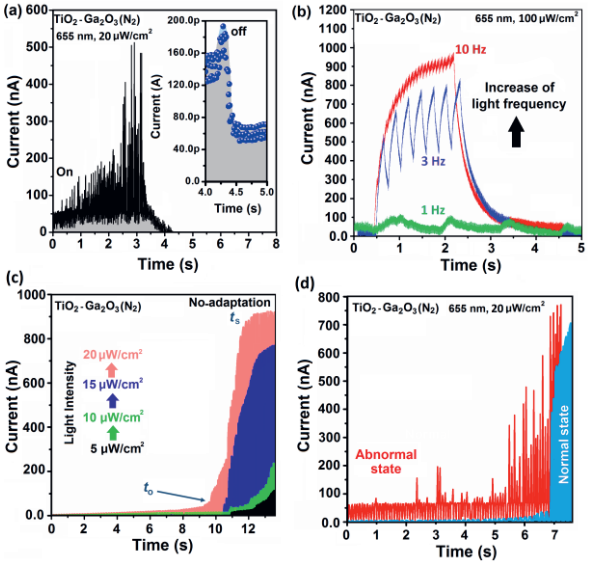

Fig. 3. (a) The relaxation time of Au/Ga_2O_3 $(N_2)/TiO_2$ (b) the light frequency dependence of post-synaptic photocurrent. (c) The dependence of ignition and saturation time to the light intensity. (d) The normal vs. abnormal photoresponse of nociceptors.

higher light frequency resulted in the longer relaxation time (larger post-synaptic current) of nociceptors (Fig. 3b). The ignition (t_0) and saturation (t_s) time are two other main properties of optical nociceptors which show the light-intensity dependence performance of Au/Ga_2O_3 $(N_2)/TiO_2$ nociceptor (Fig. 3c). It was observed that the ignition time of nociceptive sensor was the factor of light intensity where the higher light intensity evoked the nociceptor response in the shorter ignition time. Fig. 3d also shows the difference between abnormal and normal performance of a nociceptor sensor, where the ignition time of a damaged nociceptor shifted to the initiation point of experiment.

Conclusions

Heterointerface engineering enabled the fabrication of a visible light nociceptor device based on heterostructured Au/Ga_2O_3 $(N_2)/TiO_2$ ITO films. The incorporation of N_2 atoms in interlayer Ga_2O_3 assisted the control of photogenerated charge carriers at $Au/G_2O_3/TiO_2$ heterointerfaces. This sensor showed the fundamental characteristics of a visible light nociceptor including the relaxation, Ignition and saturation times.

References:

[1] M. Karbalaei Akbari, S. Zhuiykov, A bioinspired optoelectronically engineered artificial neurorobotics device with sensorimotor functionalities, *Nature Communications* 10 (2019) 3873.

DOI 10.5162/SMSI2021/B9.2

Monitoring of Composite Bicycle Components using Polymer Planar Bragg Gratings

Stefan Kefer[1], Frederick Roth[2], Michael Kaloudis[2], Bernhard Schmauss[3] and Ralf Hellmann[1]
[1] Applied Laser and Photonics Group, Aschaffenburg University of Applied Sciences, Wuerzburger Strasse 45, 63743 Aschaffenburg, Germany
[2] Laboratory for Packaging and Interconnection Technology, Aschaffenburg University of Applied Sciences, Wuerzburger Strasse 45, 63743 Aschaffenburg, Germany
[3] Institute of Microwaves and Photonics, University of Erlangen-Nuremberg, Cauerstrasse 9, 91058 Erlangen, Germany
Corresponding author's e-mail address: stefan.kefer@th-ab.de

Summary:
This study demonstrates mobile load monitoring of a composite bicycle component using an application-customized polymer planar Bragg grating sensor, evaluated by a mobile interrogation unit. After a referencing procedure, the mechanical load of a seat post is monitored while cycling through a test track.

Keywords: Bragg Grating, Composites, Cyclic Olefin Copolymer, Micromilling, Load Monitoring

Introduction

The scientific impact of Polymer planar Bragg gratings (PPBG) based on Cyclic Olefin Copolymers (COC) has grown tremendously throughout recent years. Based on their outstanding material properties [1], these polymer-based optical sensors are capable of performing temperature-referenced, humidity-insensitive and multidimensional strain or shape sensing [2]. They can also be fully integrated into commercial-grade carbon fiber reinforced polymer (CFRP) workpieces [3], wherein structural health monitoring is especially vital [4]. This study follows a straightforward approach by adhesively affixing a COC-PPBG on a bicycle's CFRP seat post. In combination with a battery-powered mobile interrogation unit, which is also capable of wireless data transmission, it is possible to monitor the load status of the seat post in the field.

Sensor Fabrication

Injection-molded COC plates are cut to bulk sensor substrates with a length of 20 mm, a width of 10 mm and a thickness of 1.5 mm. Subsequently, a micromilling process (CNC Mini-Mill/4, Minitech Machinery) is used to fabricate a microstructure on the substrate's top surface. Afterwards, a waveguide comprising a Bragg grating structure is generated within the substrate by employing a sophisticated single-writing-step procedure [5]. Finally, the PPBG's bottom side is milled to a concave shape, whereas its radius of 13.6 mm matches that of the bicycle seat post. Fig. 1 depicts the final customized COC-PPBG. The microstructure on top of the substrate is filled with a UV-curable adhesive (NOA76, Norland). Subsequently, a single-mode fiber, exhibiting a polished 8° end facet, is inserted.

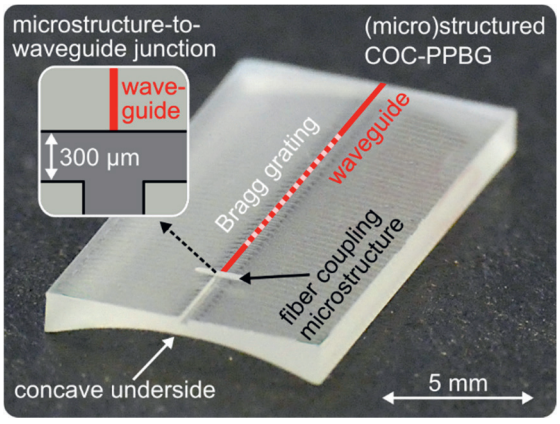

Fig. 1. COC-PPBG modified for affixation on a bicycle seat post (photonic structures are indicated).

After aligning the fiber with the integrated photonic structures, the adhesive is cured in order to obtain a durable physical connection of both components. Additionally, the optical adhesive serves as refractive index matching medium in-between fiber end facet and polymer waveguide.

Interrogation and Referencing

A battery-powered interrogator (MOFIS M400, Redondo Optics) is used to monitor strain induced shifts of the PPBG's Bragg wavelength. The device uses the longer wavelength slope of a bandpass filter to convert Bragg wavelength shifts into intensity variations, quantified and transformed to a voltage signal by means of a

photo receiver with appropriate electric conversion. After affixing the sensor at the seat post's front by means of an epoxy-based adhesive (DUOPOX AD840, DELO), the CFRP workpiece is mounted in a tensile testing machine (UD04, Step Engineering). This way, the resulting change in output voltage ΔV is referenced with the applied external load. An image of the setup is given in Fig. 2 a) while the determined reference function is shown in Fig. 2 b).

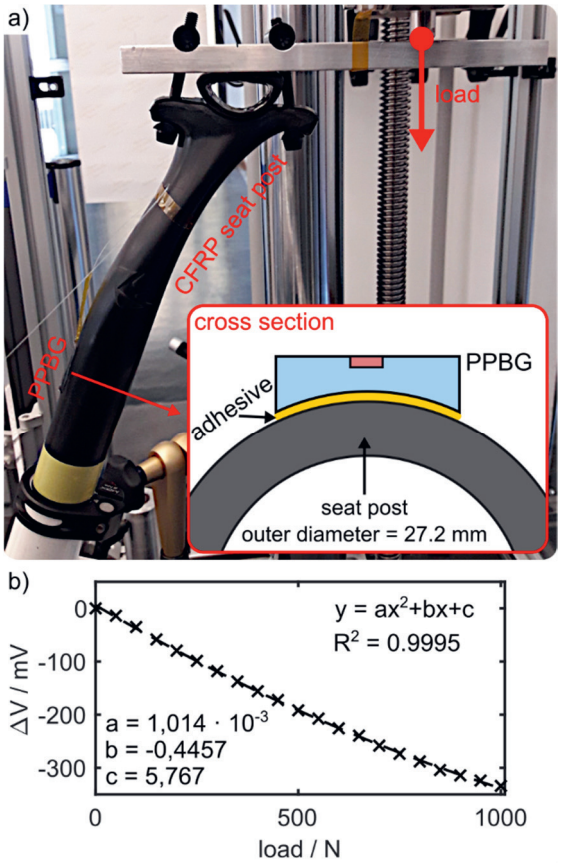

Fig. 2. a) Referencing setup. b) Voltage change ΔV as a function of the applied load.

The observed voltage change can be well-fitted with a quadratic function, whereas the nonlinear behavior is attributed to the bandpass-based wavelength shift to voltage conversion.

Field Experiments

The CFRP seat post with the affixed COC-PPBG sensor as well as the mobile interrogator are mounted on a bicycle, as shown Fig. 3 a). A cyclist with a weight of 82 kg rides the bicycle along a test track, while the load status of the seat post is monitored via the applied PPBG. Measurement data is transmitted wirelessly from the interrogator to a nearby evaluation station. Fig. 3 b) depicts the test track's pavement condition featuring four equidistant ditches. According to Fig. 3 c), which shows a time trace of the determined load, the mobile optical sensor setup is capable of quantifying the forces affecting the CFRP workpiece, whereas load impacts of the cyclist's pedaling movement as well as all ditches are discernible in the recorded data.

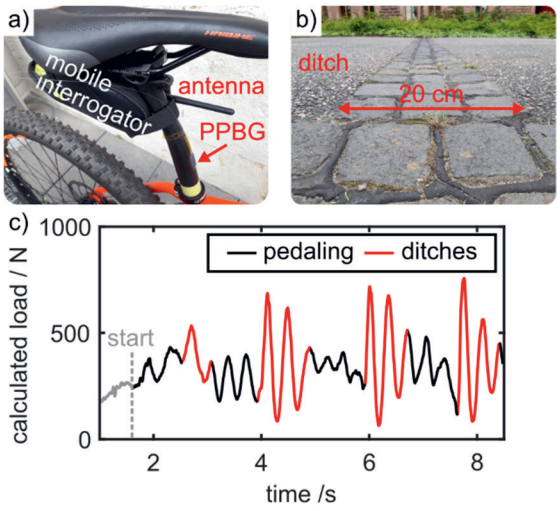

Fig. 3. a) Field experiment setup. b) Pavement conditions of the test track. c) Exemplifying time trace of the determined load profile.

Conclusion

This study demonstrates mobile load monitoring of a CFRP bicycle component by means of a shape-optimized polymer planar Bragg grating in combination with a battery-powered interrogator, which also features wireless data transmission.

Acknowledgements

The authors thank Thomas Drehmel (Winora Group) and Christian Gemperlein (all ahead composites) and acknowledge funding of the VDI/VDE-IT (ESB-1701-0005//ESB014/001).

References

[1] G. Khanarian, Optical properties of cyclic olefin copolymers, *Optical Engineering* 40, 1024–1029 (2001); doi: 10.1117/1.1369411.

[2] S. Kefer et al., "Fabrication and Applications of Polymer Planar Bragg Grating Sensors Based on Cyclic Olefin Copolymers," in *2019 Photonics & Electromagnetics Research Symposium - Fall (PIERS - Fall)* (IEEE, 2019), 647–655; doi: 10.1109/PIERS-Fall48861.2019.9021801.

[3] S. Kefer et al., Microstructure-Based Fiber-To-Chip Coupling of Polymer Planar Bragg Gratings for Harsh Environment Applications, *Sensors* 20, 5452 (2020); doi: 10.3390/s20195452.

[4] A. Zaman et al., A review on FRP composites applications and durability concerns in the construction sector, *Journal of Reinforced Plastics and Composites* 32, 1966–1988 (2013); doi: 10.1177/0731684413492868.

[5] M. Rosenberger et al., Planar Bragg grating in bulk polymethylmethacrylate, *Optics Express* 20, 27288–27296 (2012); doi: 10.1364/OE.20.027288.

DOI 10.5162/SMSI2021/B9.3

Optimization of ITO-Based Plasmonic Slot Waveguide for CO_2 Mid-IR Absorption Sensors

Parviz Saeidi[1], Bernhard Jakoby[1], Gerald Pühringer[1], Andreas Tortschanoff[2], Thomas Grille[3], and Reyhaneh Jannesari[1]

[1] Institute for Microelectronics and Microsensors, Johannes Kepler University Linz, Altenberger Str.69, 4040 Linz, Austria,

[2] Silicon Austria Labs GmbH, Europasstr. 12, 9524 Villach, Austria

[3] Infineon Technologies Austria AG, Siemensstr. 2, 9520 Villach, Austria

Parviz.saeidi@jku.at

Summary:

In this work, an ITO-based plasmonic slot waveguide is numerically analyzed for CO_2 sensing applications. Our waveguide is designed based on Indium Tin Oxide on a silica substrate layer. As for sensing application both evanescent field ratio and propagation length play an important role, our structure is optimized based on the figure of merit defined by the product of the two aforementioned quantities. From our simulations, the optimum parameters for slot width and height of 500 nm and 1100 nm were obtained, respectively, based on this figure of merit.

Keywords: Plasmonic waveguide, ITO, sensing application, mid-infrared region, figures of merit

1- Introduction

Plasmonics has reached great attention due to enabling sub-wavelength photonics applications. The existence of surface plasmon polaritons (SPPs), which are the guided electromagnetic waves propagating along metal/dielectric interfaces with strong near-field confinements, allows for high light-matter interactions [1]. Traditionally, noble metals are widely used as plasmonic materials due to their chemical stability. However, they suffer from high intrinsic loss hampering practical applications. Transparent conductive oxides (TCOs) such as Indium Tin Oxide (ITO) can be good alternatives to replace noble metals. They not only show low loss in the infrared range but also indicate CMOS compatibility making them specifically appealing for easy integration of plasmonic devices. In this work, to the best of our knowledge, we propose a plasmonic slot-waveguide sensor platform using ITO for the first time, as illustrated in Fig. 1.

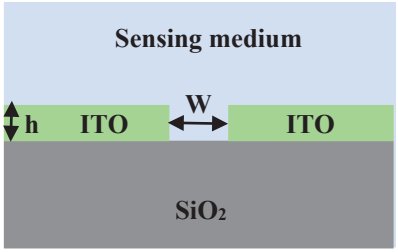

Fig. 1. The cross-sectional view of ITO-based plasmonic slot waveguide.

Our waveguide structure is designed for a wavelength of 4.26 µm, which corresponds to the absorption peak of CO_2. Two µm silica with a refractive index of 1.38 is considered as the substrate layer. ITO with a refractive index of -28.2+21.7i is placed on the top of the silica, and a small slot etched downward to form the waveguide. The sensing medium is assumed to be air. The modal properties of the proposed structure have been investigated using finite element method (FEM) implemented by COMSOL Multiphysics.

2- Results and discussions

2-1 Propagation length

The propagation wave vector of an SPP bounded mode at the metal/dielectric interface is given by [2]:

$$K_{SPP} = K_{re} + iK_{im} \qquad (1)$$

where K_{SPP} is the SPP wave vector. The propagation length of the SPP mode is given by:

$$L_{SPP} = \frac{1}{2K_{im}} \qquad (2)$$

The SPP mode on a metal/dielectric interface propagates but, owing to the presence of metal or metal-like material, gradually starts to attenuate. The propagation length of the fundamental mode of the structure as a function of ITO thickness (h) is indicated in Fig. 2 for different slot widths (w). Increasing both w and h results in an increase of the propagation length. This is due to the fact that the absorption loss in ITO reduces with the increasing w and h.

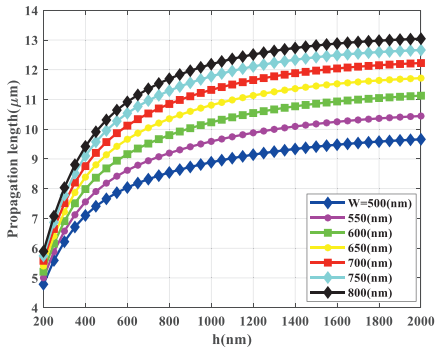

Fig. 2. The propagation length of fundamental mode as a function of h for different w.

2-2 Evanescent field ratio (EFR)

For sensing applications, the EFR plays a key role because it indicates the amount of fraction of electromagnetic field interacting with the surrounding gas. When the waveguide is surrounded by a gaseous analyte, which thus essentially forms the cladding of the waveguide, the evanescent field interacts with the gas by virtue of being absorbed by the gas. As a result, the transmitted light is attenuated at the absorption line of CO_2. The EFR is defined as the fraction of transmitted intensity in the gas to the total modal intensity:

$$EFR = \frac{\iint_{Gas} \varepsilon\left(E_x^2+E_y^2+E_z^2\right)dxdy}{\iint_{All} \varepsilon\left(E_x^2+E_y^2+E_z^2\right)dxdy} \qquad (3)$$

where E shows the electric field and ε indicates permittivity of each material and the integration is performed in the cross-sectional (xy) plane. Fig.3 presents the EFR of the fundamental mode of the proposed structure. It indicates that increasing w will lead to lower EFR. The reason is that, as the gap size increases, a part of the mode leaks into the silica results in decreasing the EFR.

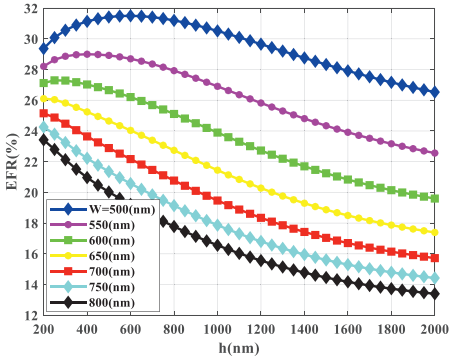

Fig. 3. EFR of fundamental mode as a function of h for different w.

As both EFR and propagation length are crucial for sensing applications, we introduce a figure of merit (FOM), which is defined as:

$$\text{FOM} = \text{EFR} \times \text{propagation length} \qquad (4)$$

The optimization of our waveguide geometries based on this FOM is plotted in Fig. 4. It is observed that the maximum FOM occurs at 500 and 1100 nm for w and h, respectively corresponding to roughly 9 um propagation length and 30% EFR.

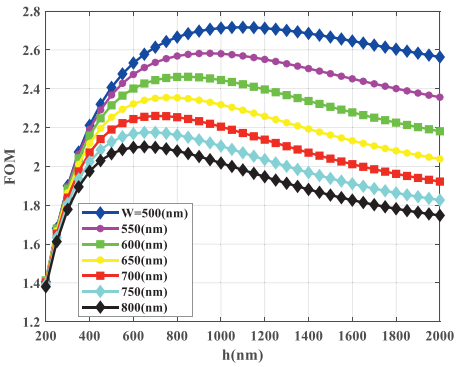

Fig. 4. FOM of fundamental mode as a function of h for different w.

The absolute value of electric field distribution (E_x) of SPP mode for the optimum values of the structure is depicted in Fig. 5 where it can be clearly observed that most of the mode is confined in the slot region, although a part of it leaks into the silica substrate.

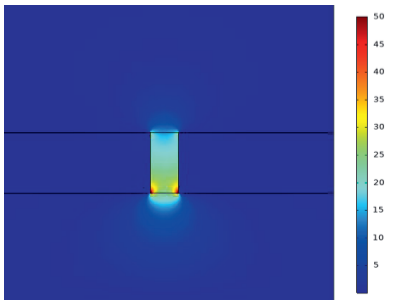

Fig. 5. The absolute value of electric field distribution (E_x) of SPP mode for optimum values of the structure.

3- Conclusion

An ITO-based plasmonic slot waveguide for the CO_2 sensing application was numerically investigated and optimized based on the figures of merit. The optimum parameters of 500 and 1100 nm for slot width and metal thickness were obtained, respectively.

Acknowledgment

"This work was supported by the PICASSO-project funded by the BMK in the framework of the program "Produktion der Zukunft" (Prj. Nr. 871417) and the COMET center "Symbiotic Mechatronics".

References

[1] Prämassing, M., Liebtrau, M., Schill, H. J., Irsen, S., & Linden, S."Interferometric near-field characterization of plasmonic slot waveguides in single-and poly-crystalline gold films". *Optics Express*, *28*(9),12998-13007, (2020). doi: 10.1364/OE.384629.

[2] Jannesari, R., Pühringer, G., Grille, T., & Jakoby, B. "Using an optimized grating as a mid-IR surface plasmon gas sensor utilizing highly doped silicon". *IEEE SENSORS*, 1-4, (2019), doi:10.1109/SENSORS43011.2019.8956904.

DOI 10.5162/SMSI2021/B9.4

Metal/semiconductor hetero-interface engineering for photocurrent controlling in plasmonic photodetectors

, Serge Zhuiykov[1], Mohammad Karbalaei Akbari[1]
[1] Gent University Global Campus, 119 Songdomunhwa-ro, Yeonsu-gu, Incheon 21985, South Korea
serge.zhuiykov@ugent.be

Summary:
The heterointerface engineering at metal/semiconductor (MS) hetero-interfaces in Au/Ga_2O_3/TiO_2 plasmonic photosensors enabled the modulation of charge transfer and photoconductance of detectors for adaptive perception of visible optical lights. The photoconductance at heterointerface between plasmonic Au antenna and main TiO_2 semiconductor was modulated by deposition of ultra-thin Ga_2O_3 film at the Au/TiO_2 hetero-interface. The fast and improved photoresponsivity were achieved by the surface functionalization of Au plasmonic antenna with N_2 doped Ga_2O_3 ultra-thin film.

Keywords: Meta/semiconductor heterointerface, Plasmonic Sensors, Atomic layer deposition

Introduction

The photodetectors have been developing for few decades as the artificial extension of the human eye receptors. Smart photodetecting gadgets with capability of the coverage of optical signals in the entre visible light spectrum with the self-adapting characteristics are highly required in various fields of visible light optical sensing. The state-of-the-art self-adaptive photodetectors can mimic the human eye's receptors functionalities.

The modulation of charge transfer at the metal/semiconductor hetero-interfaces is one of the key parameters for development of performance of the optical photosensors based on all-oxide optoelectronic semiconductors. Specifically, the charge transfer at hetero-interface between Au antenna and semiconductor body in plasmonic photodetectors should be controlled to decrease the undesired dark current and also control the charge transfer at Au/Semiconductor hetero-interfaces [1]. An Au/WO_3/TiO_2 plasmonic photodetector was recently developed where the dark current of device was tangibly decreased by the employment of ultra-thin WO_3 film at Au/TiO_2 hetero-interfaces [1]. The present research has proposed the employment of *high-k* ultrathin Ga_2O_3 film as interlayer between plasmonic Au antenna and TiO_2 semiconductor film to control the charge transfer at Au/TiO_2 hetero-interfaces (Fig. 1). The incorporation of nitrogen atoms in ultra-thin Ga_2O_3 film via rapid thermal annealing in N_2 atmosphere enabled the modulation of

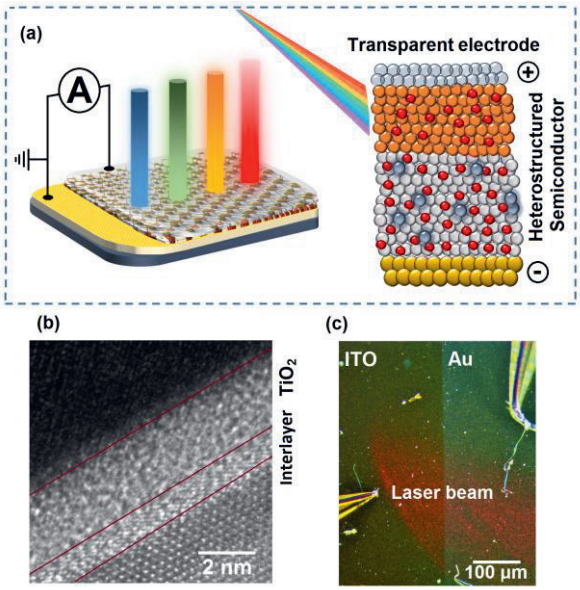

Fig. 1. (a) The graphical scheme depicts the heterostructured Au/Ga_2O_3/TiO photosensor with its (b) cross sectional TEM struture. (c) The actual top view optical photograph of photosensor with transparent ITO and Au plasmonic electrodes.

charge transfer at the Au/Ga_2O_3/TiO_2 hetero-interfaces in plasmonic photodetector.

Results

Atomic layer deposition was used to deposit 4.0 nm thick Ga_2O_3 film on the Au plasmonic substrate accompanied by the following deposition

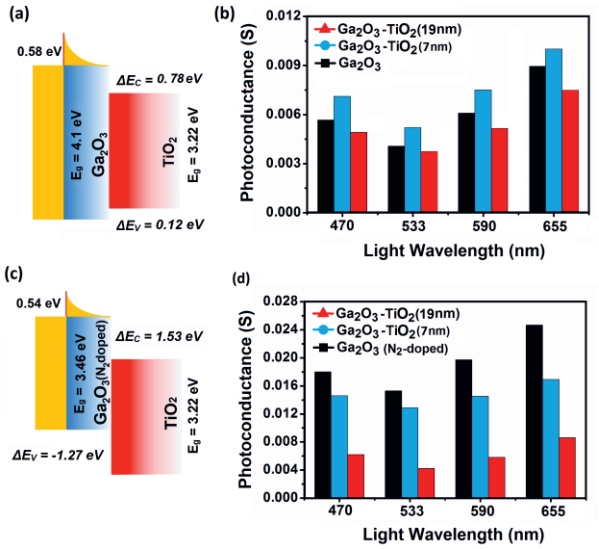

Fig. 2 (a) & (c) respectively show the energy band alignment of heterostructured Ga_2O_3/TiO_2 and Ga_2O_3 (N_2)/TiO_2 films. (b) & (d) respectively demonstrate the photoconductance of Ga_2O_3/TiO_2 and Ga_2O_3 (N_2)/TiO_2 plasmonic photodetectors.

Of TiO_2 films. It enabled the fabrication of Au/Ga_2O_3/TiO_2 and Au/Ga_2O_3 (N_2)/TiO_2 plasmonic sensors (Fig. 1 a, b, c).

The hetero-interface engineering at metal/semiconductor interface was accompanied by the alteration of Schottky barrier height (SBH) at Au/Ga_2O_3/TiO_2 hetero-structures. The SBH at MS interface can alter the charge transfer mechanism at the plasmonic hetero-interfaces. Results showed that the nitrogen doping was accompanied by a small decrease of SBH (Fig. 2a, c). Considering the mechanisms of charge injection and charge tunneling through the Schottky barrier, the Ga_2O_3 (N_2) film with lower Schottky barrier height is more favorable option for transfer of plasmonic photogenerated charge carriers from Au antenna to main TiO_2 film. The hetero-interface engineering with nitrogen doped Ga_2O_3 film considerably altered the energy band alignment at Ga_2O_3/TiO_2 hetero-interfaces (Fig. 2 a, c). The energy band alignment at Ga_2O_3/TiO_2 hetero-structure is type I, while the Ga_2O_3 (N_2)/TiO_2 hetero-interface is type II. To investigate the photoconductance of fabricated plasmonic heterostructured photo-receptors, several light sources (blue 470 nm, green 530 nm, yellow 590 nm and deep red with tunable intensities were employed. Results confirmed that the photoconductance of Au/ Ga_2O_3 (N_2)/TiO_2 plasmonic photodetectors was considerably increased (Fig. 2b, d). It was found that Plasmonic photodetectors showed the highest photoconductance at higher wavelength of visible light, including λ=590 and λ=655 nm.

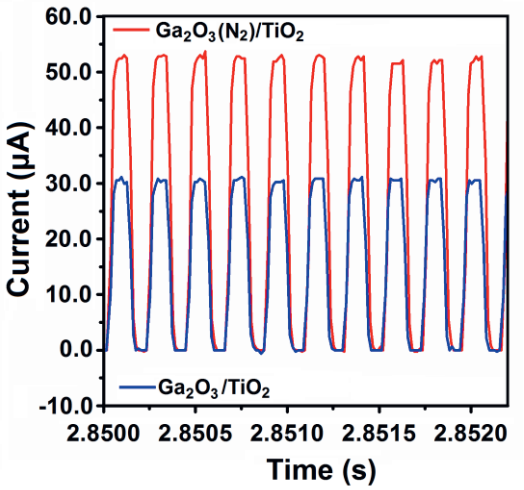

Fig. 3. The ultra-fast response of Ga_2O_3/TiO_2 and Ga_2O_3 (N_2)/TiO_2 photodetectors to visible light (λ=650 nm) pulses.

The fabricated plasmonic photodetectors already presented ultra-fast response to the visible light laser pulses (Fig. 3). A λ=655 nm pulsed laser light was employed to excite the visible light generated photoelectrons in Au antenna accompanied by the following transfer of them into TiO_2 film through Ga_2O_3 or Ga_2O_3 (N_2) inter layer barrier. The optoelectronic measurements confirmed higher photoresponse of Au/Ga_2O_3 (N_2)/TiO_2 visible light sensors compared with that of Au/Ga_2O_3/TiO_2 photodetectors.

Conclusions

The control of charge transfer at metal/semiconductor hetero-interface enabled the photoresponsivity of plasmonic Au/Ga_2O_3/TiO_2 photodetectors. The Ga_2O_3 interlayer has altered the charge transfer mechanism at Au/TiO_2 hetero-interfaces, where the photoconductance of metal/semiconductor was altered by employment of Ga_2O_3 and Ga_2O_3 (N_2) interlayer films. The hetero-interface engineering enabled the alteration of Shockey barrier height at metal/semiconductor interface and already reshaped the energy band alignment at Ga_2O_3/TiO_2 semiconductors. The photoelectrical measurement confirmed considerable improvement of photoconductance and photocurrent of plasmonic photodetectors.

References:

[1] M. Karbalaei Akbari, et al. ALD-developed Plasmonic two-dimensional Au–WO_3–TiO_2 heterojunction architectonics for design of photovoltaic devices. *ACS Appl. Mater. Interfaces*. 10 (2018)10304-10314.

DOI 10.5162/SMSI2021/B10.1

A 64 x 48 BSI SPAD Sensor Based on 8” Wafer 3D Stacking Technology

Simon Grosse[1], Andrei Steuer[1], Peter vom Stein[1], Christopher Zeidler[1], Jan Haase[1]
[1] Fraunhofer IMS, Finkenstraße 61, 47057 Duisburg, Germany
simon.grosse@ims.fraunhofer.de

Summary: A 3D stacking process by direct wafer bonding and the resulting sensor are presented to emphasize the potential of this technology for future sensor developments. By using the Fraunhofer IMS own 0.35 µm CMOS and micro systems technology, a 64 x 48 pixel sensor containing backside-illuminated low-noise single-photon avalanche diodes and in-pixel time-to-digital converters was fabricated. It is being applied om light detection and ranging applications as well as quantum imaging and characterized in both photon timing and counting mode.

Keywords: BSI SPAD, wafer bonding, 3D integration, 3D stacking, single-photon detection, LiDAR, ToF, quantum imaging

Background and Motivation

Single-photon detection with high temporal resolution is crucial for many rising application and research fields like light detection and ranging (LiDAR), quantum imaging, quantum random number generation (QRNG), fluorescence lifetime imaging (FLIM), spectroscopy and more. Single-photon avalanche diodes (SPADs) provide the preferred solution due to high performance in terms of detection efficiency, noise and timing jitter as well as the possibility of integration into complementary metal-oxide-semiconductor (CMOS) technology. On-chip circuits to obtain timing information are complex and introduce a high space consumption which eventually limits the fill factor and sensor sensitivity. Smaller CMOS technology nodes offer improvement but come with a higher dark count rate (DCR) which ultimately increases the sensor noise level [1]. 3D integration techniques allow vertical arrangement of readout electronics and SPADs to increase the fill factor and enable backside-illumination (BSI). While chip-to-wafer bonding offers a viable solution, direct wafer bonding with post-processing is the preferred option for higher volumes. Another crucial benefit is introduced by the possibility to combine different technology nodes and thus exploit both small-scale electronics and high performance SPADs.

Architecture

The presented sensor has an area of 10.25 mm by 9.2 mm while the active area claims 8.3 mm by 6.2 mm. The array consists of 64 x 48 pixels with 4 SPADs in each pixel which are connected by an adaptive coincidence circuitry which enables background light rejection [2]. Time-to-digital converter (TDC) sharing of 4 pixels with two storable timestamps per measurement cycle allows for a pixel pitch of 130 µm. The sensor is capable of photon counting (9 bit) and timing with 312.5 ps bin width during a 1.28 µs full scale range.

Direct wafer bonding

The readout integrated circuit (ROIC) and SPAD 8” wafers are fabricated separately in 0.35 µm automotive certified P1M4 and custom sensor technology, respectively. Surface roughness is a crucial parameter for the bond reliability and quality with a widely accepted threshold for successful hydrophilic bonding of a root mean square (RMS) roughness of below 0.5 nm [3]. This was achieved by a multi-stage chemical mechanical planarization process with several oxide depositions. Additionally, both wafer layouts are optimized to enhance homogeneity and avoid sites for possible topography variances. Typical values of the surface roughness before the bonding process were determined to be 0.25 – 0.3 nm RMS.

Hydrophilic low-temperature direct wafer bonding is used to establish a stable connection. Therefore, the wafer pairs are being aligned and put into contact with an alignment precision below 1 µm. Finally, the wafer pair is annealed at a temperature of 350°C.

Post-processing

To give access to the SPAD active areas that are close to the interface after bonding, the top wafer is thinned down to approximately 5 µm thickness. This is done by silicon etching with

an etch stop on the buried oxide layer of the silicon-on-insulator (SOI) wafer. The electrical contact between the wafers is established by front side through-silicon-vias (TSV). Here, bi-level silicon oxide etching exposes the ROIC and SPAD wiring metal which are then connected by sidewall deposition of an optimized material stack via physical vapour deposition (PVD) and atomic layer deposition (ALD). The bond pads are exposed in a subsequent etching step for accessibility during packaging. The schematic cross section of a wafer stack after post-processing can be seen in Fig. 1.

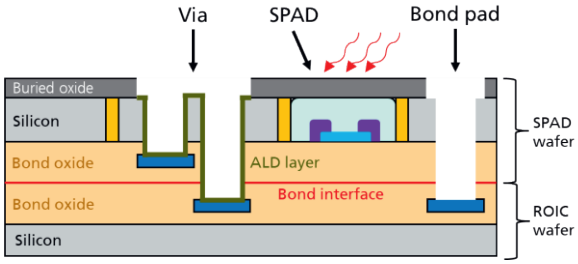

Fig. 1. Schematic cross-section of the final wafer stack configuration

Results

Scanning acoustic microscopy (SAM) was used to prove the bond result with the ability to reveal voids in the interface. An exemplary SAM image is shown in Fig. 2. It shows that a stable bond connection was established with few voids covering only dies near the wafer edge which were not fully exposed.

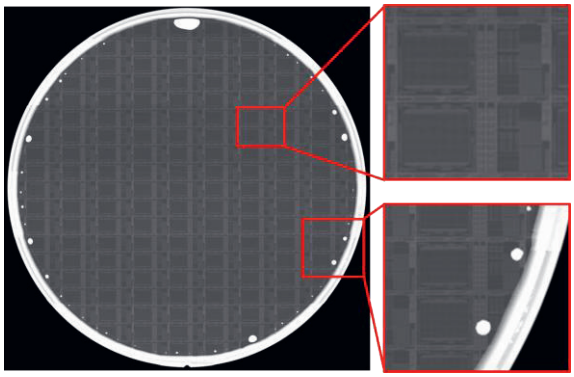

Fig. 2. SAM images of an 8" wafer bond with few voids near the wafer edge

The TSV design and processing forms a reliable electrical interconnection between the wafers with an average resistance of 14 Ω/TSV. This value was determined by testing a series connection of up to 170 TSVs in daisy chain structures. The TSV reliability was examined according to AECQ100 grade 1 and JESD2A104E, including 500 temperature cycles from -65 to 150 °C. No failures and a neglectable resistance change of < 5% were observed.

The BSI SPADs show a very low median DCR of 0.9 cps/µm^2, which is one of the lowest recorded and can compete with frontside illuminated SPADs, which typically show lower values [4]. The overall performance of the BSI SPAD sensor was evaluated in both photon timing and photon counting mode, as exemplary shown in 3D (time-of-flight) and 2D images of a street view with a row of garages in Fig. 3.

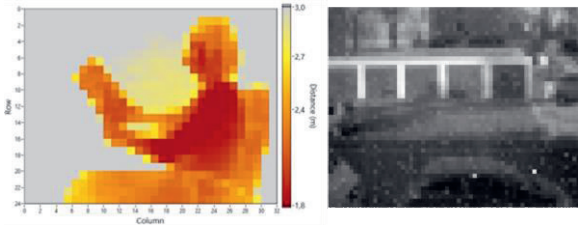

Fig. 3. Sensor operation in photon timing (left) and counting mode (right)

For time-of-flight imaging, this sensor provides a maximum range of 192 m with a depth resolution of 4.7 cm. The coincidence circuit reduces the probability for the detection of background generated events and thus improves the ability to separate between ambient light and laser signal while being able to adapt to the background event rate.

Conclusion

A reliable process for wafer bonding and post-processing for 8" CMOS wafers was developed and demonstrated with the fabrication of a 64 x 48 BSI SPAD sensor. A stable bond interface, reliable via structures and low DCR SPADs are presented. The sensor functionality and performance can be shown in photon timing and counting mode. The developed 8" wafer 3D stacking process enables the combination of technology nodes aiming at both small-scale electronics and low DCR BSI SPADs with the possibility of low to high volume production in future sensor developments.

References

[1] Bruschini, C. et al., Single-photon avalanche diode imagers in biophotonics: review and outlook, *Light Sci Appl.* 8:87 (2019); doi: 10.1038/s41377-019-0191-5

[2] Beer M. et al., Background Light Rejection in SPAD-Based LiDAR Sensors by Adaptive Photon Coincidence Detection, *Sensors (Basel)*, 18(12):4338 (2018); doi: 10.3390/s18124338

[3] L. Nie et al., Pressure Aided Low Temperature Direct Bonding of Silicon Wafers with High Surface Roughness, *1st IEEE International Conference on NEMS*, Zhuhai, 334-338 (2006); doi: 10.1109/NEMS.2006.334753

[4] Accarino, C. et al., A 64x64 SPAD array for portable colorimetric sensing, fluorescence and x-ray imaging, *IEEE Sensors Journal*, 1-1 (2019); doi: 10.1109/JSEN.2019.2916424

DOI 10.5162/SMSI2021/B10.2

A Novel Approach to Identify Wood Species Optically using Fluorescence Lifetime Imaging Microscopy

Nina Leiter[1], Maximilian Wohlschläger[1], Veronika Auer[1], Martin Versen[1], Christian Laforsch[2]
[1] Technical University of Applied Sciences Rosenheim, Hochschulstr. 1, 83024 Rosenheim, Germany
[2] University Bayreuth, Universitätsstr. 30, 95447 Bayreuth, Germany
martin.versen@th-rosenheim.de

Summary:
This contribution presents the results obtained with fluorescence lifetime imaging microscopy (FLIM) within the optical identification and differentiation of the four wood species walnut, beech, spruce, and maple. The experimental setup as well as the evaluation algorithm, with which the experiments were carried out, is explained briefly.

Keywords: Fluorescence Lifetime, wood species identification, Fluorescence, wood, FLIM

Introduction

Wood is the world's most important renewable raw material, which can be used several times within a life cycle, as material and for energy production at the end of the life cycle. The areas of material application are manifold and span from building, construction, engineered material and interior products. After the specific product life time, the then so called post-consumer wood can be recycled and reprocessed. Actually, recycled wood is mainly used within particle boards (up to 33% [1]). However, this material flow represents only 17% of the yearly resulting post-consumer wood in 2016. If the 6 % of polluted wood is taken into account, approximately 77 % of the post-consumer wood would potentially be available [2]. Therefore, the non-invasive and in-situ identification of wood species opens new material utilisation pathways of post-consumer wood, e.g. in massive wood products or in biorefineries.

At the moment, there are two main techniques under research to identify wood: near-infrared spectroscopy (NIRS) and X-ray fluorescence spectroscopy (XRF). According to [3], it is possible to identify wood types using NIRS. Unfortunately, the detection is complicated because the NIR spectrum is superimposed with the absorption band of the variable moisture content in wood. The second method to identify wood is XRF [4]. This method is not appropriate for an automated wood identification, since only pollutants such as heavy metals with high atomic numbers can be identified.. Thus, there is a demand for the development of a reliable and automatable method of wood identification and sorting.

The main component responsible for fluorescence signal of wood under excitation in the ultraviolet (UV) of visual (VIS) region is lignin in the cell walls [5]. The spectral fluorescent properties can be used for an identification purpose of wood, but vary in a significant manner [6]. Also, the fluorescence lifetime, measured in time-domain, can be used to identify wood species [7, 8]. In order to use the method of fluorescence decay time measurement in the time domain, fast synchronization and expensive equipment is required, which seems uneconomical.

Alternatively, the fluorescence decay time can be measured in the frequency domain with a FD-FLIM (frequency domain fluorescence lifetime imaging microscopy) camera. In this case, larger areas can be examined at once and the costs are considered to be lower. For this reason, the FD-FLIM method is investigated in this contribution.

Description of the New Method

In the FD FLIM method, the sample is excited by a sinusoidal or rectangular modulated light signal. The resulting fluorescence signal (emission) is phase shifted to the excitation signal. If the phase shift ϕ is measured at a known modulation frequency ω, the fluorescence lifetime τ can be calculated according to eq. (1).

$$\tau = \frac{1}{\omega} \cdot \tan(\phi) \quad (1)$$

The PCO AG from Kelheim has developed an FD-FLIM camera system, which can measure fluorescence decay times from 100 ps up to 100 µs with a dynamic range of 10 bit [9]. For

each of the 1008x1008 pixels, the intensity, the phase shift, the modulation depth and the phase and modulation lifetime can be determined.

The experimental setup consists of a laser diode Omicron PhoxX-488 that emits a sinusoidal modulated light signal of 488 nm wavelength with a definite modulation frequency ω. As fluorescence detector a pco.flim camera is used. Two optical filters placed in the excitation and emission paths narrow the bandwidth and block stray and reflected light. All components are assembled to a Motic PSM 1000 microscope, which contains a 20x magnification objective.

Four images of each sample at random positions are captured with the experimental setup and evaluated with a Gaussian analyzation as described in [10].

For the experiments wooden probes of walnut, beech, spruce and maple with a size of 2x2x0.5 cm are prepared.

Results

The measured fluorescence decay times for each wood specie are presented in Fig. 1. The measured values fit very well to Gaussian distributions. With this representation, a graphical differentiation and identification of the individual types of wood is possible.

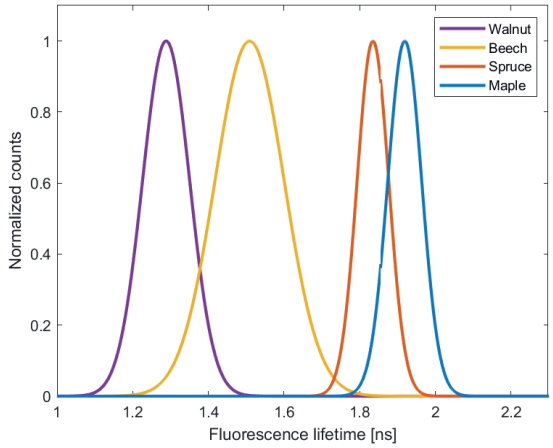

Fig. 1. Visualization of the measured fluorescence lifetimes of the four different wood species.

In addition, the calculated mean values of the fluorescence lifetimes and the corresponding standard deviations show similar results assuming a Gaussian distribution (see Tab. 1). Thus, an identification is also possible by calculation.

In summary, the wood species are unambiguously distinguishable and identifiable graphically and by calculation due to their characteristic fluorescence lifetime. This study clearly reveals the potential of the FD-FLIM technique for wood identification procedures. In the future, additional wood species should be investigated to exploit the full potential.

Tab. 1: Calculated mean values of the fluorescence lifetime and corresponding standard deviation.

Wood species	Fluorescence lifetime [ns]
Walnut	1.29 ± 0.06
Beech	1.51 ± 0.09
Spruce	1.84 ± 0.04
Maple	1.92 ± 0.04

References

[1] Klinker G., In praise of recycled wood. PFL Inspirations, 2016 http://inspirations.pfleiderer.com/13680-in-praise-of-recycled-wood. (Last Accessed 23 Nov. 2020)

[2] Flamme S., Hams S., Bischoff J., Fricke C., Evaluierung der Altholzverordnung im Hinblick auf eine notwendige Novellierung, Umweltbundesamt, Münster, 2019, ISSN 1862-4804

[3] Mauruschat, D., Plinke, B., Aderhold, J., Gunschera, J., Meinlschmidt, P., Salthammer, T., Application of near-infrared spectroscopy for the fast detection and sorting of wood–plastic composites and waste wood treated with wood preservatives. Wood Sci Technol 50, 2016, pp. 313–331. DOI: 10.1007/s00226-015-0785-x

[4] Hasan R., Solo-Gabriele, H.; Townsend T., Online sorting of recovered wood waste by automated XRF-technology: part II. Sorting efficiencies. In: Waste management, 31, 4, 2011a, pp. 695–704. DOI: 10.1016/j.wasman.2010.10.024.

[5] Albinsson, B., Li, S., Lundquist, K. & Stomberg, R. (1999) The origin of lignin fluorescence. J. Mol. Struct. 508, 19–27.

[6] Donaldson L.A., Softwood and hardwood lignin fluorescence spectra of wood cell walls in different mounting media. IAWA J 34, 2013, pp. 3–19. DOI: 10.1163/22941932-00000002

[7] Donaldson L.A., Radotic K, Fluorescence lifetime imaging of lignin autofluorescence in normal and compression wood. J Microsc., 251, 2, 2013, pp. 178-187, DOI: 10.1111/jmi.12059

[8] Burkhardt, H. Die Fluoreszenzlebensdauer in der Holztechnologie. Holztechnologie 60,6 , 2019, pp. 26–30.

[9] Chen H., Holst G., Gratton E., Modulated CMOS Camera for Fluorescence Lifetime Microscopy, Microscopy Research & Technique, 78, 12, 2015, pp. 1075-1081. DOI: 10.1002/jemt.22587

[10] M. Wohlschläger, G. Holst, M. Versen, A novel approach to optically distinguish plastics based on fluorescence lifetime measurements, IEEE Sensor Applications Symposium 2020, Kuala Lumpur, Malaysia, 2020, pp. 1-6. DOI: 10.1109/SAS48726.2020.9220084

DOI 10.5162/SMSI2021/B10.3

Differential Channel Optical Readout System for Color Changes of Gas Sensitive Colorimetric Dyes

C. Weber[1,2], M. El-Safoury[1], C. Pannek[1], L. Engel[1], A. Eberhardt[1], M.-L. Bauersfeld[1], J. Wöllenstein[1,2]
[1] Fraunhofer Institute for Physical Measurement Techniques IPM, Heidenhofstr. 8, 79110, Freiburg, Germany
[2]Department of Microsystems Engineering–IMTEK, Laboratory for Gas Sensors, University of Freiburg, Georges-Köhler-Allee 102, 79110, Freiburg, Germany
Christian.weber@ipm.fraunhofer.de

Summary:
We present a simple sensor setup for detecting very small color changes of gasochromic materials. The sensor includes up to ten LEDs for capturing different spectral channels, ranging from ultraviolet to the near infrared. The System features a differential optical structure that intrinsically allows comparing the reflectance of the gas sensitive dye to that of a reference dye. This allows for detecting diminutive color changes of dyes at gas concentrations in the sub ppm range with a better signal-to-noise ratio and drift stability compared to single channel systems.

Keywords: optical readout, differential, dyes color, gas sensor, colorimetric

Motivation

Current smoke detectors for residential use are predominantly based on the stray light principle. Detecting the light scattered by smoke particles, they feature two main disadvantages: The detection method can hardly differentiate between particles emitted from fires and harmless dust or fog particles. In addition, the detectors can only identify fires, which emit larger amounts of smoke particles. Especially for smoldering fires, this is not always the case.

In order to overcome these disadvantages, the combination with sensors for the detection of gases, emitted by fires, is advantageous [1]. The emission of carbon monoxide (CO) is a very specific indicator for burning processes and therefore, the detection of CO is ideally suited for this application. Measuring CO at an early fire stage requires a highly sensitive and selective detection method. The colorimetric gas sensing principle (also known as gasochromic principle) meets these requirements. It relies on a color changing chemical reaction of the target gas with a specifically tailored dye. In this work, we present a setup that is able to read out even very tiny color changes of gasochromic dyes in the presence carbon monoxide for fire detection purposes.

Readout System for Gas Dependent Color Change

In the presented measurement system, the color detection is accomplished by illuminating the dye with ten different LEDs and measuring the reflected light intensities in their respective spectral ranges.

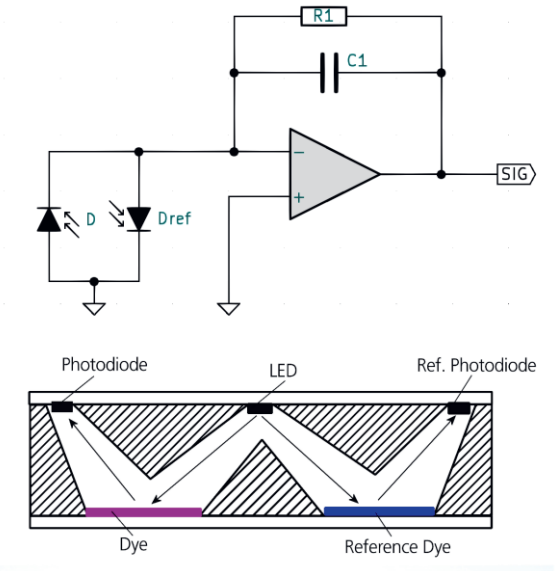

Fig. 1. Principle of the proposed optical differential circuit. The signal of the photodiode D and the reference photodiode Dref are subtracted intrinsically. Together with a completely symmetric optical layout, the output signal only depends on the difference between dye and reference dye.

In a single channel measurement system, the light reaching the detector is partly also reflected by the chamber walls and carries no information of the dye color. This fraction of the light represents an unwanted offset and might even lead to sensor drift. While the offset typically 50-80% in such a single channel signal, the color

changes to be resolved can be as small as 10^{-3} %. In order to decrease the offset fraction, we propose a differential detection principle consisting of two antiparallel photodiodes with a symmetrical arrangement (see Fig. 1). The antiparallel interconnection of the photodiodes enables a intrinsic differential measurement where the offset cancels out and only the reflection difference generates a signal. For an absolute reflection measurement, there are also two single channel photodiodes placed beside the differential detectors.

As shown in Fig. 1, the system comprises a W-shaped beam path. This ensures a defined symmetrical light distribution, blocking direct light from the LEDs to the detector

The ten LEDs with wavelengths ranging from 395 to 940 nm are operated successively. The photodiode current signals of the single channels are amplified with $2.7 \cdot 10^6$ V/A, while the photodiode signal of the differential channel is amplified with $2.7 \cdot 10^8$ V/A. An average LED current of 900 µA is modulated sinusoidal at 5 kHz, while the detector signals are captured and filtered by a digital lock-in algorithm having 1s averaging time and running on an onboard PSoC6 microcontroller. Fig. 2 shows the assembled readout system

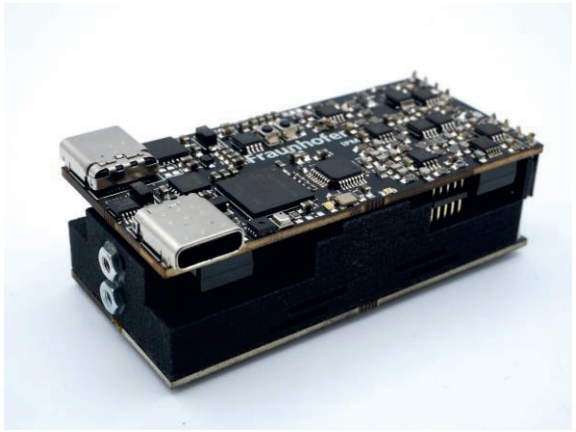

Fig. 2. Picture of the assembled system. The upper PCB contains the LEDs and the detectors on the bottom side, while the dyes are located on the lower PCB. In between, a 3D-printed chamber assembles the W-shaped light path.

Measurement Setup for CO

In order to detect CO with the developed sensor system, it is equipped with a gasochromic dye based on a binuclear rhodium complex, which was synthesized as described in [2]. The complex reacts with CO, showing a color change from purple to yellow. It is adsorbed on nanostructured silica particles, which were glued to PET foil and applied to the sensor system with adhesive. As reference dye, uncoated silica particles were used. The measurements with the developed setup were performed at the Fraunhofer IPM gas laboratory. The sensor system was placed in a gastight box with a volume of 500 cm³. A flow of synthetic air through the box with 50% r.h. at 2 l/min was established. By adding CO to the gas mixture, concentrations of 1, 10 and 100 ppm CO were realized.

Comparison of the Differential and the single Channel

In Fig 3, the sensor signals of the differential channel and the single channel with the orange LED (630 nm) while applying different CO concentrations are depicted. In the differential channel, the color change initiated by 1 ppm of CO can be resolved easily while the single channel hardly resolves 10 ppm. This can be attributed to the higher analog amplification that is possible in the offset free differential channel.

The differential channel is also less prone to drift introduced by the chamber optical properties (swelling, temperature change, etc).

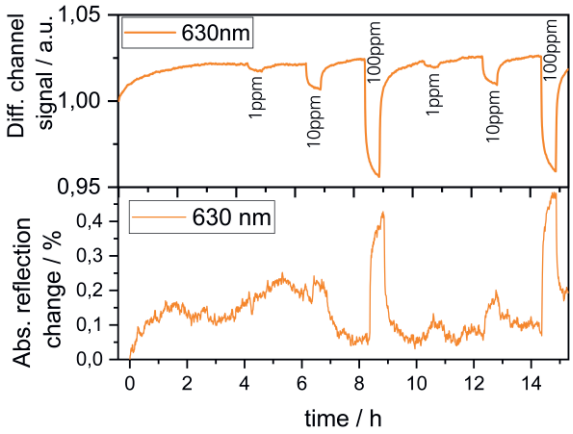

Fig. 3. Comparison of the Normalized signal of the differential detector (top) with the single channel delivering an absolute reflection change (bottom)

Conclusion

Within the scope of this work, we developed a multispectral readout circuit, which enables the detection of diminutive color changes of gasochromic dyes. Our measurement results, with a rhodium complex based dye, show the possibility to detect 1 ppm CO while showing less drift compared to a single channel measurement

References

[1] A. Duric, H. Ebner, M. Forster, I. Vinage: “Development of a multi-sensor detector for fire detection and life safety applications”, 14th International Conference on Automatic Fire Detection AUBE09, Duisburg Germany 2009.

[2] F. Cotton, A. Chakravarty, D. Tocher, J. Tocher, Structural and Electrochemical Characterization of the Novel Ortho-Metalated Dirhodium(II) Compounds Rh2(O2CCH3)2[(C6H5)2P(C6H4)2*2L, Organometallics 4 (1985) 8–13

DOI 10.5162/SMSI2021/C1.1

Spatial homogeneity of the radiance of a large-diameter integrating sphere in the SWIR measured with an InGaAs camera

Sebastian König[1], Berndt Gutschwager[1], Ingmar Müller[1], Richard D. Taubert[1]
[1] Physikalisch-Technische Bundesanstalt, Abbestr. 2-12, Berlin, Germany,
sebastian.koenig@ptb.de

Summary:
We present the investigation of the spatial homogeneity of radiance of a large-diameter integrating sphere in the SWIR measured with an InGaAs camera. A procedure developed at PTB is used to correct the non-uniformity of the infrared camera used. Various configurations are examined and the suitability of the examined sphere for characterizing IR cameras. The integrating sphere was found having a homogeneity of ± 1% in the integral wavelength range from 0.9 µm to 1.7 µm.

Keywords: Infrared camera, infrared, non-uniformity, metrological characterization

Introduction

InGaAs (Indium Gallium Arsenide) detectors provide the highest specific detectivity (D*) of all detectors used in SWIR wavelength range at the lowest acquisition and operating costs [1]. This makes contactless temperature measurement with thermographic SWIR cameras available to a large number of users. For the characterization and calibration of infrared cameras, large-area radiation sources with a homogeneous radiation temperature distribution are required in order to be able to irradiate the entire field of view of the IR cameras homogeneously. For temperatures above 500 °C, there are no large-area emitters available that would be capable of irradiate the entire field of view of an IR camera and have a good homogeneity of their radiation temperature over the entire area. Furthermore, when measuring in front of a large-area radiation source at high temperatures, the camera housing heats up. The effect of thermal load on cameras and methods for compensation have been investigated previously for cameras systems based on uncooled, shutterless microbolometer detector arrays [2]. Since InGaAs detector arrays differ fundamentally from thermal detectors with respect to the detection mechanism and spectral responsivity behavior, thermal loads and the associated, photon detector specific effects cannot be compensated applying methods for thermal detectors. Consequently, different approaches for characterization and calibration are required.

Hence, integrating spheres, especially when equipped with LEDs tailored for the spectral range of the device under test (DUT), are tunable radiance sources without introducing a noticeable heat load on the DUT. However, the radiometric characterization of integrating spheres is cumbersome and time consuming, especially when the spatial dependence of the radiance is concerned [3]. In this work, the feasibility of a fast measurement method that can obtain the relative spatial uniformity of the radiance without being affected by the non-uniformity of the responsivity of the applied SWIR camera, the so-called DRM [4], is investigated. The DRM was originally developed as a non-uniformity correction for LWIR cameras. Here, it is used in SWIR for the first time.

Measurement setup

The large-aperture variable-radiance source (LAVRAS) [3] is based on an integrating sphere with a diameter of 1.2 m, the radiating area has a diameter of 400 mm (Figure 1). The inner surface of the sphere is coated with $BaSO_4$ for high reflectivity. As optical radiation sources 64 reflector type, 50 W tungsten halogen lamps with aluminum-coated reflectors (type OSRAM 64607 EFM) are used. 2 lamps are each connected in parallel as a pair. All 32 pairs can be controlled individually, each lamp can be continuously dimmed by means of a mechanical shutter. 3 broadband-filtered Si-photodiode detectors are used as monitor detectors in the UV, VIS and SWIR wavelength range. A more comprehensive description can be found in [3], whereas the theory of integrating spheres is explained in detail in [5].
The camera used is a SWIR InGaAs camera, sensitive between 0.9 µm and 1.7 µm. The camera can only provide integral information

Fig. 1. The Large-Area, Variable Radiance Source (LAVRAS) of PTB

within its spectral range. However, by means of suitable optical filters, the spectral range can be narrowed and chosen as desired.

Characterization of an integrating sphere

The temporal stability of the sphere was monitored with the integrated detectors [3]. Sufficient stability over time is a prerequisite for using DRM. To determine the spatial homogeneity of the radiance from an integrating sphere, typically the aperture is scanned, with an imaging optical device e.g. with a radiation thermometer, which is very time-consuming. Therefore, the DRM is chosen to record the radiance proportional signals with a SWIR camera and to determine the spatial homogeneity of the radiance from this recording. However, a camera image is always a superposition of the recorded spatial radiation distribution and the non-uniformity of the spatial camera signal. By using the DRM, developed at PTB we are able to measure the spatial homogeneity of the radiance of the integrating sphere without being affected by the camera non-uniformity.

Measurements

The spatial homogeneity of the radiance of LAVRAS was measured for different settings. First, with the aid of the integrated lamp mechanical shutters, the radiance of LAVRAS was varied and the spatial homogeneity of the radiance was then examined. For this purpose, measurements were taken both with fully open shutters and with shutters half closed. In addition, the radiance homogeneity was examined when using all lamps and when using every second pair of lamps. In the third variation, the lights were turned off in the upper right quarter of the sphere.

Results

Figure 2 shows an example of the distribution of the radiance ratio based on a reference pixel in the center of the image. The lamp apertures of the integrating sphere were half-closed. The imaging geometry was chosen so that the corners of the field of view of the camera are just inside the integrating sphere aperture.

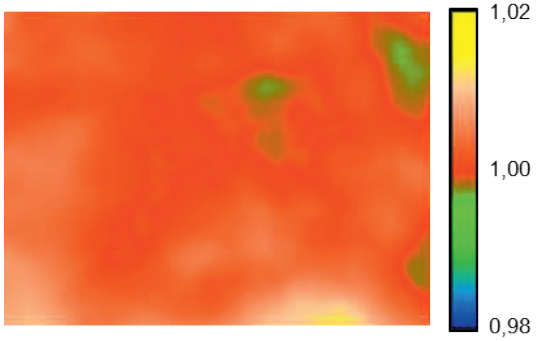

Fig. 2. Calculated distribution of the radiance ratio based on a reference pixel in the center of the integrating sphere, based on the measurement results with the InGaAs camera.

Conclusion

The integrating sphere was found having a homogeneity of ± 1 % in the integral wavelength range from 0.9 µm to 1.7 µm, measured with the DRM corrected InGaAs camera. This result is consistent with the results obtained in the UV up to the NIR [3]. If the radiance is reduced by closing the diaphragms on the lamps, it has been shown that the homogeneity of the radiation is only lightly affected. Similar results occur when the irradiation is varied by switching off different lamps. This indicates that the sphere coating is a close realization of a Lambertian reflector.

Outlook

In a next step, the measured radiance proportional values should be assigned to radiance temperatures. For this purpose, the SWIR camera is spectrally matched by optical filters to radiation thermometers or filter radiometers that are used to obtain the radiance temperatures of LAVRAS.

References

[1] Marc P. Hansen, Douglas S. Malchow: Overview of SWIR detectors, cameras, and applications, Proc. SPIE 6939, 2008

[2] A. Tempelhahn, H. Budzier, V. Krause, G. Gerlach: Improving the shutter-less compensation method for TEC-less microbolometer-based infrared cameras, SPIE Defense + Security. Baltimore, 2015. Bellingham: SPIE, Vol. 9451, 2015

[3] R. D. Taubert, C. Baltruschat, S. Schiller, and J. Hollandt: Radiometric characterization of a large-aperture variable-radiance calibration source for remote sensing applications, NEWRAD 2014, 25-26, 2014

[4] Gutschwager B. and Hollandt J.: Nonuniformity correction of imaging systems with a spatially nonhomogeneous radiation source, Applied Optics 54, Issue 36, 10599-10605, 2015

[5] David G. Goebel: Generalized Integrating-Sphere Theory, Appl. Opt. 6, 125-128, 1967

DOI 10.5162/SMSI2021/C1.2

Thermopile Arrays for IR Imaging and body temperature screening applications

Schieferdecker, J.; Schnorr, M., Forg, B.; Herrmann, F., Schmidt, C.; Leneke, W.; Simon, M. Heimann Sensor GmbH, Maria-Reiche-Str. 1, 01109 Dresden, Tel. +49-351-888885-0; E-mail: info@heimannsensor.com

Infrared arrays found their way into wide spread applications in various industries. Due to increasing resolutions and decreasing costs the growth rates for Infrared (IR) imaging sensors and cameras are assumed to continue having double digit annual growth rates also for the coming decade of the twenties. While photon IR detectors have been the drivers for thermal imaging in last century, the innovations in Si microelectronics and MEMS paved the way of success for uncooled thermal detector arrays. Pyroelectric arrays, which lead to the very first automotive night vision camera with 80000 pixels in year 2000 /1/, fell back due to their need of continuous mechanical modulation and the difficulty to integrate pyroelectric sensitive materials into monolithic CMOS structures. After that, micro-bolometers dominated the high resolution imaging markets /2/; while fully monolithic Poly-Si type IR thermopiles where the trendsetters for lower resolution consumer applications.

Unlike the other array technologies the thermopile arrays allow to build true shutterless radiometric IR cameras. The reason is, that thermopile arrays are DC sensitive devices and do not need to be biased. Thermopile arrays with pixel numbers from 8x8, 16x16, 32x32 resp. 32x24 were introduced to mass production for various consumer applications. In addition, the pixel size of 90 µm allowed a first thermopile array with 80x64 pixels /3/. Especially the 32x32 arrays and the 80x64 found large acceptance for automatic fever screening applications in the fight against the spread of actual COVID-19 worldwide pandemic.

In first part of this paper we describe, how fast the lower resolution thermopile arrays could be integrated into body temperature screeners to fight against COVID-19 pandemic spread. Second part will introduce first thermopile arrays with 60 µm pixel size, which allow to extend the application range into thermal Imaging and surveillance. All necessary signal conditioning and readout electronics including SPI interface are monolithically integrated on the sensor chip and allow thermopile arrays up to 120x84 pixels to fit in a standard TO-8 housing.

Most thermopile arrays going into the body temperature screeners using simple 32x32 arrays with a single Ge lens using special coating for the 8-14 µm range. Due to small chip, simple fixed focus optics and no need for vacuum packaging, they can be produced in very high volumes. Due to low pixel count, the screening was only for one person in narrow range up to about 1 m or so – sufficient for building entrance control. 80x64 arrays were bigger and more costly, but could be used to measure temperatures at up to three or four persons simultaneously.

The digital output via SPI interface reduces the number of necessary connections of both 80x64 and the new 120x84 arrays to 6-pin only. Thanks to integrated 16 Bit AD converters on-chip the sensor arrays can be operated with Frame Rates up to 12 Hz (full resolution) and allow a very wide dynamic range with object temperatures up to 1000 °C. Higher frame rates are possible by setting the ADC resolution to 15 or 14 Bit. Since the new 120x84 array chip has 60 µm pixels vs the 90 µm pixels of the 80x64, both chips come with similar focal plane and chip sizes. Due to their identical SPI interface both chips can be mounted in same housing with same optics, allowing a fully compatible “drop in” solution.

Thermopile arrays are low cost but efficient sensors in 2020 fighting the COVID-19

Fig. 1 shows a selection of devices for body temperature measurement in the market.

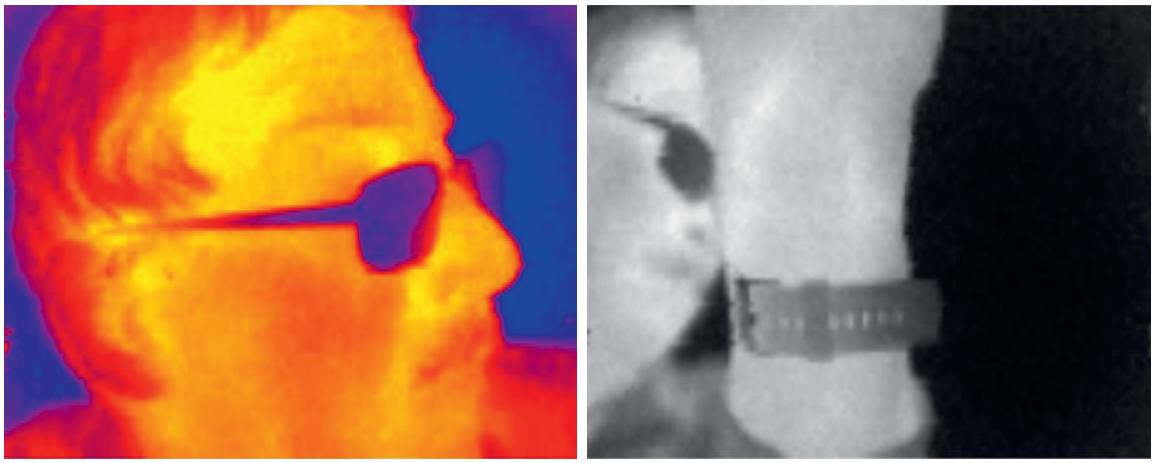

Fig. 2 shows examples for thermal images created by the 120x84 array module.

References

[1] Martinelli, N., Boulanger S.: “Cadillac de Ville Thermal Imaging Night vision system”, SAE Technical Paper 2000-01-0323, 2000

[2] T. Hoelter, A. Kathman, A. Richards, M. Walters; “Key Technology Trends and Emerging Applications for Compact Thermal Imagers”, Proceedings, Conference Sensor & Test, Nuremberg, 2015, p. 938.

[3] Schieferdecker, J.; Schnorr, M., Forg. B.; Herrmann, F., Schmidt, C.; Leneke, W.; Simon, M.: A new family of digital Thermopile Arrays for high volume applications; Proceedings Conference Sensor & Test 2019, Nuremberg, Germany

DOI 10.5162/SMSI2021/C1.3

A Novel Approach to Model the Thermal-electrical Behavior of Pyroelectric Infrared Sensors

Robin Lehmkau[1], Jens Lienig[2]
[1] InfraTec GmbH, Gostritzer Str. 61, 01217 Dresden (Germany),
[2] TU Dresden, Institute of Electromechanical and Electronic Design, 01062 Dresden (Germany)
r.lehmkau@infratec.de

Summary:
The combined evaluation of the thermal and electrical domain of a pyroelectric system is a challenging task. The proposed approach precisely models the thermal system with FEM. The output data is approximated with a fit function and transferred to SPICE creating a universal and adaptable model for the whole pyroelectrical signal chain. For validation, the *InfraTec* detector *LRM-244* is used.

Keywords: FEM, SPICE, pyroelectric detector, thermal-electrical model, *LRM-244*

Motivation

Pyroelectric detectors are used for high-performance contactless gas analysis and fast flame detection. To accelerate the design and development process of improved detectors with new materials or geometry, a precise and customizable model is needed. The main dependencies of the generated pyroelectric current I_{pyro} are the pyroelectric coefficient p of the material, the effective surface A and the time derivation of the temperature change dT/dt shown in Eq. (1).

$$I_{pyro} = p \cdot A \cdot \frac{\mathrm{d}T}{\mathrm{d}t} \qquad \text{Eq. (1)}$$

The prediction of the temperature behavior is a challenging task. Specifically, the transfer of the temperature data to the electrical domain in order to evaluate the resulting pyroelectric current and output voltage are an open problem.

The contribution of this paper is an optimized approach to model the signal behavior of pyroelectric detectors regarding the whole signal chain from the incident thermal radiation to the electrical output signal. The method can be used for any detector geometry, pyroelectric material, and electrical readout circuit.

Thermal System

Often, the thermal behavior is modeled by a simple low-pass consisting of a thermal resistance R_{th} (K/W) and a thermal capacitance C_{th} (J/K). An analytical method is to solve the equation for the one-dimensional thermal conduction, by which the temporal and additionally spatial resolution can be analyzed [1].

A more precise approach uses several RC-elements building the dominating conducting paths of a thermal system, which can be connected like a possibly multidimensional Cauer or Foster ladder as shown in Fig. 1. Note that inaccuracies of this model can occur due to the limited number of lumped RC-elements [2].

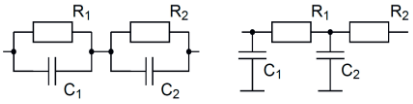

Fig. 1: Foster- (left) and Cauer (right) ladder of a simple thermal system

The most precise solution is achieved by using a software with the finite-element-method (FEM). Moreover, any detector shape can be modeled fast with CAD. It is helpful to define an interface between the thermal and electrical subdomains, as the calculation of a multiphysics problem with FEM needs much setup and computing effort.

Therefore, we simulate the thermal system with the FEM-tool *COMSOL Multiphysics™*. The pyroelectric detector *LRM-244* of *InfraTec* serves as demonstration example. It is sufficient to model the sensor chip, the absorption layer, the optical filter, glue dots, the gold coated chip holder and a small part of the circuit board surrounded by air, illustrated for one signal channel in Fig. 2. We noticed further details can be neglected.

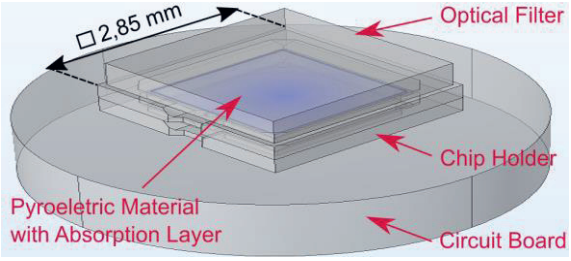

Fig. 2: FEM model of LRM-244 with the thermal dominating parts. The surrounding air block is hidden.

The input signal is modeled as thermal flux with the property “thermal perturbation” and fed into the absorption layer. The outer faces of the circuit board are kept at ambient temperature. As result the temperature change $\Delta T(f)$ of the pyroelectric material depending on discrete steps of the excitation frequency can be investigated.

Thermal-electrical Interface

The next step is to fit a continuous regression function $A(s)$ to the simulated discrete behavior $\Delta T(f)$. Simplified pyroelectrical systems have two dominating thermal time constants, depending on the sensitive material itself τ_1 and the absorption layer τ_2. They each can be described by a classical first order low-pass in Laplace notation with the complex frequency parameter s. Besides, there can be deviations from a typical low-pass behavior due to a special detector geometry or additional material layers. That is why $A(s)$ in Eq. (2) is extended by the terms containing τ_3 and τ_4 to support the precise evolving of the regression function.

$$A(s) = \boldsymbol{v} \cdot \frac{1}{1+s\cdot\boldsymbol{\tau_1}} \cdot \frac{1}{1+s\cdot\boldsymbol{\tau_2}} \cdot \frac{1+s\cdot\boldsymbol{\tau_3}}{1+s\cdot\boldsymbol{\tau_4}} \qquad \text{Eq. (2)}$$

Here, the variable v is a linear conversion factor considering the used incident radiation flux of 1 W/m² in FEM. The parameters of $A(s)$ are calculated by a function of *SciPy* using the least-square-method. A weigh function is implemented to ensure a small relative error over the relevant frequency range from typically 0,1 Hz … 1 kHz.

Figure 3 shows the fit function of the thermal system compared to a simple first order low-pass with τ_{th} = 150 ms. Especially at higher modulation frequencies, the relative error between simulation and fit stays below 0,5 % for f < 10 kHz.

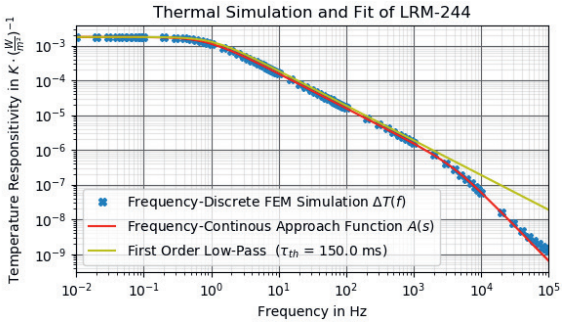

Fig. 3: Comparison of the discrete simulation data, continuous fit function and a first order low-pass

Simulation of the Pyroelectrical System

The thermal fit function $A(s)$ can be transferred to a circuit analysis program like *LTSpice* using an arbitrary behavioral voltage source V_1. Referring to Eq. 1, the time derivate of the temperature change can be simulated using V_2. Finally, a voltage dependent current source I_1 with the gain factor “$p{\cdot}A$” generates the frequency dependent pyroelectric current for an input radiation $\Phi(t)$.

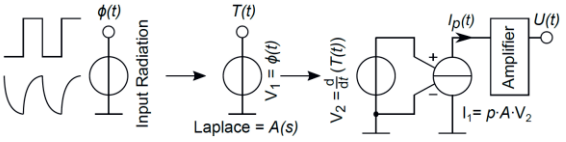

Fig. 4: Signal chain of the pyroelectrical system

The current $I_p(t)$ is fed into an electrical amplification circuit. For the LRM-244, a transimpedance amplifier with 100 GΩ feedback is used.

Model Validation

The results of the novel approach are demonstrated in Fig. 5. The relative errors of noise and relative amplitude between simulation and measurement are typically below 10 % and deviations mostly depend on the thermal and electrical component tolerances.

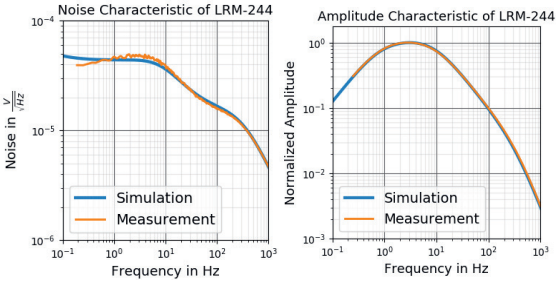

Fig. 5: Noise (left) and amplitude (right) characteristic of LRM-244 compared to the measured signals

The following table shows the results of an absolute signal simulation compared to a measurement with a lab setup and blackbody emitter (500 K, 10 Hz, no filter).

Intensity	Simulation	Measurement	Rel. Error
3,26 W/m²	1,15 V_{rms}	1,27 V_{rms}	9,4 %

Conclusion

The proposed new model for pyroelectric systems offers a fast and precise prediction of the signal and noise behavior of any detector geometry. Both the thermal and the electrical system can be largely adapted and combined with arbitrary material parameters. Even in early stages of the design process, the frequency dependent signal-to-noise-ratio (SNR) and the specific detectivity D* can be assessed and optimized.

References

[1] H. Budzier, G. Gerlach: “Thermische Infrarotsensoren: Grundlagen für Anwender“ *Wiley-VCH* (2010), ISBN: 978-3-527-40960-0

[2] M. Touzelbaev et al.: “High-Efficiency Transient Temperature Calculations for Applications in Dynamic Thermal Management of Electronic Devices“ *Journal of Electronic Packaging (2013),* DOI: 10.1115/1.4024747

DOI 10.5162/SMSI2021/C1.4

Mobile Near Infrared Spectrometer with a MEMS-FPI Sensor

Artem Ivanov[1], *Arne Kulinna*[1]
[1] *Landshut University of Applied Sciences, Am Lurzenhof 1, 84036 Landshut, Germany*
Artem.Ivanov@haw-landshut.de

Summary:
A fast, user friendly and inexpensive hand-held NIR Spectrometer is described. Spectra in the range of 1550 nm–1850 nm are acquired using a MEMS-FPI spectrum sensor. Device control and visualisation of data is accomplished using a software application running on Windows- or Android-devices. Implementation details and experimental results are discussed.

Keywords: NIR, Spectrometer, hand-held, MEMS-FPI, screening.

Introduction

Currently just a few mobile NIR spectrometers are available on the market. These devices focus on use in quality control for agriculture and food industry as well as in the recycling sector [1, 2]. Presented spectrometer was built during a bachelor thesis project with the main goal to develop a low cost hand-held device for measuring reflection Spectra in NIR region in combination with a smartphone or a PC. As the spectrum sensor a Hamamatsu MEMS-FPI (Fabri-Perot Interferometer) was chosen [3]; the manufacturer proposes it for applications like screening of plastics and textiles, moisture detection and ingredient analysis of food. Starting from the 3rd quarter of 2020 Hamamatsu also offers complete spectroscopic modules with MEMS-FPI spectrum sensors [4].

The presented mobile device features a C13272-03 spectrum sensor working in the wavelength range from 1550 nm to 1850 nm [5], a control circuitry, a secondary Li-ion cell, USB connection for data communication and battery charging and wireless connectivity via Bluetooth. The device is controlled from the cross-platform software app which offers an easy access to all necessary functions for taking, saving and loading spectra. It runs on Windows- or Android-based systems (Fig. 1).

Description of the System

The tuneable MEMS-FPI filter is controlled by the applied voltage in the range from 23 V to 38 V; its spectral resolution lies below 15 nm FWHM. To acquire a spectrum the current of the integrated photodiode is recorded for different values of control voltage. In the presented device all necessary tasks are performed by microcontroller-based electronics. Thanks to a high number of available peripherals of the used controller (PIC24FJ128GC006) it was possible to implement the majority of functions in a single chip.

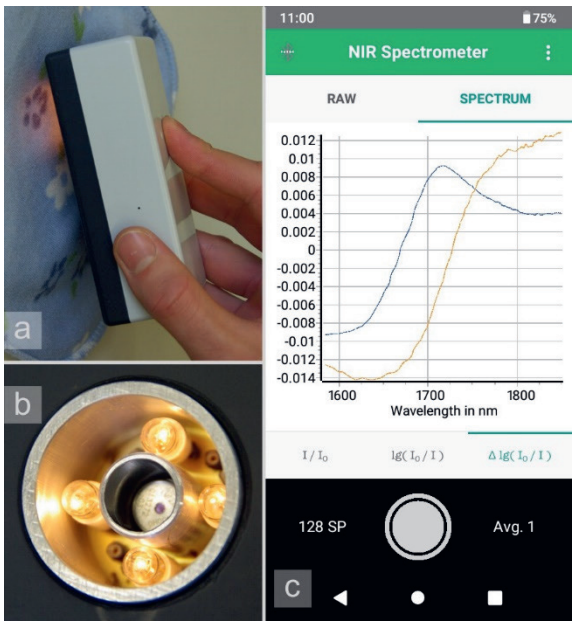

Fig. 1. The mobile NIR spectrometer (a), a close-up view of the illumination optics (b) and a screenshot of the visualization and control app (c) showing spectra of PET (blue) and HDPE (red).

The control voltage for the MEMS-FPI filter is generated internally using a step-up converter and is ramped during a spectral scan; the number of steps is set in the app. During every step 1 ms time is allowed for the mirror of the MEMS-FPI filter to stabilise, afterwards the photodiode signal is acquired by a 16-bit sigma-delta ADC for 1 ms. The total time needed for one spectrum scan depends on the required number of points in the spectrum, for example one scan with 128 points takes 0.25 s. Currently the number of samples can be set in the range between 64 and 1024 which stands for the equivalent step

of 5 nm to 0.3 nm wavelength. To reduce the noise several scans can be performed and averaged as set in the app.

Standard miniature T-1¾ bi-pin base incandescent lamps are used as the light source, the device can be equipped with up to eight lamps. Based on their intensity to current ratio the lamps of 7361 type (5 V/60 mA nominal, driven at 3.15 V/45 mA) were chosen. In case of using only one lamp, a lamp of type 7868 (2.5 V/0.35 A nominal) driven at 2.5 V or 2.0 V is suggested for a higher intensity.

The system uses simple reflective optics for illumination of the test sample in front of the sensor. It consists of two blank aluminium tubes and the metallisation of the circuit board below the lamps and is used to direct the light onto the sample while obstructing the direct light path between the lamps and the detector (Fig. 1 b). An additional aperture in front of the sensor can be used to restrict the incidence angle. This lowers the signal amplitude but improves the spectral resolution. A significant positive effect on the obtained spectra of plastics due to the installed aperture was observed, while spectra of textiles remained almost unchanged. Such beam aperture can be added to the design in form of a cap either mounted into the interior tube or placed directly on the sensor housing.

According to [4] it is important to track the temperature of the spectrum sensor to compensate for the temperature induced shifts in the transmission wavelength of the MEMS-FPI filter and to avoid the pull-in of the upper interferometer mirror which can destroy the sensor. This function is accomplished in the presented system by a continuous measurement of integrated thermistor resistance.

The acquired spectrum data can be visualised in the control app in four different representation variants: as raw data in ADC counts, as transmittance ($T = I/I_0$) and absorbance ($A = lg(1/T)$) as well as the relative absorbance (with constant offsets eliminated). Currently no additional evaluation of spectra is performed. The measurement of the reference spectrum (I_0) is carried out with a “white” reflector (e.g. alumina or a matted metal sample) and contains a dark signal measurement taken with the light source switched off.

Results and Discussion

Notwithstanding the relative simplicity of the presented device SNR of about 10^4 was achieved; spectra of different materials can be acquired in a fast and simple manner. Fig. 2 gives exemplary results for three textile materials showing clear differences in the measured spectral range.

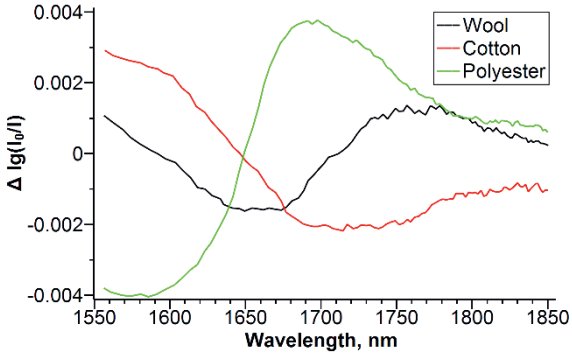

Fig. 2. Spectra of three textile materials measured with 128 sample points in ten scans (spectrum acquisition time 2.5 s).

In a plastic sorting application the thickness of the typical items (soft-drink bottles, yoghurt cups, etc.) is low, generally leading to a low reflection and poor spectral data in a direct measurement. It has proven useful to conduct such measurements on a reasonably white surface taking its reflection spectrum as the reference. Spectra acquired in this setup are not strictly reflective but represent a mix of transmission and reflection measurements. Nonetheless, the spectral features remained similar to the pure reflection of thick samples for all tested materials. In tests with textile samples the reflection of the sample alone was always sufficiently high.

The presented project demonstrates a possibility to build a low cost mobile NIR spectrometer (the total hardware effort well below 100€ in addition to the spectrum sensor) capable of fast distinguishing between different sorts of materials. In the next steps optimisations of the illumination optics and control circuitry as well as integration of spectral evaluation features and material identification algorithms in the software app are planned.

References

[1] Consumerphysics.com, SCIO by Consumer Physics. [Online]. Available: https://www.consumerphysics.com. [Accessed: 27-Nov-2020]

[2] TrinamiX, Mobile NIR Spectroscopy Solutions. [Online]. Available: https://trinamixsensing.com/nir-spectroscopy/. [Accessed: 27-Nov-2020]

[3] Hamamatsu, MEMS-FPI spectrum sensors. [Online]. Available: https://www.hamamatsu.com/eu/en/product/optical-sensors/spectrometers/mems-fpi-spectrum-sensor/index.html. [Accessed: 27-Nov-2020]

[4] Hamamatsu, MEMS-FPI spectroscopic module. [Online]. Available: https://www.hamamatsu.com/eu/en/product/optical-sensors/spectrometers/spectroscopic-modules/index.html. [Accessed: 27-Nov-2020]

[5] Hamamatsu, MEMS-FPI Spectrum Sensor C13272-03, Datasheet (Feb. 2020)

DOI 10.5162/SMSI2021/C2.1

Laser excited super resolution thermal imaging for nondestructive testing

S. Ahmadi[1], J. Lecompagnon[1], P. D. Hirsch[1], P. Burgholzer[2], P. Jung[3], G. Caire[3], M. Ziegler[1]
[1]Bundesanstalt für Materialforschung und -prüfung, 12200 Berlin, Germany,
[2]RECENDT, Research Center for Non-Destructive Testing, 4040 Linz, Austria,
[3]Technical University of Berlin,10587 Berlin, Germany
samim.ahmadi@bam.de

Summary:
The work to be presented focuses on our most recent studies to laser excited super resolution (SR) thermography. The goal of nondestructive testing with SR is to facilitate the separation of closely spaced defects. Photothermal SR can be realized by performing structured illumination measurements in combination with the use of deconvolution algorithms in post-processing. We explain that stepwise as well as continuous scanning techniques are applicable to generate structured illumination measurements. Finally, we discuss the effect of experimental parameters and image processing techniques to find the optimal SR technique which leads to the highest reconstruction quality within laser thermography.

Keywords: super resolution, laser thermography, nondestructive testing, laser scanning, photothermal imaging

Introduction

The diffuse nature of the heat is mainly responsible for the fact that two defects located close to each other cannot be resolved with an infrared (IR) camera. The IR camera measures a Gaussian-shaped temperature rise over both defects.

SR techniques have already been used in other scientific fields and are known e.g. in optics [1]. Even in non-destructive testing, SR techniques have been applied, for example in photoacoustics [2]. SR can be realized in different ways, but all these SR techniques have the same goal, namely to increase the spatial resolution (artificially) to improve the details in the image.

In the recent past, photothermal super-resolution techniques have shown that it is possible to overcome the conventional resolution limits in thermography. Through appropriate experiments and the application of appropriate image processing algorithms to the measured data, we have been able to obtain more information in our thermal images [3,4,5].

Since laser scanning can easily be combined with thermography and is therefore of high interest for the industry in terms of non-destructive and non-contact testing [6], we conducted investigations on the applicability of SR techniques. We investigated the influence of experimental parameters like laser line width or laser pulse length on the reconstruction quality. We also analyzed the influence of image processing techniques such as the superposition of different measurements or the selection of suitable regularization parameters to optimize our reconstruction results, e.g., by using compressed sampling-based algorithms such as the iterative joint sparsity approach (IJOSP) [7].

Methods

To understand how super resolution techniques can be used in laser line thermography, it is advisable to describe the measured temperature data of the IR camera mathematically. For the reflection configuration (we measure with the IR camera from the same side where we illuminate) our temperature field can be described as follows [8]:

$$T(r, z=0, t) = T_0 + \frac{2}{\rho c_p \pi 4\alpha} \cdot \int_0^t \int_{-\infty}^{\infty} q(r-\tilde{r}, t-\tilde{t}) e^{-\frac{(r-\tilde{r})^2}{4\alpha(t-\tilde{t})}} \frac{d\tilde{t}}{\tilde{t}}\, d\tilde{r}\,, \qquad (1)$$

where T_0 stands for the initial temperature, ρ for the mass density, c_p for the specific heat, α for the thermal diffusivity, q for the heat flux density. The variation of the laser pulse length is considered by the convolution in time with the variable $\tilde{t}$ and the variation of the laser line width is considered by the convolution in space with the variable $\tilde{r}$.

Within our SR studies [3,4,5] we rewrite equation (1) by using the following equation which describes temperature differences:

$$\Delta T(r, z = 0, t) = T(r, z = 0, t) - T_0 = A * x, \quad (2)$$

whereby A represents the thermal point spread function (PSF) which can be described as a Green's Function as a solution of the underlying heat diffusion equation considering the laser line width and laser pulse length. x simply stands for the defect structure in our investigated material, hence x represents absorption coefficients in space.

Since the exact position of illumination is in reality hard to determine, we decided to put the information about the spatial information into x whereas the temporal information that is known pretty well can be kept in A. Therefore, we talk about blind structured illumination. As structured illumination means that multiple measurements have to be performed to scan the whole sample surface, the equation (2) changes to:

$$\Delta T^m = A * x^m \quad (3)$$

All measurements m from structured illumination have in common that the same sparse defect pattern is considered. For this reason, we are using iterative joint sparsity algorithms (IJOSP) [4] to estimate x^m from the underlying ill-posed problem in equation (3) and thus, to obtain the defect pattern.

Results

Figure 1 (b) shows an exemplary result after applying the so-called Block-Elastic-Net optimization to the measured data shown in Figure 1 (a).

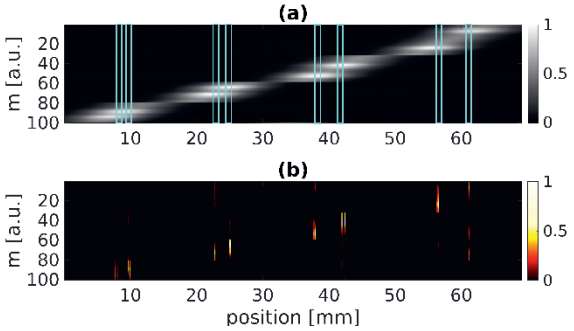

Fig 1. (a) Measured temperature difference data normalized by the maximum temperature value is shown in white. The defect pattern to be reconstructed is shown in blue and consists of four defect pairs with a distance of 0.5, 1, 2, 4 mm, respectively. We measured films with the infrared camera in transmission configuration for each position with a position shift of 0.2 mm. To create this diagram we took the maximum thermogram and calculated the mean over the vertically arranged pixels of the maximum thermogram. One measurement number refers to a measurement at one position. (b) estimated x^m after applying IJOSP with Block-Fast-Elastic-Net. The resulting amplitude values are again normalized by the maximum amplitude.

In our studies we have investigated different scenarios by varying experimental parameters such as the laser pulse length and the laser line width. It turned out that it is beneficial to use narrow laser lines as well as short pulses due to the fact that the thermal PSF does not get wider which makes sense from a super resolution point of view.

Furthermore, we discovered post-processing algorithms which enable us to increase the reconstruction quality of our defects (see the comparison of Figure 1 (a) and (b) by applying Block-Fast-Elastic-Net). However, the effectiveness of these algorithms relies on priors such as the joint sparsity of all measurements [3, 4, 5, 7].

References

[1] Thomas A. Klar and Stefan W. Hell, Subdiffraction resolution in far-field fluorescence microscopy, Optics Letters 24 (14), 954-956 (1999); doi: 10.1364/OL.24.000954

[2] M. Haltmeier et al., Compressed sensing and sparsity in photoacoustic thermography, Journal of Optics 18 (11).

[3] S. Ahmadi et al., Photothermal super resolution imaging: A comparison of different thermographic reconstruction techniques, NDT & E International Journal 111, 102228

[4] S. Ahmadi et al., Super resolution laser line scanning thermography, Optics and Lasers in Engineering 134, 106279.

[5] S. Ahmadi et al. "Laser excited super resolution thermal imaging for nondestructive inspection of internal defects." arXiv preprint arXiv:2007.03341 (2020).

[6] Schlichting et al., Flying Laser Spot Thermography for the Fast Detection of Surface Breaking Cracks, 18th World Conference on Nondestructive Testing (2012)

[7] P. Burgholzer et al., Super-resolution thermographic imaging using blind structured illumination, Applied Physics Letters 111 (3)

[8] K. D. Cole et al., Heat Conduction Using Green's Functions, 2nd Edition, CRC Press (2010)

[9] P. Burgholzer et al., Blind structured illumination as excitation for super-resolution photothermal radiometry, Quantitative InfraRed Thermography Journal (2019) 1–11

DOI 10.5162/SMSI2021/C2.2

2D-Photothermal super resolution with sparse matrix stacking

J. Lecompagnon[1], S. Ahmadi[1], P. D. Hirsch[1], M. Ziegler[1]
[1]Bundesanstalt für Materialforschung und -prüfung, 12200 Berlin, Germany,
Julien.Lecompagnon@bam.de

Summary:
Thermographic super resolution techniques allow the spatial resolution of defects/inhomogeneities below the classical limit, which is governed by the diffusion properties of thermal wave propagation. In this work, we report on the extension of this approach towards a full frame 2D super resolution technique. The approach is based on a repeated spatially structured heating using high power lasers. In a second post-processing step, several measurements are coherently combined using mathematical optimization and taking advantage of the (joint) sparsity of the defects in the sample.

Keywords: super resolution, laser thermography, nondestructive testing, laser scanning, photothermal imaging

Introduction

Photothermal super resolution (SR) is based on a combination of an experimental scanning strategy and a numerical optimization, which has been proven to be superior to standard thermographic methods in the case of one-dimensional linear defects. Due to complexity constraints, laser scanning SR techniques have been mostly limited to evaluation of one-dimensional defect patterns and/or small Regions of Interest (ROI) [1, 2, 3]. Extending the SR problem to more dimensions significantly increases the amount of measurement data and the number of measurements required to achieve sufficient defect resolution to cover large areas. With the incorporation of a limited number of priors, such as a sparse representation of the defect density, and with a purposeful exploitation of the sparse nature of the underlying physical models, the increased complexity can be made manageable.

Methods

The surface temperature of a thin plate exposed to a heating Q with spatial structure $I_{x,y}$ and temporal structure I_t can be described by:

$$T_{meas}(x,y,z=0,t) = T_0 + \Phi_{PSF}(x,y,t) \; *_{x,y} \; a(x,y) \tag{1}$$

$$\Phi_{PSF}(x,y,t) = \frac{2\cdot \mathrm{Q}}{c_p \rho (4\pi\alpha t)^{3/2}} \cdot e^{-\frac{(x-\hat{x})^2+(y-\hat{y})^2}{4\alpha t}} \cdot \sum_{n=-\infty}^{\infty} R^{2n+1} \, e^{-\frac{(2nd)^2}{4\alpha t}} \; *_t \; I_t(t) \tag{2}$$

$$a(x,y) = a_0(x,y) \; *_{x,y} \; I_{x,y}(x,y) \tag{3}$$

where T_0 denotes the initial system temperature, ρ the mass density, c_p the specific heat, α the thermal diffusivity, $(\hat{x},\hat{y})$ the coordinates of the centroid of the excitation, R the thermal wave reflexion coefficient ($R \approx 1$), d the plate thickness and a_0 the heat source distribution. The operators $*_{x,y}$, $*_t$ represent the convolution operator in the indicated dimensions [2].

The spatial and temporal dimensions can be discretized as follows:

$$x_i = i \cdot \Delta x, \quad y_j = j \cdot \Delta y, \quad t_k = k \cdot f_{cam}^{-1} \tag{4,5,6}$$
$$i \in \{1,\dots,n_x\}, \qquad j \in \{1,\dots,n_y\}, \qquad k \in \{1,\dots,n_t\}$$

A series of $m \in \{1,\dots,n_m\}$ independent measurements can be described by:

$$T_{meas}[x_i,y_j,t_k,m] = T_0 + T_{diff}[x_i,y_j,t_k,m] \tag{7}$$

with T_0 representing the initial temperature of the sample at $t = 0$ s and T_{diff} being the differential temperature caused by thermal excitation.

In order to reduce the problem complexity, the time dimension can be eliminated by choosing a timestep $t = t_{eval}$ and only take the temperature change with respect to T_0 further into account:

$$T_{diff}[x_i,y_k,m] = T_{meas}[x,y,t=t_{eval},m] - T_0 \tag{8}$$

The spatial dimensions can then be merged by flattening to a single dimension r, applying a bijective transform assigning an index $n \in \{1,\dots,n_y \cdot n_x\}$ to every pixel coordinate $[x_i,y_j]$:

$$T_r[n,m] = T_{diff}[x_i,y_j,m] \tag{9}$$

$$[i,j]_{\mathrm{n}} = \left[\left\lfloor \frac{n-1}{n_y} \right\rfloor + 1, n - \left\lfloor \frac{n-1}{n_y} \right\rfloor n_y\right] \tag{10}$$

The inverse transform of Eq. (10) can be applied to reshape the data back to a two-dimensional image.

As an approximative model, the defect response can be defined as the convolution of the thermal PSF as a Green's function kernel and the heat source distribution $a_r[n,m]$ [4]:

$$\Phi_{PSF,r}[n] *_n a_r[n,m] = T_r[n,m] \tag{11}$$

The single measurement solutions can then be merged by summation.

$$a_{rec}[n] = \sum_m a_r[n,m] \tag{12}$$

To efficiently solve Eq. (11), it can be transformed to a multiplicative problem by introducing the discrete convolution matrix h(Φ_{PSF}) , such that:

$$h\left(\Phi^{\mathrm{m}}_{PSF,r}\right) \cdot a^m_r = \begin{bmatrix} 0 \\ T^m_r \\ 0 \end{bmatrix} = T^m_{r0} \qquad (13)$$

with dimensions $\Phi^{\mathrm{m}}_{PSF,r} \in \mathbb{R}^{n_x \cdot n_y}$, $h\left(\Phi_{PSF,r}\right) \in \mathbb{R}^{2n_x \cdot n_y - 1 \times n_x \cdot n_y}$ and $T^m_{r0} \in \mathbb{R}^{2n_x \cdot n_y - 1}$. The convolution matrix h is a sparse lower triangular matrix with Toeplitz-structure, allowing it to be stored memory-efficient despite its large dimensions.

This leads to solving n_m multiplicative inversion problems. In order to be able to exploit the joint sparsity between measurements in all n_m equations, they need to be solved simultaneously. This can be achieved by stacking:

$$H \cdot A = \begin{bmatrix} h & 0 & 0 \\ 0 & \ddots & 0 \\ 0 & 0 & h \end{bmatrix} \cdot \begin{bmatrix} a^1_r \\ \vdots \\ a^{n_m}_r \end{bmatrix} = \begin{bmatrix} T^1_{r0} \\ \vdots \\ T^{n_m}_{r0} \end{bmatrix} = T_{R0} \qquad (14)$$

with dimensions $H \in \mathbb{R}^{(2n_x \cdot n_y - 1) \cdot n_m \times n_x \cdot n_y \cdot n_m}$, $A \in \mathbb{R}^{n_x \cdot n_y \cdot n_m}$ and $T^m_{R0} \in \mathbb{R}^{(2n_x \cdot n_y - 1) \cdot n_m}$. H is a sparse diagonal block matrix, which makes it efficient to store. To enhance sparsity even further, a threshold to H is applied where $H < 10^{-6} = 0$.

Since all measured data is prone to noise and due to the ill-posed nature of the problem, H can not be inverted easily. Therefore the “Blocksoft” regularization method is applied [5]:

$$\min_A \frac{1}{2} \|\mathrm{H\,A} - T_{R0}\|_2^2 + \lambda_{21} \|A\|_{2,1} + \lambda_2 \|A\|_2 \qquad (15)$$

Where $\|A\|_{2,1}$ denotes the $L_{2,1}$-norm $\|A\|_{2,1} = \sum_m \sqrt{\sum_n A_n^{m\,2}}$ and λ_{21}, λ_2 are free regularization parameters. This $L_{2,1}$-norm couples the single measurements to achieve super resolution. Eq. (15) can be solved for A iteratively with the ADMM algorithm [6].

Results

To test the performance of the proposed algorithm we have examined a purpose made sample with blind structured heating. For this a diode laser with a wavelength of $940\ \mathrm{nm}$ and a total output power of $P_{total} = 500\ \mathrm{W}$ has been utilized while measuring the sample surface temperature with an IR camera ImageIR 9300 with a framerate of $f_{cam} = 100\ \mathrm{Hz}$ and a spatial resolution of $\Delta x, \Delta y = 60\ \mu\mathrm{m}$.

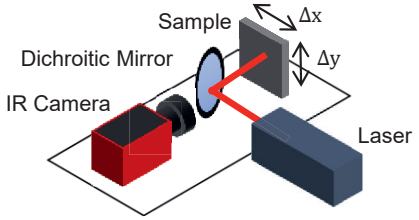

Fig. 1. Schema depicting the experimental setup for active thermography measurements with laser excitation in reflection configuration

The sample under investigation has been additively manufactured from 316L stainless steel ($\alpha = 3.76 \cdot 10^{-6} \frac{\mathrm{m}^2}{\mathrm{s}}$, $\rho = 7950 \frac{\mathrm{kg}}{\mathrm{m}^3}$, $c_p = 502 \frac{\mathrm{J}}{\mathrm{kg\,K}}$) and features several cubical defect pairs $0.5\ \mathrm{mm}$ beneath the front surface. Each defect has an edge length of $2\ \mathrm{mm}$ with decreasing distances within the pairs.

220 blind measurements with randomly sampled excitation positions across the ROI with a laser power of $P = 15\ \mathrm{W}$, a pulse duration of $t_{on} = 0.2\ \mathrm{s}$ and a laser spot size of $d_{spot} = 1.5\ \mathrm{mm}$ have been conducted. Applying our previously described 2D-SR evaluation technique, the resulting defect reconstruction a_{rec} is displayed in Fig. 2.

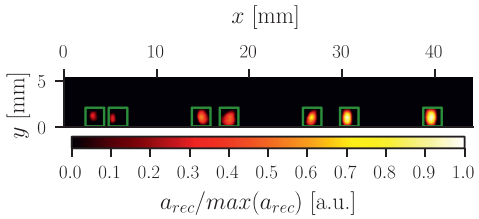

Fig. 2 Resulting defect density $a_{rec}(x_i, y_j)$ from solving Eq. (15) with an ADMM penalty $\rho_{ADMM} = 16$, $\lambda_{21} = 375$, $\lambda_2 = 20$ for $t_{eval} = 0.3\ \mathrm{s}$. The green boxes indicate the defect position and sizes. All defects and even close defect spacings up to $0.5\ \mathrm{mm}$ are resolved.

For reference, a single measurement with homogenous illumination across the sample surface has been performed. The measured data is shown in Fig. 3.

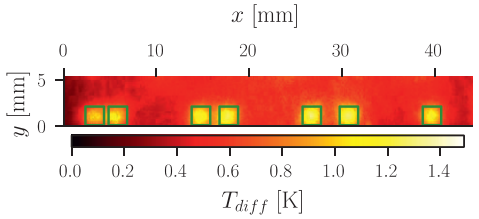

Fig. 3. Thermogram for full area homogeneous illumination for reference. $P = 450\ \mathrm{W}$, $t_{on} = 0.5\ \mathrm{s}$ sampled at $t_{eval} = 0.5\ \mathrm{s}$. All defects are clearly visible but closer defects cannot be resolved independently.

References

[1] S. Ahmadi, P. Burgholzer et al., Photothermal super resolution imaging: A comparison of different thermographic reconstruction techniques, NDT & E International,Volume 111 (2020); doi: 10.1016/j.ndteint.2020.102228

[2] S. Ahmadi, P. Burgholzer et al., Super resolution laser line scanning thermography, Optics and Lasers in Engineering, Volume 134 (2020); doi: 10.1016/j.optlaseng.2020.106279

[3] S. Ahmadi, J. Lecompagnon et. al., Laser excited super resolution thermal imaging for nondestructive inspection of internal defects, ArXiv preprint (2020), ArXiv:2007.03341

[4] K. Cole, J.V. Beck et al., Heat conduction using green’s functions, second edition. Taylor & Francis (2010); doi: 10.1201/9781439895214

[5] T. W. Murray, M. Haltmeier et al., Super-resolution photoacoustic microscopy using blind structured illumination, Optica 4, 17-22 (2017); doi: 10.1364/OPTICA.4.000017

[6] S. Boyd, N. Parikh et al., Distributed Optimization and Statistical Learning via the Alternating Direction Method of Multipliers, Foundations and Trends in Machine Learning 3, 1-122 (2011); doi: 10.1561/2200000016

DOI 10.5162/SMSI2021/C2.3

Thermographic method to locate concealed defects in Exterior Wall Insulation Panels of Prefabricated Houses

Veronika Putz[1], Richard Schmidt[1], Simon Haunschmid[2], Christian Kastl[1]
[1] Linz Center of Mechatronics GmbH, Altenberger Straße 69, 4040 Linz, Austria
[2] Synthesa Chemie Gesellschaft m.b.H., Dirnbergerstraße 29-31, 4320 Perg, Austria
Veronika.Putz@lcm.at

Summary
This contribution proposes using passive thermography to locate concealed defects in the exterior wall insulation of prefabricated houses, which may lead to spots with higher residual moisture. The method can be applied within approx. 3 days after plastering. Its usability is illustrated in several experiments.

Keywords: Non-destructive Testing, Quality Control, Thermography, Image Processing

Introduction

In prefabricated house construction, wall modules are fabricated in a factory hall, transported to the building site, and assembled. At the production site, a high degree of prefabrication is achieved: For example, all layers of a load-bearing exterior wall in timber frame construction, including vapor barrier, facade insulation (panels e.g. made of polystyrene), exterior plaster and a fiber glass reinforcement grid, can be assembled in the factory building. After construction, the modules are left in an indoor interim storage for drying before they are transported to the building ground. Due to space constraints, storage time needs to be as short as possible. However, to avoid damages during transportation, the plaster needs to be sufficiently dry before loading. Caused by local thickness variations of the plaster, spots with higher residual moisture may remain. Thickness variations occur at local defects (e.g. dents with depths of a few mm caused by storage and handling) of the underlying insulation panels or height deviations and gaps between neighboring panels. In this contribution, an NDT method to locate areas with residual moisture using thermography, which allows assessing concealed defects after plastering, is presented.

Measurement Principle and Setup

Freshly applied plastering material dries by the evaporation, which (without external heating) cools the plaster (evaporation cooling [1]). If a plastered wall is inspected in the infrared (IR) domain, moist segments are colder than dry areas. Applications of the method lie e.g. in the inspection of historic masonry [2] or in the detection of water damages in buildings. To adapt for locating small geometric errors in prefabricated exterior walls, an IR camera with high sensitivity is required[1].

Experiment 1: Plaster thickness and plaster material type

To measure the influence of layer thickness and different plaster types, the following sample was prepared: Three polystyrene panels with different heights (h_1 = 10.7 mm, h_2 = 10.55 mm, and h_3 = 10.8 mm) were aligned on a wooden carrier panel, then plastered by trained craftsmen. A layer of fiber reinforcement grid was wrought into the plaster. Three types of plaster (A: *Capatect CarbonSpachtel*, B: *Capatect CarboNit Easy*, C: *Capatect CarbonSpachtel Easy,* see [3] for details) were applied[2]. Figure 1 shows a cross-sectional and a top view of the sample: The boundaries between segments of different plaster thickness (boundary type 1) and segments of different plaster material (boundary type 2) were arranged orthogonal to each other. The plastered sample was monitored for 120h while drying (an IR image was captured every 30s) in an empty and windowless room with stable room temperature and humidity. To reduce image noise, the images were averaged across 30 consecutive recordings, yielding a temporal resolution of 15 min. In the processed data, in the first 15h, neither thickness nor material boundaries are visible. Between 24h and 48h, segments with different thickness can clearly be distinguished. Areas covered with plaster C strongly deviate from areas covered with types A and B (Fig. 2).

[1] Optris PI 450i (spectral range 7.5 to 13 µm, sensitivity 40 mK, resolution 382 x 288, field of view: 53° x 40°)
[2] A sharp transition between the three plaster types was achieved using masking tape, which was removed after applying the plaster.

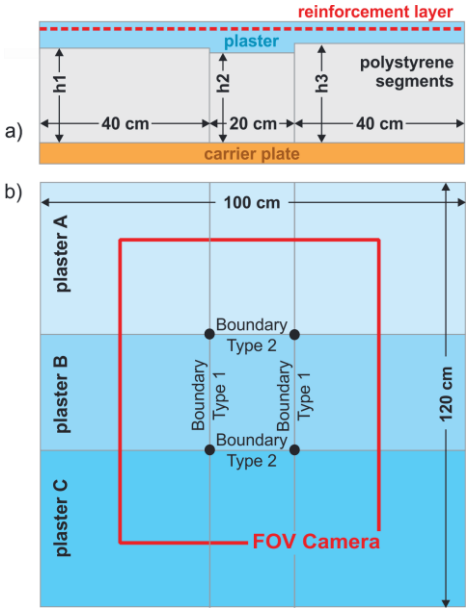

Fig. 1. Cross-section (a) and top view (b) of the sample used in Experiment 1 (not drawn to scale)

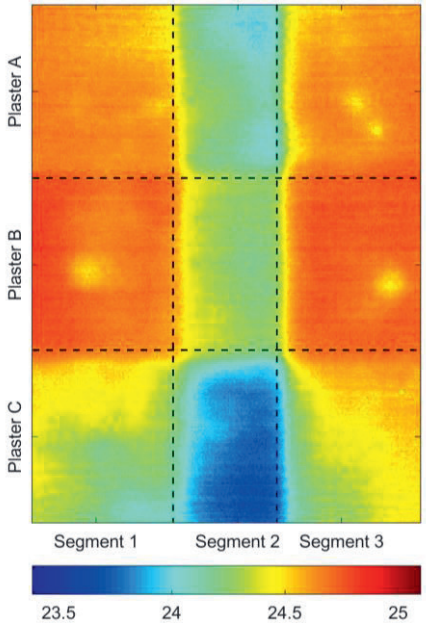

Fig. 2. Processed thermal image (captured 48h after start, all temperatures are color-coded in °C)

Experiment 2: Detecting smooth defects

To verify the proposed method for detecting flat defects with smooth contour, a polystyrene plate (25 x 25 x 5 cm) was damaged with a hot air gun, yielding 4 dents with depths between 1 and 2 mm). The plate was fit into a wooden frame and plastered (type A, see Fig 3). Again, the IR camera was used to monitor the sample. Figure 4 shows the images after preprocessing (averaging, detrending using the Gauss-Newton method, see e.g. [4]). 30 hours after plastering, the dents are visible, best results are achieved 48 hours after plastering. Even after 66 hours, the defects can be detected, although the measured temperature deviations are small.

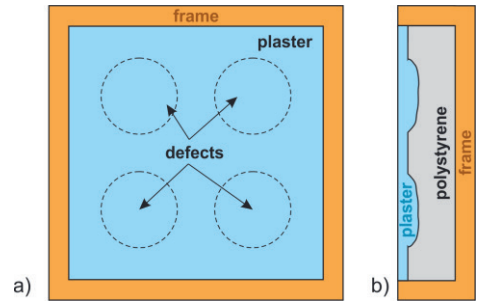

Fig. 3. Top view (a) and cross-sectional drawing (b) of the sample used in Experiment 2

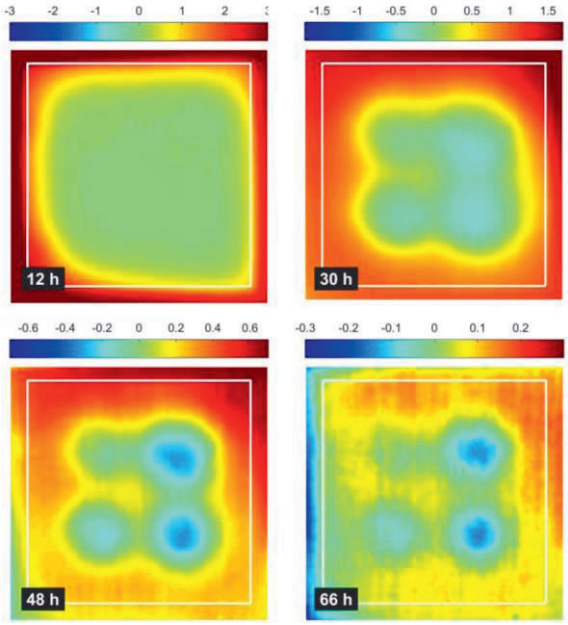

Fig. 3. Processed thermal images

Conclusion and Outlook

The proposed method obtained promising results in two experimental settings. Upcoming experiments will include measurement using a complete wall segment in a realistic setting.

Acknowledgement

This contribution was partly carried out within a cooperative research project, funded by the Austrian Research Promotion Agency (FFG, Grant No. 864811). It has furthermore been supported by the COMET-K2 ”Center for Symbiotic Mechatronics” of the Linz Center of Mechatronics (LCM) funded by the Austrian federal government and the federal state of Upper Austria.

References

[1] D. Meschede, *Gerthsen Physik*, 24th edition, Springer, 2010.

[2] M. Solla et al. “A multidisciplinary non-destructive approach to analyze moisture in historic masonry structures,” in 14th *Int. Conference on Ground Penetrating Radar (GPR)*, 2012.

[3] www.synthesa.at

[4] E. Chong et al. *An introduction to optimization*. John Wiley & Sons, 2004.

DOI 10.5162/SMSI2021/C2.4

3D Thermography for the Measurement of Surface Heat Dissipation

Robert Schmoll[1], *Sebastian Schramm*[1], *Tom Breitenstein*[1], *Andreas Kroll*[1]
[1] *University of Kassel, Department of Measurement and Control,*
Mönchebergstraße 7, 34109 Kassel, Germany,
robert.schmoll@mrt.uni-kassel.de

Summary:
3D thermal imaging can be realized by sensor data fusion of a depth and a thermal camera. In the resulting 3D thermogram thermal and spatial information of an object is available. This information is used to calculate the surface heat dissipation caused by thermal radiation and natural convection.

Keywords: 3D Thermography, Sensor Data Fusion, Heat Dissipation, Heat Loss

Introduction

In contrast to the identification of thermal bridges and insulation leaks by qualitative thermal imaging it is hard to determine quantitative heat flows through object surfaces. If the geometry and the surface temperature of an object are known, it is possible to calculate the heat dissipation (or the heat loss) by thermal radiation and natural convection. A 3D thermography system enables the simultaneous measurement of the required information.

3D thermography systems differ mainly by the acquisition of the geometric 3D data. Especially for outdoor scenes, e.g. to scan buildings, laser scanners are used [1]. For reasons of scanning speed and costs, it is possible to use so called depth cameras [2]. These cameras work with structured light, often in the near-infrared (NIR) range. They have a limited range (approx. up to 10 m) and, caused by the sensitivity for external NIR radiation, are mainly used for indoor measurements [2].

3D Thermography System

The used 3D thermography system in this work consists of a long-wave infrared (LWIR) camera and a depth camera, see Fig. 1 and [4] for details. The thermal information of the LWIR camera has to be projected into the geometric 3D data (e.g. point clouds) of the depth camera. To avoid holes in the 3D data caused by occlusion at one viewing angle it is beneficial to capture the object from different views, e.g. by moving the measurement system around the object. For this reason, multiple point clouds resulting from different viewing angles have to be registered into a single 3D model.

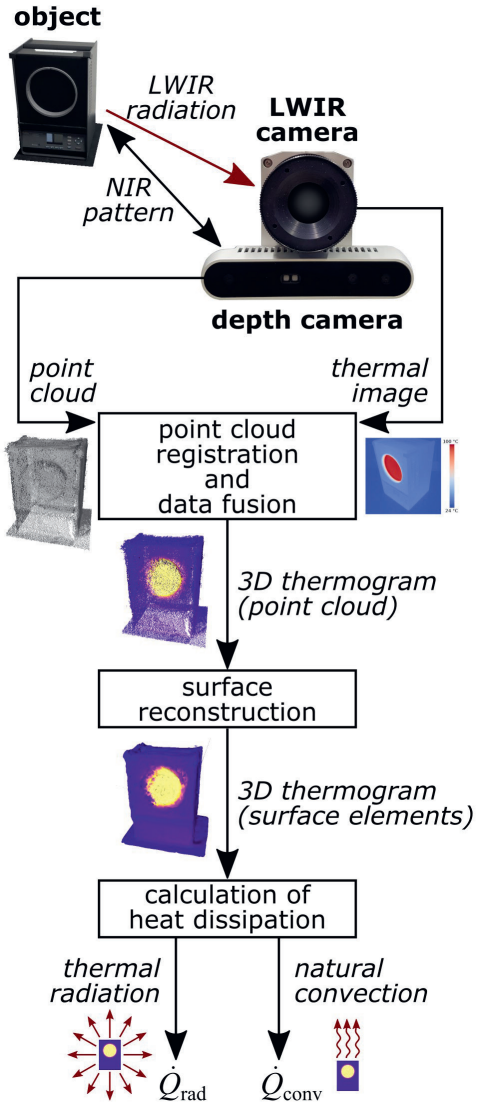

Fig. 1. Workflow of measuring surface heat dissipation using 3D thermography.

The point cloud registration and the fusion of spatial and thermal information is carried out in real-time. Therefore, self-localization and mapping algorithms, running on a graphics card of a portable high-performance computer, have to be adapted to include the thermal data [3]. For this task, the intrinsic and extrinsic calibration of the involved cameras is needed [4].

In the next step, the point cloud is converted to surface elements by a Poisson surface reconstruction [5]. For these surface elements, it is possible to calculate the radiated heat power and the heat transport by natural convection.

Calculation of Heat Dissipation

After this step, the 3D thermogram consists of surface elements (triangles) with the temperature T_i, $i = 1 \ldots N$. For the temperature measurement, the object was assumed as a grey body and the emissivity ε_i of each surface has to be determined. The area A_i of each surface element is known from the geometric data. At least, the Stefan-Boltzmann constant σ and the ambient temperature T_{amb} have to be known to calculate the heat flow caused by thermal radiation [6]:

$$\dot{Q}_{\mathrm{rad}} = \sum_{i=1}^{N} A_i \cdot \varepsilon_i \cdot \sigma \cdot \left(T_i^4 - T_{\mathrm{amb}}^4 \right) \qquad (1)$$

In order to calculate the heat flow by natural convection the air temperature T_{air} is needed. For the determination of the heat transfer coefficient α_i each surface element i is treated separately and assumed to be alone in an infinite space with known orientation to the gravity. With this information the heat flow by natural convection is calculated by [6]:

$$\dot{Q}_{\mathrm{conv}} = \sum_{i=1}^{N} A_i \cdot \alpha_i \cdot \left(T_i - T_{\mathrm{air}} \right) \qquad (2)$$

Test Object for Verification

An infrared radiator is chosen as a test object, see Fig. 2. The emissivities $\varepsilon_{\mathrm{front}}$ = 0.95 and $\varepsilon_{\mathrm{rear}}$ = 0.84 were determined by the use of reference tape.

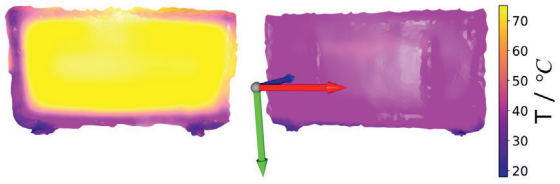

Fig. 2. Front (left) and rear (right) view of a 3D thermogram (surface elements) of an infrared radiator.

The results of the measured heat dissipation could be compared to the electrical power consumption measured by a wattmeter, see Tab. 1.

Tab. 1: Calculated heat dissipation of the infrared radiator and power consumption.

	Measured	Reference
Surface area	1.66 m²	~1.60 m²
Heat dissipation	618.1 W	612.0 W

Conclusions

The used test object gives very good results for the measurement of the surface area and the heat dissipation. An uncertainty analysis has not been carried out.

Summary and Outlook

In this work the information of a 3D thermogram is used, to calculate the heat dissipation of scanned objects. It should be mentioned, that internal heat flows, forced convection or the use of e.g. slits in the surface could not be covered by the measuring system. Additionally, newer algorithms of point cloud registration, see [3], allow 3D thermograms of larger objects. Finally, the method enables the direct measurement of surface heat dissipation by thermal radiation and natural convection e.g. to calculate losses and to optimize the efficiency.

References

[1] A. Costanzo, M. Minasi, G. Casula, M. Musacchio, M. F. Buongiorno, Combined use of terrestrial laser scanning and IR thermography applied to a historical building, *MDPI Sensors*, 15(1), 194–213 (2015); doi: 10.3390/s150100194

[2] A. O. Ordonez Müller, A. Kroll, Generating high fidelity 3-D thermograms with a handheld real-time thermal imaging system, *IEEE Sensors Journal*, 17(3), 774–783 (2016); doi: 10.1109/JSEN.2016.2621166

[3] S. Schramm, P. Osterhold, R. Schmoll, A. Kroll, Generation of Large-Scale 3D Thermograms in Real-Time Using Depth and Infrared Cameras, *In 15th Quantitative InfraRed Thermography Conference (QIRT)*, Porto, Portugal, 6.-10. July (2020)

[4] S. Schramm, J. Rangel, D. A. Salazar, R. Schmoll, A. Kroll, Target Analysis for the Multispectral Geometric Calibration of Cameras in Visual and Infrared Spectral Range, *IEEE Sensors Journal*, to appear in print (2020); doi: 10.1109/JSEN.2020.3019959

[5] M. Kazhdan, H. Hoppe, Screened poisson surface reconstruction, *ACM Transactions on Graphics*, 32, 1-13 (2013); doi: 10.1145/2487228.2487237

[6] VDI-Wärmeatlas, 11. Auflage, Springer Berlin Heidelberg (2013)

DOI 10.5162/SMSI2021/C3.1

Mid-Infrared Dual-Comb Spectroscopy as sensor: Fast and precise quantification of multiple gases

Leonard Nitzsche[1], Jens Goldschmidt[1], Jens Kießling[1], Sebastian Wolf[1], Frank Kühnemann[1], Jürgen Wöllenstein[1,2]
[1] Fraunhofer Institute for Physical Measurement Techniques IPM, Georges-Köhler-Alle 301, D-79110 Freiburg, Germany
[2] University of Freiburg, Department of Microsystems Engineering IMTEK, Laboratory for Gas Sensors, Georges-Köhler-Allee 102, D-79110 Freiburg, Germany
juergen.woellenstein@imtek.uni-freiburg.de

Summary:
Dual-comb spectroscopy allows to record broadband transmission spectra fast and precisely. This bridges the gap between classical methods, where Fourier-Transform infrared spectroscopy excels in spectral bandwidth or tunable laser absorptions spectroscopy in sensitivity. Here we present a dual-comb based spectrometer for gas sensing in mid-infrared from 3 µm to 5 µm. Using the spectrometer as a sensor for a mixture of nitrous oxide (N_2O) and carbon monoxide (CO) results in 48.3(2) ppm N_2O and 29.10(7) ppm CO in 10 s. The limits of detection are 90 ppb N_2O and 49 ppb CO in 25 s.

Keywords: dual-comb spectroscopy, spectrometer, mid-infrared, trace gas, process analytics

Motivation

Dual-comb spectroscopy allows to record broadband transmission spectra composed of thousands of equidistant independent spectral elements. Although this method is well established in many laboratories around the world its potential of being used as a sensor for e.g. process analytics is yet not fully developed. This target in mind we design a spectrometer especially suited for the detection of multiple trace gases in a single and short measurement. This is a necessity to first optimize and potentially enable active control over processes where high purity of the educts is needed, e.g. a low carbon monoxide content in hydrogen for fuel cells [1]. It is important for many catalytic reactions as methane synthesis based on nickel catalysts, where hydrogen sulfide poisons the catalyst leading to decreasing efficiency [2], as well. In contrast to being precise, our spectrometer allows fast acquisition rates (kHz) which is important for testing exhaust or optimizing combustion processes. To demonstrate that our spectrometer bridges the gap between fast acquisition rates and high precision measurements we investigate a mixture of nitrous oxide and carbon monoxide, both occurring with concentrations below 50 ppm in the chosen gas matrix.

Working principle of the spectrometer

A single frequency comb can be described as a pulsed laser where its optical spectrum is composed of multiple discrete modes with identical spacing f_r. As the comb spectrum covers a broad spectral range, the attenuation caused by a sample, here two gases, can be determined. By superimposing the probing comb with a reference comb with a slightly different mode spacing - often referred to as dual-comb spectroscopy [3] - beatings between pairs of comb modes are generated. From the beat signal - interferogram - the transmission spectrum can be reconstructed in analogy to Fourier-transform infrared spectroscopy (FTIR). No moving parts are required nor does any instrument function bias the recorded spectra. In addition, the high optical powers and beam properties allow using gas cells with longer absorption length or even open-path applications. With the possibility to build such spectrometers robust and space-efficient, it is a promising alternative to classical analytical methods as gas chromatography or FTIR.

Fig. 1. Hardware modules of the spectrometer. The near-infrared dual-frequency comb (DFC) at 1550 nm is converted to the mid-infrared. By using a tunable pump from 1.0 µm to 1.3 µm the converted mid-infrared combs can be positioned in the spectral range from 3 µm to 5 µm. The DFC is split into two branches. One propagates through a multi-reflection flow cell and the other is detected directly serving as reference.

Experimental setup

To realize such a spectrometer we make use of a fiber-based dual-comb generator emitting a superimposed dual-frequency comb (DFC) at 1550 nm further explained in [4]. The mode spacing can be tuned from 0.008 cm^{-1} to 0.016 cm^{-1} and the spectral bandwidth can be chosen from 6 cm^{-1} to 20 cm^{-1}. To reach the MIR we convert the near-infrared DFC via difference frequency generation to the mid-infrared. Combined with a tunable pump laser for this process we are able to reach the spectral region from 3 µm to 5 µm, which is of special interest as many gases show strong and characteristic absorptions in this region. The converted DFC is split into two branches. In the sample branch channel the dual-comb signal passes a multi-pass cell with 7.2 m. The signal from the reference branch is used to normalize the spectra from the sample branch.

Results

With this configuration we first record a reference spectrum of nitrogen - not absorbing -, fill the cell with a mixture of nitrous oxide (N_2O) and carbon monoxide (CO), and record a transmission spectrum of the sample.

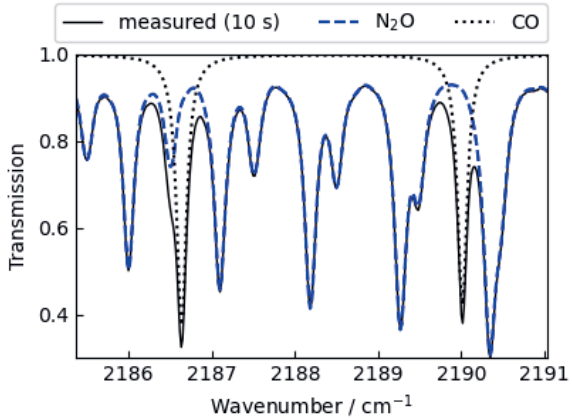

Fig. 2. Measured transmission spectrum of 48.3 ppm nitrous oxide (N_2O) and 29.1 ppm carbon monoxide (CO) in synthetic air. For convenience, the dashed lines indicate the contributions from both compounds to the spectrum.

To derive the concentrations of both compounds we fit a simulation using the HITRAN database to the sample spectrum corrected by the reference spectrum. This results in 48.3 ppm N_2O and 29.10 ppm, both with ±3 ‰ uncertainty (1σ), which is in accordance with our expectation and is shown in Fig. 2. Evaluating sample spectra with 10 Hz acquisition rate, as provided in Fig. 3, shows that after already 25 s of measurement time the relative uncertainty (1σ) of the determined gas concentration is as low as 0.6 ‰ for N_2O and 0.5 ‰ for CO, which corresponds to a 90 ppb limit of detection of N_2O and 49 ppb for CO likewise.

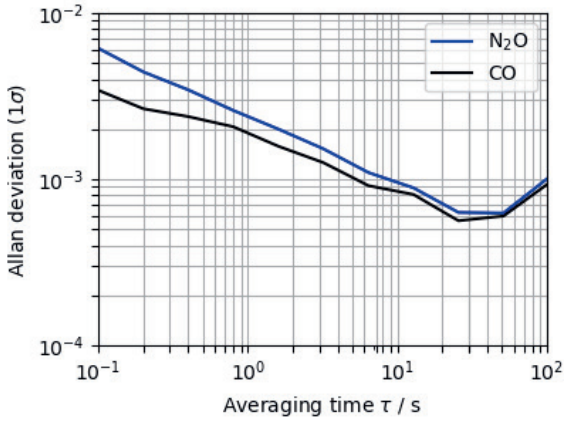

Fig. 3. Allan deviation of determined gas concentrations - 48.3 ppm for N_2O and 29.1 ppm for CO - acquired with 10 Hz rate. The minimum is reached after 25 s at 0.6 ‰ for N_2O and 0.5 ‰ for CO.

References

[1] V. F. Valdés-López, T. Mason, P. R. Shearing, D. J. L. Brett, Carbon monoxide poisoning and mitigation strategies for polymer electrolyte membrane fueal cells – A review, Progress in Energy and Combustion Science 79, 10084 (2020), doi: doi.org/10.1016/j.pecs.2020.100842

[2] C. H. Bartholomew, Mechanisms of catalyst deactivation, Appl. Catalysis A 212, 17-60 (2001), doi: 10.1016/S0926-860X(00)00843-7

[3] I. Coddington, N. Newbury, W. Swann, Dual-comb spectroscopy, *Optica* 3, 414-426 (2016); doi: 10.1364/OPTICA.3.000414

[4] L. Nitzsche, J. Kießling, S. Wolf, F. Kühnemann, J. Wöllenstein, Ultra-fast gas spectroscopy with a dual-comb spectrometer, SMSI 2020, 123 – 124, doi: DOI 10.5162/SMSI2020/B4.4

[5] R.V. Kochanov, I.E. Gordon, L.S. Rothman, P. Wcislo, C. Hill, J.S. Wilzewski, HITRAN Application Programming Interface (HAPI): A comprehensive approach to working with spectroscopic data, *J. Quant. Spectrosc. Radiat. Transfer* 177, 15-30 (2016); doi: 10.1016/j.jqsrt.2016.03.005

DOI 10.5162/SMSI2021/C3.2

Detection of Stable Isotopes of CO_2 using Quantum Cascade Laser based Absorption Spectroscopy

Ponkanok Nitzsche[1], Cem Dinc[1], Jürgen Wöllenstein[1,2], Katrin Schmitt[1,2]
1 Department of Microsystems Engineering (IMTEK), University of Freiburg, 79110 Freiburg, Germany
2 Fraunhofer Institute for Physical Measurement Techniques (IPM), 79110 Freiburg, Germany
Tel.-Nr.: +49 761 203-96808, E-Mail: ponkanok.nitzsche@imtek.uni-freiburg.de

Summary:
A spectroscopic approach to measure ^{13}C and ^{18}O isotopic ratios in carbon dioxide (CO_2) gas using a quantum cascade laser (QCL) is presented. The measurement was performed near 2310 cm^{-1}, where three absorption lines of CO_2 including $^{12}C^{16}O_2$, $^{13}C^{16}O_2$ and $^{16}O^{12}C^{18}O$ isotopes are located. The simultaneous detection of three spectral lines permits the determination of simple concentration ratios (R^{13} and R^{18}) in atmospheric CO_2. With an averaging time of about 20 s both R^{13} and R^{18} reached a precision (1σ) of 0.08 ‰ and 0.01 ‰, respectively.

Keywords: Gas Sensors, Isotopic Composition Analysis, Optical Measuring System, Absorption Spectroscopy, Quantum Cascade Laser

Motivation

Since atmospheric CO_2 is an important indicator for many climate change researches, the attention focusing on fluxes of CO_2 between the different sources and sinks have been growing. The studies of stable CO_2 isotope ratios offer the possibility to identify such CO_2 pools via the isotopic fingerprint [1]. Traditionally, the stable isotopes are measured by means of sample preparation and isotope ratio mass spectrometry (IRMS). An alternative method for this measurement is tunable laser absorption spectroscopy (TLAS). In contrast to IRMS, TLAS permits a real-time measurement of the isotopic ratio. Tuzson et al. showed a precision of 0.03 ‰ and 0.05 ‰ for R^{13} and R^{18} after an integration time beyond 100 s [2].

Spectral Absorption Lines

A mid-infrared, tunable QCL was continuously tuned across three spectral absorption lines of CO_2 isotopes. These spectral lines were chosen in such a way that there is a sufficiently high absorption line strength and low interference with other atmospheric gases. Moreover, there must be at least one absorption line of each isotope of interest within the laser tuning range. All measured isotopes should possess a similar absorption line intensity to avoid any detector saturation.

The spectroscopic information, including the vacuum wavenumber ($\tilde{\nu}_0$), low-state energy (E_L) and spectral line intensity ($S(T_0)$) of the selected $^{12}C^{16}O_2$, $^{13}C^{16}O_2$ and $^{16}O^{12}C^{18}O$ isotopes are shown in Table 1 [3]. To minimize line overlapping caused by pressure broadening, the measurement must be performed in a negative pressure condition. The low state energies of these spectral lines are considerably different, which implies that the isotope ratio measurement is sensitive to temperature variation [4].

Tab. 1: Spectroscopic data of the selected lines [3].

Isotopes	$\tilde{\nu}_0$ in cm^{-1}	E_L in cm^{-1}	$S(T_0)$ in $cm^{-1}/mol \cdot cm^{-2}$
$^{12}C^{16}O_2$	2310.002	1454.97	$4.86 \cdot 10^{-21}$
$^{13}C^{16}O_2$	2310.347	639.63	$6.72 \cdot 10^{-21}$
$^{16}O^{12}C^{18}O$	2310.206	278.28	$4.52 \cdot 10^{-21}$

Experimental Setup

Figure 1 depicts a schematic of an optical configuration of the system. A temperature controller and current driver are used with a function generator to control the QCL (HHL680, AlpesLaser) and tune the laser with a frequency of f_{mod} = 100 Hz. An optical isolator is employed to protect the QCL from back-reflected light. A 10 cm long, hermetically sealed spectroscopic cell filled with a known concentration of CO_2 was applied for the calibration of QCL wavelength. The optical path length of the measurement chamber was L_{cham} = 109±1 cm. Two photodetectors (PVI-3TE-5, Vigo System) were used to detect the optical signals simultaneously. With a diaphragm vacuum pump and a fine-metering valve, the pressure inside the chamber can be reduced and regulated to about

100 mbar. Pre-chamber and measurement chamber were temperature-regulated and heat isolated. A temperature and pressure sensor were integrated inside the measurement chamber.

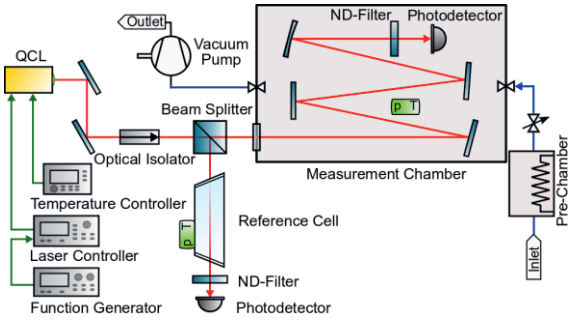

Fig. 1: Scheme of the experimental set-up.

Time series of temperature and pressure inside the chamber were measured. The Allan-deviation of the recorded temperature and pressure were calculated. A precision (1σ) of 9 mK and 0.03 mbar after an integration time of 20 s were achieved.

Measurement Results

396±8 ppm CO_2 gas in synthetic air was measured over 500 s. The transmission spectrum was defined as shown in Figure 2 (top). The black line represents the measured data after baseline correction. A HITRAN simulation [3] with the defined concentration and measured ambient conditions is illustrated with the red line. Figure 2 (bottom) shows their residual.

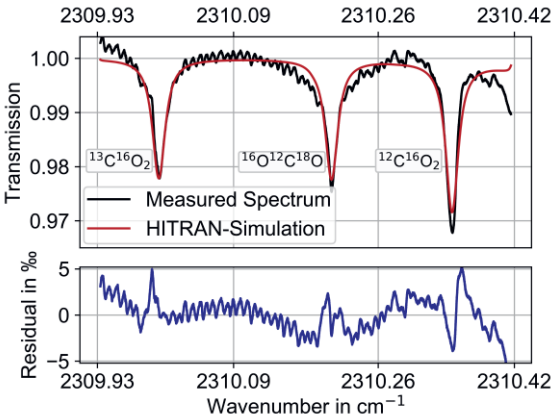

Fig. 2: Transmission spectrum of measured and simulated data and their residual.

The concentration of each isotope was calculated thus, the ratio as $R^{13} = [^{13}C^{16}O_2]/[^{12}C^{16}O_2]$ and $R^{18} = [^{16}O^{12}C^{18}O]/[^{12}C^{16}O_2]$. By employing the Allan deviation method, an optimum averaging time of 20 s can be derived, as illustrated in Figure 3. With this integration time, the system can achieve a precision (1σ) of ~0.08 ‰ and ~0.01 ‰ for R^{13} and R^{18}, respectively. However, in order to determine the actual and accurate concentrations and isotopic ratios of CO_2, the system must be calibrated.

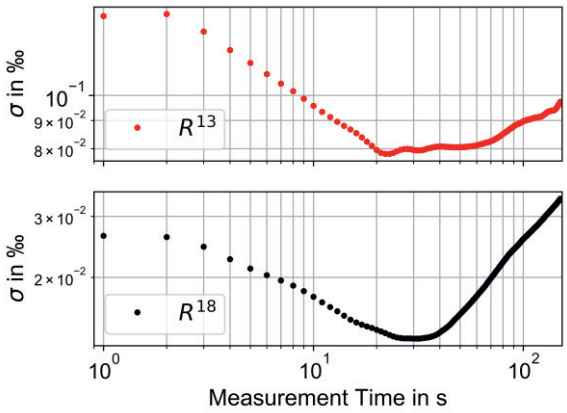

Fig. 3: Allan plot for both concentration ratios R^{13} (above) and R^{18} (below).

Conclusion

In this study, we present the design and construction of QCL-based tunable absorption spectroscopy for an analysis of CO_2 isotopic compositions. After an integration time of 20 s the temperature and pressure inside the measurement chamber show a sufficient stability. The detection limits (1σ) for R^{13} and R^{18} were estimated by the Allan deviation method as ~0.08 ‰ and ~0.01 ‰, respectively.

Acknowledgements

This work is funded by Georg H. Endress foundation.

References

[1] D. E. Pataki, D. R. Bowling, and J. R. Ehleringer, “Seasonal cycle of carbon dioxide and its isotopic composition in an urban atmosphere: Anthropogenic and biogenic effects,” *J. Geophys. Res. D Atmos.*, vol. 108, no. 23, pp. 1–8, 2003, doi: 10.1029/2003jd003865.

[2] B. Tuzson *et al.*, “High precision and continuous field measurements of δ 13C and δ 18O in carbon dioxide with a cryogen-free QCLAS,” *Appl. Phys. B Lasers Opt.*, vol. 92, no. 3 SPECIAL ISSUE, pp. 451–458, 2008, doi: 10.1007/s00340-008-3085-4.

[3] R. V. Kochanov, I. E. Gordon, L. S. Rothman, P. Wcisło, C. Hill, and J. S. Wilzewski, “HITRAN Application Programming Interface (HAPI): A comprehensive approach to working with spectroscopic data,” *J. Quant. Spectrosc. Radiat. Transf.*, vol. 177, pp. 15–30, 2016, doi: 10.1016/j.jqsrt.2016.03.005.

[4] P. Bergamaschi, M. Schupp, and G. W. Harris, “High-precision direct measurements of $^{13}CH_4/^{12}CH_4$ and $^{12}CH_3D/^{12}CH_4$ ratios in atmospheric methane sources by means of a long-path tunable diode laser absorption spectrometer,” *Appl. Opt.*, vol. 33, no. 33, p. 7704, 1994, doi: 10.1364/ao.33.007704.

DOI 10.5162/SMSI2021/C3.3

Single Photon LiDAR Technology for Gas Imaging

Peter Droegmoeller[1], Murray Reed[2]
[1] AMETEK Land, Stubley Lane, Dronfield S18 1DJ, UK,
[2] QLM, Unit DX, Albert Road, St Philips, Bristol, BS2 0XJ, UK
peter.droegmoeller@ametek.com

Summary:
A LiDAR camera system combined with a laser tuned across a specific gas absorption can measure the distance and the quantity of gas present in the surrounding area. New technology now enables this measurement to be taken without the use of large expensive lasers.

Keywords: LiDAR, rapidly tunable laser, gas imaging, Single Photon Avalanche Diodes, SPADS

Background, Motivation an Objective

Monitoring greenhouse gases in becoming a focus in the effort to reduce global warming. Gases can be detected by measuring the specific absorption bands, e.g. methane absorbs at 1651nm. To monitor gases with existing technology infrared cameras tuned to the specific absorption band are used. To be visible the gas needs to be either at a different temperature, e.g. colder due to a release from high pressure vessel or illuminated by a broad band head source like the sun. Alternatively, the illumination can be done with a wavelength specific laser, where new developments in the field of single photon avalanche diode (SPADS) will allow the use of much smaller lasers. The goal was to build a camera system using LiDAR technology for gas imaging and quantification. LiDAR stands for Light Detection And Ranging and is already more commonly adopted in the automotive industry on autonomous vehicles and driver support systems. The range of these systems are limited to 30-40m when high powered NIR lasers (905nm) are used. The range can be extended to 200m by using SWIR lasers at 1550nm [1].

Description of the New Method or System

The active imager consists of a rapidly tunable distributed feedback (DFB) laser diode, scanning optics, a single photon detector and electronics for signal processing. The laser is sending out at various wavelength close to the desired absorption band of the to be measured gas. The signal will scatter on solid objects and parts of the signal received back into the camera. If the gas was present in the sight path, the gas specific absorption will be visible in the spectral return signal. For methane, the strong absorption band at 1651nm can be used.

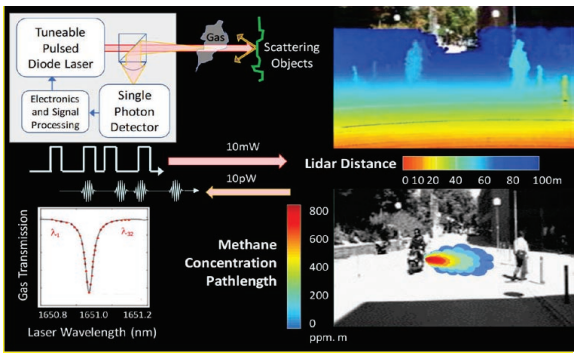

Fig. 1. System diagram of Single-Photon Diode Laser Gas Imaging LiDAR

The main challenge besides the fast tuning of the laser diode is the small return signal from the objects in the range of pW. It has been overcome with the use of uncooled InGaAs SWIR Single Photon Avalanche Diodes, which are commonly used in telecommunication fibre optics. The absorption band of methane matches the spectral response of the detector (1000 to 1700nm).

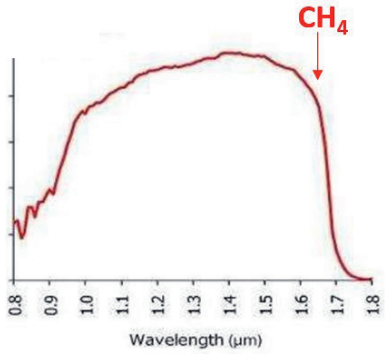

Fig. 2. Spectral response of InGaAs SWIR Single-Photon Diode

Results

The sensitivity of the novel SWIR SPAD enabled the use of a low power semiconductor laser. The laser beams through the gas and reflects off the surroundings, whereas the methane concentration levels detected were in the PPM range even at long distances above 100m.

A highspeed scanning system was used to generate a 2D image of the gas concentration with was then overlayed onto the visible camera image. The result in Fig 3 are taken at 100m distance with the full image scan completed within 1 minute.

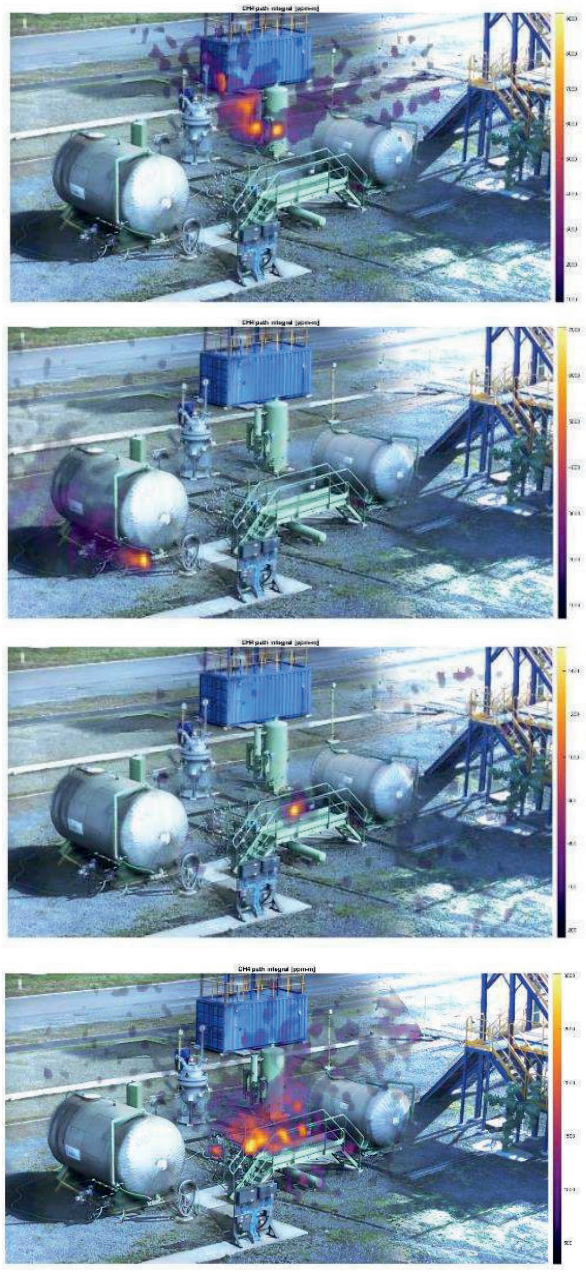

Fig. 3. Methane leak detection at test site

Blind leak simulation trial have confirmed a good correlation between the measured leak rate and the actual leak rate (Fig 3).

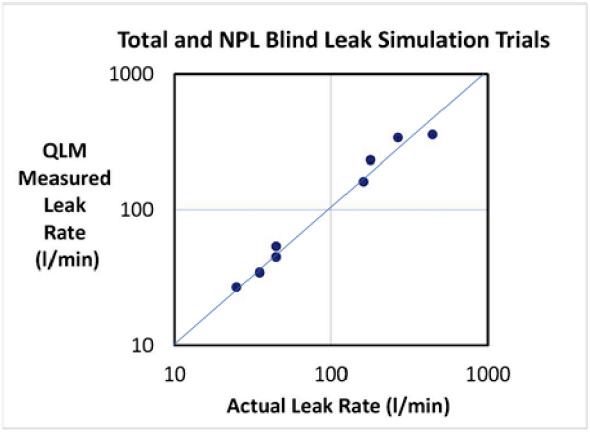

Fig. 4. Methane leak detection at test site

The availability of new laser and SPAD wavelength will allow the detection of other gases besides methane. Possible candidates for SWIR based detections are CO and CO_2. An expansion into the MWIR spectrum will be of particular interest to the petrochemical industry for the qualification and quantification of process gases.

Aknowledgement

The results are based on research funded by the UK national quantum technologies programme as part of the SPLICE project.

References

[1] Corneliu Rablau, Lidar: a new self-driving vehicle for introducing optics to broader engineering and non-engineering audiences, Proceedings Volume 11143, 15th Conference on Education and Training in Optics and Photonics; Quebec, 2019

[2] Ai, Xiao, et al. "Pseudo-random single photon counting for space-borne atmospheric sensing applications." Aerospace Conference, 2014 IEEE. IEEE, 2014.

[3] BRITESPACE consortium, “BRITESPACE High Brightness Semiconductor Laser Sources for Space Applications in Earth Observation FINAL PUBLISHABLE REPORT”, 2016

DOI 10.5162/SMSI2021/C3.4

Measurement and calculation of surface temperature on tyre samples

Frederik Bartz[1], Frederik Bartz, S. Gehrmann[2], S. Augustin[2], V. Ackermann[2], T. Fröhlich[2]
[1] Dr. Ing. h.c. F. Porsche AG, Porschestrasse 911, 71287 Weissach, Germany,
[2] Dr. Ing. h.c. F. Porsche AG, Porschestrasse 911, 71287 Weissach, Germany & TU Ilmenau, Institute PMS, Gustav-Kirchhoff-Str. 1, 98693 Ilmenau, Germany, stephan.gehrmann@porsche.de, silke.augustin@tu-ilmenau.de, v.ackermann@tu-ilmenau.de, thomas.froehlich@tu-ilmenau.de

Summary:
For a better understanding of the temperature behaviour of vehicle tyres, measurements have been carried out on a specially developed test bench. Various measuring instruments have been used to determine the surface temperature. Different influences such as the external radiation effects have been investigated. Furthermore, the heat transport in the tyre samples and the exchange with the surrounding environment has been estimated by means of numerical simulations.

Keywords: surface temperature, simulation of the radiation exchange, heat transfer in tyre samples

Introduction

With the increasing performance of vehicles and a more compact vehicle package, the external influences on the temperature of vehicle tyres are sometimes increasing. Too high temperatures can damage the tyre [1] - [3]. Therefore, the temperature behaviour under different environmental conditions has been investigated on a test bench using tyre samples. In addition, the heat transport in the test stand was numerically calculated. In this way, the different power ratios of the heat flows could be broken down. Furthermore, measured surface temperatures were compared with the simulations.

It is usually assumed that the temperature of the measuring object (solid body) is different from that of the surrounding fluid. Consequently, the surface temperature of a measurement object is located at a point of discontinuity in the temperature profile. Hence, measuring the surface temperature is a difficult task. In this lecture, the determination of the surface temperature without using a contacting thermometer will be addressed. The reason for these investigations are the changes in heat flux density resulting from the contact measurement. The difference between the undisturbed and disturbed heat flux density makes it difficult to draw conclusions about the correct surface temperature, see Fig. 1 [4].

In addition, previous investigations have shown that the reproducible installation of thermometers on the surface cannot always be guaranteed [5]. Furthermore, it is not always possible to contact the surface directly in every measuring situation (e.g. rotating components).

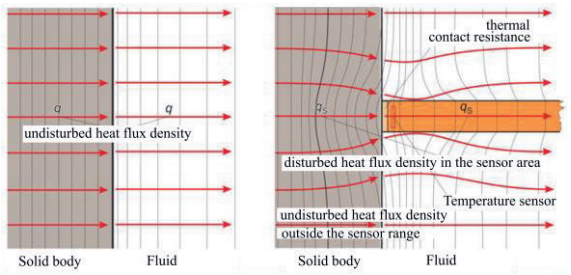

Fig. 1. Comparison of undisturbed and disturbed heat flux density [4]

Measurement and calculation methods

Due to the conditions mentioned above, the challenge arises to measure the surface temperature without contact or to determine it by calculation using suitable methods. In the submitted lecture, three different strategies are presented. In the first approach, the surface temperature is measured by means of radiation thermometers. For the second and third approach, the surface temperature is calculated. In the second approach, the surface temperature is determined by extrapolation from several temperature measuring points in the test object.

In the third approach, the calculation is based on numerical FEM methods of the heat transport and the fluid dynamics. All three methods have different advantages and disadvantages. For the radiation temperature measurement the correct emission coefficient of the surface is of particular importance. [4]

To calculate the surface temperature and the heat flow, the thermal conductivity and other important parameters of the system components (tyre sample, adhesive, intermediate layers, etc.) must be known [4], [6]. Further influencing variables and their uncertainty contributions are shown in the full article.

The metrological investigations were carried out on a specially developed test bench (see Fig. 2). This test bench is able to reproduce the fundamental types of heat transfer (heat conduction, convection, and heat radiation). Reproducible measuring conditions have already been proven in earlier studies [5], [7]. The measurement objects are from different tyres. The emission coefficient and thermal conductivity of these samples have been determined in experimental investigations. The respective methods and results are also presented in the article [8].

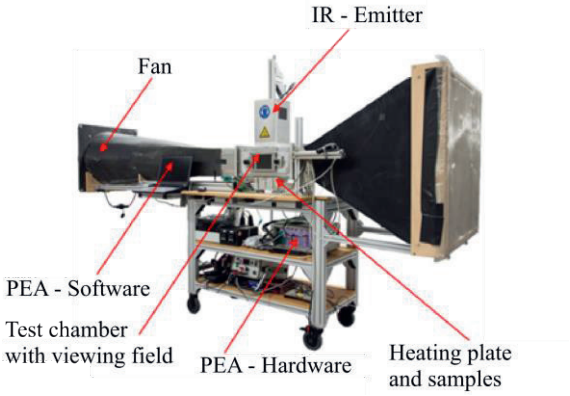

Fig. 2. Test bench for measuring the surface temperature

Results

The results for different test parameters on the test bench are presented in the submitted paper. The measured and calculated surface temperatures are compared with each other. Surface temperatures, which deviate from each other, are discussed and analysed.

It is shown that an additional external radiation source increases the differences between the extrapolated temperature and the temperature measured by radiation thermometers. These differences probably result from reflected radiation components in the radiation temperature measurement. For extrapolation based on several temperatures, the positioning of the individual thermocouples and the resulting difference is not reliable. The influences of an external radiation source and the temperature profile in the samples have been further investigated with FEM calculations [9]. By calculating the view factors, the proportions of emitted and reflected radiation components could be determined.

Both the test bench investigations and the numerical calculations have contributed to a better understanding of measuring surface temperatures. With the help of the investigations different influencing factors could be shown, which will be considered in future measurements.

Future prospect

In further investigations, which are part of the future prospect, an additional strategy for the contactless determination of the surface temperature is presented. Specially developed heat flow sensors could be used for this purpose. The thermal conductivity of actual heat flow sensors does not correspond to the required thermal conductivity. The different thermal conductivities result in different thermal resistances, which strongly influence an accurate measurement of the heat flow. The development of new heat flow sensors should compensate this disadvantage. The surface temperature is then determined from the measured heat flow and a known temperature within the measured object.

References

[1] Kraftfahrt-Bundesamt (KBA): Downsizing - nicht in jedem Segment ein Thema. KBA Fahrzeugstatistik, 08/2018.

[2] M. Trzesniowski, Handbuch Rennwagentechnik - Fahrwerk, 2. Auflage, Springer Vieweg, 2019.

[3] Continental Reifen Deutschland GmbH: Reifenschäden: Ursachen und Vermeidung, In Pkw-Reifen 2013 - 14. Technisches Handbuch, Continental Reifen Deutschland GmbH, 09/2013.

[4] Bernhard F.: Handbuch der Technischen Temperaturmessung. VDI-Buchreihe. Springer Vieweg, Berlin, Heidelberg, 2014

[5] Gorajski M., Entwicklung eines indirekten Messverfahrens zur Untersuchung des statisch-thermischen Messfehlers von Oberflächen-Thermoelementen, Masterarbeit, Porsche AG, TU Ilmenau, 2016

[6] Baehr H.D., Stephan K.: Wärme- und Stoffübertragung. Springer Vieweg, 2016

[7] Schweickhardt J.: Optimierung eines Probenträgers zur Ermittlung der Messunsicherheit bei der Oberflächentemperaturmessung, Bachelorarbeit, Porsche AG, Hochschule Esslingen, 2019

[8] Manara J., Arduini M., Hemberger F.: Bestimmung des Emissionsgrads und der Wärmeleitfähigkeit, ZAE Bericht, Report ZAE 2-0119-02 und Report ZAE 2-0719-03, 2019

[9] Ackermann V., Numerische Berechnung des Einflusses verschiedener Faktoren auf die Oberflächentemperatur von Fahrzeugreifen, Masterarbeit, TU Ilmenau, 2020

DOI 10.5162/SMSI2021/C4.1

Photonic Thermometry at PTB – Promising First Results for Contact Temperature Metrology Utilizing Optical Sensors

Stephan Krenek[1], René Eisermann[1], Georg Winzer[2], Tobias Habisreuther[3], Daniel Schmid[1], Hoang Viet Lai[1], Steffen Rudtsch[1]
[1] Physikalisch-Technische Bundesanstalt, Abbestr. 2 - 12, 10587 Berlin, Germany
[2] Leibniz-Institut für innovative Mikroelektronik, Im Technologiepark 25, 15236 Frankfurt/O., Germany
[3] Leibniz-Institut für Photonische Technolgien (IPHT), Albert-Einstein-Str. 9, 07745 Jena, Germany
stephan.krenenk@ptb.de

Summary:
Photonic sensors offer new possibilities for the metrological temperature determination in specific applications including high electric fields or harsh environments. Within two EU projects the PTB develop and validate different photonic thermometers from 0 °C to over 1500 °C. The aim of this work is to develop and validate novel accurate photonic thermometers with uncertainties in the mK range and sensors for application within harsh environments at high temperatures. We show first results using silicon ring resonators which achieve high quality factors ($Q \approx 160\,000$) and over 15 dB filter contrast.

Keywords: photonic thermometry, temperature sensor, fiber Bragg grating, ring resonator, photonic integrated circuit

Introduction

In the industrially most relevant temperature range from about −100 °C to 1000 °C temperature measurements are commonly based on the measurement of electrical resistance (e.g. Pt100) or voltage (thermocouple). Photonic sensors, in contrast, use the light-matter interaction to measure temperature or strain with the additional advantage of a metal free, chemical inert and mechanical robust sensor design. For example, a change of the refractive index due to temperature results in a resonance wavelength shift of an optical resonator. Fibre optical sensors using Bragg gratings (FBG) or distributed fibre optic methods are commercially available and are highly promising for industrial monitoring applications [1]. Approaches using photonic thermometers show great potential to reach measurement uncertainties comparable to conventional electrical sensors [2,3]. Nevertheless, the determination and reduction of temperature uncertainty is still a challenging task.

The Physikalisch Technische Bundesanstalt (PTB) is working on special photonic sensors for temperature measurement within two European research projects.

The first project "Enhancing process efficiency through improved temperature measurement 2" (EMPRESS 2) has the overall aim of improving the efficiency of key industrial manufacturing processes through improved temperature measurement and control. The project focuses on accurate and SI traceable temperature measurement with different stable, reliable, durable and robust sensors. One objective is the introduction of traceable fibre optic measurements at high temperatures above 500 °C. PTB is working together with the Leibniz-Institut für Photonische Technolgien (IPHT) on FBGs in sapphire fibres which can be used at temperatures exceeding 1500 °C.

The second project "Photonic and Optomechanical Sensors for Nanoscaled and Quantum Thermometry" (PhotOQuant) deals with fundamental research for high-precision or primary temperature sensors. Two micrometre-sized chip-based techniques are designed, manufactured, characterized and calibrated: optomechanical sensors, in which the temperature-dependent Brownian motion of nanostructures is optically detected, and photonic resonators, in which planar waveguides (e.g. ring resonators) allow very high-resolution measurements of the refractive index change. Together with the Leibniz-Institut für innovative Mikroelektronik (IHP), PTB investigates Si / SiO_2 structures which are manufactured by standardized masking processes.

Perspective and First Results

Our efforts are concentrated in two directions, first, the validation and improvement of photonic resonators (PhotoQuant) for moderate environments and temperatures up to 100 °C with measurement uncertainties below 10 mK. Secondly, the metrological characterization of sapphire based fibre Bragg gratings (SFBG) for applications in harsh environments with temperatures above 1500 °C (EMPRESS 2). Both photonic thermometer principles are mainly based on the determination of frequency (or wavelength) changes of an optical resonance.

Photonic ring resonators offer a high temperature coefficient (≈ 73 pm/K) together with a very high quality factor of the resonant frequency. In this work a photonic integrated circuit with over 130 resonator structures on a 2 mm x 2 mm chip were manufactured with IHP's BICMOS silicon photonic platform [4] on a standard multi project wafer. The resonators were characterised using a tuneable laser with a tuning range from 1520 nm to 1630 nm, variable gain preamplified photodiodes and a highly stable thermostat stage. Reference gas cells (HCN and C_2H_2) were used for an in-situ SI traceable wavelength calibration [5]. Figure 1 shows an example of the normalised transmissions spectrum of three ring resonators with rip waveguide design. All three resonator are coupled to a single bus waveguide, but with different spacing between bus and ring. Each ring resonators have a radius of $r \approx 35$ µm, resulting in a free spectral range of $FSR \approx 3$ nm. Due to the long tuning range of the laser it is possible to track the temperature shift of up to 50 resonance peaks simultaneously. In the lower part of Fig. 1 the shift of one peak per resonator is depicted. The resonators achieve very high quality factors of $Q \approx 160\,000$ and strong filter contrasts of $\Delta\tau \approx -15$ dB. These outstanding values for temperature applications [6-8], enable a very precise determination of the resonance wavelength. According to our preliminary results our photonic integrated circuits are potential suitable for temperature uncertainty below 10 mK.

Another solution suitable for even higher temperature above 1500 °C (probably up to 1900 °C) are Sapphire-FBG's, which offer a temperature coefficient of 26 pm/K [9]. Since they are intrinsically multimodal the corresponding resonance spectra is more complex compared to conventional single mode FBG [9]. Due to that, the precise determination of wavelength shift is the limiting factor for temperature uncertainties (1 K region), which is still under investigation.

In summary, photonic thermometry sensors are suitable to compete with conventional electrical sensors, however some effort and research have to be done in the future.

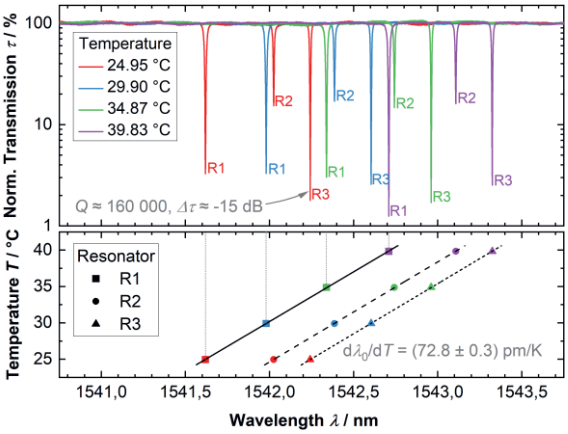

Fig. 1. Normalised Transmission of three ring resonators and temperature dependant shift of the resonance wavelength.

Acknowledgment

This work has received funding from the EMPIR programme co-financed by the Participating States and from the European Union's Horizon 2020 research and innovation programme.

References

[1] K. Hicke et al. *Proc. SPIE 10323, 25th International Conference on Optical Fiber Sensors, 103230J* (2017), doi: 10.1117/12.2272463.

[2] N. Klimov et al. *Sensors Actuators A: Physical*, **269**, 308 (2018), doi: 10.1016/j.sna.2017.11.055

[3] Z. Ahmed, et al., *Proc. SPIE 10923, Silicon Photonics XIV*, 109230L (2019), doi:10.1117/12.2505898

[4] D. Knoll *et al*., *16th Topical Meeting on Silicon Monolithic Integrated Circuits in RF Systems*, p. 46 (2016), doi: 10.1109/SIRF.2016.7445464.

[5] X. Fan, et al., *Opt. Expr.* **26**, 22944 (2018), doi: 10.1364/OE.26.022944

[6] N. Klimov, et al., *Sensors & Transducers*, **191**, 63 (2015)

[7] H.Xu et al., *Opt. Express* **22**, 3098 (2014), doi: 10.1364/OE.22.003098

[8] W. Bogaerts et al., *Laser Photonics Rev.* **6**, 47 (2012), doi: 10.1002/lpor.201100017

[9] D. Grobnic, et al., *Proc. SPIE 5855, 17th International Conference on Optical Fibre Sensors*, (2005), doi:10.1117/12.623592

DOI 10.5162/SMSI2021/C4.2

Reliable multipoint temperature profiling in hydroprocessing units

Stefano Mella[1], *Amar Löffler*[2], *Marc Schalles*[3]
[1] Endress+Hauser Temperature and System Products, Pessano con Bornago, Italy
[2 3] Endress+Hauser Temperature and System Products, Nesselwang, Germany
stefano.mella@endress.com

Summary:
Multipoint thermocouple probes are frequently used in oil and gas industry and chemical applications to detect temperature profiles. Because of the critical process conditions inside the vessels, the sheaths of such probes might be affected by crack phenomena. Due to that the process fluid might penetrate through the sheath, causing electrical insulation drops, measurement drift and in the worst case overall short circuits. A new thermometer design aims to be a more robust solution thanks to its double sealing layers, double insulation layers and completely independent sensors.

Keywords: industrial thermometer, profile temperature, advanced measurement, multi-thermocouple cable

Introduction

In the oil and gas refining industry, catalytic hydroprocessing units such as hydrotreaters (HDT) or hydrocracker units (HCU) rely on high-performance catalyst technologies to maximize product conversion while efficient reaction control seeks to keep the environmental footprint and cost down. Precise and reliable temperature mapping of densely packed reactor catalyst beds therefore makes an essential contribution to stable and profitable unit operations.

Multipoint temperature instruments with thermocouple sensors are widely used in the industry as they monitor optimum heat distribution, preventing hotspots and premature catalyst deactivation under high-temperature, high-pressure and corrosive conditions. However, most conventional multipoint thermocouple probe designs have two major weaknesses:

• Reliability: A phenomenon known as hydrogen sulfide (H2S) contamination affects conventional magnesium oxide (MgO) cables under extreme process conditions. H2S contamination can alter measurement accuracy or even lead to a loss of control over the reaction with potentially disastrous consequences.

• Size: They are comparatively invasive, taking up valuable space in catalyst beds, leading to undesired pressure drops and channeling effects.

Standard thermocouple sensors are embedded in insulating magnesium oxide (MgO) powder and surrounded by a stainless steel sheath, providing some level of protection. However, under extreme conditions, even microscopic cracks form in the outer sheath allow hydrogen sulfide to permeate into the MgO powder, causing detrimental contamination of the cable internals that may go unnoticed by operators [1].

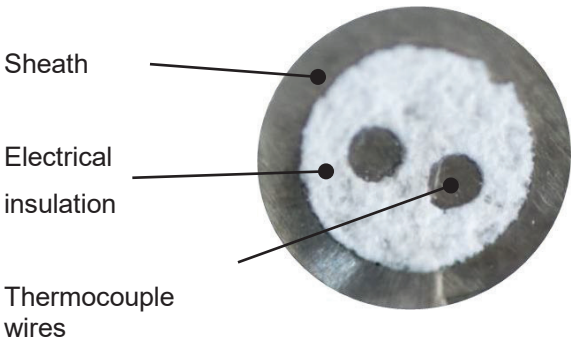

Fig. 1. Cross section of typical mineral insulated Thermocouple

Ageing mechanisms: Hydrogen stress-induced cracking (HSC)

It is standard practice to bend (route) sensor cable probes inside a reactor according to the required layout. This flexible installation ensures that measurement points are adequately distributed, for example across a catalyst bed, to provide the desired temperature profile. However, the bending of metal induces expansion and compression stress, causing weak spots along sharp bends in particular.

In hydrogen-rich atmospheres, HSC may occur at such spots, which in time can grow enough

to break through the metal sheath entirely [2]. This loss of integrity leads to larger molecules of the process fluid (e.g. H2S) reaching inside the insulating MgO powder, contaminating it.

Ageing mechanisms: H2S contamination

Magnesium oxide powder reacts with certain chemicals, including sulfur and nickel. The now contaminated MgO powder enables the formation of electrically conductive Ni3S2 by combining nickel from the thermocouple conductor leads, the metal sheath and sulfur from the process. This can be seen in Fig. 2 to 4. Here, the contaminated area 5 grows, the electrical leads form a short circuit, restricting the sensor accuracy or migrating the location of the thermocouple hot junction. The probe risks becoming blind to process temperature changes.

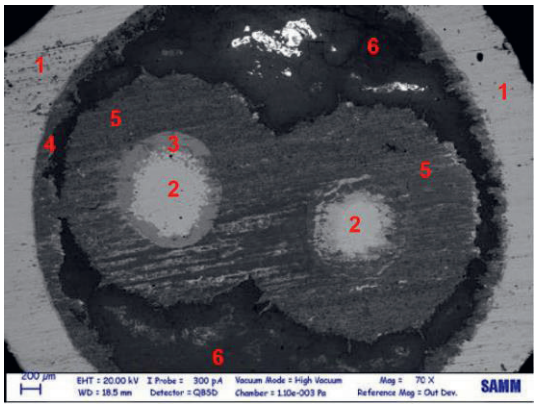

1 - Outer sheath (standard thermocouple)
2 - Thermocouple legs (+/-) kernels
3 - Thermocouple legs (+/-) polluted crowns
4 - Nickel migration from the outer sheath
5 - MgO powder, polluted by Ni and S
6 - Magnesium or aluminium powder

Fig. 2. Electron microscopy scan of a cross section of a standard mineral insulated sheathed thermocouple of Type N

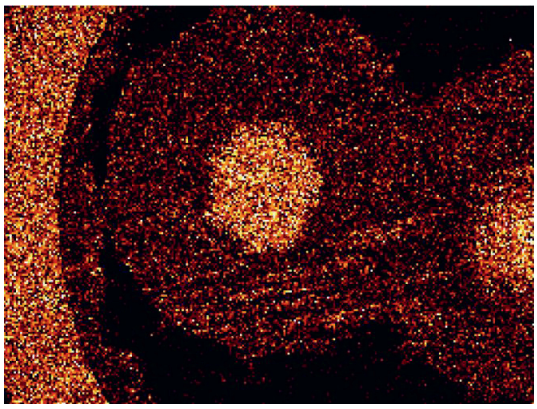

Fig. 3. Distribution of Nickel

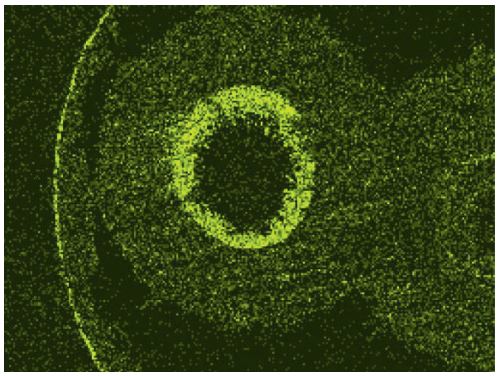

Fig. 4. Distribution of Sulfur

Description of the new thermocouple design

To provide a higher process safety, a new, robust multipoint thermocouple probe design was developed. It combines a thermowell and multiple thermocouple sensors in a single space-saving probe (Fig. 5). Here the thermowell/ outer sheath provides a first process barrier. In case of its leakage the internal MgO powder could be polluted. But, this does not distort the thermocouple measurement since each of the thermocouples is surrounded by a second sheath. This is a second layer of protection to thermocouple measuring systems.

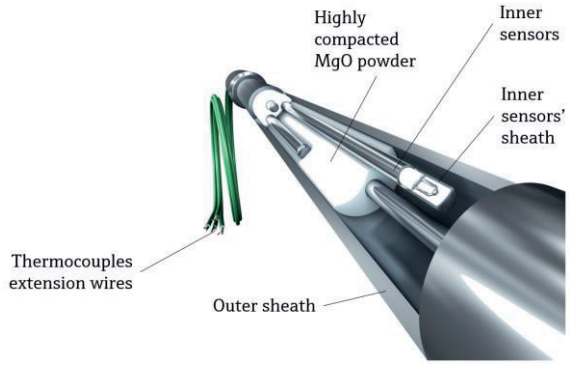

Fig. 5. Sketch of the new designed ProfileSens

Multiple thermocouple sensors can be grouped within a single probe, each delivering ultra-high measuring performance even under the most challenging operation conditions. The probe layout (routing), length and the number of sensors is individually adapted to process specifications. The design is proven in use to significantly lower the risk of premature sensor drift, corrosion or short circuits.

References

[1] E. S. Webster, Low-Temperature Drift in MIMS Base-Metal Thermocouples, *International Journal of Thermophysics* 35, 574-595 (2014); doi: 10.1007/s10765-014-1581-9

[2] M. S. Rana et. Al., Degradation of thermocouple in a temperature programmed sulphidation reactor, *Eng. Fail. Anal.* 55, 79-86 (2015); doi: 10.1016/j.engfailanal.2015.05.012

DOI 10.5162/SMSI2021/C4.3

Modelling Considerations for Resistance Wire Thermometers Applied to Internal Combustion Engines

Varun Venkataraman[1], Yushi Murai[2],
Michael Liverts[2], Ramis Örlü[2], Jens H.M. Fransson[2], Ola Stenlåås[1,3], Andreas Cronhjort[1]
[1]CCGEx, Dept. Machine Design, KTH Royal Institute of Technology, 100 44 Stockholm, Sweden
[2]CCGEx, Dept. Engineering Mechanics, KTH Royal Institute of Technology,
100 44 Stockholm, Sweden
[3]Scania CV AB, 151 87 Södertälje, Sweden
Varun Venkataraman: varunve@kth.se

Summary:
This study delves into the modelling of resistance wire thermometers (RWTs) within the application context of measuring the exhaust gas temperature pulse in internal combustion engines. The model was developed in a commercial simulation software utilizing the heat balance equation. Disparities were found between different model representations of the prongs due to differences in the heat transfer within the sensor, which impacts its expected dynamic response. The appropriate modelling choice will be made upon validation with shock tube experiments for different RWT designs.

Keywords: cold-wire anemometry, lumped parameter, resistance thermometry, time-resolved temperature measurement

Background, Motivation and Objective

Measurements of the time-resolved exhaust gas flow in internal combustion engines (ICEs) remains complex and challenging. As ICEs are expected to play a significant role in the broader effort to curb climate change, continuous and often radical improvements are demanded on its efficiency and emission mitigation levels [1]. As temperature is a crucial parameter to meet this objective, its measurement on a time-resolved basis would aid in the further development of turbocharging, waste heat recovery and aftertreatment systems.

A recent study indicated the potential to address the challenge of measuring the time-resolved exhaust gas temperature pulse in ICEs using specially designed resistance wire thermometers (RWTs) [2]. An outcome of this preliminary assessment was the need to characterise the dynamic behaviour of the RWTs based on its construction and application environment. This study initiates the assessment using models to complement experimental investigations.

Modelling of RWTs is a well-studied topic primarily concerned with resolving the heat loss from the sensing wire to the prongs to account for end conduction heat losses. These models provide a design guideline for RWTs to minimise end conduction and can be used for dynamic response correction through the frequency response function of the sensor system. While literature in this topic is expansive, two particular modelling approaches are currently examined.

Model-1 developed in Ref. [3] used the lumped parameter approach of heat transfer modelling wherein each element of the RWT (wire, stub and prongs) was lumped as a single element. Model-2 developed in Ref. [4] represented the RWT as a weighted sum of first-order systems representing the sensing wire and the prongs discretized into four distinct elements. Hence, the two models differ primarily in their representation of the prongs.

In this study, the implications of the modelling approach proposed in model-1 and model-2 are evaluated on the response of an RWT to a simulated flow profile.

Sensor Modelling Methodology

One of the RWTs analysed in Ref. [4] was modelled in the powertrain oriented system simulation software, GT-Power. Fig.1 illustrates a schematic of the modelled RWT along with the modelling approaches. When the prongs are identical, it is sufficient to model one-half of the sensor system due to assumed symmetry over the wire. The Biot number (Bi) of the element determines the validity of the lumped parameter approximation. It is defined by the ratio of the conductive to convective thermal re-

sistance. A Bi≪1 provides a better lumped parameter approximation of the modelled system. An additional thermal resistance is included to account for the unexposed length of the prongs which act as a heat sink. All of the exposed lumped elements of the RWT experience a forced convective component from the flow in addition to the conduction between them. The effect of radiation was insignificant and not included in the current evaluation.

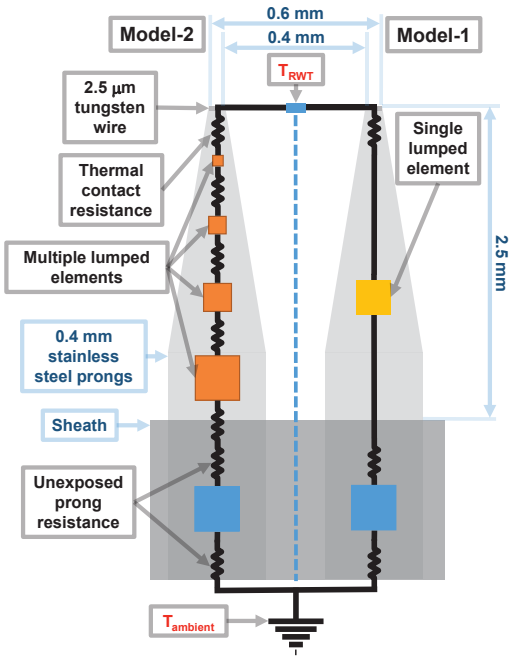

Fig. 1. Sensor schematic and modelling approach

While the overall probe dimensions were available in Ref. [4], approximations were made on dimensions and material properties not explicitly stated in the study. This especially applies to the thermal contact resistance induced by the joining process between the sensing wire (tungsten) and the prongs (stainless steel). The model-1 study [3] states a thermal contact resistance of the order of 50000 K/W although it was derived for soldering of a 50 µm silver stub onto conical stainless steel prongs of root diameter between 0.3-0.4 mm. Despite the wire being welded in the modelled sensor and not containing a stub, the thermal contact resistance suggested in Ref. [3] was used to assess the modelling approaches. The contact (weld) area between the wire and prong along with the prong mass were constant between the modelling approaches.

Implications of the Modelling Approach

To ascertain the sensitivity of RWT modelling, the experimental setup used in Ref. [4] was modelled. The temperature and velocity over the RWT were increased as a ramp depicted in the inset of Fig. 2. The ramp represents a sensor immersed in a heated jet at 0.5 m/s from the ambient condition. The Biot number criterion was valid for elements in both modelling approaches over the ramp. Fig. 2 shows the simulated response based on the two models. While the initial portion of the response of the sensing wire is comparable between the approaches, the attenuation imposed by end conduction to the prong is more severe in model-1. This is an expected observation from a theoretical viewpoint as a larger lumped element interacts directly with the sensing wire in model-1. Additionally, model-2 accounts for the length scale of the exposed prong with four lumped elements of varying size, unlike model-1.

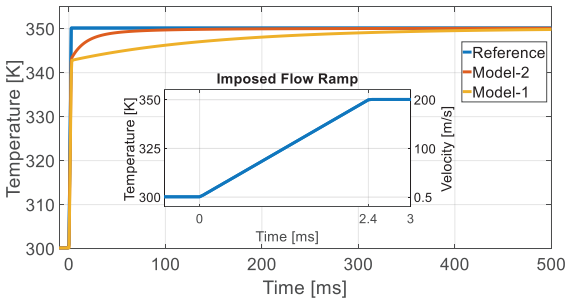

Fig. 2. Modelled RWT wire response to flow ramp

Conclusion

Despite the validity of the lumped parameter approach, differences were observed in the RWT dynamic response based on the choice of prong modelling. Experiments of RWTs with different design features in a shock tube will help validate the appropriate modelling choice associated with the prongs. The derived understanding can subsequently be extended to more complex flows as that of an ICE exhaust.

Acknowledgements

This study was financed by the Swedish Energy Agency and the Competence Center for Gas Exchange (CCGEx).

References

[1] J. R. Serrano *et al.*, Why the development of internal combustion engines is still necessary to fight against global climate change from the perspective of transportation, *Appl. Sci.*, 9, 4597 (2019), doi: 10.3390/app9214597.

[2] V. Venkataraman *et al.*, Resistance Wire Thermometers for Temperature Pulse Measurements on Internal Combustion Engines, in *SMSI2020*, 252–253, (2020) doi: 10.5162/SMSI2020/P2.14.

[3] G. Arwatz *et al.*, Dynamic calibration and modeling of a cold wire for temperature measurement, *Meas. Sci. Technol.*, 24, 125301 (2013), doi: 10.1088/0957-0233/24/12/125301.

[4] R. Dénos, C. H. Sieverding, Assessment of the cold-wire resistance thermometer for high-speed turbomachinery applications, *J. Turbomach.*, 119, 140–148 (1997), doi: 10.1115/1.2841002.

DOI 10.5162/SMSI2021/C4.4

Monte-Carlo analysis of challenges and limitations of dispersion-based optical thermometry

Anni Röse[1], Paul Köchert[1], Günther Prellinger[1], Eberhard Manske[2] and Florian Pollinger[1]
[1]Physikalisch-Technische Bundesanstalt (PTB), Bundesallee 100, 38116 Braunschweig,
[2]Ilmenau University of Technology, Max-Planck-Ring 14, 98693 Ilmenau
anni.roese@ptb.de

Summary: Using the dispersion models, it is possible to derive the effective temperature in an optical beam by the measurement of the optical path length at two well-known optical wavelengths. We are currently developing a gradient thermometer based on this principle, deploying multi-wavelength interferometry for the length measurement. This shall enable beam bending compensation in optical levelling of large structures. A Monte-Carlo investigation reveals practical obstacles and limitations of this promising temperature measurement approach.

Keywords: dispersive thermometry, measurement uncertainty modelling, multi-wavelength interferometry, Monte-Carlo Simulation

Motivation

When performing large-scale dimensional measurements outside, the measurement is mainly influenced by the inhomogeneity of the index of refraction. Vertical temperature gradients, e.g., induces beam bending. This limits the achievable accuracy of optical levelling. To improve the accuracy this effect must be properly compensated. But outdoor capturing of the temperature gradients by classical sensors requires dense and impractical sensor networks. Therefore, our group develops an alternative temperature sensor based on multi-wavelength absolute interferometry [1]. In this contribution, we present a Monte Carlo study of the achievable measurement uncertainty for this highly complex sensor design.

Dispersive Thermometry

The Edlén equation in the version by Bönsch und Potulski [2] describes the functional dependence of the refractive index of air by

$$n(\lambda, T, \mathrm{p}, \mathrm{x}, \mathrm{p_w}) = K(\lambda) \cdot D(\mathrm{T}, \mathrm{p}, \mathrm{x}) - p_w g(\lambda) \quad (1)$$

with the wavelength λ and the thermodynamic parameters pressure p, temperature T, carbon-dioxide contents x, partial pressure of water vapor p_w, and the dispersion term $K(\lambda)$, the density term $D(\mathrm{T}, \mathrm{p}, \mathrm{x})$, and the humidity term $g(\lambda)$ [2]. Dispersive thermometry is based on a measurement of the same geometric path l with two different vacuum wavelengths λ_1 and λ_2. If performed in air, the optical pathlength will differ by their difference in refractivity.

$$\mathrm{d}_1 = (DK_1 - \mathrm{p_w} g_1) \times l + l \quad (2)$$

$$\mathrm{d}_2 = (DK_2 - \mathrm{p_w} g_2) \times l + l \quad (3)$$

This equation system can now be solved for the temperature (in °C) including the humidity terms $K(\lambda)$, $D(\mathrm{T}, \mathrm{p}, \mathrm{x})$ and $g(\lambda)$:

$$\mathrm{T_{eff}} = \frac{d_2 - d_1 + (K_1 - K_2) l \mathrm{p} \alpha (1 + \beta \mathrm{p}) - \mathrm{p_w} l (g_1 - g_2)}{-\delta (d_2 - d_1) + \alpha \mathrm{p}^2 \gamma l (K_1 - K_2) + \mathrm{p_w} \delta l (g_1 - g_2)} \quad (4)$$

with β, γ, δ representing numerical constants and α a function of the CO_2 contents x [4].

The effective temperature along a beam path can hence be derived from the path $(\mathrm{d}_2 - \mathrm{d}_1)$ if pressure and water vapor information is available from auxiliary sensors.

Measurement and Uncertainty

We measure the optical path lengths d_1 and d_2 using fixed synthetic wavelength interferometry [4]. We use two Nd:YAG laser with wavelengths $\lambda_1 = 532$ nm and $\lambda_2 = 1064$ nm. The frequency difference $\Delta\nu_i$ between both lasers can be varied between 20 GHz and 60 MHz. This corresponds to synthetic wavelengths between metres and millimetres. For the actual measurement, we detect the optical phases of all four fundamental optical beams and calculate the phase of the corresponding synthetic wavelengths. This measurement strategy, however, is very complex and suffers from highly unfavourable uncertainty scaling. Figure (1) shows an Ishikawa diagram which summarizes the various uncertainty contributions. Their individual impact as well as consequences on the instrument design can be better understood by a Monte Carlo simulation.

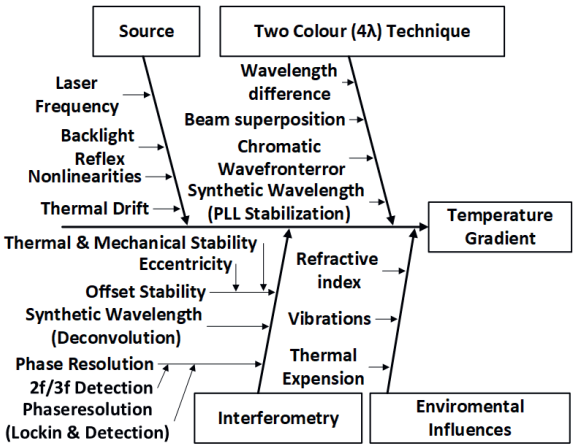

Figure 1: Ishikawa diagram summarizing uncertainty contributions of the dispersive thermometer.

Results

As discussed before, the measurement principle depends on an accurate measurement of the optical path difference. Any uncertainty of this measurement is unfavourably scaled up and impedes the achievable measurement uncertainty of the temperature measurement. As an example, Figure (2) shows the influence of thermal expansion of the reference path due to changes in temperature during the interference measurement. For an aluminium base plate with a thermal expansion of $23.1 \times 10^{-6}\mathrm{K}^{-1}$, an interferometer reference path longer than 2 mm would make an uncertainty of 0.1 K very difficult to achieve.

It appears logical that the resolution of the optical phases is critical. But Figure (3) reveals how crucial this influence really is. For a measurement distance of 50 m, and a synthetic wavelength 3.75 mm, a resolution of the phase of at least $\pi/10000$ is needed for a useful temperature uncertainty in the below 1 K. Similarly, the Monte Carlo simulation shows that

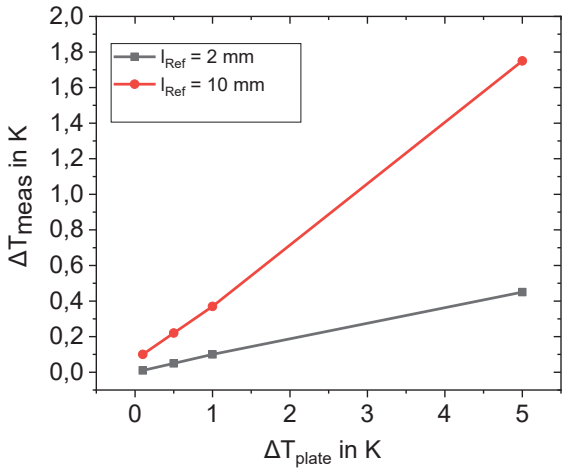

Figure 2: Thermal expansion base plate during the experiment with reference length between 2 mm and 10 mm.

for distances below 10 m, the chosen setup with a synthetic wavelength of 20 GHz is not capable to resolve temperatures better than 1 K. For shorter distances, phase resolutions better than $\pi/10000$ would be necessary.

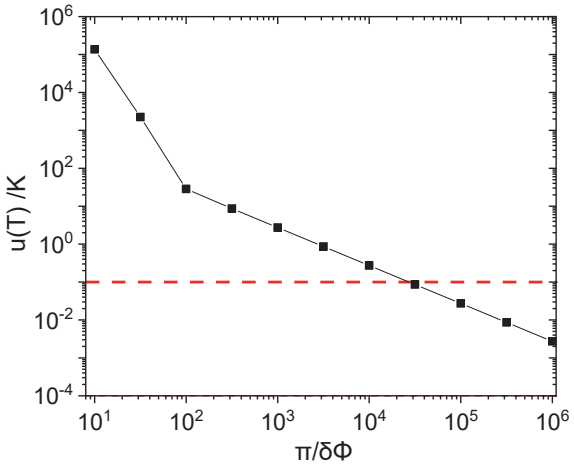

Figure 3: Dependence of the effective temperature uncertainty $u(T)$ (coverage factor k=1) on phase resolution $\delta\phi$.

Conclusions

In general, the phase resolution required by the Monte Carlo simulation poses a great challenge for the modulation and stabilization of the laser source, especially for an outdoor measurement. To achieve this, considerable integration times will probably be necessary, too. The lower limit of 10 m for this measurement is another interesting result, but less critical here since the targeted application, the reference point measurement of large VLBI telescopes, implies longer distances. In conclusion, this study shows that the realization of an optical thermometer for this purpose is, though challenging, feasible, with the Monte Carlo analysis pointing to critical issues for the instrument design.

Acknowledgement

This project has received funding from the EMPIR programme cofinanced by the participating States and from the European Union's Horizon 2020 research and innovation programme.

References

[1] Meiners-Hagen K, Meyer T, Prellinger G, Pöschel W, Dontsov D, and Pollinger F 2016 Opt. Expr. 24 24092

[2] Bönsch G and Potulski E 1998 Metrologia 35 133

[3] Meiners-Hagen K, Schödel R, Pollinger F, and Abou-Zeid A 2009 Meas. Sci. Rev. 9 16

[4] Meiners-Hagen K and Abou-Zeid A 2008 Meas. Sci. Technol. 19 084004

DOI 10.5162/SMSI2021/C5.1

Inline Inspection of Ceramic Tape Casting Processes by Means of Optical, Eddy Current and Machine Learning Methods

Manuela Heymann[1], Stefan Münch[1], Martin Schulze[1], Beate Capraro[2], Dirk Schabbel[2], Vidit Gupta[1], Andy Vogel[2], Christiane Schuster[1], Thomas Härtling[1,3]
[1] Fraunhofer Institute for Ceramic Technologies and Systems IKTS, Maria-Reiche-Strasse 2, 01109 Dresden, Germany,
[2] Fraunhofer Institute for Ceramic Technologies and Systems IKTS, Michael-Faraday-Strasse 1, 07629 Hermsdorf, Germany
[3] Technische Universität Dresden, Institute of Solid State Electronics, Mommsenstraße 15, 01069 Dresden, Germany
thomas.haertling@ikts.fraunhofer.de

Summary:
Tape casting is a ceramic forming technology used to produce planar ceramic components by means of a doctor-blade process. However, industrial casting plants are currently not equipped with inline measurement tools which allow detecting of defects and determine quality parameters of the ceramic tape. Here we use laser triangulation, camera-based monitoring, and eddy current measurement tools to acquire different tape quality parameters. Results of the implementation of these tools and the insights gained by applying machine learning algorithms for automated defect detection and classification are presented.

Keywords: tape casting, process monitoring, ceramics, optical inspection, eddy current, machine learning

1 Introduction

Tape casting is a high-throughput method for producing large, flexible tapes of functional materials very efficiently and cost-effectively in roll-to-roll processes. Applications of such tapes range from classic ceramic microsystem technologies (LTCC and HTCC) and the current strategic field of battery research to filtration, gas separation, and a variety of special functionally tapes. Finely ground ceramic powders are dispersed under addition of suitable dispersants, organic binders, and plasticizers. The resulting viscous casting slurry undergoes a doctor-blade process and subsequent drying done in a drying channel of several meters of length. The result is a very thin ceramic tape with flat surface.

The tapes produced can show several defects such as air pockets, bubble formation, large particle / object inclusions, density fluctuations of the slurry and fluctuations of the tape thickness. At present, industrial casting plants are not equipped with process monitoring tools which allow detecting defects and determine quality parameters inline. As a result, defects and parameters outside specification margins are only detected after the manufacturing process and the operators face high costs due to returned batches.

The authors intend to evaluate measuring methods for defect detection, to develop an inline application and in future adapt the information of the different methods to an overall description of the tape quality.

The inspection methods used here are laser triangulation for thickness determination at the beginning and end of the drying channel (measurement of wet and dry film thickness), camera-based optical inspection, and eddy current measurements at the end of the drying line (detection of inclusions, material defects, holes, deviation in dielectric constant). The methods have been evaluated and optimized regarding hardware, location and method of implementation, data generation and evaluation, and were integrated in a demonstration casting plant.

In this contribution we show results of the different monitoring systems and first results on

defect prediction based on machine learning algorithms and the effects on operating tape casting machines.

2 Measurement System

For thickness measurement, four laser triangulation sensors (Keyence LK-H087) were installed (a static reference and a dynamic sensor each at the beginning and the end of the drying line). Hence, they were applied in differential mode to determine the film height. Furthermore, optical inspection was carried out with a single line camera (Teledyne Dalsa Linea) and alternating illumination in reflection and transmission mode. Images were acquired exploiting the movement of the ceramic foil under the line sensor of the camera. This system was intended to detect defects in the ceramic foil. As a third component, an inline eddy current array probe setup by Fraunhofer IKTS [1] was installed at the backend of the drying line. This system allows to evaluate especially the (di)electric properties of the cast foil. It was operated in reflection mode.

3 Results

After the implementation of the described measurement tools results were obtained which allow a first inline characterization of the ceramic tape. For demonstration, a sample casting with an Al_2O_3 slurry was carried out. The tape width was 150 mm, the doctor-blade gap 400 µm (tape wet thickness) and casting velocity 0.4 m/min.

The thickness measurement was proven feasible at the backend of drying line (see results depicted in Fig. 1).

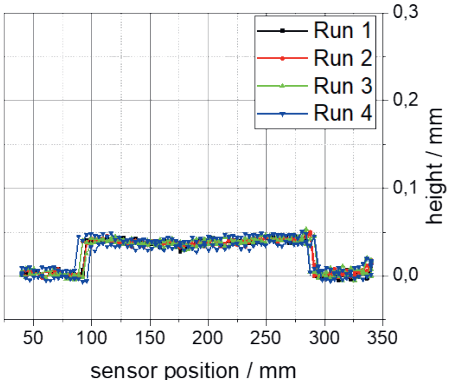

Fig. 1 Feasibility proof of inline thickness measurement of the dry ceramic green tape.

The camera-based optical inspection tool allows to detect specific defects. As an example, a small defect (a hole) is shown in Fig. 2 in reflection mode (left) and transmission mode (right). These images were used as training database for image classification with machine learning (ML) algorithms. The following steps have been pursued: image classification and labeling, image preprocessing, setting up of ML model including training and evaluation, and assessment of accuracy. For binary classification (either no defect or any kind of defect), a model based on the EfficientNet B5 showed best results. For multiclassification (four defect classes), best results were achieved by applying a U-Net model which uses an encoder and decoder approach.

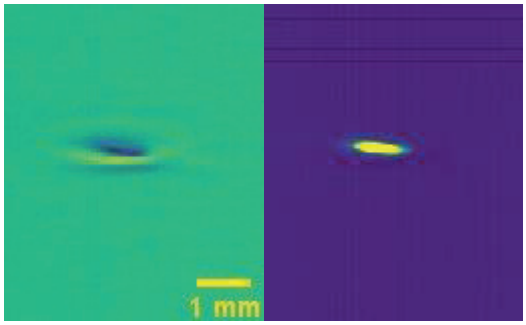

Fig. 2 Optical inspection with alternating illumination. Left: reflecting mode. Right: transmission mode. In both images a small defect (hole) is visible which leads to rejection in further material processing.

Finally, a first test of the eddy current setup allows to detect NdFeB particles in the foil. They are marked as blue spots in the image in Fig. 3.

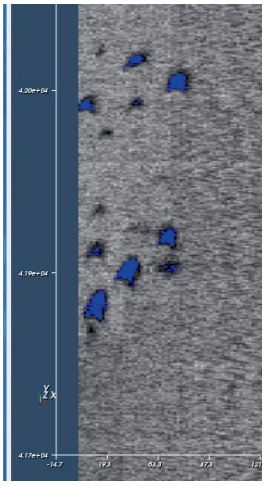

Fig. 3 Detection of NdFeB particles (blue spots) by means of the eddy current system.

Based on the current results and the ongoing work, our contribution will provide a detailed description of the measurement system in use, a classification of detectable defects, results on defect detection based on machine learning algorithms, and a discussion of the benefits by fusing the data of all three measurement tools.

References

[1] M. Wild, A. du Barét, S. Reuber, M. Schulze, H. Heuer, M. Wolter, A. Michaelis, Analysis and

monitoring of the percolating network of battery electrode films during the drying process using eddy current technology, Lecture, *International Battery Production Conference IBPC 2019,* 5.11.2019

DOI 10.5162/SMSI2021/C5.2

Indirect geometry measurement for laser chemical machining using a model-based signal processing approach

Merlin Mikulewitsch[1], Dirk Stöbener[1,2], Andreas Fischer[1]
[1] University of Bremen, Bremen Institute for Metrology, Automation and Quality Science (BIMAQ), Linzer Str. 13, 28359 Bremen, Germany
[2] University of Bremen, MAPEX Center for Materials and Processes, Germany
m.mikulewitsch@bimaq.de

Summary:
The optical geometry measurement of submerged micro-surfaces in chaotic fluid environments, e.g., for electric discharge machining (EDM) or laser chemical machining (LCM), is challenging when the specimen features high aspect ratios and steep surface gradients. To avoid reflection-caused artifacts at steep gradients, fluorescent molecules are added to the fluid and the geometry of the fluid layer is measured using a confocal fluorescence microscope. A model-based signal processing enables a robust, indirect measurement in fluid layers > 1 mm, since it is capable to cope with process-inherent bubbles and surface gradients up to 85°.

Keywords: micro geometry, optical measurement, in situ, fluorescence, signal modeling

Introduction

Laser chemical machining (LCM) uses an electrolytic fluid and localized heating by a laser to generate a material removal in submerged workpieces. It produces microstructures with high aspect ratios, high surface gradients and small edge radii. In contrast to competing processes such as micro-milling or laser ablation there is no thermal stress induction or tool wear [1]. However, the in situ conditions hinder conventional optical geometry measurement methods.

Interferometric methods such as white light interferometry suffer from measurement deviations caused by thermal gradients and refractive index fluctuations in the fluid [2]. Confocal microscopy is prone to artifacts caused by the high surface angles and curvatures [3] typically produced with the LCM process. However, an indirect measurement approach using confocal fluorescence microscopy is promising for in situ application, since it does not capture the light reflected by the specimen, but the light emitted by a fluorescent liquid covering it. The detected fluorescence signal $S(z)$ can be limited to a small volume around the focal plane of the objective by axial light sectioning produced by confocal microscopy, where a pinhole, confocal to the objective lens, attenuates light far outside the focal plane. This way, a signal is only detected when the so-called confocal volume intersects the fluorescent fluid. The surface geometry is then determined by the change of the fluorescence signal produced by pointwise scanning of the confocal volume from the fluid surface to the specimen surface.

The principle was successfully used on metallic microspheres with high curvatures by coating their surface with a thin fluorescent film < 100 nm [3]. It was shown that a measurement was possible even at angles > 75° from the surface normal with a lateral resolution comparable to conventional confocal microscopy without causing artifacts. The influence of gas bubbles and high surface inclinations on the measurement in thick fluid layers > 1 mm present during LCM has not yet been studied and is the aim of this work.

Model-based indirect measurement method for thick fluid layers

To determine the specimen surface position z_0 with micrometer precision in thick fluid layers, a model-based evaluation of the fluorescence signal $S(z)$ is required [4]. The signal model is based on a simplified confocal volume function (CVF) in the shape of a 3D-Gaussian function. It represents the spatial distribution of the contributions of all infinitesimal volume elements to the total fluorescence signal. The signal function $S(z)$ at the position z is obtained by weighting the CVF with a depth dependent absorption term and integrating it over all spatial dimensions [4]. To cope with small deviations due to inclined surfaces, the model was heuristically extended by two additional terms, resulting in

$$S(z) = S_0\, e^{\epsilon(z-z_1)}\left[\operatorname{erf}\left(\frac{z-z_0}{2\Xi}+\epsilon\Xi\right)-\operatorname{erf}\left(\frac{z-z_1}{2\Xi}+\epsilon\Xi\right)+K_1\cdot\left(\operatorname{erf}\left(\frac{z-z_2}{2\xi}+\epsilon\xi\right)-\operatorname{erf}\left(\frac{z-z_1}{2\xi}+\epsilon\xi\right)\right)\right]+K_2 e^{-\frac{(z-z_2)^2}{2\sigma^2}}, \quad (1)$$

with ϵ being the attenuation coefficient, ξ/Ξ confocal volume parameters and S_0, $K_{1,2}$, σ and z_2 weighting parameters. The desired position z_0 (specimen surface) is finally obtained by using the model function $S(z)$ for a non-linear least-squares approximation of the measured data.

Results

The fluorescence intensity signals along a line on the inclined surface of a submerged specimen were measured for the three inclinations 35°, 65° and 85°. The specimen surface positions z_0 resulting from the model-fit using Eq. (1) are shown in Fig. 1 (left). To determine the influence of the surface angle on the indirect measurement, the deviations δ from a linear fit of the surface positions were calculated. Although the standard deviation of δ increases with the angle, a comparison with a reference measurement using conventional confocal microscopy shows an equal magnitude as the indirect measurement. In contrast to the reference measurements however, no artifacts in form of systematic measurement deviations were observed during indirect measurement for surface angles up to 85°.

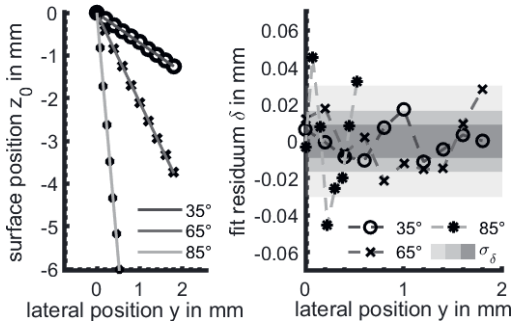

Fig. 1. Left: Surface positions for three different inclinations (with linear fit). Right: Fit residuum δ with standard deviations (shaded areas).

Since gas bubbles occur in the LCM process and may cross the optical path of the measurement system, the influence on the indirect measurement needs to be determined. For that purpose, a bubbly fluid environment was emulated by chemical reactions of phosphoric acid and a non-passivating metallic specimen material. The fluorescence intensity signals for two different bubble densities in the optical path are shown in Fig. 2. The fluorescence signal exhibits an increased noise with higher bubble density, particularly near the fluid surface. The determination of the surface position z_0 using the model-based signal approach is possible nonetheless, even with the increased signal noise. The result is merely an increased uncertainty of z_0, see measurements on a flat surface shown in Fig. 3.

In conclusion, the indirect geometry measurement method is suitable for in situ measurements in thick and contaminated fluid layers as they appear in the LCM or EDM process environments. In particular, it enables measurements on surface angles up to 85°.

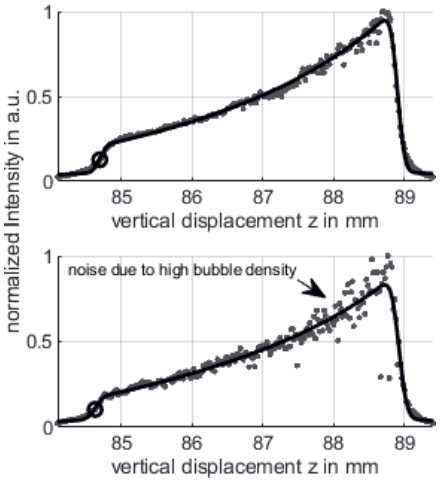

Fig. 2. Fluorescence intensity signal and model fit for a low (top) and a high (bottom) gas bubble density in the optical path (circle: z_0).

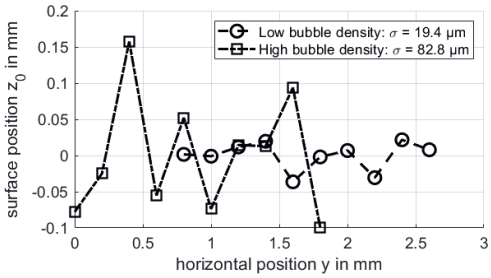

Fig. 3. Surface positions z_0 along the y-axis on a level surface. The standard deviation σ of the surface position $z_0(y)$ increases with bubble density.

Funding DFG – SFB747.

References

[1] H. Messaoudi, M. Mikulewitsch, D. Brand, A. von Freyberg, A. Fischer, Removal behavior and output quality for laser chemical machining of tool steels, *Manuf. Rev.* 6, 13 (2019); doi: 10.1051/mfreview/2019015

[2] C. Gerhard, F. Vollertsen, Limits for interferometric measurements on rough surfaces in streaming inhomogeneous media, *Prod. Eng. Res. Devel.* 4, 141-146 (2010); doi: 10.1007/s11740-010-0224-7

[3] J. Liu, C. Liu, J Tan, B. Yang, T. Wilson, Super-aperture metrology: overcoming a fundamental limit in imaging smooth highly curved surfaces, *J. Microsc.* 261, 300-306 (2016); doi: 10.1111/jmi.12334

[4] M. Mikulewitsch, A. von Freyberg, and A. Fischer, Confocal fluorescence microscopy for geometry parameter measurements of submerged micro-structures. *Opt. Lett.* 44, 1237-1240 (2019); doi: 10.1364/OL.44.001237

DOI 10.5162/SMSI2021/C5.3

Process monitoring by impedance spectroscopy in the field of used-sand regeneration

Luca Bifano[1], Marco Weider[2], Alice Fischerauer[1], Gerhard Fischerauer[1]
[1] Chair of Measurement and Control Systems, Universität Bayreuth, 95440 Bayreuth, Germany, mrt@uni-bayreuth.de
[2]Foundry Institute of the TU Freiberg, TU Bergakademie Freiberg, 09599 Freiberg, Germany

Summary:
It would be very advantageous if the condition of molding materials (sand-binder systems) in regenerator units used in foundries could be monitored in real-time. This work presents the results of investigations in this direction. In [1] it is shown that the condition monitoring can possibly be based on impedance spectroscopy because the resulting curves are characteristic of the material used. This has now been confirmed by measurements on a regenerator typical of the actual application.

Keywords: Foundry, regeneration process, condition monitoring, impedance spectroscopy

Background

The raw material sand is mined more than the natural regeneration of the sand deposits can compensate [2, 3]. One reason for this is that the foundry industry needs the sand to produce so-called lost forms and cores with binders like bentonite. As a consequence, used sand is now routinely recycled to save on raw material and to avoid the expensive disposal of used sand in landfills.

As the type and quality of sand play an important role in foundry applications, the qualification of the raw and regenerated materials is defined by industry regulations. In Germany, e. g., the guidelines are drafted by the Bundesverband der Deutschen Gießerei-Industrie (Federal Association of the German Foundry Industry, BDG). As yet, laboratory tests are the standard method [4].

To achieve optimum results at the lowest possible cost, the sand condition needs to be monitored during the recycling process. Our goal is to base such a condition monitoring on impedance spectroscopy. Known results from the literature indicate that the characteristics of different raw materials such as grain size distribution, crystal structure, and moisture may be distinguishable with this method. For example, [5] shows how the permittivity of bentonite depends on its water content. Ref. [6] describes the complex permittivity of sand-bentonite-water mixtures by a plausible model. We have now extended this approach and have investigated whether the process state in a state-of-the-art regenerator is observable by impedance measurements.

Measurement Setup

For our field measurements, the measuring cell presented in [1] was replaced by a cell in the form of a circular cylindrical capacitor (radial electrode distance: 1 cm, electrode height: 10 cm, electrode material: aluminum). In this way, the impedance measurement could be performed with a significantly smaller sample volume of the material under test (MUT). The electrodes were contacted via two coaxial cables. The electrode arrangement was fixed by a polymer sheath. The impedance of the MUT-filled cell was measured by an LCR meter E4890A from Agilent in the frequency range from 500 Hz to 1 MHz.

The sequence in a typical regeneration run is shown in Table 1. The speed of the regeneration progress can be adjusted by the rotational speed of the whetstone that is responsible for the regeneration effect. For this test series, the speed was respectively set to 1,830 rpm (batch 1, MUT 1) and 3,190 rpm (batch 2, MUT 2).

Tab. 1: Sequence of a typical regeneration run for used sand.

Step	Regeneration progress	MUT	
		1	2
1	Used sand	a	a
2	5 minutes of pre-dedusting	b	b
3	10 minutes of regeneration	c	c
4	20 minutes of regeneration	d	d
5	30 minutes of regeneration	e	e
6	10 minutes of post-dedusting	f	f

For the impedance measurements the cell was filled with the MUTs, a frequency sweep was run 5 times, and the cell was emptied again. This was repeated 5 times for each MUT.

Results

Figure 1 shows the respective mean value curve of the different regeneration states of MUT 2 as

Nyquist plots. The maximum uncertainties for the real and imaginary parts were 13.64 % (at f = 14 kHz) and 16.17 % (at f = 48 kHz) for MUT 2b. At other frequencies and for other MUTs, the uncertainties were well below these values. For example, for the MUTs 2c and 2d, the maximum uncertainties of the real and imaginary parts did not exceed 4 %. The measurements are obviously quite reproducible, although refilling the measuring cell does not lead to the exact same conditions. This reproducibility justifies our working with mean-value impedance curves.

The impedances shift to higher values as the regeneration progresses (Fig. 1). The initially observed semicircular arc at high frequencies (MUT 2a–c) disappears and the Nyquist curves become steeper. This indicates that the regeneration process reduces the electrical conductivity of the material composition (higher impedances) and that it removes components from the sand (disappearing semicircular arc). This very removal of components is the aim of the process and, as shown, it can be monitored by impedance spectroscopy.

The same observations have been made for MUT 1. Due to the slower movement of the whetstone, the regeneration progress is slower, and this is revealed by the impedance data. This will be shown in more detail in the full contribution.

Conclusion

The current field tests corroborate our conclusions from laboratory measurements on sand/binder mixtures, viz., that impedance spectroscopy is suitable for monitoring sand regeneration processes. Of course, the method will unfold its full potential when an industrial-grade LCR meter rather than laboratory equipment is used.

Acknowledgement

This work was supported by the German Federal Ministry for Economic Affairs and Energy, grant number ZF4152305DB8.

References

[1] L. Bifano et al., “Investigation of complex permittivity spectra of foundry sands,” *Tech Mess*, Vol. 87, pp. 372–380, May 2020.

[2] J. Götze, M. Göbbels, *Einführung in die Angewandte Mineralogie* (Introduction to Applied Mineralogy; in German). Berlin: Springer, 2017.

[3] N. N., *Sand and sustainability*. *UN Environmental Programme*, Geneva, Switzerland, 2019.

[4] W. Tilch, H. Polzin, and M. Franke, *Praxishandbuch bentonitgebundener Formstoff* (Practical manual for bentonite-bound molding material; in German). Berlin: Schiele & Schön, 2019.

[5] H. Kaden et al., “Low-frequency dielectric properties of three bentonites at different absorbed water states,” *J. Colloid Interface Sci.*, Vol. 411, pp. 16–26, Dec. 2013.

[6] T. A. Belyaeva et al., “The effect of very low water content on the complex dielectric permittivity of clays, sand-clay and sand rocks,” *Meas. Sci. Technol.*, Vol. 28, No. 1, (8pp), Jan. 2017.

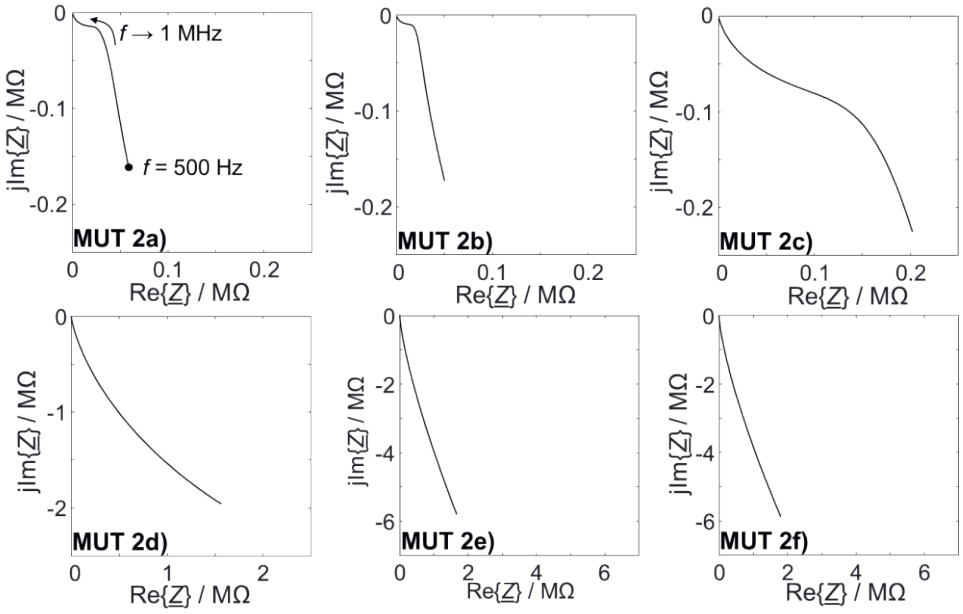

Fig. 1 Measured test-cell impedance with MUT 2a through 2f during the regeneration process.

DOI 10.5162/SMSI2021/C5.4

Online Washing Process Monitoring with Wireless Textile Impedance Measurement

Andreas Hennig[1], Hartmut Prinz[2], Mathias Roth[3], Felix Essinghold[1], Lukas Krupp[1], Anton Grabmaier[1], Hans-Günter Hloch[2], Jürgen Bohnen[2]
[1] Fraunhofer IMS, Germany, [2] wfk - Cleaning Technology Institute e.V., Germany,
[3] Textilforschungsinstitut Thüringen-Vogtland, Germany
andreas.hennig@ims.fraunhofer.de

Summary:
In this paper a sensor system for the in-situ monitoring of dirt removal in the running washing process is presented. In this work, a sensor is presented for adjustment or optimization of washing processes in textile service companies. The developed impedimetric performance sensor consists of a dirt and reference sensor area as well as a measuring and RFID communication module. At the sensor areas the impedance is measured during the washing process, recorded and transferred to an external evaluation unit. The impedance values can be used to determine the dirt removal during the washing process.

Keywords: washing process monitoring, RFID sensor, impedimetric sensor

Introduction

In Germany, 1.8 million tons of textiles for professional use, are processed by service companies every year with a turnover of about 3.2 billion €. Due to constantly increasing customer requirements regarding the cleanliness and hygiene of textiles, up to 2.5% of the processed textiles (depending on the type of textile or laundry) are sorted out within the scope of quality control. On the other hand, excessive use of heat and detergents, bleaches or disinfectants leads to increased energy costs and premature damage to textiles. Hence there is a need to adjust and optimize the washing process at regular intervals or permanently in a feedback-loop.

State-of-the-Art

Today primary wash monitors are used. These consist of defined soiled test textiles, which are colorimetrically evaluated after the washing process. However, an evaluation of the washing process is only possible afterwards. Furthermore, no direct conclusions on the effect of the process parameters are possible, so that an iterative adjustment is necessary. The process is therefore laborious and complex for the user.

An RFID module including an impedimetric performance sensor shall enable the in situ online acquisition of relevant process parameters.

Concept

The concept provides an in-situ detection of the dirt removal via impedance measurements and online data transfer during a running washing process by means of RFID technology. Essential characteristics are:

- The sensor should pass through the process with the laundry items and behave like a textile in its mechanical properties
- The dirt removal is to be measured by recording the residual dirt on a sensor area
- Measurement data transmission should be feasible out of the washing machine drum.

The impedimetric performance sensor consists of a sensor area and a RFID transponder with a textile-based antenna. The in-situ detection of the dirt removal enables the identification of functional correlations between the dirt removal and the process parameters (e.g. drum drive, chemical dosing; temperature; time) during the running washing process.

Sensor Principle

The sensor area is based on a textile electrode structure, which is soiled with a practice relevant type of dirt. This textile electrode structure consists of electrically conductive yarns (textile electrodes) included in a textile matrix. The geometry of the textile electrodes determines the measuring accuracy and response threshold to be achieved. The dirt load dependent dielectricity of the textile electrode structure (residual dirt on the sensor area of the impedimetric performance sensor) is detected by impedance measurements.

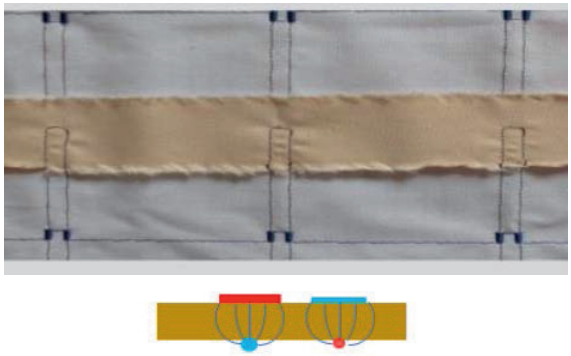

Fig. 1. Electrode structure and sensor area

Different electrode structures were evaluated. Figure 1 shows the chosen structure were higher proportion of the impedance signal comes from the textile and is therefore influenced by the contamination, compared to other arrangements. At the same time, the total value of the impedance is kept at a minimum level. Since the impedance must not be too low for the measuring circuit of the RFID module. The optimal sensor area consists of an electrode structure with electrodes that are guided at right angles to each other and attached to both sides of the soiled textile. The electrodes cross over each other at two points, so that the total impedance is still sufficiently high. Due to the improved electrode structure, commercially soiled textiles as well as specially produced soiled textiles could be used for the sensor area.

Measuring Circuit and Data Transmission

An RFID-module had to be developed, that performs the impedance measurement and enables wireless data transmission from the washing machine drum. Evaluation of textile electrodes have shown, that the impedance ranges from 10 Ω to 500 Ω, when excited by a measurement frequency of 1 kHz.

The RFID-Module is composed of an integrated impedance converter circuit from analog devices (AD5933), which performs the impedance measurement, a microcontroller and a semi-passive RFID-Frontend ASIC and a textile dipole antenna working in the UHF-RFID-Band. The dipole antenna is realized using an embroidered conductive yarn. The electronic components were encapsulated with **"**Silikonharz Elastosil RT 646**"**. The flexible textile antenna is connected via inductive coupling with a loop within the encapsulation. This allows the size of the rigid RFID module to be reduced.

To assess the feasibility, a reader antenna was mounted in the glass door of a front loading machine and the communication with a test transponder placed inside the washing machine was checked.

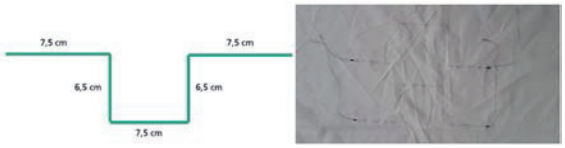

Fig. 2. Textile RFID antenna.

Results

To verify the measuring principle, the impedimetric sensor was placed in a washer extractor. The impedance measurement was performed at a frequency of 1 kHz.

Experiments with the impedimetric performance sensor in the washing machine during a washing program with a low mechanical agitation and a high liquor level (wool washing program) were done. A measurement frequency of 1kHz was used for the impedance measurement.

Figure 3 shows the impedance over time. A percentile filter was used for averaging in order to remove disturbances caused by the environment, especially the wash liquor, different soaking or covering of the sensor areas by other items of the laundry batch.

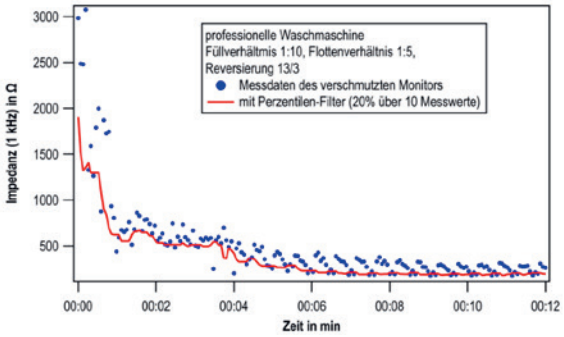

Fig. 3. Impedance curve during the washing process.

In summary, the impedimetric performance sensor allows the monitoring of the washing process and can be used to adjust temperature and concentration of the detergent or bleaching agent. In contrast to conventional wash monitors, there is no need for time-staggered removal and drying, which makes the readjustment of wash processes easier and faster.

It could be shown that inductively coupled dipole antennas can be realized with the help of conductive yarns. It could also be shown that RFID transponders can be read in metallic environments like a washing machine.

The IGF-project 19950 BG of the research as-sociation Forschungskuratorium Textil e.V., Reinhardtstr. 14-16, D-10177 Berlin, was supported via the AiF within the funding program „Industrielle Gemeinschaftsforschung und -entwicklung (IGF)" by the Federal Ministry of Economic Affairs and Energy (BMWi) due to a decision of the German Parliament.

DOI 10.5162/SMSI2021/C6.2

Operando State Diagnosis of Supported Ionic Liquid Phase Gas Purification Processes by a Resonant Perturbation Method

Vladimir Malashchuk[1,2], *Andreas Jess*[1], *Ralf Moos*[2]
[1] *Department of Chemical Engineering, University of Bayreuth, 95440 Bayreuth,*
[2] *Department of Functional Materials, University of Bayreuth, 95440 Bayreuth,*
Vladimir.malashchuk@uni-bayreuth.de

Summary:
The ionic liquid (IL) 1-Ethyl-3-methylimidazolium methanesulfonate [EMIM][$MeSO_3$] impregnated on silica 90 packed to fixed-bed was analyzed by the resonant perturbation method. Therefore, the sample was positioned within a glass reactor in a microwave cavity to analyze resonance frequency and the inverse quality factor under sorption conditions. Two humidity sensors located before and after the fixed bed and allowed to calculate the amount of stored water in the IL. This allows for operando observation of changes of the resonant frequency and the inverse quality factor with the amount of water in the sample. The results showed a decrease in the resonant frequency and an increase in the inverse quality factor with increased water-sorption in the IL. Both parameters thus allow to derive the average water load on the system.

Keywords: Resonant-perturbation method, Water loading, Supported ionic liquid phase, Operando diagnosis

Motivation

The removal of water vapor from gas streams is a pretreatment process in the chemical industry to prevent catalyst poisoning, equipment damage caused by corrosion and the build-up of hydrates in natural gas pipelines [1]. For economical usage and efficiency, adsorption plants are used to reduce the water content in feed gases to very low dew points [2]. The commonly used setup contains fix-bed reactors filled with adsorbent materials such as silica gels, activated alumina, or molecular sieves [3]. Thereby, the water vapor flows through the fixed-bed until a breakthrough downstream of the fixed-bed is detected (by a humidity sensor) or a threshold value is reached. Then, a regeneration is initiated. Mathematical models based on the data from the humidity sensors up- and downstream of the fixed-bed predict the breakthrough time and state of the fixed-bed with respect to the load, the height of the mass transfer zone and the height of the unused bed.

In a recent approach, supported ionic liquid phase (SILP) materials are used as adsorbent agents in fixed bed reactor units. In a previous investigation, [EMIM][$MeSO_3$] supported on silica 90 was tested as adsorbent material for water, and the experimental data have shown their ability for storing water in the ionic liquid phase of the SILP material. This makes these systems interesting for technical application [4]. As the SILP material stores water, the ionic liquid phase changes gradually due to the increasing water content.

The analysis of the SILP material in a microwave resonator allows for observing operando changes in material properties during a sorption experiment. By analyzing scattering parameters while water vapor flows through the fixed bed, changes in the resonant frequency and quality factor are detected due to changes in the electrical material parameters of the bed.

Experimental Method

As a representative for an industrial fixed-bed adsorber, immobilized [EMIM][$MeSO_3$] on silica 90 with a pore filling degree of 35% is placed in a quartz glass reactor in the center of a cavity resonator. The height of the fixed-bed corresponds to the cavity-height to minimize polarization effects. The resonator is connected to a network analyzer via two coaxial lines. Two loop coupling elements are used to excite the electromagnetic field into the cavity. Both resonant frequency and quality factor are calculated from the spectrum of the S_{21} scattering parameters. At the resonant frequency, the maximum

electric field strength is in the center of the cavity and does not change along the height of the fixed-bed (TM-mode, TM_{010}). Details of the setup can be found in [5]. Due to the sorbed water in the supported IL, the dielectric properties of the fixed-bed spatially change and influence both the resonant frequency and the inverse quality factor. Since the electric field completely penetrates the whole sample, no spatial resolved but averaged changes of the dielectric material properties can be measured. The changes in the resonant frequency and the inverse quality factor are caused by the much higher electrical conductivity of the pure ionic liquids [EMIM][$MeSO_3$] compared with its support silica 90. At constant temperature, the electrical conductivity of the pure IL increases with the amount of stored water. During the experiment, the water content of the nitrogen water mixture was verified by two humidity sensors upstream and downstream of the fixed bed. To consider the pressure loss along the fixed-bed, two absolute pressure sensors were used before and after the fixed-bed. With the data from the pressure sensors, humidity sensors, and the measured flow rate, the stored water content in the sample was calculated.

Results

Fig. 1 shows the sorbed amount of water L_{H2O} in kg_{H2O} per kg_{silica} over time (A), the change in the resonant frequency f_{res} (B), and the inverse quality factor 1000/Q (C). Before the sorption starts at 0.5 h, the sample was flushed with dry nitrogen. At 0.5 h, the sorption was initiated and the nitrogen/water mixture with water a partial pressure of 20 mbar flows through the fixed-bed. Apparently, the sorbed amount of water in the sample increases (see. Fig. 1 (A)), the resonant frequency decreases (B), and the inverse quality factor increases (C). At 1.5 h, the steady state is reached and no more water can be sorbed in the sample at the operating conditions. From that point in time, the sorbed amount of water, the resonant frequency as well as the inverse quality factor do not change anymore. At 3 h, the drying process (regeneration of the IL) was initiated by flushing the fixed-bed with dry nitrogen. This leads to decreasing amount of sorbed water in the sample (Fig. 1 (A)), increasing resonant frequency (B), and decreasing of the inverse quality factor (C). As the point, when the sample is fully dry, no water is stored in the sample and the resonant frequency and the inverse quality factor return to their original values before the sorption. The increase in the inverse quality factor is related to increase in losses. At that point, the origin of the electrical losses, i.e. dielectric or ohmic losses, cannot be identified and further investigations are required.

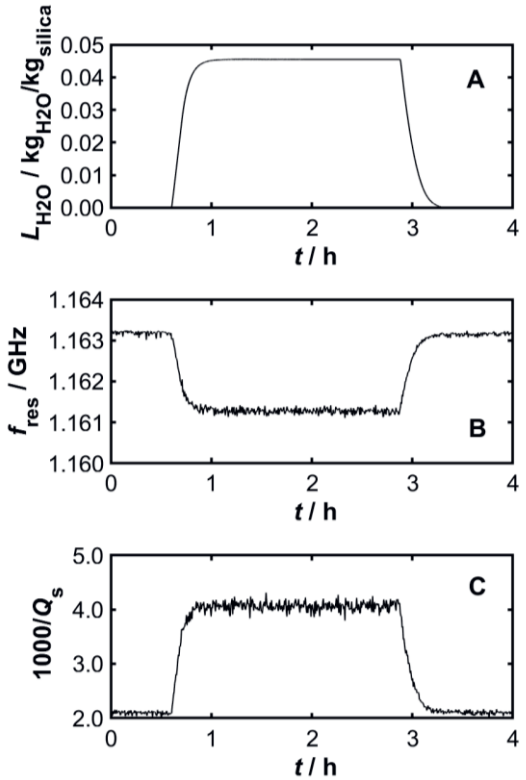

Fig. 1. Increase of sorbed water content L_{H2O} correlates with decrease in resonance frequency f_{res} and increase in inverse quality factor 1000/Q*; 50 °C, P_{H2O} = 20 mbar, P_{abs} = 1 bar, m_{sample} = 3.48 g, total volume flow rate of 50 L/h (STP), pore filling degree α = 0.35, mass loading of ionic liquid on the silica gel ϑ = 0.38 kg_{IL}/kg_{silica}*

Acknowledgements

All authors are indebted to the German Research Foundation (DFG) for funding under grant (JE 257/21-2 and MO 1060/27-2)

References

[1] Arthur L. Kohl, Richard B. Nielsen: Gas Purification, Elsevier (1997), doi: 10.1016/B978-0-88415-220-0.X5000-9

[2] A. Mersmann, B. Fill, R. Hartmann, S. Maurer: The Potential of Energy Saving by Gas-Phase Adsorption Processes, *Chem. Eng. Technol*., 23, 937–944 (2000)

[3] A. Jess, P. Wasserscheid: Chemical technology: An integral textbook, Wiley-VCH, Weinheim (2013), ISBN 978-3527304462

[4] F.R. Radakovitsch, A. Jess: Gas dehydration using the ionic liquid [EMIM][MeSO3] supported on silica gel – Structural and water vapor sorption properties, *Chemical Engineering Journal*, **398**, 124689 (2020), doi: 10.1016/j.cej.2020.124689

[5] M. Dietrich, D. Rauch, A. Porch, R. Moos: A laboratory test setup for in situ measurements of the dielectric properties of catalyst powder samples under reaction conditions by microwave cavity perturbation: set up and initial tests, *Sensors*, **14**, 16856–16868 (2014), doi: 10.3390/s140916856

DOI 10.5162/SMSI2021/C6.3

Advanced Fluid Models for Multi-Parameter Condition Monitoring Systems for Lubricants and Hydraulic Fluids

Thomas Voglhuber-Brunnmaier[1], Alexander O. Niedermayer[2], Friederich Feichtinger[2], Bernhard Jakoby[1]
[1] Johannes Kepler University, Altenbergerstr. 69, 4040 Linz, Austria
[2] Micro Resonant Technologies GmbH, Franz-Kain-Weg 37, 4040 Linz, Austria
thomas.voglhuber-brunnmaier@jku.at

Summary

A compact measurement unit for fluid monitoring based on simultaneous measurement of viscosity and density is introduced. It will be shown that a new fluid model allows to achieve higher accuracies, which is demonstrated by comparison to earlier models.

Keywords: viscosity, density, tuning fork, oil sensor

Introduction

In order to reduce maintenance costs as well as the risk of unplanned downtimes, industry gradually adopts online condition monitoring (OCM) methods combined with predictive or proactive maintenance approaches. Enabled by the increasing level of automation, plenty of data can be made available to maintenance personnel and condition monitoring algorithms, and sophisticated evaluation methods can be implemented to assist in planning of maintenance actions. With the implementation of such data-based decision methods, the reliability and precision of the collected data obviously has significant impact on the effectiveness of the maintenance actions triggered. Furthermore, the sooner a problem can be identified, the easier and cheaper the appropriate maintenance action will be. So, in many cases, the benefit of a sensor increases over proportionately with its accuracy and long-term stability.

In this contribution, we present an innovative method to increase data reliability, as implemented in a novel fully automated online condition monitoring system for hydraulic fluids and lubricating oils. The device continuously monitors the viscosity, mass density, and several other relevant parameters of the fluid. With the integrated active temperature control, measurement data can be acquired at any desired reference temperature and thus are independent of the operating conditions of the machine. By cyclic variation of the temperature, additional information is provided and used for validating the consistency of the data.

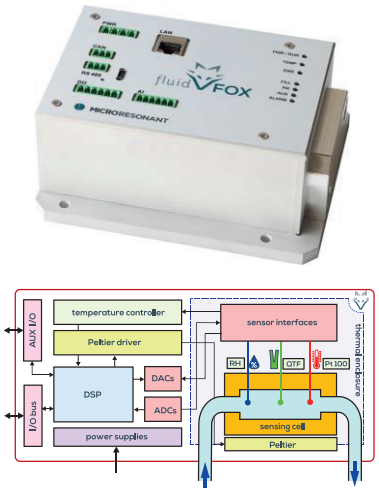

Fig. 1. Condition monitoring system for industrial use.

Monitoring System

Fig. 1 (above) shows the compact OCM system. The temperature-controlled measurement cell within the system houses the vibrating quartz tuning fork sensor (QTF), a Pt100 temperature sensor and a capacitive relative humidity sensor as shown in Fig. 1 (below). From the fluid induced resonance changes of the QTF the viscosity and density of the fluid are determined [1].

Fluid Model

The fluid models linking the resonance parameters (f_r,Q) of a vibrating sensor to density ρ and viscosity η of the fluid are mostly based on truncated Taylor series approximations whose truncation is limited to an order of two to keep the inversion of the model manageable. The most accurate model of this class to date is the model of Heinisch [2] shown in eq. (1) featuring 6 instrument parameters c_1 to c_6.

$$f_r = \left(c_1 + c_2\rho + c_3\sqrt{\rho\eta/f_r}\right)^{-\frac{1}{2}}, \quad (1a)$$

$$Q = \frac{1}{f_r}\left(c_4 + c_5\eta + c_6\sqrt{\rho\eta f_r}\right)^{-1}, \quad (1b)$$

We propose an alternative model shown in eq. (2), which allows for an arbitrary degree of approximation, not limited to second order.

$$\underline{G}(f_r, Q) = \rho\sum_{i=0}^{N}\underline{c_i}\delta^i \quad (2a)$$

$$\delta = \sqrt{\frac{\eta}{\pi f_r \rho}} \quad (2b)$$

We found an elegant new form where $\underline{G}$ represents a complex-valued function of the resonance parameters and $\underline{c_i}$ are complex-valued instrument parameters obtained by adjustment measurements using test fluids. δ is the characteristic decay length of plane shear waves. The inversion of the model is straight-forward and its complexity remains similar, when the order of approximation is extended to any arbitrary truncation N of the Taylor series. Furthermore, new physical insights could be obtained using basic dimensional analysis [3]. It could be shown that this model is applicable for mechanical resonators of any shape, given that effects due to fluid compressibility and nonlinearity can be rendered negligible by design. The QTF sensor implemented in the fluidFOX in Fig. 1 is such a candidate.

Tab. 1: Table of the nominal values of the fluids measured using the fluidFOX. Deviations for viscosity are shown in Fig. 2

fluid #	Fluid	Temp. (°C)	Density (kg/m³)	Dyn. visc. (mPas)
1	N2	50	740.1	1.2760
2	* N2	40	747.2	1.5060
3	N2	25	757.8	1.9930
4	N2	20	761.4	2.2120
5	N7	50	781.1	4.4050
6	N7	40	787.7	5.7680
7	N14	50	793.3	8.2420
8	N7	25	797.5	9.2720
9	N7	20	800.8	11.110
10	N14	40	799.7	11.290
11	N26	50	801.9	14.350
12	N14	25	809.3	19.670
13	* N26	40	808.2	20.470
14	N44	50	808.7	23.410
15	N14	20	812.5	24.320
16	N44	40	814.8	34.540
17	N26	25	817.6	38.050
18	N26	20	820.8	48.140
19	* N44	25	824.1	68.120
20	N140	50	819.1	71.950
21	N44	20	827.2	87.860
22	N140	40	825.1	112.20
23	* N140	25	834.1	242.90

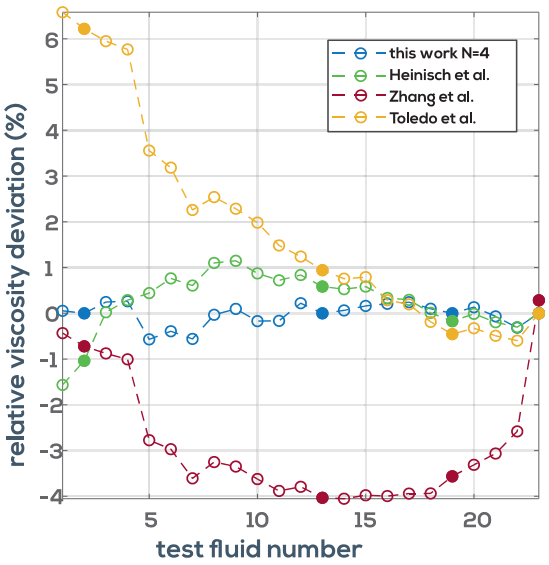

*Fig. 2. Deviations between different fluid models. The viscosities of the fluid range from 1.27mPas to 242.9mPas. Fluids indicated by a filled marker correspond to fluids marked with * in Tab. 1 and were used to adjust the model parameters c_i (see [5] for details).*

We applied various models to the raw data available from the fluidFOX. Fig. 2 shows viscosity deviations where the new model used a truncation of N=4. The used respective NIST traceable reference fluids are listed in Tab. 1. The fluid marked with * were used to adjust the model parameters.

Conclusions

A new fluid model for simultaneous measuring of viscosity and density was established showing distinct advances over existing models.

Acknowledgement

This research was partly supported by Linz Center of Mechatronics (LCM) in the framework of the Austrian COMET-K2 programme.

References

[1] A.O. Niedermayer, T. Voglhuber-Brunnmaier, M. Heinisch, B. Jakoby, Accurate Determination of Viscosity and Mass Density of Fluids using a Piezoelectric Tuning Fork Resonant Sensor, Proceedings SENSOR 66-71. (2015), doi: 10.5162/sensor2015/A2.4

[2] M. Heinisch, T. Voglhuber-Brunnmaier, E.K. Reichel, I. Dufour, and B. Jakoby. (2014). Reduced order models for resonant viscosity and mass density sensors. *Sensors and Actuators A: Physical*, *220*, 76-84.

[3] T. Voglhuber-Brunnmaier, and B. Jakoby (2020). Higher-order models for resonant viscosity and mass-density sensors. *Sensors*, *20*(15), 4279.

DOI 10.5162/SMSI2021/C6.4

Investigating the Condition Monitoring of Gearboxes using Magnetoresistive Sensors

Dr. Rolf Slatter
Sensitec GmbH, Lahnau, Germany
rolf.slatter@sensitec.com

Summary:
Intelligent sensors, that can monitor the condition of critical machine components, are an essential ”enabling technology” for availability-oriented Product-Service-Systems (PPS). Furthermore, intelligent sensors can provide information that can be offered as a service. Pay-per-Use business models are now appearing in the machine tool, printing machine and packaging machine industries, which rely on accurate information about machine condition, in order to guarantee an agreed level of machine availability [1,2]. Many different approaches are applied to gather information about the condition of machine elements, such as gears, rolling bearings or ballscrews. Magnetoresistive (MR) sensors in combination with newly developed algorithms open up interesting new opportunities for more cost-effective and accurate condition monitoring.

Keywords: Condition Monitoring, Machine Elements, Sensors, Magnetic Sensors, Magnetoresistive effect

A classic approach for condition monitoring of Spur Gears is to measure vibration and an associated method is to measure acoustic emissions. Furthermore, the temperature may be measured or wear debris monitored. [3,4] However, new approaches such as the measurement of „Instantaneous Angular Speed“ (IAS) are gaining in popularity [5]. This method makes special demands of the sensors used. They must not only be small, precise and robust, but must also have a wide bandwidth and a low power requirement. In addition to this, the machine builder often wishes to use existing sensors or measurement points for this extra functionality, that is, they wish to avoid the implementation of additional sensors if possible. Magnetoresistive (MR) sensors fulfil this complex set of requirements to a very high degree [6].

For condition monitoring of spur gears, accelerometers mounted on the gearbox housing are still the state of the art. However, these have limitations due to transfer path effects and vibrations caused by other machine elements and the environment. Therefore, to distinguish the damage-related frequencies from noise is a major challenge. Recent research has shown the potentials of measuring IAS for condition monitoring. In previous papers, optical encoders have typically been used to measure IAS [7,8]. With MR sensors the IAS can be measured at the gear wheel, i.e. near the source of the damage inside the gearbox, so a high signal to noise ratio can be achieved (see Figures 1 and 2).

In a joint project with the Institute for Product Development and Machine Elements (pmd) of the Technical University of Darmstadt the application of MR sensors for the condition monitoring of gearboxes has been investigated. This paper describes the integration of MR sensors in a single-stage spur gear and presents measurement results from these sensors for both undamaged and damaged conditions (Figure 4). Different measuring positions are evaluated according to measuring concept and location, including the use of a spur gear as measuring standard (see Figure 3). A comparison of the acquired IAS signals to accelerometer measurements shows that MR sensors are a promising alternative to conventional vibration measurement. Finally, an outlook of further condition monitoring applications of MR sensors is shown.

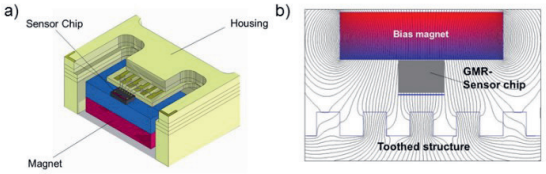

Fig. 1: GMR Tooth Sensor Module (Source: Sensitec GmbH)

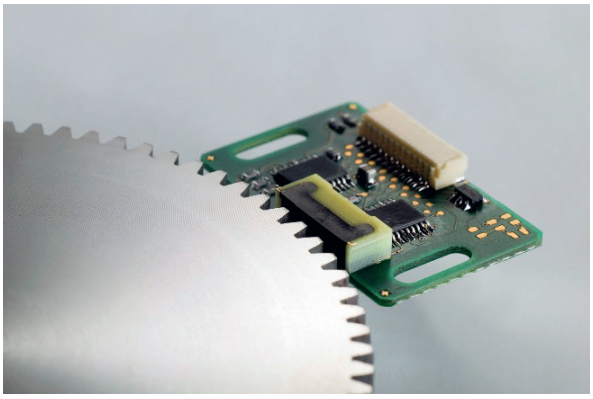

Fig. 2: Application Example (Source: Sensitec GmbH)

Fig. 3: Implementation of MR sensors using the spur gear as measuring standard (Source: pmd, TU Darmstadt)

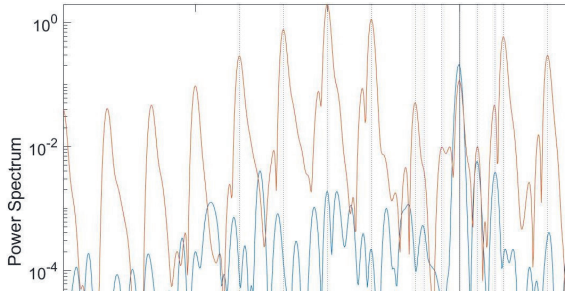

Fig. 4: Spectrum of IAS signal clearly shows sidebands around gearmesh frequency. The spacing of the sidebands correctly indicates a fault on the input shaft side of the gearbox (Source: pmd, TU Darmstadt)

References

[1] Kölsch, P. et al: “A novel concept for the development of availability-oriented business models”, Procedia CIRP 64 (2017) pp. 340 – 344

[2] Schmitt, R. & Voigtmann, C.; “Sensor information as a service – component of networked production”, J. Sens. Sens. Syst., 7, 389–402, 2018

[3] Zeng, Q. et al: “Planetary Gear Fault Diagnosis Based on Instantaneous Angular Speed Analysis”, Proc. of 23rd International Conference on Automation and Computing, University of Huddersfield, September 2017

[4] Slatter, R.: “Emerging magnetic sensor technologies for condition monitoring and non-destructive testing”, Proc. of Smart Systems Integration Conference, Copenhagen, March 2015

[5] Slatter, R..: “Intelligente Sensoren als Enabler smarter Produktsysteme“, Proc. of SysLM Tagung 2017, Kaiserslautern, October 2017

[6] Wiegel, T. & Seewig, J.: “Robust wear-detecting sensor concepts to realize innovative services and availability-oriented business models in capital goods industry”, Proc. of 14th MR-Symposium, Wetzlar, March 2017

[7] Helwig, N.: „Modular Sensor Systems for real time Process Control and Smart Condition Monitoring using XMR sensor technology”, Proc. of 14th MR-Symposium, Wetzlar, March 2017

[8] Slatter, R.; “Condition Monitoring of Gearboxes using Magnetoresistive Sensors”, Proc. of 8th International Conference on Gears, Munich, September 2019

DOI 10.5162/SMSI2021/C10.1

Integrated Differential Transformer on a Single Printed Circuit Board

Marc Berger, Anne Zygmanowski, Stefan Zimmermann
Leibniz University Hannover, Institute of Electrical Engineering and Measurement Technology,
Appelstr. 9A, 30167 Hannover, Germany,
berger@geml.uni-hannover.de

Summary:
The electrical and dielectric properties of samples can be used for various sensing tasks. For specific applications, e.g. continuous in-line measurement of the blood conductivity as a measure of sodium concentration in the blood during dialysis treatment or the determination of the polarizability as a measure of biomass in disposable bioreactors, a contactless measurement method is essential to avoid any contamination of the sample introduced by the sensor. One promising approach is a sensing concept based on a differential transformer [1–3]. In this work, we present a new integrated differential transformer structured on a single printed circuit board (PCB). The differential transformer is characterized with sodium chloride solutions and compared to a highly sensitive but larger multi-layer differential transformer from an earlier work [4].

Keywords: differential transformer, contactless measurement, miniaturized PCB coils, inductive sensor, integrated differential transformer

Introduction

The basic setup of the differential transformer consists of three coils placed on a ferrite core as can be seen in Fig. 1.

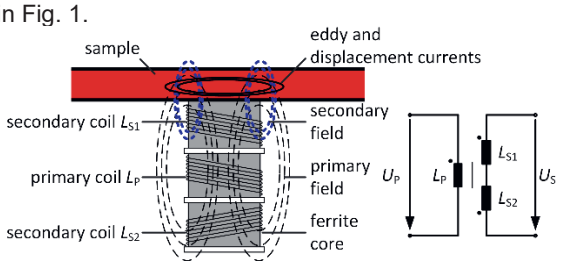

Fig. 1: *Depiction of a differential transformer for the analysis of the electrical and dielectric properties of a sample (loaded) and its electrical equivalent circuit for the unloaded case.*

Depending on the electrical conductivity κ and the polarizability ε' of the sample, the primary magnetic field caused by the exited primary coil L_P with an AC voltage U_P induces eddy and displacement currents within the sample. Since the secondary coils L_{S1} and L_{S2} have the same inductance and are arranged symmetrically to L_P, but are differentially connected in series to each other, no secondary voltage U_S can be measured due to the primary field for the unloaded (symmetric) differential transformer. This enables precise measurement of the weak induced currents within the sample. A detailed description of the measuring principle can be found in [5], where it is also shown that U_S can be calculated according to Eq. 1 and separated into a real and an imaginary part. The imaginary part is indicated by the imaginary unit j. The real part depends on ε' and the imaginary part depends on κ as well as the primitive losses ε''.

$$U_S = U_P\, K \left(-\omega^2 \varepsilon' + \mathrm{j}\,\omega(\kappa - \omega\varepsilon'')\right) \qquad (1)$$

K describes the magnetic coupling of the coils to each other as well as between the coils and the sample. ω is the angular frequency. Based on theoretical considerations, in [4] we have shown that the sensitivity of the differential transformer can be enhanced by optimizing the distance between the primary and secondary coils, as the difference in magnetic coupling of the two secondary coils to the sample should be as high as possible. However, at the same time, the magnetic coupling between the primary coil and the medium should not be reduced significantly by moving the coil too far away from the medium resulting in an optimal distance between the coils. These considerations could be proved by theoretical calculations as well as measurements.

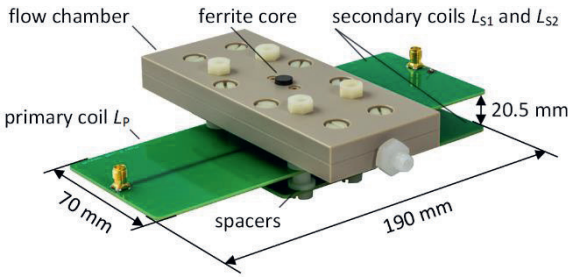

Fig. 2: *Photograph of the previously used differential transformer with flow chamber [4]. L_{S1} and L_{S2} are differentially connected via electrical wires.*

To obtain a differential transformer with adjustable distance between the coils, we used each coil on a separate printed circuit board (PCB). Each PCB has a size of 120 mm times 70 mm. A photo of this previously used differential transformer is shown in Fig. 2. Spacers are used to adjust the distance between the PCB coils. The transformer in Fig. 2 uses 8 mm spacer corresponding to the optimal distance of this

arrangement, resulting in a total height of the differential transformer excluding the measuring chamber of 20.5 mm. The objective of this work is to optimize the differential transformer regarding its size to have a smaller transformer improving usability, even if this is accompanied by an inevitable reduction of sensitivity. Therefore, we present a new integrated differential transformer, where all coils are located on a single PCB.

Integrated Differential Transformer Structured on a Single Printed Circuit Board

Fig. 3 shows the side view of the new differential transformer structured on a single PCB (a) as well as the top view (b).

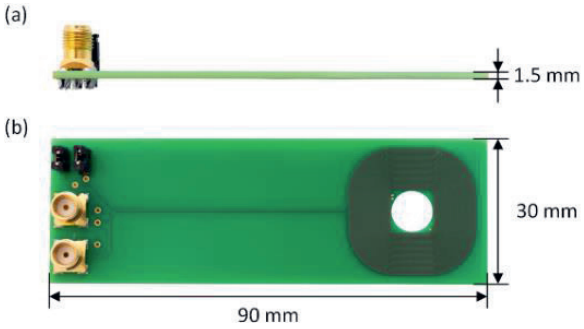

Fig 3: *Photograph of the new differential transformer structured on a single PCB in side view (a) and top view (b).*

All coils were realized on one 90 mm times 30 mm multi-layer PCB, giving the differential transformer an overall height of only 1.5 mm. In total, the PCB has six layers. Each layer has a distance of 0.3 mm to the next layer. The secondary coils L_{S1} and L_{S2} are realized on the two top and two bottom layers respectively. The maximum outer radius of L_{S1} and L_{S2} are 14.5 mm. Each secondary coil has a total number of turns of 70 and an inductance of 102 µH (without ferrite core). The secondary inductances are thus significantly lower compared to the previously used differential transformer with L_{S1} and L_{S2} of 23.8 mH, representing a disadvantage in terms of sensitivity [4]. However, an advantage of this lower inductance is the higher resonant frequency of 2 MHz compared to the secondary coil of the previously used differential transformer, operating at 155 kHz. This has a positive effect on sensitivity, as it increases with higher frequency [4]. However, to ensure that the coil still has an inductive characteristic, the measuring frequency should be below the resonance frequency. Here, we choose a frequency of 1 MHz. The primary coil with an outer radius of 9.5 mm and 30 turns, resulting in an inductance of L_P is 17 µH (without ferrite core) is located on the two middle layers. The differentially connected secondary coils as well as the primary coil can be easily connected via SMA connectors. For testing purposes, the differential connection of L_{S1} and L_{S2} is made via two jumpers, so that the connection can be opened to determine the inductance of each individual coil. A ferrite core with a diameter of 8 mm can be inserted through the center hole of the coils and hence improving the inductive coupling between the coils and the sample. Here we use a core with a relative permeability of 300.

Experimental Investigation

In order to test the integrated differential transformer, it simply replaces the previously used differential transformer shown in Fig. 2. Using a peristaltic pump, a synthetic test solution consisting of deionized water and different concentrations of sodium chloride (NaCl) flows through the flow chamber. The conductivity of the solution can be influenced by the NaCl concentration, affecting the imaginary part of the output voltage U_S. Fig. 4 shows the imaginary part of U_S versus the NaCl concentration. It can be seen that the imaginary part of U_S depends linearly on the NaCl concentration within this concentration range. This concentration range represents the clinical relevant pathological concentration range in blood serum. The sensitivity S of the integrated differential transformer was determined by the slope of the linear regression with a coefficient of determination R^2 of 0.99 and is about 11 mV/mol/L at an excitation voltage U_P of 1 V_{PP} peak to peak and a frequency of 1 MHz. As expected, the previously used differential transformer shown in Fig. 2 has a higher sensitivity of 192 mV/mol/L. Nevertheless, the main objective was to miniaturize and simplify the setup robust enough for everyday clinical use.

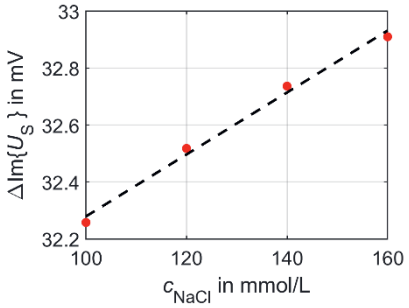

Fig 4: *Imaginary part of the measuring voltage U_S vs. the NaCl concentration and the linear regression (R^2 = 0.99) with a sensitivity S of about 11 mV/mol/L.*

Conclusion

In this work, we have presented a new miniaturized differential transformer structured on a single PCB. This transformer was characterized using synthetic sodium chloride solutions at a concentration range from 100 mmol/L to 160 mmol/L. Compared to the previously used much larger differential transformer the sensitivity is reduced. Nevertheless, this very compact, easy-to-use and robust design suitable for everyday clinical use has a sensitivity of 11 mV/mol/L with very good linearity.

References

[1] M. Allers et al., Differential Inductive Sensor for Continuous Non-Invasive Cell Growth Monitoring in Disposable Bioreactors, Proceedings 1 (2017) 518.

[2] M. Berger et al., A Differential Transformer for Noninvasive Continuous Sodium Monitoring During Dialysis Treatment: 2019 IEEE SENSORS, pp. 1–4.

[3] M. Berger et al., Continuous Non-Invasive Sodium Monitoring in Extracorporeal Circuits: 17th International Meeting on Chemical - IMCS, pp. 683–684.

[4] M. Berger et al., Contactless and continuous sodium concentration monitoring during continuous renal replacement therapy, Sensors and Actuators B: Chemical 320 (2020) 128372.

[5] T. Reinecke, et al., Continuous noninvasive monitoring of cell growth in disposable bioreactors, Sensors and Actuators B: Chemical 251 (2017) 1009–1017.

DOI 10.5162/SMSI2021/C10.2

Rotary Encoder Magnet Inspection with Noise Elimination

Dr. Koen Vervaeke
Magcam NV, Romeinse straat 18, B-3001 Leuven, Belgium
koen.vervaeke@magcam.com

Summary:
We report on a method to measure a noise-free magnetic field distribution of rotary encoder sensor magnets, based on Magcam's established 3-axis magnetic field camera technology. This method involves measuring the 3-axis magnetic field distribution in a 2D plane at close distance above the magnet and extrapolating this field distribution into a 3D volume using a patented algorithm that yields virtually noise-free data at larger distances. This powerful method allows to evaluate the magnetic field distribution and the magnet's intrinsic angular error, with a resolution better than the measurement resolution of the originally measured plane.

Keywords: sensor magnet, magnet inspection, magnetic field camera, magnetic field mapping, magnet

Background, Motivation and Objective

A method is presented for magnetically characterizing 2-pole rotary encoder magnets, which are widely used in angular encoders in e.g. electric motors and rotary positioning systems. The method uses a proprietary 'Distance Filter' algorithm, which allows to extrapolate a magnetic field distribution recorded at one certain (close) distance above a magnet or magnet assembly to another (larger) distance in a very fast way and with a strong suppression of measurement noise. This allows very fast and at the same time highly accurate measurements, making the method suitable for production quality control.

Description of the Extrapolation Method

The 'Distance Filter' extrapolation algorithm is used in combination with Magcam's magnetic field camera systems. When the extrapolation is in the direction away from the magnet, there is a strong suppression of noise, resulting in µTesla magnetic field resolutions. This makes the Distance Filter algorithm very powerful for determining magnetic field distributions far away from a magnet, since a direct measurement at the farther distance would suffer from a poorer signal-to-noise ratio.

For accurate results with the Distance Filter, the recorded magnetic field distribution must contain the full magnetic field of the measured magnet or magnet assembly, meaning that at all edges of the measured magnetic field image the magnetic field should be monotonically decreasing towards zero when going outwards towards the image edges. In practice, this means that a sufficiently large area should be measured, including extra space around the magnet.

Results

Consider a cylindrical axially magnetized 2-pole rotary encoder magnet, with the cylindrical symmetry axis pointing in the Z direction. The same principle applies for diametrically magnetized cylinder magnets. The original measurement is in the XY plane at a certain height Z0 above the magnet surface. The magnetic field distribution at a different height Z1 is obtained by the Distance Filter method by supplying one single input parameter Delta, namely the distance between the original measurement plane and the desired plane: Delta = Z1 - Z0. When Delta = 0 the original data is retained.

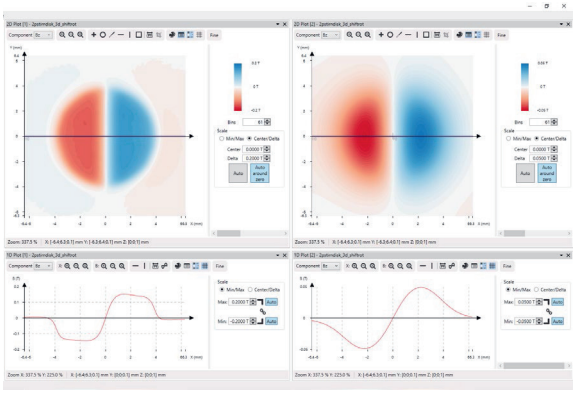

Fig. 1. Measured Bz magnetic field distribution and cross section along the X direction at Z0 = 0.3mm (left) and Distance Filter result at Z1 = 2mm (right).

Fig. 1 shows the measured Bz magnetic field distribution and cross section along the X direc-

tion at Z0 = 0.3mm (left) and Distance Filter result at Z1 = 2mm (right). Hereby the value for Delta is: Delta = 2mm - 0.3mm = 1.7mm.

Analyzing the in-plane magnetic field and azimuthal angle error in 2-pole rotary encoder magnets

In typical end applications, a Bx,By sensor is positioned in the center of the rotary encoder magnet at a certain distance from the magnet surface, which is typically several mm. At such distance the Bxy magnetic field is typically of the order of 50mT. The Bx,By sensor then measures Bx and By and from those calculates the in-plane angle of the magnetic field using atan2(By,Bx). Inhomogeneities of the magnetic field distribution can cause errors on this measured angle value. During quality control on such magnets, this angle error needs to be determined with high accuracy, typically in the order of 0.1° or better. By using a magnetic field camera in combination with the Distance Filter this can be achieved in a superior way as is shown below.

A magnetic field distribution measurement directly at the working distance of the Bx,By sensor in the above application would result in a poorer signal-to-noise ratio than a measurement very close to the magnet (typically 0.3-0.5mm). The Distance Filter makes it possible to 'preserve' the signal-to-noise ratio at close distance to remote distances, resulting in virtually noise-free magnetic field distributions.

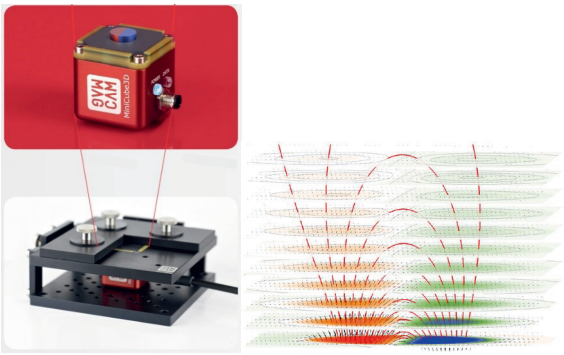

Fig. 2. 2-pole axially magnetized cylinder magnet measured with MiniCube3D magnetic field camera.

The 3D magnetic field distribution is measured at a close distance above the magnet surface using a Magcam MiniCube3D magnetic field camera (see Fig. 2).

As mentioned higher, the relevant magnetic field components for this application are the in-plane (Bxy) magnetic field and the in-plane direction (azimuthal angle) of the field in a region in the center of the magnet. These components can be analyzed as explained below.

Bxy field and azimuthal angle

The Bxy component of the magnetic field distribution is readily obtained from the Bx and By components (Fig. 3). A circle is interpolated centered on the magnet center and with a certain radius, taken to be 0.25mm in this example (see Figure 8), typically determined by the tolerance region where the Bx,By sensor will be located in the end application. In the obtained line plot, the maximum and minimum values can be automatically detected, which can be directly used in a pass/fail test to check if they are within the tolerance window.

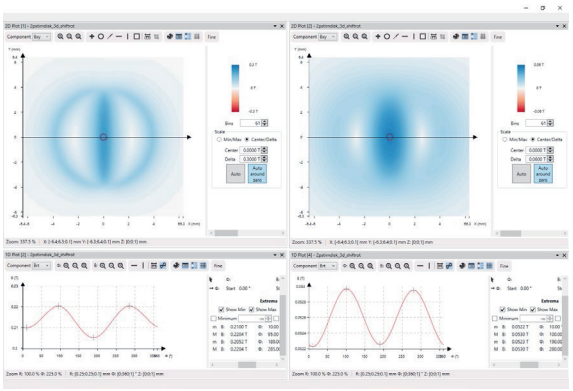

Fig. 3. Bxy (in-plane) magnetic field distribution with a circle section in the middle of the magnet for Z = 0.3mm (left) and Z = 2mm (right). In the 1D Plots the minimum and maximum values are automatically detected.

The second important quantity of the magnetic field distribution is the in-plane direction (azimuthal angle) distribution of the magnetic field. This quantity is also readily calculated from the Bx and By components of the magnetic field by using atan2(By,Bx). By analyzing the extreme values of the azimuthal angle on the same circle section as before, the angle error is directly obtained, as shown in Fig. 4. By combining the results of Bxy and the azimuthal angle, a full quality control of rotary encoder magnets can be performed within seconds.

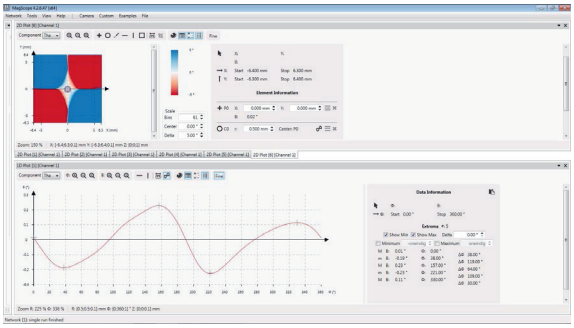

Fig. 4. Azimuthal (in-plane) angle distribution with a circle section in the middle of the magnet for Z = 2mm. In the 1D Plot, the minimum and maximum values are automatically detected and give a direct measure of the angle error of the Bxy magnetic field distribution on the circle.

DOI 10.5162/SMSI2021/C10.3

Calibration Method for an Inductive Localization System of Wireless Sensors in Photoreactors

David Demetz[1], Alexander Sutor[2]
[1] Institute of Measurement and Sensor Technology, UMIT – Private University, Hall in Tirol, Austria
david.demetz@umit.at
[2] Institute of Measurement and Sensor Technology, UMIT – Private University, Hall in Tirol, Austria
alexander.sutor@umit.at

Summary:
We present a calibration method for an inductive localization system used to trace wireless sensors for the future use in photoreactors. Photoreactors are used to cultivate photosynthetic active microorganisms and cells or to perform photocatalytic reactions. Due to the limited penetration depth of light inside those reactors, a novel internal illumination system have been presented in past. The illumination system consists of so called Wireless light emitters (WLE) which are small glowing spheres floating around in the reactor. The WLE are powered through an inductive link where the driving coils are placed at the outer diameter of the reactor. They produce an intermediate frequency (178 kHz) electromagnetic field with a magnetic flux density of approx. B = 1 mT [1] - [3]. The next step in this project is the inclusion of sensors for measuring various parameters inside the reactor. Additionally, the information about the sensor position leads to a spatial resolution of the measured quantity. Therefore, wireless sensors are needed as well as a suited localization method.

Keywords: inductive communication, inductive localization, calibration method, wireless sensors

Introduction

To control the processes in those photoreactors various parameters have to be measured e.g. temperature, pH-value, UV-illumination or other chemical concentrations. To avoid the drawback of measuring the named parameters always at the same position inside the reactor, wireless traceable sensors are being developed. Because of the promising propagation properties of magnetic fields in water and in salty water, we chose the inductive layer for the communication and the localization task. The authors of [4] also make use of this advantage for the inductive communication through human tissue for assistive listening devices. For our photoreactor use, we set the modulation frequency of the data transmission link (297 kHz) at a factor 1.66 above the frequency of the WLE power link in order to prevent interferences by harmonics. The drawback of using higher frequencies would be their high damping factor in electrically conducting media.

Inductive communication and localization

As a modulation technique for the data transmission, we use the on-off-keying (OOK); this is implemented like in [4] with an on-off switched hartley-oscillator as transmitter. In this first step, we do not use real sensors. We use a square wave generator based on the integrated circuit LMC555 to simulate the digital sensor data stream. We already presented the electrical circuit of the mentioned transmitter before [5]. To solve the localization task, we make use of the well-defined spatial propagation properties of the magnetic dipole field, which is used to describe the field of our transmitting coil. At a frequency of 297 kHz, the wavelength is big compared to the distances between the transmitter and the receivers in our setup. Therefore, only the quasi-static field component must be considered [6]. In the publication [7] we already presented the analytical coupling equation system used to calculate the directional vectors, which point to the transmitter position from every measuring point of its magnetic field. The transmitter position is calculated by finding the point where two or more directional vectors comes closest to each other (the intersection in an ideal case).

Receiver design and setup

The main requirement to our receivers is the ability to measure all three spatial components of the transmitter magnetic field. This requirement is satisfied by using three coils placed orthogonally to each other. This design minimalizes the mutual inductions between them. Since each coil is directly connected to the input of an operational amplifier, no current flows through them. This fact additionally ensures that the receiver coils

do not influence each other. The received signals are filtered with operational amplifier based amplifiers and active filters and are then digitalized by the I/O device *National Instruments USB-6366*. The software *Matlab* by *MathWorks* is used to control the I/O device and for solving the coupling equation in order to calculate the directional vectors and consequently the transmitter position. We build a setup for performing inductive localization measurements in which two receivers are each placed in a corner of our cubic room of interest (ROI). This is needed because by solving the coupling equation due to the symmetry properties of the magnetic dipole field, we get multiple possible solutions for the directional vector. By placing the receiver in a corner of the ROI, the multiple solutions are automatically diminished to one right solution. This because the other solutions would not point into the ROI. The size of our ROI is 50 cm in width and height and 30 cm in depth.

Receiver calibration

The receivers are calibrated using a Lidar depth Camera. Therefore, we chose the *Intel Realsense Lidar Camera L515*. The camera is mounted above the ROI pointing downwards in order to capture the whole setup. According to its datasheet, the depth accuracy of the camera is lower than 5 mm at VGA (640 per 480 pixel) resolution and a maximal distance of 1 m. In our setup, the maximal distances are always under 1 m. Additionally, the depth camera is used with the resolution set to XGA (1024 per 768 pixel) which further increases its depth accuracy. For the calibration, both systems are used to locate the transmitting coil; the depth camera and the inductive system. The position measured with the camera is considered to be the correct one. In order to calibrate the receivers, the transmitter position measured with the depth camera is used to calculate the amplitudes in each receiver coil. A comparison between the normalized measured receiver amplitudes and the normalized calculated amplitudes enables an adjustment of the gain factor of each coil signal amplifier. Since the used transmitter coil does not have ideal properties, the calibration of our system needs a second step. Due to inaccuracies in winding the coil by hand, the magnetic dipole equation does not accurately model our real coil. Even if the distance between the transmitter and the receivers is big compared to the coil dimensions, the system needs some further adjustments. Therefore, a defined grid of points are selected in the ROI. The transmitter coil is placed on each of those points and its position is measured with the depth camera as well as with the inductive localization system. We calculate a displacement vector between the correct position and the inductively measured position for each grid point. Those vectors are saved in a so called displacement map. We use the map in a second step to tune each further inductive localization measurements by adjusting the measured position by means of the displacement vectors from the map.

Discussion and outlook

The feasibility of the described calibration method has been tested with some first test measurements. We were able to observe a clear improvement in the localization accuracy. The next step is the registration of a good resolved calibration map in order to best increase the overall accuracy. The recorded calibration map can also be used to analyze the influence of e.g. nearby standing electrically conducting materials that would affect the magnetic field and so the accuracy of our localization system. This can be done by comparing it to a second calibration map with the same grid points registered with the interfering objects near the ROI.

References

[1] M. Heining, A. Sutor, S. Stute, C. Lindenberger und R. Buchholz, „Internal illumination of photobioreactors via wireless light emitters:," *Journal of Applied Phycology, vol. 27,* pp. 59-66, 2015, doi:10.1007/s10811-014-0290-x.

[2] A. Sutor, M. Heining und R. Buchholz, „A Class-E Amplifier for a Loosely Coupled Inductive Power," *Energies,* Bd. 12, Nr. 6, 2019, doi: 10.3390/en12061165.

[3] B. O. Burek, A. Sutor, B. W. Bahnemann und J. Z. Bloh, „Completely integrated wirelessly-powered photocatalyst-coated spheres as a novel means to perform heterogeneous photocatalytic reactions," *Catal. Sci. Technol.,* Bd. 7, Nr. 21, p. 4977–4983, 2017, doi: 10.1039/c7cy01537b.

[4] J. Edelmann, R. Stojakovic, C. Bauer und T. Ussmueller, „An Inductive Through-The-Head OOK Communication Platform for Assistive Listening Devices," *2018 IEEE Topical Conference on Wireless Sensors and Sensor Networks (WiSNet),* p. 30–33, 2018, doi: 10.1109/WISNET.2018.8311556.

[5] D. Demetz, O. Zott und A. Sutor, „Wireless and Traceable Sensors for Internally Illuminated Photoreactors," *Proceedings of the IEEE International Conference on Industrial Technology (ICIT),* pp. 582-286, 2020, isbn: 978-1-7281-5754-2.

[6] F. H. Raab, E. B. Blood, T. O. Steiner und H. R. Jones, „Magnetic position and orientation tracking system," *IEEE Transactions on Aerospace and Electronic Systems,* p. 709–718, 1979, doi: 10.1109/TAES.1979.308860.

[7] D. Demetz und A. Sutor, „Inductive Communication and Localization of Wireless Sensors in Photoreactors," *SMSI 2020 - Measurement Science,* pp. 325 - 326, 2020, doi: 10.5162/SMSI2020/P3.5.

DOI 10.5162/SMSI2021/C10.4

Embedded Multi-Frequency Eddy Current Measurement System for In-Situ Assessment of Metals

Rohan Munjal, Frank Wendler and Olfa Kanoun
[1] *Chemnitz University of Technology*
Professorship for Measurement and Sensor Technology
Reichenhainer Straße 70, 09126 Chemnitz
rohan.munjal@s2014.tu-chemnitz.de

Abstract:
In this paper, we propose a novel portable multi-frequency embedded sensor system for eddy current assessment of metal pieces, which is capable to realize in-situ measurements over a wide frequency range. The aim of the sensor system is to measure characteristic changes in conductivity and permeability in regards to working distance between sensor coil and work-piece. Thus, realizing a non-contact in-process measurement with a maximum standard deviation of 0.013 µH. The obtained data of the electric and magnetic parameters can be used to analyze mechanical state and phase transitions of the material [1].

Keywords: Impedance Spectroscopy, Inductance Spectroscopy, Multi-Frequency Measurement, Embedded Sensor System

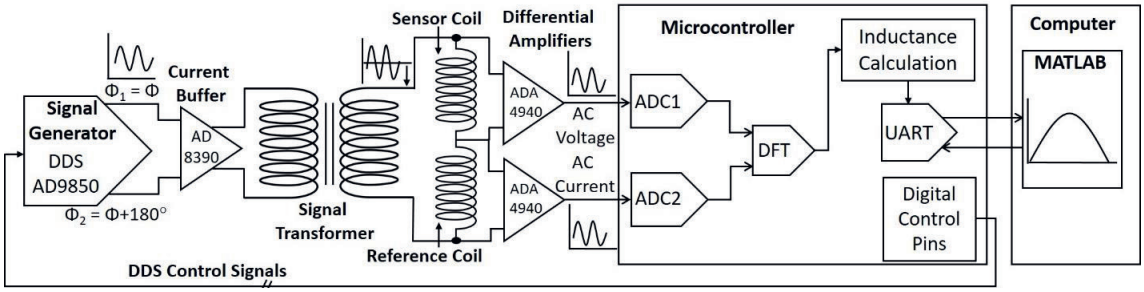

Fig. 1: Block diagram of real-time embedded sensor system

Introduction

The evolution of manufacturing has led to automization of industry, which requires a more autonomous production processes. Therefore, quality and process control tasks needs sophisticated measurement systems for data acquisition and analysis. In this paper, we discuss the properties of a developed cost effective, portable in-situ, real time and non-contact embedded sensor system, which is targeted for in-process measurements in steel manufacturing.

Embedded Sensor Measurement System

In [2], we proposed an embedded system for impedance measurement, which can be adopted for the eddy current measurements.

In the Fig. [1], the schematic of the sensor system is shown. The signal generator, current buffer and signal transformer is used to supply the sufficient current for the sensor coil. The current through the sensor coil is calculated in terms of voltage using a reference coil with a similar value as that of sensor coil. The serial combination of sensor and reference coil eliminates the influence of ambient temperature. In this configuration, voltage drop over the both coils are proportional to the individual inductance values over the full frequency range. The time domain signal of both coils are conditioned by differential amplifiers and are digitized by in-built ADCs of the microcontroller. In the microcontroller DFT is performed to obtained amplitude and phase value of both signals and to calculate the inductance of the sensor coil.

Results

A partial hardened sample of C-75 steel is used to compare between laboratory device and implemented embedded sensor system.

The unhardened region and hardened region of C-75 steel are measured using impedance analyzer and compared with the simulated Dodd and Deeds model [3]. The obtained results in Fig.[2] show that the unhardened point matches with the relative permeability of 100 and fits to the model simulation, while the hardened point does not matches with the model simulation results and the relative permeability varies between 100 to 125.89 depending upon the frequency as shown in Fig. 2. The measured inductance from the hardened section is shifted to the simulated model inductance curves with higher permeability values at high frequency around 500 kHz. Due to low penetration depth at high frequencies, the obtained information

from the C-75 steel is confined to the top layer. There is an increase in the variation of permeability in the hardened section as frequency increases, thus higher permeability values are observed at layers close to the metal surface. This is expected from the hardening process as the highest hardening value is expected close to the metal surface, where, highest cooling rate is achieved.

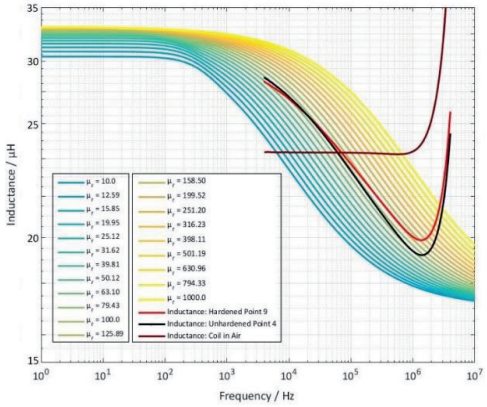

Fig. 2. Model simulation results at logarithmic distributed permeability values and experimental results using impedance analyzer for a C-75 Steel Work Piece

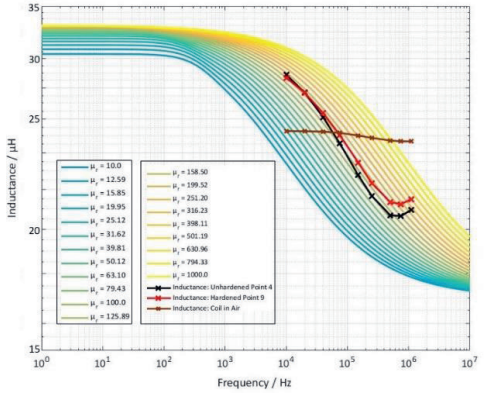

Fig. 3. Model simulation results at logarithmic distributed permeability values and experimental results using embedded sensor system for a C-75 steel work piece

With similar parameters and distance as used in the laboratory measurements, the embedded sensor system measures the inductance of sensor coil with C-75 steel. It shows a higher inductance value in comparison to the measurements on impedance analyzer. Thus, the permeability value for unhardened region fits to 125.89. For the hardened region the permeability varies between 125.89 and 158.50 depending upon the frequency as can be seen in Fig. 3. The obtained higher inductance value from embedded sensor system is due to the presence of uncorrected parasitic inductance on the printed circuit board (PCB), which leads to a constant higher inductance value over the whole frequency range. In the case of the embedded system, the effect of parasitic capacitance decreases the operating frequency range of the sensor in comparison to the measurements with the impedance analyzer as can be seen in Fig. 3.

For the quality evaluation of embedded system design, the standard deviation using C-75 metal was calculated. The 10 measurements were taken for the value of inductance and the standard deviation was calculated out of these measurements. The maximum standard deviation for unhardened and hardened C75 steel is 0.013 µH at 20 kHz.

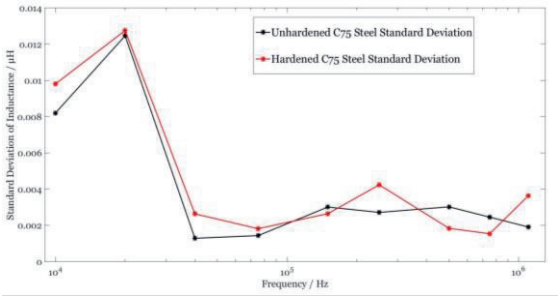

Fig. 4. Standard Deviation of Measurement System

Conclusion

The presented embedded measurement system could successfully retrieve broadband impedance data from the sensor coil. This impedance data was used to calculate the spectra of the inductance. In comparison to the model of Dodd & Deeds, the measured inductance spectra display the same characteristic drop of inductance as predicted in the model. A more detailed comparison with a commercial impedance analyzer confirms this characteristic behavior. In the direct comparison to the impedance analyzer data, the embedded system has a characteristic inductance offset and a reduced frequency range due to the resonance of the sensor coil. Both effects are accounted to the parasitic inductance and capacitance on the PCB of the embedded system. A calibration procedure and adjustment of those systematic errors might improve the obtained inductance spectra in the future.

References

[1] R. Munjal, F. Wendler and O. Kanoun, "Embedded Wideband Measurement System for Fast Impedance Spectroscopy Using Undersampling," in *IEEE Transactions on Instrumentation and Measurement*, vol. 69, no. 6, pp. 3461-3469, 2020.

[2] R. Munjal et al., Effect of hardening on electrical and magnetic properties of C-75 steel and characterization with multi-frequency inductance spectroscopy, *Measurement Science and Technology*, vol. 32, no. 2, 2020.

[3] C. Dodd and W. Deeds, Analytical Solutions to Eddy-Current Probe-Coil Problems, *Journal of Applied Physics*, vol. 39, no. 6, pp. 2829-2838, 1968.

DOI 10.5162/SMSI2021/D10.1

Poly-harmonic Signal Characterization Method and ADC Characterization Using Josephson Converter and Linear Regression Analysis

Sergey V. Sherstobitov[1], *Mariia V.Karpova*[1]
[1] *All-Russian Scientific Research Institute of Physicotechnical and Radio Engineering Measurements (VNIIFTRI), Mendeleevo, Moscow region, Russia, 141570*
s_sherstobitov@rambler.ru; Lab-610@vniiftri.ru

Summary:
The features and limiting accuracy characteristics of the method for measuring the characteristics of poly-harmonic signals and the main characteristics of the ADC such us effective number of bits, signal-to-noise ratio, harmonic distortion, dynamic range are considered, depending on the number of ADC bits using a Josephson converter and linear regression analysis method.

Keywords: ADC, DAC, Josephson voltage standard, linear regression method, harmonic test signal.

Introduction

ADCs are widely used in modern measuring instruments. The conversion accuracy and, accordingly, the measurement accuracy strongly depends on their characteristics. In many methods, to determine the characteristics of the ADC, input voltage signals of a constant or step type are used. However, often such signals are not included in the class of ADC working signals, for example, due to the presence of an input filter that cuts off the DC component of the signal. Most ADCs work with harmonic sinusoidal signals of alternating voltage, in which the useful information is in the values of amplitudes, phases of fundamental tone and harmonic components. Traditionally TRUE RMS thermoelectric converters have been used at the top level of AC voltage metrology, but their usage is limited by sinusoidal signals with low harmonic components. In the case of analog instruments, input filters are used to measure signal harmonics contents. In the case of digital processing, FFT, DFT algorithms are often used, which have their own limitations on application and limit the measurement error. The construction of reference generators of the test signals based on Josephson arbitrary waveform synthesizer and the development of techniques for determining the characteristics of the ADC is an urgent task.

Description of the Method

Progress in the field of AC voltage measurements is associated with the development of AC voltage standards based on the Josephson effect [1, 2]. At the output of such a device, it is possible to obtain both a programmable DC voltage output signal with an exact value and almost zero non-linearity, and AC waveform signals with an exact value of the RMS value of a sinusoidal signal or an exact value of harmonic components [3]. Authors developed algorithms for determining the characteristics of harmonic signals and the characteristics of the DAC/ADC using the regression analysis method. The process of measuring of the ADC characteristics can be implemented in the following sequence: 1. Submission to the ADC input of an exemplary analog test signal included in the class of permissible signals with specified parameter values. 2. Recording a sequence of digital readings obtained in real-time operating mode in a digital storage device. 3. Recovery of signal parameter values by compute of the recorded sequence using software based on linear regression method. 4. Comparison of the obtained parameter values with the given ones and calculation of the values of the ADC characteristics as signal conversion errors. The software consists of two blocks - a computer Generator of digital signals and a processing unit for digital implementations. The Generator creates sequences of digital samples for digital-to-analog converters on Josephson binary array, and for other types of DACs. It is also used to generate digital test signals when characterizing another signal processing software. The Generator module generates a digital signal corresponding to the harmonic signal model of the following form:

$$A(t,N)=A_0+\sum_{l=1}^{M} A_l \sin(2\pi l F_0+\Psi_l)+B(t,\sigma) \quad (1)$$

where A_0 is the constant component of the signal $A\ (t, N)$; A_l, $2\pi l F_0$ and ψ_l -amplitude, angular frequency and phase of the l-th harmonic of the sinusoidal signal component $A(t, N)$; M is the number of harmonics of the fundamental tone of the sinusoidal component in the signal $A(t, N)$, $B(t,\sigma)$ is a random function describing the additive "white" noise with zero mean and with standard deviation equal to σ.

For processing digital implementations, regression analysis method is used. The internal scale parameter of the implementation is the number of samples per period of the fundamental tone. With its known value, the task of reconstructing the parameters of a sinusoidal signal is formulated as a linear regression by the principle of least squares in the class of sums of trigonometric functions. Then, the algorithm calculates the amplitudes and phases of the fundamental tone and harmonics, the coefficient of nonlinear distortion, the effective number of bits of the ADC, the signal-to-noise ratio, dynamic range, etc. To obtain the uncertainty errors in determining the frequency and amplitude parameters, a statistical modeling process was used.

Results

Modeling and processing were carried out taking into account five harmonics with a harmonic coefficient equal to 0.01%. The noise model is normal white noise.

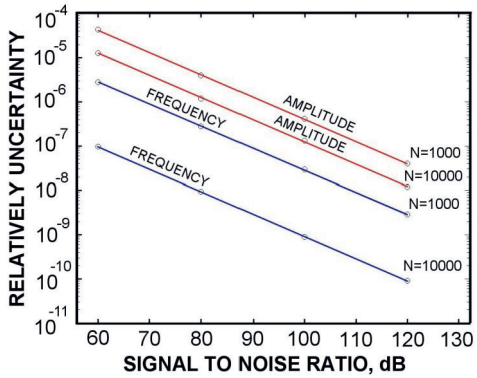

Fig. 1. The dependence of the relative errors in measurement the frequency and amplitude on the signal-to-noise ratio from 60 dB to 120 dB and number of samples N = 1000, N =10000.

The number of sample parameter values for statistics was 500 – 10000. The study of the graphs above shows that the error in the amplitude of the fundamental tone is inversely proportional to the signal-to-noise ratio and the number of counts in the signal implementation.

In practice, an increase in the implementation length (the number of processed samples) does not always lead to a decrease in the measurement error, since due to the instability of the real signal frequency, a phase error can accumulate, limiting the measurement accuracy. Implementation of the signal samples was loaded into the binary Josephson voltage converter and use to generate test signal for ADC. The output signal from the Josephson setup was fed to 24-bit ADC. Signals with a number of samples from 30 to 4000 for the period of the fundamental tone of the generated signal were used. Experiments were carried out to generate and measure the characteristics of signals with a different set of harmonic components, different coefficient of nonlinear distortion. In all cases, the method showed good accuracy in measuring both the amplitude of the fundamental tone and the harmonic components, which, makes it possible to estimate with high accuracy both the characteristics of the signal itself and the characteristics of the DAC/ADCs.

Conclusion

The results of statistical modeling using this method showed possible accuracy characteristics for measuring the parameters of the amplitude, phase, frequency of the fundamental tone of the signal and harmonics, which depend on the signal-to-noise ratio and the length of the processed implementation. The errors of the method when processing real signals will depend on the accuracy of the DAC/ADCs used, the accuracy and stability of the signal frequency and sampling frequency. Measurements with a Josephson setup, good results were obtained that were not achievable for other processing methods, such as FFT, DFT. The authors use these algorithms in the development of methods and instruments for measuring the characteristics of the ADCs and the characteristics of the AC Josephson setup to obtain uncertainty of amplitudes 1 ppm and less.

References

[1] Hamilton C. A., Burroughs C. J., Kautz R. L., Josephson D/A converter with fundamental accuracy, *IEEE Trans. Instrum. Meas,* 1995, vol. 44, no. 2, p. 223–225; doi**:** 10.1109/19.377816

[2] M. Sira, O. Kieler, R. Behr, A Novel Method for Calibration of ADC Using JAWS, *EEE Trans. Instrum. Meas, 2019,* vol. 68, no. 6, *p. 2091-2099;* doi:10.1109/TIM.2018.2888918

[3] S.P. Benz, F.L. Walls, PD Dresselhaus, C.J. Burroughs Low-Distortion Waveform Synthesis with Josephson Junction Arrays, *IEICE Trans. Electron*. 2002 vol. E85-C(No.3) p. 608-611

DOI 10.5162/SMSI2021/D10.2

Feasibility Study for Safe Workplaces through automation and digitalization technology with redesigned Smart Sensors and LoRaWAN Monitoring System

Sergej Johann[1], Carlo Tiebe[1], Harald Kohlhoff[1], Matthias Bartholmai[1]
[1] Bundesanstalt für Materialforschung und -prüfung, Unter den Eichen 87, 12205 Berlin, Germany
Sergej.Johann@bam.de, Carlo.Tiebe@bam.de, Harald.Kohlhoff@bam.de,
Matthias.Bartholmai@bam.de

Summary:
This project addresses the application of safe and healthy workplaces in offices, chemical laboratories and other workplaces where indoor air quality plays an important role. The LoRaWAN (Long Range Wide Area Network) is used as a communication interface to make sensor data globally accessible. The objectives of the project are to create a sensor node and an online and offline system that collects the data from the sensor nodes and stores it on a local server, in a cloud, and also locally on the node to prevent communication failures. An important point in this project is the development of the sensor nodes and the placement of these in the premises, thus no development work is involved in building the infrastructure.

Keywords: smart sensors, air quality monitoring, LoRaWAN, VOC, multisensor system

Idea

The idea of the project is to create a safe and healthy workplace for safe and unimpaired work. The implementation is based on the current technology LoRaWAN [1], which allows to cover a large area with a range of up to 15 km under optimal conditions and a calculated range from the link budget of even 800 km [2]. Regarding occupational safety, important air quality parameters should be detected and measured to avoid endangering people. In the office, in the laboratory, etc. limits for hazardous volatile gases must be observed [3,4,5]. The proposed sensor network with the low power sensor nodes should continuously record all necessary data and issue a warning if the limit value is exceeded.

Implementation

The concept envisages the development of several sensor nodes and their equipment with different sensors to determine indoor air quality. Sensors for measuring the following parameters are implemented as a basis: volatile organic compounds (VOC), temperature, humidity and pressure. The network can be operated in two ways to make the collected data available. Online via a cloud and via the associated network infrastructure, that is provided in cooperation project partners and is implemented as the primary solution. A local computer is configured as a server and provided with a user interface.

Figure 1 shows the overall concept of how the network should look like. A room under investigation (office or laboratory) is equipped with sensor nodes, each sensor node contains several sensors to determine the parameters for room air quality measurement. The first step is to collect experiences and measured values to be able to make a statement about the requirements. The red marked communication paths and components are currently being implemented.

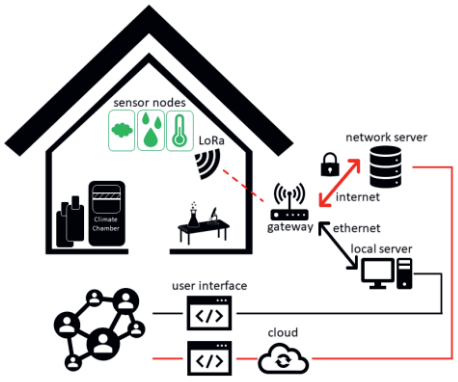

Fig. 1. Implementation of the System Network.

To keep the sensor node as simple as possible some components were removed from the predesign (GPS, Multisensorport and IC). The system is powered by a 4800 mAh rechargeable battery. It can be recharged via wired power supply or an external power source. A powerful

but energy saving ESP32 microcontroller controls all the peripherals and offers the possibility to connect to the local WiFi or Bluetooth network. A LoRa module provides the interface between the sensor accounts and the network. A commercially available 4in1 environmental sensor was used for the sensor node (BME680 from Bosch). The acquired measurement values are stored on the local SD card before being sent to the network to still record the measurement data in case of network problems.
Figure 2 shows the first prototype which is inserted into a housing that allows air access to the sensor, providing good ventilation.

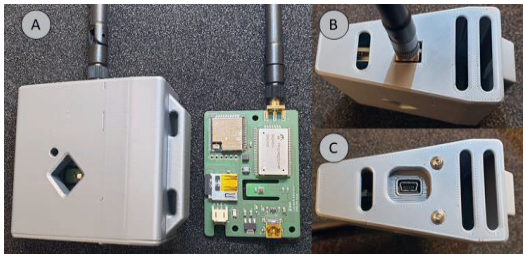

Fig. 2. Sensor node with 3D printed housing. A: side view, the sensor access and PCB. B: top view, C: bottom view.

Results

In a first publication with the conceptual design, the sensor (BME680) was successfully validated for stability with gas consisting of ethanol (C_2H_6O) and synthetic air at different molar fraction amounts 20, 40 ,80, 100, 200 and 300 µmol/mol with an uncertainty of about 4 % and an air flow rate of 1000 ml/min ±1 % [6]. Another test which lasted about 2 days started under real conditions. The sensor was installed in an office which was not used during this time. All raw values were stored locally on the SD card of the sensor node in with a sampling rate of 5 sec. and 1 sec. for the data processing. Figure 3 shows the signal course of the sensor parameters, temperature, relative humidity, pressure and the VOC signal Due to an individual mixing ratio of the air, the curves in Figure 3 are different from the calibration curve [6].

The signal curve shows a change of all signals over time. A trend can be seen where the values are moving into the stabilization. Environmental influences such as the changing temperature and humidity values in the room show a clear deflection of the VOC signal and cause a fluctuation. The temperature value is increased due to too frequent polling (approx. 25 % more often than recommended) due to self-heating. The end of the measurement was influenced with a direct human approximation. The change can be seen in the increase in relative humidity, temperature and the sudden change in the VOC value, which indicates that a gas source has approached the sensor.

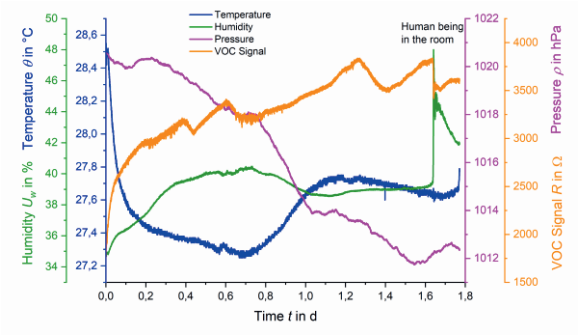

Fig. 3. Validation under real conditions. Acquired raw data from the BME680 multisensor at approx. 2 days.

Outlook

The selected sensor shows first promising results for indoor air quality measuring even under real operating conditions so that a rough statement about the activities in the room can be made. Further tests are in progress, e.g. to validate how robust and reliable the sensor nodes are. As well as that collect further knowledge. Another important aspect that should be investigated is the power management of the LoRaWAN, where the runtime of the system and the signal integrity until shutdown is examined.

References

[1] LoRa Alliance Inc., 2017, LoRaWAN Specification 1.1.

[2] https://smartmakers.io/lorawan-reichweite-teil-1-die-wichtigsten-faktoren-fuer-eine-gute-lorawan-funkreichweite/, 2020-11-20.

[3] Technical instructions for keeping the air clean - TA Luft (in German) https://www.bmu.de/fileadmin/Daten_BMU/Download_PDF/Luft/taluft.pdf, 2020-11-22.

[4] Directive (EU) 2016/2284 of the European Parliament and of the Council of 14 December 2016 on the reduction of national emissions of certain atmospheric pollutants, amending Directive 2003/35/EC and repealing Directive 2001/81/EC, http://data.europa.eu/eli/dir/2016/2284/oj, 2020-01-23.

[5] Arbeitsgemeinschaft ökologischer Forschungsinstitute e.V. (AGÖF), AGÖF-Orientierungswerte für flüchtige organische Verbindungen in der Raumluft Datenbank AGOEF-VOC-Orientierungswerte Stand: 2013-11-28, https://www.agoef.de/fileadmin/user_upload/dokumente/orientierungswerte/AGOEF-VOC-Orientierungswerte-2013-11-28.pdf

[6] Design and Implementation of Smart Multisensor Monitoring System for Safe Workplaces with LoRaWAN, SMSI2020 proceedings, 388 – 389.

DOI 10.5162/SMSI2021/D10.3

Adaptive Spiking Sensor Electronics Inspired by Biological Nervous System Based on Memristor Emulator for Industry 4.0 Applications

Hamam Abd[1], Andreas König[1]
[1] Lehrstuhl Integrierte Sensorsysteme (ISE), TU Kaiserslautern Deutschland,
{abd, koenig}@eit.uni-kl.de

Summary:
Modern devices have become more vulnerable to noise as well as to failure with leading-edge technologies. Thus, a spike-processing based ADC design is pursued with promising features, e.g., low-power, low-voltage operation, robust to noise and technology scaling issues. This supports both the self-x properties as well as machine learning in advanced sensor electronics system for practical use in industry 4.0 and IoT. In this work, an adaptive spike-to-rank coding has been designed based on an emulated memristor CMOS circuit, which is the main part of the novel ADC.

Keywords: Spiking neuron, Adaptive spiking sensor electronics, CMOS Memristor, Industry 4.0.

Background, Motivation and Objective

The rapid advance and down-scaling of integration technologies face many issues due to manufacturing deviations, noise, signal swings, etc. This advocates the transition from amplitude coded signals to time-coded signals or spike domain information processing. The memristor spiking neural network (SNN) architecture offers learning, scalability, self-x, noise-robustness, low power, small on-chip footprint, and robustness to technology scaling [1]. SNN has many advantages, however, the memristor is not expected to be feasible in the commercial chip soon, because a lot of open issues , such as compatibility with CMOS technology, unstable switching behavior, the fabrication complexity of memristor systems, and the finite number of resistance levels [1] have to be tackled. To implement memristor SNN on contemporary chips, many researchers have focused on memristor emulators [2]. Inspirations from biological sensory systems can be combined with this approach to advance sensor electronics. Jeffress in [3] had theorized sound localization in human ears. Acoustic localization uses spatially separate sensor pairs to determine the location of the objects. The design of an ADC inspired by such biological sensory systems based on acoustic localization requires two parts. The first one is to generate spikes with the time difference from the sensor is called a sensor-to-spike converter (SSC). The second one will convert this spike to digital and called a spike-to-digital converter (SDC) [4]. Prior work [4] did not make use of adaptivity in the ADC for self-x properties as required, e.g., for Industry 4.0. The primary goal of this research is to design an adaptive spike to rank coding (SRC), which is the main part of the aspired SDC and an adaptive spiking neural ADC.

Proposed Methodology

In this research, the Adaptive Coincidence Detection (ACD) has been designed, which is the main part of the SRC. The proposed ACD design uses two synapses and one neuron, as shown in Fig. 1 A. The synapses have been designed using the memristor from [2], which has been modified to be adaptive, as shown in Fig. 1 B.

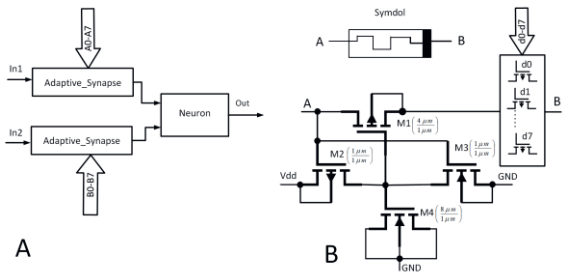

Fig. 1. (A) Adaptive Coincidence Detection. (B) adaptive synapse.

In [5], authors have designed leaky-integrate and-fire (LIF) neuron using memristors. We have designed a neuron using emulated memristor based on a CMOS circuit, as shown in Fig. 2. The memristor circuit in [6] has been modified to serve for the design of a spiking neuron. M1 has been added as a current limiter transistor. C is the membrane capacitor. The

neuron will fire, when the membrane capacitor voltage rises above the crossing point of the inverter. The output is sent back through the delay line (inverter chain) to M6, which discharges the membrane capacitor and limits the width of the spike.

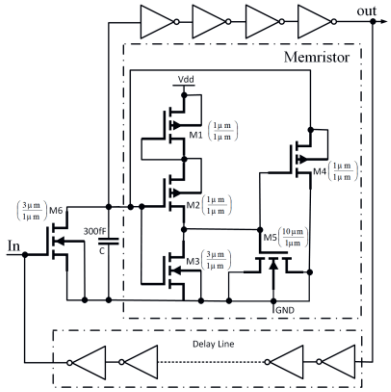

Fig. 2. Implemented memristor-based neuron.

Fig. 3 shows the ACD as the main part of the SRC. SRC shown in Fig. 3 consists of nine ACD. The proposed SDC is designed using Cadence tools and AMS 0.35 μm CMOS technology.

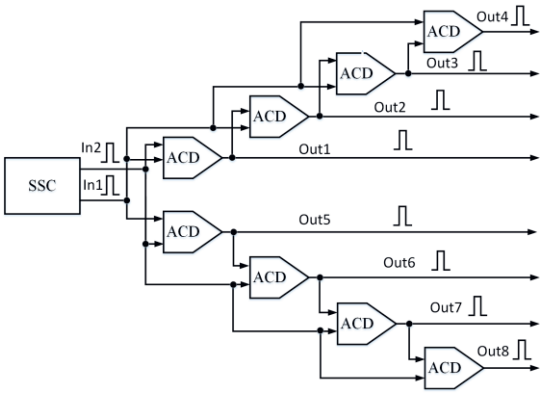

Fig. 3. Adaptive spike-to-rank coding circuit.

Results

Fig. 4 shows for the proposed ACD the three states that usually occur in biological neural networks. The first state generates an output spike if the input spikes arrive at the same time. The second state generates an output spike if the input spikes arrive slightly delayed to each , but the output spike still is generated with delay. In the third state, an output spike will not be generated if two input spikes arrive with significant delay to each other. The currently implemented SRC can achieve up to 5 steps, and each step, the outputs have different order as shown in Fig. 5. The results show that the proposed SRC can generate 2.5-bit value resolution in the digital representation. By increasing the delay chain length and number of ACDs, we can get more bits. However, the upper limit is bounded by the maximum obtainable output order. Fig. 5 shows the rank coding simulation for time differences from 0 ns to 60 ns between the inputs In1 and In2. The SRC performance has been checked under the temperatures (-40 °C, 27°C, 85 °C), and any deviations have been compensated by adapting the synapses weights, which can be achieved by changing the value of the memristor through 8-bit binary digitized transistor. In future work, the resolution will be increased and the design of a complete adaptive spiking sensor conditioning and to-digital conversion electronics be advanced.

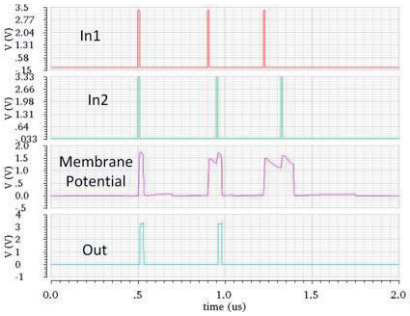

Fig. 4. Adaptive Coincidence Detection simulation.

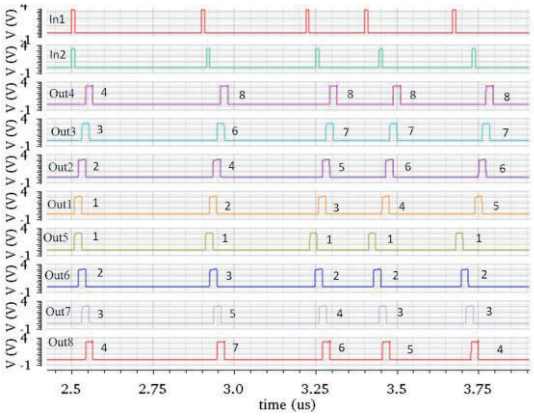

Fig. 5. Rank coding simulation of Fig. 3 SRC circuit.

References

[1] O. Krestinskaya, A.P James, and L. O. Chua. "Neuromemristive circuits for edge computing: A review." *IEEE TNNLS* 31.1 (2019). DOI: 10.1109/TNNLS.2019.2899262.

[2] H. Abd, and A. König. "A Compact Four Transistor CMOS-Design of a Floating Memristor for Adaptive Spiking Neural Networks and Corresponding Self-X Sensor Electronics to Industry 4.0." *tm-Technisches Messen* 87.s1 (2020).

[3] Ashida, Go, and Catherine E. Carr. "Sound localization: Jeffress and beyond." *Current opinion in neurobiology* 21.5 (2011).

[4] Kammara AC, A König. "SSDCα–Inherently robust integrated biomimetic sensor-to-spike-to-digital converter based on peripheral neural ensembles." *tm-Technisches Messen* 83.9 (2016).

[5] Z. Wang, et al. "Fully memristive neural networks for pattern classification with unsupervised learning." *Nature Electronics* 1.2 (2018).

[6] Y. Babacan, A. Yesil, and F. Gul. "The fabrication and MOSFET-only circuit implementation of semiconductor memristor." *IEEE TED* 65.4 (2018).

DOI 10.5162/SMSI2021/D10.4

Predicting the Analog Integrated Circuit Performance Using Indirect Measurements Based on Simulations

Senan Alraho[1], Qummar Zaman, Andreas König[1]
[1] Lehrstuhl Integrierte Sensorsysteme (ISE), TU Kaiserslautern, Deutschland,
aube@eit.uni-kl.de

Summary:
This paper presents a low-cost indirect measurement method to predict the performance of analog integrated circuits (ICs). The method is based on integrating simple sensors near to the main circuit to capture circuit properties under different conditions expected by real fabrication. Monte Carlo with corner simulation results is used to train neural network for modeling and mapping the sensor outputs to the design output performance. The achieved correlation performance metrics is 91.68%. The circuit is designed using AMS 0.35 µm technology and Cadence tools.

Keywords: Neural Network, Artificial Intelligence, Indirect Measurements, Non-intrusive sensors.

Background, Motivation an Objective

The merging of AI and ML with other developing technologies, such as industrial internet of things I(i)OT and cyber-physical production systems (CPPS) is empowering the significant revolution in the industrial domain [1] known as industrial 4.0 [2]. In industry 4.0 and IoTs devices, smart integrated sensors perform a central role in data generation [1]. Normally the performance of smart sensory electronics (SSE) is decayed with the passage of time [3]. To address the aging and process variations effects, commonly, analog ICs are overdesigned, that leads to consume more power and or larger chip area. Nevertheless, ML in SSE will enable the self-x (self-optimize, self-calibration, self-healing, etc.) properties [4]. One of the primary calibration methods is designing the analog ICs with controllable tuning knobs and performance measurement set-up [5] for chip performance monitoring [6]. So, the main objective in this research work is to find out a cost-effective indirect performance evaluation method (IMs) for SSE toward reducing the number of real expensive chip measurements.

Proposed Methodology

The block diagram of the proposed IMs is presented in Fig. 1, the non-intrusive sensors (NS) are integrated on chip in close proximity to the main design under test (DUT) to face the same conditions imposed on the DUT, that is PVT variations (process, voltage, temperature). An artificial neural network (ANN) is used to map NS and DUT performance and creates accurate regression model to indirectly and more easily predict DUT performance based on the sensors data. The flow diagram of the proposed measurement approach is depicted in Fig. 2.

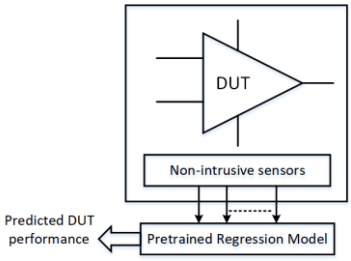

Fig. 1: Block diagram of the proposed IMs method

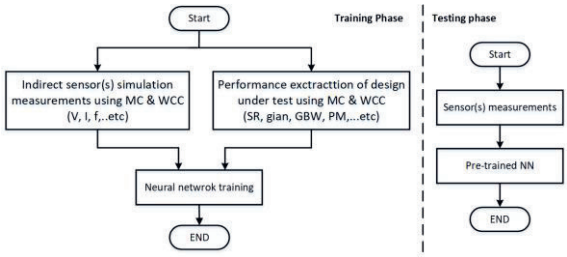

Fig. 2: Flow chart of the proposed IMs methodology

During training phase, both DUT and NS are simulated and subjected to the same PVT condition using combination of worse case corners (WCC) and Monte Carlo (MC) with enough samples (200 samples) to accurately capture real fabrication process profile. 80% of data samples are randomly selected to train the ANN while the remaining 20% are used to evaluate its performance. In the testing phase, the data provided by NS to the pre-trained ANN is used to indirectly predict the DUT performance.

A single-ended operational amplifier is used as DUT in this experiment to verify the proposed

concept. The measurements quantities of the DUT are slew rate, DC gain, gain-bandwidth product, and phase margin. The remaining simple characteristics are left for the real measurement because it will consume considerable time during simulation. A feasible solution is to increase computational resources to cover more tests by simulation. The clock generator based on ring oscillator (RO) circuit shown in Fig. 3 is designed as PVT monitoring circuit.

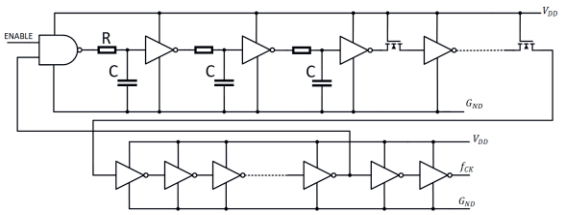

Figure 3: Ring oscillator for process monitoring.

RO shares almost the same circuit devices of the DUT to increase data correlation between both and thus improving the ANN modelling and prediction accuracy. The first test result shows weak prediction level of the ANN with adjusted R squared value (ARS) of 30.48%. It concludes that although RO alone is showing good sensitivity to the PVT variations, however, its performance is mostly dominated by RC components, thus not providing enough correlation information with the DUT to the ANN. Hence, additional NS with different sensitivities to PVT is required to further enhance ANN modelling. Authors in [7] presented a circuit to monitor the transistors threshold voltage (Vth) variation with the process by reading the voltage drop on PMOS diode connected transistor working in the weak inversion. Though, we count that is not enough to monitor Vth of PMOS only while the NMOS can go in opposite process corner. Hence, we proposed a modified version of this circuit as shown in Fig. 4 to monitor both of NMOS and PMOS Vth variations.

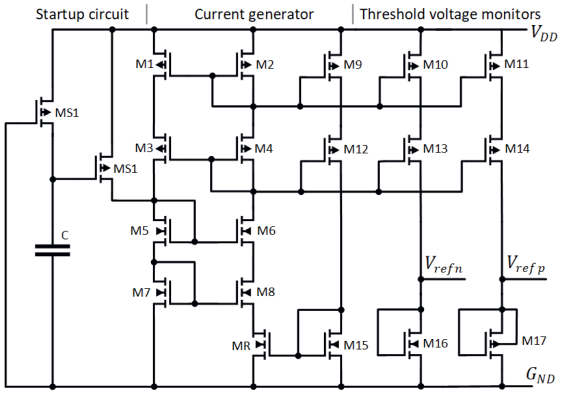

Figure 4: Threshold voltage monitor circuit.

The resistor-less current biasing circuit [8] is used to generate reference current insensitive to supply voltage and has small positive temperature coefficient. All transistors in the circuit work in the subthreshold region, except for MR that is in the triode region functioning as MOS resistor. By including PMOS threshold voltage readings from Vrefp together with the RO frequency data, the measurement prediction is improved with ARS of 70.5%. In the last experiment the Vrefn data is added and the prediction accuracy improved significantly with ARS equal to 91.68%. The performance of the proposed methodology is illustrated graphically in Fig. 5. In the future, we are working to have all types of NS outputs in digital form to have more immune outputs to the observer noise.

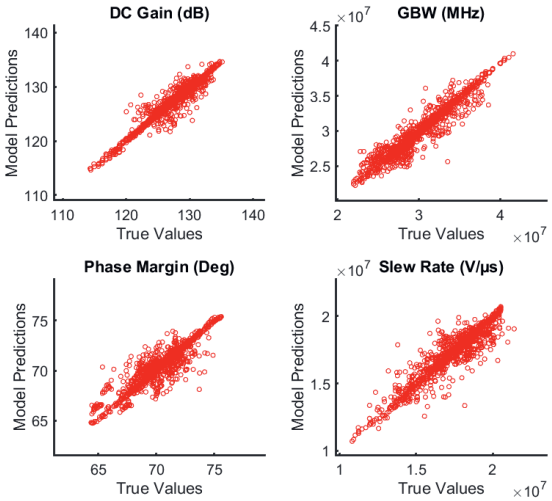

Figure 5: Scatter plot of the predicted and true values.

References

[1] Diez-Olivan, Alberto, et al. "Data fusion and machine learning for industrial prognosis: Trends and perspectives towards Industry 4.0." Information Fusion 50 (2019).

[2] Henning, Kagermann. "Recommendations for implementing the strategic initiative INDUSTRIE 4.0." (2013).

[3] Lee, Sanghoon, et al. "A built-in self-test and in situanalog circuit optimization platform." IEEE Transactions on Circuits and Systems (2018)

[4] Andraud, Martin, Haralampos-G. Stratigopoulos, and Emmanuel Simeu. "One-shot non-intrusive calibration against process variations for analog/RF circuits." IEEE TCS 2016.

[5] Andraud, Martin, Haralampos-G. Stratigopoulos, and Emmanuel Simeu. "One-shot non-intrusive calibration against process variations for analog/RF circuits." IEEE TCS 2016.

[6] In chip monitoring, telemetry and analytics", 2020 (accessed 2020). URL https://www.moortec.com.

[7] Osaki, Yuji, et al. "Delay-compensation techniques for ultra-low-power subthreshold CMOS digital LSIs." IEEE, 2009 52nd IEEE International Midwest Symposium on Circuits and Systems.

[8] Oguey, Henri J., and Daniel Aebischer. "CMOS current reference without resistance." IEEE Journal of Solid-State Circuits 32.7 (1997).

Pillar

Measurement Science

DOI 10.5162/SMSI2021/A10.1

Optimised Multi-Electrode Topology for Piezoelectric Material Characterisation

Leander Claes[1], Nadine Feldmann[1], Benjamin Jurgelucks[2], Veronika Schulze[2], Stephan Schmidt[2], Andrea Walther[2], Bernd Henning[1]
[1] Measurement Engineering Group, Paderborn University, Warburger Straße 100, 33098 Paderborn, Germany
[2] Mathematical Optimization, Humboldt-Universität zu Berlin, Rudower Chaussee 25, 12489 Berlin, Germany
claes@emt.uni-paderborn.de

Summary:
The increase in availability of computational resources resulted in the advent of simulation-driven design of sensor and actor systems. A prerequisite of this design process is a sufficiently accurate and complete set of material parameters. When it comes to piezoelectric materials, these data sets are especially hard to acquire, as they must include the mechanical, electrical and piezoelectric properties, resulting in a minimum of ten material parameters to be determined. In this work, the authors describe an approach of designing a test specimen with an optimised electrode topology that is to be used in a material characterisation procedure using only electrical impedance measurements. The aim is to increase the sensitivity of the measured impedance with respect to each of the material parameters, so that these parameters can be identified from an electrical impedance measurement in an inverse procedure.

Keywords: Piezoelectricity, material parameters, optimisation, topology, inverse procedure

Motivation

Identification of piezoelectric material parameters is typically done by applying the well-known IEEE Standard on Piezoelectricity [1]. However, this standard requires measurement on four differently conditioned specimens for the identification of a full set of material parameters. As different processing procedures are required for each of those specimens, they are prone to have different material parameters, which in turn will lead to inconsistencies in the determined data set. An alternative approach using a single disc-shaped specimen with a three-electrode setup is developed by Feldmann et al., which shows that a full set of piezoelectric parameters (the elements of the stiffness matrix c_{11}, c_{12}, c_{13}, c_{33} and c_{44}, of the permittivity matrix ε_{11} and ε_{33} and of the piezoelectric coupling matrix e_{15}, e_{31} and e_{33}) can be determined from a single specimen [2]. However, the presented approach requires three different impedance measurements, resulting from the three electrodes of the specimen. This in turn results in a highly complex, four-terminal impedance measurement setup, as sense and load contacts have to be switched between the three electrodes of the specimen as well as open and short reference measurements. Thus an evolution of the aforementioned approach is developed, with the premise of evaluating only a single frequency-dependent impedance measurement. This is realised by the optimisation of a multi-electrode configuration, in which the electrodes are either connected to the high potential terminals or to the ground terminals of the impedance analyser.

Optimised Electrode Topology

The configuration of the electrode topology is derived using an iterative approach based on a finite-element model of a piezoelectric disc, which is similar to the sequential element rejection and admission method (SERA) [3]. For the initial electrode configuration, the faces of the disc are fully covered with the high potential and the ground electrodes respectively. Using this initial configuration, frequency-domain simulations yield the frequency- and radius-depended induced electrical charge density $\sigma(f,r)$ for each radial position r on each of the disc's faces. By varying the parameters of the piezoelectric material model, the sensitivity $\Upsilon_\sigma(f,r,p_i)$ of the charge density with respect to each material parameter p_i is determined. It is assumed that, in order to obtain a high sensitivity of a measured impedance, electrodes should be placed where the sensitivity of the induced charge density is high. To keep axial symmetry, only a one-dimensional, radially dependent criterion value $C(r)$ for the SERA is required for the lower and upper face of the specimen. In the presented procedure, a high potential electrode is placed where $C(r)$ is above a certain threshold value t, and a ground electrode is placed where $C(r)$ is below the negative of the same value $(-t)$:

$C(r) \leq -t$: Ground electrode
$-t < C(r) < t$: No electrode
$C(r) \geq t$: High potential electrode

As the determined sensitivity of the charge density is dependent on frequency and the respective material parameter as well as on the radius, a method to resolve this additional dependencies is required. Two approaches are presented here. The first one being a simple sum with respect to frequency f and the material parameters $p_i \in \{c_{11},\ c_{12},\ c_{13},\ c_{33},\ c_{44},\ \varepsilon_{11},\ \varepsilon_{33},\ e_{15},\ e_{31},\ e_{33}\}$:

$$C(r) = \sum_f \sum_{p_i} \Upsilon_\sigma(f, r, p_i)\ .$$

This translates to placing electrodes wherever the overall sensitivity is high. However, one might prefer placing electrodes where the sensitivities of different material parameters each show a different behaviour in frequency domain. One way of determining such a criterion value is based on the determinant criterion [4]:

$$C(r) = \begin{vmatrix} \langle \Upsilon_\sigma(f,r,p_1), \Upsilon_\sigma(f,r,p_1)\rangle & \langle \Upsilon_\sigma(f,r,p_1), \Upsilon_\sigma(f,r,p_2)\rangle & \cdots \\ \langle \Upsilon_\sigma(f,r,p_2), \Upsilon_\sigma(f,r,p_1)\rangle & \langle \Upsilon_\sigma(f,r,p_2), \Upsilon_\sigma(f,r,p_2)\rangle & \cdots \\ \cdots & \cdots & \ddots \end{vmatrix}.$$

The two criteria are smoothed in radial direction using a Gaussian filter to prevent electrodes that are too small to realise. Using the threshold value t, the placement of electrodes is determined. The procedure is then repeated using the now modified electrode topology until the topology converges.

Results

Figure 1 shows the resulting electrode topology when using the sum of sensitivities as a criterion value (a) and the determinant criterion (b), along with the sensitivities of the electrical impedance Υ_Z for each of the material parameters. While the first approach yields an overall higher sensitivity with respect to most material parameters, the electrical impedance is nearly independent of c_{12}. In contrast, the overall sensitivity of the second approach is slightly lower but varies less over the different material parameters, which is preferable for a material parameter identification process. In addition, the fact that only electrodes with the same potential occur on each side of the specimen facilitates the measurement with standard impedance analysis equipment. In an optimisation procedure similar to the one presented by Jurgelucks et al. [5] the topology of specimen b is parameterised by the four electrode bound radii and optimised based on the sensitivity of the electrical impedance calculated via automatic differentiation. The determinant criterion [4] is again used to define the target function. The resulting electrode configuration (Figure 1 c) shows a further reduced variance of the sensitivities of the material parameters. The optimised electrode radii for a piezoelectric disc with a radius of $5\ \mathrm{mm}$ and a thickness of $1\ \mathrm{mm}$

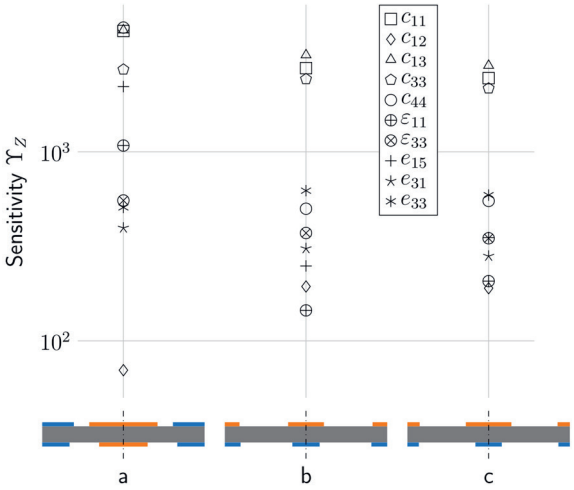

Figure 1: Sensitivities of the electrical impedance for different electrode topologies, generated using the sum of sensitivities (a) and the determinant (b) as criterion value, as well as the optimised configuration of the latter (c). Blue electrodes are on ground, orange electrodes are on high potential.

are $1.4\ \mathrm{mm}$ and $4.3\ \mathrm{mm}$ on the upper face as well as $0.8\ \mathrm{mm}$ and $4.3\ \mathrm{mm}$ on the lower face.

Conclusions

Applying a combination of the sequential element rejection and admission method and optimisation, an electrode topology for piezoelectric discs is determined. The resulting configuration has two electrodes on both faces of the disc, each with a ring at the outer edge of the disc and a circle at the centre. The impedance of this configuration shows significant sensitivity to all material parameters and is sufficiently simple to be analysed using standard measurement equipment. Using this sample as a specimen the authors aim to realise a full material characterisation procedure based on a single electrical impedance measurement.

References

[1] American National Standards Institute. *IEEE Standard on Piezoelectricity*, (1987)

[2] N. Feldmann, V. Schulze, L. Claes, B. Jurgelucks, A. Walther and B. Henning, Inverse piezoelectric material parameter characterization using a single disc-shaped specimen, *tm - Technisches Messen* (2020); doi: 10.1515/teme2020-0012

[3] O. M. Querin, M. Victoria, C. A. Gordoa, R. Ansola and P. Martí, *Topology Design Methods for Structural Optimization* (2017); isbn: 978-0-08-100916-1

[4] V. V. Fedorov, *Theory of Optimal Experiments,* (1972); isbn: 0-12-250750-9

[5] B. Jurgelucks, L. Claes, A. Walther and B. Henning, Optimization of triple-ring electrodes on piezoceramic transducers using algorithmic differentiation. *Optimization Methods and Software* (2018); doi: 10.1080/10556788.2018.1435652

DOI 10.5162/SMSI2021/A10.2

Inverse determination of elastic material parameters from ultrasonic guided waves dispersion measurements using Convolutional Neuronal Networks

Mathias Held[1], Abdalla Rashwan[1], Maik Lauschkin[1], Jannis Bulling[1], Yevgeniya Lugovtsova[1], Jens Prager[1]

[1] *Bundesanstalt für Materialforschung und -prüfung, 12205 Berlin, Deutschland,*

E-Mail: Mathias.Held@bam.de, Abdalla.Rashwan@bam.de, Maik.Lauschkin@bam.de, Jannis.Bulling@bam.de, Yevgeniya.Lugovtsova@bam.de, Jens.Prager@bam.de

Introduction

In the context of Industry 4.0 and especially in the field of Structural Health Monitoring, Condition Monitoring and Digital Twins, simulations are becoming more and more important. The exact determination of material parameters is required for realistic results of numerical simulations of the static and dynamic behavior of technical structures. There are many possibilities to determine elastic material parameters. One possibility of non-destructive testing are ultrasonic guided waves. For the evaluation of the measurement results, mostly inverse methods are applied in order to be able to draw conclusions about the elastic material parameters from analysing the ultrasonic guided wave propagation. For the inverse determination of the elastic material parameters with ultrasonic guided waves, several investigations were carried out, e.g. the determination of the isotropic material parameters through the point of zero-group-velocity [1] or anisotropic material parameters with a simplex algorithm [2]. These investigations are based on the evaluation of dispersion images. Machine learning and in particular Convolutional Neural Networks (CNN) are one possibility of the automated evaluation from image data, e.g. classification or object recognition problems. This article shows how the dispersive behavior of ultrasonic guided waves and CNNs can be used to determine the isotropic elastic constants of plate-like structures.

Concept

For using supervised learning algorithms and CNNs, a diverse data set of dispersion images with known material parameters is required. For this reason, the Scaled-Boundary-Finite-Element-Method (SBFEM) [3] is used to generate synthetic data and create dispersion images comparable to real measurement results, as it is shown in Figure 1. The dispersion images are computed using a 2D Fast Fourier Transform of the surface displacement take along a line simulated with the SBFEM to calculate the Frequency and Wavenumber. Python with the software framework Keras from Tensorflow is used to implement the CNN and train the model on the dispersion images to predict the isotropic elastic material constants.

Data and Preprocessing

For generating dispersion images using the SBFEM, random elastic material parameters are used in the range of 0.2 to 0.45 for the Poisson's ratio and for the Young's modulus normalized to density in the range of

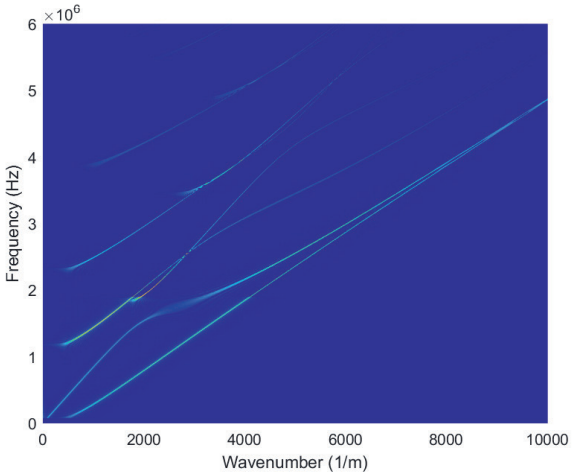

Figure 1: A dispersion image obtained using the SBFEM

$26 * 10^6[m^2/s^2$ to $28 * 10^6[m^2/s^2]$ which includes various metallic materials like aluminum or steel. The generated dataset contains 1000 labeled samples which are converted into 8 bit gray scale images with a resolution of 656x875 pixels. For training a neuronal network a normalization of the input and output data is recommended. Therefore, each pixel is normalized into the value range zero to one, dividing by 255. The material parameters, which the CNN is predicting, are also normalized into the range from zero to one by applying a normalization related to the minimal and maximum value. For evaluating and training the model, the dataset is split into 600 training, 300 validation and 100 test samples.

Architecture

For the baseline architecture, a simple feed forward CNN architecture as usually used for classification problems is chosen and applied to the regression problem. The structure of the 2D convolutional layers is the same in each layer, only the number of filters doubles for each layer. The filter kernel size is always three by three and step size of the kernel is one in every direction, as well as the dilation rate. This is intended to prevent information loss, as is the use of "same padding" in the border area of the images while applying the kernel. The initial values of the kernel are initialized using the Keras "$glorotuniform$" method. The biases are initialized to zero and no regularizers are applied to biases or kernels. Due to the regression problem and the normalization of the input and output, a ReLU activation function is used

in each layer. To downsize the feature map while processing, max pooling with a two by two filter size and step size of two is applied. The sequence of these layers remains the same and is repeated several times until the transition to the decision layer. A short summary is listed in Table 1. The transition between the last convolutional layer and the fully connected layers is done by a flattening layer. The hyperparameters of the fully connected layers are equal to the convolutional layers. A separate model is trained for predicting Poisson's ratio and density-normalized Young's modulus separately, while the architecture is the same for both models.

Table 1: Summary of the baseline model architecture

Layer (type)	Output Shape	Param
conv2d	(None, 656, 875, 16)	160
activation	(None, 656, 875, 16)	0
max pooling2d	(None, 328, 437, 16)	0
	...	
max pooling2d 5	(None, 10, 13, 1024)	0
conv2d 6	(None, 10, 13, 2048)	18876416
activation 6	(None, 10, 13, 2048)	0
flatten	(None, 266240)	0
dense	(None, 1)	266241
activation 7	(None, 1)	0

Number of trainable parameters: 24,549,761

Training

For training of the model only Keras functions are used. The Adam Optimizer ($beta1 = 0.9$, $beta2 = 0.999$, $epsilon = 1 * 10^{-7}$) with the mean squared error (MSE) as a loss function. Due to the normalization of the output data, the loss function is called the normalized MSE (NMSE). The batch size is set to 5 for a general result considering there are only little changes in the behavior of the dispersion curves for different material parameters. The training data is shuffled every epoch to avoid learning from sequences. The learning rate is initialized to 0.0001 and regulated using the ReduceLROnPlateau callback function($monitor = "valloss"$, $factor = 0.1$, $patience = 10$, $verbose = 1$, $mode = "min"$, $mindelta = 0.0001$, $cooldown = 5$, $minlr = 0$). The training is carried out for 50 epochs and the best model achieved up to then is saved for each epoch. To achieve reproducible results a random seed and some environment parameters are fixed.

Results

First results for the mean absolute error (MAE) of the testdata and the percent error of the testdata related to the maximum value of the simulation are shown in Table 2. These first results for the testdata are based on the model which achieved the best result for the validation data during training. The best result on the validation data for Poisson's ratio was achieved in the 30th epoch and for the density-normalised Young's modulus in the 40th epoch. These first results show that a good prediction of the elastic material parameters is possible. As expected, the error for predicting values close to min and max of the range of values is higher than for values which are in the mid-range of the simulated material parameters, as is the error of the test data compared to training- and validation data.

Table 2: Test results for the baseline model.

Dataset	Test	
	MAE	Percent
Poisson's ratio	$9,56 * 10^{-4}$	0,027%
Young's modulus/density	8842,16	0,032%

For further evaluation of the CNN, the Grad-CAM Algorithm, which is normally used for classification methods, is applied to ensure that the neuronal network is predicting from the behavior of the curves. Figure 2 shows that the area of low wavenumbers and frequencies has a higher influence on the calculation of the Poisson's ratio.

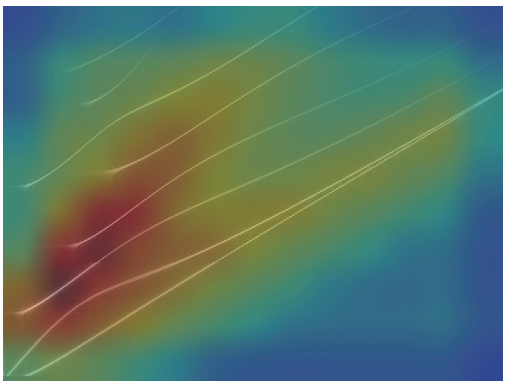

Figure 2: A "heat-map" for predicting the Poisson's ratio calculated using the Grad-CAM Algorithm

Summary

This article shows that it is possible to extract material parameters from the dispersive behavior of guided waves using SBFEM simulation data and Convolutional Neuronal Networks. In future studies, this method could be extended to the determination of anisotropic material parameters and other arbitrary boundary parameters from real measurement dispersion images.

References

[1] Dominique Clorennec, Claire Prada, and Daniel Royer. Local and noncontact measurements of bulk acoustic wave velocities in thin isotropic plates and shells using zero group velocity lamb modes. *Journal of Applied Physics*, 101(3), 2007.

[2] Manuel Webersen, Sarah Johannesmann, Julia Düchting, Leander Claes, and Bernd Henning. Guided ultrasonic waves for determining effective orthotropic material parameters of continuous-fiber reinforced thermoplastic plates. *Ultrasonics*, 84:53–62, 2018.

[3] Hauke Gravenkamp, Carolin Birk, and Chongmin Song. Simulation of elastic guided waves interacting with defects in arbitrarily long structures using the scaled boundary finite element method. *Journal of Computational Physics*, 295:438–455, 2015.

DOI 10.5162/SMSI2021/A10.3

Model-based optimization for acoustic characterization of thin hidden layers

Sebastian Wöckel, Hendrik Arndt
ifak - Institut für Automation und Kommunikation e.V.,
Werner-Heisenbergstr. 1, 39106 Magdeburg (Germany),
sebastian.woeckel@ifak.eu

Summary:
This contribution discusses a model-based optimization method to identify hidden layers and estimate selected material properties gathered from acoustic data. The procedure is exemplified by non-contact air-coupled ultrasound inspections. The method implies a model fitting of the sound propagation in the multi layered media and a derivation of media properties with a genetic algorithm. The modelling and the estimation technique are evaluated with measurement and simulation data of ideal stacked solid and fluid layers, which are “thin” (< 1…10 mm) in relation to the acoustic wavelength (> 5 mm).

Keywords: ultrasound inspection, parameter estimation, material characterization

Motivation

The non-destructive physical evaluation of hidden in-between (mostly adhesive) layers is a sophisticated task. Physical parameters of the thin adhesive layer, including its thickness, material distribution, density and elasticity, determine the stability and durability of the assembly. Already, there exists a variety of measurement system that are used for multi-layer inspection. Some apply high frequency electromagnetic signals in the THz-range [1] or high frequency ultrasound to identify stacked layers in size above the wavelength of the corresponding signal. This contribution concerns the common inspection technique based on ultrasound in conjunction with a model-based algorithm to separate single layers reflections out of the signal. Depending on the application a direct contact, immersion or air-coupled techniques are applied. Although the first provides the highest signal-to-noise ratio and resolution, it is limited to point-selective measurements. The second water-coupled technique provides an automatic scanning, keeping the SNR and resolution, whereat the construction component needs to be immersed in a waterbed. The inspection with air-coupled ultrasound provides the highest degree of freedom – concerning the technical realization. Its main drawbacks are the low defect sensitivity caused by the high reflection loss at the air-solid interface (power balance $P_{out}/P_{in} \sim 10^5$) and the low resolution due to the wavelength accordingly frequency ranges (< 1 MHz).

In this context, a signal-oriented method is discussed to overcome the mentioned drawbacks of e.g. air-coupled inspections. The idea bases on the fast estimation of the sound propagation in the multi layered media [2] including an automated derivation of acoustic media properties (mainly density, sound velocity, effective damping and elasticity) by using a mathematical optimization algorithm like a genetic algorithm. The modelling and the estimation technique are exemplified on simulation and empirical data of multiple stacked solid and elastic (adhesive) layers, which are “thin” (< 1 mm) in relation to the acoustic wavelength (> 5 mm). This contribution focuses on the algorithm itself exemplified on the estimation of the parameters of a hidden layer, using a simple laboratory measurement setup. This measurement rig provides the ultrasonic air coupled transmission (S_{21}) or reflection (S_{11}) measurement on a planar multilayer structure. The thicknesses of the plates, the in-between layer as well as the transducers distances can be adjusted in steps of Δh = 100 µm. For continuous variation of (ρ_1, c_1, h_1) the hidden layer forms an open cavity filled with a viscous liquid.

The main outcome is an algorithmic method, which delivers supplemental information by a complete acoustic characterization of the medium.

Method: linear propagation model

The sound propagation through a system of layers can be modelled as a two-port network which is characterized by its transfer (S_{21}) and reflection (S_{11}) functions. In time-domain the relative distances and the amplitudes contain the information on the velocity (c_i) and damping (α_i) within each layer and the reflection and acoustic contrast (ρi, c_i) at each interface. To extract that information a Mason-graph is used, which converts the sound propagation to a deterministic

two port network. Such graph delivers an analytic expression for the transient wave at each knot of the graph, including all multiple propagation paths, reflections due to acoustic contrasts (ρ, c) and delays (Δt) caused by different sound velocity (c). The analytic form of the transfer function S_{21} of a 3-layer-system (Fig. 1) including the transmission within the layers (T_i) and the reflection at the interfaces (R_i = Γ_i) can be expressed by:

$$S_{21} = \frac{1}{\Delta} T_1 T_5 \prod_{i=1}^{4} \sqrt{1 - R_i^2}\, T_{i+1} \qquad (1)$$

$$\Delta = 1 + T_2^2 R_1 R_2 + T_3^2 R_2 R_3 + T_4^2 R_3 R_4 + T_2^2 T_3^2 R_1 R_3 + T_3^2 T_4^2 R_2 R_4 + T_2^2 T_3^2 T_4^2 R_1 R_4 + T_2^2 T_4^2 R_1 R_2 R_3 R_4$$

The main advantage of such an analytic expression is the higher processing speed in an iterative optimization procedure instead of a simulation.

Layer Peeling with Parameter Estimation

For adapting the model parameters p to the measurement y_{meas} a minimization of the cost-function f calculating the residual $r(p)$ is applied. The residuals combine the deviation between the model $y_i(p)$ and the measurement y_{meas} by using the difference of the absolute values (signal envelopes via Hilbert-transform) according to the first order Laplace-formulation:

$$\min f_{L1} = \min \|r(\tilde{\boldsymbol{p}})\|_1 = \min \sum_{i=1}^{m} \left| \tilde{y}_i(\tilde{\boldsymbol{p}}) - y_{Meas,i} \right| \qquad (2)$$

$$f_{L1}(\rho, c, \alpha) = \sum \left\| \begin{matrix} log[\|Hilbert(y_{Model})\|] \\ - \, log[\|Hilbert(y_{Meas})\|] \end{matrix} \right\|$$

The logarithmic version of the first order norm delivers a smooth curve for prediction of the global minima and a steep decent in the region of the minimum itself. The latter supports an effective and fast gradient optimization. The parameter estimation is divided in two consecutive steps using a differential evolution algorithm for predicting the starting values p_0 [3] and a gradient based algorithm calculating the material parameters p.

Conclusion

The model equation exemplified here (1) is adequate for a perpendicular incidence only. The accuracy of the 1D-Model estimation mainly depends on the mechanical setup of the measurement the radial symmetry of the transducers and the angular deviation of the incident acoustic field. According to the idealized transmission function for an angular incident acoustic field [4] the error for the layer thickness, the sound velocity and the density of the hidden (unknown) layer will be in size of 5% for each 1° deviation of the incident angle. In laboratory measurements and according to the method above, the thickness of the unknown hidden layer can be estimated with an absolute deviation of 5%. The corresponding error for the density and damping coefficient are <10% and >20% respectively, mainly due to the error propagation. By the help of empiric data as well as 2D-simulations, the performance of the algorithm was evaluated (Fig. 2). According to the bandwidth of the transducers (B = 90 kHz) only a reduced region along the theoretical trace of the transmission function S_{21} (white dotted line) can be used for the calculation. However, even in that case, such algorithm delivers quantitative values of the hidden material and the thickness of the layer.

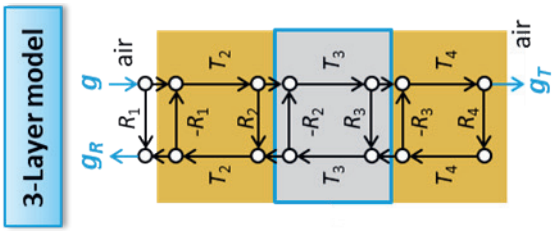

Fig. 1. Mason-Graph of a 3-layer-system; T-transmission function, R – reflection function, g – signal

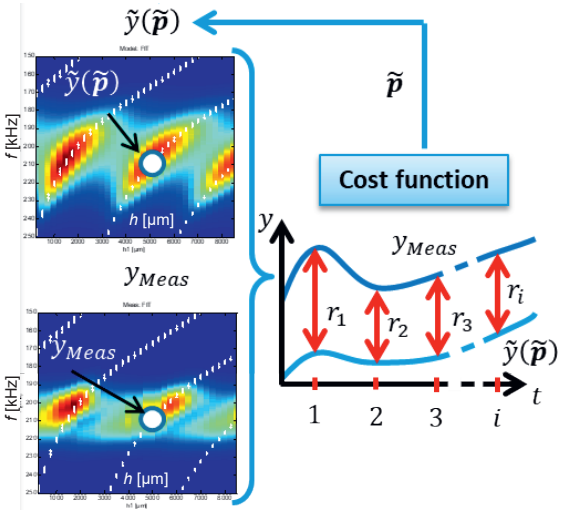

Fig. 2. Schematic for the optimization of the model function y(p) and the Measurement y_{Meas} in frequency domain for an ultrasonic transmission on a 3-layer-system (Acrylic (6 mm) – Water (h - variable) – Acrylic (6 mm)) with burst-excitation of (207.5 kHz +/- 45kHz).

References

[1] J. Jonuscheit, et.al 'Contact-Free Multilayer Thickness Determination of Industrial Coatings using THz Measuring Techniques', TM 2/2012.

[2] F. Hägglund, et.al 'Model-based estimation of thin multi-layered media using ultrasonic measurements', IEEE UFFC, vol.56, no.8, 2009.

[3] J. E. Carlson, 'Characterization of thin layers in multi-layered structures: on the problem of finding starting values for numerical solutions to inverse problems', in 2009 IUS: Italy, 2009.

[4] Rose, Ultrasonic waves in solid media, 2008

DOI 10.5162/SMSI2021/A10.4

Phononic Crystals Applied as Ultrasonic sensor for Liquid Systems

R. Lucklum, N. Mukhin, U. Steinmann, Otto-von-Guericke-University

Abstract

Ultrasonic sensors have a long tradition. One realization applies an ultrasonic resonator achieved by a liquid analyte confined in a solid structure. When working at MHz frequencies the characteristic dimension of the resonator, d_{res}, is in the mm- or upper µm-range. The primary measurement value is the resonance frequency, f_{res}, which is directly related to speed of sound in the liquid, c_{liq}:

$$f_{res} = \frac{c_{liq}}{2\, d_{res}} \tag{1}$$

A second measurement value is the *Q*-factor of resonance:

$$Q_{res} = \frac{f_{res}}{f_{FWHM}} \tag{2}$$

where f_{FWHM} is the full frequency difference at half peak maximum. Both, f_{res} and Q_{res} depend on liquid properties like the concentration of one component in a liquid mixture. The measurement becomes an inverse problem. Quite often, one just calibrates the sensor with proper substances, although theory is available to calculate a functional relation. The resolution achievable directly depends on Q_{res}.

In reality, one cannot realize full reflection of the ultrasonic wave at the walls of the cavity. One actually needs a certain amount of coupling, when a piezoelectric transducer realizes electromechanical signal transduction. In consequence, both, f_{res} and Q_{res} systematically deviate from eq. 1 by some amount.

A fascinating idea to design a resonant sensor is the exploitation of phononic crystals. A phononic crystal (PnC), an engineered material characterized by a periodic array of scattering inclusions in a homogeneous host matrix, exhibits bandgaps, where propagation of acoustic waves is forbidden (significantly decreased in experiment). This property allows for an optimization of ultrasonic resonant sensors via control of acoustic wave propagation within the sensor. We shortly introduce the transduction concept behind 1D- and 2D-PnC sensors. Whereas the 1D-PnC sensor can be analytically treated e.g. via a chain matrix approach, the 2D-PnC requires advanced methods of numerical computation. The measurement chain allows a direct calculation of the electrical response, e.g. to changes in liquid properties. The other way around is not possible. For example, the effective acoustic impedance, $Z_{a\ liq}$, is a function of the characteristic acoustic impedance, Z_{liq}, of the material and the phase shift the ultrasonic waves undergoes while propagating through this layer:

$$Z_{a\ liq} = \mathrm{j}\, Z_{liq} \tan\left(\frac{\omega d_{res}}{Z_{liq}}\right) \tag{3}$$

Since $Z_{liq} = \rho_{liq} c_{liq}$ (ρ is the density), c_{liq}, cannot be analytically isolated. It is a complex number, which considers acoustic energy dissipation as well. The optimal relation of resonance bandwidth and amplitude of the resonance is the key to an enhanced sensitivity of the sensor to liquid analyte properties and an example of the analysis of a 1D-PnC ultrasonic sensor.

We finally extend our view to a new 2D PnC sensor design concept: The analyte-filled point defect extends to an analyte-filled capillary in the 3rd dimension. This is the step toward the integration of a PnC with microfluidic elements.

We conclude from our analyses, that the ultrasonic PnC-sensor can reach a frequency resolution better than 10^{-6} the probing frequency. This results in a resolution in speed of sound of appr. 1 mm s^{-1} taking water as an example or a resolution in the molar fraction of alcohol in water of about $5\,10^{-5}$.

DOI 10.5162/SMSI2021/D2.1

Electric Field Meters – Application of the GUM

Carola Schierding[1], Martin Thedens[1], Michael Beyer[1]
[1] Physikalisch-Technische Bundesanstalt, Bundesallee 100, Braunschweig, Germany
carola.schierding@ptb.de

Summary:
For the development of a model for the identification of the measurement uncertainty according to the "Guide to the Expression of Uncertainty in Measurement" it is necessary to obtain knowledge of the influencing variables and possible application conditions. For this purpose, the measuring method of the electric field meter is investigated. Based on this, the capability of electric field meters as traceable measuring instruments in a static electric field is considered.

Keywords: GUM, electric field meter, traceability, electrostatics, measurement uncertainty

Introduction

It is necessary to characterize metrologically the measuring method of a FM to obtain a traceable measuring instrument. In order to measure electrostatic charges on surfaces by means of an electric field meter (FM) with corresponding indication of the measuring accuracy. By using a FM to determine the electrostatic field of the surface charges, a measurement without discharge can be obtained. This is possible due to the non-contact and discharge-free measuring method of a FM. The measuring method is based on the principle of electrostatic induction [1]. The FM used here [1, 2, 3] consists of a grounded measuring head and electronic measuring equipment in a grounded enclosure. With this measurement method, the FM does not directly influence the electrostatic charge. However, it is necessary to consider that the FM changes the shape of the E-field distribution. This is caused due to the characteristics of the FM, in particular, the edge of the grounded measuring head, which is not homogeneous (Fig. 1 top) [1]. This kind of distortion can be prevented by placing the measuring head into a grounded electrode.

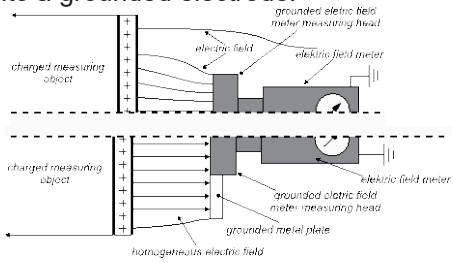

Fig. 1. Top: E-field distortion due to measuring head; Bottom: E-field homogenization by a grounded electrode (according to [1]).

As a result of the homogenization, the measuring head causes no significant influence on the distribution of the E-field, see Fig. 1 bottom. That optimization is used by manufactures to indicate the measurement deviation of their FM. Hereby is the problem that the indication of the deviation applies for just one particular case, the so-called “one point calibration”. For this one homogenous E-field configuration: Measuring head placed centered in a ground electrode, a plate electrode as measuring object, both electrodes with the same diameter and are also placed centered and parallel to each other in a set distance [2].
However, no further indications on the measurement deviations for applications without a ground electrode, other measuring object sizes or shapes (homogenous and inhomogeneous E-field configurations) and measuring distances are provided. Establishing the FM as a measuring instrument requires precise knowledge of the measuring method, the characterization of influencing parameters and the traceability of the measured values to national standards. Therefore, a test setup was developed, which ensures correct and reproducible measurements [4]. Due to the investigation results [4], and additional considerations on the mode of operation of the FM within the E-field, it could be determined that measuring objects are detected by means of a measuring cone defined by a measuring angle (depending on the diameter of the measuring head) [5]. Thus, the influencing variables and conditions for the correct application of an FM could be identified [6]. Based on these results it is possible to develop a model for the indication of the measurement uncertainty according to GUM [7].

Modelling and Results

The GUM provides a consistent method for the determination and indication of the measurement uncertainty. The determination of the influencing variables, the application conditions and the modelling are the main challenges and are discussed here for the measuring method FM. The influencing variables and conditions for the correct application of FM measurement are identified [6]. All other influences are considered as not relevant.

Conditions:

- Environmental conditions (temperature *T*, relative humidity *rh*)
- Optimal measuring distance depends on measuring object size, measuring angle and measuring range of FM.
- Tilting of FM to measuring object, indicated by tilt angle *δ*. Depends on optimal measuring distance and volume of measuring cone.

Influencing variables:

- Measuring distance (set distance, deviation according to calibration certificate, handling).
- FM measured value recording (accuracy recorder output, display output voltage FM).
- Voltage generation and measuring system (HV-divider, display voltage standard, nominal voltage deviation).
- Inhomogeneity of FM (correction factor of field distortion by measuring head for measurements without ground electrode).
- Inhomogeneity of the measuring objects (correction factor of field distortion by measuring real objects).

Fig. 2 shows the influencing variables for the measurement of the E-field caused by the measuring object and the symbol of the equation for the following consideration.

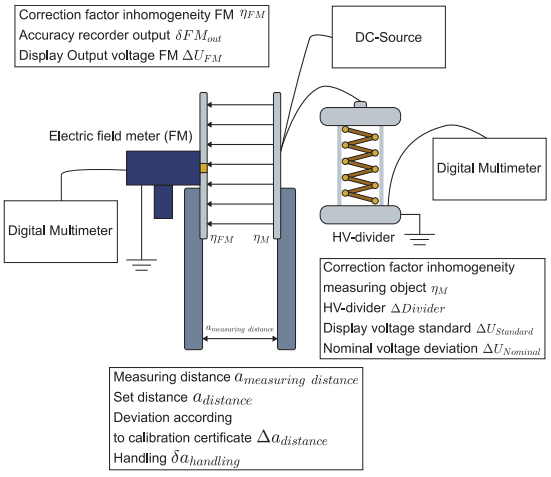

Fig. 2. Influences on electric field meter by means of the schematic test setup.

The model equation is based on several analytical terms. In the equations, all quantifiable influences are indicated by *Δ*. The measurement result is corrected by these terms. All influences which cannot be quantified are indicated with *δ*. These do not change the measurement result, but only contribute to the measurement uncertainty.

As a result, the model provides the value $\Delta E_{\%}$, which is the difference between the expected E-field E_h and the determined E-field $E_{h,\ measure}$ in percent. Here, the influence variables and the conditions on the measurement method as such, as well as the influences resulting from the specific measurement and measurement object after the measurement are considered according to the correction factors in the measurement uncertainty. With the measurement method, it is therefore possible to indicate the measurement deviation with extended uncertainty of the measurements with the extension factor $k = 2$ and a coverage probability of 95% (normal distribution), if the following applies:

- Environmental conditions:
  T = 15 °C to 31 °C and rh = 25% to 65%
- Measurements with or without homogenizing electrode (η_{FM})
- Homogeneous measuring objects with a diameter d_{HVe} = 100 mm to 400 mm
- Inhomogeneous measuring objects with round-, angle- or corner geometries (η_M)
- Depending on the respective optimal measuring distance $a_{optimal}$ and the acceptable tilt angle δ of FM

References

[1] G. Lüttgens, et. al., “Statische Elektrizität Durchschauen - Kontrollieren – Einsetzen”, 1. Auflage, Wiley-VCH Verlag, 2020.

[2] J. N. Chubb, “Two New Designs of „Field Mill“ Type Fieldmeters not Requiring Earthing of Rotating Chopper“, IEEE Transactions on industry applications, Vol.26, No. 6, 1990.

[3] Eltex- Elektrostatik- GmbH, “Betriebsanleitung Influenz- Elektrofeldmeter EMF58”, Weil am Rhein, Germany, 1994.

[4] C. Schierding, et. al., “Messtechnische Charakterisierung der berührungslosen Messung elektrostatischer Aufladungen mittels Feldmühlen“, 13. Fachtagung Köthen, Germany, Nov 2017.

[5] C. Schierding, et. al., „Further Developments of metrological and simulation-based characterization of the non-contact measurement of electrostatic charge by means of electric field meters”, 21st ISH, Budapest, Hungary, Aug 2019.

[6] C. Schierding, et. al., “Überblick zum aktuellen Stand der messtechnischen Charakterisierung der berührungslosen Messung elektrostatischer Aufladung mittels Feldmühlen“, 14. Fachtagung Köthen, Germany, Nov 2019.

[7] Guide to the Expression of Uncertainty in Measurement, ISO, Switzerland, corrected and reprinted 1995.

DOI 10.5162/SMSI2021/D2.2

Uncertainty-Aware Sensor Fusion in Sensor Networks

Maximilian Gruber[1], Wenzel Pilar von Pilchau[2], Varun Gowtham[3], Nikolaos-Stefanos Koutrakis[4], Matthias Riedl[5], Sascha Eichstädt[1], Jörg Hähner[2], Eckart Uhlmann[4], Julian Polte[4], Alexander Willner[3]
[1] PTB, Berlin, Germany
[2] University of Augsburg, Augsburg, Germany
[3] Fraunhofer FOKUS, Berlin, Germany
[4] Fraunhofer IPK, Berlin, Germany
[5] ifak, Magdeburg, Germany
team@famous-project.eu

Summary:
Uncertainty assignment for measurement values is a common process for single sensors, but this procedure grows in complexity for sensor networks. Often measured values are processed further in such networks and uncertainty must be evaluated for virtual values. A simple example is the fusion of homogeneous values and faulty or drifting sensors can harm the virtual value. We introduce a method from the field of key-comparison into the domain of sensor fusion. The method is evaluated in three different scenarios within an agent-framework.

Keywords: sensor networks, sensor fusion, measurement uncertainty, digital twin, emulated sensor

Motivation

Sensors always have some degree of uncertainty in the values they provide. This uncertainty can be related to time and/or measurement. As the number of sensors increase, for example in cases of large sensor networks, the accumulated uncertainty grows as well. In our previous work [1] uncertainty propagation was part of the use cases described, in particular within the context of sensor fusion. Sensor fusion is the combination of sensory data such that the resulting information is better than those obtained from individual sensors [2]. Sensor fusion is especially important for capturing industrial processes in the form of a digital twin. In our project FAMOUS[1], digital twins are virtual representations of sensors and sensor networks in the fields of discrete manufacturing and process engineering. There is plethora of literature that use statistical and stochastic models to address uncertainty in sensor fusion [3, 4, 5, 6]. This paper presents methods to reduce the effect of failing/drifting sensors and evaluates the uncertainty [7] in sensor fusion by drawing parallels to key comparison methods in metrology [8].

Uncertainty-Aware Sensor Fusion

The propagation of uncertainties is evaluated according to the formalism of the *Guide to the expression of uncertainties* (GUM) [9]. Suppose N independent measurements $x_1, \dots, x_N$ are taken by sensors and the corresponding uncertainties $u(x_i)$ are known from datasheets. It is of interest to combine these values into a fused value y_{fusion} and evaluate the uncertainty of that using Eq. 1 and Eq. 10 from GUM. A naive approach would use a weighted mean with weights $\gamma_i = \frac{1}{u(x_i)^2}$. With $k = \sum_{i \in I_c} \gamma_i$ this results in

$$y_{fusion} = \frac{1}{k} \sum_{i \in I_c} \gamma_i x_i$$

$$\mathrm{u}(\mathrm{y}_{\mathrm{fusion}})^2 = \sum_{i \in I_c} \left(\frac{\gamma_i}{k}\right)^2 u(x_i)^2$$

The presented homogenous sensor fusion is structurally similar to key comparisons in metrology. We therefore take a method developed by Cox [9] to calculate a more informed fusion value. The procedure uses the same weighted mean as our naive choice but extends it by a χ^2-test to detect outliers. If outliers are detected, the fusion value is recalculated.

Implementation Details

Sensors, sensor datasheet information and sensor fusion are represented as agents within an agent-framework suited for metrological information processing[2]. Raw sensor data is simulated and fed into the datasheet agent. There,

[1] http://famous-project.eu/

[2] https://github.com/bang-xiangyong/agentMET4FOF

the sensor value is transformed into an SI-unit and uncertainty information is added based on the datasheet. Thereafter, a uniform disturbance is added based on the given uncertainty and the uncertainty is recalculated for the disturbed sensor reading. The simulated sensor is an acceleration sensor of type LIS3DH[3]. Sensor readings are provided in multiples of earth's gravitational "constant" g. Conversion to an SI-unit is necessary. Uncertainty assignment considers variation of gravitation across the earth, non-linearity offset error and ADC-conversion.

$$x_{SI} = a * (x_{raw} + b)$$

$$u(x_{SI})^2 = (x_{raw} + b)^2 * u_a^2 + a^2 * (u_b^2 + u_x^2)$$

If operated at range $\pm 4g$ with 10bit resolution:

$$a = 9.81\ \frac{m}{s^2} \qquad b = 0 \qquad x_{raw} \in [-4, 4]$$

$$u_a = 0.025\ \frac{m}{s^2} \qquad u_b = 0.08 \qquad u_x = 0.5 * \frac{8}{2^{10}}$$

Scenarios

We chose three scenarios to evaluate different methods for sensor fusion in networks. We use in every scenario eight sensors that propagate their values to a virtual sensor that aggregates the incoming measurement values and uncertainties to a new *virtual* value. The incoming signal is a sinusoidal function of the time *t*. In the first scenario all sensors work as intended. In the second scenario, one of the sensors fails after $10\ s$ and returns a faulty value of $0\ m/s^2$ for every following measurement. The third scenario simulates a sensor that starts drifting after $5\ s$. The drift increases linearly for the next $10\ s$ where it remains till the end of the scenario.

Evaluation

Fig. 1 compares both presented methods for the drift scenario. The naive approach shows a smaller uncertainty throughout the simulation but is also strongly biased by the drifting sensor. The advanced method by Cox matches the lower uncertainty of the simple method during normal operation of all sensors but adopts a more robust behavior in case of sensor drift – at the cost of a higher uncertainty value of that result.

Conclusion and Future Work

By taking a known methodology from the field of metrology we can provide robust and uncertainty-aware sensor fusion for homogenous sensor networks. Comparing an informed fusion to a rather naive approach shows robust behavior in two anomalous scenarios. Furthermore, the fusion values are assigned a higher uncertainty, if fewer sensors contribute to it (due to outlier removal).

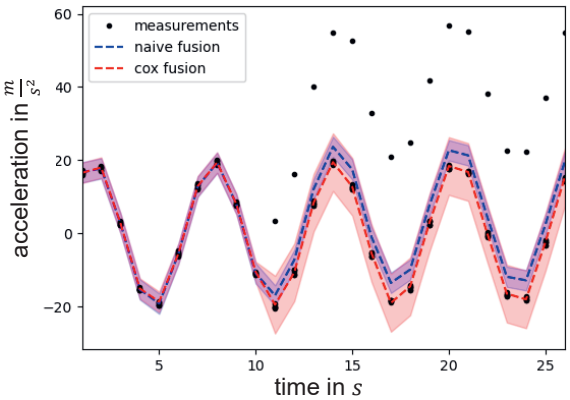

Fig. 1. Comparison of the naive and informed fusion methods with a single drifting sensor. Bands of uncertainties are exaggerated by factor 10 for visualization.

Acknowledgments

Research for this paper is funded by the Federal Ministry of Education and Research (BMBF) project FAMOUS (01IS18078).

Bibliography

[1] W. Pilar von Pilchau et al., „An Architectural Design for Measurement Uncertainty Evaluation in Cyber-Physical Systems," in *Position Papers of the FedCSIS 2020*, Sofia, Bulgaria, 2020.

[2] Y. Zou and K. Chakrabarty, „Uncertainty-Aware and Coverage-Oriented Deployment for Sensor Networks," *Journal of Parallel and Distributed Computing Vol. 64,* pp. 788-798, 2004.

[3] M. R. Senouci et al., Uncertainty-Aware Sensor Network Deployment, 2011.

[4] T. Youngchuan et al., „A Weighted Belief Entropy-Based Uncertainty Measure for Multi_Sensor Data Fusion," *Sensors Vol. 17,* p. 928, 2017.

[5] C. Papatsimpa and J. P. M. G. Linnartz, „Propagating Sensor Uncertainty To Better Infer Office Occupancy in Smart Building Control," *Energy and Buildings Vol. 179,* pp. 73-82, 2018.

[6] K. Shen et al., „A Consensus Nonlinear Filter With Measurement Uncertainty in Distributed Sensor Networks," *IEEE Signal Processing Letters Vol. 24,* pp. 1631-1635, 2017.

[7] BIPM, IEC, IFCC, ILAC, ISO, IUPAC und OIML, „International vocabulary of metrology (VIM)," 2012.

[8] M. G. Cox, "The evaluation of key comparison data", Metrologia Vol. 39, pp. 589, 2002

[9] BIPM, IEC, IFCC, ILAC, ISO, IUPAP and OIML, „Guide to the expression of uncertainty in measurement," 2008.

[3] https://www.st.com/resource/en/datasheet/lis3dh.pdf

DOI 10.5162/SMSI2021/D2.3

Spectrometry of pulsed photon radiation

Rolf Behrens[1], Hayo Zutz[1], Julian Busse[1]
[1] Physikalisch-Technische Bundesanstalt (PTB), Bundesallee 100, 38116 Braunschweig
Rolf.Behrens@PTB.de

Summary:
The energy distribution (spectrum) of pulsed photon radiation can hardly be measured using active devices. Therefore, a thermoluminescence detector (TLD)-based few-channel spectrometer is used in combination with a Bayesian data analysis.

Keywords: Spectrometry, Pulsed photon radiation, Bayesian analysis, Uncertainty

Background, Motivation and Objective

Pulsed photon radiation arises in more and more situations, e.g. from small pulsed X-ray tubes for material (like weld seam) testing or linear accelerators in tumor therapy. In this work, spectra at such radiation fields are measured.

Measurements and Data Evaluation

For the measurements, a TLD-based few-channel spectrometer (FCS) is used (see Fig. 1) [1],[2]. The photons' penetration depth in the spectrometer depends on the energy so that the energy-resolved and absolute spectrum of the radiation, including the uncertainties of the spectrum, can be determined from the dose values in the TLD layers using Bayesian data evaluation (deconvolution).

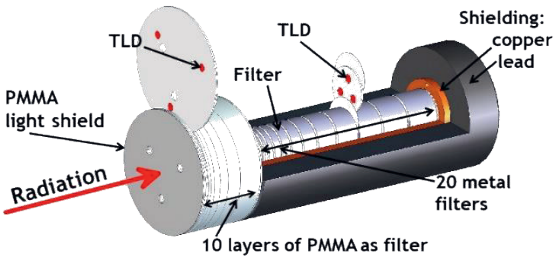

Fig. 1. Sketch of the TLD-based spectrometer. Basic principle: The deeper the radiation penetrates the spectrometer, the higher its energy.

The experimental setups are shown in Fig. 2: At the top, the spectrum of an industrial type open beam X-ray generator, XRS4 with a tube voltage of 370 kV, is measured. In the same way the spectrum of the XR200 with a tube voltage of 150 kV is measured. At the bottom, the spectrum of a medical accelerator at nominal 25 MV (which is actually 20 MV real) high voltage behind a shielding wall, is measured. The latter field is considered as reference field of pulsed high energy photons for dosemeter testing.

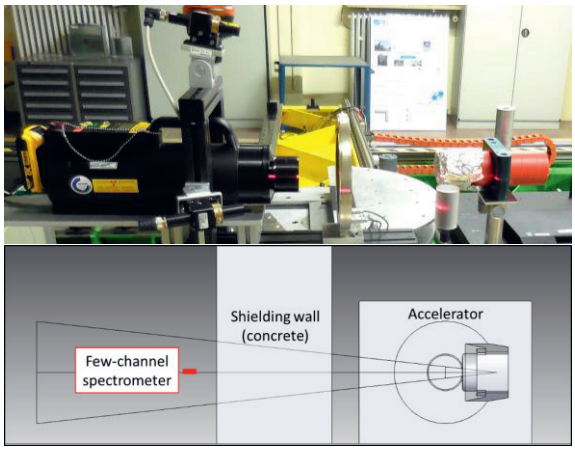

Fig. 2. Experimental setups. Top: industrial type open beam X-ray generator, XRS4, left, and FCS (red), right. Bottom: sketch of the medical accelerator, right, 2 m shielding wall, middle, FCS (red), left.

The TLDs are calibrated absolutely in terms of air kerma at PTB's corresponding reference field (Cs-137 radiation).

The Bayesian data evaluation is performed using the WinBUGS software [3] which, besides the absolute photon spectrum and total doses, also supplies the corresponding uncertainties and coverage intervals.

The following prior information for the photon spectra is included in the data evaluation: i) a smooth rise with increasing energy, ii) an exponential decrease at higher energies and iii) a peak in the spectrum at the energy of the characteristic fluorescence radiation of the anode material (for the XRS4 and XR200). This prior information is used due to the well-known form of bremsstrahlung spectra. Further details, including the validation of the method, (irradiation in known photon fields and subsequent data evaluation with the same prior information) are given in the literature [2],[5],[6].

Results

Fig. 3 shows the absolute photon fluence per pulse from the XRS4 and XR200 normalized to a distance of 1 m, top, and the absolute photon fluence per absorbed dose to water at the ISO center of the medical accelerator (at 1 m distance) at a total distance of 5.5 m from the accelerator. The latter one is measured at two different cross-sectional beam areas (at 1 m from the accelerator): 40 x 40 cm² and 10 x 10 cm². In both graphs, also the spectrum used as starting point for the Bayesian data evaluation is given. The fluence spectra are converted to ambient dose equivalent, $H^*(10)$, using the corresponding conversion coefficients [4]. The resulting doses are given in the legends together with the spectra's mean energies, $\bar{E}$, and their conversion coefficient from air kerma, K_a, to $H^*(10)$: $h^*_K(10)$.

The top of Fig. 3 reveals that the data evaluation clearly identifies the end point energies of the X-ray tubes. Furthermore, for the XRS4 compared to the XR200, the mean energy is approximately 1.5 times, the dose per pulse 2 times and the conversion coefficient rather similar. The differences are as expected due to the larger tube voltage of the XRS4.

The bottom of Fig. 3 shows that the data evaluation also identifies the end point energy of the accelerator. Furthermore, for the 40 x 40 cm² field compared to the 10 x 10 cm² field, the mean energy is approximately 30 % smaller, the dose per reference dose almost 2 times larger and the conversion coefficient nearly the same. The differences are as expected due to the larger beam area of the 40 x 40 cm² field resulting in a larger contribution of stray radiation at the spectrometer's position from within the shielding wall. As the photons lose energy during their scattering in the wall, the mean energy is smaller.

Conclusions

The measurements clearly show that the few-channel spectrometer in combination with the Bayesian data evaluation can be used in different areas of application to reliably measure the spectrum of pulsed photon radiation, including uncertainties, coverage intervals and doses.

Funding

This work is supported by the Bundesamt für Strahlenschutz (BfS) with project no. 3619S2236 / FV-63014 „Aufbau und Charakterisierung eines Referenzfeldes zur Sicherstellung des Strahlenschutzes an Beschleunigeranlagen in Medizin und Forschung und zur Prüfung und Kalibrierung entsprechender Messgeräte“.

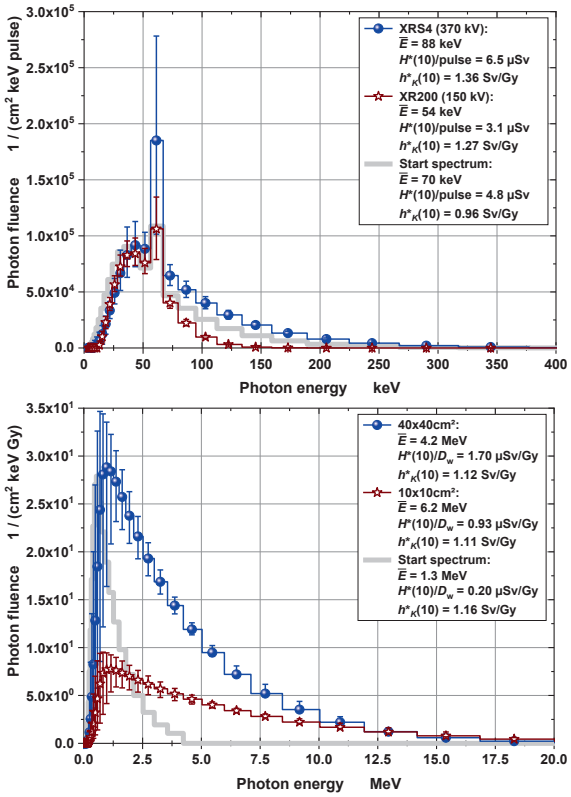

Fig. 3. Photon fluence spectra together with their 95 % coverage intervals. Top: X-ray generator, XRS4 (370 kV tube voltage) and XR200 (150 kV tube voltage); bottom: shielded, pulsed high energy photon field from a medical accelerator at nominal 25 MV high voltage.

References

[1] R. Behrens and P. Ambrosi, A TLD-based Few-channel Spectrometer for Mixed Photon, Electron, and Ion Fields with High Fluence Rates, *Radiat. Prot. Dosim.* **101**, 73 (2002) *doi: 10.1093/oxfordjournals.rpd.a006062*

[2] R. Behrens, A spectrometer for pulsed and continuous photon radiation, *J. Instrum.* **4**, P03027 (2009) *doi: 10.1088/1748-0221/4/03/P03027*

[3] D.J. Lunn, A. Thomas, N. Best, D. Spiegelhalter, WinBUGS – a Bayesian modelling framework: Concepts, structure, and extensibility, *Statistics and Computing* **10**, 325 (2010) *doi: 10.1023/A:1008929526011*

[4] International Commission on Radiation Units and Measurements (ICRU), Conversion Coefficients for use in Radiological Protection against External Radiation. *ICRU Report 57* (1998) *doi: 10.1093/jicru/os29.2.Report57*

[5] R. Behrens, B. Pullner, M. Reginatto, X-Ray Emission from Materials Processing Lasers, *Radiat. Prot. Dosim.* **183**, 361-374 (2019); *doi: 10.1093/rpd/ncy126*

[6] R. Behrens, M. Reginatto, Bayesian Spectrum Deconvolution Including Uncertainties and Model Selection: Application to X-Ray Emission Data Using WinBUGS, *Radiat. Prot. Dosim.* **185**, 157-167 (2019); *doi: 10.1093/rpd/ncy286*

DOI 10.5162/SMSI2021/D2.4

Evaluation of precision of measurement results in medical laboratory

A.Tumilovich[1], T.Martynova[2], A.Chunovkina[1]
[1] D.I. Mendeleyev Institute for Metrology (VNIIM).
[2] Federal State Budgetary Educational Institution of Higher Education «Academician I.P. Pavlov First St. Petersburg State Medical University» of the Ministry of Healthcare of the Russian Federation (Pavlov Medical University)
a.a.koroleva@vniim.ru

Summary:
This paper analyzes an approach to evaluation of measurement uncertainty in medical laboratory. In particular, special attention is paid to precision of measurement results carried out by a medical laboratory on identical materials in precision conditions.

Keywords: medical laboratory, measurement uncertainty, certified reference material, measurement traceability, measurement precision, bias.

Introduction

Ensuring metrological traceability in the field of medical measurements aimed at realizing the possibility of comparing the measurement results obtained in different laboratories. Metrological traceability is realized through the chain of calibration performed using certified reference material and reference measurement procedure. Calibration implies calculation of associated measurement uncertainties. Knowledge of the measurement uncertainty provided by the medical laboratory is an important factor in clinical decision. The Guide to the Expression of Uncertainty of Measurement GUM [1] is a fundamental document for the calculation of measurement uncertainty. Unfortunately, uncertainty calculation methods based on measurement model are not always feasible in the field of medical measurements, therefore the document ISO/TS 20914 "Medical laboratories - Practical guide for the estimation of measurement uncertainty" was developed [2]. This document follows the basic ideas of the GUM and presents a simplified method for estimating measurement uncertainty within a medical laboratory, which is based on the analysis and evaluation of measurement precision within the laboratory and information on the accuracy of reference materials/certified reference material (CRM) used by the laboratory to establish and control a bias in the measurement results.

Evaluation of measurement uncertainty in medical laboratory

According to ISO/TS 20914:2019, the uncertainty of the measurement result $u(x)$ in a medical laboratory is consists of the three main components:

$$u(x) = \sqrt{u_{bias}^2 + u_{cal}^2 + u_{Rw}^2}, \quad (1)$$

where u_{bias}– is uncertainty of a bias value, u_{cal}– uncertainty of the value assigned to an end-use calibrator, u_{Rw}– uncertainty estimate based on data observed under intermediate precision conditions of measurement.

In turn, the uncertainty of a bias value calculated in accordance with the formula:

$$u_{bias} = \sqrt{SD_{mean}^2 + u_{ref}^2}, \quad (2)$$

where SD_{mean}– is standard deviation of the mean value of a measurand obtained from a repeatability study, u_{ref} – uncertainty of the value assigned to a reference material.

Estimation of precision of measurement results

This article is devoted to the assessment of the precision of measurement results[3] based on all information available in a medical laboratory. The laboratory can assess the precision of its measurements using data from regular internal quality checks. The precision of measurements is assessed in the form of the standard deviation (SD) of the results obtained for control materials similar in their properties to the clinical samples analyzed by the laboratory. The reason for the discrepancy in the measurement results in terms of precision are: sample inhomogeneity; instrumentation; reagent and calibrator instability; reagent and calibrator lot-to-lot

variability; fluctuations in laboratory environment; operator bias introduced by reading analogue instrument indications; more than one of the same measuring systems for the same measurand. Combining several groups into one when estimating u_{Rw} is performed in order to increase the accuracy of the SD estimates. The application of the Cochran test for pooling SD is discussed below.

Evaluation of the precision of measurements in a medical laboratory using the example of measuring WGB, RBC, HBL

The processing of the results was carried out jointly with the laboratory of Pavlov Medical University in which measurements were performed. Two sets of certified reference material (CRM) were analyzed for certified values of the characteristics of WGB (leukocytes), RBC (erythrocytes) and HGB (hemoglobin). Each set of CRMs consisted of two vials of certified "pathology" values (CRM1 and CRM2). In the specification for these CRMs, in addition to the certified values, their limits of the relative error for a confidence level of 0.95% were indicated. Also measurement results for control material (CM), consisting of the values ”pathology” for the investigated characteristics of WGB, RBC, HGB were obtained.

In order to evaluate the precision for each characteristic of CRMs and CM, 10 measurements were carried out on the same measuring instrument under the same precision conditions. Thus, the medical laboratory received 10 values of characteristics related to "pathology" from the 1st set, 10 values of characteristics related to "pathology" from the 2nd set and 10 values of characteristics related to the measurement of CM. Further, according to ISO/TS 20914:2019, the SD was estimated for each characteristic from each set. To characterize HGB, instead of the SD, the range was estimated, since distribution of measurement results differs from the normal distribution.

Cochran's criterion was used to analyze the homogeneity of the variance of the measurement the characteristics of WBC and RBC, in accordance with formula (3):

$$\frac{SD_{\max}^2}{\sum SD_i^2} \le G_{0,95}(3,10) \qquad (3)$$

where SD_{max}– is the largest value of the variance of each characteristic, $G_{0,95}(3,10)$ – is the critical value of the Cochran criterion for the significance level 5%, equal to 0.617.

The data on the estimated variances of characteristics and the analysis of homogeneity by the Cochran test are presented in Table 1:

Tab. 1: Analysis of homogeneity

SD \ Material	WGB, 10^9/l	RBC, 10^{12}/l
SD (CRM1)	0.079	0.034
SD (CRM2)	0.089	0.026
SD (CM)	0.075	0.046
Cochran criterion	0.032<0.617	0.020<0.617
$SD_{\Sigma} = \sqrt{\frac{\sum SD_i^2}{3}}$	0.081	0.036

The range of measurement results of HGB is 2 g/l for RCMs and 4g/L for CM that corresponds to 2% and 6% accordingly.

Conclusions

According to the obtained results, the hypothesis about the homogeneity of the variances of measurement results of WGB, RBC and HGB is confirmed. Therefore, for each of the analyzed characteristics, the pooled variance (SD_{Σ}) can be attributed to the measurement results of WBC, RBC, obtained in further measurements in this medical laboratory. The article describes the procedure for evaluating the SD of the precision of measurements in a medical laboratory based on the pooled estimate of variance. The obtained estimate can be used in carrying out the internal laboratory control of the measurement precision and in the estimation of the measurement uncertainty. In the extended paper the method of combining information on the variance of precision based on the Bayesian approach will be presented and compared the one considered.

References

[1] JCGM 100:2008 Evaluation of measurement data — Guide to the expression of uncertainty in measurement (GUM);

[2] ISO/TS 20914 «Medical laboratories — Practical guidance for the estimation of measurement uncertainty»;

[3] JCJM 200:2008 International vocabulary of metrology – Basic and general concepts and associated terms (VIM);

[4] ISO 5725-2:2019 Accuracy (trueness and precision) of measurement methods and results — Part 2: Basic method for the determination of repeatability and reproducibility of a standard measurement method.

DOI 10.5162/SMSI2021/D3.1

IoT-middleware requirements for context-sensitive processing of data to enable predictive maintenance through augmented reality

Marc Philipp Jensen[1]
[1] *University of Applied Sciences, Schellingstr. 24 70174 Stuttgart Germany, marc.jensen@hft-stuttgart.de*

Summary:
Increasing numbers of sensors and actuators are being used in IoT systems. This generates a huge volume of data. To extract valuable information for a company based on this rich source of data, a computerised processing of the data is essential. However, the user plays a crucial role in the evaluation. Information must therefore be context-sensitive and adapted to sensory needs.

Keywords: IoT, industrial IoT, MQTT, Augmented Reality, Data modelling.

Introduction

The number of devices connected to the internet is continuously increasing year by year. This trend is spread across different fields of application, like operation of industrial plants, automation of buildings, in healthcare and connecting smart homes. For companies in particular, the Industrial Internet of Things (IIoT) provides access to a strong and growing market [1]. This creates versatile integration possibilities for sensors and expands the fields of application for the Internet of Things (IoT). A large amount of data is generated through the communication of sensors, actuators, and IT systems. In recent years, various IoT standards have been developed; these include the specification of communication protocols for connectivity, data models and data structuring, device management and security requirements. These developments lead to a high degree of fragmentation in the context of IoT standardisation, highlighting a uniform data exchange between IoT systems as a major challenge.

This short paper aims to identify possibilities of IoT communication protocols to provide a user with contextual data of industrial equipment via an augmented reality interface.

Background

Operating industrial plants requires constant monitoring of devices. The highly dynamic nature of the complex interaction between different departments imposes special requirements for IT systems. Information about people, machines and the control of overarching processes must be extracted based on the available data. With the architecture of IoT-based systems, harmonisation of the connections between sensors, communication, application and processes is particularly important [2]. However, a digital transformation in this area is often extremely complicated due to the number of different system types and protocols. To enable seamless status monitoring at any point, interfaces are essential that meet the requirements of real-time and machine-to-machine communication. The authors [3] point out the importance of not overlooking humans as actors in the design of IoT standards and the development of more efficient machine-to-machine communication. An effective data interpretation can be presented to a consumer based on the contextual analysis of the available data.

Objective

Different system architectures and requirements of industrial machines complicate the implementation of IoT standards. Proprietary standards, applied data formats and the complexity of structured data, as well as security requirements for securing data transmission, pose significant challenges in this context [4]. With sensor networks usually involving a high number of interconnected sensors and actuators, which are also increasingly running on embedded devices, communication protocols designed to meet these requirements are therefore highly recommended. A variety of IoT protocols are available, namely Message Queue Telemetry Transport (MQTT), Constrained Application Protocol (CoAP) and Representational State Transfer (REST), all of which are used extensively in IoT applications [5]. The OASIS organisation has standardised the IoT protocol MQTT, which was developed as a lightweight

and robust communication protocol that is well suited for IoT applications. Both communication and data exchange are based on the Publish/Subscribe principle. The architecture's central server (broker) enables connected clients to subscribe to topics. This way, clients can both send and receive messages to and from each other. Because of the simple structure, MQTT is notably easy to use and is currently supported by numerous systems [6]. Data transmitted via an MQTT broker can be ambiguous to the consumer if no information is provided about the characteristics of the data. As discussed in [7], MQTT by itself does not allow typification of data and association of metadata. However, a structured definition can be achieved through the hierarchical structure of a MQTT topic. The user can interpret the data on a topic by defining the topics in a well-structured format. By configuring the broker, a bridge functionality can be enabled with MQTT. The Broker simultaneously operates as a MQTT client. As a result, communication can be established with different MQTT networks and messages can be transmitted between different systems. In order to design this mechanism dynamically, the goal of this research is to separate the bridge functionality into an independent software component.

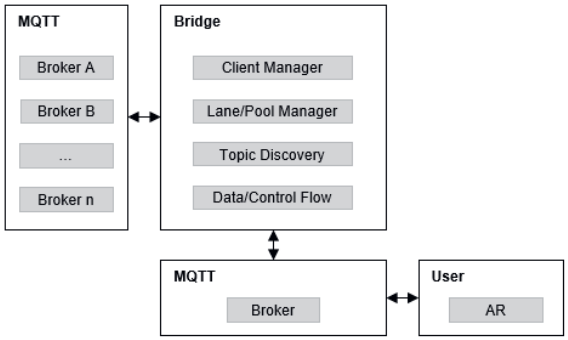

Fig. 1. Data and control flow of the MQTT bridge.

This enables the user to access sensor data from different MQTT networks. In the process, the user can consolidate the sensor data into structured data channels by remapping the topics.

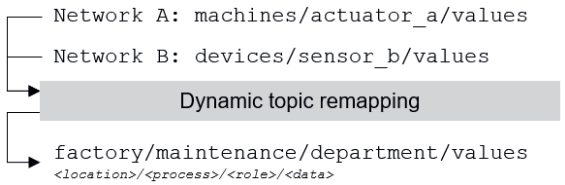

Fig. 2. Restructuring the MQTT data flow by remapping available topics.

A context-sensitive structuring of the data can be enabled and thus, as an example, a reference to spatial awareness, the role of a user or process classification can be achieved. A prototypical test bed consists of a RFID measurement cabinet and a head-mounted display through which a user can access streams of data. The RFID measurement cabinet is used to measure RFID transponder performance on different substrates. The MQTT IoT middleware transmits the measurement results in real-time in the user's context. Using augmented reality, this human-machine interface (HMI) enables the user to visualise the information in the real world in a user-friendly way.

Conclusion

IoT gateway or adapter solutions must still be used to merge IoT data from different systems. Achieving interoperability of IoT standards remains a major challenge due to different data models, communication protocols and system requirements. The concept of a virtual MQTT bridge enables the user to dynamically merge sensor data from different MQTT brokers and enrich it with additional sensor data.

References

[1] ‘Forecast: Enterprise IoT Platforms, Worldwide, 2018-2024’. https://www.gartner.com/en/documents/3982172/forecast-enterprise-iot-platforms-worldwide-2018-2024 (accessed Jan. 15, 2021).

[2] ‘A framework for rapid integration of IoT Systems with industrial environments - IEEE Conference Publication’. https://ieeexplore.ieee.org/document/8767224/ (accessed Jan. 15, 2021).

[3] D. Sahinel, C. Akpolat, O. C. Görür, and F. Sivrikaya, ‘Integration of Human Actors in IoT and CPS Landscape’, in *2019 IEEE 5th World Forum on Internet of Things (WF-IoT)*, Apr. 2019, pp. 485–490, doi: 10.1109/WF-IoT.2019.8767276.

[4] K. Fysarakis, I. Askoxylakis, O. Soultatos, I. Papaefstathiou, C. Manifavas, and V. Katos, ‘Which IoT Protocol? Comparing Standardized Approaches over a Common M2M Application’, in *2016 IEEE Global Communications Conference (GLOBECOM)*, Dec. 2016, pp. 1–7, doi: 10.1109/GLOCOM.2016.7842383.

[5] P. Nguyen-Hoang and P. Vo-Tan, ‘Development An Open-Source Industrial IoT Gateway’, in *2019 19th International Symposium on Communications and Information Technologies (ISCIT)*, Sep. 2019, pp. 201–204, doi: 10.1109/ISCIT.2019.8905157.

[6] S. Shin, K. Kobara, Chia-Chuan Chuang, and Weicheng Huang, ‘A security framework for MQTT’, in *2016 IEEE Conference on Communications and Network Security (CNS)*, Oct. 2016, pp. 432–436, doi: 10.1109/CNS.2016.7860532.

[7] N. Tantitharanukul, K. Osathanunkul, K. Hantrakul, P. Pramokchon, and P. Khoenkaw, ‘MQTT-Topics Management System for sharing of Open Data’, in *2017 International Conference on Digital Arts, Media and Technology (ICDAMT)*, Mar. 2017, pp. 62–65, doi: 10.1109/ICDAMT.2017.7904935.

DOI 10.5162/SMSI2021/D3.2

Simultaneous Signal Acquisition by Synchronous Detection of Orthogonal Frequency Components

Matthias Baer[1], *Panayiota Demosthenous*[2], *Bernhard Schmauss*[1]
[1] *Institute of Microwaves and Photonics (LHFT) and Erlangen Graduate School for Advanced Optical Technologies (SAOT), Cauerstr. 9, 91058 Erlangen, Germany*
[2] *Cyprus Research & Innovation Center Ltd (CyRIC), 72, 28th Octovriou Ave, Off.301, Engomi, 2414 Nicosia, Cyprus*
matthias.baer@fau.de

This paper is an outcome of the Project POST-DOC/0718/0186 which is co-funded by the European Regional Development Fund and the Republic of Cyprus through the Research and Innovation Foundation.

Summary:
We describe a multiplexing technique to simultaneously measure the absorption properties of gas at two different wavelengths using just one photodetector and an orthogonal frequency synchronous detection technique with non-sinusoidal modulation. This concept is demonstrated in a near infrared (NIR) spectroscopic application, measuring ethanol vapor in air.

Keywords: Near infrared, spectroscopy, integrating sphere, lock-in, synchronous detection

Synchronous Detection and Integrating Spheres in Spectroscopy

To gather even the smallest signal or signal change in spectroscopic applications, the usage of lock-in amplifiers is a commonly used technique. Synchronous detection, the principle behind lock-in amplifiers has been described in a historical overview already in 1954 [1]. However, some more detailed and application specific literature can be found in [2][3][4]. A principle schematic of a synchronous detector is depicted in Fig. 1. At this point, it shall be pointed out, that the reference signal does not necessarily need to be a sinusoidal signal, but can be more generally the excitation signal of the system.

Integration spheres are known to be beneficial in some spectroscopic applications, especially in scattered reflectance or transmittance measurements [5][6]. Especially integrating spheres are beneficial in gas sensing applications, as they easily increase the effective optical path length from the light source to the detector. Hence, the interaction length between light and gas sample becomes higher [7].

Application and Optical Setup

In the work presented here, an integrating sphere is used to measure ethanol vapor in air. The setup is sketched in Fig. 2. Two light sources (LS) are mounted to the sphere. The first LS is a DFB Laser with a wavelength of 2274 nm, which is close to an absorption band of ethanol. The second LS is a NIR-LED at a wavelength of roughly 1550 nm, which is intended to measure any other analyte but ethanol.

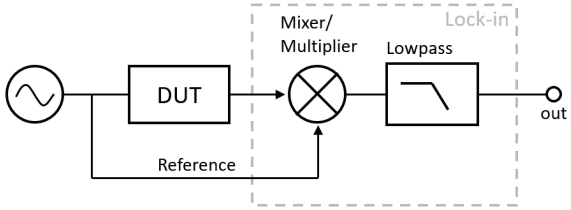

Fig. 1: Simple schematic of a synchronous detector.

The light of the LSs is detected with a photodetector (PD) which is sensitive for both wavelengths. The PD is mounted to a port of the integrating sphere that is not centered. Thus, no direct illumination of the PD by any of the LSs is possible. The port at which a sample can be mounted is actually at the rear side of the integrating sphere and thus not visible.

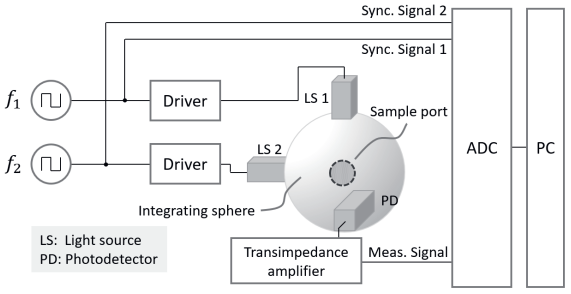

Fig. 2: Optical and electrical setup.

During measurement, both LSs are operated simultaneously and are pulsed with a rectangular waveform with a duty cycle of 50%. While LS 1 is modulated with a frequency of 480 Hz, LS 2 is modulated with a frequency of 985 Hz, which is roughly the double frequency. It shall be emphasized that the ratio of these frequencies was chosen consciously. A synchronous

detector with a rectangular waveform (duty cycle of 50%) as reference signal does not only show a sensitivity at the fundamental frequency, but also at all odd harmonics, though with decreasing sensitivity. Thus care has to be taken, that the modulation signals of LS 1 and LS 2 do not share any harmonics. For the given case only odd harmonics are expected and by choosing the modulation frequencies with a ratio of two, the constraint of no common harmonics is fulfilled. Thus both signals are mathematically orthogonal to each other, which guarantees cross sensitivity freedom. However, in the considered case the frequency ratio is not exactly two and at some point two harmonics will come to lie at almost the same frequency. Fortunately, as mentioned before, the sensitivity of the synchronous detector decreases for higher harmonics, so that this problem is not severe.

The actual synchronous detection of the PD signal is done digitally by sampling the measurement and excitation signals (Sync. Signal 1/2) and processing them with a PC. Fig 3 shows snippets of the two synchronization signals and the measurement signal. It can be seen, that the measurement signal is a superposition of both excitation signals scaled by any factor.

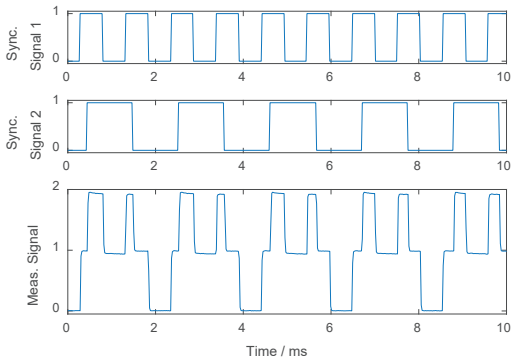

Fig. 3: Sampled signals according to Fig. 2.

Fig. 4 sketches the digitally implemented lock-in algorithm. With a rectangular excitation signal beeing used for both LSs, the algorithm is basically a multiplication of the measurement signal with the sign of the mean value free synchronization signal.

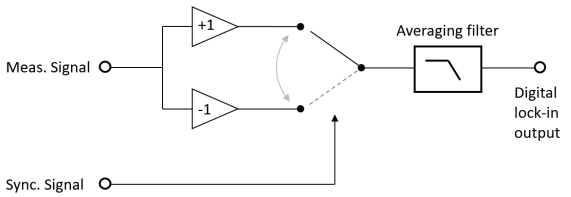

Fig. 4: Principle of the digitally implemented synchronous detector.

Results

A measurement (Fig. 5) has been performed by first flushing the integrating sphere with air. Then the sample port was left open for some time to measure the signal amplitude from both LSs at the detector when no analyte is present. After roughly 200 seconds, a cotton wool ball soaked with a 37.5%vol. ethanol solution was brought to the sample port. As the ethanol vapor fills the integration sphere, the detected intensity of LS1 decreases while the intensity of LS 2 is unaffected.

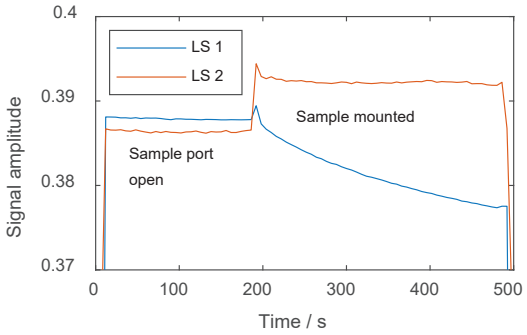

Fig. 5: Measured light intensity of LS 1 and LS 2 at the photodetector. The separation of both is done by using synchronous detection.

Simultaneous measurement of two different light intensities by orthogonalization of both signals using different modulation frequencies has been demonstrated.

References

[1] D. G. Tucker, "The history of the homodyne and synchrodyne," in Journal of the British Institution of Radio Engineers, vol. 14, no. 4, pp. 143-154, April 1954, doi: 10.1049/jbire.1954.0021.

[2] Bentham Instruments Ltd. Technical Note, Lock-in amplifiers, 2017, http://support.bentham.co.uk/support/solutions/articles/13000036065-lock-in-amplifier-tutorial

[3] Zürich Instruments AG Whitepaper, Principles of lock-in detection and the state of the art, 2016, https://www.zhinst.com/sites/default/files/li_primer/zi_whitepaper_principles_of_lock-in_detection.pdf

[4] Stanford Research Systems Application Note #3, About Lock-In Amplifiers, https://www.thinksrs.com/downloads/pdfs/applicationnotes/AboutLIAs.pdf

[5] Perkin Elmer Application Note, Applications and Use of Integrating Spheres With the LAMBDA 650 and 850 UV/Vis and LAMBDA 950 UV/Vis/NIR Spectrophotometers, https://www.perkinelmer.com/CMSResources/Images/44-74191APP_LAMBDA650IntegratingSpheres.pdf

[6] Leonard M. Hanssen and Keith A. Snail, Integrating Spheres for Mid- and Near-infrared Reflection Spectroscopy, Chapter of "Handbook of Vibrational Spectroscopy", John Wiley & Sons Ltd

[7] Sébastien Tranchart and Ikhlef Hadj Bachir and Jean-Luc Destombes, Sensitive trace gas detection with near-infrared laser diodes and an integrating sphere, APPLIED OPTICS Vol. 35, No. 36 20 December 1996, doi: 10.1364/AO.35.007070

DOI 10.5162/SMSI2021/D3.3

Approximate sequential Bayesian filtering to estimate Rn-222 emanation from Ra-226 sources from spectra

Florian Mertes[1], Stefan Röttger[1], Annette Röttger[1]
[1] Physikalisch-Technische Bundesanstalt, Bundesallee 100, Braunschweig, Germany
florian.mertes@ptb.de

Summary:
A new approach to assess the emanation of ^{222}Rn from ^{226}Ra sources based on measurements of the residual ^{222}Rn is presented. The method incorporates the dynamics into the inference procedure, rather than resorting to previously available steady-state approximations. The algorithm is based on approximate Bayesian filtering in a switched linear dynamical system to identify regimes of changing emanation behavior from a time-series of spectral data.

Keywords: State-Space model, switched linear dynamical system, Rn-222, integrating measurements

Introduction

For the calibration of ^{222}Rn measurement devices at low activity concentrations, decaying ^{222}Rn reference atmospheres produced through gaseous standards do not yield satisfactory statistical uncertainties. A different approach to realize reference atmospheres of low activity concentrations is provided by ^{222}Rn emanation sources. Emanation sources are ^{226}Ra sources constructed so that some fraction of the generated ^{222}Rn is released from them. In [1, 2], an approach to measure the released amount of ^{222}Rn based on measuring the residual ^{222}Rn in the source is presented. However, this approach is only valid for times in which steady state has been reached. Moreover, it has been suggested that environmental conditions can impact the emanation behavior, which leads to erroneous results when assuming steady state. In the following, a new approach is presented based on Gaussian sum filtering in a switched linear dynamical system (SLDS) which more accurately models the emanation behavior, given the deterministic dynamics of the radioactive decay, with the possibility for on-line operation. Additionally, the method allows one to probabilistically identify regimes of constant emanation behavior.

Model and filtering algorithm

The basis of the new method is to model the ^{226}Ra source as a switched linear dynamical system, in which its latent state vector $x \in \mathbb{R}^{n\times 1}$, $x = \left[A^S_{Rn-222}, A^S_{Ra-226}, \eta, \frac{d\eta}{dt}\right]^T$, where A^S_i is the activity of the i-th nuclide in the source and η is the number of escaping ^{222}Rn atoms per unit time, evolves through the Itō stochastic differential equations (1).

$$dx = F_s x dt + L_s dW_{s,t} \tag{1}$$

where $F_s \in \mathbb{R}^{n\times n}$ is the fundamental matrix of the s-th model and $L_s \in \mathbb{R}^{n\times 1}$ is a matrix which controls how the increments of a Wiener-process $dW_{s,t}$ of power-spectral density $Q_s \in \mathbb{R}$ enter the system. The index s of the active dynamics is modeled as a discrete Markov process with transition matrix Π. For each $s \in \mathbb{N}$, the solution to (1) is an initial value problem [3] and resembles a Gaussian process for Gaussian x_0. $F_s = F$ and $L_s = L$ are chosen to be

$$F = \begin{bmatrix} -\lambda_{Rn-222} & \lambda_{Rn-222} & -\lambda_{Rn-222} & 0 \\ 0 & -\lambda_{Ra-226} & 0 & 0 \\ 0 & 0 & 0 & 1 \\ 0 & 0 & 0 & -\gamma \end{bmatrix}, L = \begin{bmatrix} 0 \\ 0 \\ 0 \\ 1 \end{bmatrix}$$

Generally, measurements with spectrometric devices $y \in \mathbb{R}^{m\times 1}$ (2) are performed over non-overlapping intervals $l_k \in \mathbb{R}$ indexed by $k \in \mathbb{N}$, such that $t_k \in T$, where T represents the set of measurement time instants.

$$y_{k,l_k} = H \int_0^{l_k} x(t_k + \tau)\, d\tau + r_k \tag{2}$$

where $H \in \mathbb{R}^{m\times n}$ maps the state integral to the measurement space, r is an uncorrelated Gaussian white noise sequence of variance R_k indexed by k that is computed from the observed y_k (Gaussian approximation to counting statistics). This approximation is crucial, since it preserves the conjugacy of the model. H is assumed to be deterministic. Given a time-series of spectra, we are interested in the filtering distribution $p(x_k, s_k | y_{0:k}, H) = p(x_k | s_k, y_{0:k}, H) p(s_k | y_{0:k}, H)$, which is defined recursively [3, 4], since both x and s are Markov processes. y is a linear transformation of x, so for given s_k, x_k and y_k are jointly Gaussian.

$$p(x_k, y_k | s_k, H) = \mathcal{N}\left(\begin{bmatrix} \mu_{x_k} \\ K_{l_k}\mu_{x_k} \end{bmatrix}, \begin{bmatrix} \Sigma_{x_k} & \Sigma_{x_k}K_{l_k}^T \\ K_{l_k}\Sigma_{x_k} & K_{l_k}\Sigma_{x_k}K_{l_k}^T + J_{s_k,l_k} + R_k \end{bmatrix}\right)$$

with

$$K_{l_k} = H\int_0^{l_k} e^{F\tau}d\tau, J_{s_k,l_k} = \int_0^{l_k} K_{l_k\text{-}\tau} L Q_{s_k} L^T K_{l_k\text{-}\tau}^T d\tau.$$

For the specific F,L and Q in the models, the discretization of (1), K_{l_k} and J_{s_k,l_k} are available analytically and were implemented using symbolic computation, using the diagonalizability of F. To obtain the approximate filtering distributions, Algorithm 1 in [4] was adapted to include the additional terms K_{l_k} and J_{s_k,l_k}. As discussed in [4], it is infeasible to compute the exact filtering distribution. In our implementation, the arising Gaussian mixtures are collapsed to smaller mixtures based on an upper bound of the KL-divergence [5], where we chose to collapse to 3 Gaussian components per model. The unknown parameters (Q, Π, γ) are tuned with respect to approximate maximum marginal likelihood [3].

Experimental Results

The SLDS approach was chosen because the time-series of interest is comprised of regimes of constant η and those of changing η, where it is of interest to know when stable regimes are reached. The choice was made to model this behavior by having two linear dynamic models, one of them with fully deterministic dynamics e.g. $Q_1 = 0$.

For the collection of data, an electroplated ^{226}Ra (104.4 ± 0.4) Bq source was mounted on top of a high-purity Germanium γ-ray detector, inside of a climate chamber. Spectra were recorded over the course of approx. 85 days in intervals of 10800 s live time. At specific times, the relative humidity was changed to induce changes in η. From each γ-ray spectrum, the total number of counts that were recorded at energies over 200 keV was calculated, a background count rate was subtracted, and the algorithm was applied to the result. The threshold of 200 keV was chosen because above this threshold the spectrum is only made up of events that are due to the background or the short-lived ^{222}Rn progeny (SLP) within the source. The SLP is assumed to always be in equilibrium with ^{222}Rn, which is a valid approximation on these time-scales.

Figure 1 shows the raw-counts that were computed from the spectra (input data), the relative humidity inside the chamber as measured by a SHT-35 sensor (red curve), the inferred filtering distributions and the results that would have been obtained from the method in [1, 2]. It can be observed from these results that once the dynamics of ingrowth are modeled in this way it becomes apparent that the methods in [1, 2] lead to deviations from the true value. The new method extends the validity to regimes of non-constant η and allows for an estimate of the naturally expected increased uncertainty in these regimes. Moreover, all obvious switching points within the time-series are detected.

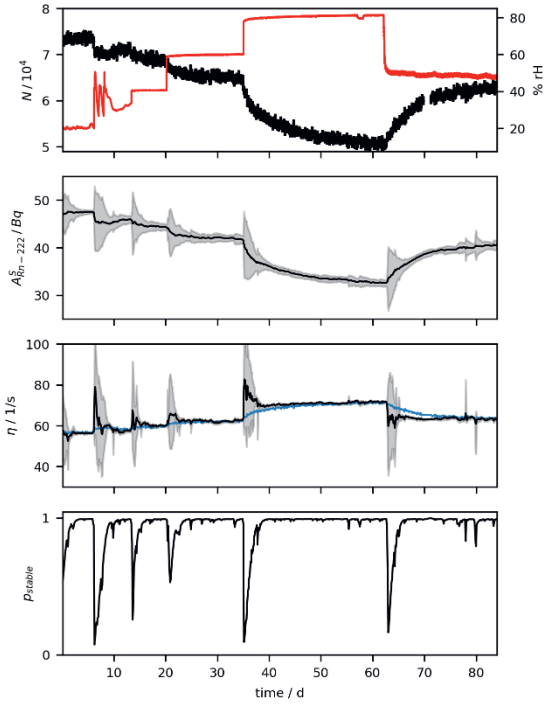

Figure 1: Filter output (black) with estimated 90 % quantiles (grey) and comparison with results of the methods [1, 2] on the same dataset (blue)

Acknowledgment

This project 19ENV01 traceRadon has received funding from the EMPIR programme co-financed by the Participating States and from the European Union's Horizon 2020 research and innovation programme.

References

[1] D. Linzmaier, A. Röttger, Development of a low-level radon reference atmosphere, Applied Radiation and Isotopes, 81, 208-211, (2013), doi: 10.1016/j.apradiso.2013.03.032

[2] F. Mertes, S. Röttger, A. Röttger, A new primary emanation standard for Radon-222, Applied Radiation and Isotopes, 156, (2020), doi: 10.1016/j.apradiso.2019.108928

[3] S. Särkkä, A. Solin, Applied Stochastic Differential Equations, Cambridge University Press, (2019)

[4] D. Barber, Expectation Correction for Smoothed Inference in Switched Linear Dynamical Systems, Journal of Machine Learning Research, (2006)

[5] A. R. Runalls, Kullback-Leibler Approach to Gaussian Mixture Reduction, IEEE Transactions on Aerospace and Electronic Systems, 43, (2007), doi: 10.1109/TAES.2007.4383588

DOI 10.5162/SMSI2021/D3.4

The analysis and correction of transfer function of film measuring transducers of the microwave power

Igor Zakharov[1,2], Pavel Neyezhmakov[1]
[1]National Scientific Centre "Institute of Metrology", 42, Myronosytska str., 61002, Kharkiv, Ukraine
[2]Kharkiv National University of Radioelectronics, 14, Nauky ave., 61166, Kharkiv, Ukraine
E-mail (Igor Zakharov) newzip@ukr.net.

Summary:
Results of determination of transient response of film thermoelectric measuring transducer of the microwave power are stated. On the basis of the analysis of their transfer function synthesis of the correctional device is made, allowing to reduce inertial properties of the transducer by three orders.

Keywords: film thermoelectric transducer, transient response, transfer function, correction, correctional device

Introduction

For measuring microwave power, film thermoelectric measuring transducers (FMT) are widely used. The advantages of FMT include high sensitivity, independence of readings from ambient temperature, and the ability to calibrate with low frequency alternating current. A considerable drawback of FMT is their significant inertia (15-20 ms), which prevents their use for dynamic measurements of microwave power. The problem of reducing the inertia of measuring transducers is most effectively solved by applying methods of electrical correction of their dynamic characteristics. To implement the corrective device, it is necessary to conduct a detailed analysis of the dynamic characteristics, which have a number of features.

Transient response of FMT

The experimental determination of the transient response (TR) of the microwave FMT was carried out on the basis of the method [1] of step-by-step measurement of TR by feeding power pulses with decreasing duration to the FMT input with an inversely proportional increase in their amplitude. This provided an increase in the signal-to-noise ratio during measurements in the initial sections of the TR. The instantaneous values of the FMT output signal were measured with a stroboscopic transducer. The processing of the measurement results was reduced to the normalization of TR in different areas. The identification of the normalized TP was carried out by the sequential logarithm method [2].

The identification of the FMT transient response showed that it is well described by the sum of 3 exponentials with positive coefficients A_i $(\sum_{i=1}^{3} A_i = 1)$:

$$h(t) = 1 - \sum_{i=1}^{3} A_i e^{-\frac{t}{\tau_i}}, \qquad (1)$$

where $\tau_i > \tau_{i+1}$ are the time constants of the FMT.

Analysis of FMT transfer function

The transition characteristic (1) corresponds to the transfer function

$$H_{FTP}(s) = \sum_{i=1}^{3} \frac{A_i}{\tau_i s + 1}. \qquad (2)$$

As a result of studying the structure of the FTP transfer function, its following regularities were determined:

1) the FTP transfer function of the form (2) at has 3 real negative poles $-\frac{1}{\tau_i}$ and 2 real negative zeros $-\frac{1}{\alpha_i}$;

2) the zeros of the FTP transfer function are located between its poles, and there is one zero between two adjacent poles:

$$-\frac{1}{\alpha_i} \in \left(-\frac{1}{\tau_{i+1}}; -\frac{1}{\tau_i}\right), i = 0,1,2..$$

Based on the revealed patterns, the transfer function of the FTP can be written in the following form:

$$H_{\Pi}(s)=\frac{(\alpha_1 s+1)(\alpha_2 s+1)}{(\tau_1 s+1)(\tau_2 s+1)(\tau_3 s+1)}, \quad (3)$$

where $\alpha_i \in (\tau_{i-1};\tau_i)$.

The values α_1, α_2 can be found from the following system of equations:

$$\begin{cases} \alpha_1\alpha_2 = A_1\tau_2\tau_3 + A_2\tau_1\tau_3 + A_3\tau_1\tau_2 \\ \alpha_1+\alpha_2 = A_1(\tau_2+\tau_3)+A_2(\tau_1+\tau_3)+A_3(\tau_1+\tau_2). \end{cases}$$

Correction device synthesis

With sequential correction in the basis of the first-order aperiodic link with a time constant τ_b, it is possible to write for the investigated FTP:

$$H_{CD}(s)=\frac{k_b}{\tau_b s+1}\cdot\frac{(\tau_1 s+1)(\tau_2+1)(\tau_3 s+1)}{(\alpha_1 s+1)(\alpha_2 s+1)} \quad (4)$$

Assuming that $\tau_b=\tau_3$, we get:

$$H_{CD}(s)=k_b\frac{(\tau_1 s+1)(\tau_2 s+1)}{(\alpha_1 s+1)(\alpha_2 s+1)}. \quad \textbf{(5)}$$

Considering that $\alpha_i \in (\tau_{i-1};\tau_i)$ it can be concluded that the structure of the correcting device (CD) with a transfer characteristic of the form (5) is 2 sequentially connected simplest corrective links with a correction factor $k_{ci}=\frac{\tau_i}{\alpha_i}$ and a time constant τ_i [3].

Thus, the static conversion factor of the synthesized CD when it is implemented in the specified form on passive elements will be equal to

$$k_b=\frac{\alpha_1\alpha_2}{\tau_1\tau_2}, \quad (6)$$

and the correction factor is determined by the expression

$$k_c=\frac{\tau_1}{\tau_3}. \quad (7)$$

The coefficient of transformation of the CD is calculated by the formula

$$k_0=\tau_3\sum_{i=1}^{3}\frac{A_i}{\tau_i} \quad (8)$$

The value of the conversion coefficients can vary from $\frac{\tau_3}{\tau_1}$ (at $A_1 = 1$, $A_1 = A_2 = A_3 = 0$, i.e., for a transducer without films) to 1 (at $A_3=1$, $A_1 = A_2 = 0$). Therefore, for any positive A_i, $k_0^{-1} < k_c$.

Thus, the correction of the FTP with the largest time constant τ_1 in the basis of the first-order aperiodic link with a time constant τ_n with equal correction coefficients (the smallest time constant of the FTP) compared to the correction of the first-order aperiodic transformer with a time constant τ_1 with equal coefficients correction, gives a gain in the amplitude of the output signal in

$$r_n=\tau_3\sum_{i=1}^{3}\frac{A_i}{\tau_i} \quad (9)$$

time.

For the FTP investigated in subsection 1 of the article with the parameters indicated in Table 1, the gain in signal amplitude will be 20.4 times, i.e. with a decrease in the result of the correction of the FTP time constant by 1000 times, its output signal will decrease only by 49 times.

Conclusion

1. As a result of the study of the structure of the transfer function of the FTP, the following regularities were determined:

- the transfer function of the FTP has 3 real negative poles and a 2 real negative zeros;
- the zeros of the FTP transfer function are located between its poles,
- there is only one zero between two adjacent poles.

2. As a result of the implementation of the sequential correction, the model of the corrected FTP is the aperiodic link of the first order, which is equivalent to lowering the order of its differential equation to 1. In this case, the time constant of the corrected FTP is equal to the smallest time constant of the uncorrected FTP, which is 3 less than its maximum time constant, and the amplitude of the output signal (and the signal-to-noise ratio) decreases only by 49 times.

References

[1] I.P. Zakharov. Method for determining the normalized transient response of a microwave power converter. A.C. SSSR No. 1651243, B.I. No. 19, 1991. (In Russian).

[2] I.P. Zakharov, M.P. Serhiienko. Determination of dynamic characteristics of measuring instruments. Kharkov, NURE, 2019, 210 p. (In Ukrainian).

[3] V.E. Shukshunov Corrective links in devices for measuring non-stationary temperatures. Moscow, Energiya, 1970, 120 p. (In Russian).

DOI 10.5162/SMSI2021/D3.5

Development of a Low-Cost Sensing Node with Active Ventilation Fan for Air Pollution Monitoring

Nicolas P. Winkler[1], Patrick P. Neumann[1], Harald Kohlhoff[1], Jessica Erdmann[1], Erik Schaffernicht[2], Achim J. Lilienthal[2]
[1] Bundesanstalt für Materialforschung und -prüfung, Unter den Eichen 87, 12205 Berlin, Germany
[2] Örebro University, SE-701 82 Örebro, Sweden
Contact e-mail address: mro@bam.de

Summary:
A fully designed low-cost sensing node for air pollution monitoring and calibration results for several low-cost gas sensors are presented. As the state of the art is lacking information on the importance of an active ventilation system, the effect of an active fan is compared to the passive ventilation of a lamellar structured casing. Measurements obtained in an urban outdoor environment show that readings of the low-cost dust sensor (Sharp GP2Y1010AU0F) are distorted by the active ventilation system. While this behavior requires further research, a correlation with temperature and humidity inside the node shown.

Keywords: wireless sensing node, low-cost, air pollution, sensor network, occupational health

Background and Motivation

Air pollution is the biggest environmental health risk in the European Union (EU). It is estimated that 400,000 premature deaths are caused by air pollutants per year. The EU aims to reduce this number by 52% by 2030 compared to 2005 [1]. Especially in industrial environments, where workers are exposed to airborne by-products, continuous monitoring is crucial to develop and comply with occupational health standards.

Rapid developments in sensor technology enable new and cost-efficient possibilities for long-term monitoring of air parameters. A concept that combines the advantages of stationary low-cost and mobile high-quality sensors in one system was proposed in [2] and is the objective of the research project “Robot-assisted Environmental Monitoring for Air Quality Assessment in Industrial Scenarios” (RASEM).

Related Work

Although many approaches and projects aim to leverage low-cost devices for a next-generation air pollution monitoring system, research shows that state-of-the-art devices cannot replace traditional reference monitoring stations, because they lack accuracy and require extensive calibration in laboratory and field [3][4][5].

Hardware platforms used by other researchers were analyzed and compared in [6]. An Arduino microcontroller with similar low-cost sensors used in this project has been used for dense pollution monitoring in foundries [7]. While previous research papers focus on the performance of specific sensors (e.g., [4]) or ready-to-buy-solutions (e.g., [3]), there is little information on the overall manufactured design (e.g., casing) or how important an active ventilation system is.

Sensing Node Setup

Compared to the state of the art, this sensing node includes a fan for active ventilation. The sensors are sheltered by a commercially available weather protective casing, which enables passive ventilation through its lamellar structure.

The Arduino framework is used, which comes with a high variety of available software libraries. An ESP32 microcontroller (Espressif ESP32-DevKitC-32U), which is compatible with Arduino, a real-time clock (Adafruit DS3231), and a micro SD breakout board (Adafruit MicroSD) are housed in a 3D-printed casing at the bottom of the sensing node. Data is transmitted via antenna and WLAN to a central server unit.

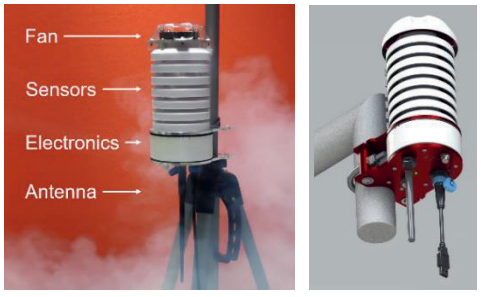

Fig. 1: Left: Sensing node during tests with a fog machine. Right: 3D rendering of a sensing node.

Environmental Sensors

A. DHT22 Temperature & Humidity Sensor

An Adafruit AM2302 is used, which is a wired DHT22 temperature and humidity sensor.

According to the datasheet, operating ranges (and accuracies) are -40 to 80 °C (± 0.5 °C) for temperature and 0 to 100% (± 2%) for relative humidity, however [4] indicates that the error for humidity readings is up to 5%.

B. WaveShare Dust Sensor

This *WaveShare* dust sensor board is a Sharp GP2Y1010AU0F optical dust sensor with resistors on board. The manufacturer specifies the measurement range with up to 500 $\mu g/m^3$, however, previous research by [5] shows that the sensor signal outputs are not well correlated to the mass concentration. To adapt the sensor board to the ESP32's analog-to-digital converter, the existing resistors are changed to increase the maximum sensor output to 1.1 V.

C. SPEC Digital Gas Sensor

The digital gas sensor module by SPEC Sensors can be used with different electrochemical sensors. 8 CO and 16 Indoor Air Quality (IAQ, CO-calibrated) are three-point calibrated with dry reference gases at room temperature (Fig. 2).

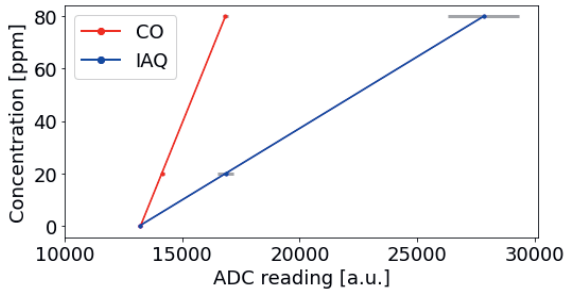

Fig. 2: Three-point calibration results with standard deviation σ and fitted function ax + b (CO: a= 0.0222, b= -293.8; IAQ: a =0.0055, b= -72.3).

Influence of Active Ventilation

All sensors are sampled directly before and after a two-second runtime of the fan (measurement period = 30 s). Fig. 3 shows the dust sensor readings of three consecutive days in an urban outdoor environment in Berlin-Lichterfelde in early June 2020. The sensor readings taken directly after the fan runtime suffer from noticeably high variance. This effect correlates with the temperature and humidity measurements inside the node. According to external weather data, the first day was cloudy, whereas the following two days were mostly sunny. Probably, the sun heats the casing, which leads to distorted sensor measurements. This is also indicated by the recurrent drop in temperature in the afternoon, which is most likely caused by the neighboring building shadowing the sensing node. The calculated global Pearson correlation coefficient r is $r = 0.28$ (dust and temperature), $r = 0.012$ (dust and humidity) and $r = -0.79$ (temperature and humidity). An influence of the fan on the other sensors is not visible.

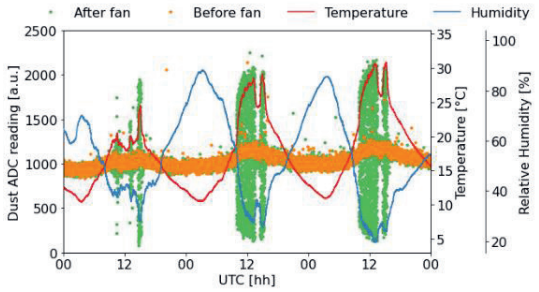

Fig. 3: Three days of dust and temperature sensor readings. Variance in dust samplings correlates with the temperature inside the sensing node.

Conclusion

More investigations are needed to explain and verify the influence of an active fan on dust sensor readings. Future experiments will investigate how this effect diminishes after turning off the fan. Apart from that, further research may identify how low-cost sensors can support traditional reference sensors for environmental monitoring.

Acknowledgment

The authors express their gratitude to SAFЄRA for funding the project in the scope of the 2018 joint call and thank the involved colleagues from the Finnish Institute for Occupational Health.

References

[1] European Union, *A Clean Air Programme for Europe (COM(2013) 918 final)*, (2013);

[2] N.P. Winkler, P.P. Neumann, A. Säämänen, E. Schaffernicht, A.J. Lilienthal, High-quality meets low-cost: Approaches for hybrid-mobility sensor networks, *Materials Today: Proceedings* 32, 250-253 (2020); doi: 10.1016/j.matpr.2020.05.799

[3] N. Castell et al., Can commercial low-cost sensor platforms contribute to air quality monitoring and exposure estimates?, *Environment International* 99, 293-302 (2017); doi: 10.1016/j.envint.2016.12.007.

[4] T. Araújo, L. Silva, A. Moreira, Evaluation of Low-Cost Sensors for Weather and Carbon Dioxide Monitoring in Internet of Things Context, *IoT* 1, 286-308 (2020), doi: 10.3390/iot1020017

[5] J. Li, P. Biswas, Optical Characterization Studies of a Low-Cost Particle Sensor, *Aerosol and Air Quality Research* 17 7, 1691–1704 (2017); doi: 10.4209/aaqr.2017.02.0085

[6] F. Karray, M.W. Jmal, A. Garcia-Ortiz, M. Abid, A.M. Obeid, A comprehensive survey on wireless sensor node hardware platforms, *Computer Networks* 144, 89-110 (2018), doi: 10.1016/j.comnet.2018.05.010

[7] V.H. Bennetts et al., Towards occupational health improvement in foundries through dense dust and pollution monitoring using a complementary approach with mobile and stationary sensing nodes, *2016 IEEE/RSJ International Conference on Intelligent Robots and Systems (IROS)*, 131–36 (2016); doi: 10.1109/IROS.2016.7759045

DOI 10.5162/SMSI2021/D5.1

Image-Based Predictive Maintenance Concept for Inkjet Printing of Ceramic Inks

Peter Bischoff[1], Christoph Zeh[1], Christoph Kroh[2], Christiane Schuster[1], Thomas Härtling[1,3]
[1] Fraunhofer Institute for Ceramic Technologies and Systems IKTS, Maria-Reiche-Str. 2, 01109 Dresden, Germany,
[2] Senodis Technologies GmbH, Manfred-von-Ardenne-Ring 20D, 01109 Dresden, Germany,
[3] Technische Universität Dresden, Institute of Solid State Electronics, Mommsenstraße 15, 01069 Dresden, Germany
peter.bischoff@ikts.fraunhofer.de

Summary:
Ceramic inks can be used to mark metal sheets in hot forming for track-and-trace purposes. However, the ceramic pigments in the inks can lead to clogging of printer nozzles which results in loss of print quality. Here we report on a predictive maintenance concept including different machine- and deep-learning models as the basis of a print quality assurance strategy. Pixelwise image segmentation leads to detailed information about the printing results. The information is used to train a model, classifying the remaining useful lifetime until insufficient printing results.

Keywords: predictive maintenance, machine learning, inkjet printing, ceramic pigments, image analysis

Introduction

By printing individual part markings (e.g. data matrix codes) on metal sheets as a first step in production, continuous tracking and tracing of all produced components can be achieved. A ceramic ink enables part marking in production environments where conventional marking methods are not appliable, e.g. in hot forming. Ceramic particles are added to the ink to ensure code readability after heating the metal sheets to temperatures up to 1200° C, which is necessary for the forming process.

Due to the solid particles in the ink, several problems occur in the printing process. During long-term printing particles accumulate around the edges of the printing nozzles, affecting the inkjet. This leads to degrading printing quality and ultimately to non-readable part markings. At a testing station set up at Fraunhofer IKTS long-term testing is performed by regularly printing a test pattern. Typical printing faults observed are missing droplets in the printed test grid, large deviations compared to the desired printing position of the droplets, and the ejection of too little ink volume resulting in small and hardly visible droplets after heating the metal sheets. Currently no concept for detecting these flaws, especially in their early stages, exists, hence no automatic maintenance to restore the initial printer conditions can be performed. To address this challenge we implemented machine-learning methods and algorithms to quantify the state of the printer and to train a model which is able to reliably predict the remaining-useful-lifetime (RUL) until the quality of the printing results are not sufficient, i.e. not readable, any more.

Methods

To receive reliable data from images taken of the printed test pattern at the test station an image-segmentation model is implemented. The model is based upon the U-Net architecture and reduced in size of the output feature maps from the convolutional layers compared to the original architecture [1]. Dropout layers as well as batch normalization layers are added to stabilize the training. The model is trained on a dataset of 30 labeled images which are augmented seven times. Weighted masks for computing the loss are used to compensate for the imbalance of ink pixels vs. background pixels. The output mask computed by the model can be evaluated in terms of, e.g., drop positions, size, and shape.

The image data as well as other existing sensor data is analyzed to define an indicator of the printhead's condition. This indicator is predominantly supposed to help identify the correct labels for the training data used to train the RUL classification model. Possible indicators are e.g.

the number of ink-drops which deviate from their supposed position greater than a threshold value.

The RUL classification model uses a single long-short-term memory layer followed by a single fully connected layer. The model input consists of geometric properties for each printed drop and relevant sensor data. The dataset, which consists of 940 samples from seven long-term tests, is reduced through a principal component analysis and randomly divided into a training and test set. A random search for optimal hyperparameters is conducted.

Results

The training process for the image segmentation model clearly converges for both training loss and validation loss. The training process seems to be instable and the model is overfitted since the validation loss is constantly higher than the training loss. Nevertheless, comparing the input images from a test set with the output masks shows that the relevant ink droplets are detected reliably.

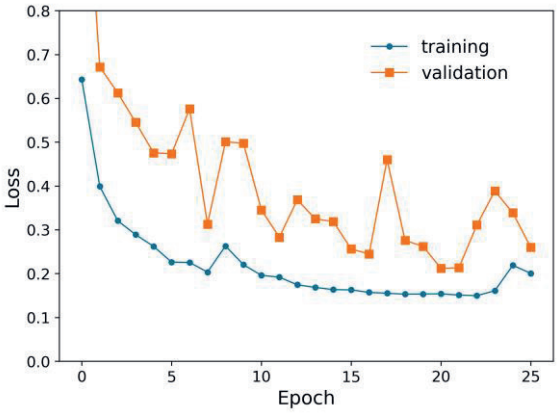

Fig. 1: Training and validation loss over the course of the training process for the image segmentation model.

The features engineered from the resulting information about the ink droplets do not explicitly indicate the time of failure for the printhead. The features often show a time depended increase for a single long-term test but none of the features is applicable to all tests. Therefore, a manual selection of the failure time is conducted to label the long-term-test data as an intermediate solution.

During the training of the RUL prediction model the computed loss converges quickly. Both, training and validation loss are equally low at the minimum after epoch 39. Analyzing the prediction results on the test set of 88 samples show that only two samples are wrongly classified. Furthermore, it shows that the wrongly classified samples are samples from the corresponding neighbor class, e.g. a sample from the class “300 min >= RUL > 200 min” is classified to the class “480 min >= RUL > 300 min”. The prediction therefore seems to be not random for the misclassified samples.

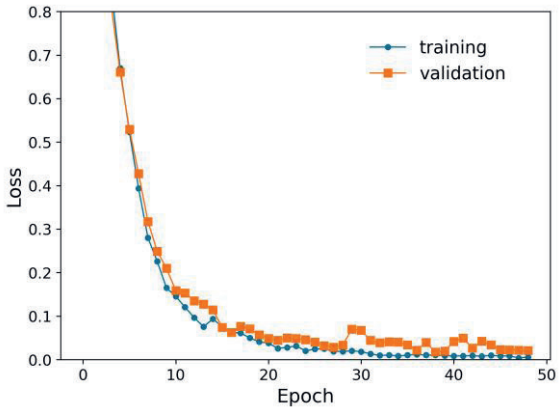

Fig. 2: Training and validation loss for the RUL-prediction model with LSTM cells.

Discussion

Our results show that the developed concept is suitable to predict printing failure eight hours in advance with high accuracy. The occurring of overfitting during the training of the U-Net model is likely caused by the model complexity. Since the segmentation task should be relatively easy to achieve by comparing brightness, the number of trainable parameters in the model can cause problems during the training process. Since the validation loss also shows instability, hyperparameter optimization could help overcome both problems. The model is still able to output relevant and useful data.

Further investigation is needed to find an accurate indicator for labeling the RUL-classification data. Nevertheless, manual labeling seems to be accurate enough to train a classification model. More accurate labels as well as more data could possibly lead to a regression model.

References

[1] O. Ronneberger, P. Fischer, T. Brox, U-Net: Convolutional Networks for Biomedical Image Segmentation, *Medical Image Computing and Computer-Assisted Intervention – MICCAI 2015. Lecture Notes in Computer Science, vol 9351* (2015); doi: 10.1007/978-3-319-24574-4_28.

DOI 10.5162/SMSI2021/D5.2

Use of adaptive learning algorithms in linear position measurement applications

Andreas Voss, Axel Bartos
TE Connectivity Sensors Germany GmbH, Hauert 13, 44227 Dortmund
Andreas.Voss@te.com

Summary:
The advancing digitalization of manufacturing ("smart factories") will create a high demand of position sensors. Besides environmental monitoring, position sensing will play a key role in future production processes. In summary, position measurement needs to become modular and scalable to different sensing dimensions with demanding accuracy requirements. xMR (magneto-resistive) technologies can give answers to achieve adaptive sensor systems under the objective of finding an optimum application solution in terms of performance, size and price.

Keywords: magneto-resistive, linear measurement, adaptive learning, contactless, sensor array

The system point of view

Designed as a miniaturized sensor system, position sensors must be as simple as possible due to customer acceptance and yet cover many requirements in terms of measuring distance, accuracy and performance. Although by definition, magnets are part of the measurement system, the sensor should work with existing magnets. For this purpose, an adaptive learning algorithm at the end of the line test (EOL) or during commissioning at the customer site is required. Miniaturization can be achieved by integration (MR sensor + ASIC) or by a new technological approach, which makes it possible to save measuring points and thus sensors, while achieving the desired measurement accuracy. Tunnel magneto resistive (TMR) technology [1] promises this simplification, since complex signal amplification can be omitted, and the technology is ready for direct chip-integration on ASICs.

Methodology of magnet movement measurement

Moving a permanent magnet on a linear path along an xMR [2][3] sensor establishes a characteristic output curve which can be used for a determination of the magnet position. Fig. 1 shows all three components of the magnetic field created by a magnet moving parallel to the z-axis with a certain distance ***d*** of the magnet to the sensor in y-direction. It stands out, that the y-component will be a good choice to use for a position determination, as it is continuous and free of singularity from its maximum to minimum. Using a simple Look-Up-Table (LUT) approach will solve the position mapping for different magnet-shapes (∅, ***h***) and distances between sensor and magnet.

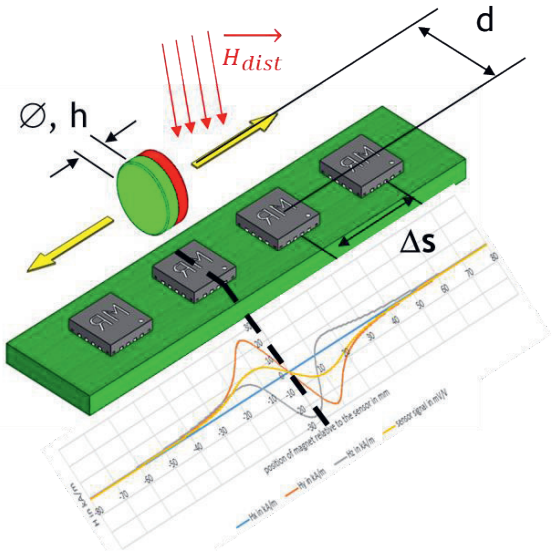

Fig. 1. Characteristic curve of magnet displacement along AMR sensor, y-component with continuous singularity-free function.

Although this single-sensor magnetic mapping only covers a short distance, it forms the basis of an absolute measurement system for the sensing of longer distances by being scalable and adaptable to customer requirements as part of a linear sensor kit [4].

Absolute algorithm approach

The logical next step is the arrangement of a series of sensors (see Fig. 1, distance ***Δs***), which cover the entire magnetic movement.

When implementing an absolute measurement, only a single screenshot of the magnetic field distribution along the sensor array is possible. Now the whole characteristic sensor curve is populated with measurement points – one or two of them are situated in the linear region of the curve - all others are arranged at the left

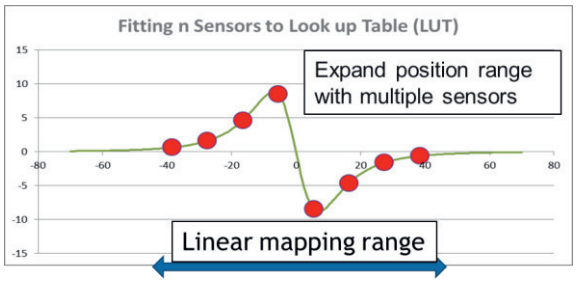

Fig. 2. Expanding range with an array of AMR sensors.

and right section of the curve. A first approach is to find an algorithm, which determines the sensor(s) in the linear region and apply the LUT approach for one sensor described above. A smarter (and more robust) way is to include the available information from all sensors to determine the position. A closer look to Fig. 2 reveals a perfect match of the characteristic curve (green) with the single sensor signals (red dots) which will be the base of the now described procedure:

One algorithm, doing that fitting tas,k is the method of least squares (LS) [5], where the square of distances between all sensor node values ***s(n)*** and correspondent look-up-table values ***LUT[s(n)]*** are summed up to find a local minimum, just where the LUT curve has its best match with the measured ***m*** sensor values as shown in the following formula:

$$Q(\Sigma \rightarrow Min) = Min\left(\sum_{n=1}^{m} \sqrt{\{s(n) - LUT[s(n)]\}^2}\right) \quad (1)$$

Runtime improvements can be achieved by using adaptive weighted averages [6] and golden ratio methods [7], resulting in up to 5 times faster position calculations than using formula (1) in stand-alone mode.

Adaptive LUT learning

Suppose to have a learning system, that can teach itself the LUT for position determination. This is very useful, when a standard sensor system needs to be adapted to a customer's application without HW changes. It requires a learning step with the application magnet, for example during the EOL Test. After the sensor installation, a full-scale movement of the magnet needs to be executed, while the sensor system is in learning mode. A prerequisite for this feature is to ensure that the movement is done with a constant velocity (which results in a constant ***Δd*** in Fig. 3). In this case the LUT learning algorithm can calculate the curve shape autonomously and normalizes the measured data as the real distance ***Δs*** of the sensor elements on the hardware is known by design.

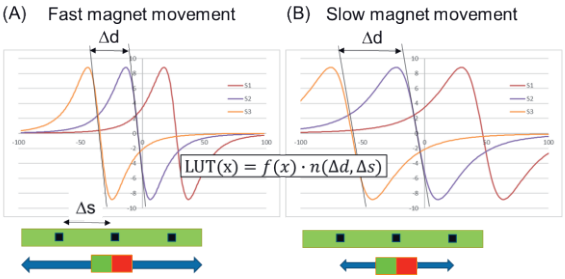

Fig. 3. Fast or slow (constant) magnet movement during learning step lead to real LUT.

A big advantage of this learning step is the possibility to map different magnets and inaccuracies of the magnet system in the LUT, as induced by e.g. slightly magnetic materials in the application housing or piston of hydraulic and pneumatic actuators.

Outlook

Since small sizes often offer an application advantage, sensor technologies are moving into focus which can make their contribution here. TMR will play a key role, as this technology provides an effect amplitude of approx. 1 Vpp at 5 V supply. This allows TMR sensors to be wired directly to the ADC of an MCU or ASIC, opening the door to direct integration of both parts into one component housing. In combination with intelligent bus interfaces [8], the hardware simplification could lead to half of the system space needed today.

The future is found in a combination of intelligent adaptive software approaches to cover platform solutions which in best case could be adapted to a wide range of customer applications by simple customizing.

[1] M. Jullière: Tunneling between ferromagnetic films. In: Physics Letters A. Band 54, 1975, S. 225–226

[2] Thomson, W., “On the electrodynamic qualities of metall: effects on the electric conductivity of nickel and of iron”, Proc. Roy. Soc. London, A8, 1857, S. 546-550

[3] R.Hunt, A Magnetoresistive Readout Transducer, IEEE Transactions on Magnetics 6(1):150 - 154 · April 1971

[4] WO2011160796A3, US20170074715A1

[5] W.Press, S. Teukolsky, W. Vetterling, B. Flannery; Numerical Recipies in C: The Art of Scientific Computing, ISBN 0-521-43108-5, p.671

[6] N. Bronstein, K. A. Semendjajew u. a.: Taschenbuch der Mathematik. 2nd. edition. 1995, ISBN 978-3817120086 p. 629

[7] Florian Jarre, Josef Stoer: Optimierung. Springer, Berlin 2004, ISBN 3-540-43575-1, S. 130 ff.

[8] DE102016002420A1

DOI 10.5162/SMSI2021/D6.1

Topography analysis in the NPMM-200

Emiljano Meta[1], Eberhard Manske[1]
[1] Technische Universität Ilmenau, Institute of Process Measurement and Sensor Technology, Ilmenau, Deutschland
E-Mail: emiljano.meta@tu-ilmenau.de

Abstract:
Using a specially developed combination of phase shifting and image processing algorithms will be performed a specific analysis of relatively rough and unknown surfaces (with or without structures). These algorithms are able to evaluate phase-shifted interference images and calculate topographic data from them. Interference images, which are used for the analysis, are acquired with the help of the high-precision nanopositioning and nano-measuring machine (NPMM-200) of the Technical University of Ilmenau [1, 2].

Keywords: NPMM-200, Topography, edge detection, phase shifting Algorithms, phase unwrapping

Introduction

Today, interferometry is one of the most versatile measurement techniques in high-precision non-contact measurement technology. The computer-aided evaluation, which led to interesting industrial measuring methods, helped to achieve a fast and very accurate optical detection of interference fringes. The electronic evaluation of the optical phase of the interference images can increase the sensitivity and measurement accuracy to fractions of the (average) wavelength of the used light source.

The phase shifting method (PSM) is one of the most accurate methods in the topography analysis. Several phase-shifted interference images are necessary for this purpose.

The measuring object is illuminated with a spectral wide light source. Unlike measuring with coherent radiation, it results in a Gaussian-shaped profile of the spectral intensity due to the spectral width. This is caused by the superposition of the object and reference wave. The phase-shifted interference images are generated while the object is moved in small equidistant steps relative to the interferometer. These are acquired and saved using a camera microscope. From these images, a three-dimensional topography of a measurement object can be calculated and graphically displayed.

Mechanical setup

The following components are necessary for the interferometer to generate interference images in the NPMM-200: *white light source, Mirau objective, camera microscope and a computer* for data acquisition and evaluation.

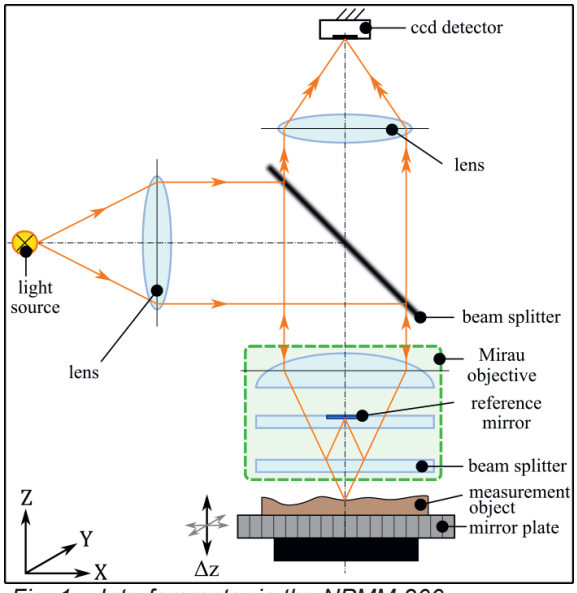

Fig. 1. Interferometer in the NPMM-200

Phase shifting method (PSM)

This is a dynamic spatial phase shifting method [3]. An interference pattern can be described in the two-beam interference arrangement as follows:

$$I = I_0 \cdot \left(1 + \gamma_0 \cdot \cos\left(\phi_0 + \delta\right)\right) \qquad (1)$$

Here, a phase shift of δ = 90° is added between the reference and the measurement object beam, see Figure 2. This is equivalent to a scanning interval of ΔZ = λ/8, see equation (2). For the solution of equation (1) are at least three phase-shifted interference images necessary.

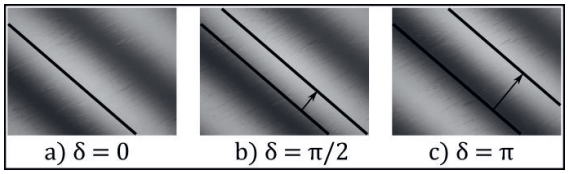

Fig. 2. Phase-shifted interference images

The phase φ_0 contains the information about the optical path difference and the following equation describes the correlation between the two quantities:

$$\frac{\Delta Z}{\lambda/2} = \frac{\phi_0}{2\pi} \Rightarrow \Delta Z = \frac{\pi/2 \cdot \lambda/2}{2\pi} = \frac{\lambda}{8} \quad (2)$$

For the phase analysis is used in this case a so-called 15-step-algorithm, which is relatively robust against small deviations of the phase angle [4]. Therefore, it is necessary to generate (at least) 15 interference images. The more images are used in the analysis, the better will be the result. However, the only disadvantage of this method is that only polished surfaces (e.g. mirror surfaces) can be analysed, which do not contain edges (e.g. in the case of studs). Edges or steps on the measuring object surface lead to phase jumps. If these are higher (lower) than π (-π), they cannot be clearly identified. In order to overcome this limitation, it will be attempted to detect and extract the different surface areas from the structural surfaces. Special edge detection algorithms are very important.

Furthermore, to avoid discontinuities and to fulfil Nyquist's sampling theorem, an interference fringe should cover at least two pixels on the detector.

Edge detection

The edge detection algorithms contribute to the detection and automatic selection of the individual surface areas of a structural surface, see figure 3.

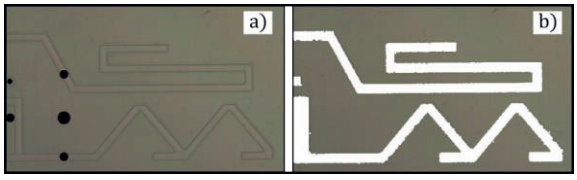

Fig. 3. Edge detection and selection of surface areas

In a first step, only the large area part of figure 3 a) is selected and then evaluated using the PSM algorithm, see figure 3 b). Phase jumps occur, which will have to be corrected, see figure 4 a).

All other surface areas that are shown in figure 3 a) (marked with black dots) are saved as objects and then evaluated one by one.

Phase unwrapping

For relatively complicated structural surfaces, phase jumps can also occur that are quite difficult to unfold, see figure 4 a). For this purpose, there are specially developed algorithms that perform phase unwrapping in two dimensions, see figure 4 b) and c).

Results

The result from the edge detection, phase shifting method and 2D phase unwrapping is shown in the next figure (d)).

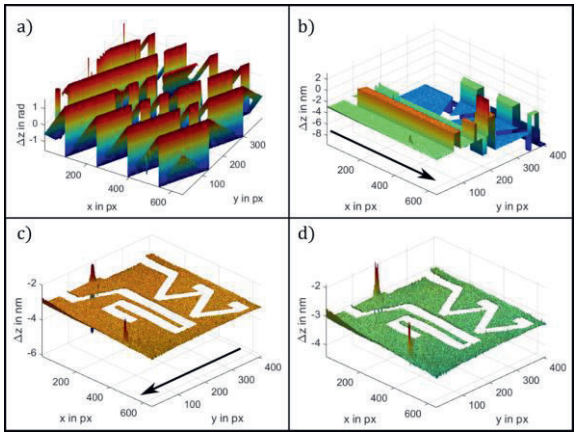

Fig. 4. Phase unwrapping and final result

The height differences of the structure shown above were successfully measured. This has been achieved by direct implementation of the 15-step and 2D phase-unwrapping algorithm without data smoothing, windowing or manual intervention. This would not have been easily possible with conventional phase-unwrapping algorithms.

References

[1] G Jäger; E Manske; T Hausotte; A Müller; F Balzer, Nanopositioning and nanomeasuring machine NPMM-200—a new powerful tool for large-range micro- and nanotechnology, *Surf. Topogr.: Metrol. Prop. (Surface Topography: Metrology and Properties)*, doi: 10.1088/2051-672X/4/3/034004

[2] NPMM-200, Nanopositionier- und Nanomessmaschine, Technische Universität Ilmenau, Link: https://www.tu-ilmenau.de/sfb622/transfer-und-verbundprojekt-npmm-200/zielstellung/

[3] H.J. Tiziani, Rechnerunterstützte Laser-Meßtechnik/ Computer aided laser measurement techniques, *tm - Technisches Messen*, 221-223; doi: 10.1524/teme.1987.54.6.221

[4] P. D. Groot, 101-frame algorithm for phase-shifting interferometry; doi: 10.1117/12.28

DOI 10.5162/SMSI2021/D6.2

Sensor and Measurement Science International
3 – 6 May 2021, Nuremberg, Germany

MECHANICAL DESIGN OF A NEW DYNAMIC FORCE TRANSFER STANDARD

Saher R. Hassan[1]/Presenter, C. Schlegel[2], R. Kumme[3], R. Tutsch[4]

[1] Physikalisch-Technische Bundesanstalt, Bundesallee, Braunschweig, Germany, saher.r.hassan@ptb.de
[2] Physikalisch-Technische Bundesanstalt, Bundesallee, Braunschweig, Germany, christian.schlegel@ptb.de
[3] Physikalisch-Technische Bundesanstalt, Bundesallee, Braunschweig, Germany, rolf.kumme@ptb.de
[4] TU Braunschweig, Institut für Produktionsmesstechnik, Braunschweig, Germany, r.tutsch@tu-bs.de

Abstract:
This paper describes the development of a new modular dynamic transfer standard for measurement of force and acceleration in the field of dynamic force metrology. The force measurement concept depends on a strain gauge based shear-type force measuring instrument. The acceleration is measured using an installed reference standard accelerometer to the longitudinal axis of the force measuring instrument. The transfer standard is traceable to the primary dynamic force and acceleration standards at PTB.

Keywords: Dynamic force; Transfer standard; Force metrology

1. INTRODUCTION

The idea is to develop a transfer standard to provide the traceability for dynamic force measurement (e.g. fatigue testing machines). The recent experience in dynamic force metrology shows the need to provide a transfer standard in the range of about 20 kN. The stiffness of the sample that are used to test the dynamic properties of metallic materials are in the range between 1.5 to 5.5×10^5 N/mm.

2. DESCRIPTION OF THE WORK

There are many concepts to design a force transducer. The most stable principle for dynamic and static applications is strain gauge based force transducers [1]. The measuring of strain depends on the type of application of force. We can measure using simple cylinder, bending or shear beam. The reason why shear beam design was selected is that the stiffness of the sensor can be changed with fixation of its force capacity.

1. Design of the elastic element

If a simple beam with rectangular cross section loaded under force F, the position of all points on the beam surface will be changed due to straining. The strain along the longitudinal axis is called normal strain ε, and the strain in beam inclination is called the shear strain γ. The strain causes normal and shear stresses (σ & τ) inside the beam body. The shear stress can be calculated from

$$\tau = \frac{F}{2 \cdot I}\left(\frac{h^2}{4} - y^2\right). \quad (1)$$

At the maximum shear stress plane with zero normal stress, the principal stress which is a pure normal stress can be measured on a 45° inclined plane to the neutral axis of the shear beam which is called the principal plane. At the principal plane, the principal strain is half of the maximum shear strain and the principal stress has the same value as the maximum shear strain. The applied force can then be estimated from

$$F = \frac{2 \cdot \varepsilon_{1,2} \cdot E \cdot b \cdot h}{\frac{3}{2}2(1+\nu)}. \quad (2)$$

Principal strain measured by strain gauge

$$\varepsilon_{1,2} = \pm\frac{\frac{3}{2} \cdot F \cdot (1+\nu)}{E \cdot b \cdot h}. \quad (3)$$

Principal stress that used as an allowable stress in the design process is calculated from

$$\sigma_{1,2} = \pm\frac{\frac{3}{2} \cdot F}{b \cdot h}. \quad (4)$$

The stiffness equation used to optimize the dynamic properties of the force transducer is

$$K = \frac{E \cdot b \cdot h^3}{4 \cdot l^3}. \quad (5)$$

While there is a dependence of the force capacity F on the third order of shear beam height h also there is a dependence of the stiffness on the third order of shear beam height which provides the ability to increase the stiffness with the same force capacity and vice versa. In the calibration of the fatigue testing machine [2], there is a need to control the stiffness of the reference force transducer for the same type of testing machine to simulate a certain type of testing specimens.

The mechanical design of the elastic element is performed in such a way so that the strain distribution over the area of the strain gauges is uniform without any peaks or strain gradients. There

is no area on the elastic element with a higher strain than the strain gauge area. In addition, the fatigue life; which is a critical criterion in the design of dynamic force transducer for periodic forces; is consequently related to the strain level. Generally, the change in resistance of the strain gauge is related to the mean value of the strain under the area of the measurement grid, but the fatigue life is given by the maximum strain along this area [3-4].

2. Acceleration Measurement

A modular acceleration measuring system was then developed to provide the compensation of inertial errors, the inertial error is thus created only by the acceleration of the masses that are applied to the force sensing element which is called top mass. The error can be calculated by measurement of the top mass and the acceleration of this mass which is measured using the accelerometer. For calibration of the acceleration compensation system, the accelerometer can in principle be recalibrated using primary methods independent of the force transducer.

A system therefore built to compensate the inertial error. Three Kistler reference standard accelerometers type 8002K were mounted as follows; one accelerometer is mounted axially to the load string at the sensing element to measure the acceleration of the top mass of the force transducer. The other two accelerometers are mounted at the base plate of the force transducer to measure the acceleration of the base mass of the force transducer. The mounting of two axial displaced accelerometers enable the measurement of alignment error during dynamic force measurement. The cables are led out through drilled holes in the outer hub of the force transducer. The outputs of the three accelerometers were amplified using a Bruel & Kjaer Nexus charge amplifier which provides an analog voltage output that can be read by many controllers. This enables an online compensation of the force transducer output in the real application, if this is desired. Traceability of the acceleration measurement is achieved by calibration of the accelerometers against the PTB primary standard according to the calibration standard ISO 16063-11:1999, this calibration can be easily repeated as a result of the modular attachment of the accelerometers mounting. The three accelerometers were mounted using electrically isolated stud plates at the force transducer with 2 N·m tightening torque.

ACKNOWLEDGEMENTS

The authors would like to acknowledge the funding of the joint research project 18SIB08 ComTraForce. This project has received funding from the EMPIR programme, which is co-financed by the European Union's Horizon 2020 research and innovation programme, and from EMPIR Participating States.

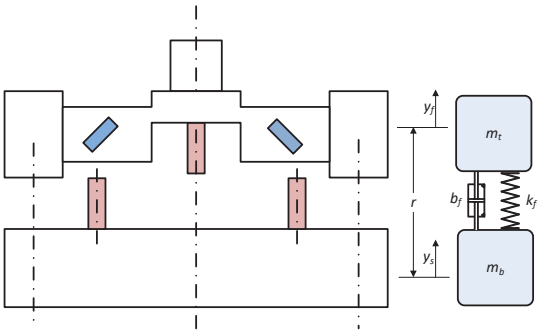

Figure1: Schematic of the force transducer with modular accelerometers to measure the acceleration of the top and base masses of the force transducer. The arrangement of the accelerometers enables the measurement of the alignment during dynamic measurements

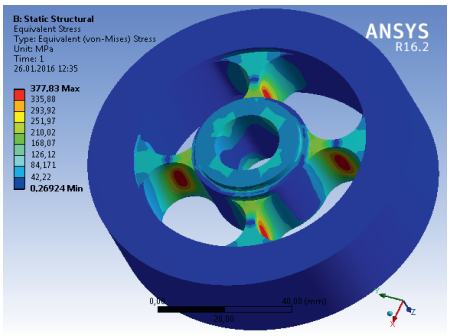

Figure2: Finite element analysis of the sensing element shows von-Mises stresses.

3. SUMMARY

A transfer standard for dynamic measurement of force and acceleration was developed and optimised to provide the traceability chain for dynamic force measurement for metrological services specially for dynamic calibration of material testing machines in the frequency range (from 0 Hz to 2000 Hz).

The dynamic characteristics were investigated to provide a model for the dynamic force measurement in applications with an estimation of the measurement uncertainty.

4. REFERENCES

[1] Kleckers T, "2018 New design for a precise, radially symmetric shear-beam reference sensors for compressive force" J. Phys. Conf. Ser. 1065 042009

[2] Sawla A 1991 "Measurment of dynamic forces and compensation of errors in fatigue testing" Proc. 12th IMEKO World Congress (Beijing, China) pp 5–10A. B. Author, Title of Book. New: IEEE Press, Ch. 6, pp. 23-25, 1992.

[3] Hessling J P 2008 Dynamic calibration of uni-axial material testing machines Mech. Syst. Signal Process. 22 451–66

[4] Dixon M J 1995 Dynamic force measurement Materials Metrology and Standards for Structural Performance (Chapman & Hall (London [u.a.])) pp 55–80

DOI 10.5162/SMSI2021/D6.3

Thermographic Stall Detection Using Model-Based Evaluations of the Surface Temperature Response to Oscillating Fluid Temperatures

Felix Oehme[1], Michael Sorg[1], Andreas Fischer[1]
[1] University of Bremen, Bremen Institute for Metrology, Automation and Quality Science
Linzer Str. 13, 28359, Bremen, Germany
Correspondence: f.oehme@bimaq.de

Summary:
In the operation of wind turbines, flow separation on rotor blades causes performance losses, structural loads and acoustic emissions. To unambiguously detect flow separation using thermographic images despite a low thermal contrast, a model-based signal processing approach is presented. The proposed signal processing approach evaluates the amplitudes of the surface temperature response to oscillating input signals selectively. Due to the direct correlation between the amplitude information and the flow-dependent heat transfer coefficient, an unambiguous detectability of stall is achieved.

Keywords: IR thermography, thermographic boundary layer measurements, flow separation, turbulent flow separation, flow separation on rotor blades

Introduction

Flow separation on rotor blades of wind turbines with pitch control is an undesirable flow state. It causes a decrease of torque producing lift, an increase in drag and acoustic emissions as well as structural loads. A measurement method with the potential to investigate the origin of flow separation on real wind turbines in operation is thermographic flow visualization using infrared light [1]. However, due to the low thermal contrast between turbulent and separated flow regions, the thermographic visualization of flow separation requires measurement conditions with a high temperature difference between the rotor blade surface and the incoming flow. For free field measurements, the available thermal contrast is only based on the absorbed solar radiation. Therefore, a signal processing approach is required which provides a high identifiability for flow separation.

The state-of-the-art signal processing approach for measurements with low thermal contrast evaluates the dynamic change of the surface temperature in thermographic image series [2]. However, the signal measurement chain is not considered, and a distinct evaluation of the influences on the dynamic surface temperature is missing. Thus, designing a model-based signal processing approach which provides a high interpretability for the unambiguous stall detection is an open task.

Therefore, the rotor blade surface response with respect to boundary layer flow characteristics and temporal fluctuations of the heat inputs is modeled using system theory. Based on the system modelling, a harmonic analysis of temporal surface temperature fluctuations around predefined operating points is then derived.

Measurement Principle

The proposed harmonic signal processing approach considers the small-scale oscillations of the surface temperature around an operating point as a thermodynamic response to the oscillating temperature of the incoming flow. The system's input-output relation shows the behavior of a linear time-invariant system and can be evaluated with an analysis of the amplitude attenuation of the output signal for selected frequency components. Here, the amplitude attenuation is a function of the selected frequency, thermal material parameters and the flow-dependent heat transfer coefficient. The resulting analogy between the spatial amplitude distribution and the distribution of the flow-dependent heat transfer coefficient enables a subsequent identification of the different flow regions including stall.

In order to calculate the amplitude of the output signal, a pixelwise discrete Fourier transformation is conducted for thermographic image series. Compared to the classical approach for thermographic flow visualization of evaluating temperature fields, the harmonic signal

processing approach provides a significant reduced influence regarding undesired cross-sensitivities. While the dynamic behavior of the heat inputs is considered as desirable input signal, the undesired influence of heat conduction and the initial rotor blade temperature distribution is reduced by the dynamic behavior of the output signal. As a result, the amplitude information correlates directly with the flow-dependent heat transfer coefficient.

Results

In order to prove the potential of the harmonic signal processing approach, wind tunnel measurements with a wind turbine rotor blade profile and free field similar Reynolds numbers are performed. The location of the different flow states is validated by surface pressure measurements. Fig. 1 shows the processed thermographic image series for the harmonic as well as the mean temperature signal processing approach as reference. Both approaches enable a distinction between the laminar/turbulent and the turbulent/separated flow regions. Compared to the mean temperature approach, the harmonic approach suffers from an increasing variance of the evaluated amplitudes within each flow region as a result of analyzing the small-signal behavior of the surface temperature oscillation as well as the reduced influence of heat conduction. In consequence, the contrast between the different flow regions is reduced, while flow-dependent features are visible.

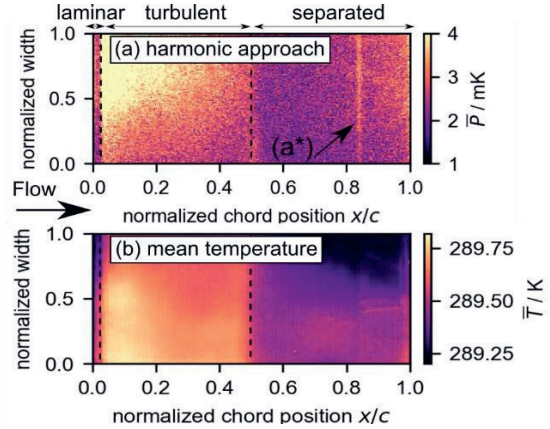

Fig. 1 Processed thermographic image series by the harmonic (a) and the mean temperature signal processing approach (b). (a): Surface modification on the measuring object.*

In order to prove the desired identifiability of flow regions based on flow-dependent features, Fig. 2 shows the expected course of the heat transfer coefficient based on theory (dotted) and experiments (dashed) over the normalized chord position as well as the normal to the flow direction averaged profiles of the presented signal processing approaches. Considering the results of the mean temperature approach, the mean temperature over the normalized chord position shows the expected signal behavior only for the transition regions. Within each flow region, the mean temperature course is mainly influenced by lateral heat conduction, characteristic separation features are not detectable.

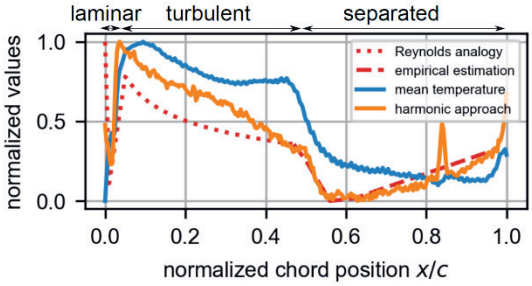

Fig. 2 Comparison of the expected (dotted, dashed) course of the heat transfer coefficient over the chord position and the measured results (solid line) of the mean temperature and the harmonic signal processing approach.

In contrast, the amplitude course of the harmonic approach reflects the theoretical estimations of the Reynolds analogy for the laminar and the turbulent flow region [3]. Inside the laminar and the turbulent flow region, a decreasing amplitude occurs as a result of an increasing boundary layer thickness. Flow separation is unambiguously identifiable based on a global amplitude minimum, a plateau near the separation point and an increasing amplitude inside the separated region. The increasing amplitude and the heat transfer coefficient over the cord position is induced by grown vortices and thus a typical feature for separated flow regions [4].

In conclusion, the proposed harmonic signal processing approach leads to an enhanced identifiability of flow separation.

The authors gratefully acknowledge the financial support of the Deutsche Forschungsgemeinschaft (DFG project number FI1989/5-1)

References

[1] E. Gartenberg, A. S. Roberts Jr., Twenty-five years of aerodynamic research with infrared imaging, Journal of Aircraft 2, 161–171 (1992), doi: 10.2514/3.46140

[2] C. Dollinger, N. Balaresque, M. Sorg; A. Fischer, IR thermographic visualization of flow separation in applications with low thermal contrast, Infrared Physics & Technology, 254-264 (2018), doi: 10.1016/j.infrared.2017.12.001

[3] H. Schlichting, K. Gersten, Boundary-Layer theory, Springer Berlin Heidelberg 9. edition (2017), doi: 10.1007/978-3-662-52919-5

[4] E. Gartenberg, A. S. Roberts Jr., Airfoil transition and separation studies using an infrared imaging system, Journal of Aircraft 4, 225–230 (1991), doi: 10.2514/3.46016

DOI 10.5162/SMSI2021/D6.4

Monitoring Inkjet Printer Condition via Image Analysis of Printed Patterns

Christoph Zeh[1], *Peter Bischoff*[1], *Marek Rjelka*[1], *Christiane Schuster*[1], *Thomas Härtling*[1,2]
[1] *Fraunhofer Institute for Ceramic Technologies and Systems, Maria-Reiche-Str. 2, 01109 Dresden Germany*
[2] *Technische Universität Dresden, Institute of Solid State Electronics, Mommsenstraße 15, 01069 Dresden, Germany*
christoph.zeh@ikts.fraunhofer.de

Summary:
Detailed information on the condition of large-character inkjet printers can be acquired by using intermediate results from standardized matrix code grading. This approach allows monitoring each individual printer nozzle which is of high importance if ceramic inks are used for printing. Inks containing ceramic pigments tend to clog printer nozzles more rapidly which may lead to loss of print quality. In several application areas such as hot metal forming code quality must be guaranteed which can be achieved with the approach reported here.

Keywords: direct part marking, data matrix code, grading, condition monitoring, image analysis

Introduction

Direct Part Marking (DPM) summarizes a variety of technologies to provide digital codes directly onto products or individual components. Each part receives a unique identifier (UID). UIDs and subsequent tracking and tracing of parts are key to industrial digitalization (Industry 4.0). Here, we show how existing code grading standards can be expanded for continuous monitoring of individual printer nozzles and how this provides in-depth information on the printer condition and possible causes for malfunctions.

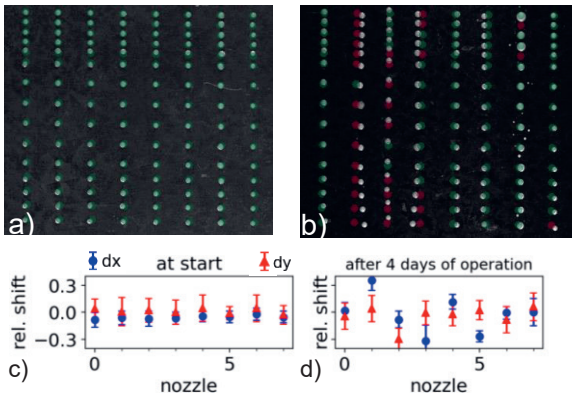

Fig. 1. Printed test-patterns a) initially and b) after 4 days of continuous operation, respectively. Color overlay indicates brightness grading. Correspondingly, c) and d) show mean and SD of position deviations.

Background, Motivation and Objective

Typically, Data Matrix ECC200 or QR codes are chosen to encode UIDs. The fastest DPM-technology in terms of coded parts per time unit is inkjet printing. When selected solid particulate materials (e.g. ceramic pigments) are brought onto the parts via the ink, high-temperature processes like hot forming (metal industry) can be addressed by inkjet technology. A drawback of using non-standard pigment materials and larger particle sizes in the ink formulations is that they can only be applied through rather coarse inject nozzles (≥ 100 µm). Suitable large-character printers are based on electro-magnetic valve technology and typically contain 16 nozzles or multiples thereof. Compared to other printing technologies, larger nozzles cause a significant increase in drop volumes and hence larger drop diameters on the destined substrate surfaces. Since the available area is limited on most product components, there is an upper limit to the matrix code dimensions and consequently a limit on the number of drops that can be used in each dimension (resolution). This means each single drop applied to the component strongly impacts the quality and readability of the resulting matrix codes. Malfunctioning of a single printer nozzle can lead to total quality loss (according to industry standards) and often, but not necessarily, to loss of decodability. Therefore, monitoring the condition of printers is of paramount importance to ensure continuous operation. Existing standards for grading matrix codes provide rules to grade and verify DPM code quality via optical inspection and image analysis. Verifying every single DPM code is common practice in

the industry, so imaging equipment is easily available and could be exploited for further analysis. However, common standards only allow for an overall print quality measure and give limited information on the printer's current condition. In particular, single nozzle malfunctions cannot be measured despite that they have to be avoided and, if possible, predicted long before the print quality is drastically reduced. Therefore, the goal of this work is to define those measures that describe the condition as completely and exact as possible only using image analysis similar to existing standards.

Monitoring gradual nozzle clogging via image analysis

The most common malfunction for inkjet printers is nozzle clogging. This can occur stochastically, going from normal operation to total nozzle blocking in a single operation if large particle agglomerates get stuck in a nozzle. But clogging can also gradually build up through continuous growth of small residue. While the first form of error is hard to predict, the second form of error should be visible in specific features of the printed codes. Gradual clogging will reduce the diameter of the nozzle and hence reduce drop volume. Although, small residue may not hinder ink flow significantly, but rather only lead to subtle changes in the drop flight direction, leading to a change in drop position with respect to the desired position.

ISO 15415 (with ISO TR 29158) provides rules to measure brightness, contrast, and modulation for each cell of a matrix code as interim results before overall grades are determined. Physically, these features mainly correspond to the lateral pigment distribution and their optical properties. Varying surface characteristics of the components, which provide the image background, shall be ignored at this point. Provided the orientation of the printer nozzles with respect to the matrix code is known, brightness and similar features can be attributed to a particular nozzle by selecting the corresponding cells of the matrix code. Via brightness, gradual nozzle clogging is detectable due to a reduction of pigments and due to shift of drop position with respect to the matrix grid which in turn translates to brightness changes at a specific matrix location. Slight positional changes might go unnoticed with this approach (Fig. 1 a, b).

EN 9132 takes position and size of each element in the code matrix into account. These measures relate more directly to the impact of gradual nozzle clogging if intermediate grading results are used to gain nozzle-wise information (Fig. 1 c, d). Noteworthy, drop size measurements can be misleading if changes in brightness or varying substrate conditions are not considered simultaneously. Moreover, drop sizes strongly depend on threshold values to separate foreground and background of the image and can be difficult to interpret if the lateral particle distribution is inhomogeneous. In these cases, AI-driven approaches for segmentation can provide much more reliable results than the purely analytical analysis defined in the grading standards mentioned above. Some of these will be presented in another contribution.

Separating nozzle clogging from other printer malfunctions

Some relevant causes for print quality degradation are ink pressure variations, filter clogging, abrasion, and temperature or humidity changes. Their effects should apply similarly to all printer nozzles. For example, all drop sizes of one printed code change following a slow pressure change, or the brightness of all dots are reduced in case of filter clogging which reduces the ink's solid particle concentration. These effects can be separated from nozzle clogging by comparing mean measures of each nozzle with the overall mean of the matrix code. Temperature has a strong impact on ink viscosity and therefore affects drop break-off from the nozzle and build-up of residues at the nozzle exit. This process will be more subtle, and the size of the effect will differ for each nozzle since it also depends on the latest history of the printer. Therefore, these effects are better described by changes of variance of the quality measures. All measurements introduced above need to be carried out for each printed matrix code and monitored over time. Only then, degradation of the printer condition can be evaluated in a useful manner.

Conclusion and Outlook

In summary, a detailed evaluation of the condition of large-character inkjet printers can be acquired by using intermediate results from existing matrix code grading standards and keeping track of nozzle-correspondence. In the future, the described measures will be used to build robust machine learning models that allow to predict nozzle clogging and other printer malfunctions for predictive and automated printer maintenance.

References

[1] ISO/IEC 15415:2011, Information technology - Automatic identification and data capture techniques - Bar code symbol print quality test specification - Two-dimensional symbols

[2] EN 9132 Aerospace series - Quality management systems - Data Matrix Quality Requirements for Parts Marking

DOI 10.5162/SMSI2021/D8.1

Investigation of a Mitigation Strategy for Thermal Effects of X-ray Sources in Computed Tomography

Felix Binder[1], *Benjamin Baumgärtner*[1], *Tino Hausotte*[1]
[1]*Institute of Manufacturing Metrology (FMT), Friedrich-Alexander-University Erlangen-Nuremberg (FAU),*
felix.binder@fmt.fau.de

Summary:
Computed tomography (CT) is a fast and non-destructive measurement method with an increasing industrial application area that demands powerful X-ray sources. Depending on factors, like the measurement settings, the environmental conditions and the effectiveness of the installed cooling system, the dissipated heat of the X-ray source can influence the measurement. In this contribution a mitigation strategy will be described, which approximates the thermal behaviour of an X-ray source in order to derive a task specific warm-up time that reduces the temperature difference during a CT measurement.

Keywords: computed tomography, temperature effects, mitigation strategy, thermal characterization, X-ray source

Introduction

Dimensional measurements in X-ray computed tomography (CT) are often carried out under stable environmental conditions to disregard temperature changes during a measurement. With increasing power consumption of industrial X-ray sources, it is reasonable to investigate the thermal behaviour of such a component.

However, a complete thermal characterization requires detailed knowledge of all active components, the cooling system, the materials, the geometrical setup and the measurement parameters. The presented approach focuses on an alternative way to approximate the thermal behaviour of an X-ray source in order to calculate a task specific warm-up time Δt_W, which reduces the total temperature difference $\Delta\vartheta$ during the critical part of a CT measurement.

Theory

The majority of the used power to produce X-rays is dissipated as heat into the CT system, which influences the stability of the projected images [1], presumed that the cooling system cannot totally compensate the heat. Furthermore, temperature variations of the X-ray source can cause geometrical displacements [2], which result in translation, rotation and dilation errors of the reconstructed volume [3].

Therefore, it is assumed that a reduction of the total temperature difference $\Delta\vartheta$, caused by the X-ray source, will also reduce geometrical displacements during the measurement. Based on that assumption, an additional warm-up time Δt_W is considered to improve a cold-start measurement procedure as described in Fig. 1.

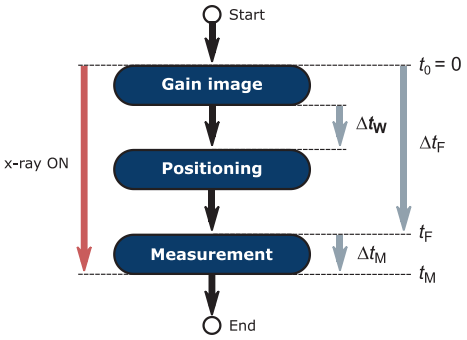

Fig. 1. Cold-start measurement procedure including an additional time Δt_W to warm-up the system.

The gain image acquisition and object positioning phase can be summarized as a pre-heat phase with the duration Δt_F. During this phase, the X-ray tube will heat-up until t_F is reached and the actual thermal sensitive measurement starts for the duration of Δt_M and ends at t_M. Since Δt_W will increase the overall measurement time, but reduces the temperature difference $\Delta\vartheta$, different strategies can be derived to find a task specific optimum.

Experiment

A Pt100 contact sensor, which has been corrected with a calibrated reference thermometer, has been installed on the housing of the X-ray tube, close to the reflection target (tungsten), which is known to be the main heat source of the system. The sensor temperature was logged

every 5 s. The X-ray tube has a peak power consumption of 500 W and is actively water-cooled. Additionally, the tube is indirectly air-cooled by two radiators, that provide ventilation of cooled air from the surrounding measurement room with a set temperature of (20.0 ± 0.2) °C and a relative humidity of (45 ± 10) % RH. A series of measurements, across the operating power range of the X-ray tube have been carried out according to the parameters in Fig. 2.

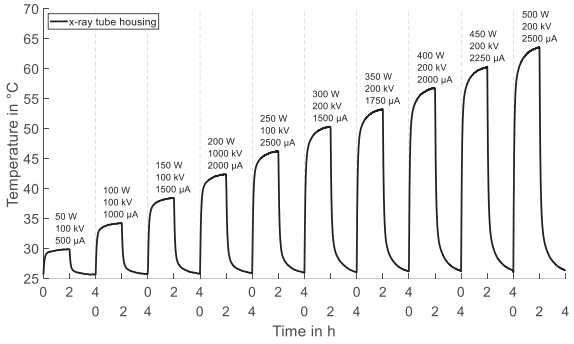

Fig. 2. X-ray tube housing temperature of a measurement series with increasing power consumption.

For the characterization of each measurement, a suitable fit function (1) has been used to approximate the constant t_c.

$$\vartheta(t) \approx \vartheta_0 + \left(\vartheta_{eq} - \vartheta_0\right) \cdot e^{-\frac{t_c}{t}} \quad (1)$$

ϑ_0 denotes the common base temperature of the system and ϑ_{eq} the equilibrium temperature for each measurement. With the determined constants t_c the total temperature difference $\Delta\vartheta$ can be calculated with (2) according to the measurement procedure defined in Fig. 1.

$$\Delta\vartheta = [\vartheta(t_M) - \vartheta(t_F)] - [\vartheta(t'_M) - \vartheta(t'_F)] \quad (2)$$

t'_F and t'_M describe the times on which the preheat and the measurement phase ends, considering an additional warm-up time $\Delta t_W > 0$.

Results

Approximation (1) and equation (2) are used to estimate the total temperature difference $\Delta\vartheta$ for $\Delta t_W \in [0, 500]\,s$ with $\Delta t_F = 230\,s$ and $\Delta t_M = 6300\,s$. Δt_F and Δt_M are task specific values, that depend on the number of gain images, the number of projection images, the integration time of the detector and a CT specific delay (e. g. rotating the axis or image processing). In this case Δt_F and Δt_M were assumed for a precise measurement with 90 gain images, 1500 projection images and a detector integration time of 2000 ms.

The resulting temperature differences $\Delta\vartheta$ for each power setting are summarized in Fig. 3 and show that without an additional warm-up time a significant temperature difference during the measurement still can be expected. Furthermore, the gradient and therefore the optimization potential increases with the power consumption.

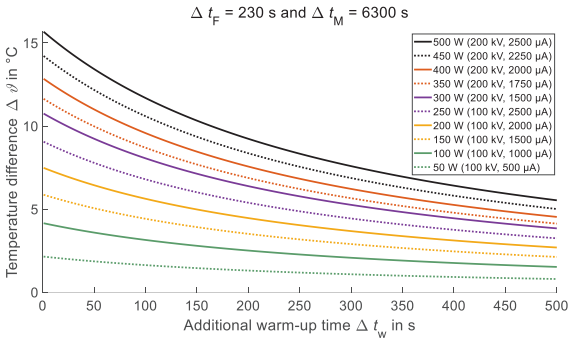

Fig. 3. Temperature differences for each power setting with an additional warm-up time Δt_W.

Conclusion

An investigation has been carried out, which is based on a series of temperature measurements across the operating range of the tube. The logged temperatures can be used to approximate the thermal behaviour of the X-ray source for the given parameter settings.

Even though a pre-heat phase has been considered, the results show that with increasing power consumptions an increasing temperature difference $\Delta\vartheta$ can be expected, which may influence the measurement if uncompensated. Integrating a task specific additional warm-up time Δt_W as a countermeasure, for example by increasing the number of gain images, yields the potential to reduce thermal effects caused by the X-ray source for a small increase of total measurement time.

Acknowledgement

This work is part of the European Metrology Programme for Innovation and Research (EMPIR) project 17IND08 AdvanCT. The EMPIR initiative is co-funded by the European Union's Horizon 2020 research and innovation programme and the EMPIR participating states.

References

[1] W. Sun, S. Brown, N. Flay, M. McCarthy, J. McBride, A reference sample for investigating the stability of the imaging system of x-ray computed tomography, *Measurement Science and Technology 27*, doi: 10.1088/0957-0233/27/8/085004

[2] M. Katic, N. Ferdelji, D. Sestan, Investigation of Temperature-Induced Errors in XCT Metrology, *International Journal of Automation Technology 14*, 484-490 (2020); doi:10.20965/ijat.2020.p0484

[3] N. Limodin, J. Rethore, J. Adrien, J. Y. Buffiere, F. Hild, S. Roux, Analysis and Artifact Correction for Volume Correlation Measurements Using Tomographic Images from a Laboratory X-ray Source, *Experimental Mechanics 51*, 959-970 (2011); doi: https://doi.org/10.1007/s11340-010-9397-4

DOI 10.5162/SMSI2021/D8.2

Influence of Continuous Scan Mode and Workpiece Positioning on Dimensional Measurements with Computed Tomography

Christian Orgeldinger[1], Florian Wohlgemuth[1], Tino Hausotte[1]
[1] Institute of Manufacturing Metrology (FMT),
Friedrich-Alexander-University Erlangen-Nürnberg (FAU), Nägelsbachstraße 25, 91052 Erlangen
florian.wohlgemuth@fmt.fau.de

Summary:
The determination of measurement uncertainties in dimensional X-ray computed tomography measurement technology is a complex task for which many different influences have to be taken into account. This work examines the influence of the scan mode in combination with the number of projections and an eccentric clamping on the quality of the measurement. It shows that the workpiece positioning has a considerable influence on the result in the case of continuous scan mode. In addition, an application-dependent potential for reducing the lead times is described.

Keywords: X-ray computed tomography, measurement uncertainty, scan mode, workpiece positioning, dimensional metrology

Background

Due to the many advantages such as non-destructive testing of internal geometries, X-ray computed tomography (CT) has become increasingly important in recent years [1]. The complex influences on the measurement result are not yet fully understood at this point and therefore require further investigation. While the influence of the focal spot size and detector unsharpness was evaluated in previous studies [2], the aim of this work is to investigate the effects of continuous scan mode on dimensional measurements. So far, the influence of object movements during a single exposure on the resulting deteriorated image quality has only been investigated in medical applications [3]. These investigations are also necessary to decide whether the influence of the continuous scan mode needs to be accounted for when attempting to numerically evaluate measurement uncertainties (compare to [4]).

Theory

While a commonly used CT measurement mode works according to the start-stop principle, the measurement time can be reduced considerably by continuously rotating the turntable at a constant angular velocity. It can be assumed that a continuous movement only leads to a deterioration in the measurement if the movement of an individual projected object point during a single projection leads to an unsharpness that is in the order of magnitude of the detector unsharpness. The following conservative estimate then applies to the minimum number of projections n_{min}:

$$n_{min} = \frac{2\pi \cdot R_{max} \cdot M}{\sigma_D} \qquad (1)$$

R_{max} is the maximum distance of an object point from the centre of rotation and M describes the magnification of the image on the detector. σ_D is the detector unsharpness (compare to [2]).

Experimental Setup

To examine the influence of the measurement strategy, measurements with start-stop scan mode as well as continuous scan mode with centric and eccentric clamping (approximately 20 mm eccentricity) are carried out by using different numbers of projections. The CT system used is a Zeiss Metrotom 1500 (OS version 3.2.4.17214). The number of projections is significantly below the operating software-suggested value of 1400 and thus the CT system is operated outside of its specification. To enable a quantitative comparison, a calibrated test specimen made of aluminum is used (see Fig. 1).

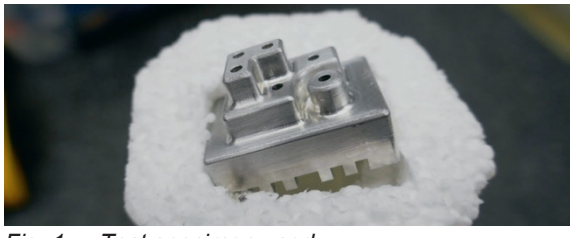

Fig. 1. Test specimen used

The tube was operated at 180 kV / 180 µA and the detector at 1000 ms and 16x gain. 20 measurement repetitions are carried out for each configuration for sufficient statistics. To determine the measurement uncertainty, standard deviations and measurement deviations for 48 lengths, 29 radii and 29 roundnesses are evaluated using Volume Graphics VGStudio Max version 3.4 and MathWorks MATLAB 2018b.

Results

Fig. 2 shows the systematic measurement error (bias) of the distance measurements, Fig. 3 the random measurement error (standard deviation). Both errors display similar behaviour; the random error is a factor of about three of the systematic error. Above 600 projections, continuous and start-stop mode are indistinguishable for centric clamping. Eccentric clamping leads to clearly higher random errors only for the continuous scan mode. The systematic measurement error also slightly increases for the start-stop mode in the case of eccentric clamping and low projection number – the effect for the continuous scan mode is however more pronounced.

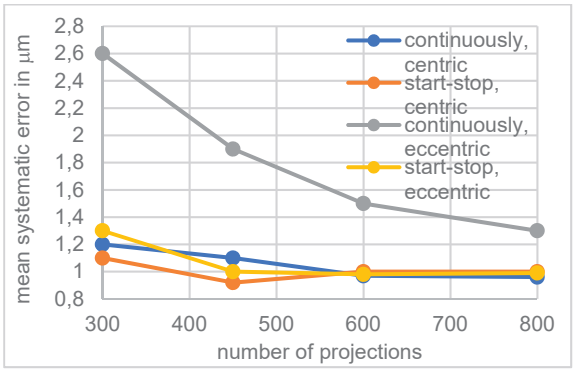

Fig. 2. Systematic error in distance measurements

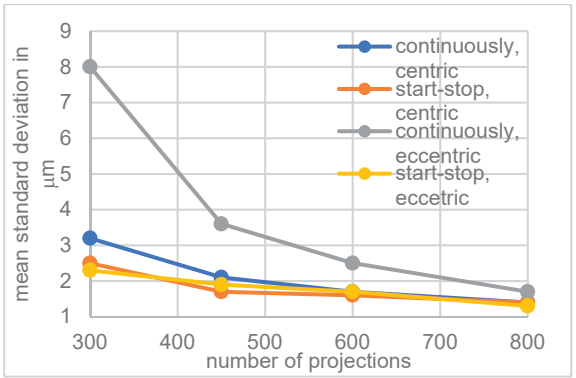

Fig. 3. Random measurement errors (standard deviation) in distance measurements

If the number of projections is very low, the measurement accuracy deteriorates due to the lack of data for the reconstruction. With projection numbers over 800, no additional improvement was achieved in further experiments. While the measurement in the start-stop mode is nearly independent of the clamping position of the workpiece, this significantly influences the measurement values in the continuous mode. With more than 800 projections, the difference in the random error vanishes. This limit value can also be determined for an offset of 20 mm with eq. (1). The differences between the scan modes become significantly smaller with an increasing number of projections, especially for centric clamping. Radius and roundness measurements show a similar behaviour.

Conclusions

Both the number of projections and the rotation axis distance have a decisive influence on the difference between start-stop and continuous scan mode. This is important because both the scan mode and the number of projections have a considerable influence on the measurement time and thus have potential to be optimized in industrial applications. For small and centrally clamped workpieces, for example, the throughput time could be significantly reduced without any major loss of information. In order to be able to estimate the potential, further measurements should be carried out with different offset configurations and suitable measurement objects. The data determined could then in turn be used to improve the simulation of measurement uncertainties. The results show that even outside of specification, the continuous scan mode of the Zeiss Metrotom 1500 can still perform as well as the discontinuous scan mode depending on measurement part, eccentricity and measurand.

Acknowledgement

The authors would like to thank the German Research Foundation (DFG) for the financial support of the acquisition of the CT system Zeiss Metrotom 1500 through Grant No. 324672600.

References

[1] J. P. Kruth, M. Bartscher, S. Carmignato, R. Schmitt, L. De Chiffre, A. Weckenmann, Computed tomography for dimensional metrology, CIRP Annals - Manufacturing Technology 60, 821-842 (2011)

[2] C. Orgeldinger, F. Wohlgemuth, A. M. Müller, T. Hausotte, Spot size and detector unsharpness determination for numerical measurement uncertainty determination, iCT 2019, Padova, Italy

[3] W. Siman, S. C. Kappadath, Comparison of Step-and-Shoot and Continuous-Bed-Motion PET Modes of Acquisition for Limited-View Organ Scans, Journal of nuclear medicine technology 45(4), 290–296 (2017)

[4] F. Wohlgemuth, A. M. Müller, T. Hausotte, Development of a virtual metrological CT for numerical measurement uncertainty determination using aRTist 2, Technisches Messen 85, 728-737 (2018)

DOI 10.5162/SMSI2021/D8.3

Accuracy Improvement of the Alternating Current Zero Potential method for Impedimetric Sensor Matrices

Zheng Hu[1], *Dayu Chen*[1], *Olfa Kanoun*[1]
[1] *Technische Universität Chemnitz, Chemnitz, 09126, Germany*
olfa.kanoun@etit.tu-chemnitz.de

Summary:
In [1], we introduced the alternating current zero potential circuit (AC-ZPC) for two-dimensional resistive sensor matrices, where each matrix row is driven by an individual AC signal at a certain frequency, so that every column can be read separately. This method enables the simultaneous measurement of all sensors in the matrix and dispenses with multiplexers. In this work, a novel calibration method for the AC-ZPC for two-dimensional sensor matrices is proposed, where the measurement deviation caused by the used operational amplifiers has been eliminated. A measurement accuracy improvement has been thereby realized. This novel calibration strategy has been carried out by simulation for matrices of impedimetric sensors composed of one resistor in parallel to one capacitor. The achieved measurement accuracy regarding the capacitors is in the pico-farad range and is for the parallel resistors in the kilo-Ohm range.

Keywords: AC-ZPC method, impedimetric, sensor matrices, calibration, measurement deviation, impedance spectroscopy

Background, Motivation an Objective

The AC-ZPC method was proposed to overcome the crosstalk effect [1] in the two-dimensional sensor matrices. It has been proved to be very accurate for resistive sensor matrices. Its potential for impedimetric units has been also demonstrated [2].

As reported in [2], one of the measurement deviation sources in the AC-ZPC method is the output impedance of the voltage source connected to each matrix row. This effect was solved in [2]. An un-solved source of deviations is the non-ideal properties of the used operational amplifiers [1, 2]. These result in an unsatisfactory deviation for impedimetric targets like the RC parallel pairs indicated in Table. 1. Especially the measurement results regarding capacitor values in the pico-farad range are worse than for parallel resistors in the kilo-Ohm range. This range is important for nanocomposite pressure [3] and strain sensors [4, 5] as well as temperature sensors [6].

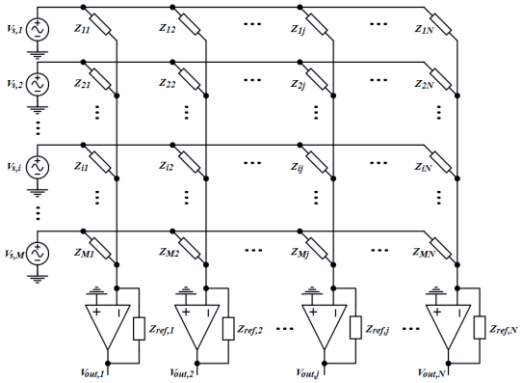

Fig. 1. The AC-ZPC method for 2D sensor matrices of M rows and N columns.

In this work, a new calibration approach is proposed for correcting the deviations resulting from the non-ideal operational amplifiers, when the output impedance value of the row signal source can be ignored.

Calibration method

For matrices of M rows and N columns, when the voltage follower (s. Fig. 1) has been used for each voltage source $V_{s,i}$ for the i^{th} row, its output impedance can be within $0.1\ \Omega$ range, i.e., such small value can be ignored. Then the read-out voltage by the j^{th} column operational amplifier

Table. 1. RC parallel pairs simulating the Impedimetric pressure sensor.

Applied weight [N]	93.4	51.6	15.3	10.2	6.9	1.6	0.1	0.0
Resistance [kΩ]	1.9	2.9	11.0	15.9	22.6	48.6	75.1	100.4
Capacitance [pF]	361.7	300.4	149.6	102.0	75.8	22.8	10.0	7.3

targeting the sensor on the i^{th} row Z_{ij} can be calculated as follows.

$$V_{out,j}\left\{1-\frac{1}{A_j}\left[1+Z_{ref,j}\left(\frac{1}{Z_{amp,j}}+\sum_{m=1}^{M}\frac{1}{Z_{mj}}\right)\right]\right\} = -Z_{ref,j}\frac{V_{s,i}}{Z_{ij}}$$

A_j and $Z_{amp,j}$ are the finite gain factor and the input impedance of this op-amp, respectively. Z_{mj} marks the other sensors connected to the same column but in different rows.

Based on this equation, we propose a new calibration method, where one extra row of given impedance value Z_{given} is inserted into the sensor matrix: In the first phase, $V_{s,i}$ is connected to the i^{th} row and the extra row is grounded. The resulting readout value by the j^{th} column is named as $V_{out,j}^{i}$ here; In the second phase, $V_{s,i}$ is switched to the extra row, while the i^{th} row is grounded. The resulting readout data by the same column is defined as $V_{out,j}^{extra}$. Both $V_{out,j}^{i}$ and $V_{out,j}^{extra}$ can be expressed using the same equation (s. above), then the expression of the targeted sensor can be recalculated.

$$Z_{ij} = Z_{given}\frac{V_{out,j}^{extra}}{V_{out,j}^{i}}$$

Hence, the unexpected deviation sources like A_j, $Z_{amp,j}$ and Z_{mj} have been calibrated out, and the measurement results regarding Z_{ij} can be improved.

Results

The proposed calibration method has been simulated in LTspice for a 4*4 sensor matrix, where the targeted sensor Z_{11} varies as the values listed in Table. 1, and the other 15 sensors are RC pairs of $1.9\,k\Omega\,||361.7\,pf$ simulating the worse crosstalk effect. When the calibration method is carried out, an extra row of given RC pairs ($1.9\,k\Omega\,||361.7\,pf$) is added to this 4*4 matrix, to keep the consistency with other un-targeted sensors. The excitation signal for each row is a single sine wave having a frequency of 7 kHz, 11 kHz, 17 kHz and 23 kHz, respectively. Different voltage source impedance $Z_{r,i}$ has been also considered in the simulation.

As indicated in Fig. 3 and 4, the proposed calibration method performs always better than the non-calibrated one, facing different $Z_{r,i}$ values. In comparison to the original AC-ZPC method (the blue/red/yellow curves), the novel calibration method (the black/magenta/cyan curves) narrows the resistance measurement deviation within $\pm 0.1\%$ range and suppresses the capacitance measurement deviation from more than -3% to less than 1%.

References

[1] Hu Z, Tan W, Kanoun O. High accuracy and simultaneous scanning AC measurement approach for two-dimensional resistive sensor arrays[J]. IEEE Sensors Journal, 2019, 19(12): 4623-4628.

[2] Hu Z, Ramalingame R, Kallel A Y, et al. Calibration of an AC Zero Potential Circuit for Two-Dimensional Impedimetric Sensor Matrices[J]. IEEE Sensors Journal, 2020, 20(9): 5019-5025.

[3] Ramalingame R, Hu Z, Gerlach C, et al. Flexible piezoresistive sensor matrix based on a carbon nanotube PDMS composite for dynamic pressure distribution measurement[J]. Journal of Sensors and Sensor Systems, 2019, 8(1): 1.

[4] Sanli A, Müller C, Kanoun O, et al. Piezoresistive characterization of multi-walled carbon nanotube-epoxy based flexible strain sensitive films by impedance spectroscopy[J]. Composites Science and Technology, 2016, 122: 18-26.

[5] Bouhamed A, Al-Hamry A, Müller C, et al. Assessing the electrical behaviour of MWCNTs/epoxy nanocomposite for strain sensing[J]. Composites Part B: Engineering, 2017, 128: 91-99.

[6] Benchirouf A, Palaniyappan S, Ramalingame R, et al. Electrical properties of multi-walled carbon nanotubes/PEDOT: PSS nanocomposites thin films under temperature and humidity effects[J]. Sensors and Actuators B: Chemical, 2016, 224: 344-350.

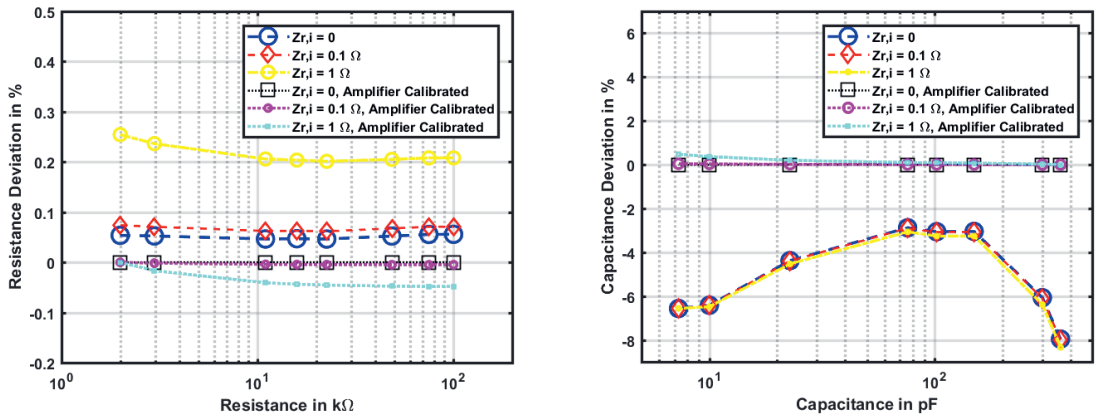

Fig. 3. Resistance and Capacitance deviation of the AC-ZPC method with/without calibrations.

DOI 10.5162/SMSI2021/D8.4

Precision Measurement of the Application dependent Current Consumption of a Wireless Transceiver Chip

Thomas R. Doebbert, Christoph Cammin, Gerd Scholl
Electrical Measurement Engineering,
Helmut-Schmidt-University, Hamburg, Germany
thomas.doebbert@hsu-hh.de

Summary:
Modern production concepts generate a demand for reliable, fast and secure wireless communication solutions. Therefore, the current consumption should not increase highly due to additional security operations. This paper shows a principle current measurement method exemplarily of a transceiver for IO-Link Wireless protocol. The results show that the current consumption increases by about 316 µA when using hardware-based encryption features, whereby an experimental standard deviation of the mean values of about 15 µA was determined.

Keywords: Wireless Security, Current Measurement, IO-Link Wireless, Current Consumption, Industry 4.0

Introduction

Reliable and secure radio-based communication systems are an important component for the enhancement of modern production concepts like Industry 4.0. An essential requirement, especially in an industrial production environment, is that fixed cycle times can be guaranteed even for secured transmissions, where security operations influence the power consumption and the timing of the data transmission of wireless transmission protocols.

Due to typical timing demands in the order of less than 1 ms and low power requirements of hardware modules, these investigations represent a demanding measurement task, because broadband measurements need to be realized with a high amplitude resolution.

In this paper, the current consumption of the data transfer in plaintext and in ciphertext using a Phytec module based on a CC2650 SoC radio transceiver chip [1] is investigated. The IO-Link Wireless protocol is used because it directly addresses the special requirements in the field of production automation in terms of latency, reliability and number of sensors [2].

Principle Measuring Method

In the first step of the measurement, the internal shunt resistor of the current measurement device is used to find an indentation of the measurement range. In the second step, an external exchangeable shunt resistor is used to achieve a better fitting measurement range for using the internal 18 bit ADC of the measurement device. In the third step, plaintext mode of operation is compared to cryptographic mode of operation. In the last step, a statistical evaluation is used to analysis the measurement accuracy.

To measure the influence of the cryptographic algorithms compared to the plaintext mode or unencrypted operation, only every other downlink, cryptographic operation is activated. In this way, within 10 ms three measurements with cryptographic operations and three with plaintext mode are recorded. Thermal effects are neglected, because the effects are subtracted with the operation without cryptographic algorithm.

Measurement Assessment

To achieve a more accurate measurement range compared to the setup with an internal shunt, a measurement setup with an external shunt is used [3], as shown in Fig. 1. The external debugger, which was connected to the Device under Test (DUT) is not shown here.

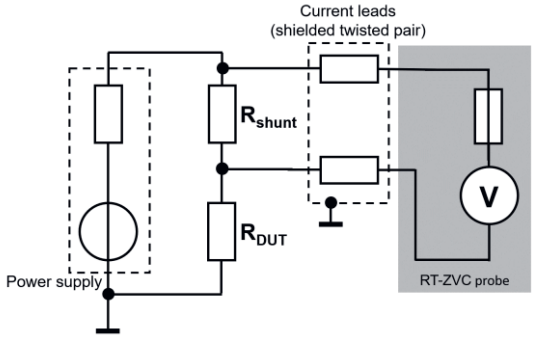

Fig. 1. Setup of measurement 3] with external shunt according to [4, p. 32].

A constant voltage source [5] provides a stable voltage supply for the DUT. The appropriate measurement range of 13.81 mA was chosen by selecting a shunt resistor, which was measured using a precision multimeter [6] to have a value of 3.259 Ω. The accuracy of the current measurement can be approximated by using the data sheet of the power probe [4]. The appropriate type of current (DC or AC) has to be selected according to the data sheet. Eq. (1) uses the AC version (10 Hz to 40 kHz) of the approximated measurement value, because the signal is characterized as a pulsed DC signal, as in Fig. 2. The abbreviated symbols in eq. (1) characterize the measured current ($I_{acc,ZVC}$), tolerance of the external resistor with additional connectors (R_{tol}), the measurement range (I_{range}) and the internal ADC tolerance of the ZVC probe (ADC_{tol}).

$$I_{acc,ZVC} = I_{meas} \pm \left[\frac{\%R_{tol}}{100\%} \cdot I_{meas} + \frac{\%ADC_{tol}}{100\%} \cdot I_{range}\right] = 8.63\ \text{mA} \pm \left[\frac{0.4\%}{100\%} \cdot 8.63\ \text{mA} + \frac{0.02\%}{100\%} \cdot 13.81\ \text{mA}\right] = 8.63\ \text{mA} \pm 0.0373\ \text{mA}\,. \quad (1)$$

Theoretically, the 18 bit ADC can resolve 105.35 nA steps over an input range of 13.81 mA. Practically, assuming that the two least significant bits cannot be used, an amplitude resolution due to amplitude quantization of 421.4 nA over the input range is feasible.

An example measurement of 16 bytes AES-ECB algorithm is shown in Fig. 2. A moving average filter smoothed the data over 125 samples.

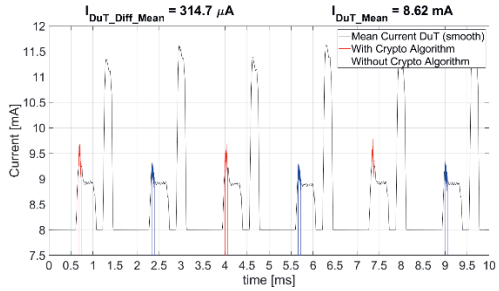

Fig. 2. AES-ECB encryption of 16 bytes using the on chip hardware accelerator.

Each measurement consists of 445 data sets with each 50 k samples (at 5 MSa/s) recorded (2.225 G samples) and used for further calculations, as in [3].

Table 1 shows the statistical parameter of 10 measurements each with 445 data sets.

Tab. 1: Measurement Results.

	Current Mean DUT	Current Difference of crypto to plaintext
Mean value	8.63 mA	316.2 µA
Experimental Standard Deviation	15.2 µA	25.0 µA

Results

The experimental standard deviation of the mean currents are factor 2.5 smaller than the accuracy according to the data sheet of the measurement equipment [4]. Furthermore, the experimental standard deviation of the mean value is about two orders of magnitude larger than the theoretical step size of the ADC, thus, the quantization effects like quantization noise have a negligible effect. The mean value of current difference is 316.2 µA (i.e. about 3.7 % of the mean value) and has therefore only a minor influence on potential battery life. The experimental standard deviation of the current difference of crypto to plaintext is 25.0 µA, which is significantly smaller than the mean current difference of crypto to plaintext.

In a future step, the frequency spectrum needs to be evaluated, because the pulsed DC signal is not considered in the datasheet [4]. The approximation of an AC current with 10 Hz to 40 kHz was used. However, the statistical parameter lead to a validation of the accuracy estimation given in the datasheet [4].

Acknowledgment

The authors would like to acknowledge Mr. Jockram and Dr. Heynicke for their support as well as the company Kunbus GmbH.

References

[1] PHYTEC Embedded Pvt. Ltd., phyWAVE-CC26xx Hardware Manual, Available: https://www.phytec.in/fileadmin/user_upload/images/content/1.Products/IoT/L-824e_1.pdf, August 2016.

[2] R. Heynicke, et al., IO-Link Wireless enhanced factory automation communication for Industry 4.0 applications, J. Sens. Sens. Syst., 7, 131–142, (2018); doi: 10.5194/jsss-7-131-2018.

[3] T. Doebbert, et al., IO-Link Wireless Device Cryptographic Performance and Energy Efficiency, submitted for publication

[4] Rohde & Schwarz, R&S RT-ZVC Multi-Channel Power Probe, User Manual, Available: https://scdn.rohdeschwarz.com/ur/pws/dl downloads/dl common library/dl manuals/gb1/r/rt zvc/RT-ZVC UserManual en 03.pdf, Version 03, 2020-10-23.

[5] Rohde & Schwarz, R&S NGM200 Power Supply Series, Data Sheet, Available: https://scdn.rohde-schwarz.com/ur/pws/dl_downloads/dl_common_library/dl_brochures_and_datasheets/pdf_1/NGM200_dat_en_3609-1685-32_v0200.pdf

[6] Keysight, Keysight 3458A Multimeter, User's Guide, Available: https://literature.cdn.keysight.com/litweb/pdf/03458-90014.pdf

DOI 10.5162/SMSI2021/D9.1

DMP41- a high-precision amplifier based on an inductive-voltage-divider, suitable to safeguard traceability for most mechanical quantities

André Schäfer; Hottinger Brüel & Kjaer - HBK,
Im Tiefen See 45, 64293 Darmstadt, Germany,
andre.schaefer@hbkworld.com

Summary:

This paper describes the newest version of the strain gauge precision instrument DMP41 with highest resolution and highest stability for the use in calibration tasks with e.g. force, torque, pressure transducers or load cells. This inductive-voltage-divider-based digital amplifier DMP41 is the world´s most precise amplifier for strain-gauge-based sensors. It has been optimized and got some new version 2020.

Keywords: DMP41, strain gauges, force, torque, pressure, sensors, mechanical calibration systems

Introduction

Since May 2, 2019, definitions based on the universal natural constants apply to all units of measurement in the SI system. With a dispute spanning two centuries, the new definitions for Amperes, Kelvin, and Mole have been set into force at the World Metrology Day 2019 [1]. While Meter and Candela have been already defined using natural constants before, the kilogram artifact, by the new system, is now also replaced. This has far-reaching consequences for the system of metrological traceability of measurements.

Primary quantities of the SI and thus fundamentally affects calibration. A current approach to this in the USA is the strategic “NIST-on-a-Chip”, for which no equivalent concept yet exists in Europe. Still, Germany is famous for its century long history in the field of mechanical engineering. With the brave new world of the many new facets of the internet of things (IoT) we presently see extensive changes in the market and even an ambivalence of new and old in metrology.

We may talk of a “sensorization” in the market, expressed in a much higher quantity of sensors affordable to be employed. The IoT, integrated sensor systems of high complexity, having a lot of wind in its sails. Thus, questions dealing with the nature of metrology, as the representation and the traceability of the measured variables and the measurement uncertainty seem to be not so important anymore [2].

However metrological traceability is defined as property of a measurement result whereby the result can be related to a reference though a documented, unbroken chain of calibration, each contributing to the measurement uncertainty. If you use strain gauges, you have to build up a high-precision measurement chain, consisting of a sensor and a precision amplifer. The following is description of the newest version of the strain gauge precision instrument DMP41 with highest resolution and highest stability [3].

Basic principle of DMP41

The inductive-voltage-divider-based digital amplifier DMP41 is the world´s most precise amplifier for strain-gauge-based sensors and can measure most mechanical quantities, such as force, torque, pressure and any other strain-based pick-up principles.

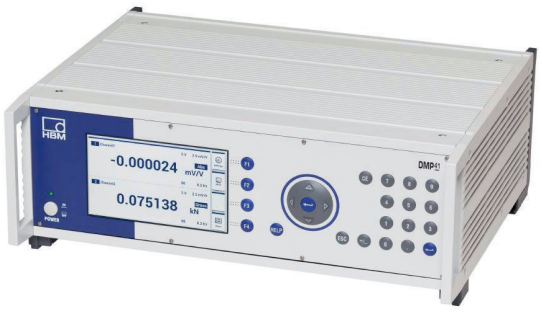

Figure 1: DMP 41 high-precision instrument

This newest member of the DMP series, which has been optimized for decades as a reference device in mechanical laboratories of National Metrology Institutes (NMIs) around the world.

In the full paper the new features of the 2020/2021 edition will be shown and explained. Figure 2 is showing its block diagram.

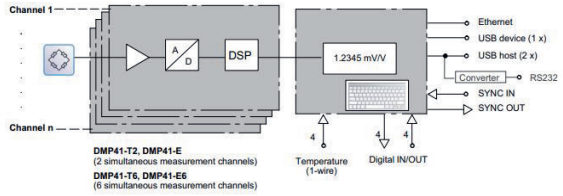

Figure 2: Block diagram of DMP41: a preamplifier is converted into Digital by the ADC; all further data processing happens on the digital side.

Long term stability of the DMP series

Although this paper is mainly about the differences between the DMP41 and the DMP40, all devices of the DMP series have basic design principles in common. The DMP39, DMP40, and DMP41 are all based on an inductive voltage divider, which lays the foundation for the DMP series' outstanding long-term stability.

Such dividers are very accurate because their accuracy is only defined by the ratio of the number of windings, meaning they allow the implementation of amplifiers with much smaller measurement uncertainties than by resistive implementations [4].

This "digitally" defined ratio of windings allows for the instrument's very small deviations. Inductive voltage dividers operate most accurately in the frequency range of 225 Hz, also reducing disturbances. Thus, implementation of the DMP family offers a radically different design to the resistive and generally less accurate designs.

To prove its long-term stability, since the introduction of the first device of the DMP series, the DMP39 in 1980, the long-term stability of a measuring chain consisting of a BN100 calibration unit with Serial Number 010 and the first-ever DMP39 with Serial Number 001 has been monitored over 40 years now. Figure 3 shows the results. The measuring chain did never exceed an error band of +/-2.5 ppm.

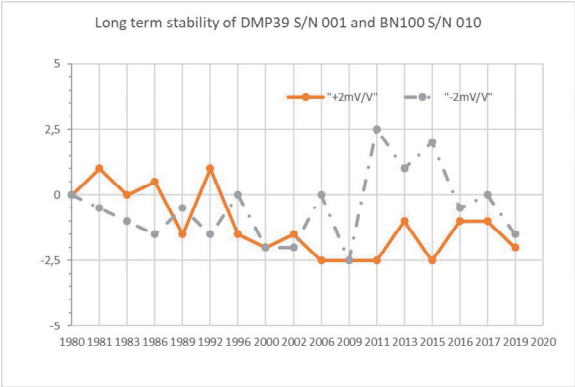

Figure 5: Monitoring of the long-term stability by internal calibration method in a measuring chain, comprising a BN100 calibration unit with S/N 010 and the first-ever DMP39 with S/N 001

Conclusion

It will be shown, that if one uses a high-precision amplifier as DMP41, it will have a significantly lower measurement uncertainty that any strain gauge based sensor, whether it is force, torque, pressure or load cells [5].

References

[1] Frank Härtig, Dorothea Knopf, Katharina Lehrmann "The kilogram in the new SI" , tm - Technisches Messen , Volume 87: Edition 4, January , 2020

[2] "Growth Opportunities in the Calibration and Repair Market, Forecast to 2022 Market Consolidation and Technological Expertise to Accelerate Growth in a Transforming Market", issued by Global Measurement & Instrumentation Research Team at Frost & Sullivan, MD2B-30, February 2018

[3] Schäfer, Calibration & Traceability Challenges and its Impact to the Development of Mechanical Engineering, International Metrology Workshop 14. – 18. May 2018"Fundamental Constants: Basics Physics and Units", Including the Helmholtz Symposium & Award Ceremony on 17 May 2018, 670.WE Heraeus, Bad Honnef, Germany 2018

[4] Schäfer, A.; "Force, strain and pressure transducers based on foil type strain gauges", Proceedings of Eurosensors XXII conference, Dresden, Germany, October 2008

[5] Kehrer, R.; Schäfer, A.; „MGC - A revolutionary structured analogue amplifier and its application at a Multi-Channel Body Test Stand"; Proceedings of NVH Symposium´95, Matsushita National Panasonic symposium ; Tokyo, Japan, Nov. 1995

DOI 10.5162/SMSI2021/D9.2

Analysis of the Oscillating Behavior of a Highway Bridge for Structural Health Monitoring

Ronny Peter, Alice Fischerauer, Sebastian Kraus, Niklas Krug, Tim Ringelmann, Johannes Welsch, Gerhard Fischerauer
Universität Bayreuth, Chair of Measurement and Control Systems, Universitaetsstrasse 30, 95447 Bayreuth, Germany,
mrt@uni-bayreuth.de

Summary:
Bridges, being concrete structures, oscillate from excitation with impulsive forces. The details of these oscillations such as amplitudes, frequencies, and their decay coefficients bear information about the structural health of the bridge. Each tire of a passing vehicle excites the bridge with a short impulse of force, which contains a broad frequency spectrum. We developed a mathematical model to describe the resulting oscillations and compared the time response of the model with measurements taken at the deck of a bridge.

Keywords: Structural health monitoring, bridge monitoring, resonance analysis, vibration behavior, acceleration measurement.

Introduction

In this work, we investigated the impulse response of a highway bridge to excitation by vehicles passing the expansion joint. If the responses to the impulses from different vehicles prove to be similar, a change in the response characteristics has to be related to changing properties of the bridge like cracks or rust. Although there has been an extensive amount of research on the problem of bridge monitoring, one still faces challenges. Some methods require a large amount of sensors throughout the bridge [1], others need an artificial ultrasound excitation [2], and RF imaging methods often lack the necessary resolution [3]. In this work, we use the natural excitation by passing vehicles to monitor accelerations in the deck of the bridge with a single sensor. This will hardly bear information about the whole bridge, but it should provide information about the abutment, expansion joint, and a part of the deck.

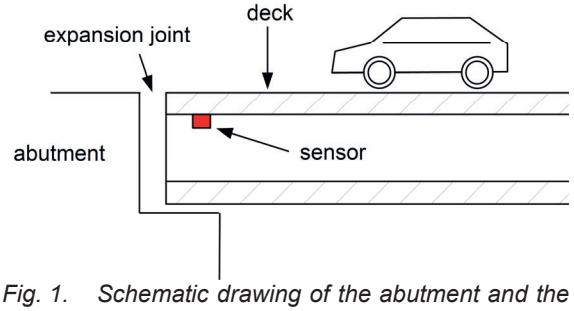

Fig. 1. Schematic drawing of the abutment and the deck of the investigated bridge.

Theoretical considerations

The bridge is regarded as a linear time-invariant (LTI) system. Every tire of a vehicle entering or leaving the bridge across the expansion joint excites the bridge with a Dirac impulse. As a consequence, impact sound waves are stimulated leading to a displacement of the surface of the deck. The impulse response as it becomes manifest in the acceleration of the deck's surface at a given point is modeled as a sum of decaying sinusoidal signals:

$$h_i(t) = \sum_j A_{ij} \cdot \mathrm{e}^{-\alpha_{ij} \cdot t} \sin(\omega_{ij} t) \cdot \varepsilon(t - t_i) \qquad (1)$$

with A_{ij} the amplitude of the *j*-th oscillation resulting from the *i*-th Dirac impulse. α_{ij} and ω_{ij} are the corresponding damping coefficients and oscillation frequencies, and $\varepsilon(t)$ denotes the Heaviside step function. In this work, we limited the number of relevant waves to three.

Measurement system and setup

The measurement system consisted of a custom-built data logger and a commercial acceleration sensor. The latter (ADXL355) had a resolution of about 4 µg/LSB, a 3 dB-bandwidth of 1 kHz, and a sample rate of 4 kHz. All three axes of acceleration were continuously logged with an Arduino-based logging system. The memory and the battery both lasted for about 36 hours. The sensor was placed on the deck of the bridge near the expansion joint (see Fig. 1).

Measurement results

To fit the model function (1) to the measured response of the bridge, we first extracted periods from the measured time-dependent vertical acceleration that are obviously associated with a passing vehicle. An example presenting fit and measurement is given in Fig. 2. The damped oscillation occurring first in chronological order is due to the first tire touching the expansion joint (which was right front in this experiment), the second oscillation is due to the second tire (left front in the example), etc. In the example, the oscillations corresponding to tires number one and three exhibit higher frequencies and lower amplitudes than those caused by tires number two and four.

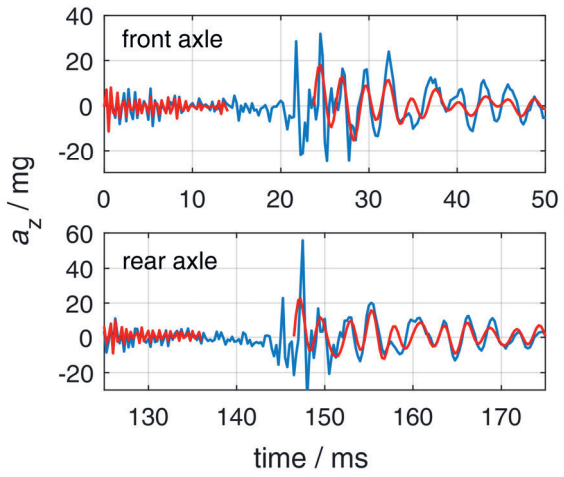

Fig. 2. Measured (blue) and fitted (red) vertical acceleration. See text for further details.

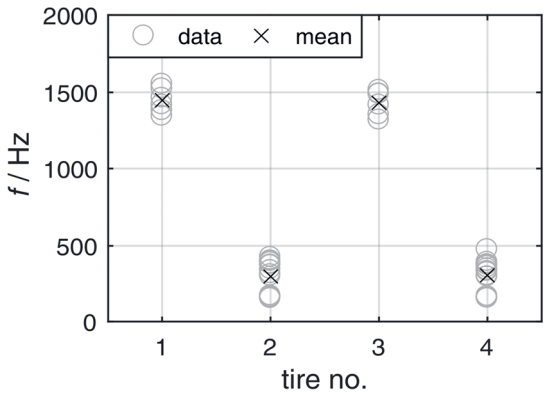

Fig. 3. Dominant frequencies excited by five different vehicles, displayed separately for each tire. Outliers were excluded.

The impulse responses to five different vehicles were fitted as described above. In order to investigate the benefits as well as the limits of the model, the three dominant frequencies from each of the four impulse responses for every vehicle were extracted from the corresponding frequency spectra and used as starting points for the fit. The fitted frequencies ω_{ij} are displayed in Fig. 3. Two clusters can be formed, one for the first and third impulses and another one for the second and fourth impulses.

Discussion

From the measurement results, it is evident that some tires cause bridge responses that are very similar between them but different from the responses to other tires. In our measurements, the tires causing similar responses belonged to the same vehicle side. The origin of this classification could be twofold: (a) The vehicle suspension characteristics belonging to the same axle could change after contact of the first tire with the expansion joint. (b) The expansion joint itself acts as a separate resonator, the characteristics of which are influenced by the tire contact. This would require the bridge to be modeled as a system of coupled resonators.

Conclusion

We analyzed the oscillating behavior of a bridge at one point originating from impulsive forces generated by vehicles crossing the expansion joint. The vehicle tires triggered different responses of the bridge, depending on the position of the tire in the vehicle (left, right, front, rear). The extracted resonance frequencies of the damped bridge oscillations formed distinct clusters, corresponding to distinct tire classes. In order to model the oscillating behavior of the bridge in a way that predicts these clusters, the present model has to be extended to describe coupled resonators. We believe that changes of the clusters over time could be an early warning signal in that they predict an emerging damage of the bridge.

Acknowledgement

The authors would like to thank Dipl.-Ing. (FH) Volker Lauterbach from the Autobahndirektion Nordbayern for providing them with access to the measured bridges.

References

[1] M. Chang, S. Pakzad, “Optimal Sensor Placement for Modal Identification of Bridge Systems Considering Number of Sensing Nodes,” *J. Bridge Eng.,* vol. 19, no. 6, (10pp), June 2014; doi: 10.1061/(ASCE)BE.1943-5592.0000594.

[2] N. K. Mutlib, S. B. Baharom, A. El-Shafie, and M. Z. Nuawi, “Ultrasonic health monitoring in structural engineering: buildings and bridges,” *Struct. Control Health Monit.*, vol. 23, pp. 409–422, March 2016; doi: 10.1002/stc.1800.

[3] S. Kharkovsky, J.T. Case, M.T. Ghasr, R. Zoughi, S.W. Bae, and A. Belarbi, “Application of Microwave 3D SAR Imaging Technique for Evaluation of Corrosion in Steel Rebars Embedded in Cement-Based Structures,” in: *AIP Conf. Proc.*, vol. 1430, pp. 1516–1523, 2012; doi: 10.1063/1.471639

DOI 10.5162/SMSI2021/D9.3

Scalable and Automatic Dynamic Excitation of Non-Linear Structures

Peter Blaschke[1,2], *Daniel J. Alarcón*[1]
[1] *Technische Hochschule Wildau, Hochschulring 1, 15745 Wildau, Germany*
[2] *NV Tech GmbH, Paul-Lincke-Weg 10, 71711 Steinheim, Germany*
peter-g.blaschke@th-wildau.de

Summary:
The mathematical foundations of modal analysis assume material linearity and time invariance on a tested structure. This is, however, rarely the case in a real modal test. Complex structures often present bolted or threaded connections, or assemblies with multiple material interfaces. These connections induce non-linear force/response relationships in the structures, which hinder the application of traditional modal excitation methods. The proposed Scalable Automatic Modal Hammer (SAM) allows testing complex structures at single force/response points for a precise material characterization.

Keywords: modal testing, automatic excitation, modal analysis, modal hammer, composite

Motivation

Experimental Modal Analysis (EMA) is the study of the dynamic properties of structures and systems in the frequency domain. The goal of EMA is to determine the resonance frequencies, mode shapes and modal damping of the studied structure. The applications of these parameters are manifold in the fields of automotive Noise, Vibration, Harshness (NVH), sound design, structural health monitoring, finite elements analysis, etc.

EMA is based on sets of equations that assume from the tested structure: 1) material linearity and homogeneity, 2) reciprocity, and, 3) time invariance [1]. These conditions are oftentimes not fully accomplished when performing modal tests in real industrial structures. For instance, bolted or screwed structures, or parts made of multiple materials such as automotive brake pads, present friction interfaces among their constructive parts. These interfaces result in non-linear modal excitation/response relationships, which are in violation of the initial EMA assumptions [2].

Traditional modal excitation techniques, such as electrodynamic shakers and handheld modal hammers, are inadequate solutions to excite these complex structures. On one hand, electrodynamic shakers require their physical attachment to the structure under study, with associated notable changes in the structure's mass and stiffness. On the other hand, handheld modal hammers are heavily operator-dependent. Double impacts and a large variability in the excitation force throughout a modal test are commonplace.

Scalable, Automatic Modal Hammer Excitation

The solution presented in this paper profits from the advantages of hammer excitation, such as the lack of mass loading effects; while eliminating the drawbacks related to human operator variability.

The Scalable Automatic Modal Hammer (SAM) is developed to guarantee a very high degree of impact repeatability and reproducibility throughout a modal test. Furthermore, the SAM can be synchronized with a Scanning Laser Doppler Vibrometer (SLDV) for the full automatization of an impact modal test.

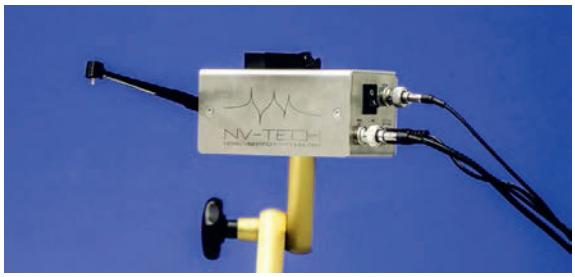

Fig. 1. The Scalable Automatic Modal Hammer (SAM).

The SAM consists of a piezoelectric impact force sensor tip built on a 3D printed ABS shaft, of proprietary topologically optimized design. The shaft is designed to be flexible enough to cause a reactionless force impulse on the structure, while keeping the sensor aligned with the structure. This assembly is driven by a stepper

motor, controlled via USB by means of a graphical user interface. Several parameters such as hammer inwards and outwards angular velocity and acceleration can be adjusted to tailor the desired force impulse and contact time between hammer tip and structure.

Repeatability Study

A study to assess the impact repeatability and reproducibility of the SAM has been carried out in comparison with a series of manual impacts with a mini-modal hammer of the same model as that installed in the SAM, performed by an expert operator.

Three different SAM tests have been performed with objective forces 28 N, 90 N and 138 N. The manual operator test was performed with an objective force of approximately 100 N. 42 impacts on a massive steel block have been recorded for each SAM test. All impacts were sampled with 250 kHz, which guarantees a proper sampling of each impact as Fig. 2 shows. Each impulse is defined with approximately 12 data points; therefore, the test results are not affected by the so-called picket-fence effect.

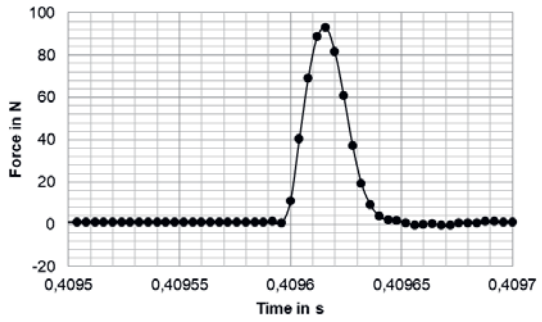

Fig. 2. 93 N impact sampled with 250 kHz.

Table 1 shows the mean, median and standard deviation across all performed tests. All three tests carried out with the SAM present comparable levels of standard deviation, of a maximum of 1.4 N, and much lower values in comparison to the manual test.

Tab. 1: Mean values, median values and standard deviations for each test.

Test	Manual	1	2	3
Objective in N	100	28	90	138
Mean	107,371	27,780	90,404	138,066
Median	106,800	27,675	90,080	138,200
Std. Dev	21,803	1,115	1,131	1,408

Reproducibility Study

The SAM was developed with the goal of exciting structures with non-linear force/response behavior at one single working point. Slight variations in the force impulses are associated to variations in the different components of a complex composite structure. The resulting frequency response functions (FRFs), are in this case different, and the modal damping of each mode cannot be estimated confidently.

Fig. 3 shows three different overlaid FRFs of a brake rotor. The SAM was used to excite the rotor three times, using the same control parameters, and therefore, obtaining the same force impulse.

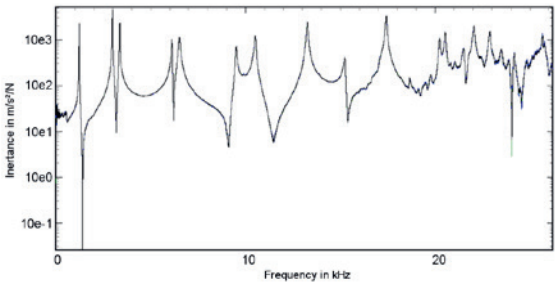

Fig. 3. Three overlaid inertance Frequency Response Functions of a brake rotor, generated with three different impacts with the SAM.

Slight differences between the black, blue and green FRFs are only observable at frequency ranges beyond 20 kHz at the anti-resonance area at 24 kHz.

Conclusions

The main goal for modal analysis is to identify and extract the modal parameters, natural frequencies, mode shape and damping. For non-linear structures the force input/response relationship is non-proportional. This is the reason why an extra effort has to be done to control the input force exact as possible. The work shown in this paper briefly summarizes repeatability and reproducibility studies undertaken in the SAM. The advantages of the SAM in front of a human operator are manifold, not only in regards to impact repeatability, but as well given the possibility of fully automatizing modal tests by synchronizing the SAM and a SLDV. Impact reproducibility is a necessity in this case to excite the structure during hundreds or thousands of impacts in exactly the same way.

References

[1] Irretier, H., Mathematical Foundations of Experimental Modal Analysis in Rotor Dynamics, *Mechanical Systems and Signal Processing*, Vol. 13, Issue 2, 183-191 (1999); doi: 10.1006/mssp.1998.1215

[2] Blaschke, P., et al., Non-Linearity Identification of Composite Materials by Scalable Impact Modal Testing, *Sensors and Instrumentation, Vol. 5, Conference Proceedings of the SEM Series*, 7-14 (2017); doi: 10.1007/978-3-319-54987-3_2

DOI 10.5162/SMSI2021/D9.4

Detection of initial subsurface defects in rotor blade leading edges of wind turbines by means of active thermography

Friederike Jensen[1], Michael Sorg[1], Andreas Fischer[1]
[1] University of Bremen, Bremen Institute for Metrology, Automation and Quality Science
Linzer Str. 13, 28359, Bremen, Germany
Correspondence: f.jensen@bimaq.de

Summary:
The surface condition of the leading edge of rotor blades has a significant influence on the lifetime and performance of a wind turbine. Initial subsurface defects like air traps can lead to a premature surface damage by erosion, and a delayed defect detection results in high maintenance and repair costs. Active thermography is proposed as a non-destructive and in situ measuring method to visualize damage patterns on the rotor blade leading edges and to make initial subsurface defects visible. In particular, it enables the investigation of the damage development for mechanical impacts such as rain drops.

Keywords: active thermography, edge zone analysis, leading edge erosion, subsurface defects, composite materials

1. Introduction

The leading edge of a rotor blade is particularly exposed to mechanical and environmental stress, such as in rain, where the drops hit the blade at an impact speed of over 300 km/h. The impact of the raindrops gradually removes the coated surface and parts of the underlying glass fiber composite material [1]. The impact of the rotor blade damage on the life and performance of a wind turbine is considerable, and repairing such a damage is complicated and expensive. Figure 1 shows a schematic representation of the leading edge structure of eroded rotor blades.

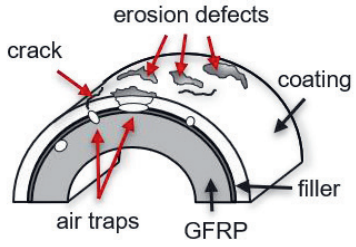

Fig. 1. Schematic sketch of a coated GFRP test specimen with initial defects (air traps) and surface defects

Studies suggest that initial subsurface defects such as pores in the interface between the coating and glass-fiber reinforced plastic (GFRP) lead to premature erosion [2]. The size of the damage-promoting subsurface defects ranges from millimeters to centimeters and remain hidden during visual inspection. Early detection and evaluation of erosion surface damage and subsurface defects, before a major damage up to and including total failure of the rotor blade occurs, leads to a reduction in maintenance and repair costs. However, the effect of certain defect properties such as the defect size on the premature damage is still unclear. Therefore it is necessary to develop a non-destructive and contactless measuring technique to visualize subsurface inhomogeneities.

2. Measurement approach

Long pulse thermography is selected as the measuring method for the contactless, non-destructive examination of erosion damage and subsurface defects [3], since, in contrast to computer tomography, it can also be used in situ. In active thermography, the test specimen is first heated by an energy source. In the subsequent cooling phase, the different temperature distribution at the surface of the test specimen is recorded by an infrared camera (IR) [4]. Thereafter, the thermograms are processed to visually highlight and, thus, to detect material inhomogeneities. The defects visibility is assessable by means of the contrast to noise ratio (CNR) [5].

3. Experimental setup

For the thermographic investigations, a test rig is set up as shown in Figure 2. The test specimen, which resembles the leading edge of a rotor blade, is fixed in a kinematic system. Using a camera of the type Vario Cam hr head (resolution: 640 x 480 px, wavelength range: 7.5 – 14 µm) from the company InfraTec with a 30 mm lens, an image of the emitted infrared light from

the test specimen surface is obtained. Furthermore, an excitation unit, consisting of two 1 kW halogen lamps, is applied under and above the camera to heat the test specimen. The kinematic system as well as the IR camera is connected to a computer to position the test specimen and to evaluate the acquired image data with the software Irbis3 from the company InfraTec. For the examination the test specimen is excited for 10 s. The recording time starts at the end of the excitation and is set to 30 s at a recording frequency of 25 Hz. Here, the first image of the raw data is considered and processed with low pass filters to identify subsurface defects.

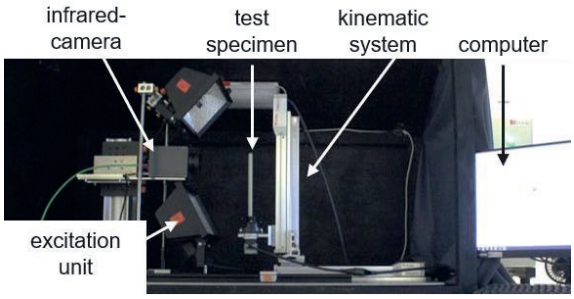

Fig. 2. Experimental setup for the thermographic examination of test specimens

4. Results

The measurements are carried out on a test specimen consisting of a hand-laminated GFRP half pipe which is covered with a coating system including a filler and a gel coating, both consisting of polyurethane. Polystyrene balls of an average diameter of 1 mm are incorporated into the coating system, which are intended to imitate air traps created during production. Figure 3 shows an image of the test specimen with its associated thermogram. Due to the prevailing temperature difference, which is caused during the cooling process by material-dependent heat storage capacities and the resulting different heat transfers, the small polystyrene balls are detected. They are recognizable as bright points in the thermograms, but remain hidden in the photograph. The CNR indicates the level of contrast between a defect and its surroundings. A high CNR stands for a high detection capability. Exemplary in the first recording, the CNR ranges between 22 and 108.

5. Conclusion and Outlook

The experimental results show that active thermography is a non-invasive, non-destructive measuring method to visualize initial subsurface defects in the millimeter range, which remain hidden during a visual inspection of the leading edge of wind turbine rotor blades. As a next step, the development of these initial material defects to premature rain erosion is investigated using computer tomography. With this knowledge, the in-situ defect measurement with thermography will also enable damage predictions for the rotor blade leading edge of real-scale wind turbines.

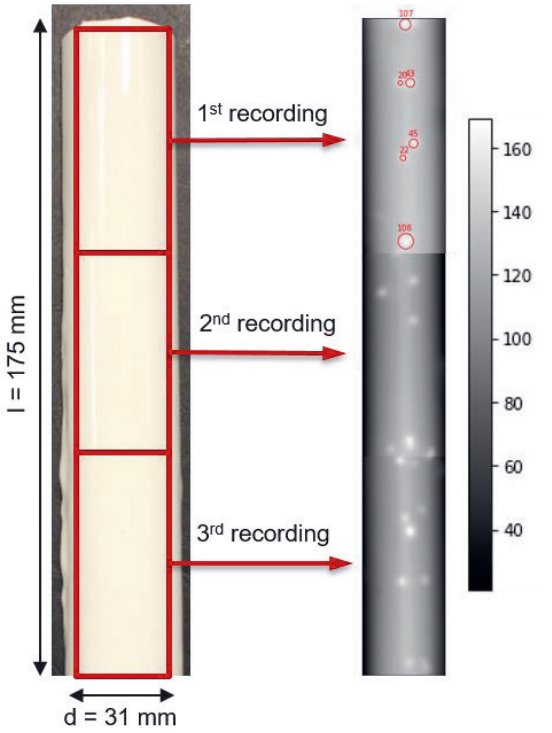

Fig. 3. Left: optical image of the modified test specimen; right: thermograms of the modified test specimen spread over three images – polystyrene balls are recognizable as bright points in the signal processed thermograms (marked with red circles and the corresponding CNR in the 1st recording as an example)

Funding: German Federation of Industrial Research Association (AiF, 20794 N / 2)

6. References

[1] A. Sareen, C. A. SAP re, M. S. Selig, Effects of leading edge erosion on wind turbine blade performance, *Wind Energy* 17, 1531-1542 (2014); doi: 10.1002/we.1649

[2] M.H. Keegan, Wind Turbine Blade Leadeing Edge Erosion: An investigation of rain droplet and hailstone impact induced damage mechanisms, Ph.D. thesis (2014), University of Strathclyde, Glasgow

[3] Z. Wang, G. Tian, M. Mea, F. Ciampa, Image processing based quantitative damage evaluation in composites with long pulse thermography, *NDT & E International*, 99 (2018); doi: 10.1016/j.ndteint.2018.07.004

[4] D. P. Almond, S. L. Angioni, S. G. Pickering, Long pulse excitation thermographic non-destructive evaluation, *NDT & E International,* 87 (2017); doi: 10.1016/j.ndteint.2017.01.003

[5] C. Dollinger, N. Balaresque, M. Sorg, A. Fischer, IR thermographic visualization of flow separation in applications with low thermal contrast, *Infrared Physics & Technology*, 88 (2018); doi: 10.1016/j.infrared.2017.12.001

System of Units and Metrological Infrastructure

DOI 10.5162/SMSI2021/C7.1

Current Measurement System for Solder Joint Quality Analysis in Photovoltaic Modules

M. Lenzhofer [1], L. Neumaier [1], P. Malago[1], J. Kosel and M. Ortner [1]
[1] Silicon Austria Labs SAL GmbH, Europastraße 12, 9524 Villach, Austria,
E-mail: martin.lenzhofer@silicon-austria.com

Summary:
This paper deals with a novel approach of using a multi frequency eddy current measurement system for analyzing the quality of solder joints in a photovoltaic (PV) module. Due to environmental conditions, thermal cycles and variable load situations the solder joints of the cell connectors inside a photovoltaic module suffer and properly lead to degradation or even worse to completely fail, which in turn can be accountable for burn marks, hotspots, arcing discharges and of course, substantial power losses. With the presented approach, the conductivity of each solder joint can be individually analyzed, enabling the possibility of early failure detection in-line or even in the field. The measurement results show that the evaluated states correlate to conductivity decrease of solder joints, which can be confirmed by electroluminescence (EL) images of a solar cell.

Keywords: Eddy current measurement system, photovoltaic module, solder joint inspection, conductivity measurement

Introduction and Principle

The photovoltaic (PV) technology plays an important role in the sector of renewable energy sources. Many companies and research institutes try to raise the efficiency of PV modules, to increase the power output and additionally reduce their manufacturing costs with novel technologies, materials and setup concepts. In addition, within the last two years, sustainability and End-of-Life (EoL) management started to gain major importance within PV technologies. In that sense, the Austrian flagship project “Sustainabe Photovoltaics - PVRe²” aims to increase the sustainability of electricity generation from PV. One of the major issues are defect solder joints (so-called “cold solder joints”). This failure is mostly resulting from solder joint cracks, which in turn can be accountable for burn marks, hotspots, arcing discharges and of course substantial power losses.
This paper deals with the analysis method of the solder joint quality control. Since the cells are fully encapsulated, a conducted measurement method for analyzing reasons is impossible. So, one particularly well-suited noninvasive method is eddy current testing, which is mainly used for detecting cracks in surfaces, but can also be used for electrical conductivity measurements, [1], [2]. The method is based on the physical phenomenon of electromagnetic induction. If a wire coil that is supplied by an alternating current thus generating an oscillating magnetic primary field is brought closely to a conductive material, a circular flow of electrons, which is known as eddy current, will appear in the conductor, refer to Fig. 1. The eddy current will in turn generate its own secondary magnetic field, which interacts with the wire coil described through mutual inductance, [3].

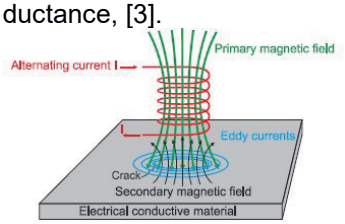

Fig. 1. Primary and secondary magnetic field generated by eddy currents in an electrically conductive material, [1].

Any change in the thickness of the metal, or other disturbances like changes in the conductivity alter the amplitude and pattern of the eddy current and its resulting magnetic field. This leads to a varying impedance of the coil, that is measured to determine the nature of the disturbance, [4]. This kind of non-destructive testing strongly depends on the penetration depth, which is influenced by the frequency of the measurement system as well as the magnetic permeability and conductivity of the test material. While the eddy current density is highest near the surface, the probing depth can be steered through frequency variation. Probing depths of several millimeters can be achieved in non-magnetic materials, which makes this method an ideal candidate for our purposes as wires, con-

nectors and solder joints in PV cells have typical thicknesses in the order of max. 0.3 mm. Eddy current measurements are always calibrated according to an appropriate reference standard like air, or to a known good sample.

Measurement Setup

As probe a handmade air coil was developed with a diameter of 12 mm and a length of 10 mm, which resulted in an inductivity value of 76 µH, refer to Fig. 2 a.). This sensing element was connected to an impedance analyzer E4990A from Keysight, which was set to the desired frequency range of 1 kHz to 5 kHz. Eddy current measurement systems are influenced by several other effects in addition to the material properties: Most important are the distance to the device under test (DUT), which is referenced to the dimensions of the probe, as well as the alignment to it, but also vibrations or movements of the sensor probe during the measurement have to be avoided. When applying this technology to PV modules, the setup is well defined, because the probe can be pressed onto the backsheet of the PV module during the measurement, so the distance remains constant and even the position is set, leading to stable and repeatable results.

Measurement Results

To verify the system setup, a single cell was laminated identically as it is used in a PV module, see Fig. 2 b.). Two interconnections (busbar ribbon & cross-connector) on the upper side were not soldered (red), while the other ones were soldered properly (green).

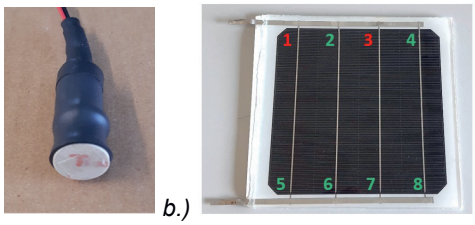

Fig. 2. a.) Sensor probe, b.) Test-cell with soldered and not soldered junctions for system verification.

To simulate a degradation of the cell due to aging effects it was artificially aged running through 100 thermal cycles from -40°C to +80°C, according to the international standard IEC 61215. This degradation effect was analyzed by electroluminescence method and quantified by greyscale values, shown in Fig. 3.

For each measurement, the probe was located over a solder joint one after the other. Additionally, a measurement without a target was performed that depicted the reference for normalizing the result. In a post processing step, the variation between the 1 kHz and 5 kHz result was calculated, according to the theoretical equations. Finally, the results were correlated to the electroluminescence image of the cell. The bright shining regions illustrate a higher current flow due to better contacts between the wires, while the darker regions lead to lower currents due to higher resistances or lower conductivities. Tab. 1 presents the achieved results of all solder joints after processing. Due to the fact of small variations, a region of fluctuation is noticed, while the bad junctions show a significant increase in value.

Table 1. Analyzed junction conductivity

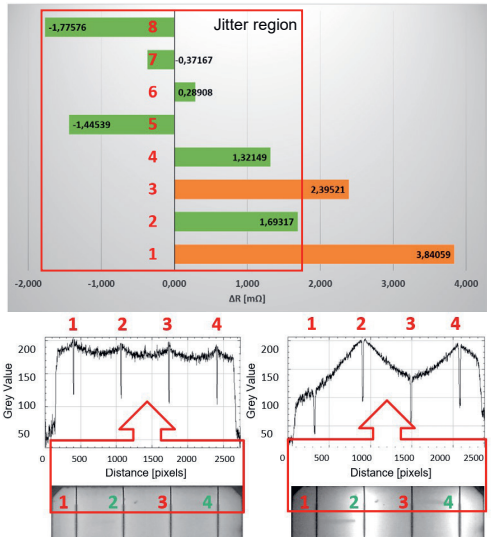

Fig. 3. Electroluminescence measurements of the PV cell before (left) and after thermal aging (right).

Conclusion

The presented multi frequency eddy current measurement method and achieved post-processing calculation results are in good agreement with the electroluminescence investigations of a PV cell.

Acknowledgement

This work was conducted as part of the Austrian “Energy Research Program” project PVRe2 - Sustainable Photovoltaics, funded by the Austrian Climate and Energy Fund and the Austrian Research Promotion Agency (FFG), both are gratefully acknowledged.

References

[1] L. Janousek, K. Capova, N. Yusa and K. Miya, “Multi-probe inspection for enhancing sizing ability in eddy current nondestructive testing”, IEEE Trans. Magn. 2008, vol. 44, pp. 1618-1621.

[2] M. K. Markelov, A. S. Ishkov and A. V. Svetlov, "Eddy Current Measuring System for Testing Conductive Objects", 2020, pp. 1-5, doi: 10.1109/MWENT47943.2020.9067468.

[3] R. Pohl, A. Erhard, H. J. Montag, H. M. Thomas and H. Wüstenberg, “NDT techniques for railroad wheel and gauge corner inspection”, NDT E Int. 2004, pp. 89-94.

[4] D. Placko and I. Dufour, “Eddy current sensors for nondestructive inspection of graphite composite materials”, In Proceedings of the IEEE Conference of the Industry Applications Society (IAS'92), Houston, TX, USA, October 1992; pp. 1676-16

DOI 10.5162/SMSI2021/C7.2

Testing of High-Power Traction Batteries

Johannes Büdel[1], Johannes Teigelkötter[1] Alexander Stock[1], Kai Kuhlmann[1], Klaus Lang[2], Patrik Ott[2]
[1] Technische Hochschule Aschaffenburg, Würzburger Str. 45, D-63743 Aschaffenburg,
[2] Hottinger Brüel & Kjaer GmbH, Im Tiefen See 45, D-64293 Darmstadt
Johannes.Teigelkoetter@th-ab.de

Summary:

Electric drives in road vehicles with a battery as energy storage are about to be introduced to the mass market. In order to guarantee the quality and operational safety of battery-powered vehicles, considerable efforts must be made by car manufacturers and their suppliers. Since the properties of the batteries significantly determine the performance of the vehicles, special test benches with precise measuring systems are required for the accurate determination of the battery properties. The safety devices of the traction batteries must also be tested on high-performance test benches. In this paper the necessary test benches and the corresponding measuring systems are presented. Estimations of the measurement uncertainty and possibilities to increase measurement accuracy are presented.

Keywords: Mobility, Batteries, Test Benches, High Performance Measurement System, Current Measurement

High-Power Traction Batteries

With a value share of approx. 40 %, the traction battery is not only an essential technical component, but also significantly determines the total manufacturing costs of an electric vehicle. The traction battery, as shown in fig. 1, consists of a combination of individual battery modules. For achieving a module voltage of approx. 32 V to 50 V, several chemical cells are connected in series. Different Li-Ion technologies are used in modern and powerful battery systems. The modules are connected in series and parallel, depending on the required power and energy of the vehicle. The total voltage of the traction battery is usually in the range of 300 V to 1000 V. The battery management system (BMS) monitors and activates the output voltage for the drive train and other consumers [1].

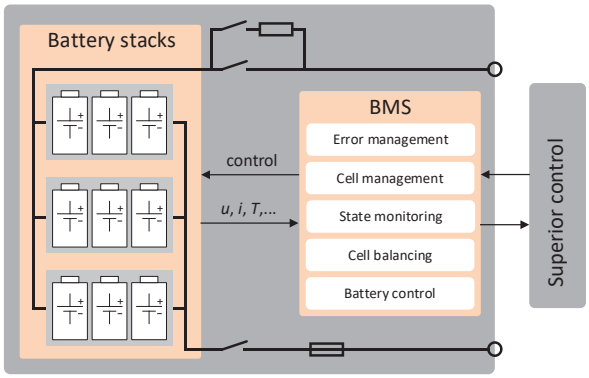

Fig. 1. Typical structure of a battery system

High-Performance Test Bench

In accordance with the individual requirements of high-power traction batteries, a corresponding test bench has to fulfil those specifications for the test procedures. The main focus of this test bench is to provide the most flexible test execution and a high power range of the future batteries. The execution of the test procedures has to be as realistic and application-oriented as possible. Considering the requirements for the process of testing a high-power traction battery, a unique high-performance test bench for these systems is presented in fig. 2 [2].

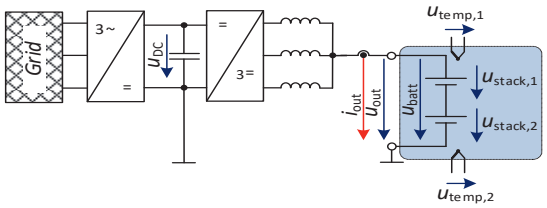

Fig 2. Basic structure of the test system

The power electronic interface of the test bench consists of two two-level converters, connected via the shared dc-link. The three half-bridges of the output dc-dc converter are controlling the battery current, while the grid side converter controls the dc-link voltage and the grid current. With this configuration, the test bench allows a bidirectional power flow, with a maximum operating power of 250 kVA, an output voltage range of 0-750 V and a maximum output current up to ± 800A.

Determination of the Battery DC Resistance

Besides the battery capacity, the internal resistance is also one of the major battery parameters. The lower the resistance, the less the restriction the battery encounters in delivering the needed power spikes. Figure 3 presents a technique to measure the DC resistance of a battery. This method is based on the voltage change during a current step. Ideally, the current jumps from a small value (e.g. 0.1 C-Rate) to a high value (e.g. 2 C-Rate). After a defined duration, the voltage drop is measured [3]. According to this procedure the resistance is calculated with eq.1.

$$R_{DC} = \frac{\Delta U}{\Delta I} \qquad (1)$$

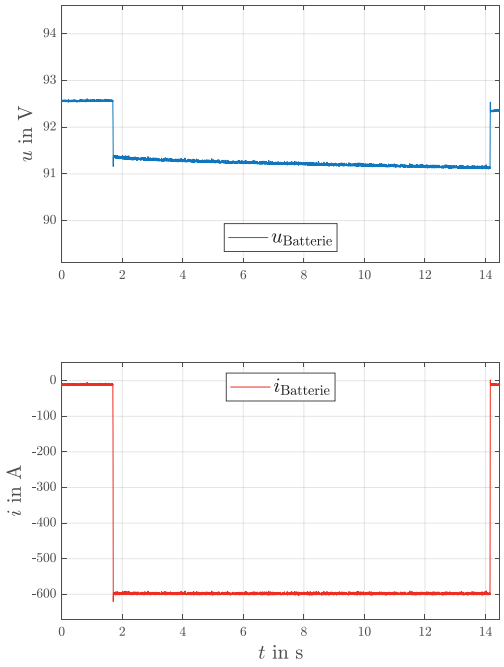

Fig. 3. Measurement of DC-Resistance

Short circuit test on a traction battery

The Battery Management System (BMS) is responsible for monitoring and protecting a battery system. During normal operation, this BMS determines the charge level of a traction battery and takes over communication with the vehicle computer. The safety electronics with the cut-off device are also installed here, which are intended to disconnect the battery from the boardnet in the event of a fault. To test this safety electronics, a low-resistance short circuit is provoked. Thereupon, a short-circuit current flows, which must be switched off by the safety electronics within a short time with the help of special switch-off devices.

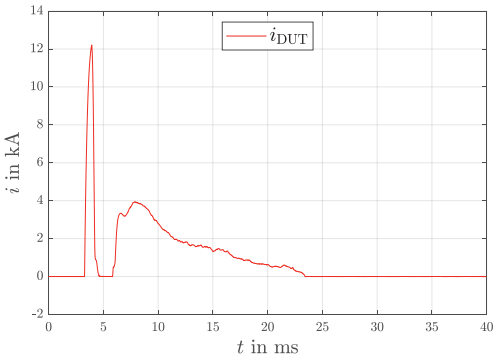

Fig. 4: Waveform of the short-circuit current measured with a shunt

The waveform of a typical short-current is shown in fig. 4. This current reaches a peak value of about 12 kA at t = 4 ms. After the short-circuit current has been interrupted, obviously, the current rises again up to 4 kA. This behavior is not acceptable for reliable operation. To find out the reason for this malfunction it has to be checked if the current was really interrupted at t = 5 ms or if a small current was still flowing.

This short-circuit current measurement sets high demands on the measurement technology. In order to absorb the strong mechanical forces, which are acting due to the large currents, the current sensors must be designed very stable. To capture the fast current changes correctly, the bandwidth of the sensors must be sufficiently high. To ensure that the relative measurement uncertainty is independent of the actual current level, a nonlinear current sensor is proposed here. This NLCS (Nonlinear Current Sensor) was developed especially for the measurement of short circuit currents [4].

References

[1] International Electrotechnical Commission (IEC): Electrical Energy Storage, White Paper, 12/2011.

[2] Büdel, J., Teigelkötter, J., Stock, A., Kowalski, T., & Lang, K. (2017, September). Qualification and verification of high-power battery systems for traction application. In 2017 19th European Conference on Power Electronics and Applications (EPE'17 ECCE Europe) (pp. P-1). IEEE.

[3] Jossen; Weydanz: Moderne Akkumulatoren richtig einsetzen. Untermeitingen: Inge-Reichardt-Verlag, 2006. ISBN: 3-939359-11

[4] Kurzschlussprüfung von Hochleistungs-Traktionsbatterien mit nichtlinearen Stromsensoren, HBM White Paper, www.HBM.com

DOI 10.5162/SMSI2021/C7.3

Quantitative Evaluation of Artefact Reduction by an Optimized Specimen Orientation for Metrology based on Industrial Computed Tomography

Manuel Kaufmann[1], *Ira Effenberger*[1]
[1] *Fraunhofer Institute for Manufacturing Engineering and Automation IPA*
Nobelstr. 12, 70569 Stuttgart, Germany
manuel.kaufmann@ipa.fraunhofer.de

Summary:
Industrial Computed Tomography is used to solve metrological tasks in quality assurance. Although CT has many advantages like complete and non-destructive data acquisition, artefacts can occur depending on the part's material and geometry. Moreover the extent of scanning artefacts strongly depends on the specimen's orientation. By a raycasting approach, the homogeneity of penetration lengths is determined and maximized in order to find the optimal orientation. The reduction of artefacts is assessed by point-based quality metrics. The results show a local contrast improvement of 80 %.

Keywords: Industrial Computed Tomography, Artefacts, Reduction, Quality

Introduction and Problem Setting

Industrial Computed Tomography (CT) is well established in industry both for inspection and metrology tasks. The concept of the CT is based on capturing a set of x-ray projection images, usually over a full rotation of the object, that are reconstructed to a 3D volume. However due to interaction between x-ray photons and the observed specimen, in the reconstruction algorithm an assumed linear x-ray propagation is violated. As a consequence artefacts occur that are defined as discrepancies between the real attenuation coefficients of the specimen and the reconstructed values [1]. Figure 1 shows typical artefacts for dense materials such as Aluminum for the analyzed use case part. Here streaks between edges and high-contrast regions, contrast loss and cupping artefacts occur.

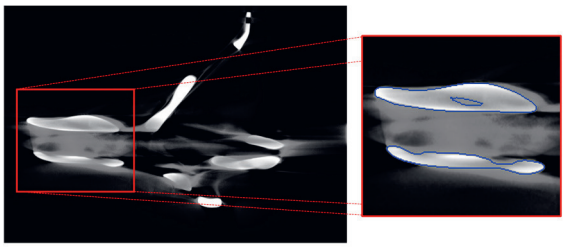

Fig. 1. Artefacts and surface extraction depicted in the detail view, which is denoted with blue lines.

Thus, the possibility to detect small geometrical features such as inner defects and the accuracy of a surface determination is impaired by these artefacts. In range of photon energies typically occurring for CT, beam hardening and Compton scattering are the main effects of photon-matter interaction. According to [2], both effects are influenced by the specimen's material, the CT parameters defining the x-ray spectrum, the specimen's geometry and its position and orientation within the x-ray beam.

Aim and Used Approach

In our work, the influence of the specimen orientation on the extent of artefacts is researched. Therefore, two orientations of a use case part, a best and a worst orientation, are studied. In order to determine an optimal specimen orientation, a raycasting approach is incorporated to gather the local penetration lengths. In the state of the art [3], a minimization of penetration lengths is performed. However in our approach, the optimal orientation is gathered by maximizing the homogeneity of penetration lengths. Figure 2 gives an example for less and more homogeneous penetration lengths, where in the prior case a higher grey value dynamic occurs.

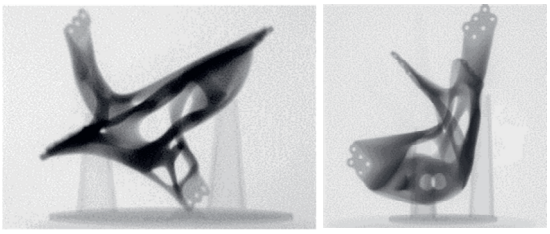

Fig. 2. Projection images of less (left image) and more homogeneous penetration lengths (right image).

The geometrical setup is shown in Figure 3, where the optimization variables ϕ and θ are depicted.

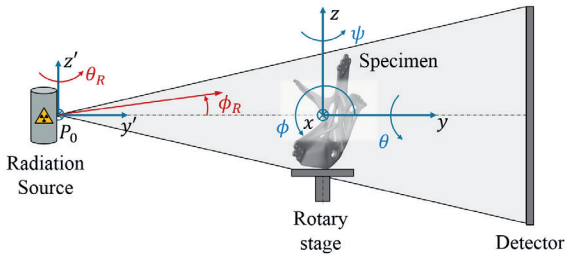

Fig. 3. Set-up for specimen orientation optimization.

Quantification of the Artefact Reduction by Point-based Quality Metrics

In order to evaluate the extent of artefact reduction, quality metrics for both best and worst case orientations are compared. As quality metrics, the Michaelson contrast C_M and parameters of a sigmoid function approximation are considered. The contrast C_M is computed according to

$$C_M = \frac{I_{max} - I_{min}}{I_{max} + I_{min}} \quad \text{with} \quad 0 \leq C_M \leq 1 \,. \quad (1)$$

Here, I_{max} and I_{min} are the maximum and minimum grey values in the reconstructed volume, respectively. The contrast C_M is gathered for each surface point P of the determined ISO 50 surface. A higher scan quality is associated with a higher contrast value. Furthermore, the parameters S_0 and S_1 of a sigmoid function are approximated for each grey value profile through the surface point P and along the corresponding surface normal $\vec{n}$. The sigmoid function is defined according to

$$\mathrm{sig}\,(q) = S_1 \cdot \frac{1}{1+e^{-q}} + S_0 \,, \quad (2)$$

where q denotes a control variable along the surface normal $\vec{n}$. A smaller S_0 value (grey value offset) indicates smaller grey values of the air surrounding the specimen and thus implies the absence of surrounding artefacts. An increased S_1 value (grey value slope) indicates a steeper grey value transition between air and material and implies a better separation of material from background.

Results

The considered quality metrics are studied for a 3D printed aircraft bracket part made from an Aluminum alloy. Both the best and worst case orientations are determined by deploying the described raycasting approach. The worst case orientation in contrast is determined by minimizing the projection image homogeneity.

In Figures 4 and 5, the local contrast C_M is shown for both orientations. For most regions on the scanned specimen, the contrast is strongly improved by scanning in the optimized orientation. On average, the contrast is increased by 79 %. The grey value offset S_0 is decreased by 31 % and the slope S_1 is increased by 36 %. These numbers allow the conclusion that a strong artefact reduction due to an optimized orientation was achieved. By evaluating point-based quality metrics, a significant improvement of the scan quality is shown for an optimized orientation of a part with complex geometry. Artefacts may be shifted to other regions on the specimen indeed, whereby quality values of former high-quality regions become smaller. For most regions however, the reduction of artefacts eventually improves the results of voxel-based evaluations like surface determinations and defect analyses.

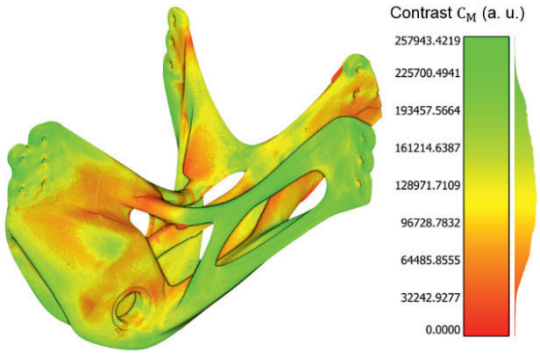

Fig. 4. Contrast values for the analyzed specimen at worst orientation.

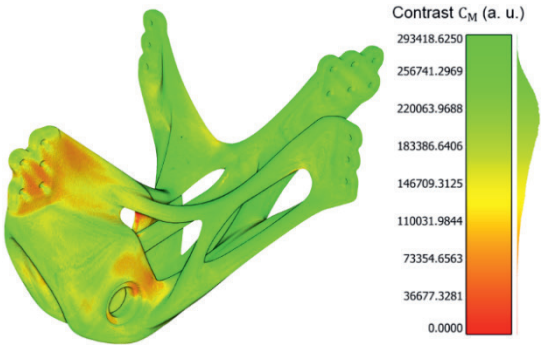

Fig. 5. Contrast values for the analyzed specimen at best orientation.

References

[1] J. Hsieh, Computed tomography. Principles, design, artifacts, and recent advances. 2nd ed., Hoboken: Wiley Interscience (2009); SPIE Press.

[2] A. Amirkhanov et al., Visual optimality and stability analysis of 3DCT scan positions. In: *Trans. Vis. Comput. Graph.* 16 (6), S. 1477–1486 (2010); doi: 10.1109/TVCG.2010.214.

[3] C. Heinzl et al., Fast Estimation of Optimal Specimen Placements in 3D X-ray Computed Tomography. In: *International Symposium on Digital Industrial Radiology and Computed Tomography* (2010).

DOI 10.5162/SMSI2021/C7.4

Application of Laser Line Scanners for Quality Control during Selective Laser Melting (SLM)

Kira Kristin Wehnert[1], Sebastian Schäfer[1], Jan Schmitt[1], Andreas Schiffler[1]
[1] Institute Digital Engineering (IDEE), University of Applied Sciences Würzburg-Schweinfurt, Ignaz-Schön-Str. 11, 97421 Schweinfurt, Germany
kirakristin.wehnert@fhws.de

Summary

The use of laser line scanners for powder bed monitoring in 3D printing processes was investigated. It was possible to analyze dependencies in terms of exposure time due to the use of two different wavelengths of the laser line scanners. With a simplified setup – in accordance to a selective laser melting machine – the behavior of materials with nearly the same particle size as metal powder could be analyzed. In order to satisfy the conditions in the building chamber a construction platform was used. The behavior and the settings of the laser line scanner got evident, especially due to the strong reflections.

Keywords: metal printing, powder bed monitoring, quality control, laser line scanner

Background, Motivation an Objective

First time right is one major goal in powder based 3D metal printing. Reaching this goal is driven by reducing life cycle costs for quality measures, to minimize scrap rate and to increase productivity under optimal resource efficiency [1]. Therefore, monitoring the state of the powder bed for each printed layer is state of the art in selective laser melting. In the most modern approaches the quality monitoring is done by computer vision systems [2]. Nevertheless, the use of computer vision systems has drawbacks. Firstly, the sensor signals for the camera image do not provide depth information directly, which would correspond to a later height profile with height deviations. Secondly, the application of computer vision systems needs to be trained and labeled with reference images for several cases. This would require the images to be evaluated by human quality control or to be generated by image processing algorithms, which are basically highly sensitive to changing exposure situations. Therefore, it would be ideal to create a height profile per shift in order to be able to identify the severity of errors and, in the worst case, to stop the print job. This not only saves material, time and costs, but also improves the process of the system.

Description of the New Method or System

The approach uses a laser line scanner to monitor the powder bed. With this new concept, several images during the print job of each layer can be taken and evaluated. The evaluation can be done online during the process and feedback to the controller to monitor each individual layer. Hence, in case of deviations the location in the printing plane is an inherent measurement and will be used to decide which severity of error is reported. With this approach, the sources of error for each layer can be analyzed with depth information to evaluate the cause of the error. Due to work safety during the development and the risks of the metal powder used, the tests with the laser line scanner were carried out on an external test set-up. This is similar in principle to the recoating process in the SLM (Selective Laser Melting) machine. Two different laser line scanners ($\lambda_{1(\text{red laser light})}$ = 660 nm; $\lambda_{2(\text{blue laser light})}$ = 405 nm) are used for generating the profiles. In order to simulate the metal powder without the risk of health-endangering risks, a similar powder with nearly the same particle size has to be utilized to exclude a risk regarding to the health of the workers. Metal powder used for a SLM machine has a particle size between 10 and 45 µm [2]. Flour and cocoa powder have proven to be the most suitable test material. The utilized flour has a particle size between 11-15 µm and the cocoa powder between 10-12 µm. Both of the powder can be used for the experiments due to the similar particle sizes as the metal powder.

Results of the flour and the cocoa powder

For the first measurements with the laser line scanners, the surfaces of the flour and the cocoa powder were smoothed. The results obtain that flour does not have a satisfactory surface layer, whereas the cocoa layer is satisfactory and can be used for further tests. The roughness of the cocoa layer was determined using

white light interferometry. The arithmetic mean value R_a is 25.8 µm. Based on this value a technical surface can be assumed where a speckle effect occurs. To compare the two sensors with each other, the process parameters are set and images of surface defects are generated. Since the exposure time and the surface condition of the measured surface have a significant impact on the sensor functionality, the experiments are carried out on cocoa powder layers and a reflective building platform with an already melted part. Another aspect why the mentioned platform is used is to get close to the environmental conditions in the building chamber. Because of the lighting in the chamber and trough reflective areas, additional external light can be caused.

Results of the scanned cocoa powder

In order to detect errors caused by incorrectly set parameters, such as the exposure time, these are added (Figure 1, left) manually. For example, the laser line scanner with red laser light produces underexposed areas at 400 µs (Figure 1, middle) and overexposed areas at 2000 µs.

Figure 1 left: foto of the coca powder with caused creases; middle: red laser light underexposed areas at 400 µs; right: red laser light exposure at 1500 µs

The laser line scanner with the blue laser light has different error patterns. Defects due to underexposure appear after 240 µs (Figure 2, left). By increasing the exposure time to 2600 µs (Figure 2, right), no defects due to overexposure were found. By adjusting the exposure time exactly, it is possible to take images of powder layers with both sensors.

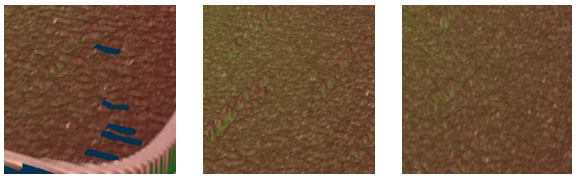

Figure 2 left: blue laser light underexposed areas at 240 µs; middle: blue laser light at 1700 µs; right: blue laser light at 2600 µs

Results of the scanned building platform with red laser light

The tests on the building platform are carried out with the same parameters that have already been used in the failure simulation. Significant defects occure at an exposure time of 1500 µs. Up to 4960 µs, defects increase due to overexposure. Starting at an exposure time of 500 µs, defects continue to decline, but there are areas that are no longer sufficiently exposed. Defects disappear completely at 10 µs due to overexposure, but there are areas of the component that can no longer be detected. The results clearly show that reducing the exposure time reduces the amount of defects due to overexposure. It is possible to reduce the overexposure, but areas are still created that cannot be exposed sufficiently. It can be assumed that the sensor cannot provide meaningful measurement values for reflective areas that may occur in the production process.

Results of the scanned building platform with blue laser light

Since blue laser light can be used to acquire images from 960 µs onward, that do not show any errors due to overexposure or underexposure, only the smallest adjustable range of 15 µs and the maximum adjustment range of 9600 µs were demonstrated. Errors due to underexposure increase by reducing the exposure time. Increasing the exposure time eliminates the errors due to underexposure, but the errors due to overexposure increase. The results clearly show that with the blue laser light at an optimal adjusted exposure time, images of reflecting surfaces can be captured without disturbing errors due to under- or overexposure.

Final result and further outlook

It was not possible to display reflective surface profiles using the red laser light, since errors occurred despite manual changes in exposure time. In contrast, an error-free display of the reflecting surface was achieved with the blue laser light. Therefore, it can be assumed that these are errors due to the speckle effect, which causes noise at the sensor receiver. Based on the investigations it seems that a lower wavelength of the blue laser light is more suitable for powder bed measurements. The results carried out for the approach to use laser line scanning for powder bed monitoring are promising. Additionally first feasibility tests within the real application confirm the results.

References

[1] Thiede, S., 2012. Energy Efficiency in Manufacturing Systems. Sustainable Production, Life Cycle Engineering and Management, Springer Berlin Heidelberg, Berlin, Heidelberg. doi:10.1007/978-3-642-25914-2.

[2] Grasso, M., Colosimo, B.M., 2017. Process defects and in situ monitoring methods in metal powder bed fusion: a review. Measurement Science and Technology 28, 044005. doi:10.1088/1361-6501/aa5c4f.

DOI 10.5162/SMSI2021/C8.1

Methodology for Diagnosing Sensor Faults on Engine Test Benches

Michael Wohlthan[1], Gerhard Pirker[1], Andreas Wimmer[2]
[1] LEC GmbH, Inffeldgasse 19, A-8010 Graz, Austria
[2] Graz University of Technology, Institute of Internal Combustion Engines
and Thermodynamics, Inffeldgasse 19, A-8010 Graz, Austria
michael.wohlthan@lec.tugraz.at

Summary: This paper presents a new approach for a diagnostic system that detects and isolates sensor faults at engine test benches. The modular system as well as the combination of physics-based and data-driven modelling concepts allow highly flexible application on various types of engine test benches. The adaptability of the system is validated using measurement data from two different engine test benches.

Keywords: fault diagnosis, engine test bench, model-based diagnosis, sensor faults, adaptable system

Motivation and Objective

Experimental investigations on engine test benches are a significant cost factor in current combustion engine development. To keep the number of required tests and their associated costs low, it is essential that sensor faults and measurement errors are detected in an early stage [1]. Fritz [2] estimates that up to 40% of test bench time is lost due to faults that are detected too late. Because of the increasing number of sensors and actuators in combustion engines, reliable validation of test results by one person alone has become nearly impossible. On the whole, there is a need for an automated diagnostic system that evaluates measurement data quality and identifies faulty measurement sensors. The great challenge in applying a diagnostic system at engine test benches is that they are often subject to frequent changes in the test engine. Therefore, the diagnostic system must be able to be adapted easily to different types of test engines.

System Description

The proposed diagnostic system works according to the procedure shown in Fig. 1. The test bench produces measurement data (x stands for the measured value of any sensor) which is then checked by a diagnostic procedure consisting of three steps: symptom generation, fault detection and fault isolation. In the symptom generation step, the diagnostic system is adapted to the changeable test engine. This is done by defining limits, formulas (e.g. redundancies or simple physical relations) or by using models.

Modeling is either done online and automatically with data-driven methods [4][5] or initially before the test is started using an engine component-specific (cylinder, turbocharger, throttle valve, etc.) model library containing physics-based models [6]. Each model, formula or limit check ultimately delivers a residual r, which serves as a fault symptom based on the deviation between measurements and model equation-based computations [3].

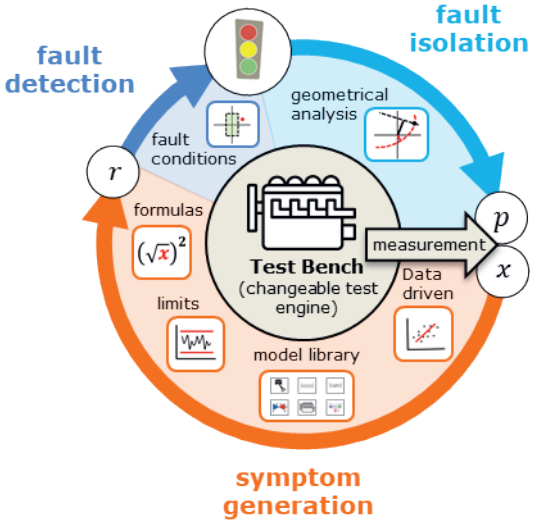

Fig. 1. Scheme of diagnostic procedure

In the second step, fault detection is performed in order to determine whether a fault has occurred in the respective measurement. This is done by checking fault conditions (1).

$$|r| > thr \qquad (1)$$

Thus, a fault is detected if the value of the residual exceeds a certain threshold thr. Finally, it is determined which sensor is faulty. In this third and final step, fault probabilities p_i are calculated for all considered sensor values x_i using a geometrical classification method based on the distance evaluation between error propagation curves and residual state points [7].

Results

The following figure shows the diagnostic results of two different test engines. The first engine is a multicylinder diesel engine (layout in Fig. 2, left) and the second a single-cylinder research engine (layout in Fig. 2, right). The diagnostic system is adapted to these engines using different models. This happens either automatically through the online training of data-driven models or by choosing different component-specific modules from the physics-based model library.

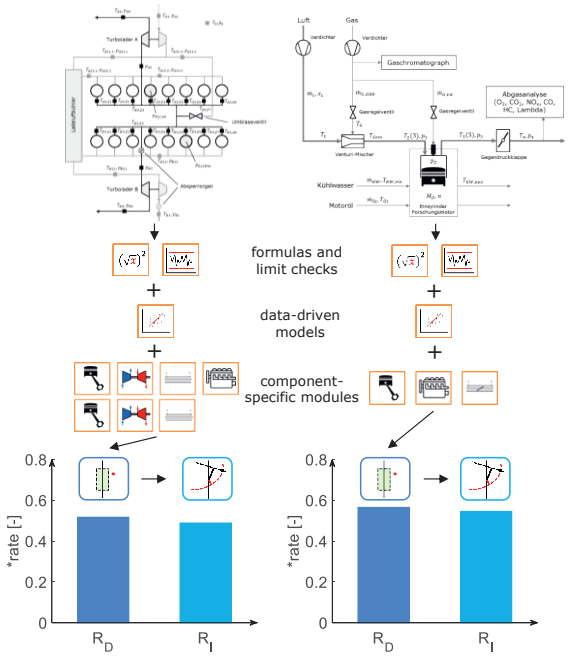

Fig. 2. Comparison of the diagnostic results of a multicylinder diesel engine (left) and a single-cylinder research engine (right)

Evaluation quantities are necessary for an objective validation of the diagnostic system. To evaluate fault detection independently of fault isolation, two quantities are introduced: the detection rate (2) and the isolation rate (3).

$$R_{\mathrm{D}} = \frac{\text{number of correctly detected faults}}{\text{number of actual faults}} \qquad (2)$$

$$R_{\mathrm{I}} = \frac{\text{number of correctly isolated faults}}{\text{number of actual faults}} \qquad (3)$$

Fault-free measurements from real test bed operation provide the initial basis for the analysis. In order to obtain the large number of faulty measurements necessary for the evaluation of the two quantities, abrupt faults with different timings and different intensities are simulated for all implemented sensors. Fault diagnosis is then performed with all measurement data obtained in this way. Finally, the overall detection rate and the overall isolation rate are calculated.

Conclusions

Two important conclusions can be derived from the results shown in Fig. 2. Despite the great differences between the test engines, comparable diagnostic results are achieved. This shows that the diagnostic system can be used flexibly with different test engines because of its adaptability. At this point, it should also be mentioned that the scope of application is not limited to combustion engines. The modular approach can generally be applied to other test bed systems as well if the corresponding model library has been developed for it. Furthermore, it can be seen in Fig. 2 that in both cases, the isolation rate R_{I} is only slightly below the detection rate R_{D}, which means that nearly every fault that is detected is also correctly isolated.

References

[1] A. Flohr, Konzept und Umsetzung einer Online-Messdatendiagnose an Motorprüfständen. Dissertation, Technische Universität Darmstadt (2005)

[2] S.C. Fritz, Entwicklung und Umsetzung einer zentralisierten Messdatendiagnose für Motorprüfstände als integrierter Bestandteil des Prüstandssystems. Dissertation, Technische Universität Darmstadt (2008)

[3] R. Isermann, P. Balle, Trends in the Application of Model Based Fault Detection and Diagnosis of Technical Processes. *Control Engineering Practice, Vol.* 5 (1997); doi: 10.1016/S0967-0661(97)00053-1

[4] D. Schadler, Model based methods for fault diagnostics at engine test beds, *ISCCRO18: 2nd International Statistical Conference in Croatia* (2018)

[5] D. Schadler, E. Stadlober, Fault detection using selected data and updated regression models, *Measurement Vol. 140* (2019); doi: 10.1016/j.measurement.2019.04.010

[6] M. Wohlthan, Methoden zur Fehlerdiagnose an Motorprüfständen, Dissertation, Technische Universität Graz (2019)

[7] M. Wohlthan, D. Schalder, G. Pirker, A. Wimmer, A multi-stage geometric approach for sensor fault isolation on engine test beds, *Measurement Vol. 168* (2021); doi: 10.1016/j.measurement.2020.108313

DOI 10.5162/SMSI2021/C8.2

Near Process Coolant Flow Field Measurements in a Grinding Machine

C. Vanselow[1], B. Espenhahn[1], L. Schumski[2], D. Stöbener[1,3], D. Meyer[2,3], A. Fischer[1,3]
[1] University of Bremen, Bremen Institute for Metrology, Automation and Quality Science (BIMAQ), Linzer Str. 13, 28359 Bremen, Germany,
[2] Leibniz-Institut für Werkstofforientierte Technologien (IWT), Badgasteiner Straße 3, 28359 Bremen, Germany
[3] University of Bremen, MAPEX Center for Materials and Processes, Postbox 330440, 28359 Bremen, Germany
c.vanselow@bimaq.de

Summary:
An extension from qualitative to quantitative flow measurements of the cooling lubricant supply during grinding is achieved using shadowgraphy and particle image velocimetry. As a result, the measurement results in a grinding machine show the general feasibility of optical measurements despite severe optical disturbances in the two-phase flow. While using tracer particles enables closer measurements to the grinding wheel, both measurement approaches provide similar results. This enables investigations for the identification of flow characteristics, which are responsible for an efficient cooling.

Keywords: Optical flow field measurement, shadowgraphy, particle image velocimetry, grinding, liquid jet flow

Motivation

In order to prevent grinding burn, coolant flows are used for lubrication and cooling of grinding processes [1], which are an important manufacturing step for metallic and optical components. However, only qualitative coolant flow characteristics were analyzed to optimize the jet inflow conditions yet [2]. A deeper insight in the cooling process can be obtained with quantitative flow field measurements enabling a recourse conservation, a more efficient process control and a better surface finish.

State of the art

Besides analyzing the jet exit velocity, the angle of impact on the grinding wheel and the nozzle shape [2], qualitative flow visualizations were conducted with shadowgraphy imaging in order to optimize the cooling efficiency in the grinding process [3]. Shadowgraphy uses a homogeneous background illumination to observe the fluid with a camera. Curvatures in the refractive index field of the fluid lead to deflected light rays that propagate from the background to the camera and corresponding parts of the camera image appear only weak or not at all illuminated. Shadowgraphy was used to determine the fluid breakup length of different nozzle flows. However, shadowgraphy is also capable of quantitative flow velocity field measurements as it is shown in [4] for a turbulent sonic helium jet in air and a 2d turbulent boundary layer at Mach 3. Here the visible turbulence structures in the flow, as they also occur in the visualized coolant flows in grinding processes, are tracked in successive images by an algorithm based on cross-correlation. In principle, this allows a measurement of two velocity components of the coolant flow field in the grinding process.

Particle image velocimetry (PIV) utilizes tracer particles which follow the flow with negligible slip [5]. The particles are illuminated with a light sheet from a double pulsed laser and observed by a camera. A cross-correlation algorithm is used to measure two components of the flow velocity field and may also be capable of measuring the coolant flow in the grinding process. However, in contrast to shadowgraphy, PIV measurements are disturbed by inhomogeneous refractive index fields which lead to an unpredictable measurement error [6].

Approach

Shadowgram imaging and PIV are used as complementary measurement techniques to measure the flow velocity fields of the coolant in the grinding machine for the first time. As a first step, the considered coolant flow is measured without a workpiece.

The signal evaluated with shadowgraphy is generated by undisturbed light rays propagating from the homogeneous background illumination through the flow field. In contrast, PIV evaluates the light reflected from particles located inside the light sheet, which can be disturbed on its

way to the camera by the inhomogeneous refractive index field of the flow field. Thus, the PIV signal can be disturbed by light refraction whereby most of the signal for shadowgraphy is not affected by inhomogeneous refractive index fields. However, the image contrast vanishes in the shadowgram, if the illuminated flow field is too thick and the observed turbulence structures conceal each other. Here, PIV with a thin light sheet is advantageous since the light does not have to propagate through the whole flow field. As a result, when both techniques are used, shadowgraphy serves as a reference measurement when a sufficient contrast is available, and PIV allows velocity estimations when shadowgraphy is not working.

Results

The average velocity fields of different coolant volume flows are measured, whereby 1000 shadowgraphy images each are recorded by a high-speed camera with a repetition rate of 12 kHz. Furthermore, 700 PIV single measurements with a repetition rate of 15 Hz and a laser light pulse interval of 20 µs are performed. The light sheet optics are integrated into the grinding machine with a waterproof box and the laser light is provided by a light guiding arm. The velocity fields are evaluated by a commercial iterative algorithm with an adaptive interrogation window size using a minimum of 32×32 px^2. The measured velocity field with PIV for a volume flow of 55 Lmin^{-1} and the difference Δv to the measured velocity field with shadowgraphy imaging is depicted in Fig. 1. The free jet flows from x=y=0 cm to the positive x-direction and impinges on the rotating grinding wheel at about x=25 cm, where the grinding wheel rotates with a circumferential velocity of 25 ms^{-1}. The difference Δv between the measurement techniques is in most elements of the measurement volume near zero, which indicates valid measurement results. However, at the region near the grinding wheel surface occur high differences in the measured velocity. Here, the contrast in the shadowgraphy images does not allow an evaluation of the fluid velocity. As a result, the velocity field can be measured closer to the rotating grinding wheel with PIV.

As an example, in Fig. 2a), a raw image is displayed with the evaluated velocity field. The transition between grinding wheel and fluid is hardly noticeable. Especially in the region at the grinding wheel surface with x<80 cm, a lack of velocity vectors is apparent. Here, the PIV raw image displayed in Fig. 2b) shows a much higher contrast. There are no seeding particles observables, but the velocity evaluation works using the droplets and the turbulence structures in the flow for the correlation. As a result, the velocity field of the coolant flow was measured for the first time. Thus, an experimental flow study to identify the flow characteristics responsible for an efficient cooling is feasible.

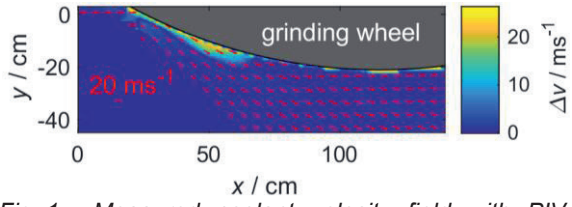

Fig. 1. Measured coolant velocity field with PIV visualized by the arrows, while the color indicates the difference Δv to the measured velocity with shadowgraphy imaging.

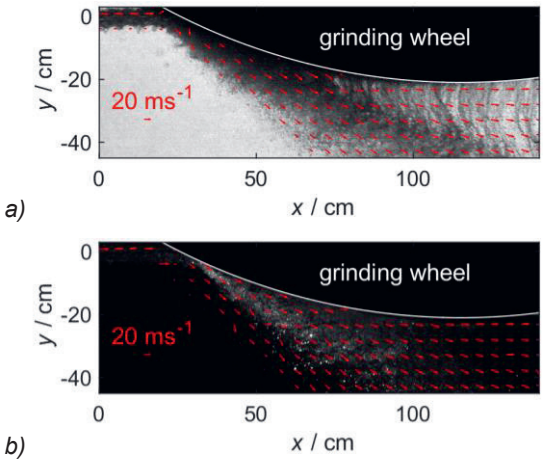

Fig. 2. a) Shadowgraphy and b) PIV raw images together with the resulting velocity flow field.

Acknowledgement

This research is funded by Deutsche Forschungsgemeinschaft (DFG, German Research Foundation) project number 415003387.

References

[1] E. Brinksmeier, D. Meyer, A. Huesmann-Cordes, C. Herrmann, CIRP Annals 64(2), 605-628 (2015); doi: 1016/j.cirp.2015.05.003

[2] C. Heinzel, D. Meyer, B. Kolkwitz, J. Eckebrecht, CIRP Annals 64(1), 333-336 (2015); doi: 10.1016/j.cirp.2015.04.009

[3] P. Geilert, C. Heinzel, A. Wagner, Inventions 2(4), 27 (2017); doi: 10.3390/inventions2040027

[4] D. R. Jonassen, G.S. Settles, M.D. Tronosky, Optics and Lasers in Engineering 44(3-4), 190-207 (2006); doi: 10.1016/j.optlaseng.2005.04.004

[5] M. Raffel, C. Willert, J. Kompenhans Particle Image Velocimetry: A Practical Guide (Experimental Fluid Mechanics), Springer, 2002; doi: 10.1007/978-3-319-68852-7

[6] C. Vanselow, A. Fischer, Optics and Lasers in Engineering 107, 221-230 (2018); doi: 0.1016/j.optlaseng.2018.03.020

DOI 10.5162/SMSI2021/C8.3

Wireless Measurement of Moisture Entry in SYLGARD-527

Kirsten J. Dehning, Moritz Hitzemann, Stefan Zimmermann
Leibniz University Hannover, Institute of Electrical Engineering and Measurement Technology,
Appelstr. 9A, 30167 Hannover, Germany,
dehning@geml.uni-hannover.de

Summary:
Humidity highly affects the failure rate of silicone-potted frequency converters in wind turbines. In order to understand the entry process of moisture, in this work, possible pathways for humidity e.g. by diffusing through the silicone-potting compound or passing along boundaries are investigated by potted humidity sensors. To avoid the effect of cables as additional entry gateways and the diffusion through sidewalls humidity sensors were potted into silicone inside an open toped glass vessel at different positions, and inductively powered and read out via Bluetooth. The results show that under the experimental conditions the moisture mainly diffuses through the silicone and does not pass along the boundary layer between the silicone and the glass.

Keywords: silicone-potting compound, wind turbine converter failure rate, moisture

Introduction

Due to the high failure rate of frequency converters in wind turbines and the associated repair costs and loss of earnings, Germany suffers major economic damage in the region of 200 million euros per year. Various research projects have indicated that moisture is a major cause of failure. Especially the work of Harley et al. shows that water vapor is absorbed in silicone-potting compounds damaging the converter electronics [1]. Furthermore Zorn et al. determined the effect of humidity on failure rate of converters [2].

To investigate possible entry pathways of moisture and its transport in silicone-potting compounds used to seal and protect the semiconductor modules from the environment, humidity and temperature sensors from *Sensirion* (Switzerland, Model SHT35-DIS-B) are fully potted into silicone inside an open glass vessel at different positions. To avoid additional gateways for humidity by cables, in this work, both the energy supply and the data transmission are wireless by inductive powering and Bluetooth. A QI coil placed at the bottom of the vessel is used for inductive powering the potted electronics, while data are transferred from a potted Arduino to an external Arduino connected to a computer using the Bluetooth low energy protocol. Furthermore, the open toped vessel is made of glass to prevent moisture from penetrating from the side.

The used silicone-potting compound is the cold-curing two-component silicone SYLGARD-527 (*Dow*, USA), that is chemically known as polydimethylsiloxane and which is very similar to the silicones used in the semiconductor industry. The temperature and humidity sensor SHT35-DIS-B has an accuracy tolerance of ±1.5 % r.H. [3]. Here, we use eight of such sensors at different positions inside the silicone-potting compound. Four sensors are placed in the middle at different heights and four sensors are placed at one height but with different distances to the sidewall. The different sensor positions inside the silicone-potting compound are given in Tab. 1. The internal Arduino and the energy supply coil are placed far below the sensors. The setup is shown in Fig. 1.

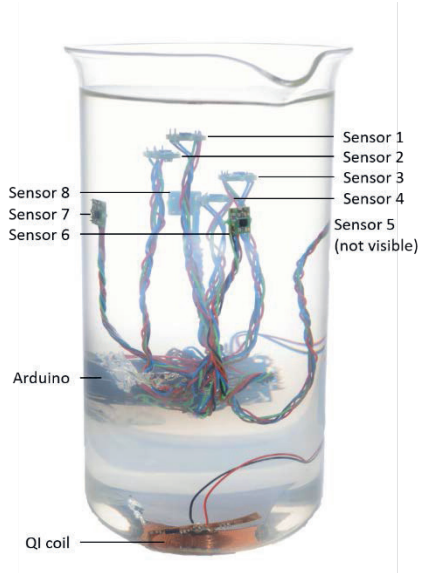

Fig. 1: *Wireless measuring setup with eight sensors silicone-potted in an open toped vessel.*

Tab. 1: Sensor positions

Sensor no.	Distance from the top of the silicone-potting compound [mm]	Distance to sidewall [mm]
1	20	35
2	30	35
3	40	35
4	50	35
5	60	2
6	60	7
7	60	12
8	60	17

Results

In order to investigate the path of moisture through the silicone-potting compound a temporal step profile of relative humidity at constant temperature of 60°C was generated in a climatic chamber. The signals of all eight sensors are shown in Fig. 2. Obviously, the sensors 1 to 4 measure the rising moisture delayed according to the increasing distance from the top of the silicone potting. Even more important, the sensors 5 to 8 show similar response. This clearly indicates that the moisture does not pass along boundary layer between glass vessel wall and the silicone potting.

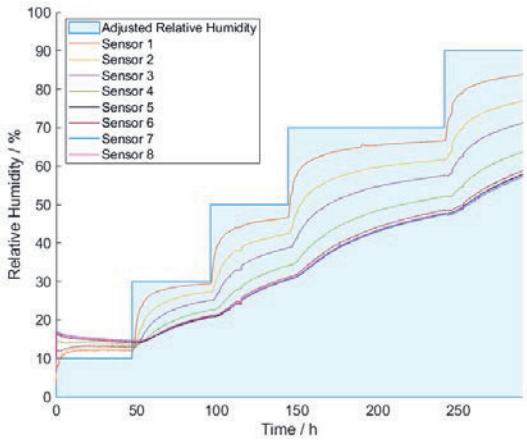

***Fig. 2:** Sensor signals of all eight silicone-potted humidity sensors responding to a temporal step profile of relative humidity at 60°C.*

Furthermore, we calculated the time constants of the sensor responses. Therefore, we used an exponential function fitted to the sensor responses 1 to 4 for the first step from 10 % r.H. to 30 % r.H. This is exemplarily shown in Fig. 3 for the first sensor. The time constants are given in Tab. 2. As expected, the second sensor has about twice the time constant compared to the first sensor although the distance to the surface is just 50% larger.

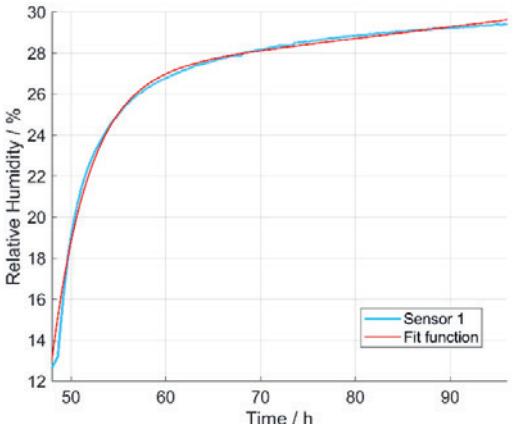

***Fig. 3:** Step from 10 to 30 % r.H. for Sensor 1 with fitted function:* $f(x) = 24.57 \cdot e^{0.002x} - 3157234.10 \cdot e^{-0.26x}$

Tab. 2: Sensor response time constants

Sensor No.	Time to 30% r.H. t_{99} [h]
1	36.9
2	70.3
3	133.0
4	210.3

Conclusion

In this work, the entry process of moisture e.g. by diffusion through the silicone-potting compound SYLGARD-527 and/or passing along the boundary between glass and the silicone is investigated by using wireless humidity sensors potted inside the silicone. The sensors were inductively powered and read out via Bluetooth. This way, other possible moister gateways e.g. via cables were excluded. From the experimental results in becomes clear, that under experimental conditions that the moisture just diffuses through the silicone and does not pass along the boundary layer between the glass and the silicone. In order to transfer this result to the converters, we will use the same setup in a converter module housing and add additional moister gateways, as cables and printed circuit boards, to be presented at the conference.

Acknowledgment

Supported by the German Federal Ministry of Economics and Technology (BMWi) upon decision of the German Bundestag under the Grant 0324336E.

References

[1] S. Harley, E.Glascoe, R. Maxwell, Thermodynamic Study on Dynamic Water Vapor Sorption in Sylgard-184, *The Journal of Physical Chemistry B 116 (48),* 14183-14190 (2012); doi: 10.1021/jp305997f

[2] C. Zorn, M. Piton, N. Kaminski, Impact of Humidity on Railway Converters, *PCIM Europe 2017, Nürnberg,* 715-722 (2017); ISBN: 978-3-8007-4424-4

[3] Sensirion AG, Datasheet SHT3x-DIS (2019)

DOI 10.5162/SMSI2021/C8.4

Measurment methods for understanding water uptake processes in polymers

Paul Gierth, Uta Gierth, Lars Rebenklau, Michael Schneider
Fraunhofer IKTS, Winterbergstrasse 28, 01277 Dresden, Germany
paul.gierth@ikts.fraunhofer.de

Summary:
Harsh environmental conditions may cause corrosion processes in electronics. They are mainly induced by water uptake of polymer embedding, housing or molding compounds. Therefore, longtime stability of these materials is critical for many applications. This work is focusing on demonstration and discussion of suitable measurement methods to determine the water uptake of polymers. Electrochemical impedance spectroscopy (EIS) and Fourier Transform Infrared spectroscopy (FTIR) were used to investigate polymer degradation before and after multiple loading scenarios. Degradation models could have been derived from these results.

Keywords: Electrochemical impedance spectroscopy, Fourier transform infrared spectroscopy, polymers, water uptake, degradation

Motivation

Main purpose of polymers are corrosion protection of conductors and electronic components. Therefore, the longtime stability of these materials against different loading scenarios is critical for many applications. Usually, modern test scenarios just focus on pass or fail results, e.g. mechanical characterization [1]. Such tests are regularly performed before and after defined loading scenarios like damp heat, temperature cycling or pressure cooker treatment. Unfortunately, the results only summarize the accumulated alteration at the time of test. A deep understanding of the fundamental reaction processes or kinetics can´t be achieved in that way but is necessary for further improvement of materials and technologies. In addition to conventional shear test, the Methods EIS and FTIR were applied.

EIS and FTIR for electronic industry

EIS and FTIR is commonly used in corrosion research. By means of EIS the determination of electrical impedance as a function of the measuring frequency can be realized. Standardly, this method is applied to investigate material characteristics, such as dielectric permittivity and capacitance. In insulating materials, a capacitive characteristic appears, whereas in electrical conductors an ohmic characteristic dominates. Polymers present a shifting characteristic between these two main states in dependency of their degradation state. A fast condition check is possible, especially water uptake, due to voids, blister, or insufficient cross-linking of the polymer structure. In addition, FTIR helps to investigate the molecular changes by stimulation of functional groups. For example, formation of intramolecular hydrogen bonds within the polymer network is detectable. Additionally, analyzing destruction of chemical bonds is possible.

Experimental

Two kinds of epoxy coatings were selected and cured on printed circuit boards (PCB) with electroless nickel immersion gold (ENIG) finishes. These samples were aged for up to 96 h in a pressure cooker test or up to 14 days in a damp-heat-treatment and further inspected regarding their shear strength stability. The degradation process was investigated with EIS and corelated with FTIR measurement, but discussion is focused on EIS.

Results

Shear strengths are summarized in Fig. 1 and 2.

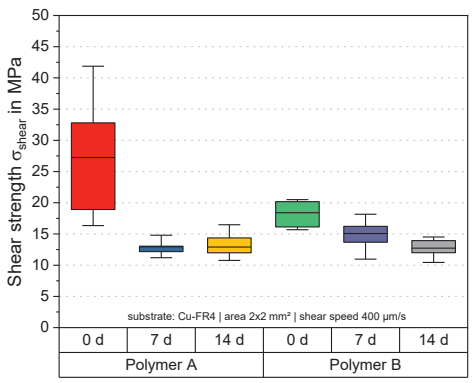

Fig. 1. Shear strengths of epoxies on ENIG surfaces before and after damp heat treatment

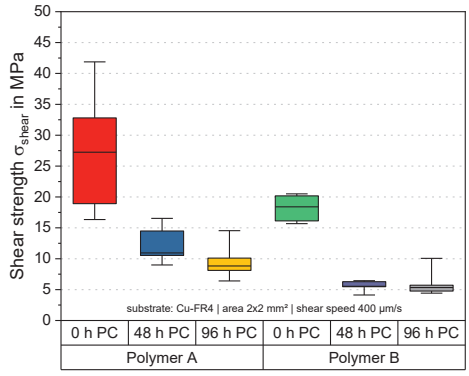

Fig. 2. Shear strengths of epoxies on ENIG surfaces before and after pressure cooker treatment (PC)

Both loading scenarios show strong mechanical degradation of the inspected epoxies. The pressure cooker treatment leads to a faster degradation overall. The optical inspection of all fracture zones shows adhesive as well as cohesive failure mechanisms. Consequently, no clear degradation mechanism could be observed. Optical inspection of the polymers revealed that polymer *A* occurs defects like blisters, pinholes, or inclusions in certain regions. Polymer *B* seems to be nearly free of defects.

Samples were analyzed with EIS before and after PCT to obtain a better understanding of the degradation mechanism.

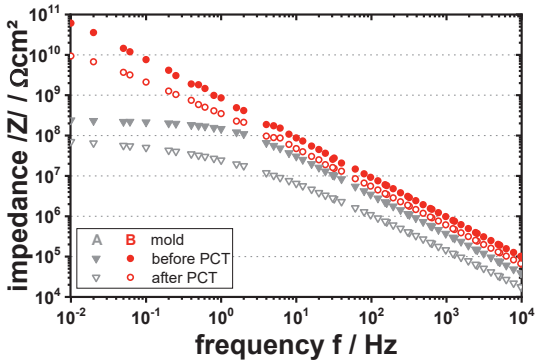

Fig. 3. EIS: Impedance of polymer A and B before and after pressure cooker treatment (PC).

The change of capacitive reactance on high frequency region during different loading scenarios is used to calculate water uptake WU of the material by using eg. (1) according [2].

$$WU = \frac{\lg\left(\frac{C_t}{C_o}\right)}{\lg 80} \cdot 100\ (Vol.\%) \qquad (1)$$

The water uptake was calculated to approximately 21 Vol.% for polymer A and 11 Vol.% for polymer B. The different results indicate different water penetration scenarios. For the nearly perfectly cured Polymer B, liquids could only penetrate the material by a homogeneous diffusion across the material. A polymer with several surface defects (A) offers the possibility for inhomogeneous penetration of any kind of liquids into deeper material regions along preferred paths and accelerates the degradation in this way. Selective penetration could be found in phase shift of the impedance during EIS measurement and was used to generate following equivalent circuits according [4, 5].

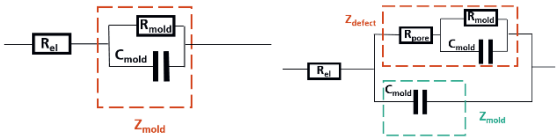

Fig. 3. Equivalent circuits of polymers on metallic surfaces without surface defects (left) and with liquid penetrated pores (right).

Therefore, pre-existent defects previously detected by optical microscopy of polymer A could clearly been seen in the initial EIS measurement (lower frequencies) and their influence on environment stability could be described using the shown methods. In that way, a better understanding of different degradation mechanisms could be found without destruction of the samples, which demonstrates the usability of this measurement method as material and application controlling method.

For a complete understanding of the ongoing degradation mechanisms during the applied loading scenarios FTIR inspections must be applied. The obviously change in intensity ratio of characteristic bands provides information like an increase of hydroxide ion content or decreasing of epoxide bond. That indicates a significant change of the material during the loading scenario. These results are appropriate to generate better understanding in material degradation mechanism and material state monitoring over product lifetime cycles. Therefore, methods like EIS and FTIR are highly recommended to be transferred from the corrosion research to the electronic industries.

References

[1] Military Specification (MIL)-883, Method 2019.9 Die shear strength, revision E, Department of Defense, 1991.

[2] D. M. Brasher, A. H. Kingsbury, electrical measurment in the study of immersed paint coatings in metal, Journal of Applied Chemistry, 1954.

[3] U. Rammelt, habilitation thesis, TU Dresden 1991.

[4] G. Grundmeier et al.: Electrochim. Acta 45 (2000) 2515

DOI 10.5162/SMSI2021/C9.1

Temporal Hygrometer Characterization: Design and First Test of a New, Metrological-Dynamic-Testing-Infrastructure

Felix Witt[1], Dominik Bergmann[2], Florian Bubser[1], Volker Ebert[1]
[1] Physikalisch- Technische Bundesanstalt, Bundesallee 100, 38116 Brunswick, Germany,
[2] Institut für Flugführung der Technischen Universität Braunschweig, Hermann-Blenk-Str. 27, 38108 Brunswick, Germany
Corresponding Author volker.ebert@ptb.de

Summary:
A new, metrological-dynamic-testing-infrastructure (MetDynTI) for hygrometers is presented, comprising a flow test section driven by a switching water vapor (H_2O) step change generator, capable of fast, well defined, H_2O steps from 300 to up to 15000 µmol/mol. The step response of the test section is detected in real-time by means of an integrated, fast, direct tunable diode laser absorption spectroscopy (dTDLAS) hygrometer. The exact knowledge of the dynamic behavior of the driving section enables the dynamic characterization of subsequent test hygrometers exposed to the H_2O step change.

Keywords: Dynamic Characterization, Hygrometer, Laser Spectroscopy, dTDLAS, Metrology

Introduction

Water vapor (H_2O) in air is an essential parameter that is monitored in many home or workplace applications e.g. air conditioning or ventilation and is also key for industrial process control systems [1], or for weather forecast or for climate studies. Accurate monitoring of dynamic H_2O concentration [H_2O] changes which may be caused by opening a window or changing process parameters is key for process control systems and poses a significant challenge for most hygrometers used commonly [2]. Hygrometers are almost exclusively calibrated under quasi-static conditions. An accurate or even traceable characterization of their dynamic response, however, is often lacking, or needs to be strongly improved. Inaccurate dynamic coefficients often cause temperature oscillations. These may lead to discomfort or energy losses in a home setting or can have significant implications for an industrial process control system. One reason for this deficiency is the lack of a (metrologically) standardized dynamic hygrometer characterization. Here, we present a newly designed dynamic hygrometer test setup comprising: A) Generation of fast, defined [H_2O] step changes in air. B) A fast, absolute and sampling-free, optical reference [H_2O] analyzer. C) A gas flow test section in which the device under test (DUT) can be inserted and which is optimized to “maintain” the steep H_2O gradients. By comparison of traceable, H_2O step changes with the DUT dynamic behavior we can extract the DUTs dynamic characteristics and their dependence on step height, step direction, flow speed etc.

H_2O Step Generation and Flow Conditioning

Fig. 1 schematically shows the H_2O step generation, flow conditioning and optical measurement section (similar to [3]). A base flow of dry air ([H_2O] < 20 ppm), at ambient pressure, is dynamically mixed with humid air from one of the two thermodynamic static humidity generators. Two 3/2 valves enable fast switching between the generators without interrupting their flow. The upper and lower H_2O values can be adjusted between 300 and 15000 µmol/mol (= ppm). The air is injected into the measurement section (80 mm diameter) and homogenized using a sintered glass filter. A honeycomb flow rectifier is used to reduce the flow turbulences. The axial gas velocity inside the flow tube ranges from 0.06 to 0.33 m/s (20 to 100 l/min). The generated gas travels axially along a two-meter-long open pipe to prevent ambient effects on the measurement zone.

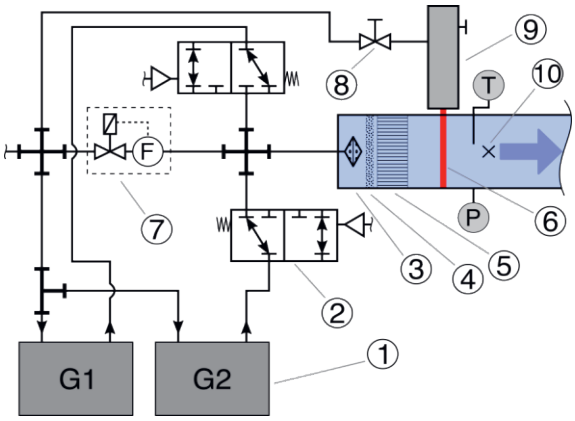

Fig. 1. Schematic test setup. 1: Humidity generators, 2: 3/2 valves, 3: Injection nozzle, 4: Sintered filter,

5: Honeycomb flow rectifier, 6: dTDLAS laser measuring plane, 7: Flow controller, 8: Needle valve, 9 dTDLAS optic unit, 10: DUT Position

dTDLAS as a fast, reference Hygrometer

An optical multipath ring cell (#6 in Fig. 1), forming a thin, planar laser sheet, perpendicular to the flow, is used to analyze the generated [H_2O] step changes in front of the DUT via high-speed, sampling-free and SI-traceable, direct tunable diode laser absorption spectroscopy (dTDLAS) [4]. From the cell's spectral transmission dTDLAS derives calibration-free absolute H_2O concentration using a 1st-principles model based on the Lambert-Beer law, high accuracy H_2O spectral data as well as measured path length and gas temperatures/pressures [4]. The current setup uses an H_2O absorption line at 1370 nm. Measurements from 50 to 30000 ppm with a resolution of 1 ppm are feasible. The current max. time resolution lies near 14 Hz and will be improved further by a faster data acquisition. Fig. 2 shows a typical H_2O absorption profile with a fitted Voigt line shape indicating 315 ppm H_2O at 1013 hPa.

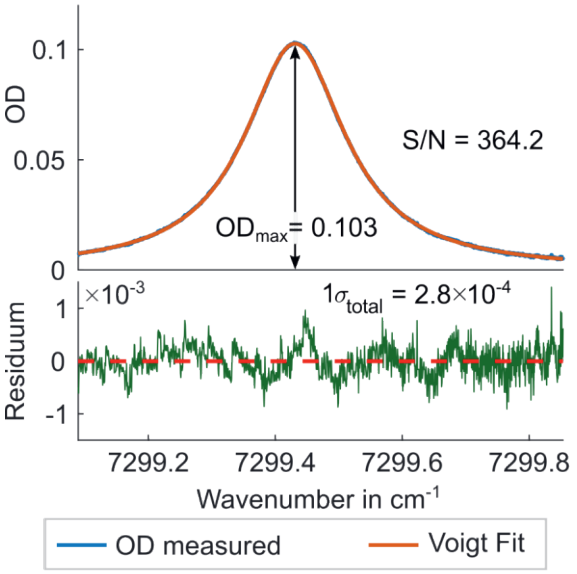

Fig. 2. Measured and fitted optical density (OD) of a single scan of the absorption line. Below: the residual be-tween fitted and measured data. The signal to noise ratio (S/N) defined by OD_{max} / $1\sigma_{total}$ is 364.

Results

Fig. 3 shows the dynamic [H_2O] at the optical cell measured with the dTDLAS-Hygrometer for a step from 315 ppm to 3731 ppm. At a total flow rate of 20 l/min it takes about 0.6 s for the changed concentration to reach the measurement plane of the laser and an additional 0.4 s to reach 10 % of the "final" step concentration. At t_{10} the local [H_2O] temporal "gradient" exceeds 3050 ppm/s, which is not achievable with most other hygrometers. t_{90} is reached 3.1 s after the [H_2O] change arrived at the laser. After t_{10}, i.e. after the early transition phase between t_{dead} and t_{10}, the [H_2O] dynamics is well described with a first order low pass. This well predictable behavior in combination with planned improvements to further reduce the step time will make it possible to mathematically remove the "influence" of the setup and to isolate the dynamic response behavior of a potential DUT in the test section.

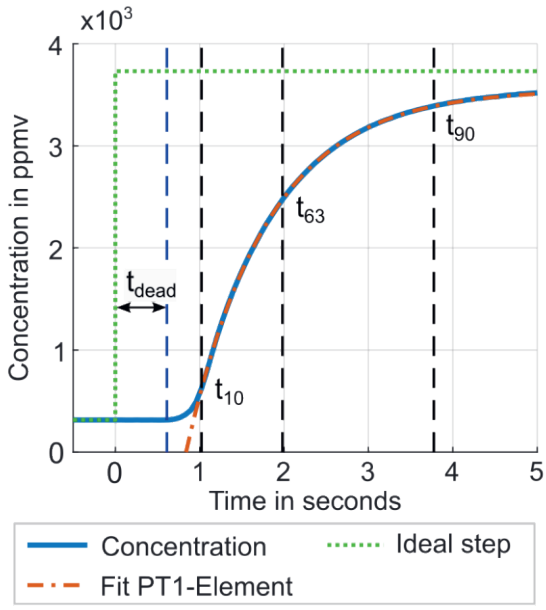

Fig. 3. [H_2O] step from 315 to 3731 ppm measured with the dTDLAS-Hygrometer. The new gas mix arrives at the measurement plane after a transport time of 0.6 s after the valves were actuated. An ideal low pass behavior (PT1-Element) is fitted to the step response between t_{10} and t_{90}. The fits coefficient of determination (R^2) is 1.000 the RMSE is 3.796. The "$t_{10} \rightarrow t_{90}$ response time" is 2.7 s.

References

[1] S. Bell, R. Benyon, N. Böse, et al., A Roadmap for Humidity and Moisture Measurement, Int J Thermophys 29, 1537–1543 (2008); doi: 10.1007/s10765-008-0419-8

[2] B. Buchholz, A. Afchine, A. Klein, et al., HAI, a new airborne, absolute, twin dual-channel, multi-phase TDLAS-hygrometer background, design, setup, and first flight data, Atmospheric Measurement Techniques 10, 35–57 (2017); doi: 10.5194/amt-10-35-2017

[3] E. Georgin, F. Bubser, R. Deschermeier, V. Ebert, Metrology of Transient Humidity Measurements: Dynamic Generation and Measurement of Humidity, Conference: TEMPMEKO 2019, Chengdu, China

[4] B. Buchholz, N. Böse, V. Ebert, Absolute validation of a diode laser hygrometer via intercomparison with the German national primary water vapor standard, Appl. Phys. B 116, 883–899 (2014), doi: 10.1007/s00340-014-5775-4

DOI 10.5162/SMSI2021/C9.2

Towards the assessment of the accuracy of measuring the integral characteristics of physical quantities using the sensors of discrete values of these quantities

P. Neyezhmakov[1], A. Prokopov[1], T. Panasenko[1], V. Skliarov[1], A. Shloma[1]
National Scientific Centre "Institute of Metrology",
Myronosytska Str., 42, 61002 Kharkiv, Ukraine
pavel.neyezhmakov@metrology.kharkov.ua

Summary:
The methodology of accuracy analysis of measurement results for the case when the required value is an integral of a continuous function, and the measuring instruments are sensors for determining the discrete values of this function on the integration interval, is presented.

Keywords: sensor, integral, discrete values, quadrature formula, accuracy

Background, Motivation an Objective

Among the measurement tasks, a special place is occupied by measurements, in which not just a certain value of the physical quantity is to be determined, but an integral of the function of this quantity, the arguments of which are time or spatial coordinates. Examples of such measurements include determination of the mean temperature by volume at thermal measurements; determination of the effective (operating) value of the electrical voltage at electromagnetic measurements; determination of the mean along the trajectory of propagation of electromagnetic signal of (the mean integral) refractive index of air, which takes into account the difference between the velocity of propagation of this signal in the Earth's atmosphere and the velocity of light in vacuum in length measurement in geodesy.

If, in the above cases, sensors are used as measuring instruments to obtain local values of physical quantities that determine discrete values of the corresponding sub-integral functions on the integration interval, then, in order to assess the accuracy of the expected result, it is necessary to perform the following: firstly, to assess the accuracy of the representation of the original integral in the form of a combination of ratios determined by discrete values of the sub-integral function (i.e., the accuracy of the used variant of the quadrature formula); secondly, to establish the requirements to the accuracy of the used sensors and to the measurement procedure (ensuring the fulfillment of the initial requirements to the accuracy of the measurement result): thirdly, to estimate the contribution of external factors influencing the measurement result.

Description of the New Method

The possible variant of the solution of the above problem is considered further on the example of geodetic length measurements performed on near-Earth baselines with electromagnetic waves of optical range. The case of measuring lengths of up to 5 km with uncertainty of not more than 1 mm is analysed.

The ratio for the length L between the end points of the baseline being measured in neglect of the rangefinder signal trajectory refractive curvature, which is insignificant for this case, is as follows

$$L = \frac{c \cdot \tau}{\overline{n}} \qquad (1)$$

where c is the speed of light in vacuum (known constant); τ is the propagation time of the signal on the baseline being measured (it is measured directly or obtained from the measured phase incursion of the signal that has passed the baseline);

$$\overline{n} = \frac{1}{L}\int_0^L n(x)\,dx \qquad (2)$$

mean integral value of the refractive index of air (x is a coordinate along the trajectory).

The formula for the expanded measurement uncertainty L according to (1) has the form

$$u_L = 2L\sqrt{\frac{u_\tau^2}{\tau^2} + \frac{u_{\overline{n}}^2}{\overline{n}^2}}, \quad (3)$$

where u_τ, $u_{\bar{n}}$ are the measurement uncertainties τ and $\bar{n}$, respectively. From (3) for $U_L \leq 1$ mm at $L \leq 5$ km, taking into account that for modern rangefinders in this range $\frac{u_\tau}{\tau} < 2 \cdot 10^{-8}$, we obtain the requirement for measurement uncertainty $\bar{n}$

$$u_{\bar{n}} \leq 5 \cdot \frac{10^{-7}}{L}, \qquad (4)$$

where L in km.

The quantity $u_{\bar{n}}$ includes components that depend, respectively, on the accuracy of the used variant of the quadrature formula, instrumental error of the meteorological sensors (since the well-known formulas for $n(x)$ [1] determine $n(x)$ precisely through the values of temperature T, pressure p, humidity e at a point x), accuracy of accounting for external influencing factors.

The analysis of the requirements for the measurement uncertainty carried out with the meteorological sensors (provided that the components of the uncertainty due to the influence of external conditions and the inaccuracy of the used variants of the quadrature formulas are negligible) was performed in [2] and made it possible to establish the ranges of change of meteorological parameters and the values of the measurement uncertainties for pressure, humidity and temperature for which condition (4) is satisfied.

The conditions with the influence of external factors (atmospheric turbulence) on the value $u_{\bar{n}}$ are considered in [3].

A preliminary analysis of the accuracy of the quadrature formulas being used is made in [4] on the basis of comparison of the values of the remainders of these formulas. The assessments indicate higher precision capabilities of the gradient method using Euler-Maclaurin quadratures or Hermite polynomials (in comparison with the trapezium quadrature formula).

The results of these assessments are confirmed by a numerical experiment carried out during the preparation of this publication. The profiles $n(x)$ experimentally obtained at a baseline of 1 km of the reference baseline geodetic polygon of the NSC “Institute of Metrology” are used. For the function $n(x)$, exact values $\bar{n}$ are calculated according to formula (2), as well as approximate values according to the above-mentioned quadrature formulas (depending on the number of intervals N, into which the baseline is divided by the measurement points of local values of meteorological parameters). It is shown that the difference between the exact and approximate value $\bar{n}$ for the gradient method reduces to a value of ~10^{-8} already at two end and one intermediate measurement points of meteorological parameters on the 1 km baseline.

Results

Within the framework of the task of measuring quantities that are time or spatial coordinate integrals using sensors for discrete measurements, an analysis was made of the possibility of ensuring the accuracy required in precision length measurement in determining the refractive index of air $\bar{n}$ averaged along the trajectory of propagation of an electromagnetic signal.

It was shown that for baselines of up to 5 km, the combined uncertainty of the length measurement of 1 mm can be ensured by the gradient method based on the Euler-Maclaurin quadrature and Hermite polynomials.

References

[1] P. Ciddor, R. Hill. Refractive index of air. 2. Group index. *Applied Optics* 38(9):1663–1667, 1999. doi:10.1364/AO.38.001663.

[2] P. Neyezmakov, V. Kupko, T. Panasenko, A. Prokopov, V. Skliarov, A. Shloma. Analysis of accuracy requirements to the meteorological sensors used to compensate for the influence of the Earth’s atmosphere in high precision length measurement. Proceedings of SMSI 2020 Conference, 22–25 June 2020, Nuremberg,Germany, doi:10.5162/SMSI2020/D3.3.

[3] A. Andrusenko, A. Prokopov, Ye. Remayev. Methods for evaluating the error in determining the mean integral refractive index of air at the High Accuracy Calibration Rig UVT 5-84. In book Metrologiya v lazernoy dal'nometrii. Kharkov. NPO Metrologia, 1991. P. 34–42 (In Russian).

[4] P. Neyezhmakov, A. Prokopov. Analysis of the accuracy of the gradient method for determining the mean integral refractive index of air. Ukrainian Metrological Journal, 2018, No. 4, pp. 43-48. doi: 10.24027/2306-7039.4.2018.155754.

Acknowledgement

This study was performed under the European joint research project named EMPIR 18SIB01 GeoMetre Large-scale dimensional measurements for geodesy. This project has received funding from the EMPIR programme cofinanced by the Participating States and from the European Union’s Horizon 2020 research and innovation programme.

DOI 10.5162/SMSI2021/C9.3

Detecting Local Delamination of Power Electronic Devices through Thermal-Mechanical Analysis

H. Huai, G. Laskin, M. Fratz, T. Seyler, T. Beckmann, A. Bertz, J. Wilde
[1] Albert-Ludwigs-University, Georges-Koehler-Allee 103, 79110 Freiburg
[2] Fraunhofer IPM, Georges-Koehler-Allee 301, 79110 Freiburg
haosu.huai@imtek.uni-freiburg.de

Abstract:
Die attachment delamination is one of the most common defects that happen over the life-time of a power electronic module [1]. It is usually the consequence of thermal mechanical stress that occurs during active operation of the device due to CTE (coefficient of thermal expansion) mismatch of its components. Additionally, even during the production cycles, errors can emerge, where the chip is not fully attached to the substrate. This can lead to premature failure of the final product. Aim of this paper is the detection of local delamination spots through pre-existing optical techniques. This novel non-destructive method will allow the isolation of defective devices during production or warn the overall system during operation, if a failure is imminent.

Keywords: Power electronics, Reliability, Non-destructive testing, Thermal-Mechanical Analysis, Die attachment

Optical Measurement Methods

Thermal-Mechanical stress in a power module will result into warpage of the system. One way to observe this deformation is by using the Digital Image Correlation (DIC). Here, the sample is first prepared with a stochastic black and white pattern. Two high resolution cameras observe the movement of the black dots during heating and calculate the stress and strain by comparing the reference image taken at the start of the measurement with subsequent images shot [2].

Another way to measure the deformation is by using the Electronic Speckle-Pattern Interferometry (ESPI) (Fig. 1). In this method, a continuous laser is used to illuminate the measurement area constantly. The Interference between reference and measurement beam will provide phase information that is used to calculate the result.

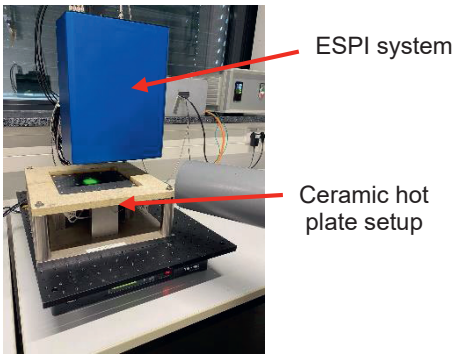

Fig. 1. Measurement setup for ESPI during passive heating.

Modelling of Delamination Effects

The main focus of this paper are IGBTs (Insulated Gate Bipolar Transistors) and power diodes. Samples with intentionally built in defects are manufactured with an established silver sintering process on top of PCB substrates (Fig. 2) [3]. During the step of printing the SnAg paste on the PCB with a stencil, we use custom made stencils with smaller openings compared to the regular process. By varying the geometry of the openings, we can produce chips that are not attached to the substrate at specific locations. Thus, we achieve samples that model the delamination process perfectly. Finally, the deformation is captured with the help of DIC and ESPI systems. Through comparing the warpage of healthy and defective samples, we want to correlate the behavior of the deformation with the magnitude and location of the defect. FE-simulation of samples with varying sinter layers are created to serve as a base for comparison for the measurements.

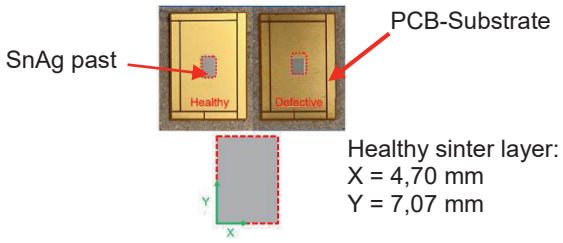

fig. 2. IGBT samples with healthy and defective sinter layers through variation of their x and y value.

Results

Simulation results for the warpage of an IGBT chip with a reduced length in Y-direction of 5,57 mm at increased temperatures show significant overshoot in the area of local delamination. (Fig. 3).

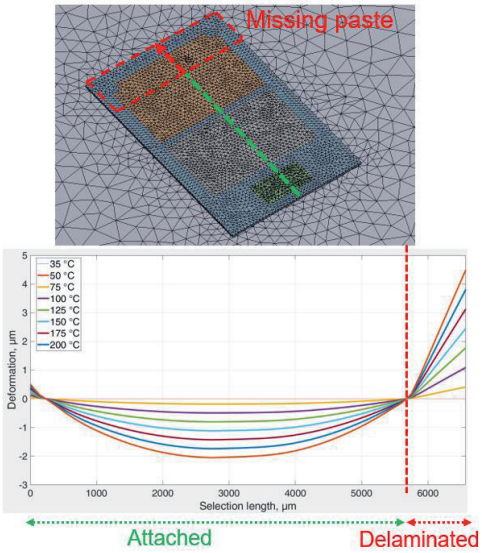

Fig. 3. FE-simulation of delamination effects with Ansys Workbench.

This behavior is to be compared to the measurement results with DIC and ESPI. A phase image taken with the ESPI already shows the area of delamination clearly (Fig. 4).

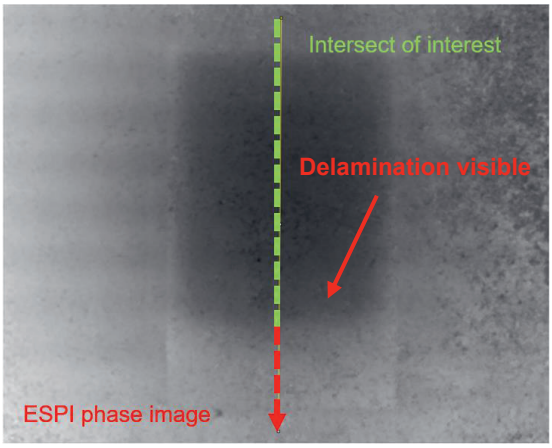

Fig. 4. ESPI phase image of IGBT with delamination.

It is notable that the same overshoot behavior seen in the simulation can also be found in the measurements. Comparing the simulation (Fig. 4) with the DIC and ESPI results (Fig. 5 and Fig. 6), one can clearly see that the delamination starts at a section length of about 5,5 mm, which matches with the new length in Y-direction of the sinter layer. The graphs also show that the ESPI provide much better results with less noise.

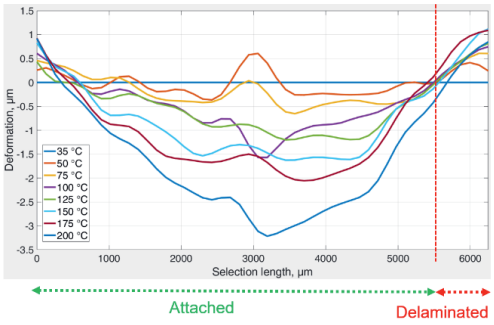

Fig. 5. Deformation along IGBT chip at various temperatures monitored with DIC.

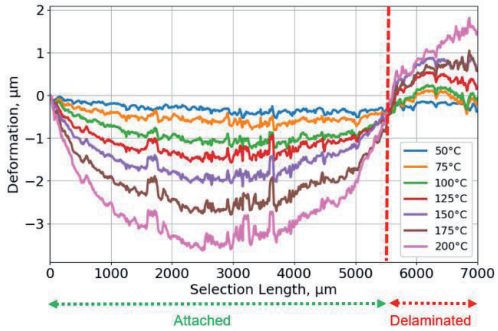

Fig 6. Deformation along IGBT chip at various temperatures monitored with ESPI.

Conclusion

In this paper, we have proposed a novel non-destructive method to test power electronic devices of delamination defects by performing a thermal-mechanical analysis. For this purpose, an established sinter process is varied to allow the user to intentionally create locations of low attachment between chip and substrate. Following, the warpage of healthy and defective samples during passive heating on a hot plate are recorded with optical methods and compared. This shows that locations of delamination show characteristic behaviors in their warpage, which can be used as an indication for fault detection.

References

[1] *A. Schiffmacher, J. Wilde, C. Kempiak, A. Lindemann, J. Rudzki and F. Osterwald, "Thermomechanical deformations of power modules with Sintered Metal Buffer Layers under Consideration of the Operating Time and Conditions," 2020 ECTC Orlando, FL, USA*

[2] *Siebert, Thorsten, Hans-Reinhard Schubach, and Karsten Splitthof. "Recent Developments and Applications for Optical full field strain measurement using ESPI and DIC." Fourth International Seminar on Modern Cutting and Measurement Engineering. Vol. 7997. International Society for Optics and Photonics, 2011.*

[3] N. Subbiah, A. Schiffmacher, X. Song and J. Wilde, "Comparison of silver sintered assemblies on Non-DCB Substrates," CIPS 2020

DOI 10.5162/SMSI2021/D1.1

GUM2ALA – Uncertainty propagation algorithm for the Adaptive Linear Approximation according to the GUM

Tanja Dorst[1], Sascha Eichstädt[2], Tizian Schneider[1,3], Andreas Schütze[1,3]
[1] ZeMA – Center for Mechatronics and Automation Technology gGmbH, Saarbruecken, Germany,
[2] Physikalisch-Technische Bundesanstalt, Braunschweig and Berlin, Germany,
[3] Saarland University, Lab for Measurement Technology, Saarbruecken, Germany
E-mail (corresponding author): t.dorst@zema.de

Summary:
In machine learning, many feature extraction algorithms are available. To obtain reliable features from measured data, a propagation of measurement uncertainty is necessary for these algorithms. In this contribution, the Adaptive Linear Approximation (ALA) as one feature extraction algorithm is considered, and analytical formulas are developed for an uncertainty propagation in line with the Guide to the Expression of Uncertainty in Measurement (GUM). This extends the set of uncertainty-aware feature extraction methods, which already contains the discrete Fourier and Wavelet transform.

Keywords: measurement uncertainty, uncertainty propagation, feature extraction, adaptive linear approximation, machine learning

Motivation

The increasing demand for performance and efficiency in Industry 4.0 has led to the growing adoption of smart sensors, which allow data acquisition combined with internal signal processing, e.g., based on machine learning (ML). To analyze recorded data and develop data based evaluation models, a fully automated machine learning toolbox [1] can be used without knowledge of any physical process model and without expert knowledge. The best combination of five complementary methods for feature extraction (FE) and three for feature selection (FS) is calculated using a simple, but efficient classifier and k-fold cross validation for the training data set.
Whenever decisions are based on data, reliable data are important. Measurement uncertainties, sensor calibration and thus traceability to the SI units are the key principles in metrology. To be able to evaluate data quality and thus the quality of the ML results, it is necessary to consider the uncertainty information associated with the sensor data, ideally from calibration. However, calibrated sensors are seldomly used due to cost reasons or because removal and recalibration of the sensors may be difficult or even impossible. In these cases, information from the data sheets of the manufacturers could be used to obtain an indication of the data quality in form of a measurement uncertainty.
The available measurement uncertainty information associated with the raw sensor data then needs to be taken into account in the subsequent data processing. However, the measurement uncertainty evaluation within the above-mentioned software toolbox has been neglected so far. To extend the toolbox for uncertainty analysis, the uncertainty associated with the raw sensor data must be propagated through the FE and FS methods. The reduction of the number of features is carried out by the FS methods. The classification afterwards is carried out in two steps: a further dimensionality reduction by Linear Discriminant Analysis (LDA) followed by the classification itself based on the Mahalanobis distance to the class centers. The selection and classification methods can use the measurement uncertainty information of the extracted features or methods of Bayesian statistics. It is worth noting that a Bayesian approach can also be implemented for FS and classification.
In this contribution, an algorithm for the uncertainty propagation in the Adaptive Linear Approximation (ALA) is developed in line with the *Guide to the Expression of Uncertainty in Measurement (GUM)* [2] and validated using a Monte-Carlo simulation corresponding to Supplement 2 to the GUM [3].

Results

ALA approximates a signal in linear segments of variable length. Mean and slope are extracted for each segment as features. The number of segments is calculated automatically, depending on the tradeoff between number of features and approximation error. The calculations for every

segment are the same, therefore they are shown here only for one segment.

Let $Y = (y_1, \dots, y_n) \in \mathbb{R}^{1\times n}$ denote the real-valued time-domain values of a signal. The result of the ALA for Y is given by

$$F = \left(\overline{y_1}, \dots, \overline{y_{u_3+1}}, b_1, \dots, b_{u_3+1}\right) \in \mathbb{R}^{1\times 2(u_3+1)},$$

where $\overline{y_k}$ denotes the mean value and b_k the slope of the k-th segment, respectively. The index u_3 is the number of splits and therefore, $u_3 + 1$ the number of segments into which the signal is divided. The mean value and slope for the k-th segment are determined by

$$\overline{y_k} = f(y_i) = \frac{1}{v_{k+1}-v_k+1}\sum_{i=v_k}^{v_{k+1}} y_i$$

and

$$b_k = h(y_i) = \frac{\sum_{i=v_k}^{v_{k+1}}(t_i - \overline{t_k})(y_i - \overline{y_k})}{\sum_{i=v_k}^{v_{k+1}}(t_i - \overline{t_k})^2}.$$

For the propagation of uncertainties according to GUM, the sensitivities of the mapping $Y \mapsto F$ are calculated as

$$c_{k,j} = \frac{\partial \overline{y_k}}{\partial y_j} = \frac{1}{v_{k+1}-v_k+1}$$

and

$$d_{k,j} = \frac{\partial b_k}{\partial y_j} = \frac{t_i - \overline{t_k}}{\sum_{i=v_k}^{v_{k+1}}(t_i - \overline{t_k})^2},$$

for $j = v_k, \dots, v_{k+1}$, where v_k denotes the index of the input quantities at the beginning of a segment and v_{k+1} at the end, respectively. These coefficients can be stored in a sensitivity matrix

$$\mathbf{J}^{\mathbf{m}}_{\bar{\mathbf{y}},\mathbf{b}} = \begin{pmatrix}\mathbf{C}\\ \mathbf{D}\end{pmatrix} \in \mathbb{R}^{2(u_3+1)\times n},$$

where $\mathbf{C} \in \mathbb{R}^{(u_3+1)\times n}$ denotes the upper submatrix with sensitivity coefficients for the mean values, and $\mathbf{D}$ the lower submatrix with sensitivity coefficients for the slopes. The covariance matrix $\mathbf{U} \in \mathbb{R}^{n\times n}$ of the input quantities leads to the following expression for the covariance matrix $\mathbf{U_F} \in \mathbb{R}^{n\times n}$ associated with F:

$$\mathbf{U_F} = \mathbf{J}^{\mathbf{m}}_{\bar{\mathbf{y}},\mathbf{b}} \cdot \mathbf{U} \cdot \mathbf{J}^{\mathbf{m}}_{\bar{\mathbf{y}},\mathbf{b}} = \begin{pmatrix} \mathbf{C}\mathbf{U}_\mathbf{y}\mathbf{C}^\mathbf{T} & \mathbf{C}\mathbf{U}_\mathbf{y}\mathbf{D}^\mathbf{T} \\ \left(\mathbf{C}\mathbf{U}_\mathbf{y}\mathbf{D}^\mathbf{T}\right)^T & \mathbf{D}\mathbf{U}_\mathbf{y}\mathbf{D}^\mathbf{T} \end{pmatrix}$$

The block structure of the covariance matrix $\mathbf{U_F}$ can be used to deal with computer memory issues. Since $\mathbf{U_F}$ is symmetric, only three blocks need to be stored, see also [4].

Fig. 1 shows the features for one signal and the validation of the features with a Monte Carlo simulation with 1.000.000 trials. The comparison of the GUM2ALA to the Monte Carlo results shows that the features and their associated uncertainties are the same for both approaches. However, the application of a Monte Carlo simulation is much more time-consuming. Furthermore, a straightforward implementation of the Monte Carlo simulation is in most cases not feasible for standard computers due to the amount of computer memory required.

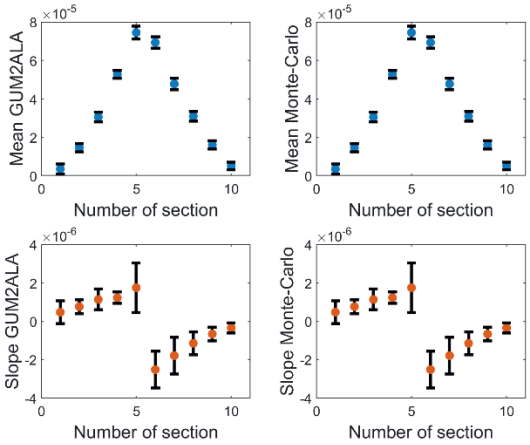

Fig. 1: Mean (top) and slope (bottom) as features for one cycle divided into 10 sections, calculated by the GUM2ALA algorithm (left) and validated by a Monte-Carlo simulation with 10^6 runs (right).

Outlook

After extending the approach to all FE methods in the toolbox, the feature uncertainty will be considered in the FS and classification steps for improving the stability and performance of the automated ML toolbox.

Acknowledgement

Part of this work has been developed within the Joint Research project 17IND12 Met4FoF of the European Metrology Programme for Innovation and Research (EMPIR). The EMPIR is jointly funded by the EMPIR participating countries within EURAMET and the European Union.

References

[1] T. Schneider, N. Helwig, and A. Schütze, “Industrial condition monitoring with smart sensors using automated feature extraction and selection,” *Meas. Sci. Technol.*, vol. 29, no. 9, 2018, doi: 10.1088/1361-6501/aad1d4.

[2] Joint Committee for Guides in Metrology, “JCGM 100: Evaluation of measurement data — Guide to the expression of uncertainty in measurement,” *JCGM100:2008*, 2008.

[3] Joint Committee for Guides in Metrology, “JCGM 102: Evaluation of measurement data – Supplement 2 to the ‘Guide to the expression of uncertainty in measurement’ – Extension to any number of output quantities,” *JCGM102:2011*, 2011.

[4] S. Eichstädt and V. Wilkens, “GUM2DFT – a software tool for uncertainty evaluation of transient signals in the frequency domain,” *Meas. Sci. Technol.*, vol. 27, no. 5, 2016, doi: 10.1088/0957-0233/27/5/055001.

DOI 10.5162/SMSI2021/D1.2

Representing Semantic Information in Sensor Networks

Maximilian Gruber[1], *Sascha Eichstädt*[1]
[1] *Physikalisch-Technische Bundesanstalt, Berlin, Germany*
maximilian.gruber@ptb.de

Summary:
To pave the way towards (semi-) automated data-analysis, self-describing sensors and measurements become a key component in the context of Industry 4.0. We map concepts from existing knowledge bases into a coherent new ontology to fulfill metrological requirements of sensor and measurement descriptions. Use cases considered for this ontology cover sensor networks, network topology, network robustness, information fusion, calibration models for dynamic uncertainty, correct metrological representation and implementation performance.

Keywords: metadata, ontology, sensor network, information fusion, uncertainty

Introduction and Considered Use Cases

Automating the analysis of an ever-growing number of sensors in industrial plants requires sensors that can self-provide information about themselves in an appropriate and machine-interpretable format [1-4]. Promising approaches to achieve these goals can be found by considering the developments of the semantic web group [5] and ontology engineers coming from diverse disciplines [6].

Consider a use case with a set of calibrated dynamic sensors with topological and geometrical relations. A physical effect that is constant in its intensity moves relative to the array of sensors, leading to spatial and temporal dependent sensor observations. Multiple questions arise in this context: (1) estimation/location of the physical effect, (2) detect sensor failures and (3) recalibration of sensors through information redundancy. Answering these questions requires the raw sensor readings, but also meta information about sensor properties and their relations. A common, flexible and machine-interpretable approach is to use an ontology to represent the meta information.

Merge of Existing Data Schemes

Given the considered use cases, it is necessary to provide descriptions of the following three key components: (1) sensor, (2) observation and (3) calibration model. This can be achieved by merging and extending existing data schemes, vocabularies and ontologies, namely [7]:

- Digital SI (D-SI, [8])
- Semantic Sensor Network (SSN, [9])
- Sensor, Observation, Sampling and Actuation (SOSA, [10])
- Ontology of Units of Measure and Related Concepts (OM, [11])
- Geographic Query Language (GeoSPARQL, [12])
- Mathematical Markup Language (MathML, [13])

Calibration model information is represented by a merge of OM, MathML and D-SI. These data schemes are used to define the concepts of `Parameter`, `Variable`, `Equation`, `EquationModel` and `CalibrationModel`.

General sensor information such as identifiers, manufacturing details, measurement principle and location are represented using the SOSA/SSN ontologies. OM allows to specify the measurement quantity of the sensor. The location information is extended by GeoSPARQL for geometric and topological relations. A sensor is linked to its calibration model by the `hasCalibrationModel` attribute.

Observations are described by combining SOSA, D-SI and OM. The OM concept of `om:Measure` is extended to cover uncertainties of values. An observation is then characterized by time aspects from SOSA and a result of type `dsi:MeasureWithUncertainty`, which follows the D-SI data model. Observations are connected to a sensor via the `sosa:madeBySensor` attribute.

A brief overview of the suggested combination is illustrated in figure 1.

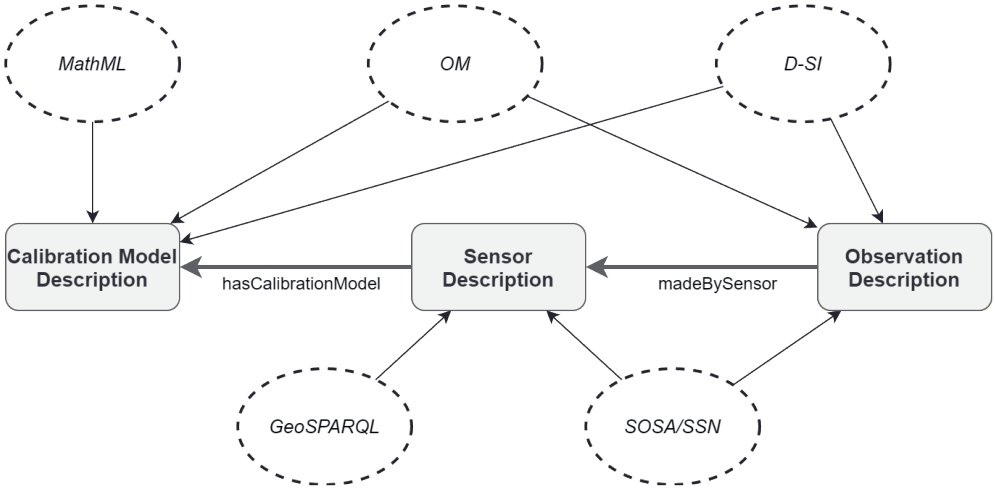

Figure 1: Overview of proposed merge

Outlook

We presented a possible merge of ontologies to represent sensor networks and relations therein from a metrological viewpoint. Further research will focus on the semantic description of sensor models and their transfer behavior.

References

[1] Plattform Industrie 4.0, and Federal Ministry for Economic Affairs. 2019. “Details of the Asset Administration Shell - Part 1.”

[2] Pfisterer, Dennis, Kay Romer, Daniel Bimschas, Oliver Kleine, Richard Mietz, Cuong Truong, Henning Hasemann, et al. 2011. “SPITFIRE: Toward a Semantic Web of Things.” IEEE Communications Magazine 49 (11): 40–48. https://doi.org/10.1109/MCOM.2011.6069708.

[3] Schütze, Andreas, and Nikolai Helwig. 2017. “Sensorik Und Messtechnik Für Die Industrie 4.0.” Tm - Technisches Messen 84 (5): 310–19. https://doi.org/10.1515/teme-2016-0047.

[4] Eichstädt, Sascha, and Björn Ludwig. 2019. “Metrologie Für Heterogene Sensornetzwerke Und Industrie 4.0.” Tm - Technisches Messen 0 (0). https://doi.org/10.1515/teme-2019-0073.

[5] Sheth, Amit, and Cory Henson. 2008. “Semantic Sensor Web.” Internet Computing, IEEE 12 (August): 78–83. https://doi.org/10.1109/MIC.2008.87.

[6] Padmavathi, Thimmaiah, and Madaiah Krishnamurthy. 2017. “Semantic Web Tools and Techniques for Knowledge Organization: An Overview.” KNOWLEDGE ORGANIZATION 44 (4): 273–90. https://doi.org/10.5771/0943-7444-2017-4-273.

[7] Gruber, Maximilian, Sascha Eichstädt, Julia Neumann, and Adrian Paschke. 2020. “Semantic Information in Sensor Networks: How to Combine Existing Ontologies, Vocabularies and Data Schemes to Fit a Metrology Use Case” 2020 IEEE International Workshop on Metrology for Industry 4.0 & IoT. https://doi.org/10.1109/MetroInd4.0IoT48571.2020.9138282

[8] Hutzschenreuter, Daniel, Frank Härtig, Wiebke Heeren, Thomas Wiedenhöfer, Alistair Forbes, Clifford Brown, Ian Smith, et al. 2019. “Smart-Com Digital System of Units (D-SI) Guide for the Use of the Metadata-Format Used in Metrology for the Easy-to-Use, Safe, Harmonised and Unambiguous Digital Transfer of Metrological Data,” November. https://doi.org/10.5281/zenodo.3522631.

[9] Janowicz, Krzysztof, Armin Haller, Simon J. D. Cox, Danh Le Phuoc, and Maxime Lefrancois. 2019. “SOSA: A Lightweight Ontology for Sensors, Observations, Samples, and Actuators.” Journal of Web Semantics 56 (May): 1–10. https://doi.org/10.1016/j.websem.2018.06.003.

[10] Haller, Armin, Krzysztof Janowicz, Simon Cox, Maxime Lefrançois, Kerry Taylor, Danh Le Phuoc, Josh Lieberman, Raúl García-Castro, Rob Atkinson, and Claus Stadler. 2018. “The Modular SSN Ontology: A Joint W3C and OGC Standard Specifying the Semantics of Sensors, Observations, Sampling, and Actuation.”

[11] Rijgersberg, Hajo, Mark van Assem, and Jan Top. 2011. “Ontology of Units of Measure and Related Concepts.” Semantic Web – Interoperability, Usability, Applicability.

[12] Open Geospatial Consortium. 2012. “GeoSPARQL - A Geographic Query Language for RDF Data.”

[13] W3C. 2014. “Mathematical Markup Language (MathML) Version 3.0 2nd Edition.”

DOI 10.5162/SMSI2021/D1.3

Ensemble Learning for Computational Optical Form Measurement

Lara Hoffmann[1], Ines Fortmeier[1], Clemens Elster[1]
[1]Physikalisch-Technische Bundesanstalt, Braunschweig and Berlin, Germany
E-mail (corresponding author): lara.hoffmann@ptb.de

Summary:

Deep learning has become a powerful tool of data analysis with applications in such different areas as medical imaging, language processing or autonomous driving. Recently, deep learning techniques have also been applied to an inverse problem in optical form measurement. In a proof-of-principle study it was shown that an accurate solution of the inverse problem can be achieved by a deep neural network that is trained on a large data base. This work augments the developed method with a quantification of its uncertainty by considering an ensemble of networks. The approach is tested using virtual experiments with known ground truth.

Keywords: deep learning, uncertainty, inverse problem, virtual experiment, optical form measurement

Motivation

Deep learning techniques have already been successfully used in many different domains such as medical imaging quality assurance [4], natural language processing [8] or autonomous driving [2]. In this study deep learning is applied to computational optical form measurements. The goal is to extend the deep learning approach proposed in [3] by quantifying the uncertainty associated with predictions made by a trained network ensemble.

Deep neural networks are neural networks with many hidden layers. Each layer consists of neurons, which are connected to the previous layer through a linear combination of its neurons and an additional bias. The nonlinear behavior of the network results from a nonlinear activation function per layer. The architecture can get arbitrarily deep by adding more layers, which makes neural networks a powerful tool to emulate highly complex functions. Fig. 1 shows an example of a deep neural network architecture. It has three input neurons, two output neurons and several hidden layers. The network parameters can be optimized via gradient-descent techniques using backpropagation by minimizing a chosen loss function on given training data. A common problem with deep learning models is their black-box behavior. In general, it is not possible to understand why the network made a certain prediction which challenges the trust in its prediction. Different techniques have been developed to tackle this problem, for example by using the Fisher information [5]. In this work we focus on estimating the uncertainties of the network predictions.

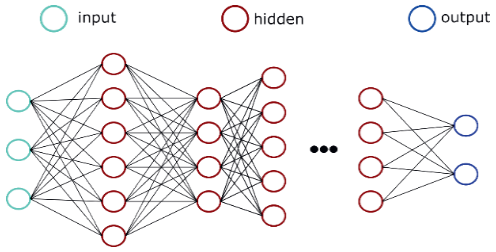

Fig. 1: Example of a deep network architecture.

The continuous technological advancements imply a growing relevance of accurate measurement techniques. The deep learning application here is based on the tilted-wave interferometer (TWI) [1]. The TWI is a highly accurate measurement technique for the reconstruction of optical aspheres and freeform surfaces using contact-free interferometric measurements. Topographies are reconstructed by solving a numerically expensive inverse problem from the measured intensity images using a numerical model for the wave propagation through the optical system.

Methods

A database of virtual measurement results has been constructed using the simulation toolbox SimOptDevice [7]. First, the test topographies were generated by adding randomly chosen difference topographies to a specified design. Then, the optical path length differences were calculated by the simulation toolbox. The task of

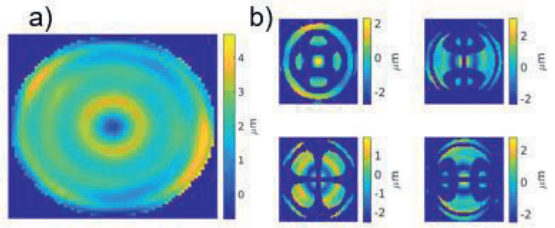

Fig. 2: Example of a data sample consisting of a) a test topography deviation and b) the corresponding differences of optical path length differences.

the inverse problem is to reconstruct a topography deviation from the corresponding deviations of optical path length differences. Fig. 2 shows an example of a data sample consisting of a test topography deviation and the corresponding differences of optical path length differences. The quantity and quality of the data have an essential impact on the network performance, especially considering its generalization capability. The constructed data base consists of $40{,}000$ test topographies (one channel output of the network), together with the corresponding optical path length differences (four channel input of the network) for training. A disjoint set was generated containing $2{,}000$ randomly generated samples for testing. The generated data are very diverse ranging from a root mean squared deviation of 20nm to several µm.

A U-Net architecture [6] was chosen to solve the inverse problem of reconstructing the test topography deviations from the optical path length differences. The U-Net is a deep neural network with bottleneck structure and skip-connections and has been already successfully applied in various computational imaging tasks. It is desirable to have an idea of the trustworthiness of individual network predictions in addition to the overall accuracy on a test set. A relevant quantity in this context is the uncertainty of an output generated by the network. Uncertainty quantification was realized by learning an ensemble of networks and computing its standard deviation per output pixel. The ensemble prediction is given as the mean of the different network predictions.

Results and Conclusion

The topography deviations were predicted together with their corresponding uncertainties from the optical path length differences in the test set after having trained the ensemble of U-Nets on the disjoint training set. Some results are shown in Fig. 3. More precisely, the profiles of some reconstructed topography deviations are shown together with their uncertainties and the known ground truth. The obtained results show that the estimated uncertainties cover the errors of the prediction. Furthermore, the root mean squared error of the predictions is an order of magnitude smaller than the variability of the

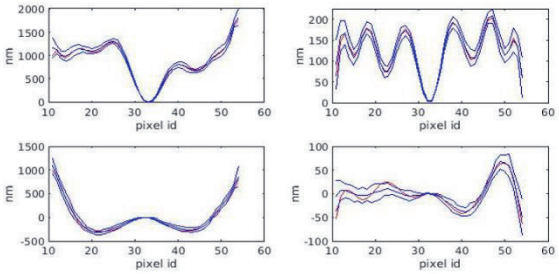

Fig. 3: Profile plots of the ensemble results on random test data. The prediction with uncertainty interval is shown in blue and the underlying ground truth in red.

topography deviations within the test set. The median error is even less.

We conclude that deep learning can be successfully applied in the context of computational optical form measurement, assuming ideal measurement conditions. Uncertainty quantification in terms of an ensemble of networks yields a reliable uncertainty characterization of network predictions. Comparing the proposed approach to the conventional method [1] as well as incorporating calibration errors and testing on real measurements are referred to future work.

Acknowledgement

The authors thank Manuel Stavridis for providing the software tool SimOptDevice and Michael Schulz for helpful discussions about optical form measurements.

References

[1] I. Fortmeier, M. Stavridis, A. Wiegmann, M. Schulz, W. Osten, C Elster, “Evaluation of absolute form measurements using tilted-wave interferometer”, Optics Express, vol. 24, no. 4, pp. 3393-3404, 2016.

[2] S. Grigorescu, B. Trasnea, T. Cocias, G. Macesanu, “A survey of deep learning techniques for autonomous driving”, Journal of Field Robotics, vol. 37, no. 3, pp. 362-386, 2020.

[3] L. Hoffmann, C. Elster, „ Deep neural networks for computational optical form measurements”, JSSS, vol. 9, no. 2, pp. 301-307, 2020.

[4] T. Kretz, K.-R. Müller, T. Schäffter, C. Elster, „Mammography Image Quality Assurance Using Deep Learning”, IEEE Transactions on Biomedical Engineering, 2020.

[5] J. Martin, C. Elster, „Detecting unusual input to neural networks”, arXiv preprint, 2020.

[6] O. Ronneberger, P. Fischer, T. Brox, “U-Net: Convolutional Networks for Biomedical Image Segmentation”, MICCAI, pp. 234-241, 2015.

[7] R. Schachtschneider, M. Stavridis, I. Fortmeier, M. Schulz, C. Elster, “SimOptDevice: a library for virtual optical experiments”, J. Sens. Sens. Syst., vol. 5, pp. 105-110, 2019.

[8] T. Young, D. Hazarika, S. Poria and E. Cambria, "Recent Trends in Deep Learning Based Natural Language Processing", IEEE Computational Intelligence Magazine, vol. 13, no. 3, pp. 55-75, 2018.

DOI 10.5162/SMSI2021/D1.4

Dynamic calibration of sensors with exclusive digital output

Benedikt Seeger[1], *Thomas Bruns*[1]
[1] *Physikalisch-Technische Bundesanstalt, Berlin, Germany*
benedikt.seeger@ptb.de

Summary:
For the processing of dynamic data (e.g. vibrations) an exact knowledge of the temporal relations is necessary. In this topic we present a GPS based method for time stamping of dynamic signals. As well as dynamic calibration methods based on this data for sensors with exclusively digital output.

Keywords: dynamic calibration, MEMS, uncertainty

In the field of accelerometry, MEMS accelerometers and gyroscopes have become ubiquitous.
Unlike typical analog sensors, the analog to digital conversion in digital MEMS sensors is performed asynchronously in the sensor. This offers the advantage from a system integration point of view that no interference-prone analogue signals have to be transmitted. From a meterological point of view, however, it is disadvantageous that the sampling time is determined by the sensor. The sensors normally signal at least the beginning or the end of the AD-conversion by an interrupt signal. In this session we will show how this signal can be absolute timestamped with an uncertainty of about 200 ns using common microcontroller hardware, our own open source software and a GPS module. Synchronous to the data of the digital sensor, analog reference values are read in from the µC system. Thus a synchronization signal can be acquired, which can be e.g. the excitation signal in a classical dynamic calibration system. This allows to make the analog calibration system fit for digital sensors without changing them. Figure 1 shows a classical calibration system which has been extended by a digital Data Aqusitiuon Unit (DAU). The calibration system and the DAU sample the same reference signal, so a time reference can be established between both systems, which is essential for the determination of the phase response. Since the DAU is based on low-cost hardware, it also serves as the basis for a smart sensor in networked systems. Since the DAU delivers the measured values acquired by the sensors as an absolute-time stamped data stream with metadata. The meta data are physical size, unit, quantization resolution and fulls scale values. The description of the units is based on the D-SI [1]. In this session we will introduce the microcontroller system and a Python based open source software for the dynamic calibration of one and more axis MEMS accelerometers and gyroscopes.

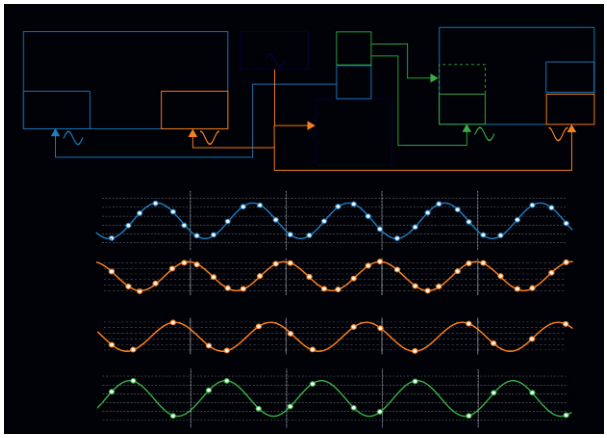

Figure 1 An Analog Calibration System (ACS) extended with a Digital Aquisition Unit (DAU) for dynamic calibration of digital acceleration sensors.

References [1] Hutzschenreuter, D., et al. "SmartCom Digital System of Units (D-SI) Guide for the use of the metadata-format used in metrology for the easy-to-use, safe, harmonised and unambiguous digital transfer of metrological data." *Available:*. 2019.

DOI 10.5162/SMSI2021/D4.1

Hydrogen Chloride Optical Gas Standards (OGS) at PTB

Javis Nwaboh, Zhechao Qu, Olav Werhahn, Volker Ebert
Physikalisch-Technische Bundesanstalt (PTB), 38116 Braunschweig, Germany,
Corresponding Author: javis.nwaboh@ptb.de

Summary:
Accurate and reliable measurements of hydrogen chloride (HCl) are required in applications such as biomethane quality control, clean room monitoring or stack emissions monitoring. In order to perform HCl measurements, standardized measurement methods as well as accurate reference gases are required to calibrate typical HCl measurement instruments. However, there is a lack of SI-traceable HCl reference gases and reliable quality control test methods for many of these applications, once future more challenging limit values have been put into force by new regulations to come. To this end, PTB is developing optical gas standards (OGS), e.g., for HCl quantifications in those applications and to complementing existing gaseous reference standards. In this paper, we report on the HCl-OGSs developed in PTB for different applications.

Keywords: Metrology, Gas Analysis, Optical Gas Standard (OGS), TILSAM, dTDLAS.

1. Introduction

Gaseous hydrogen chloride (HCl) poses severe health effects when inhaled and can form corrosive hydrochloric acid on surfaces when it meets water. These properties accelerate the need for accurate HCl detection e.g. for quality control measurements in biomethane, airborne molecular contaminations monitoring in clean rooms or stack gas emissions [1]. Accurate HCl measurements typically require validated test methods [1]. Reliable test methods are lacking for HCl quantifications in biomethane, an energy gas that is seen to replace parts of the fossil natural gas sources in existing grids [1]. For stack emissions, HCl measurements are referred to the HCl - standard reference method described in EN 1911 (on the determination of mass concentration of gaseous chlorides). EN 1911 is based on wet chemistry. Hence, a gas sample is extracted, particle-filtered and dried and then dissolved in water, to analyze the Cl^--ion concentration in the liquid. This sampling procedure can easily lead to systematic deviations. HCl amount factions in biomethane and clean room air are required to stay at low µmol/mol to the nmol/mol levels. HCl sensor calibration requires calibration gas standards in the same range. However, generation and provision of gaseous reference materials traceable to the international system of units (SI) has proven to be difficult [1], e.g. there are no calibration and measurements capabilities (CMCs) reported for HCl amount fractions below 10 µmol/mol (https://kcdb.bipm.org/). Only a few National Metrology Institutes (NMIs) have CMCs for HCl (10-1000 µmol/mol) in N_2. For HCl in more complex gas matrices (e.g. biomethane), there are no CMCs available at all. Optical gas standards [3], [4] provide the option to be mandated as test methods for HCl measurements in the above mentioned applications. Due to the 1st principles measurement approach, OGSs do not require calibration with a calibration gas mixture, and therefore can be used to complement gaseous reference standards in the low µmol/mol down to the nmol/mol levels [2, 3]. Furthermore, an OGS can also be used for HCl measurements directly in the field in situ. In this paper, we present HCl OGS instruments compliant with the TILASM method [4] and developed or currently being developed at PTB.

2. An Optical Gas Standard (OGS)

The measurement technique employed in an OGS instrument (see Fig. 1) is direct tunable diode laser absorption spectroscopy (dTDLAS) [2-3], [5-6]. dTDLAS is a variant of TDLAS that combines TDLAS with a 1st principles data evaluation approached to derive absolute gas species amount fractions that are directly traceable to the SI. An OGS laser spectrometer is thus similar to the National institute of Science and Technology (NIST) ozone standard reference Photometer (SRP). Employing the Beer-Lambert law on a continuously scanned diode laser spectrometer and deriving the line area (A_{line}) underneath an absorption line, a SI-

traceable HCl amount fraction is inferred. Figure 1 shows an HCl absorption profile in N_2 matrix gas measured at a wavelength of about 3.6 µm and evaluated according to equation 1 as resulting a 518.4 µmol/mol HCl amount fraction without the need to calibrate the instrument with a gaseous calibration standard [3], [4]. Repeated measurements are shown in Fig. 2.

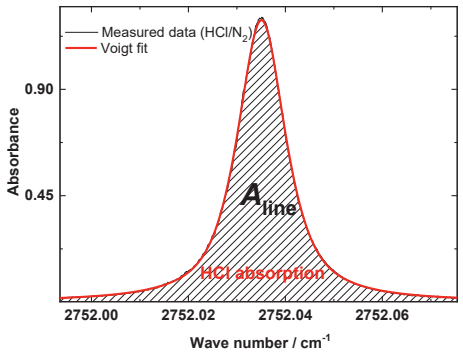

Fig. 1: Typical HCl single line absorbance spectrum measured by an OGS instrument operated at 3.6 µm.

$$x_{\text{species}} = \frac{k_B \cdot T}{S_T \cdot L \cdot p_{\text{total}}} \cdot A_{\text{line}} \qquad (1)$$

For an HCl OGS, ensuring that all input quantities on the right-hand side of Eq. 1 are SI-traceable, the HCl amount fraction (concentration) x_{HCl} is directly traceable to the SI. The quantities k_B being the Boltzmann constant, S_T the line strength of the probed molecular transition at gas temperature T, L the path length of the light beam transmitted through the absorbing medium and p_{total} the total gas pressure. The SI-traceability of these input quantities is ensured similarly to references [2,3,4].

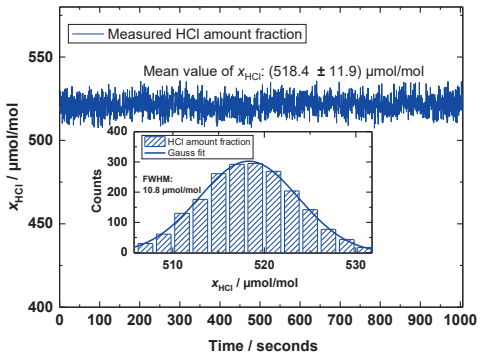

Fig. 2: HCl amount fraction (repeated measurements) as a function of time. Inset: A histogram depicting a normal distribution of the results and depicting the performance of an OGS.

Delivering SI-traceable amount fractions, an OGS is a “calibration free” instrument and can therefore be used as described to complement (support and use in the place of) calibration gases both in the lab and in the field, especially for sticky and reactive gases such as HCl, H_2O and NH_3.

3. Summary

Table 1 lists some details of HCl OGS systems developed/currently being developed at PTB. The OGS-Biomethane instrument is currently being used in a bilateral comparison with the Korean NMI, KRISS. Furthermore, the instrument will be employed in a CCQM key comparison of HCl in air, planned to be run at a 30 µmol/mol level.

Table 1: Summary of HCl OGS systems developed/currently being developed at PTB.

OGS systems of PTB cluster	Targeted range / µmol/mol	Rel. combined uncertainty (k = 1) / %	Gas Matrix
OGS-Biomethane	0.025 - 500	2.3	CH_4 (or biomethane), N_2, air
OGS-Stack	0.05 - 100	2 - 4	Flue gas (with high CO_2, H_2O)
OGS-AMC	0.001 – 1	2 - 4	Air (or N_2)

OGS-Biomethane: HCl-OGS instrument for bio-CH4 conformity assessments.
OGS-Stack: HCl-OGS instrument for stack emissions monitoring.
OGS-AMC: HCl-OGS instrument for airborne molecular contaminations tests.

Acknowledgement

Parts of this work was supported by the European Metrology Programme for Innovation and Research (EMPIR). The EMPIR initiative is co-funded by the European Union’s Horizon 2020 research and innovation programme and the EMPIR Participating States. The authors would also like to acknowledge the support from current and past members of the PTB working group ‘Spectrometric Gas Analysis’

References

[1] EMPIR project Biomethane (http://empir.npl.co.uk/biomethane/), IMPRESS 2 (http://empir.npl.co.uk/impress/), MetAMCII, (http://empir.npl.co.uk/metamcii/).

[2] J. A. Nwaboh, Z. Qu, O. Werhahn and V. Ebert, "Interband cascade laser-based optical transfer standard for atmospheric carbon monoxide measurements", Applied Optics, 56, E84-E93 (2017).

[3] B. Buchholz, N. Böse and V. Ebert, "Absolute validation of a diode laser hygrometer via intercomparison with the German national primary water vapor standard", Applied Physics B, 116, 883–899 (2014).

[4] O. Werhahn, J.C. Petersen (eds.), 2010, TILSAM technical protocol V1_2010-09-29. Available from: http://www.euramet.org/fileadmin/docs/projects/934_METCHEM_Interim_Report.pdf.

[5] Z. Qu, J. Nwaboh, O. Werhahn and V. Ebert, "Towards a dTDLAS-Based Spectrometer for Absolute HCl Measurements in Combustion Flue Gases and a Better Evaluation of Thermal Boundary Layer Effects", Flow, Turbulence and Combustion, Sept. 2020, doi: 10.1007/s10494-020-00216-z.

[6] A. Pogany, S. Wagner, O. Werhahn and V. Ebert, "Development and Metrological Characterization of a Tunable Diode Laser Absorption Spectroscopy (TDLAS) Spectrometer for Simultaneous Absolute Measurement of Carbon Dioxide and Water Vapor", Applied spectroscopy, 69, 2, 257-268 (2015).

DOI 10.5162/SMSI2021/D4.2

Development of a Traceable Dynamic Force Calibration for Applications like Material Testing Machines

Rolf Kumme[1]
[1] *Physikalisch-Technische Bundesanstalt, Bundesallee 100, 38116 Braunschweig, Germany*
rolf.kumme@ptb.de

Summary:
This paper provides an overview of the EMPIR 18SIB08 ComTraForce project and describes a general concept for the development of a traceability chain for dynamic force calibration in applications like in the field of material testing machines.

Keywords: dynamic force, force traceability, EMPIR 18SIB08, ComTraForce

Introduction

Forces are measured in many applications in industry and research and the traceability of the measurement of static forces is well established. However, in many mechanical applications such as material testing, the forces are time dependent. The vibration of the whole mechanical structure of a material testing machine results in a vibration of the force transducer and the mass distribution of the whole structure, which causes (in addition to the spring force related to the mechanical deformation) in inertia forces related to the acceleration of the mass distribution of the mechanical structure. A new joint research project within the scope of the European Metrology Research Programme (EMPIR) called 18SIB08 ComTraForce was launched on 1 September 2019 to develop methods and procedures for the measurement of static, continuous and dynamic forces with the aim of establishing comprehensive traceability for force metrology services [1].

Concept of Traceability of Dynamic Forces

The traceability of static forces is realized by means of force measuring devices used as force transfer standards and calibrated in accordance with established procedures such as ISO 376 [2], first to determine the calibration curve of a force measuring device in a national force standard machine or a force calibration machine traceable to the SI. In the second step, the calibrated force measuring devices are used to calibrate the force indication of the material testing machine in accordance with international standards such as ISO 7500-1 [3].

When applying a material testing machine, the force $F=F(t)$ is applied as a function of time to the specimen or the mechanical structure to be tested. This results in time-dependent deformations $x=x(t)$ of the force measuring device and a time-dependent deformation of the mechanical structure. The deformation of the force measuring devices takes place according to Hooke's law in first approximation proportional to the acting force:

$F = c \cdot x$, where c is the spring stiffness.

If static forces are applied or if the force as a function of time increases or decreases with a constant velocity, the acting accelerations are zero. In this case, there is equilibrium between the applied force, which is generated by the testing machine, and the force acting on the specimen or the force acting on the transfer standard installed in the testing machine for calibration. In this case the acting forces are static or continuous forces. The spring forces in the force transducer of the testing machine and in the force transducer of the force transfer standard are equal; therefore, the testing machine force indication can be calibrated directly with the force transfer standard. For precise measurement, the creep effect of the machine transducer and of the force transfer standard must be considered to allow the uncertainty of the calibration to be reduced. Another influence that must be considered is the synchronisation of the measurement of the force measurement device in the testing machine and the force measurement with the force transfer standard.

In the case of dynamic testing in the testing machine in addition to the spring forces vibrations are generated which result in not negligible accelerations which generate additional inertia forces $F_a=m \cdot \ddot{x}$. As a consequence, the force indicated by the testing machine is not identical to the force acting on the specimen. To

consider the effect of inertia forces between the machine transducer and the specimen, methods such as ASTM E467 and ISO 4965 take these effects into account [4,5,6]. These standards are good practice guides for verifying the machine performance under consideration of dynamic forces. However, such standards are only verification standards and not calibration standards for a dynamic calibration of the machine. The uncertainties of these methods are unknown and the standards lack uncertainty information.

It is the aim of the new EMPIR ComTraForce project to develop traceable dynamic calibration methods based on traceable force transfer standards for continuous and dynamic forces. This paper describes the basic concept for developing these methods.

Here, the main idea is to use force measuring devices with well known static and dynamic properties with a traceability to the SI as in the static calibration according to ISO 7500-1. To this end, in the first step, the static calibration curve of the force measuring device consisting of a force transducer, a measuring amplifier and an indication must be calibrated. In the second step, the dynamic properties must be determined.

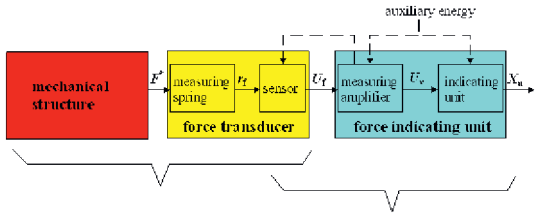

Fig. 1. Force measuring device in interaction with mechanical structure.

To establish traceability for dynamic forces in the field of material testing, it is necessary to select suitable force-measuring devices with a linear dependency between the indicated deflection and the acting force and a well-known frequency dependency of the force measuring device consisting of the force transducer and the measuring amplifier according to the block diagram in Fig. 1.

In addition to the static calibration and the frequency response of the force measuring device, the acting dynamic forces generated by the inertia force of the accelerated masses must also be considered. In addition to the calibration of the force measuring devices, it is necessary to determine the acceleration of the masses, which causes additional inertia forces between the machine force transducer and the specimen, as described in the model in Fig. 2. A traceability for dynamic forces in dynamic applications like in the field of material testing can be established by a combination of a traceable force and acceleration measurement devices. Each of these devices have to be calibrated and in addition to the uncertainty of the calibration of the force and acceleration measurement devices additional influences related to the application have to be taken into account.

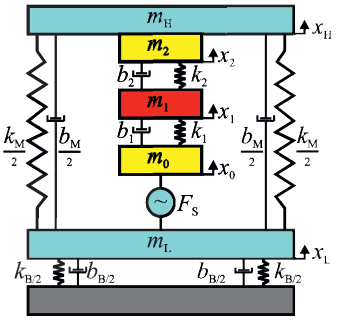

Fig. 2. Simplified model of a material testing machine.

Summary

In this paper, a concept for the development of a traceability chain for dynamic force calibration in dynamic applications like in the field of material testing machines is presented.

Acknowledgements

The author would like to acknowledge the funding of the joint research project 18SIB08 ComTraForce. This project has received funding from the EMPIR programme, which is co-financed by the European Union's Horizon 2020 research and innovation programme, and from EMPIR Participating States.

References

[1] 18SIB08 ComTraForce, Comprehensive traceability for force metrology services, https://www.ptb.de/empir2019/comtraforce/home.html

[2] ISO 376: 2011 Metallic materials - Calibration of force-proving instruments used for the verification of uniaxial testing machines

[3] ISO 7500-1: 2018 Metallic materials - Calibration and verification of static uniaxial testing machines - Part 1: Tension/compression testing machines - Calibration and verification of the force-measuring system

[4] ASTM E467 - 08(2014), Standard Practice for Verification of Constant Amplitude Dynamic Forces in an Axial Fatigue Testing System, ASTM International, West Conshohocken, PA, 2014, www.astm.org

[5] ISO 4965-1:2012 Metallic materials - Dynamic force calibration for uniaxial fatigue testing - Part 1: Testing systems

[6] ISO 4965-2:2012 Metallic materials - Dynamic force calibration for uniaxial fatigue testing - Part 2: Dynamic calibration device (DCD) instrumentation

DOI 10.5162/SMSI2021/D4.3

Ro-Vibrational Spectroscopic Gas Thermometry (RVSGT): A new primary method for gas thermometer calibrations?

Gang Li, Volker Ebert
Physikalisch-Technische Bundesanstalt (PTB),38116 Braunschweig, Germany,
Corresponding Author: gang.li@ptb.de, volker.ebert@ptb.de

Summary:

Gas temperature measurements play an important role for industrial process control, combustion technology, but also for environmental and climate science. Absolute calibration of contact gas thermometers is difficult and has a number of practical challenges when aiming on high accuracies. Rovibrational spectroscopic gas thermometry RVSGT, directly employs molecules as smallest possible "sensors", can be "read out" remotely using light absorption and can serve as a primary reference method for direct gas thermometer calibrations. Here, we present a new methodology to extract the gas temperature from a ro-vibrational spectrum of a "sensor" molecule measured by FT-spectrometry.

Keywords: gas temperature, spectroscopic thermometry, FT spectrometry, molecular spectral data

Introduction

Accurate gas temperature measurements are critical in modern science, but often hampered by the intrusive character of the contact-based techniques or the low thermal conductivity of gases causing multiple complications when calibrating contact gas thermometers. An ideal gas thermometry approach is versatile, non-intrusive, compatible with low to mid gas pressures, avoids the introduction of significant energy into the sample, allows a "remote" read-out and covers a wide temperature range. Broadband ro-vibrational spectroscopic gas thermometry (RVSGT) combines all requirements by using the gas molecules itself as temperature "sensor" and infrared spectroscopy as the remote temperature read out technique. For this RVSGT detects groups of rotationally resolved molecular transitions, preferentially in the near or the mid IR. RVSGT has the potential to derive absolute temperatures, just requiring a complete set of traceable spectral parameters as targeted in the EUMETRISPEC initiative (https://www.eumetrispec.org/). Rotationally resolved rovibrational spectra also contain a lot of "orthogonal" information, e.g. gas temperature from line intensity distribution, gas pressure from collisional or Doppler width, absorber number density from line area or band intensity, thus promising a consistent set of thermodynamic gas parameters from a single measurement. RVSGT thus can become particularly advantageous for numerous industrial as well as metrological applications, even has the potential to become a primary gas thermometry method. Until recently this was to some extend hampered by large uncertainties in the required molecular spectral parameters or their adoption to elevated temperatures. Recent advances in quantum chemical calculations now offer novel routes towards highly accurate spectral parameters and thus highly accurate non-contact gas temperature measurements. Furthermore, RVSGT can serve as primary reference method and allow a direct primary calibration of the ubiquitous contact gas thermometers without the need for assumption/corrections for possibly ill-described thermal coupling of the contact sensor and the gas.

Methodology

The relationship between intensities (S_i) of rotational lines within a vibrational band and the thermal dynamic temperature T at a local thermal equilibrium (LTE) condition is described by:

$$S \propto \cdot v \cdot \frac{1}{Q_T} \cdot HL \cdot g_I \cdot exp^{(-E_{Low}/k_B T_{rot})} \cdot \left(1 - exp^{(-hcv/k_B T_{rot})}\right) \cdot |\langle vJ'|M(x)|0J''\rangle|^2$$

where $\mathbf{v}$ is the frequency of the transition, $\mathbf{Q_T}$ is the partition sum at temperature T, HL is the Hönl-London Factor, $\mathbf{g_I}$ is the statisitical weights, $\mathbf{E_{Low}}$ is the lower state energy of the transition, $\mathbf{h}$ is the Planck constant, c is the speed of light, $\mathbf{T_{rot}}$ is the thermal dynamic temperatue assuming a LTE condition, $\mathbf{M(x)}$ is the Matrix element. The equation shows three

terms influencing the temperature: Q_T, $exp^{(-E_{Low}/k_B T_{rot})}$, $\left(1 - exp^{(-hcv/k_B T_{rot})}\right)$. making the direct analytical determination of T_{rot} impossible.
Here, we propose a simple pseudo-T-fit approach. This method has mainly three prerequisites:

a) Accurate knowledge of the relative rotational line intensity distributions within a vibrational band from ab initio calculations or semi-empirical fits to the best experiments.

b) A probe molecule whose spectrum is measured with signal-to-noise ratio (SNR) of at least a few hundred or better.

c) Suitable high-resolution line shape model (Hartmann-Tran profile and its derivatives) adequate to model the high-SNR spectrum.

The pseudo-T-fit approach starts from assuming a trial temperature, T_{ini}. Doppler width of a spectral line, Q_T, $exp^{(-E_{Low}/k_B T_{rot})}$, $\left(1 - exp^{(-hcv/k_B T_{rot})}\right)$ are calculated using T_{ini}. The relative distribution of line intensities, i.e. $\boldsymbol{C}_v$, $\boldsymbol{D}_v$, …, is fixed, e.g. by the HITRAN database or ab initio spectral data [1,2]. The fit is implemented via an optimization algorithm, Gauss-Newton or Levenberg-Marquart, to optimize other spectral parameters and to reduce the global root mean square (rms) of the fitted residual. After the fit is converged, the rms sum, f_T^2 , is registered. Subsequently, other temperatures are iterated. f_T^2 as a function of T is then modeled with a third order polynomial function. The optimum temperature T_{opt} is extracted as the minimum on the polynomial curve. figure 1 shows an an example. A second iteration with finer T grid around the T_{opt} is preferred for a more accurate T_{opt} determination.

Results

Figure 1 shows the variations of the sum of the fitting residual squared at different input temperatures for a measured FTIR spectrum of the 2.3 µm band of N_2O [3] using speed-dependent Voigt line shape model – a subgroup of the Hartmann-Tran profile. The minimum of the red curve corresponds to the determined temperature of T(spec)=296.10(6) K, which is in agreement with the traceably measured temperature T(ref)=296.0(1) K using two PT100 sensors. The major T(ref) uncertainty comes from the spatial T inhomogeneity between top and bottom of an 80 cm long absorption cell.

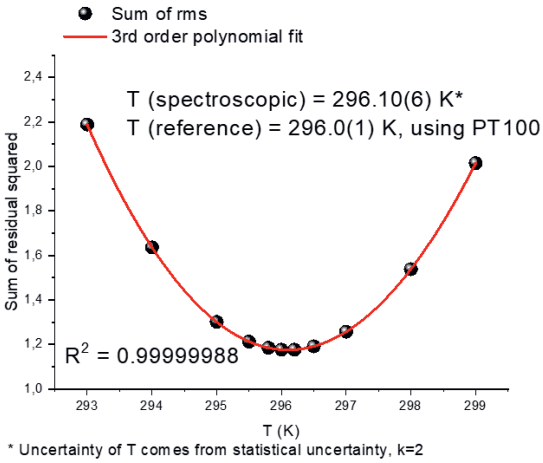

Fig. 1. Example of a pseudo-T-fit approach to extract the optimum spectroscopic gas T. The sum of the squared fit residuals between observed and calculated spectrum at different "assumed" gas T's are fitted with a cubic function. The gas T corresponding to the minimum of the fitted curve is the fitted T derived from our approach. The uncertainty of the spectroscopic T quoted in the figure arises from the statistical uncertainty of the polynomial fit. Other sources of uncertainty are still to be analysed.

RVSGT [4] has the advantage of utilizing the full spectral information for higher accuracy, compared to laser-based Doppler-width-thermometry or two-line ratio thermometry. We employ a full spectroscopic model and follow the GUM to study the accuracy requirements on different input parameters for a highly accurate spectroscopic gas thermometry from Doppler limit to atmospheric pressure at LTE conditions. These parameters include Herman-Wallis factor, line shape models, accessible temperature range, and others. The full potential and optimum uncertainty of RVSGT needs to be further studied and experimentally verified using other primary (gas) temperature realizations.

References

[1] G. Li, I.E. Gordon, L. S. Rothman, Y. Tan, S.-M. Hu, S. Kassi, A. Campargue, E. S. Medvedev, The Astrophysical Journal Supplement Series 01, 216(1-1) (2015)

[2] O. L. Polyansky, K. Bielska, J. Tennyson et al. Phys. Rev. Lett. 114, 243001 (2015)

[3] V. Werwein, J. Brunzendorf, G. Li, A. Serdyukov, O. Werhahn, and V. Ebert. Appl. Opt. 56 (2017), 11, E99 - E105.

[4] G. Li, V. Ebert, "Broadband Ro-Vibrational Spectroscopic Thermometry for Gases", TEMPMEKO2019, P5.27, Chengdu, China, 9.6.2019

DOI 10.5162/SMSI2021/D4.4

Building blocks for an adaptive software-based uncertainty estimation

Ivan Poroskun, Daniel Heißelmann, Christian Rothleitner
Physikalisch-Technische Bundesanstalt (PTB), Bundesallee 100, Braunschweig, Germany
ivan.poroskun@ptb.de

Summary:
Measurement uncertainty estimation based on Monte Carlo simulations gains more importance with the ongoing digitalization in metrology. In the field of coordinate metrology, the VCMM is a well-established tool. The concept of this digital twin is transferred to more a general software library, which is consequently applied to develop the Virtual Planck-Balance.

Keywords: uncertainty estimation, digital twins, Monte Carlo Simulation, Virtual Planck-Balance, VCMM

Introduction

In coordinate metrology, the use of the virtual coordinate measuring machine VCMM as a digital twin to calculate the task-specific measurement uncertainty is well established [1]. It is a valuable tool for DAkkS-accredited laboratories as well as in planning and evaluation of measurements in industrial quality control.

PTB's new competence center for virtual measuring instruments (VirtMet) aims at transferring the VCMM concept into other digital twins [2]. The main components and basic principles of the VCMM are identified and generalized for future applications from varying fields of metrology. As a first application, the Virtual Planck-Balance (VPB) will be set up, where the Planck-Balance is a Kibble-Balance for industrial use [3].

Currently, digital twins are independently developed and only very little of actual code is transferred between projects and organizations. Many basic components, such as random number generators (RNG) and routines for uncertainty estimation are likely to be the same and yet they are often implemented anew. From the perspective of software engineering, there is a need for a library which covers most of common needs for the development of digital twins. While there are software libraries available implementing GUM and its supplements (e.g. [6]), the aim of this work focusses on the practical applicability for the development of digital twins.

Proposed structure

In order to apply the concept of the VCMM to other digital twins it has been analyzed and divided into sub-structures. As a first step, the concept will be transferred to the VPB. For this purpose, a simple software structure (Fig. 1) is proposed. It consists of two main parts: one part which is dependent on a specific project (framed as *virtual measurement*) and a second part consisting of more general components which can be reused for different digital twins. The latter part consists of measurand(s), stopping rule(s) and a component for uncertainty estimation. A set of distributions for RNGs (visualized as red circles) might also be provided. The whole structure is framed inside a Monte-Carlo simulation loop and only the parametrization of RNGs is performed before the loop starts, whereas the uncertainty is estimated after the simulation.

The base component of the structure is the *core*: a project specific evaluation algorithm. In case of the VCMM it is represented by a set of fitting algorithms inside the CMM's application software. Preferably, the core already exists at the time the digital twin is created. The *models* map input parameters into arguments of the *core*.

The evaluation algorithm provides simulation results in each run of a Monte-Carlo loop. These are saved and observed by stopping rules. After

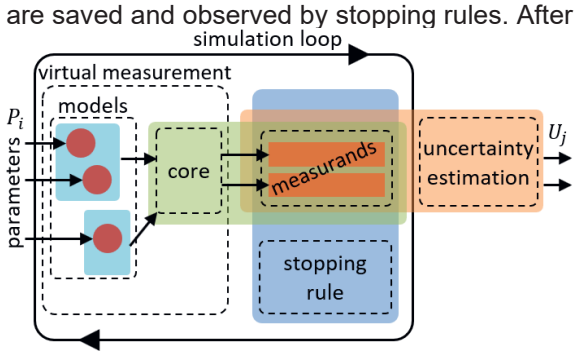

Fig. 1 Proposed structure for digital twins.

the simulation completes, the values are forwarded into the uncertainty estimation block for further analysis. In the following, we will briefly discuss some aspects of each component.

Stopping rules

In the simplest case the stopping rule for termination of a Monte-Carlo simulation is given by a fixed number of runs *N* which is known a priori. If *N* is chosen too low, the desired numerical tolerance of the result might not be achieved. For this scenario GUM S1 [3] includes an adaptive Monte-Carlo (MC) procedure. As it is done in [4] some improvements of adaptive MC are added over time. The criterion for stopping rule components must be interchangeable with minimal effort to fulfill current preferences of the developer.

Measurands

Simple measurands are realized as vectors containing simulated values. Besides the individual simulation results, the measurands also contain meta data necessary for the evaluation of the stopping rule and uncertainty estimation components.

Uncertainty estimation

This component implements algorithms for uncertainty estimation from GUM S1 [3]. The implementation details follow the specifications from [6].

Application to Virtual Planck-Balance

As all software components common to various digital twins can be covered by the supporting software library, for the devolvement of a new digital twin only the components specific to the individual application must be created.

In a first application, the feasibility of the approach shall be tested by transferring it to the Planck-Balance, thus creating the Virtual Planck-Balance. The core contains the measurement equation of the PB for a single measurement described by [5]

$$m = \frac{U_{\mathrm{dynamic}} \cdot U_{\mathrm{static}}}{v_{\mathrm{dynamic}} \cdot g \cdot R_{\mathrm{static}}}\ , \quad (1)$$

where m denotes the mass, U_{dynamic} and U_{static} are voltages, v_{dynamic} is the velocity, g is the local acceleration due to gravity, and R_{static} is the electrical resistance. The measurement equation (1) can be viewed as a tree-like structure where each of the five arguments is placed onto a separate node of the tree. Each argument is implemented inside a separate class with either a constant value, where no uncertainty of the argument is to be considered, a single RNG or with a complex combination of multiple physical models. The encapsulation of each argument provides the advantage of hiding possible complex details and making the overall model extensible and easy to comprehend.

Conclusion

A structure is proposed to enable users to create a digital twin of any complex measurement setup. The approach is based on the well-established VCMM, from which a versatile software library containing building blocks for future digital twins is derived. Thus, for any specific application, the building blocks can be used and only the individual models have to be developed. In a next step, the approach will be adapted to the Planck-Balance.

References

[1] D. Heißelmann, M. Franke, K. Rost, K. Wendt, T. Kistner, and C. Schwehn, Determination of measurement uncertainty by Monte Carlo simulation, *Advanced Mathematical and Computational Tools in Metrology and Testing XI*, 192–202, (2018); doi: 10.1142/9789813274303_0017.

[2] S. Eichstädt *et al.*, Metrology for virtual measuring systems: new competence centre “VirtMet” at PTB, *MathMet2019*, Lisbon, Portugal, (2019).

[3] JCGM, Evaluation of measurement data - Supplement 1 to the “Guide to the expression of uncertainty in measurement” - Propagation of distributions using a Monte Carlo method: JCGM 104:2009.

[4] G. Wübbeler, P. M. Harris, M. G. Cox, and C. Elster, A two-stage procedure for determining the number of trials in the application of a Monte Carlo method for uncertainty evaluation, *Metrologia*, 47(3), 317–324, (2010); doi: 10.1088/0026-1394/47/3/023.

[5] C. Rothleitner *et al.*, The Planck-Balance – A self-calibrating precision balance for industrial applications, *Engineering for a Changing World*, p. 11, (2017).

[6] M. Cox, P. Harris, and I. Smith, Software specifications for uncertainty evaluation, National Physical Laboratory (NPL), NPL Report MS 7, (2010).

Collaborating Institutions and Organizations

- AHMT German Working Group of Professors in Measurement Technology
- Federal Institute for Materials Research and Testing BAM (Germany)
- BIPM - Bureau International de Poids and Mesures (France)
- CETIIAT - Centre Technique des Industries Aèrauliques et Thermiques (France)
- COOMET, Euro-Asian Cooperation of National Metrological Institutions
- EURAMET - The European Association of National Metrology Institutes
- Federal Institute of Metrology METAS (Switzerland)
- GMA - Society for Measurement and Automatic Control (Germany)
- IMEKO - International Measurement Federation (Hungary)
- INTI - Instituto Nacional de Teconología Industrial (Argentina)
- Italian National Agency for New Technologies, Energy and Sustainable Economic Development (Italy)
- MSC (USA)
- NCSLI - National Conference of Standard Laboratories International (USA)
- NIST - National Instititute of Standards and Technology (USA)
- Physikalisch-Technische Bundesanstalt – PTB (Germany)
- RISE - The Swedish Research Institute (Sweden)
- ROSSTANDART (Russia)
- VNIIMS - All-Russian Scientific Research Institute of Metrological Service (Russia)

Supporting Institutions and Publishing Partners:

AHMT

AMA Association for Sensors + Measurement

PTB Physikalisch-Technische Bundesanstalt Braunschweig und Berlin

BAM

DKD

eurolab

VDE

VDI

Journal of Sensors and Sensor Systems